ANNUAL REPORT
OF THE
INSTITUTE OF PHYSICS
ACADEMIA SINICA
1973

Published by

The Institute of Physics, Academia Sinica
Nankang, Taipei, Taiwan, Republic of China
August 1974

中央研究院物理研究所集刊

本集刊每年在八月出版一次

非賣品

中央研究院

物理研究所集刊

第四卷

發行人：吳大猷
編輯者：中央研究院物理研究所集刊編輯委員會
出版者：中央研究院物理研究所　臺北市南港區
印刷者：崇文企業有限公司
中華民國六十三年八月出版

中央研究院物理研究所集刊

第四卷

中央研究院物理研究所印行

CONTENTS 目錄

Study of excited states of ^{75}As with the ^{74}Ge(p, γ)^{75}As reaction*

C. W. Wang, Y. C. Liu, E. K. Lin, C. C. Hsu, and G. C. Kiang
Tsing Hua University and Academia Sinica, Taiwan, China

(Received 24 October 1973)

The γ radiation following the proton capture reaction ^{74}Ge(p,γ)^{75}As has been studied with a Ge(Li) detector. From the analysis of the measured γ-ray spectra, a detailed decay scheme of ^{75}As was constructed in which the energy levels of ^{75}As up to 2938 keV excitation were determined. Spin and parities for some levels are suggested. The deduced level schemes are in good agreement with results of Wilenzick *et al*. and Moreh and Shahal.

[NUCLEAR REACTION ^{74}Ge(p,γ), E =2.531 MeV; measured E_γ, Q. ^{75}As deduced levels, J, π. Enriched target.]

I. INTRODUCTION

Early information on low-lying levels in the ^{75}As nucleus has been obtained from the radioactive decay[1,2] of ^{75}Se and ^{75}Ge, Coulomb excitation,[3] and neutron inelastic scattering.[4] Energy levels below 822 keV together with their spins and parities have been well established. Very little information on levels above 822 keV is available. In recent years investigations of the energy levels of ^{75}As above 1 MeV have been reported[5,6] from high-resolution measurements with the use of the Ge(Li) detector. Wilenzick, Dave, and Nelson[5] have observed γ-ray transitions in ^{75}As in their (n,$n'\gamma$) reaction experiment and obtained the energy levels of ^{75}As up to 1606 keV. Moreh and Shahal[6] have measured the energy levels of ^{75}As up to 2687 keV excitation in a resonance scattering experiment, and proposed a decay scheme of ^{75}As as from the resonance at 7646 keV. Among the energy levels reported in these two works, many are new. The energy levels of ^{75}As measured through the (n,$n'\gamma$) reaction experiment are apparently not all populated in the resonance scattering; additional information is necessary to verify the new levels reported.

By using the ^{74}Ge(p,γ)^{75}As reaction it is possible to measure levels of ^{75}As up to rather high excitations. A brief study on the ^{74}Ge(p,γ)^{75}As reaction was made in 1957 by Chick and Hunt,[7] who obtained many resonances in ^{75}As at excitation energies between about 8.0 and 10.0 MeV. Among these three prominent resonances at E_p = 2342, 2528, and 2664 keV were observed. In the present work we used the ^{74}Ge(p,γ)^{75}As reaction to determine the excitation energies of ^{75}As up to 2938 keV and suggested the corresponding spin values. The aim of this work was on one hand to supplement the information on the energy levels of ^{75}As higher than 822 keV and also to verify new levels reported recently, and on the other hand to confirm the 2531-keV resonance from the ^{74}Ge(p,γ)^{75}As reaction and to determine the branching ratios for γ-ray transitions and decay scheme of ^{75}As levels observed.

The experiment consists of yield measurements of γ-ray deexciting from the 9399-keV resonance at a proton energy of E_p = 2531 keV. The measurements were carried out by using a large volume, high-resolution Ge(Li) detector. Level energies were determined to within 1.5 keV.

This paper is one of a series describing experimental investigations on the decay schemes of the arsenic isotopes by using proton capture reaction. Some data of (p,γ) reactions have been recently published.[8,9]

II. EXPERIMENTAL PROCEDURE

The proton beam was provided by the Van de Graaff accelerator at Tsing Hua University. The beam intensity was a few microamperes. The beam energy was determined by the usual nuclear magnetic resonance method. Several resonances in the ^{27}Al(p,γ)^{28}Si reaction were used as a proton energy calibration standard.

The target was isotopically enriched ^{74}Ge deposited on a 0.4-mm gold backing, mounted in a specially designed target chamber.[9] The areal density of the prepared targets was between 10–30 μg/cm^2. In the course of the experiment, the target was water cooled.

The γ rays from the ^{74}Ge(p,γ)^{75}As reaction were recorded by a 50-cm^3 Ge(Li) detector and 7.6 $\times$7.6-cm NaI(Tl) crystals enclosed in lead shields. These two detectors were mounted directly opposite each other at 90° to the beam direction. The Ge(Li) detector was used for γ-ray spectra measurement, while the NaI(Tl) crystal was used for the γ-ray yields measurement. The data-taking procedure was as follows:

This paper has been published in Phys. Rev. C 9, 1396 (1974)

TABLE I. γ energies, branching ratios, and level energies in ^{75}As from the ^{74}Ge(p,γ)^{75}As reaction.

High E_γ (keV)	Branching ratio	Energy level (keV) Present work	(γ,γ')	$(n,n'\gamma)$	Spin and parity
9398	4.7	0	0	0	$\frac{3}{2}^-$
9200	6.2	199.3 ± 1.5	199	198.6	$\frac{1}{2}^-$
9133	5.2	264.9 ± 1.5	265	264.7	$\frac{3}{2}^-$
9120	2.6	278.7 ± 1.5	...	279.0	$\frac{5}{2}^-$
9093	1.6	304.1 ± 1.5	...	303.2	$\frac{9}{2}^+$
8997	2.4	400.4 ± 1.5	(404)	400.3	$\frac{5}{2}^+$
8930	4.5	468.6 ± 1.5	468	468.8	$(\frac{1}{2}^-)$
8828	4.2	572.6 ± 1.5	(568)	572.8	$\frac{5}{2}^-$
8779	4.7	619.1 ± 1.5	618	617.9	$(\frac{1}{2}^-, \frac{3}{2}^-)$
...	...	822	...	821.8	$\frac{7}{2}^-$
8536	3.9	864.8 ± 1.5	...	864.5	...
8353	<1.0	1044.0 ± 1.5	...	1043.6	$(\frac{7}{2})$ [b]
8343	<1.0	1065.4 ± 1.5	...	1063.8	$(\frac{1}{2}^-, \frac{3}{2}^-)$ [a]
8331	<1.0	1077.0 ± 1.5	1076	1076.4	...
8268	2.1	1128.6 ± 1.5	...	1129.3	$(\frac{1}{2}^-, \frac{3}{2}^-)$ [a]
...	...	...	1134	...	$(\frac{1}{2}^-, \frac{3}{2}^-)$ [a]
8193	5.5	1204.5 ± 1.5	1203	1204.4	$(\frac{1}{2}^-, \frac{3}{2}^-)$ [a]
...	...	(1262)	1262	...	
8046	3.7	1351.3 ± 1.5	...	1349.7	
...	...	...	1355	...	
7976	1.9	1422.0 ± 1.5	...	1422.1	
7966	2.1	1431.7 ± 1.5	1432	1431.9	$(\frac{1}{2}^-, \frac{3}{2}^-)$ [a]
7891	3.7	1504 ± 1.5	1505	1503.2	$(\frac{1}{2}, \frac{3}{2})$ [a]
...	...	(1595)	...	1595.4	
7793	4.2	1605 ± 1.5	1607	1606.4	$(\frac{1}{2}, \frac{3}{2})$ [a]
7591	4.1	1808 ± 2	...		$(\frac{1}{2}, \frac{3}{2})$ [b]
...	...	...	(1843)		
7524	6.0	1874 ± 2	1872		$(\frac{1}{2}, \frac{3}{2})$ [a]
7335	<1.0	2061 ± 3	2064		
7299	6.2	2098 ± 3	2097		$(\frac{1}{2}, \frac{3}{2})$ [a]
7221	2.4	2180 ± 3	2176		$(\frac{1}{2}, \frac{3}{2})$ [a]
...	...	...	2233		$(\frac{1}{2}, \frac{3}{2})$ [a]
...	...	(2470)	(2470)		
6824	<1.0	2572 ± 3	(2572)		
...	...	...	2596		
6733	4.9	2663 ± 4	...		$(\frac{1}{2}, \frac{3}{2})$ [b]
6713	5.2	2683 ± 4	(2687)		$(\frac{1}{2}, \frac{3}{2})$ [b]
6461	6.7	2938 ± 4	...		$(\frac{1}{2}, \frac{3}{2})$ [b]

[a] Reference 6.

[b] Suggested from present work.

(1.) The yield measurement was made in the proton energy range from 2450 to 2550 keV in steps of about 1 keV to confirm the 2528-keV resonance previously observed by Chick and Hunt.[7] The resonance energy was determined to be 2531 ± 2 keV.

(2.) The proton beam energy was then kept at 2531-keV for the γ-ray spectra measurement. Data were collected over a 24-h period. The obtained γ-ray spectra were stored in a TMC4096 channel analyzer with a conversion gain of 3 keV per channel.

A detailed description of the experimental method and data analysis has been described in a recent paper.[8]

III. RESULTS

A. Level scheme of ^{75}As

The results of the γ-ray spectra measurements at $E_p = 2531$ keV are summarized in Table I. Figure 1 shows the high-energy part of the measured γ-ray spectrum at $E_p = 2531$ keV. The γ-ray energies obtained were used to construct a level scheme for the ^{75}As nucleus as shown in Fig. 2. The first column of Table I shows the observed γ-ray energies. The third column lists the energy levels of ^{75}As as deduced in the present work, which seem to be in good agreement with those reported by Wilenzick, Dave, and Nelson[5] and Moreh and Shahal,[6] as given in the fourth and fifth columns.

In the excitation energy range of $E_{ex} \geq 1605$ keV we obtained 23 levels, and confirmed all levels observed in the $(n, n'\gamma)$ work by Wilenzick, Dave, and Nelson,[5] except the 1595-keV level which, because of large background, is somewhat uncertain according to the present data. It was not observed in the resonance scattering experiment.[6] In the excitation energy range of 1605 keV $< E_{ex} \leq 2938$ keV we observed 10 energy levels, 3 of which were not previously reported. These are levels at 1808, 2663, and 2938 keV.

B. Decay scheme of ^{75}As

The observed γ rays totaled 113 in number and except for a few they were all identified. The information from identified γ lines was used to construct a decay scheme as shown in Fig. 3. For the low-energy γ lines, this is similar in general detail to the scheme published in Ref. 5; however, we have not observed the γ-ray lines corresponding to the 619-265-, 822-279-, and 1422-400-keV transitions. It is seen that the decay scheme of ^{75}As is extremely complex as a result of the high level density of ^{75}As. It is remarkable that the 9399-keV resonance decays directly to all lower states except the 822 keV $(\frac{7}{2}^-)$ state. The sum of the branching ratios for the transitions is fitted to the total decay.

The broken lines in Fig. 3 indicate uncertain transitions and hence uncertain levels (the 1262, 1595, and 2470 keV). The numbers in Fig. 3 are the percentage of the branching ratio for the γ-ray transitions. These were determined from the analysis of the observed γ-ray spectra, after the proper corrections for attenuation and detector efficiency were made. Most of the error is due to the uncertainty in the peak area measurements not

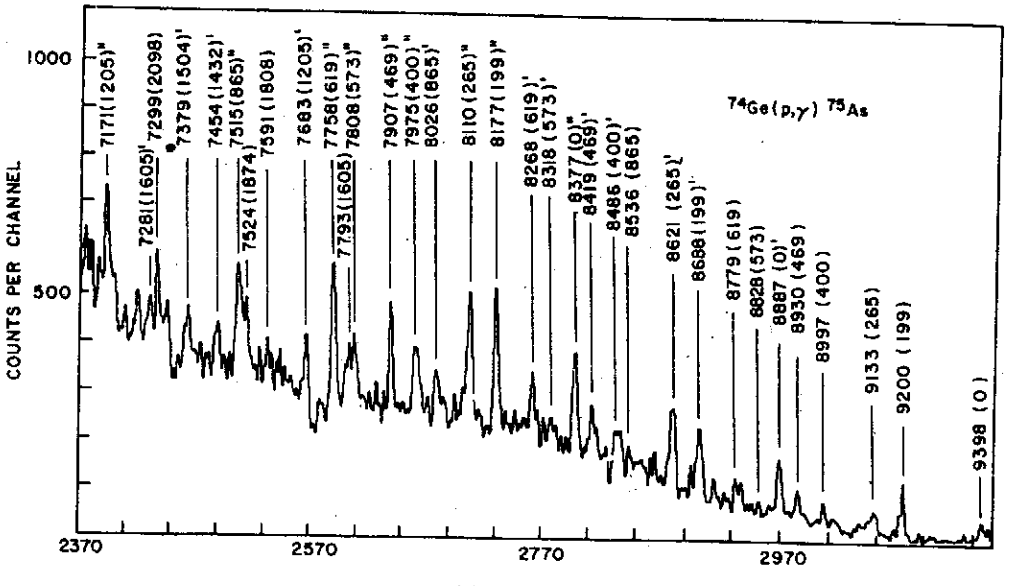

FIG. 1. Part of γ-ray spectrum of the ^{74}Ge$(p,\gamma)^{75}$As reaction at $E_p = 2531$ keV. Numbers over peaks refer to γ-ray energy. The symbols ( ), ( )', ( )", refer to the full-energy, single-escape, and double-escape peaks, respectively.

the relative accuracy is in the range 5 to 10% except for very small branchings where the error is larger.

C. *Q* value

The *Q* value of the $^{74}Ge(p,\gamma)^{75}As$ reaction was redetermined from the resonance to ground- and lower-excited-state transitions in the $E_p = 2531 \pm 2$ keV resonance. The excitation energy of the resonance was calculated to be $E_{ex} = 9398.6 \pm 5$ keV and the *Q* value obtained is 6901.6 ± 5 keV, which is in reasonable agreement with the one reported in the Nuclear Data Tables.[1]

IV. DISCUSSION

In the present experiment we obtained more information on the energy levels of ^{75}As than those reported previously.[1-6] A total of 33 energy levels up to 2938 keV were determined. Due to the use of an absorber in front of the detector, the γ lines with $E_\gamma < 270$ keV could not be observed. In general, the level scheme of ^{75}As and the decay scheme obtained in this work are in excellent agreement with recently available data of Wilenzick, Dave, and Nelson[5] and Moreh and Shahal.[6] Our data give additional evidence for the existence

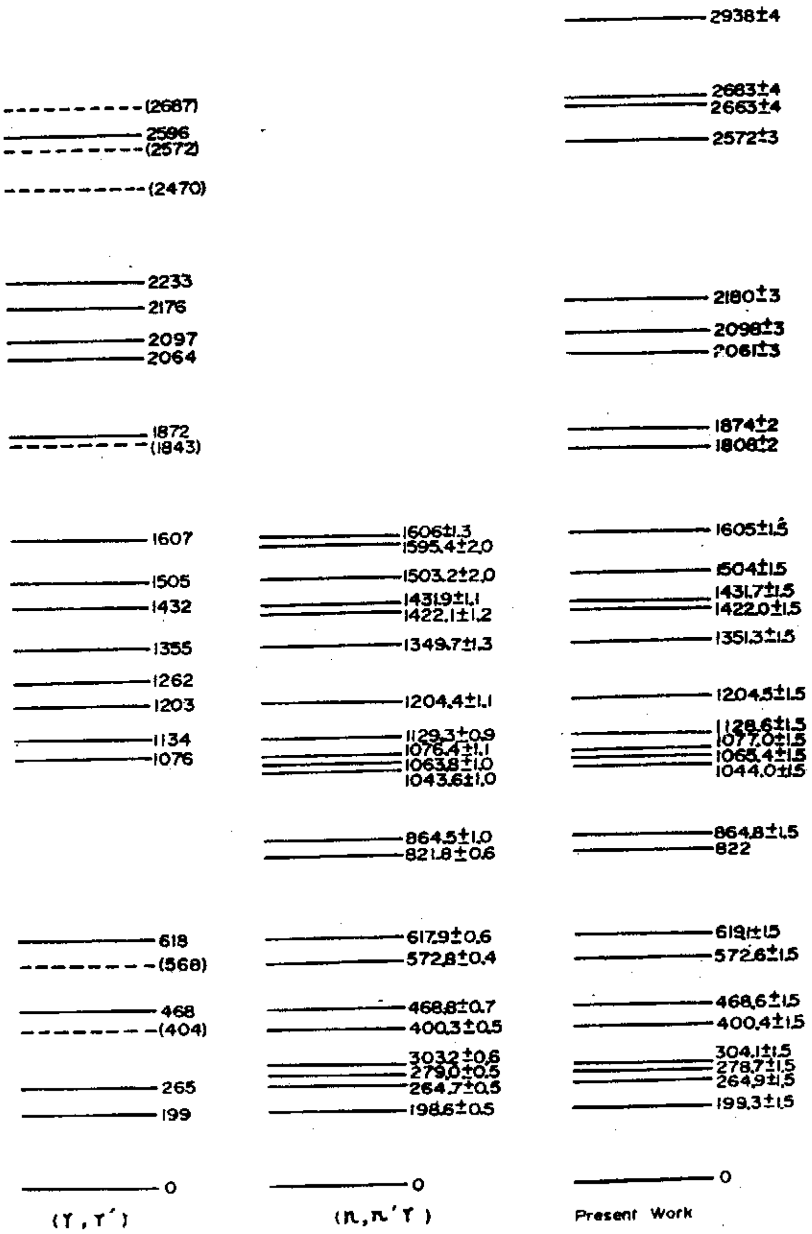

FIG. 2. A comparison of the energy levels of ^{75}As as obtained in the present work with the results of Moreh and Shahal (Ref. 6) and of Wilenzick, Dave, and Nelson (Ref. 5).

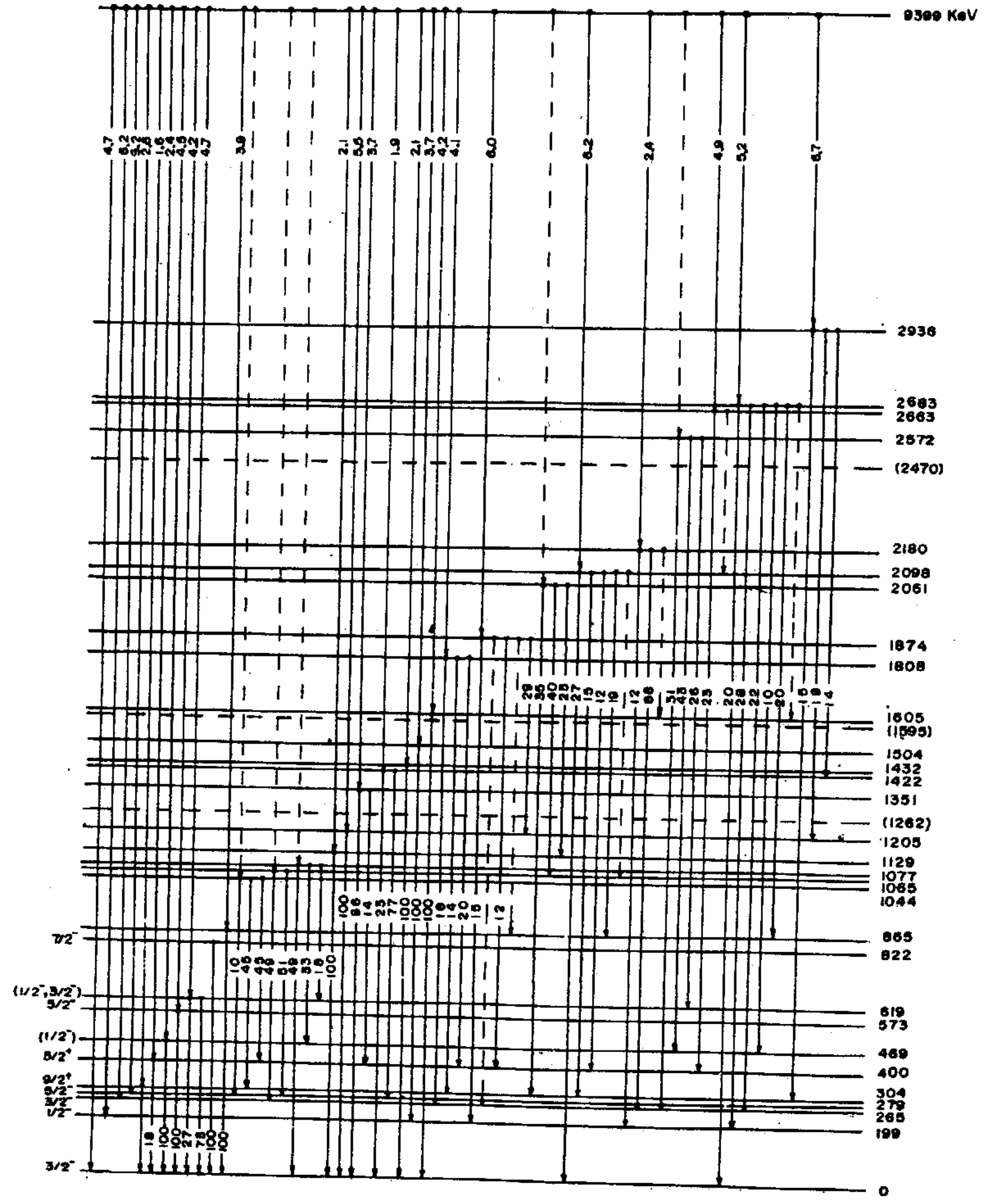

FIG. 3. The decay scheme of 9399-keV resonance in ^{75}As observed in the present work.

of the 865-keV level, and confirm the existence of the level at 1044, 1064, and 1422 keV as reported in Ref. 5, and also of the levels at 1872, 2064, 2097, 2176, 2572, and 2687 keV as reported in Ref. 6.

Levels at 1134, 1262, 1355, 2233, and 2596 keV found recently in the resonance scattering experiment[6] have not been observed in the present experiment. However, we obtained 12 energy levels between 279 keV ($\frac{5}{2}^-$) and 2683 keV which have not been found in the resonance scattering experiment.[6] These levels are most likely states with spins of $\geqslant \frac{5}{2}$. This conclusion is based on the fact that these states were not seen in the resonance scattering experiment which selectively populates only those levels which have large dipole matrix elements and consequently are only levels in ^{75}As with spins of $\frac{1}{2}$ or $\frac{3}{2}$.

In the present ^{74}Ge(p,γ)^{75}As experiment at the beam energy of $E_p = 2531$ keV, the angular momentum that the protons carry into the resonance state is mainly of value $l=0$, it is expected that the levels with spins of $\frac{1}{2}$ or $\frac{3}{2}$ have appreciable branching ratios. It is seen from Table I that for the levels which were known or previously assigned to be $(\frac{1}{2}, \frac{3}{2})$, the measured branching ratios for the transitions from the resonance to the levels up to 2098 keV are falling into values of $\geqslant 4.0\%$. Only one level at 573 keV is exceptional; the measured branching ratio is 4.2%, but it is known to be $\frac{5}{2}^-$ as reported in Ref. 1. The above consideration suggests that three new levels at 1808, 2663, and 2938 keV and also the 2683-keV level may have spins of $\frac{1}{2}$ or $\frac{3}{2}$. In the subsequent decay from the 1044-keV level, 10% of the total decay was found to feed the 279-keV level and 45% to feed the 304- and 400-keV levels, respectively. The 279-, 304-, and 400-keV levels are known[1] to be $\frac{5}{2}^-$, $\frac{9}{2}^+$, and $\frac{5}{2}^+$, respectively. Consideration of the $M1$ and $E1$ transition probabilities suggests that the 1044-keV level is $\frac{7}{2}^-$. A summary of suggested spins for the levels obtained in the present investigation and those assigned previously are listed in the last column of Table I. It is believed that the present data has contributed additional useful information on the level structure of ^{75}As.

It is a pleasure to thank all members of the Van de Graaff accelerator group for their generous assistance.

---

[*] Work performed at the Physics Research Center in Hsinchu and supported by the National Science Council.

[1] *Nuclear Data Sheets*, compiled by K. Way *et al.* (Printing and Publishing Office, National Academy of Sciences-National Research Council, Washington, D. C.).

[2] S. C. Pancholi and H. Ikegami, Nucl. Data B 6, 79 (1966).

[3] R. L. Robinson, F. K. McGowan, P. H. Stelson, and W. T. Milner, Nucl. Phys. A104, 401 (1967).

[4] D. L. Smith, Bull. Am. Phys. Soc. 15, 86 (1970).

[5] R. M. Wilenzick, V. R. Dave, and J. A. Nelson, Phys. Rev. C 4, 2126 (1971).

[6] R. Moreh and O. Shahal, Phys. Rev. 188, 1765 (1969).

[7] D. R. Chick and S. E. Hunt, Nature (Lond.) 180, 88 (1957).

[8] T. H. Hsu, E. K. Lin, C. C. Hsu, Y. C. Liu, P. K. Tseng, C. W. Wang, and W. S. Hsu, Chin. J. Phys. (Taipei) 10, 55 (1972).

[9] T. H. Hsu, P. K. Tseng, E. K. Lin, and Y.C. Liu, Nucl. Instrum. Methods 106, 513 (1973).

ANNUAL REPORT OF THE INSTITUTE OF PHYSICS, ACADEMIA SINICA 1973

TARGET CHAMBER FOR USE WITH RADIATIVE TRANSITION REACTIONS STUDIES*

T. H. HSU, P. K. TSENG, E. K. LIN and Y. C. LIU

Tsing Hua University, Academia Sinica and Taiwan University, Hsinchu, Taiwan, China

Received 19 July 1972

A target chamber with a continuously moving target holder was designed for the investigation of radiative transition reactions on the medium-weight nuclei. This chamber has been successfully used to gather data from the ^{70}Ge(p,γ)^{71}As, ^{72}Ge(p,γ)^{73}As, ^{65}Cu(p,γ)^{66}Zn and ^{27}Al(p,γ)^{28}Si reactions. Some of these results are presented and described.

1. Introduction

The radiative transition reactions induced by charged particles, such as (p,γ), (p,$\alpha\gamma$) and (α,γ) reactions etc., have been succesfully studied in various laboratories for several years$^{1-3}$). The simplicity and the usefulness of this type of reaction in yielding nuclear structure information have been hampered by the fact that the reaction cross section is rather small compared with other accessible reactions. This has resulted in the following technical obstacles:

1) target contamination due to long hours of heavy current bombardment,
2) deterioration of fragile target,
3) requirement of high efficiency and good resolution gamma-ray detectors,
4) requirement of a high accuracy beam current integration system.

Accordingly the radiative transition reactions have rarely been explored beyond the $1f_{7/2}$ shell nuclei^{4}). In order to overcome the above mentioned obstacles, considerable amount of effort has been paid in this laboratory on the improvement of design and construction of a target chamber suitable for investigation of the radiative transition reactions. In this paper, we report a target chamber constructed specially for measurements of gamma-ray spectrum, its angular distribution, and excitation functions from the radiative transition reactions induced by charged particles. With this chamber we have successfully investigated the (p,γ) reaction on the medium-weight nuclei^{5,6}), namely ^{65}Cu and ^{70,72}Ge, in the region beyond the $1f_{7/2}$ shell.

2. Chamber design and construction

The essential feature of the constructed chamber is as follows:

1) The target is surrounded by a wall of a cylindrica cold finger with a small circular window for the incident beam, and located as close to the cold trap reservoir as possible. Thus, the target could be well free from the contamination due to incoming residual vapour in the system. Viton O-rings were used for all vacuum couplings. For a better vacuum in the chamber and also for more rapid oscillation of the target, it was suggested that nickel bellows can be used for the coupling of the brass shaft to the chamber. However, in the present application, the Viton O-ring coupling was found to be satisfactory.

2) The target holder is made to move up and down uniformly and repeatedly so as to avoid deterioration due to the continuous bombardment of a heavy current beam at the same spot on the fragile target. This capability makes it possible to accumulate a gamma-ray spectrum over a long period (24 h or longer) which is necessary in order to accumulate sufficient counts for sufficient statistical accuracy.

3) The size and the shape of the target chamber are kept as small and compact as possible so that the gamma-ray detector can be brought very near to the target for a large geometrical efficiency. Thus, the requirement of high efficiency and good energy resolution of the detection can be fulfilled by the use of this target chamber together with a high-resolution Ge(Li) detector.

4) By a properly insulated coupling to the beam tube, the target chamber itself becomes a Faraday cup. The entrance for the incident beam to the target is designed to consist of a long tube (30 cm from the entrance slit to the target) and a small window at the cylindrical cold finger. This arrangement gives no way to the secondary electrons for escaping away from the Faraday cup. Therefore, an accurate current integration can be achieved through an integration system.

A schematic drawing of the target chamber is shown in fig. 1. The main body of the chamber is a T-shaped

---

* Work performed at the Physics Research Center and supported by the National Science Council of the Republic of China.

This paper has been published in Nuclear Instruments and Method 106 (1973) 513-517

stainless steel tube 4 cm in diameter and an inner copper tube 2.5 cm in diameter which was used as cold finger. At the top of the chamber is a 2.5 l liquid nitrogen cold trap reservoir. The copper tube finger is then attached to this reservoir. A 1.5 cm hole was bored through one side of this cold finger to make access for the beam to strike targets. The copper target holder is soldered directly onto a hollow brass shaft. The assembly of the target holder inside the target chamber can be made by slipping it into the cold finger at a proper position. Near the target chamber a Ge(Li) detector can be placed at a small distance of ≈ 2.5 cm from the target.

Shown in fig. 2 is the layout of the movable target holder driven by a motor. Fine threads were cut at the bottom end of the brass shaft. A gear disc made from nylon was attached to a nut which is made to fit these threads. By rotating the gear disc one may ascend or descend the target holder inside the chamber with respect to the beam.

The orientation of the target holder with respect to the beam direction was monitored by an angular scale marked on a rotating disc which was fixed at the end of the shaft. Two small slots were cut to this disc at 0° and 180°. By sliding one of the slots along the micro-switch arm, which was fixed at the outer body of the chamber, the target can then be raised or lowered without changing its angular orientation inside the chamber. Uniform and slow motion of the target holder was produced by a 1 rpm motor, driving

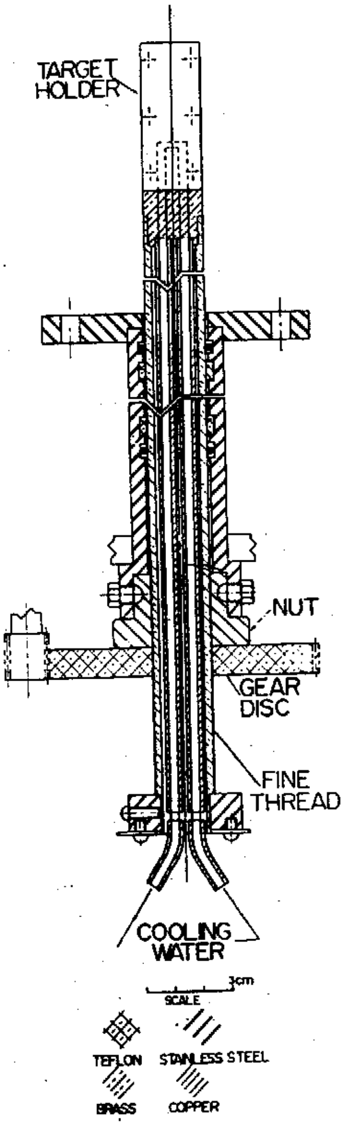

Fig. 1. Schematic view of the target chamber.

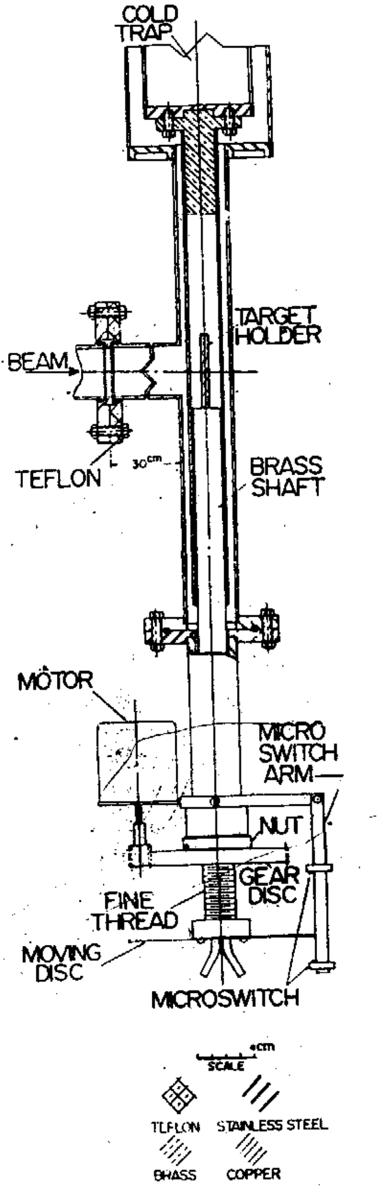

Fig. 2. Layout of the movable target holder.

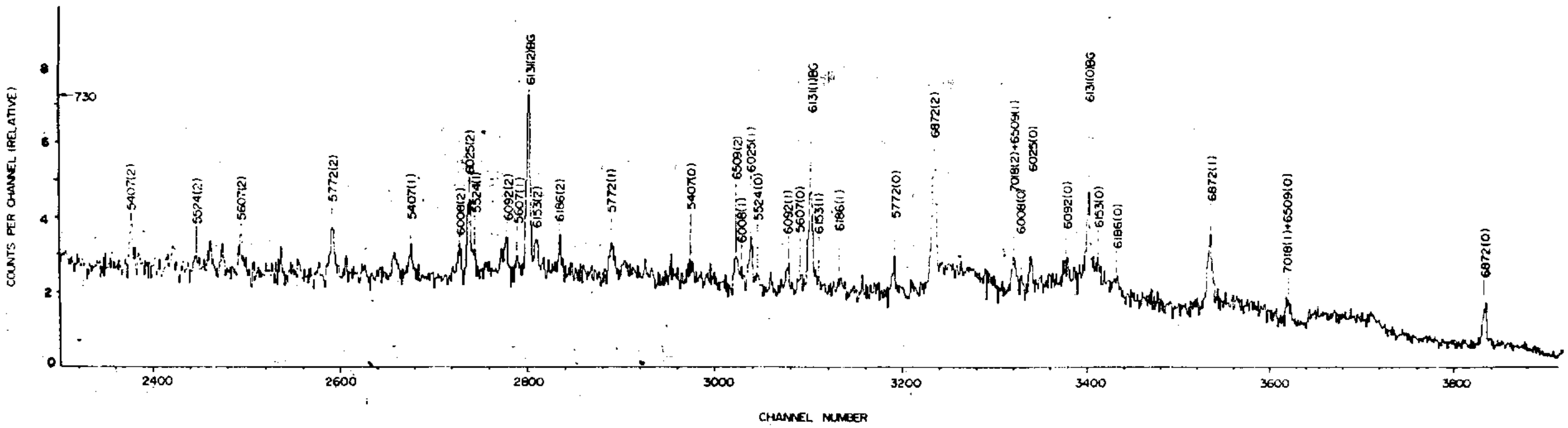

Fig. 3. A gamma-ray spectrum of the ^{70}Ge(p,γ)^{71}As reaction at $E_b = 2434$ keV. Numbers over peaks refer to gamma-ray energy. BG, background; (0) (1) (2), full-energy, single-escape, and double-escape peaks, respectively.

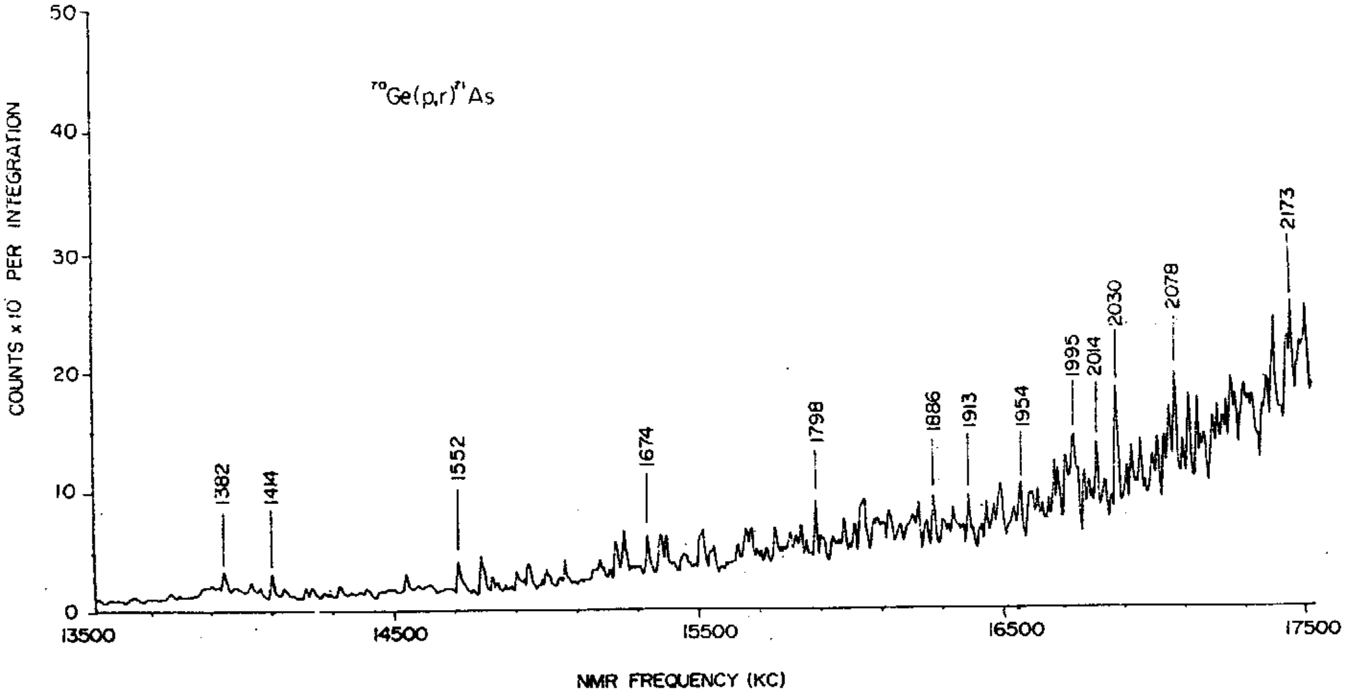

ig. 4. Yield curve from the ^{70}Ge(p,γ)^{71}As reaction in the proton-energy range 1293–2185 keV. Numbers over peaks refer to resonant energy.

ne gear disc with a gear ratio of 1:10. Two micro-witches were set on upper and lower sides of the micro-witch arm. They were activated by the contact of the noving disc. The target holder, therefore, travelled utomatically and repeatedly between an adjustable istance set by the micro-switches.

The chamber was maintained at high vacuum by a 00 l/s Vac-Ion pump which was installed just in ront of the beam entrance slit. Typical vacuum at $\times 10^{-7}$ torr can be readily obtained within a period f 30 min pumping.

As many as four targets can be mounted on the arget holder, two targets on each side of the target older, they can thus be interchanged inside the hamber as desired without breaking the vacuum. This is specially convenient for the calibration and ackground runs. Because of heavy current bombardment it is necessary to provide cooling of targets. This was done by cutting a cooling canal into the target holder as shown in fig. 2. Running tap water was used or the target indirect cooling.

3. Performance of the chamber

The constructed chamber has been used for a series of (p,γ) experiments[5,7]) in this laboratory. In the measurements, thin targets of about 2–10 μg/cm^2 were prepared by vacuum evaporation of uniform deposition of metallic elements onto a 1 cm × 3 cm gold sheet of 0.4 cm thickness. A few examples of measurements are presented in figs. 3 and 4. Fig. 3 shows part of the gamma-ray spectrum from the ^{70}Ge(p,γ)^{71}As reaction[5]) at $E_p = 2434$ keV measured by a 50 cm^3 Ge(Li) detector. The measurement was performed with a 3 MeV Van de Graaff accelerator at Tsing Hua University. The ^{70}Ge target used is ≈ 5 μg/cm^2 thick. It was found that under the bombardment by a 2434 keV proton beam at 5 μA for a period of 24 h, no noticeable deterioration of target and carbon build-up on the target were observed. Fig. 4 shows the yields of the gamma-rays from the ^{70}Ge(p,γ)^{71}As reaction[5]) measured in the proton-energy range 1293–2185 keV at a step of $\Delta E_p \approx 1$ keV. It is seen that many resonances which correspond to the energy levels of ^{71}As at energy excitation ≈ 6 MeV are sufficiently resolved.

In a similar way, we have successfully measured the gamma-rays from the ^{72}Ge(p,γ)^{73}As reaction[5]). Further measurement was made for the ^{65}Cu(p,γ)^{66}Zn reaction[6]), and performance of the chamber was found to be quite satisfactory.

In order to show the stability and resolution of our system used for the measurement, an aluminium target of ≈ 1.5 keV thickness was bombarded with a proton beam in the region $E_p = 1.38$–1.40 MeV[7]). The typical beam current was 5 μA. Well separated resonances at

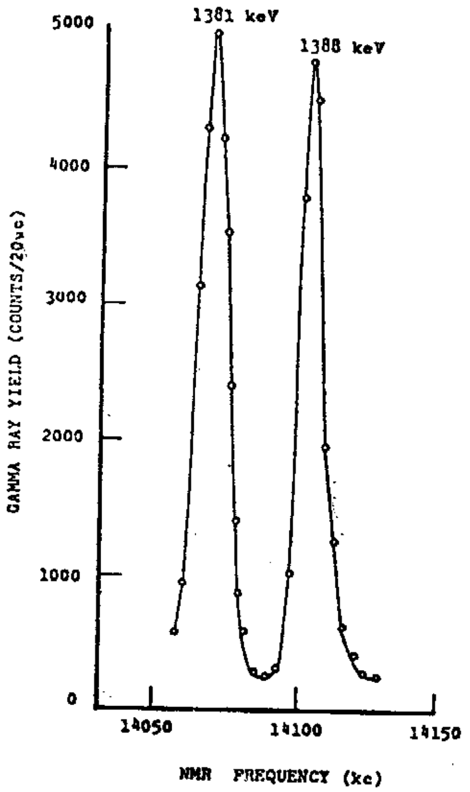

g. 5. Yield curve for the 1381 keV and 1388 keV resonances from the $^{27}Al(p,\gamma)^{28}Si$ reaction.

$_p$ = 1381 and 1388 keV as shown in fig. 5 were obtained by repeated separate measurements. These data were taken at a proton-energy step of 0.5 keV. The result shows the stability of our system to be within 0.5 keV.

The successful measurement with the constructed target chamber for the (p,γ) reaction on the medium-weight nuclei has encouraged us to take advantage of this chamber for more detailed investigation of the (p,γ) reaction. It is believed that the measurements with this chamber for the (α,γ) reaction can also be achieved.

The author acknowledges the help rendered by the members of the accelerator laboratory at Tsing Hua University.

References

1) See for instance: A. Hossain, H. A. Rashid and M. Islam, *Nuclear structure* (North-Holland Publ. Co., Amsterdam, 1967) p. 58.
2) P. M. Endt and C. Van der Leun, Nucl. Phys. **A105** (1967) 1.
3) Nucl. Data A6 (K. Way et al.; Academic Press, New York and London, 1969).
4) See for instance: G. B. Vingiani, G. Chilosi and C. Rossi-Alvarez, *The structure of* $lf_{7/2}$ *nuclei* (ed. R. A. Ricci; Padova, 1971) p. 303.
5) Y. C. Liu, T. H. Hsu, E. K. Lin, C. C. Hsu, P. K. Tseng and C. W. Wang, to be published.
6) C. C. Hsu, E. K. Lin, Y. C. Liu, T. H. Hsu, C. W. Wang and P. K. Tseng, to be published.
7) T. H. Hsu, E. K. Lin, C. C. Hsu, Y. C. Liu, P. K. Tseng, C. W. Wang and W. S. Hsu, Chinese J. Phys. **10** (1972) 55.

THE LEVEL STRUCTURE OF ^{64}Zn THROUGH THE ^{63}Cu(p,γ)^{64}Zn REACTION*

C. C. Hsu, E. K. Lin, (林爾康) C. W. Wang, (王建萬)
G. C. Kiang, (江紀成) Y. C. Liu, and M. C. Wang
National Tsing Hua University and Academia Sinica
Hsinchu, Taiwan, China

Keyward Abstract

Nuclear Reaction ^{63}Cu(p,γ), E = 1.75 - 2.95 MeV; measure σ(E); γ branching ratios; ^{64}Zn deduced levels, J^{π}; discussed shell model calculation.

Abstract

The excited states of the ^{64}Zn nucleus was investigated in the ^{63}Cu(p,γ)^{64}Zn reaction. The level scheme of ^{64}Zn was established and for a number of levels the spin-parity assignments were suggested on the basis of the measured γ-branching ratios. The level structure was compared with the theoretical calculation in the framework of the conventional shell model.

1. *Introduction*

In recent years (p,γ) reactions have been widely used for experimental studies of nuclear level structure, and there were many data of (p,γ) reactions that have been reproduced in many laboratories when the high-resolution detector of Ge(Li) for γ-ray was available. The experimental works of the (p,γ) reactions on light and medium-weight nuclei with use of a 50-cm^3 Ge(Li) detector in this laboratory have been extensively investigated to study the level scheme for several years, and the works on aluminium and arsenic isotopes have been completed and published or to be published.(1-3)

Concerning nuclear level structure of ^{64}Zn, most informations were obtained from ^{64}Zn(p,p'γ)$^{(4)}$, Zn^{64}(d,d')$^{(5)}$ and β-decay from ^{64}Ga by means of the ^{64}Zn(p,n)^{64}Ga reaction.$^{(6)}$ The work on the ^{63}Cu(p,γ)^{64}Zn reaction, however, was rarely being reported except the work of Weller and Grosskreutz$^{(7)}$ in 1956. In their investigation, the experimental work was carried out with poor energy resolution of the NaI(Tl) detector. In the present study of the ^{63}Cu(p,γ)^{64}Zn reaction, a detailed decay scheme of ^{64}Zn was constructed from the analysis of the measured γ-ray spectrum and the energy levels of ^{64}Zn up to about 4 MeV excitation energy were accurately determined. The spins-parities of a resonance of de-excitation at E_p = 2098 keV and the observed energy levels in ^{64}Zn were discussed and compared with the theoretical shell-model calculation in which a truncated model space with restriction of the low-seniority configuration was assumed. The result of the calculation is described on Section IV.

2. *Experimental Method and Results*

A target of enriched ^{63}Cu was prepared by evaporating on a 99.99% gold backing and its thickness was estimated to be 30 $\mu g/cm^2$. A 7.6x7.6-cm NaI(Tl) detector was fixed at 90° to the proton beam to measure the excitation functions for γ-rays of energy E_γ = 992 keV and E_γ>7500 keV. The proton energy was varied from E_p = 1750 to 2950 keV in steps of 1- and 2 keV around and off the resonance, respectively. The decay spectrum of the resonance at E_p = 2098 keV was measured with a 50-cm^3 Ge(Li) detector at 90° to the beam direction. The γ-energies were calibrated by the standard sources of γ-ray for the energy region < 3 MeV, and the 6.129 MeV contaminant γ-ray from the ^{19}F(p,$\alpha\gamma$)^{16}O reaction, and its single and double escape peaks for higher energy portion. The experimental techniques used in the present experiments and the relative efficiency of the Ge(Li) detector determined in the present analysis were similar to those described previously.(1-3) Figure 1 shows the excitation functions of E_γ = 992 keV and E_γ >7500 keV. Figure 2 shows a decay spectrum of the resonance at E_p = 2098 keV. The energies of the γ-rays observed in Fig. 2, the relative intensities and the corresponding transitions in ^{64}Zn are listed in Table I. The spectrum contains many unresolved weak peaks, we therefore listed only those transitions which could be identified in the spectrum. The decay scheme of ^{64}Zn constructed from the resonance of de-excitation at excited energy of 9772±2 keV (E_p = 2098 keV) is shown in Fig. 3. The branching ratios for γ-rays decayed from the ^{63}Cu(p,γ)^{64}Zn reaction were not previously reported. We have determined in the present measurement the branching ratios for many transition lines. The numbers on the transition line in Fig. 3 refer to the percentage of the branching ratio normalized by the intensity of 992 keV γ-ray. It is noted that the branching ratios for some particular levels are not completely determined due to the contaminant of natural background. Since the energies of the transitions from the 1799- and 992 keV states to the ground state are respectively the same as that from the 2794- to 992- and 1799 keV states, and also the same as that from the 3602 keV to 1799 keV state, the branching ratios for these transitions can not been obtained.

3. *Discussion*

The resonance, r, of de-excitation at the energy of E_{ex} = 9772 keV in ^{64}Zn was found to decay intensively into the excited states at E_{ex} = 1799 (2^+) and 992 keV (2^+).

If we assume that the most intensive transitions to be E1 or M1, the spin-parity of the resonance is likely to be ($1^{\pm}$, $2^{\pm}$, $3^{\pm}$). Since E3 or M3 transitions from the resonance of de-excitation is too weak to be observed, the ratio of the strength of r→992-keV (2^+) to that of r→ground state (0^+) is resonably more close to the ratio M1/E2 than that of any other decay mode, the spin-parity of the resonance is therefore favourally to be 2^+ out of the ($1^{\pm}$, $2^{\pm}$, and $3^{\pm}$). For the spins-parities of the excited levels in ^{64}Zn, we observed five characteristic groups among the measured branching ratios for γ-ray transitions from the resonance of de-excitation, they are:

(1) r → 1909 (0^+), 2610 (0^+) and 2736 keV; (2) r → 2308 (4^+) and 1794 keV; (3) r → 2980 (3^-), 3004 and 3092 keV; (4) r→3206, 3300 and 3549 keV; (5) r→3188 (1^+), 3263 (1,2), 3368 (1^+), 3428 (1^+) 3458, 3602, 3797 (1^+), 3874 and 3900 keV. Every group has about the same branching ratio corrected by its γ-ray energy. By considering the final states in every group having the same spins and parties, the spins-parities of the following excited states can be suggested: 2736 keV (0^+); 2794 keV (4^+); 3004 keV (3^-); 3092 keV (3^-); 3263 keV (1^+); 3458 keV (1^+); 3602 keV (1^+); 3874 keV (1^+) and 3900 keV (1^+). Next, if we compared the ratios, which are respectively the strength of the levels at E_{ex} = 3206, 3300 and 3549 keV feeding to the level at E_{ex} = 992 keV (2^+) to that of those levels feeding to the ground state (0^+), with the ratio of the strength of any two possible decay modes, we found that the ratio of M1/E2 is the most probable, thus the spins and parities of the group (4), i.e. the levels at E_{ex} = 3206, 3300 and 3549 keV, are likely to be 2^+.

4. *Shell-Model Calculation*

Since the theoretical discussions for ^{64}Zn have not yet been found in the literature, it is interesting to carry out a shell-model calculation of the normal-parity states for ^{64}Zn to compare with the present experimental results. In this calculation, the eight valence nucleons outside the ^{56}Ni core are assumed to be distributed among the $2p_{3/2}$, $1f_{5/2}$, and $2p_{1/2}$ single-particle orbits. Due to the size of the model space in these orbits being massive, a truncated model space with restriction of the low-seniority configurations(8) is assumed. In the present calculation, the seniority numbers of basic states of ^{64}Zn are restricted up to 2. With this restriction, the largest dimension of the matrix is reduced to 98 for J=2. The two-body residual interaction matrix elements of T=0 and T=1 are adopted respectively from the previous studies of copper(8) and Nickel(9) isotopes. The single-particle energies of $1f_{5/2}$ and $2p_{1/2}$ orbits relative to $2p_{3/2}$ orbit are varied to give a best fit between the theoretical calculation and the lowest five observed levels. The final set of single-particle energies which we used to obtain the results are given in MeV as follow: $1f_{5/2}$, 0.396; $2p_{1/2}$, 0.989; where the energy of the $2p_{3/2}$ is set to be zero. The energy levels calculated with this model are compared with the present experimental energy levels as shown in Fig. 4. Although the lowest two pairs of 0^+ and 2^+ levels are in the reverse order, the energy levels up to 2.5 MeV can be accounted for. The calculated spectrum shows an obvious tendency that the states of J=2 are lower than the observed states. This is attributed to the effect of the adopted two-body matrix elements which were determined by fitting the calculated states of 2^+ and 0^+ well with those states of the experimental levels in copper isotopes(8). For the excited states at higher than 2.5 MeV, the states of first 1^+ and second 4^+ observed respectively at 3.188- and 2.794 MeV, as compared with 3.441- and 2.806 MeV from the calculation, the agreement is quite good. As the calculation shows a 3^+ state at 3.775 MeV and a 5^+ state at as higher as 5.712 MeV, it is not surprising that the states of 3^+ and 5^+ were not observed in our experiment. There appear also some states of 2^+ and 4^+ between 3- and 4 MeV in the calculated spectrum. This suggests that it is possible to observe these states experimentally in the region above 4 MeV excitation. In general, the present shell-model calculation seems to give a satisfactory comparison with the experimental results. It is believed that if a full space of the model is used in calculation, the agreement would be improved greatly.

5. *Conclusion*

In this experimental investigation, the energy of the level in ^{64}Zn was accurately determined within the errors of ±2 keV. We have established a level scheme for ^{64}Zn and suggested the spins-parities of the levels at 3900, 3874, 3602, 3549, 3458, 3300, 3263, 3206, 3092, 3004, 2794 and 2736 keV. The spin-parity of the resonance of de-excitation at E_{ex} = 9772 keV is more likely to be 2^+, the angular distribution measurement, howeever, is needed for confirmation. For the shell-model calculation, the satisfactory agreement with experimental results indicates that the low-seniority restriction in the calculation is a useful approximation to reduces the dimensionality for the ^{64}Zn nucleus which has eight valence nucleons outside the ^{56}Ni core.

Acknowledgement

The authors wish to express their sincere thanks to all members of the THU Van de Graaff accelerator group for their generous assistance, and to the Institute of Nuclear Energy Research, Atomic Energy Council for providing computer facility for the shell model calculaiton.

References

(1) T. H. Hsu, E. K. Lin, C. C. Hsu, Y. C. Liu, P. K. Tseng, C. W. Wang and W. S. Hsu Chinese J. Phys. 10 (1972) 55.
(2) Y. C. Liu, T. H. Hsu, E. K. Lin, C. C. Hsu, P. K. Tseng and C. W. Wang to be published.

(3) C. W. Wang, E. K. Lin, Y. C. Liu, C. C. Hsu and G. C. Kiang Phys. Rev. C 9 (1974) 1396.
(4) A. K. Sen Gupta and D. M. Van Patter Nucl. Phys. 50 (1964) 17.
(5) E. K. Lin Nucl. Phys. 73 (1965) 613.
(6) J. Konijn, R. van Liashout, J. P. Deutsch and L. Grenacs Nucl. Phys. A91 (1967) 439.
(7) C. E. Weller and J. C. Grosskreutz Phys. Rev. 102 (1956) 1149.
(8) M. C. Wang, H. C. Chiang, S. T. Hsieh and E. K. Lin, to be published.
(9) S. T. Hsieh, M. C. Wang, H. C. Chiang and T. Y. Lee, Phys. Rev. C. 8 (1973) 563.

Table Caption

Table I γ-ray energies, and relative intensities from the resonance of de-excitation at E_p=2098 keV in the ^{63}Cu(p,γ)^{64}Zn reaction. The symbol r → 0 refers to the transition from the resonance to the grand state and the symbol r → 992, for example, refers to the transition from the resonance to the 992 keV state in ^{64}Zn.

Table I

γ-ray energy (photo peak) (keV)	Relative intensity	Corresponding transition in ^{64}Zn	γ-ray energy (photo peak) (keV)	Relative intensity	Corresponding transition in ^{64}Zn
9772	24.9 ± 4.5	r → 0	3205	4.0 ± 1.1	3206 → 0
8782	69.6 ± 6.3	r → 992	3191	4.1 ± 0.8	3188 → 0
7972	65.3 ± 20.0	r → 1799	3006	3.0 ± 0.5	3004 → 0
7861	7.0 ± 0.5	r → 1909	2982	0.8 ± 0.3	2980 → 0
7464	10.5 ± 4.0	r → 2308	2805	2.5 ± 0.4	3797 → 992
7162	5.5 ± 2.0	r → 2610	2560	3.1 ± 1.2	3549 → 992
7040	6.8 ± 1.8	r → 2736	2468	2.5 ± 0.3	3458 → 992
6977	12.0 ± 1.0	r → 2794	2438	1.3 ± 0.5	3428 → 992
6795	14.6 ± 1.8	r → 2980	2380	4.2 ± 1.3	3368 → 992
6768	14.5 ± 1.0	r → 3004	2306	10.6 ± 1.5	3300 → 992
6681	15.3 ± 3.6	r → 3092	2271	5.8 ± 0.4	3263 → 992
6585	8.7 ± 0.9	r → 3188	2215	3.6 ± 0.5	3206 → 992
6569	13.7 ± 1.5	r → 3206	2195	8.0 ± 0.9	3188 → 992
6514	5.8 ± 2.0	r → 3263	2103	11.9 ± 1.1	3092 → 992
6469	11.2 ± 3.0	r → 3300	2008	26.6 ± 4.7	3004 → 992
6407	8.0 ± 2.0	r → 3368	1988	10.4 ± 3.2	2980 → 992
6344	8.6 ± 1.6	r → 3428	1798	49.3 ± 2.7	1799 → 0
6313	7.8 ± 3.0	r → 3458	1747	6.5 ± 0.5	2736 → 992
6224	12.2 ± 1.6	r → 3549	1618	3.8 ± 0.3	2610 → 992
6172	7.7 ± 3.0	r → 3602	1498	3.1 ± 1.2	3300 → 1799
5975	7.7 ± 1.8	r → 3797	1407	3.0 ± 1.0	3206 → 1799
5892	6.5 ± 3.1	r → 3874	1387	2.7 ± 0.6	3188 → 1799
5873	5.2 ± 1.1	r → 3900	1316	13.2 ± 2.1	2308 → 992
3797	7.2 ± 2.1	3797 → 0	1290	4.7 ± 0.2	3092 → 1799
3602	2.0 ± 0.8	3602 → 0	1204	6.0 ± 0.4	3004 → 1799
3551	1.6 ± 0.6	3549 → 0	1180	4.2 ± 0.5	2980 → 1799
3455	4.3 ± 2.0	3458 → 0	992	362.3 ± 10.9	992 → 0
3428	9.9 ± 1.0	3428 → 0	937	4.2 ± 0.2	2736 → 1799
3367	4.7 ± 0.4	3368 → 0	917	8.2 ± 0.7	1909 → 992
3299	4.5 ± 2.0	3300 → 0	807	115.6 ± 9.8	1799 → 992
3265	5.2 ± 0.6	3263 → 0			

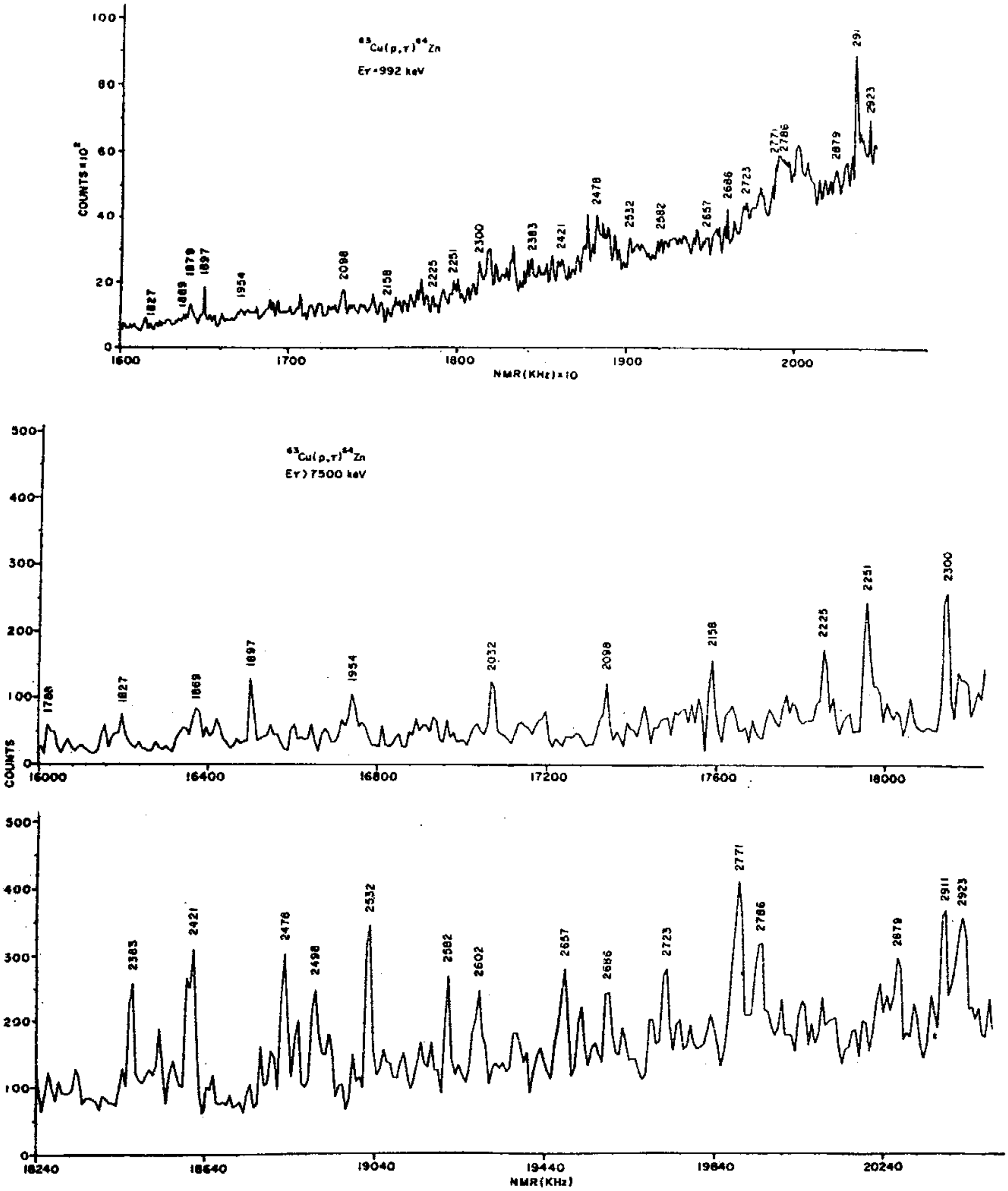

Fig. 1.

Fig. 1 The excitation functions of 992 keV γ-ray and larger than 7500 keV γ-rays. The numbers refer to the proton energy (in keV) of the resonance.

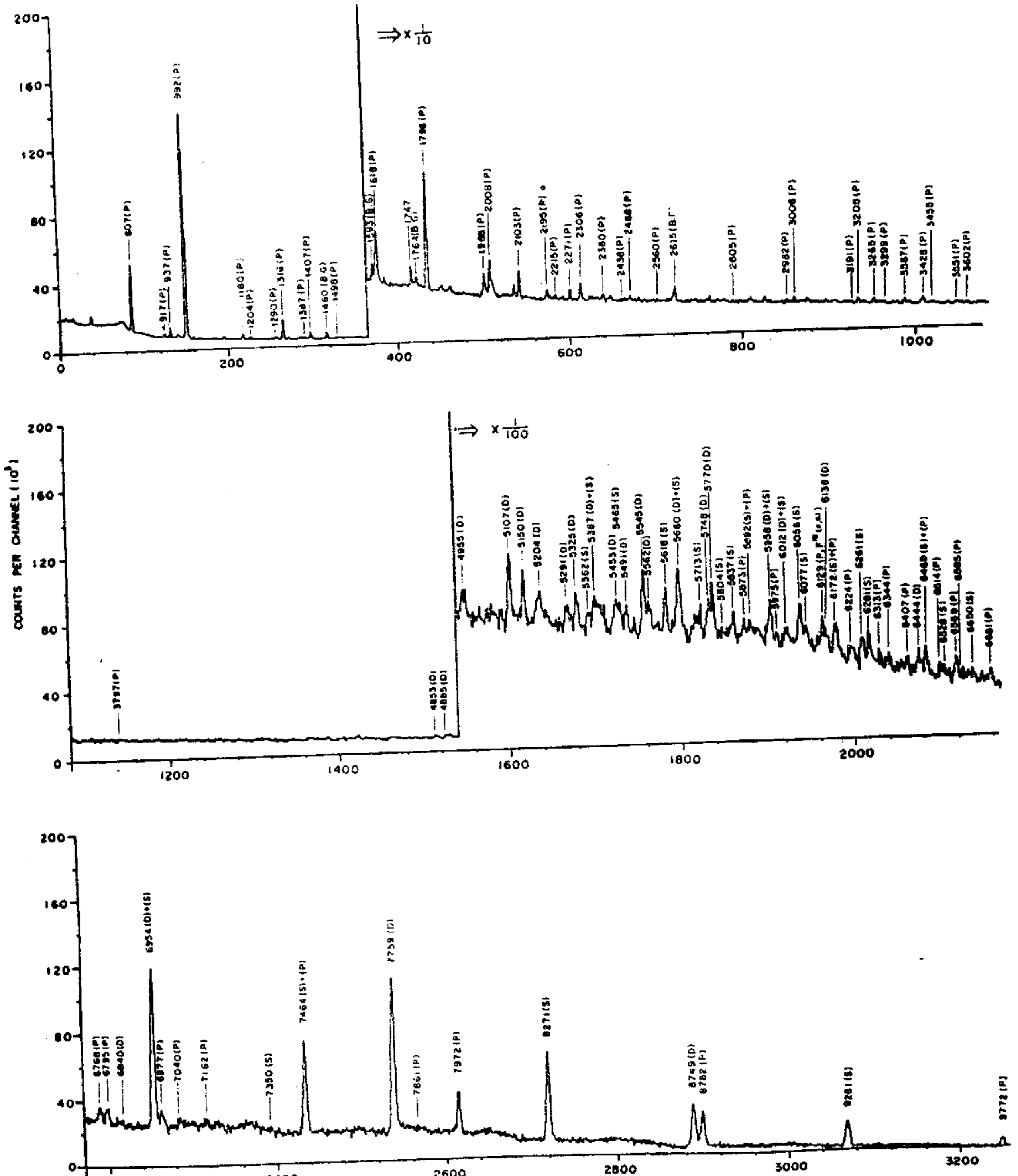

Fig. 2

Fig. 2 A decay spectrum of the resonance at E_p=2098 keV. The number, P, S and D refer to the energy of the γ-ray (in keV), photo peak, single escape and double escape peak, respectively.

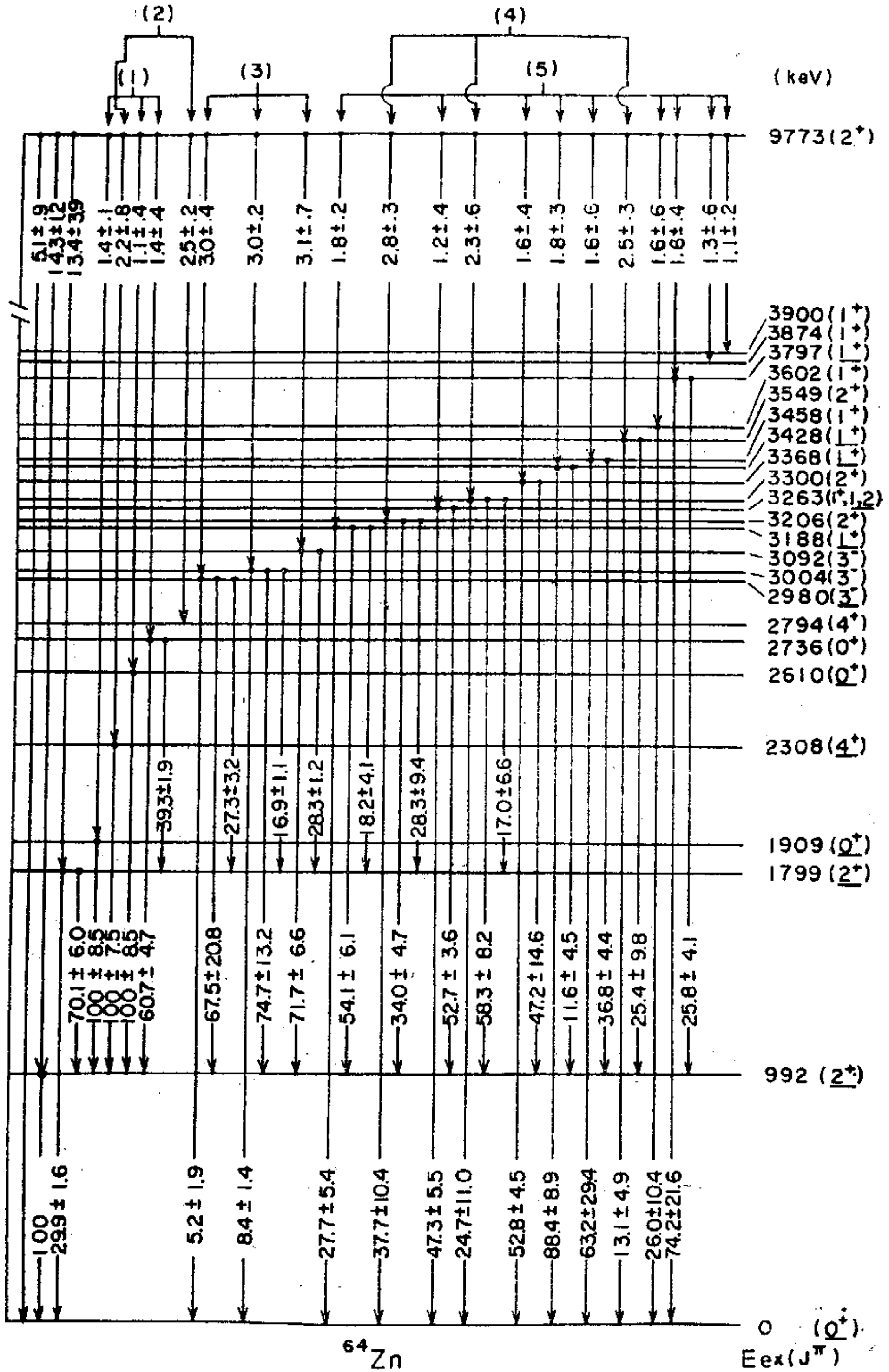

Fig. 3.

Fig. 3 The decay scheme of ^{64}Zn constructed from the resonance of de-excitation at 9772±2 keV (E_p=2098 keV). The numbers refer to the percentage of the branching ratio normalized by the intensity of 992 keV γ-ray. Five characteristic groups are denoted as the (1), (2), (3), (4) and (5) on the top of the scheme. The J^{π} with a bar underneath are taken from Refs. 4-6, while the J^{π} without bar are suggested by the present experiment.

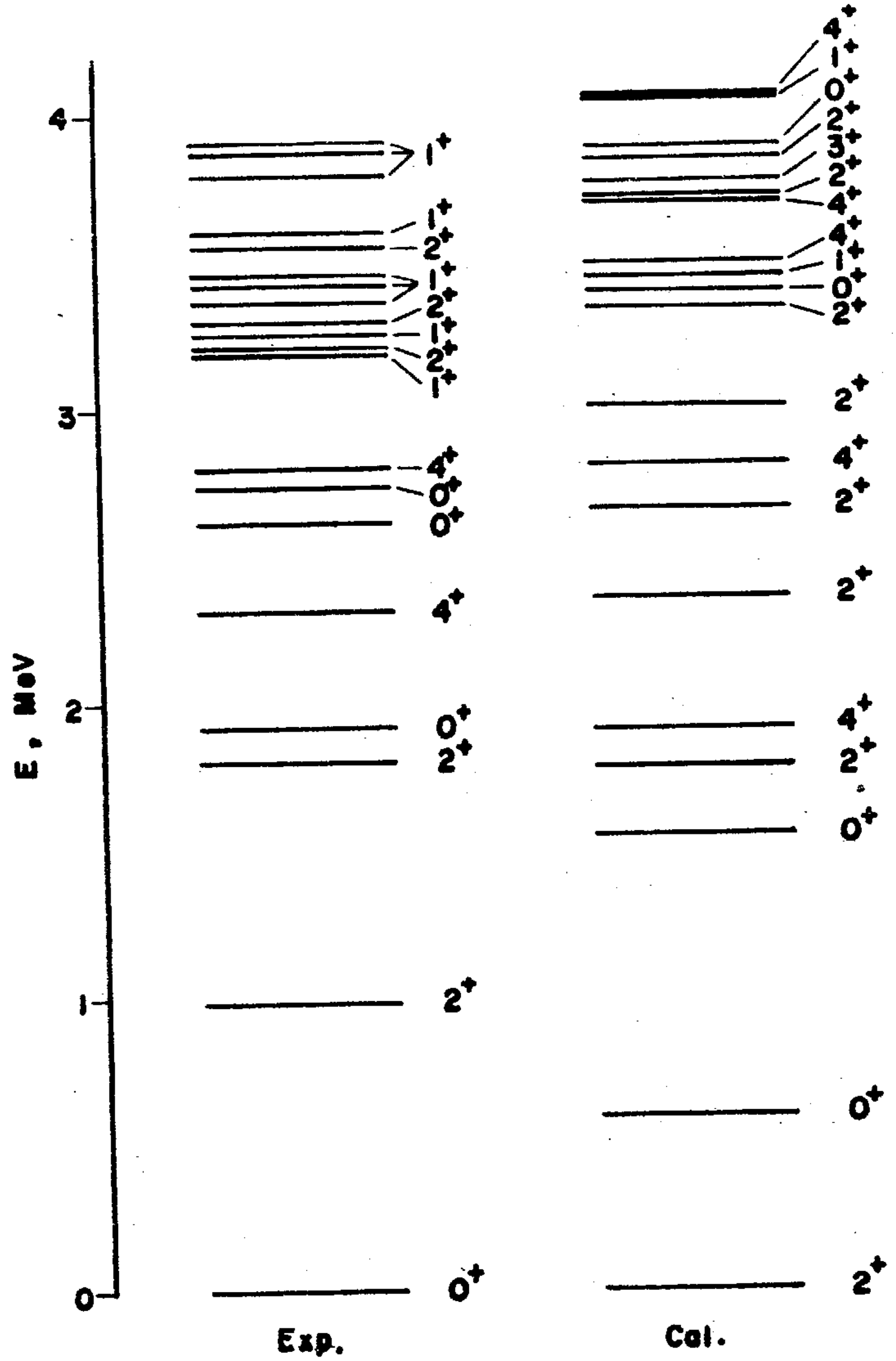

Fig. 4

Fig. 4 Level scheme of ^{64}Zn from the present experiment and the shell-model calculation.

THE STUDY OF $Li^7(d,\alpha,\alpha)n$ REACTION

Ming Wen*, W. N. Wang & D. Wang

Institute of Physics

Academia Sinica

The Republic of China

Abstract

The reaction $Li^7 + d \rightarrow \alpha + \alpha + n$ was studied at deuteron bombarding energy 1.5 MeV. The two alpha particles are detected in coincidence by two silicon surface barrier detectors, one fixed at 60° and the other varied from 75° to 130°. The reaction mechanism is found to be mainly sequential two-body decay involving the ground and broad first excited states of He^5. Contribution from the direct three-body decay and the sequential two-body decay involving the Be^8 second excited state, if present, are no more than a few percent of total reaction.

1. *Introduction*

The study of nuclear reaction with more than two particles in the outgoing channel is of great interesting theoretically and experimentally.

Deuteron bombardent of Li^7 provides a very convenient reaction to study the three-body decay process because of its large positive Q value to decay into two alpha-particles and a neutron. The recation $Li^7 + d \rightarrow \alpha + \alpha + n$ has been studied by several authors at E_d = 180 keV(1), 200 keV(2), 380 keV(3), 0.8 and 1.0 MeV(4), 0.6-2.0 MeV(5), 2.6 to 4.0 MeV(6); 3.0, 3.2, 3.6 and 5.9 MeV(7) using various techniques.

The reactions induced by deuteron bombardment on natural lithium target are mainly through the following process:

(1) $Li^7 + d \rightarrow + He^5 + \alpha$ Q = 14.165 MeV
$\quad\quad\quad\quad\quad\quad \llcorner\!\rightarrow \alpha + n$ Q = 0.957 MeV

(2) $Li^7 + d \rightarrow n + Be^8$ Q = 15.03 MeV
$\quad\quad\quad\quad\quad\quad \llcorner\!\rightarrow \alpha + \alpha$ Q = 0.094 MeV

(3) $Li^7 + d \rightarrow \alpha + \alpha + n$ Q = 15.122 MeV

---

* Present address: Institute of Nuclear Science, Atomic Energy Commission, Taipei, R.O.C.

(4) $Li^6 + d \to \alpha + \alpha$ ~~+ n~~ $Q = 22.36$ MeV

(5) $Li^6 + d \to p + Li^7$ $Q = 5.02$ MeV

The previous experiments indicated that for $E_d \leqslant 1.0$ MeV the reaction proceeds mainly through the ground state and the first excited state of He^5, and for higher energies ($E_d \geqslant 2.0$ MeV), the contribution from the intermediate states of Be^8 becomes important. However, significant contribution from the direct break-up process have not been observed.

The width of the first excited state of He^5 had been found to be within a large range from 1.5 to 2.0 MeV$^{(2)}$. Different methods had been suggested by previous authors to fit the energy spectrum of the first excited state of He^5.

The aim of the present experiment is to extend the experimental study to the energy region where no detail results have been reported and to obtain some information about the first excited state of He^5 as well as the reaction mechanism.

2. *Kinematic Relation*

The finial state of a three-body decay, $A+B \to x_1 + x_2 + x_3 + \theta_t$, has nine degrees of freedom. However, by the conservation of total energy and momentum, only five independent variables are actually needed to be measured. Using the energy and momentum conservation rules, it is easily to derive a relation between the K.E. of the particle x_1 entered the detector at angle θ_1 and that of particle x_2 entered the detector at θ_2. The relation$^{(8)}$ is:

$$\frac{1}{m_3}\,[E_1^{\ell}(m_1+m_3) + E_2^{\ell}(m_2+m_3) - 2(m_p m_1 E_p^{\ell} E_1^{\ell})^{1/2}\cos\theta_1^{\ell}$$

$$-\,2(m_2 m_p E_p E_2)^{1/2}\cos\theta_2^{\ell} + 2(m_1 m_2 E_1 E_2)^{1/2}\cos\theta_{12}^{\ell}]$$

$$= Q + E_p^{\ell}\left(1 - \frac{m_p}{m_3}\right)$$

where $\cos\theta_{12}^{\ell} = \cos\theta_1^{\ell}\cos\theta_2^{\ell} + \sin\theta_1^{\ell}\sin\theta_2^{\ell}\cos(\phi_1 - \phi_2)$

m_i : mass of particles i, i=1,2,3

E_i^{ℓ} : K.E. of particle i in lab. system i=1,2

θ_1^{ℓ} : laboratory polar angle of particle i, i=1,2

m_p : mass of the projectile
E_p : K.E. of the projectile in lab. system
Q_t : The total Q value of the reaction
θ^{ℓ}_{12} : laboratory polar angle between particle 1 and 2.

The calculated kinematical locus of the direct three-body decay process at $E_d = 1.5$ MeV θ^{ℓ}_1 at 60° and θ^{ℓ}_2 at 105° is shown in Fig. 1. The black points are the calculated positions where the ground state of He^5 located by assuming a sequential decay process: The x and Δ represent the location of the first excited state of He^5 and the 11.4 MeV excited state of Be^8 respectively which are the only other two contributions kenermatically possible.

3. *Experimental Apparatus and Procedure*

The deuterons were accelerated by the 3 MeV Van de Graaff accelerator of the National Tsing Hua University and were analyzed by a 45° degree magnet. Lithium hydride ($\sim$200 μ g/cm^2) evaporated on cabon backing ($\sim$1 mg/cm^2) was used as the target. The overrall energy resolution in our experiment was about 180 KeV. A diagram of the experimental arrangement is shown in Fig. 2.

The outgoing α -particles were detected by two ORTEC silicon surface barrier detectors. The bias voltage of the detector was chosen such that the sensitive region was just deep enough to stop 12 MeV alpha particles in the depletion layer. The signals from the detectors were amplified and analyzed by a two dimensional pulsed height analyzer. In order to reduce background from the chance coincidence, pulses from the fast coincidence circuit were used to gate the multichannel analyzer.

In order to avoid serious pile up, the beam current was limited to about 0.08 μ A for measurement at backward angles and 0.04 μ A at forward angles.

The two dimensional coincidence spectra were observed by fixed one detector at 60° (D_f) relative to incident beam and the other (D_m) was varied from 75° to 135° in stop of 5°. During the experiment, a monitor was used to check the target condition and the variation of the incident beam. The counting rate of the monitor was used to normalized the experimental cross sections.

4. *Experimental Results and Discussion*

Typical coincidence spectra are shown in Fig. 3 and Fig. 4. The data projections onto the alpha particle 1 energy axis (E_f, the energy axis of α-particles detected in fixed detector at θ_f) and the alpha particle 2 energy axis (E_m, the energy axis of the movable detector at θ_m) are also shown. The arrows in the Fig. indicate the expected positions of the ground and the first excited state of He^5. In Fig. 5 we show the results of Fig. 4 after dividing it by phase space factor. We see that the peak positions are unaltered but the relative strength are changed.

The spectra are distributed nonuniformly along the kinematic curve. There are several regions where a great number of events fall into it. These regions are just that we have expected from the assumption of the intermediate states of He^5 in the sequential decay. The second excited state of Be^8 has also been found in the experiment, but the contribution is small compaired with that of He^5 first excited state. We note also that there are several regions on the kinematic curves where counting rate is very low. This shows that the probability of direct break-up into three bodies in small.

In order to obtain the angular Correlated information of the process $^7Li(d,\alpha,\alpha)n$, The reaction was Studied at $E_d = 1.5$ MeV and $\theta_f = 60°$ and the second detector Varied in Step of 5° from 75° to 135°, which angles are kinematically possible to detector the second α particle by placing the first α-detector at 60° in this three body decay process. The three-dimensional projection of alpha-alpha Coincidence Counts of the reaction are shown in Fig. 6. The dash curves on the E_f, θ_m plane in the figure indicate the Calculated positions of the ground and first excited states of ^5He and that 11.4 excited state of ^8Be respectively by assuming sequential decay. We can see that intensity peaks are observed only above the positions corresponding to the calculated dash lines. The sharper peaks are always the He^5 ground state groups. The low yield between dash lines indicates again that the reaction is principlly sequential.

The experimental angular Correlations of this reaction is self-explained in the diagram. The correlations show pronounced dependence upon the movable counter angle with it's maximum near the center of the recoiled angle.

We conclude our discussion by saying that, at $E_d = 1.5$ MeV, the reaction is mainly a sequential decay process involving the ground and the first excited state of He^5.

References

(1) H. Heremie, Ph. Martin and A. Calamand, Nuclear Phys. A105 (1967) 689.

(2) P. Fessende and D. R. Maxson, Phys. Rev. 133 (1964) B71.

(3) P. A. Assimakopoucos, N. H. Gangas and S. Kossionides, Nuclear Phys. 81 (1966) 305.

(4) C. Milone and R. Potenza, Nuclear Phys. 84 (1966) 25.

(5) The reaction $^7Li\ (d,\alpha)^5He$ in the energy range 0.6 to 2.0 MeV. E. Friedland, I. Venter (Univ. Pretovia, South Africa), E. Phys. (Germany), Vol. 243, No. 2, P. 126-31 (1971).

(6) V. Valkovic, W. R. Jackson, Y. S. Chen, S. T. Emerson and G. C. Phillips, Nuclear Phys. A96 (1967) 241.

(7) Valkovic, C. Joseph, A. Viller and G. C. Phillips, Nuclear Physics A116 (1968) 497.

(8) G. G. Ohlsen, Nuclear Instr. and Methods 37, (1965) 240.

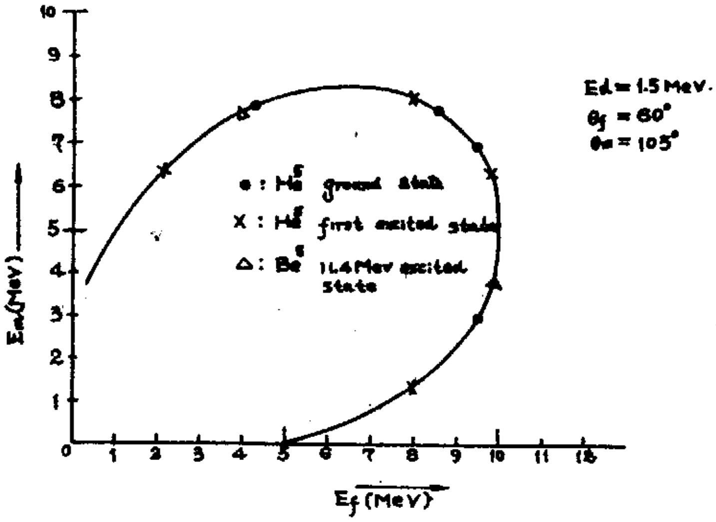

Fig. 1. The calculated kinematic curve for fixed Ed=1.5MeV $\theta_f = 60^\circ$ and $\theta_m = 105^\circ$ in $Li^7(d, \alpha, \alpha)n$ Reaction

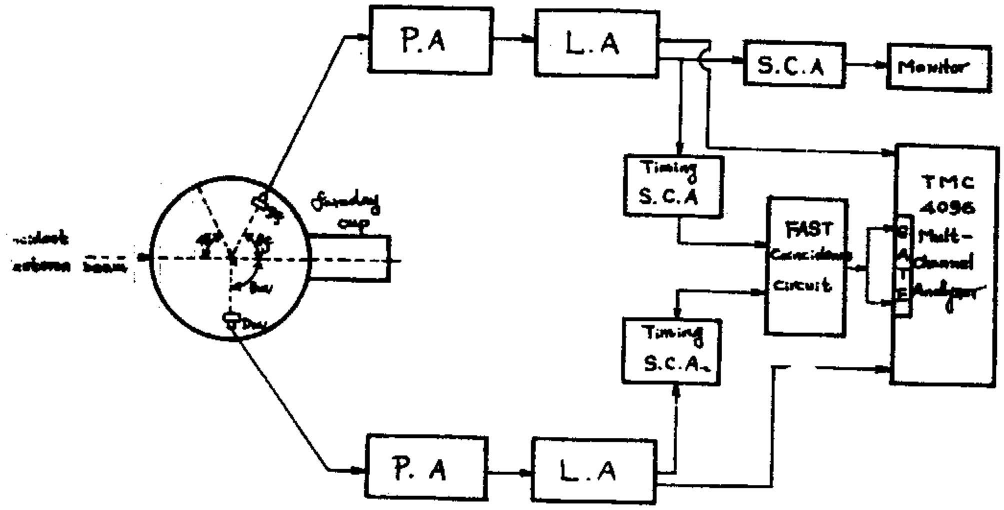

Fig. 2. Block Diagram of the circuit used for measurement of alpha- alpha coincidences.

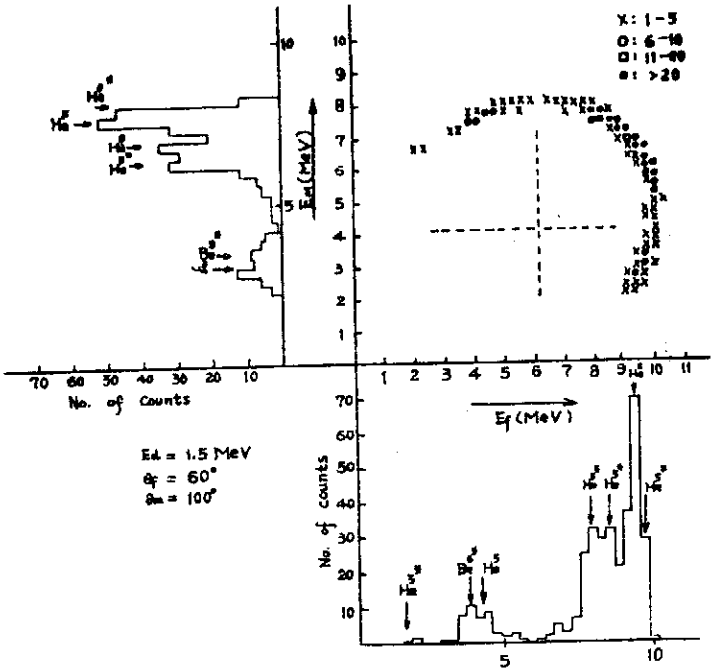

Fig. 3. The alpha-alpha coincidence spectrum at a deuteron bombarding energy of Ed=1.5MeV and angle settings θ_f= 60° and θ_m=100°. The dashed lines indicate how the data projection onto the E_f axis contains only the events above from the horizontal dash line, while the projection onto the E_m axis contains only the events on the right from the vertical dash line.

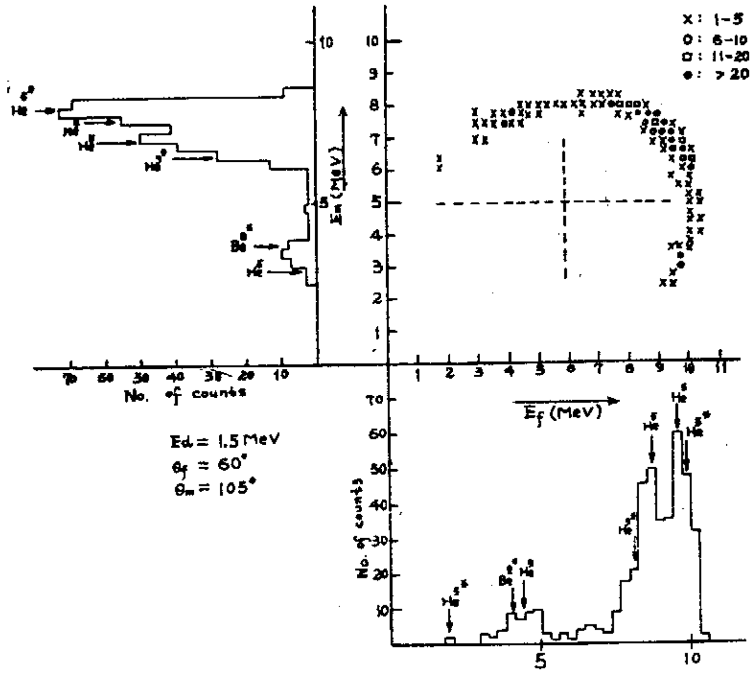

Fig. 4. The alpha-alpha coincidence spectrum at a deuteron bombarding energy of Ed=1.5MeV and angle settings θ_f=60° and θ_m=105°. The dashed lines indicate how the data projection onto the E_f and E_m axes were made. The projection onto the E_f axis contains only the events above from the horizontal dash line, while the projection onto the E_m axis contains only the events on the right from the vertical dash line.

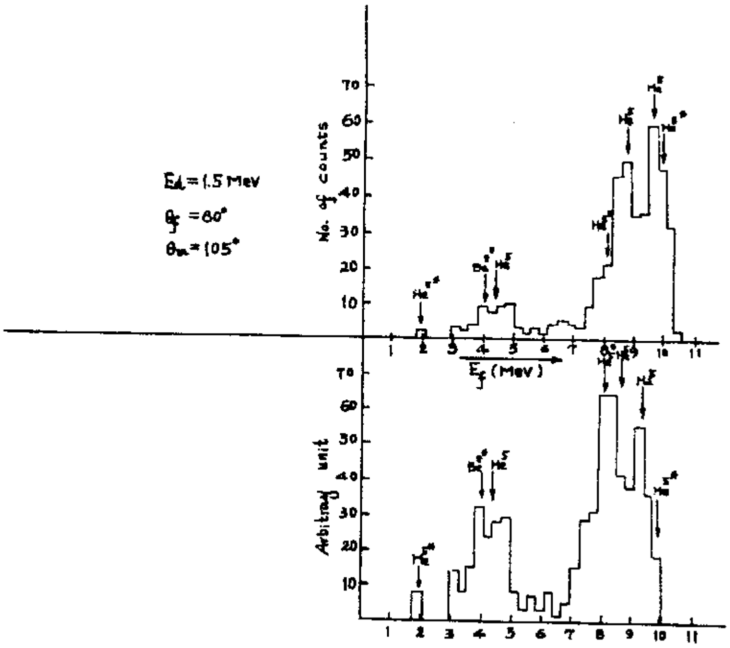

Fig. 5. The results of Fig. 4 after dividing it by phase space factor.

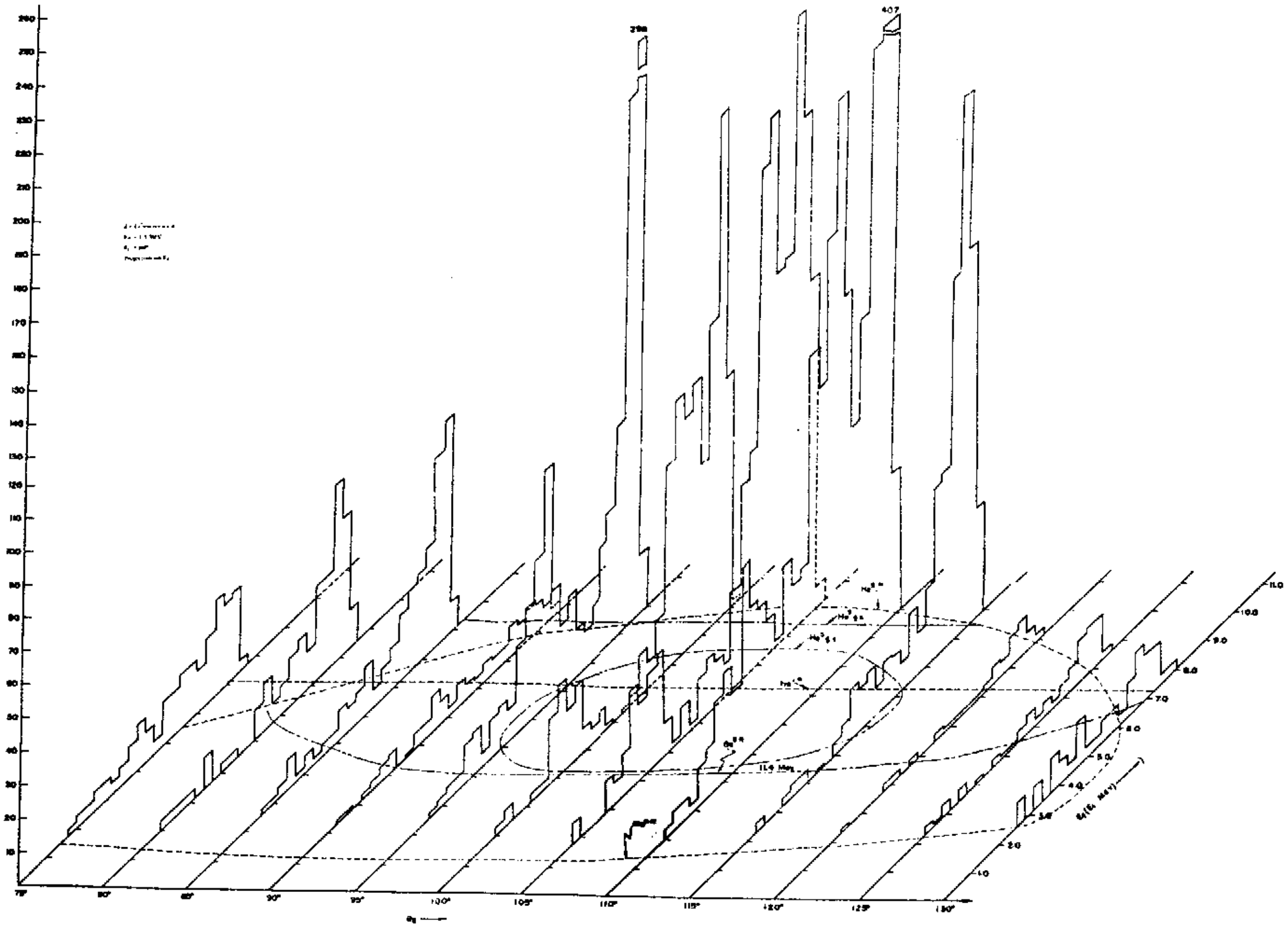

[illegible]

ANNUAL REPORT OF THE INSTITUE OF PHYSICS, ACADEMIA SINICA 1973

ANGULAR CORRELATION STUDIES OF THE $^{27}Al(p,\gamma)^{28}Si$ REACTIONS AT THE 1381- and 1388 keV RESONANCES*

E. K. Lin, (林爾康) G. C. Kiang, (江紀成)
C. W. Wang (王建萬) and S. H. Duan
Institute of Physics
Academic Sinica

Abstract

The 1381- and 1388 keV $^{27}Al(p,\gamma)^{28}Si$ resonances, corresponding to the 12.917- and 12.924 MeV states of ^{28}Si have been studied by the directional correlation method. The spin-parity of both two resonances was proposed to be 2^+. The decayed γ-rays emitted from these resonance states to the 1.78 MeV level of ^{28}Si nucleus were found to have admixture of E2 and M1 with the intensity mixing ratio 1.2% and 0.64% respectively.

1. *Introduction*

Numerious sharp resonances have been observed in the $^{27}Al(p,\gamma)^{28}Si$ reaction for proton bombarding energies below 3 MeV(1-4). By means of the large volume Ge(Li) detector with high energy resolution, the low-lying levels of the compound nucleus of ^{28}Si have been intensively investigated(1-3). Gove et al(5) measured seventeen angular distributions of capture gamma-rays emitted in the transitions to the first excited state with the result that the first excited state of ^{28}Si was 2^+. Valerio and Nelson(6) have studied the $^{27}Al(p,\gamma)^{28}Si$ resonances at 324-, 405- and 630 keV by the method of triple correlation and reported the level scheme of ^{28}Si up to E_x=12.9 MeV. However, the most structure of the excited states of ^{28}Si higher than E_o = 12.9 MeV has rarely been reported previously. Since the even-even ^{28}Si nucleus with spin 0 in its ground state and the transition from its first excited state to the ground, $2^+(2)0^+$ must be pure, only the gamma rays decayed from other higher levels to the first excited state could be mixed. This means that the ^{28}Si nucleus is especially suitable for the directional correlation measurement(7). And the interpretations of the measured correlation is considerably reduced.

In the present work, the directional correlation measurements were performed with the principal aim of determining (1) the spins of the E_p=1381- and 1388 keV resonances in the $^{27}Al(p,\gamma)^{28}Si$ reaction (corresponding to the 12917- and 12924 keV levels of

---

* Work performed at the Physics Center at Hsinchu and supported by the National Science Council

^{28}Si), (2) the mixing parameters of the gamma radiations.

2. *Experimental*

A 3 MeV Van de Graaff accelerator was used to produce proton beam and to investigate the 1381- and 1388 keV ^{27}Al(p,γ)^{28}Si resonances. The energy resolution was about 1 keV for 1.0-2.5 MeV protons. The proton beam of approximately 3 μA was analyzed by a 25° deflecting magnet and impinged on the target with a fine spot. The beam energy was determined by the nuclear magnetic resonance method. The magnetic field was controller by a Spectro-Magnetic Industries current regulator unit and a HP 5245L flux meter. Several well known resonances between E_p=992 to 2650 keV in the ^{27}Al(p,γ)^{28}Si reaction have been used for the energy calibration.

The targets were prepared by the vacuum evaporation method. Pure alumium (99.999%) was evaporated in the vacuum onto a gold backing (~ 0.4 mm thick). The thickness of prepared targets was 25 ± 5 μg/cm^2. A specially designed and constructed scattering chamber with target cooling system and cold trap was used for this experiment$^{(8)}$. The target was mounted on the target holder at 135° with respect to the beam. The water cooling system continuously cooling the target permitted the long period bombardment for the coincidence spectra measurement without noticeable target deterioration. Usually, data were collected for each run over a period of 12 hr or more.

A Harshow 3" × 3" NaI(Tl) crystal and a Ortec 50 cm^3 Ge(Li) detector were employed in the coincidence measurement. Each of the two detectors was shielded with a 2mm cylinderical lead cup in order to reduce the low energy but stong random gamma background. The NaI(Tl) detector was fixed with 90° to the beam, while the Ge(Li) detector was put on a rotatable arm which can be turned arround the target from 90° to 180° continuously. The Ge(Li) detector provided energy resolution (FWHM) of 2.1 keV for 1.33 MeV photons. The efficiency of the Ge(Li) detector was ∿10% relative to NaI(Tl) crystal for 1.33 MeV; the source-to-detector was kept at a distance of ~8cm.

In order to carry out the directional correlation measurement, a γ-γ coincidence system was set up, the block diagram is shown in Fig. 1. For coincidence measurements, the proton beam energy was kept at 1381- and 1388 keV respectively, and the geometrical conditions were kept same. In the de-excitation gamma transitions from two resonance states of ^{28}Si as investigated, the resonance →1.78 MeV state cascade was the main mode of decay, and the gamma rays emitted from the 1.78 MeV state in the subsequent decay are very prominent. We used the low efficiency Ge(Li) detector to measure the 1.78 MeV gamma rays decayed from the first excited state to the ground state of ^{28}Si, and the NaI(Tl) detector to measure the gamma rays emitted from the resonances to the 1.78 MeV state. This arrangement enables to increase the coincidence counting rate. The coincidence to establish a resonance →1.78 MeV cascade was obtained with proper gating. The output from the NaI(Tl) detector through the ORTEC 410 linear amplifier was feeded to a CI-1480 ratemeter as a reaction monitor to check the yield in stable.

3. *Data Analysis*

The experimental data from each measured directional correlation were analyzed by a IBM 1130 computer. Using the least square method, the data were fitted to a linear combination of $P_o(\theta)$, $P_2(\theta)$ and $P_4(\theta)$ Legendre polynominals as outlined by Rose(9). The correlation function for the gamma cascade $J_a(L_1)J_b(L_2)J_c$ could be simply expressed as

$$W(\theta) = A_o + A_2P_2(\theta) + A_4P_4(\theta).$$

And the anisotropy(7,10), $A = \dfrac{W(180°)-W(90°)}{1+A_2+A_4}$, is related to the coefficients A_2 and A_4 by $A = \dfrac{1+A_2+A_4}{1-\frac{1}{2}A_2+\frac{3}{8}A_4} - 1$, where A_o has been normalized to unity. However, in case of the cascade transition the correlation is in more complex mode, such as $J_a(L_1 L')J_b(L_2)J_c$ the anisotropy A becomes a function of δ(7,10,11), since the correlation function $W(\theta)$ and its cofficients, A's, not only depend on the angle θ but also depend on the mixing ratio δ of L_1 and L_1'. Where

$$\delta = \langle J_a \| L_1 \| J_b \rangle / \langle J_a \| L_1 \| J_b \rangle, \qquad L_1' = L_1 + 1$$

Based on the known decay mode, $2^+(2)\,0^+$, from the first excited state to the ground state of ^{28}Si nucleus, we have computed $A(\delta)$ for each possible J and L values, where J = 1,2,3,4 and L=1,2,3, in the range of $-20<\delta<80$.

The directional correlation data at E_p=1317 keV (E_x=12.855 MeV) for θ=90°, 120°, 150°, and 180° were also taken. Since the 12.855 MeV→1.78 MeV→0 cascade mode is 4^+ (2) 2^+ (2)0^+, the obtained data were used as the known standard. All of the other directional correlation measurements were normalized with the known standard in order to minimize the geometrical effects.

4. *Results and Discussions*

The coincidence measurements were carried out at E_p=1317-, 1381- and 1388 keV for θ=90°, 120°, 150° and 180° for three cascades 12855 keV→1778 keV→0, 12917 keV →1778 keV→0 and 12924 keV→1778 keV→0 of ^{28}Si. The typical coincidence spectra of the cascade transition 12924 keV→1778 keV→0 for different angles are shown in Fig. 2. Only one sharp clean and simple gamma line appears in the spectra for each angle, there are no difficults in the elimination of the background and the other interference factor during the data analysis.

A. The 1381 keV resonance

The angular correlation function obtained in the cascade 12917 keV→1778 keV→0 of ^{28}Si is shown in Fig. 3. It is seen that the data were fitted very well. The fitted correlation function after normalization is

$$W(\theta) = 1.+(0.1711 \pm 0.0047)\, P_2(\cos\theta) + (0.00619 \pm 0.00606)\, P_4(\cos\theta),$$

Based on the two coefficients $A_2 = 0.1711 \pm 0.0047$, $A_4 = 0.00619 \pm 0.00606$, the calculated anisotropy A=0.28423 is very close to the experimental value of $A_{exp} = 0.28120 \pm 0.0738$.

If we assumed that, the decay mode of the 12917 keV level is $J_a(L_1)2^+\ (2)0^+$ then, the possible values for J_a are 1,2,3 and 4. However, the theoretical values of A_2 and A_4 for these J_a values are in clear disagreement with the above experimental values. Thus, the decayed gamma-rays from the 12917 keV level of ^{28}Si to its first excited level are likely in mixed polarity; and the cascade transition is of the $J_a(L_1, L_1')2^+\ (2)0^+$ mode.

In the process of determination for the J_a, L_1 and L' a computer program has been written to compute the $A_2(\delta)$, $A_4(\delta)$ as well as the anisotropies $A(\delta)$ values for the different J_a, L_1, and L_1'. The obtained values from computation are $A_2=0.1683$, $A_4= 0.00390$, $\delta=-0.11$ for $J_a=2$, $L_1=1$, $L_1'=2$ In comparision of the experimental values with the computed ones, we found that the cascade transition 12917 keV→1778 keV→0 is likely of the $2(1,2)2^+\ (2)0^+$ mode. And the mixing ratio of L=2 and L=1 is $\delta=-0.11$.

In Fig. 4, the anisotropy is plotted vs δ. The most possible admixture of γ_1 from $E_p=1381$ keV resonance is E2 and M1; the J^π of the 12917 keV level of ^{28}Si is 2^+. And the intensity ratio of E2 mixed with M1 in the 12917 keV→1778 keV transition is $\delta^2 = 0.012 \pm 0.001$ or 1.2%.

B. The 1338 keV resonance

For the cascade transition 12924 keV→1778 keV→0, we obtained the correlation function $W(\theta)$ as follows

$$W(\theta) = 1+(0.2173 \pm 0.0336)\, P_2(\cos\theta) + (0.0311 \pm 0.0415)\, P_4(\cos\theta),$$

and the experimental anisotropy $A_{exp}=0.4040 \pm 0.1158$. The angular distribution and the fitted curve are presented in Fig. 5.

From the measured coefficients for this cascade transition $A_2=0.2173\pm0.0336$, and $A_4=0.0311\pm0.0415$, the 12924 keV→1778 keV transition might be in mixing palority. The coefficient A_4 with a considerable large uncertainty of 0.0415, in comparision with 0.0311, which could lead either $A_4>0$ or $A_4<0$. In case of $A_4<0$, which implied $J_a=3$ or 1, the cascade mode is $3\ (L_1,\ L_1')2^+\ (2)0^+$ or $1(L_1,\ L_1')2_1^+\ (2)0^+$, where $L_1'=L_1+1$, $|J_a-2|\leqslant L_1'\leqslant J_a+2$. However, according to the possible values of L_1' and $J_a=1,3$, the calculated anisotropy $A(\delta)$ disagree with the A_{exp}. When $A_4>0$, $J_a=2$, $L_1=1$, the calculated A_2, A_4 and $A(\delta)$ are 0.1907, 0.0021 and 0.3824 respectively for $\delta=-0.08$. The anisotropy $A(\delta)$ was plotted vs δ as shown in Fig. 6. The calculated values are quite match with experiment. We conclude that the 1388 keV resonance state in the ^{27}Al(p,γ)^{28}Si reaction has spin 2 and proposed symmetric parity, the gamma ray decays from the 12924 keV level of ^{28}Si to its first excited level is in admixture polarities $L_1=1$, $L'=2$ or E2 and M1 transition. The intensity ratio of E2 to M1 is $\delta^2=0.0064\pm0.0020$ or int(E2)/int(M1)=0.64%.

Based on the measured branching ratios, Meyer et al$^{(2)}$ have tentatively assignment the spin-parity of the 1381- and 1388 keV resonances to be $(2^+,3,4^+)$ and $(2^+,3^-)$, respectively. In the present investigation as discussed above, we confirm the 2^+ out of other possible assignments for both two resonances.

Acknowledgement

The authors would like to express their deeply appreciation to Dr. C. C. Hsu for his suggestions and discussions. The gratitude also goes to the staff members of the Van de Graaff accelerator lab. at Tsing Hua University for their assistance.

References

(1) T. H. Hsu, E. K. Lin, C. C. Hsu, Y. C. Lin, P. K. Tseng, C. W. Wang, W. S. Hsu, Chin. J. Phys. 10, (1972) 55.
(2) M. A. Meyer, N. S. Welmarans and D. Eeitmann, Nucl. Phys. A144, (1970) 261.
(3) F. Ajzenberg-Selove and T. Lauritsen, Nucl. Phys. 11 (1959) 140.
(4) S. E. Hunt and W. M. Jones, Phys. Rev. 89 (1953) 1283.
(5) H. E. Gove, E. B. Paul, G. A. Baitholomev and A. E. Litherland, Phys. Rev. 94 (1954) 749.
(6) J. I. Valerio and E. B. Nelson, Nucl, Phys. 29 (1962) 70.
(7) H. Frauenfelder, in Beta and Gamma Spectroscopy (edited by K. Siegbahn), North Holland, 1955, p. 531.
(8) T. H. Hsu, P. K. Tseng, E. K. Lin and Y. C. Liu, Nucl. Instrum. Methods 106 (1973) 513.
(9) M. E. Rose, Phys. Rev. 91 (1953) 610.
(10) L. C. Biedenharn and M. E. Rose, Rev. Mod. Phys. 25 (1953) 729.
(11) M. E. Rose, Phys. Rev. 93 (1954) 477.

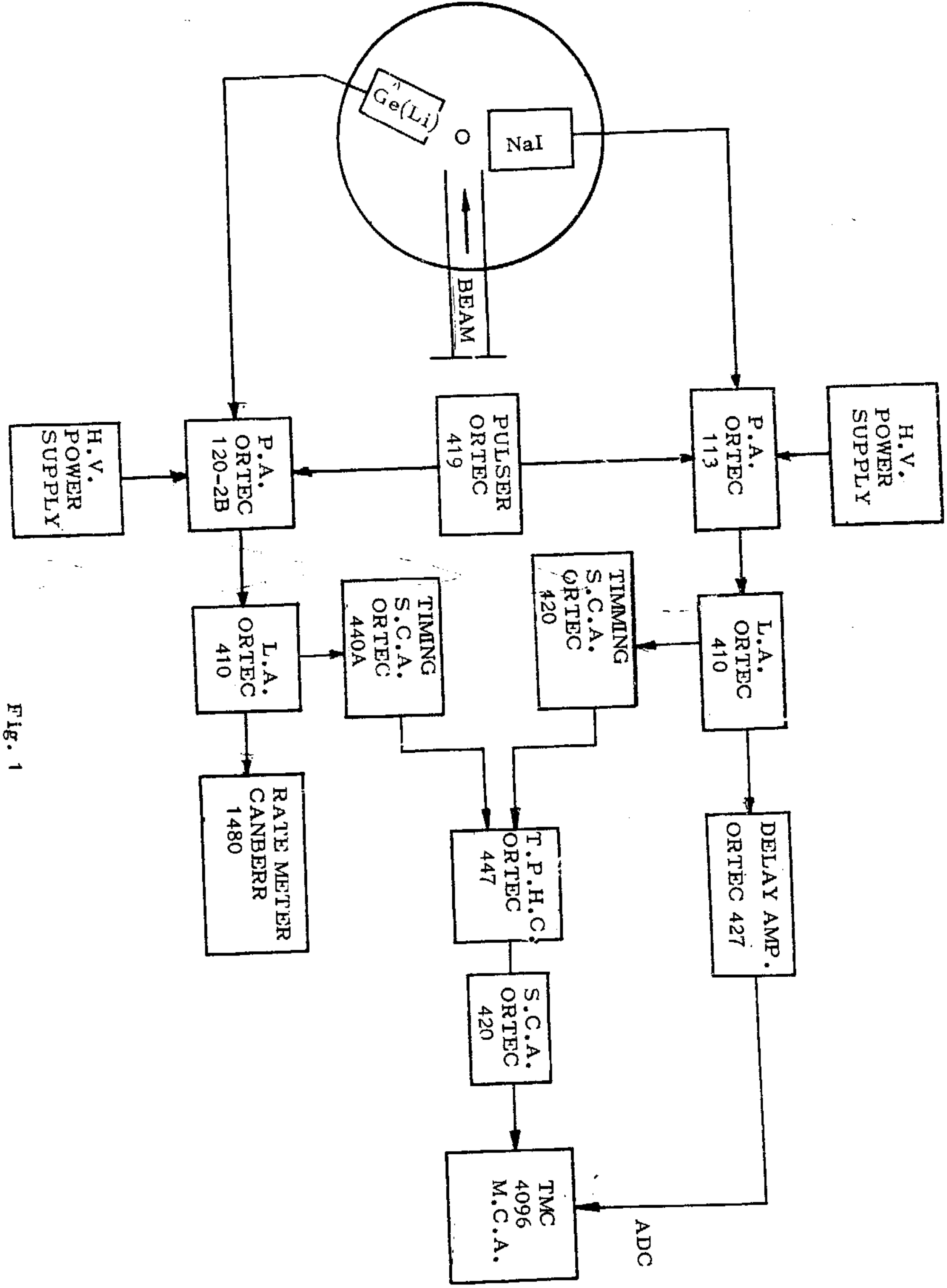

Fig. 1 Block diagram of the electronics used for the directional coincidence measurement.

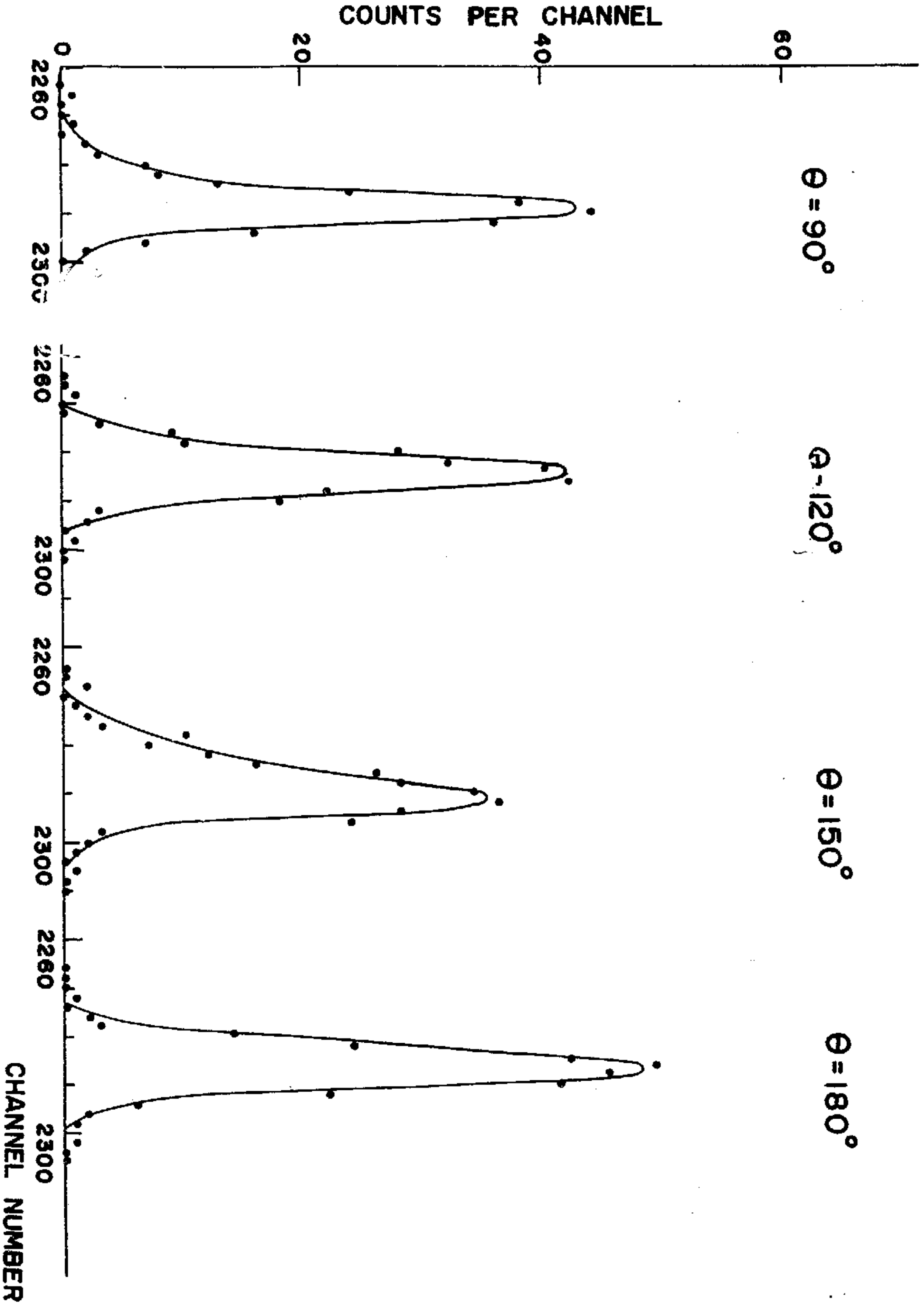

Fig. 2

Fig. 2 A typical coincidence spectra of the cascade 12924 keV→1778 keV→0 transition, observed from a 50cm^3 Ge(Li) detector at E_p= 1388 keV in the ^{27}Al(p,γ)^{28}Si reaction.

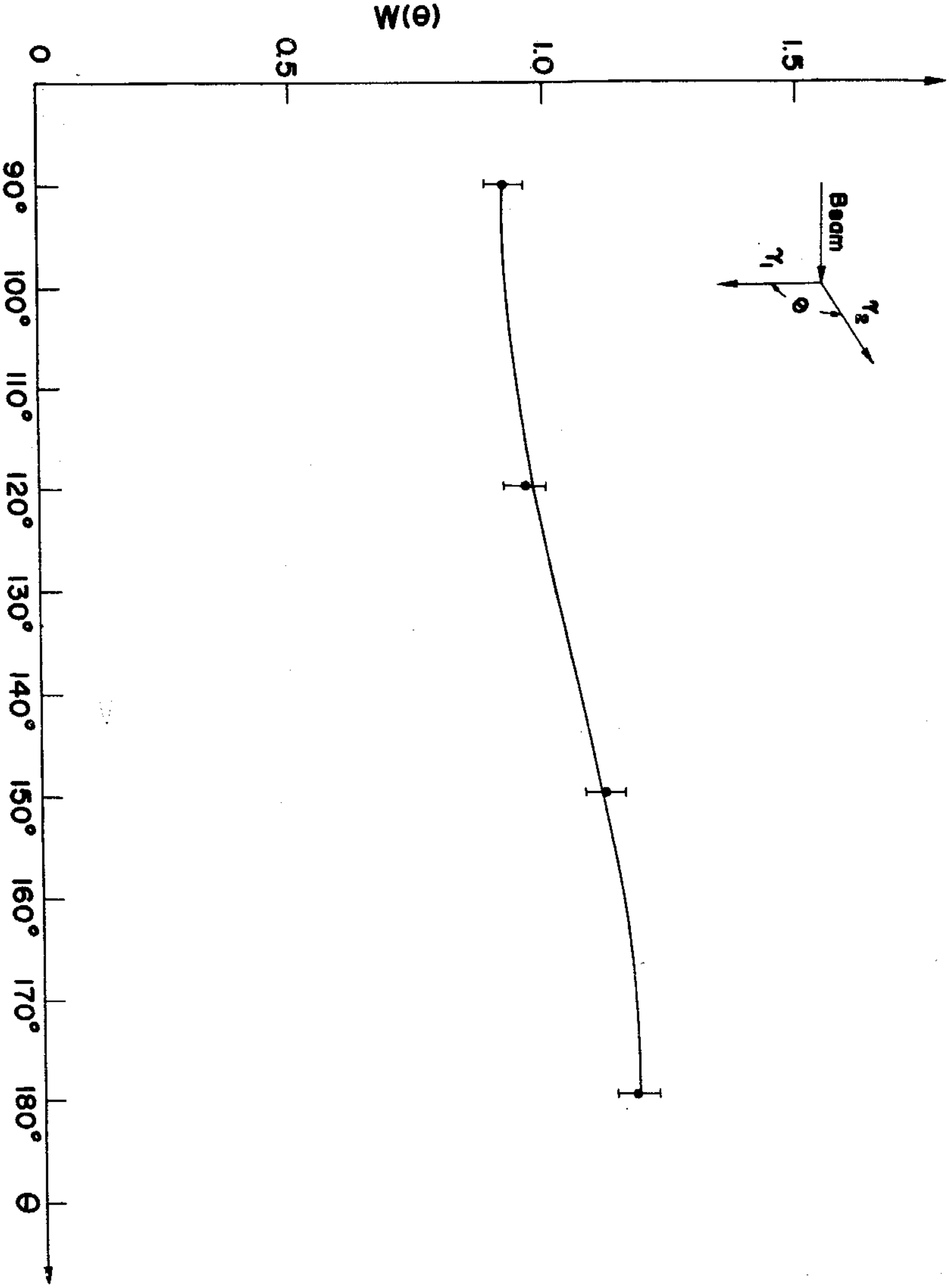

Fig. 3

Fig. 3 The fitted angular correlation function and the experimental data of the E_p=1381 keV resonance in the $^{27}Al(p,\gamma)^{28}Si$ reaction.

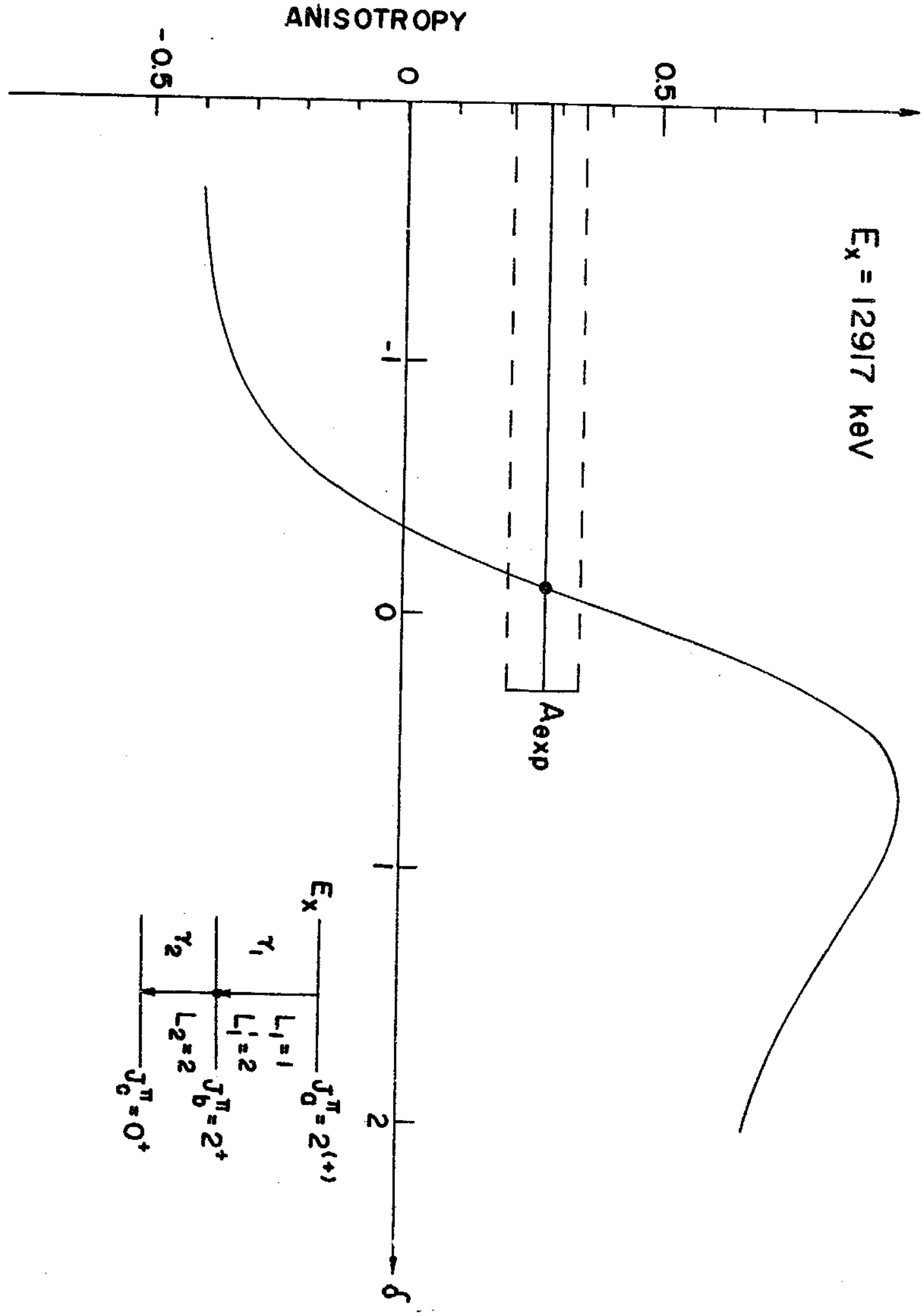

Fig. 4

Fig. 4 The anisotropy A(δ) for $J_2=2$, $L_1=1$, $L_1'=2$. The dotted lines represent the region of the experimental values for $E_p=1381$ keV resonance.

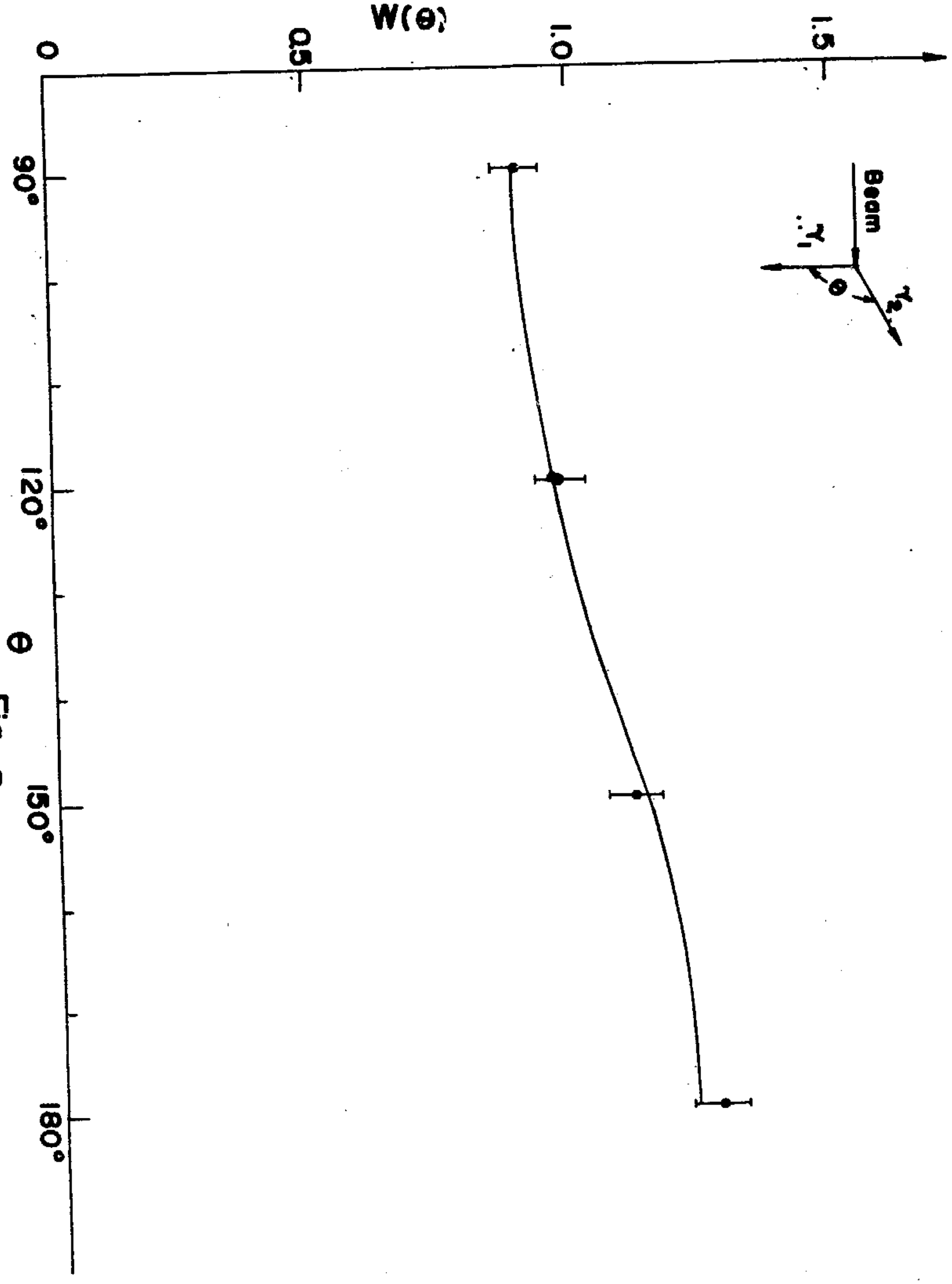

Fig. 5

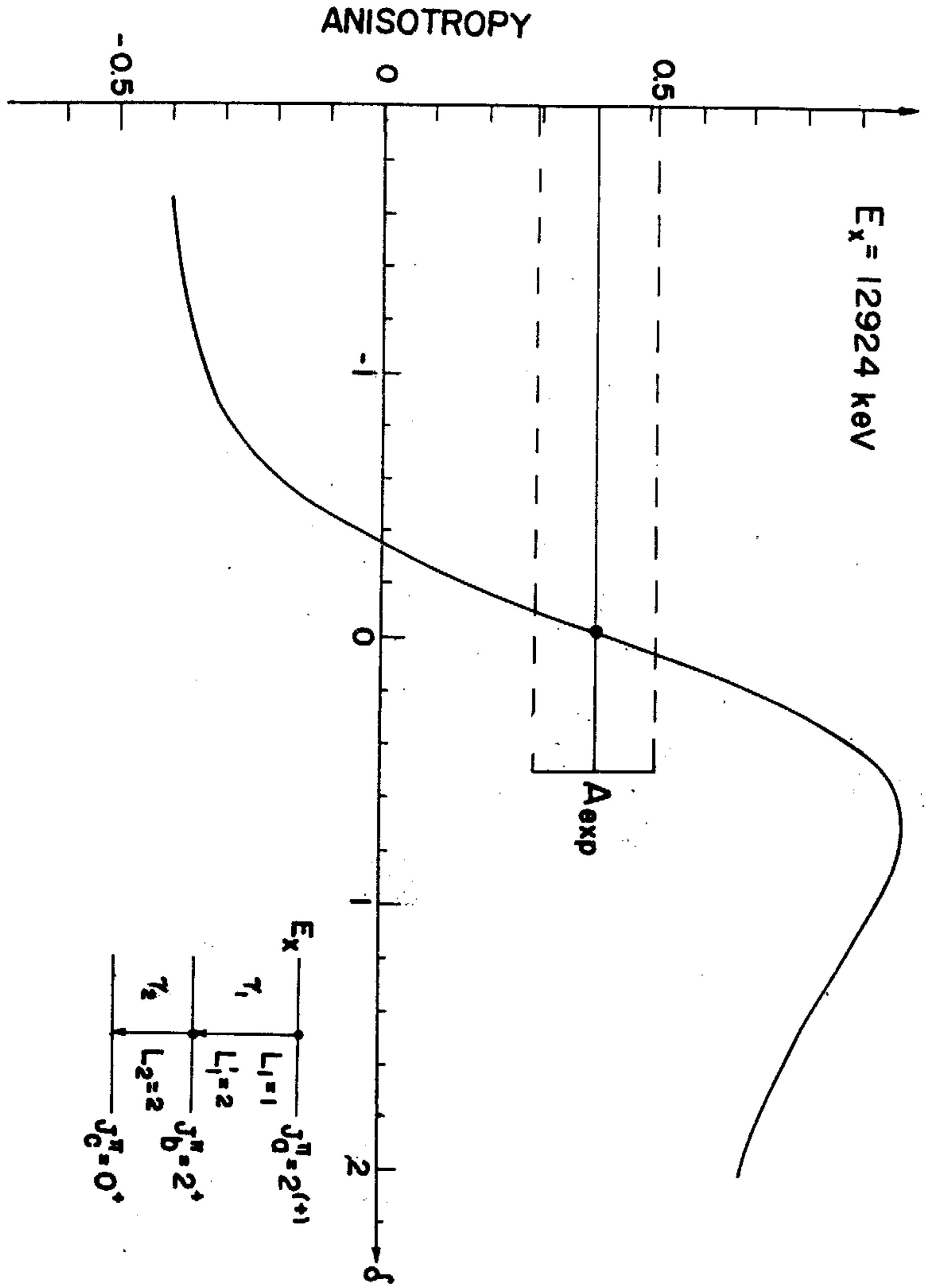

Fig. 6

Fig. 6 The anisotropy A(δ) for J_a=2, L_1=1, L_1'=2. The dotted lines represent the region of the experimental values for the resonance at E_p=1388 keV in the ^{27}A(p,γ)^{28}Si reaction.

METHOD OF RADIO WAVE COUPLING FOR PRECISE SIZE EFFECT MEASUREMENT

Yu-Tung Yang

Physics Institute, Academia Sinica, Nankang

Taiwan, Republic of China

Abstract

For power absorption line shape study in the RF range a condenser coupled transmitter receiver system has been designed. The RF size effect indicates a result that agrees with other types of results reasonably well. The crossed coil coupling method which has been used for NMR study is found not suitable for the size effect experiment at all.

Introduction

The crossed-coil coupling method of a fixed radio wave transmitter receiver system has been used for years for high resolution NMR measurements(1),(2),(3). We tried the same technique on the size effect experiment based on the theory deduced by Fischer and Kao(4),(5), but we could only obtain qualitative results and meanwhile, the RF marginal oscillator method for signal detection used before(4) is already ruled out for such a line shape study for good reasons(4,5). It was realized only recently that even the fixed frequency crossed-coil coupling method did not work so well as expected as far as the solid state size effect experiment is concerned. According to the size effect theory(4), the RF power absorption line shape should be symmetrical with respect to both directions of the applied DC magnetic field, because the magnetoresistance is a function of H^2. When the experiment is carried out, the sample being tested is put in a slab receiver coil whose axis is perpendicular to the DC magnetic field H. If the electric field of the receiver coil is E″ and the magnetic field H″, then the theoretical requirement is $H \perp E'' \perp H''$, and nothing else.

In fact, the crossed-coil technique can not fulfill the theoretical requirement because there are extra interfering electric field E′ and magnetic field H′ of the transmitter coil which make the strict $H \perp E'' \perp H''$ impossible. The result of an experiment based on the crossed-coil technique is shown in Fig. 1.

In order to avoid the complicacy, we abandon the crossed-coil technique and use

---

** Because a diode was used for making the record.

the new condenser (charge) coupling method instead, (Fig. 2). Since there is no more transmitter coil, therefore the interfering fields due to the transmitter coil disappear.

The size effect* is so strong that no lock-in amplifier is needed, and the arm of the probe head can be extended to 20 inches without difficulty.

Fig. 3 shows the RF sine wave oscillation in the receiver tank.

Fig. 4 shows the correct size effect power absorption curve which is symmetrical with respect to ± H field. It is due to the new condenser coupling technique. The curve is for demonstration only.**

The signal detection by a diode is not good for line shape study either because of the nonlinear characteristic of the diode. The power absorption curve can be determined by recording the RF output voltage amplitude A, which is shown on the screen of the Tektronix 7403N oscilloscope. The oscilloscope has been calibrated. Our aim is to find the A^2 vs. H curve.

Fig. 5 shows the experimental result (one typical example) compared with the theoretical calculation (solid line). The curve matching(5) shows the characteristic value of the curve $\Delta = 5.2$, and from the value of Δ we obtain(4),(5) the size effect mobility of electrons in InSb, $\mu = 6.8 \times 10^4$ cm^2 volt^{-1} sec^{-1}, and the corresponding carrier concentration $n = 3.1 \times 10^{16}$ cm^{-3}. The DC galvanomagnetic measurements done in this laboratory show that $\mu_{DC} = 6.1 \times 10^4$ cm^2 volt^{-1} sec^{-1}, and $n_{DC} = 1.7 \times 10^{16}$ cm^{-3}. The error of the size effect measurement is less than 10% due to curve fitting, and that of the classical galvanomagnetic measurements is less than 15% due to voltage measurements. All the values are obtained at 300° K.

Fig. 6 shows the 8 digits fixed frequency NMR pattern of pure H_2O obtained by using the new condenser coupling technique. The circuit for that experiment is also simple and is designed according to a new circuit principle. The detail of the spectrometer will be published soon elsewhere.

Acknowledgement

I am very grateful to the National Science Council, Republic of China, for the support of the project.

Reference

(1) F. Bloch, W. W. Hansen, and M. E. Packard, Phys. Rev., **70**, 474, 1946.

(2) W. G. Proctor and F. C. Yu, Phys. Rev. **77**, 716, 1950.

(3) A. K. Saha and T. P. Das, "Theory and Applications of Nuclear Induction", Saha Institute of Nuclear Physics, Calcutta, India, 1957.

(4) H. Fischer and Y. H. Kao, Solid State Comm. **67**, 275, 1969, and Bull. Am. Phys. Soc. **12**, 533, 1967.

(5) Y. T. Yang, H. T. Ho, C. C. Pei, S. C. Yang and B. S. Yu, Il Nuovo Cim. **16**,**B**,188, 1973.

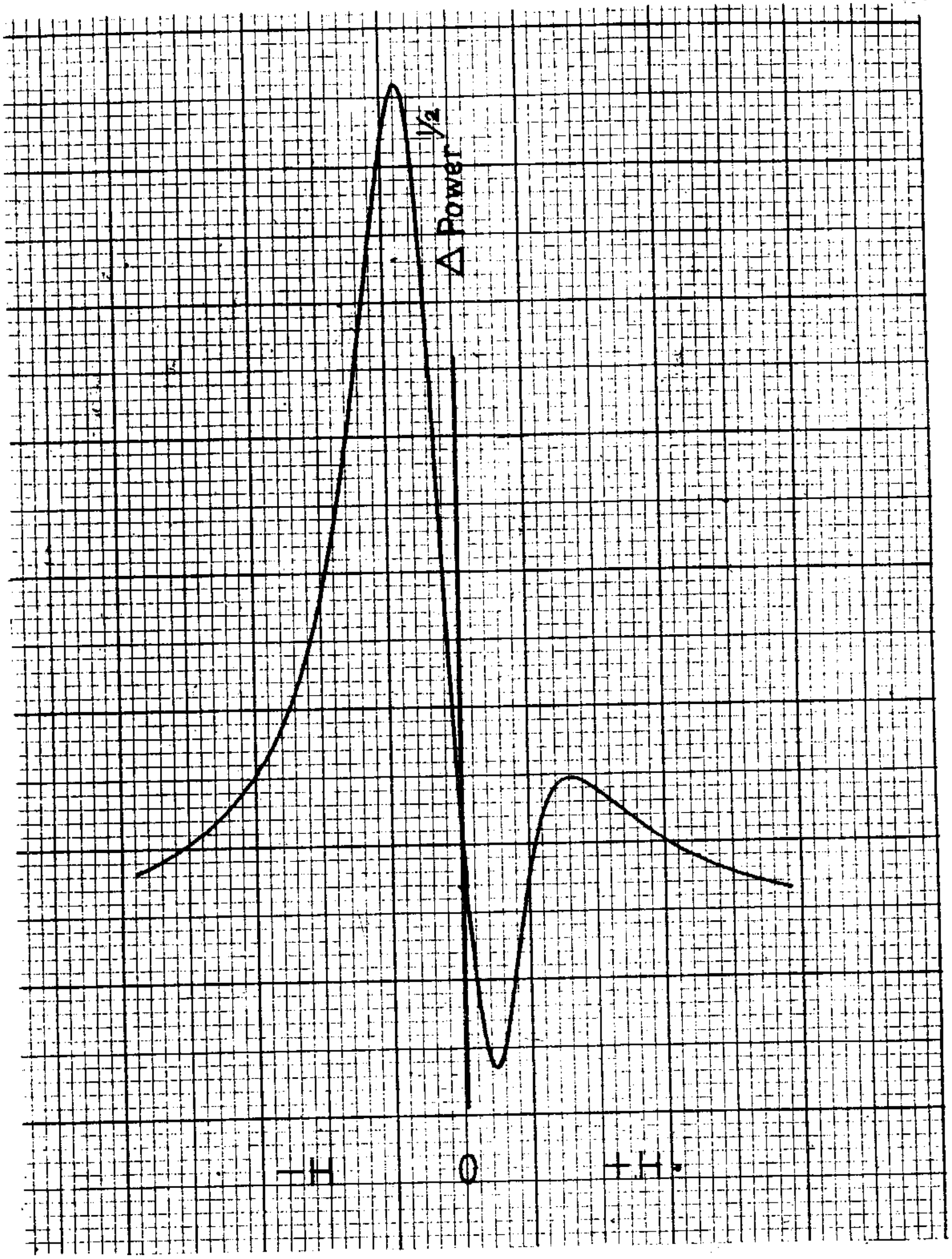

Fig. 1

Fig. 1 Result of a size effect experiment based on the crossed-coil technique. The power absorption curves are asymmetrical with respect to the DC magnetic field ± H.

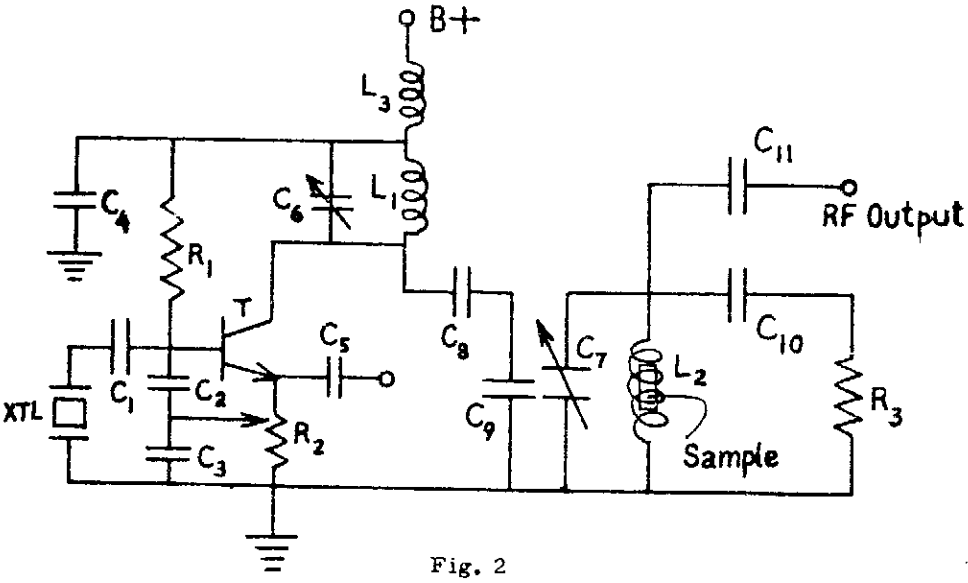

Fig. 2

Fig. 2 Fixed frequency transmitter receiver system coupled by condensers. In the circuit, $C_1 = C_2 = C_3 = 33$ pf, $C_4 = 220$ pf, $C_5 = 47$ pf, $C_6 = C_7 = 5$ to 100 pf, fine tuning, $C_8 = 100$ pf, $C_9 =$ 5 to 10 pf and is coupled with C_7, and yet C_7 is tunable, $C_{10} = 100$ pf, $C_{11} = 100$ pf, C_{11}, when connected with HP 7403N oscilloscope, is for the RF output wave amplitude A observation, and when connected with HP 5245L frequency counter, is for the frequency measurement. Moreover, $R_1 = 220$ k-ohm, $R_2 = 0$ to 1 k-ohm, fine tuning, $R_3 = 100$ k-ohm, $L_1 = 18$ turn, silver wire, SWG 24, 1 cm dia. 30 mm long, $L_2 = 18$ turn, close wound, SWG 24 copper wire. The cross section of L_2 is rectangular, the inner volume of the coil is 1.8 cm x 0.9 cm x 0.26 cm to fit the sample properly. L_3 = RF choke, mh order. T = BC409C or equivalent.

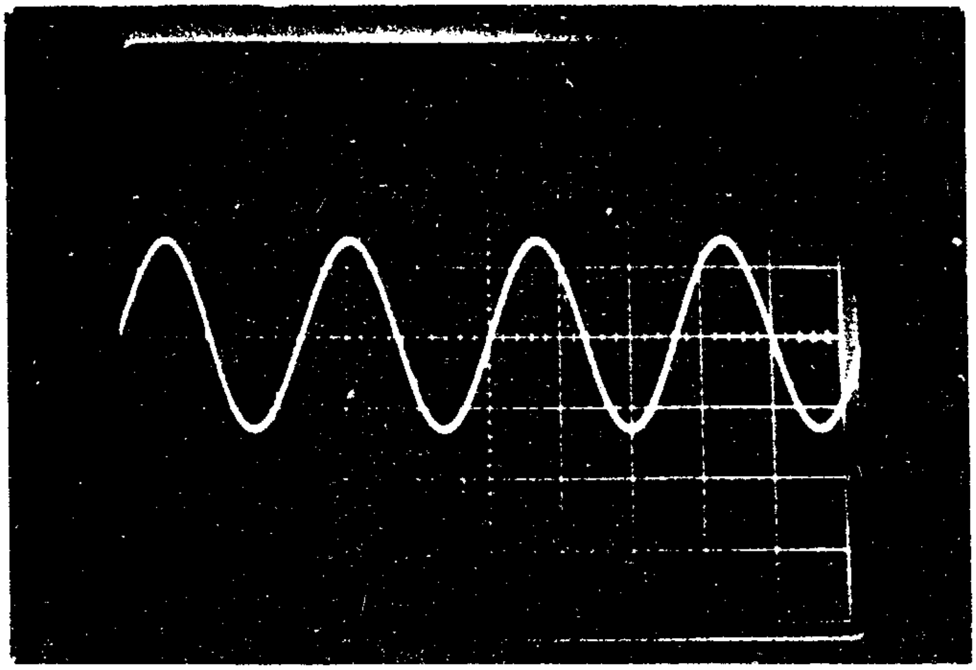

Fig. 3

Fig. 3 RF sine wave oscillation in the receiver tank circuit L_2C_7.

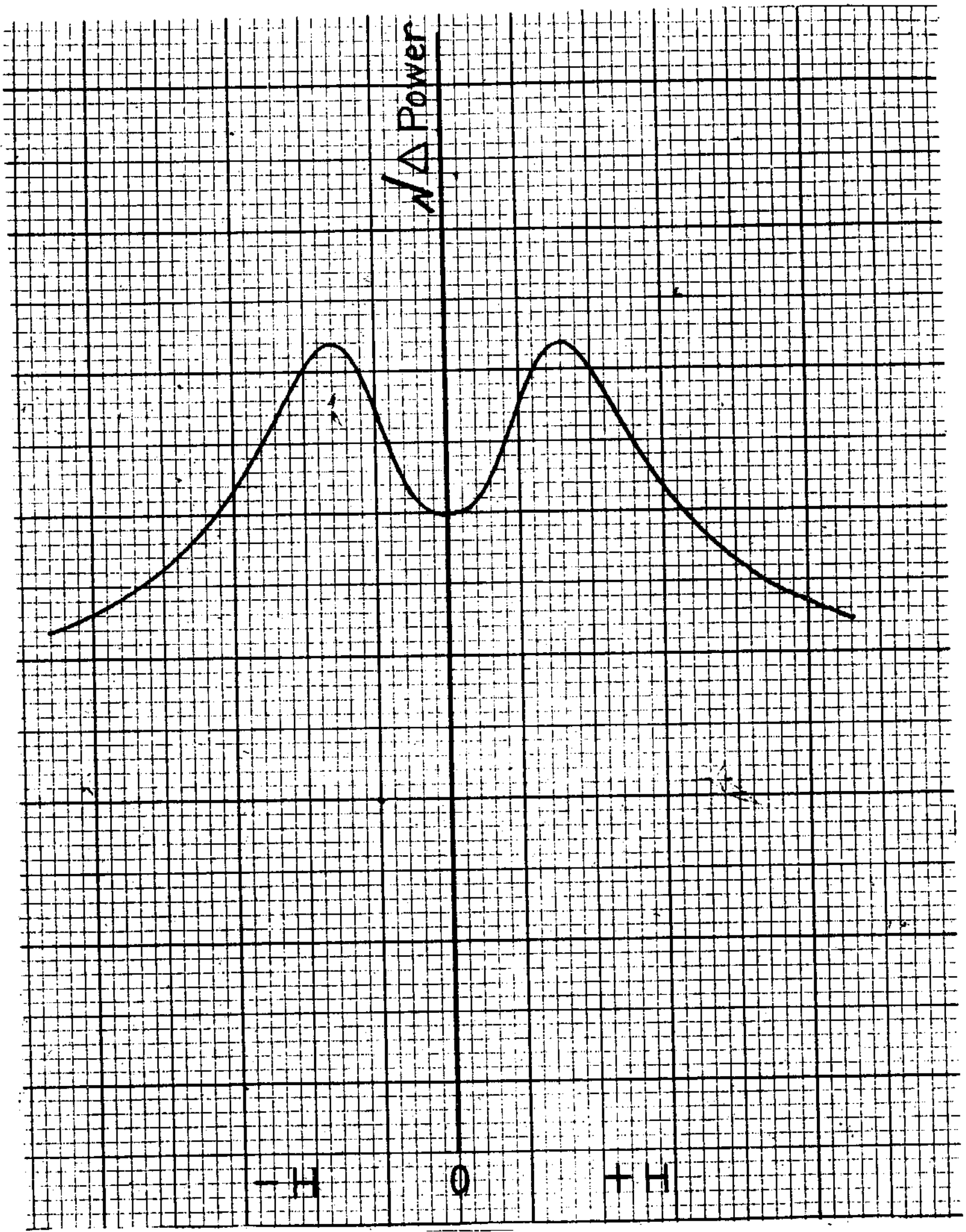

Fig. 4

Fig. 4 The correct size effect power absorption curves which are symmetrical with respect to the DC ± H field. It is due to the new condenser coupling technique.

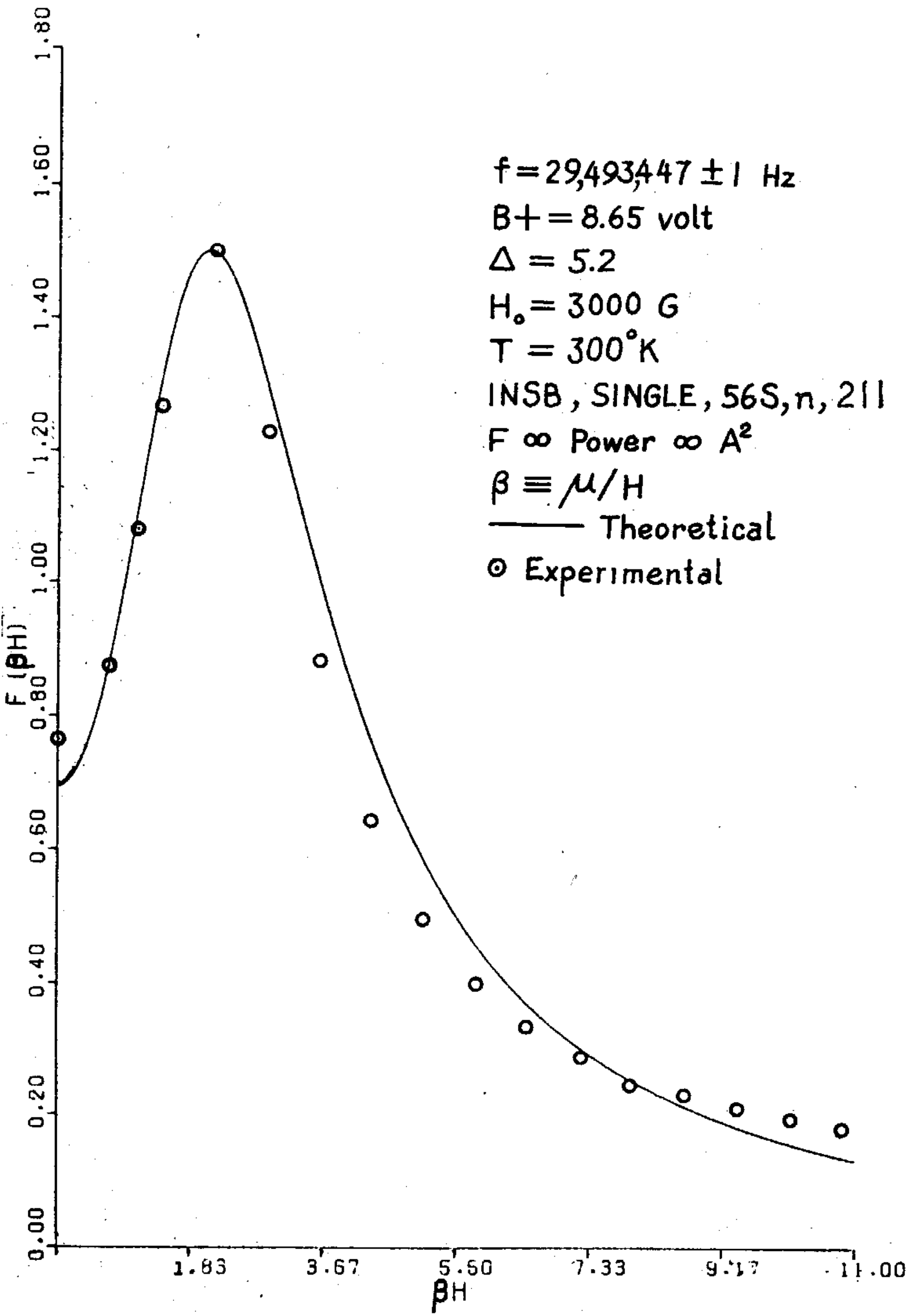

Fig. 5

Fig. 5 A typical experimental result. The solid curve is due to theoretical calculation. The dots are the experimental A^2 vs. βH points.

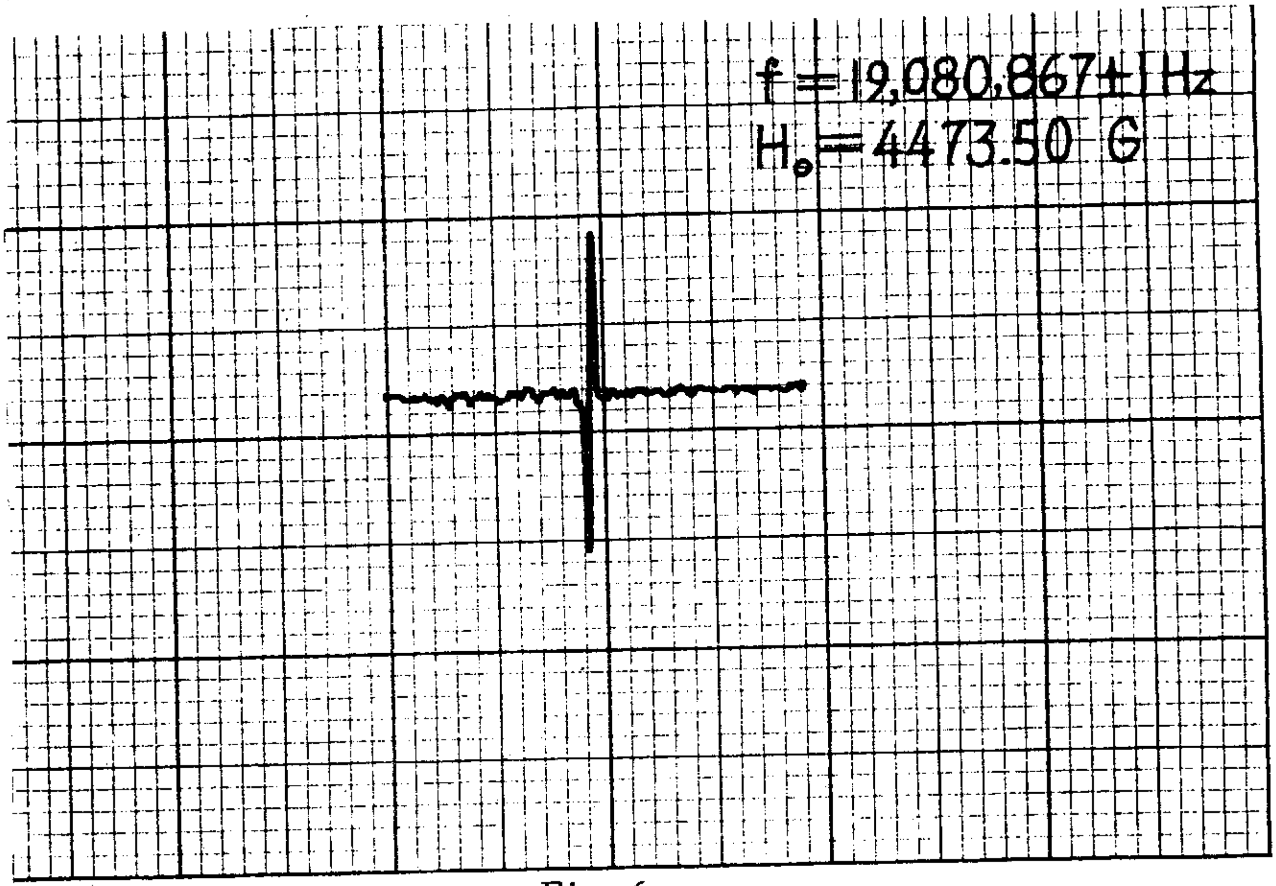

Fig. 6

Fig. 6 NMR pattern of pure H_2O obtained by using the new condenser coupling technique. The frequency is arbitrarily fixed at 19,080,867 ± 1 Hz. The simple circuit for such an experiment will be shown soon elsewhere. The NMR pattern shows the usefulness of the condenser coupling technique as far as the line shape study is concerned.

ELECTRONIC CONDUCTIVITY AND PERCOLATION THEORY IN ULTRA THIN FILMS*

N. T. Liang and Shou-Yih Wang
Solid State Phys. Division, Institute of Physics
Academia Sinica
The Republic of China

Abstract

Experiments on electronic conductivity in ultra thin films have been performed. The average potential Barrier of glass substrate as seen by tunnelling electrons of Bi particles was estimated. The nature of electronic conduction in aggregated Bi films was found likely to be described by percolation theory.

1. *Introduction*

It is well known that the resistivity of an aggregated film shows an abrupt fall over several orders of magnitude as the effective thickness of the ultra thin film increases from zero to a suitably thicker value. Neugebauer(1) displayed such a resistivity dependence on thickness of mercury films at various temperatures. R. M. Hill(2) has reported a series of papers specifically on the electric conduction in ultra thin metal films. Since the phenomena of huge abrupt change behave something like a percolation problem the electric conductivity is often related to percolation theory. Ambegaokar, Halperin and Langer(3) explained the conductivity dependence on temperature, the well known $T^{1/4}$ law of Mott's result, using a percolation approach to electronic hopping in disordered systems. Last and Thouless(4) applied classical percolation theory to the electric conductivity of a system of conducting paper with macroscopically punched holes. The purpose of this work is to provide a more natural, fully quantum mechanical system for testing the correlation between electric conductivity and percolation theory in addition to discussions on some properties of electronic tunnelling in the ultra thin films.

In section II we will give a short account of our experimental apparatus. In section III the unactivated tunnelling process will be described and an average potential barrier Φ will be determined specifically for Bi. In section IV we will concentrate on percolation

---

* This work was sponsored by National Science Council of The Republic of China.

problem and the critical probability will be given as a criterian that our Bi ultra thin film appear likely to be describable by percolation models. Finally in section V we will discuss some relevant problems and difficulties that we have encountered.

2. *Description of the Experiment*

Our experimental apparatus was mainly an ultra high vacuum evaporator (NEVA Type 507) with an electron-gun heating facility. We also used U.S. made varian vacuum system model 61 for evaporation. The vacuum of some 10^{-7} torr was mostly used. Typical experimental run was to evaporate film material with either e-gun or Ta boat to deposit adatoms on substrates usually of micro slide glass or quartz with indium electrodes previously made on them. The substrates were neither heated nor cooled. Measurement of resistance across the film with electrometer (Keithley 610B) was done gradually during the evaporation. The rate of evaporation was controlled rather slow of about 10 Å/min to allow for careful reading of the resistance change with the film thickness. The thickness of film was monitored with a microbalance whose output was coupled to an electronic frequency counter model (HP5245L). The calibration of such microbalance was made by use of a multi-beam interference microscope with resolution of about ±30 Å.

A scanning electron microscope had been used with no result because the conductivity of our aggregated film was too low to allow sufficient electron beam for observation. Another factor was insufficient contrast since our films were ultra thin, or in other words they were too even to observe variations of the aggregated islands with respect to the substrate surface. However, transmission electron microscope was employed to offer better and direct observation of the island films. We have also evaporated SiO to support the film(5) for handling in using the transmission electron microscope.

We have evaporated several kinds of metallic elements as our aggregated films. In particular, we found semi-metal bismuth films formed a type of structure with relatively large islands (or particles) and relatively small separations. As R. M. Hill noted(2), this type (type III according to his classfication) was hard to make experimentally and very little experimental data have been reported yet. The feature of this type of film is that the electronic conductivity is predominated by substrate tunnelling without the need of activation energy. From transmission electron microscope observation we estimated its average particle size to be 160 Å, its average separation to be 17 Å for one Bi film. It was also this type of film structure that made the resistivity-thickness curve drops much faster than other metal films.(5) Thus we report mainly in this article relevant properties of ultra thin films of Bi.

3. *Tunnelling Conductivity in Bismuth Ultra Thin Films*

According to R. M. Hill(2), the state of ultra thin films may be classified into 4 types: (I) small size of particle, small gap; (II) small size, large gap; (III) large size, small gap and (IV) large size, large gap. The tunnelling process would occur only in type (I) and type (III) films due to the small gap between 2 metallic particles or islands so that the tunnelling probability is large enough. If the particle size is small (e.g. smaller than 100 Å, see ref. 2) which is the case for a number of metallic elements, the activation energy δE is large, $\delta E > KT$, (K the Boltzman constant, T the absolute temperature). This tunnelling process is known as activated tunnelling. On the contrary when particle size is as large as the Bi film we made, the E is small and the tunnelling is practically unactivated. It is just the tunnelling processes which depend exponentially on particle separations (or gaps) that the resistivity exhibites sudden change for several orders of magnitude for a thickness change of only about 10 angstroms.(5) If we think of WKB approximation(6) for the tunnelling, the average barrier height Φ of the substrate as seen by tunnelling electrons must appear exponentially in the formula of conductivity or resistivity for the tunnelling currents. For detailed formula we simply employ Hill's result(7) for unactivated tunnelling:

$$J(V,T) = \frac{3.95 \times 10^{10}\Phi}{(\Delta S)^2}\ Sinh\left(\frac{eV}{KT}\right) \cdot \frac{(\pi BKT)^2}{Sin(\pi BKT)} \cdot \frac{KT}{\delta E} \cdot exp\{-1.025\Delta S(m^*\Phi)^{1/2}\} \qquad (1)$$

To compare with our experimental results, this equation may be rewritten in the following form:

$$\ell_n(J/V) \cong -1.025\Delta S(m^*\Phi)^{1/2} - 2\ell_n(\Delta S) + constant \qquad (2)$$

in which we have used low field approximation $eV \ll KT$ (V the applied potential difference between 2 particles) and neglected the activation energy (δE) dependence upon ΔS (Justified for type III films). The notations and units for the above equation are: J the current density in amp/cm^2, V in volts, ΔS the reduced barrier width in angstroms. Φ the overall effective average potential barrier in electron volts, m* the effective mass of the tunnelling electron in units of rest electron mass. Further simplification allows us to write

$$\frac{\partial \ell_n \sigma}{\partial(\Delta S)} = -1.025\sqrt{m^*\Phi} - \frac{2}{\Delta S} \cong -(\Phi)^{1/2} - \frac{2}{\Delta S} \qquad (3)$$

in which the conductivity of the ultra thin film $\sigma = \text{constant} \times \frac{J}{V}$ is used and m^* is taken to be unity.

In figure (1), we show the plot of $\ln\sigma$ vs ΔS in order to be able to compare with eq. (3). From this figure and eq. (3) clearly we should choose the slope of the lower portion for $(\Phi)^{1/2}$ since it is practically independent of ΔS. The result of Φ is thus

$$\Phi = 0.88\, eV. \tag{4}$$

We must note that the plot of Fig. (1) is based on electron microscope findings and a model of simple particle distribution on substrate. The model assumed particles of spherical shape and of uniform size and located uniformly with equal spacings. Changes in ΔS follow with the change in effective film thickness and in turn with the conductivity. We remark here that this simple model does allow us to look into the islands of the film and that the data both from evaporation process and from electron microscope are in good agreement with this model. Further, the value of eq. (4) appears reasonable if we compare Hill's result$^{(8)}$.

4. *Pereolation and Electrical Conductivity*

As mentioned before the sudden drop of resistivity for several orders of magnitude as film thickness starts to increase suggests a kind of percolation phenomenon to occur. Among a number of investigators, Ambegaskor et al. treated very successfully the hopping conductivity problem in a three dimensional disordered system.$^{(3)}$, Last and Thouless$^{(4)}$ tested the porcolation theory by punching holes randomly in a sheet of colloidal graphite paper and measuring the conductivity. They claimed the conductivity to behave quite different from that of percolation probability. However, as they noted, punching holes of macroscopical size is of classical nature. It therefore awaits a quantum mechanical case to further resolve the percolation and electrical conductivity.

In our evaporation experiment, metallic particles or islands are formed during evaporation on the plane surface of some insulating substrate. The transition probability that an electron in a certain particle hops into a neighboring particle depends mainly on the separation between the two particles and the difference of the fermi levels of the two particles. When the evaporated particles on the substrate are only few in number the conductivity is practically zero (assuming the substrate is a perfect insulator). As more and more particles are randomly formed with closer and closer spacings on the substrate this transition probability increases and eventually reaches a value such that the network formed by all those island-particles is critically connected. By "critically connected" here we mean that the electron wavefunction of the system is no longer localized but starts to be in Bloch form. At this state of film the resitivity would drop several orders of magnitude within some 10Å of change in film thickness. The conductivity in units of bulk conductivity of the film material (σ/σ_b) would suddenly rise from practically zero to some finite value. The electrical conductivity of the ultra thin film thus behaves somewhat like the percolation probability P(p) and the effective film thickness (or equivalently, the randomly-distributed-islands mass per unit area or more precisely the fraction of the substrate surface area occupied by islands) acts somewhat like the probability p in percolation problems.

To determine whether it is a percolation problem in a similar fashion as Last and Thouless did we made enlargement of transmission-electron-microscope photo pictures of a Bismuth island film. We chopped off portions of the enlarge picture which correspond to the area occupied by Bi particles we then weighed these portions against the total weight of the picture and estimated the fractiona p of the area occupied by metallic islands. The fraction was 70%. Let us use monte carlo estimates of percolation Probabilities for various 2 dimensional lattices as given by Frisch et al.$^{(9)}$ We read from their curves the atom and bond critical probabilities p_c^A, p_c^B, with lattices:

Square lattice : $p_c^B = 0.487$, $p_c^A \cong 0.57$,
Triangular lattice : $p_c^B \cong 0.33$, $p_c^A \cong 0.48$
Hexagonal lattice : $p_c^B \cong 0.62$, $p_c^A \cong 0.66$.

In comparison with the tabulated values our value 0.70±0.04 is rather close to the atom percolation of hexagonal lattice. Furthermore, since the distribution of particles is of random nature, it is very likely that the tunnelling electronic conductivity in Bi island film was a percolation problem. Clearly. the films were of two-dimensional nature because the critical probabilities for three-dimensional lattices are much smaller.

5. *Remarks and Discussions*

Several points are worthy to mention in the following. In using the titanium sublimation pump we were suspecious that the substrate surface was considerably contaminated by titanium atoms. This was overcome to some extent by using a close shade to cover the substrate before evaporation. However, the titanium-adatom contamination deserves a separate study itself.

In the high impedance measurement of island-film resistance, the shunt impedance of the feedthrough (which the lead wires of island-film in vacuum system were connected out in open air for easy measurement) was found considerably low. As the result we could not use those data for such high impedance region.

The calibration of our thickness monitor showed some difference between the films made by e-gun and those by Ta-boat heating. The thickness of e-gun-made films as observed by our interference microscope were found thinner than those of boat-made ones when microbalance monitor recorded the same frequency difference. The reason, we believe, was that the e-gun-made films had larger mass densities.

Acknowledgement

The authors wish to thank Professors Y. C. Lee, F. Y. Wu and I. L. Fu for their useful and stimulating discussions.

References

(1) C. A. Neugebauer, Phys. of Thin Films, Vol. 2, p.23 (1964).
(2) R. M. Hill, Proc. Roy. Soc. A, 309, 377-395, 397-417 (1969); contemp. Phys. Vol. 10, No. 3, 221-240 (2969).
(3) Vinay Ambegaokar, B. I. Halperin, J. S. Langer, Phys. Rev. B, Vol. 4, No. 8, p. 2612 (1971).
(4) B. J. Last and D. J. Thouless, Phys. Rev. Lett. Vol. 27, No. 25, p. 1719 (1971).
(5) N. T. Liang and Shou-yih Wang, Annual Rep. of Institute of Phys. Academia Sinica p. 163 (1971)
(6) Any textbook on Quantum Mechanics, e.g. L. I. Schiff, Quantum Mechanics, p. 184, Second Edition (1955).
(7) R. M. Hill, Proc. Roy. Soc. A, 309, p. 383 eq. (12), (1969).
(8) R. M. Hill, Proc. Roy. Soc. A, 309, p. 406, Table 2 (1969).
(9) H. L. Frisch, J. M. Hammersley, D. J. A. Welsh, Phys. Rev. Vol. 126, No..3, p. 949 (1962).

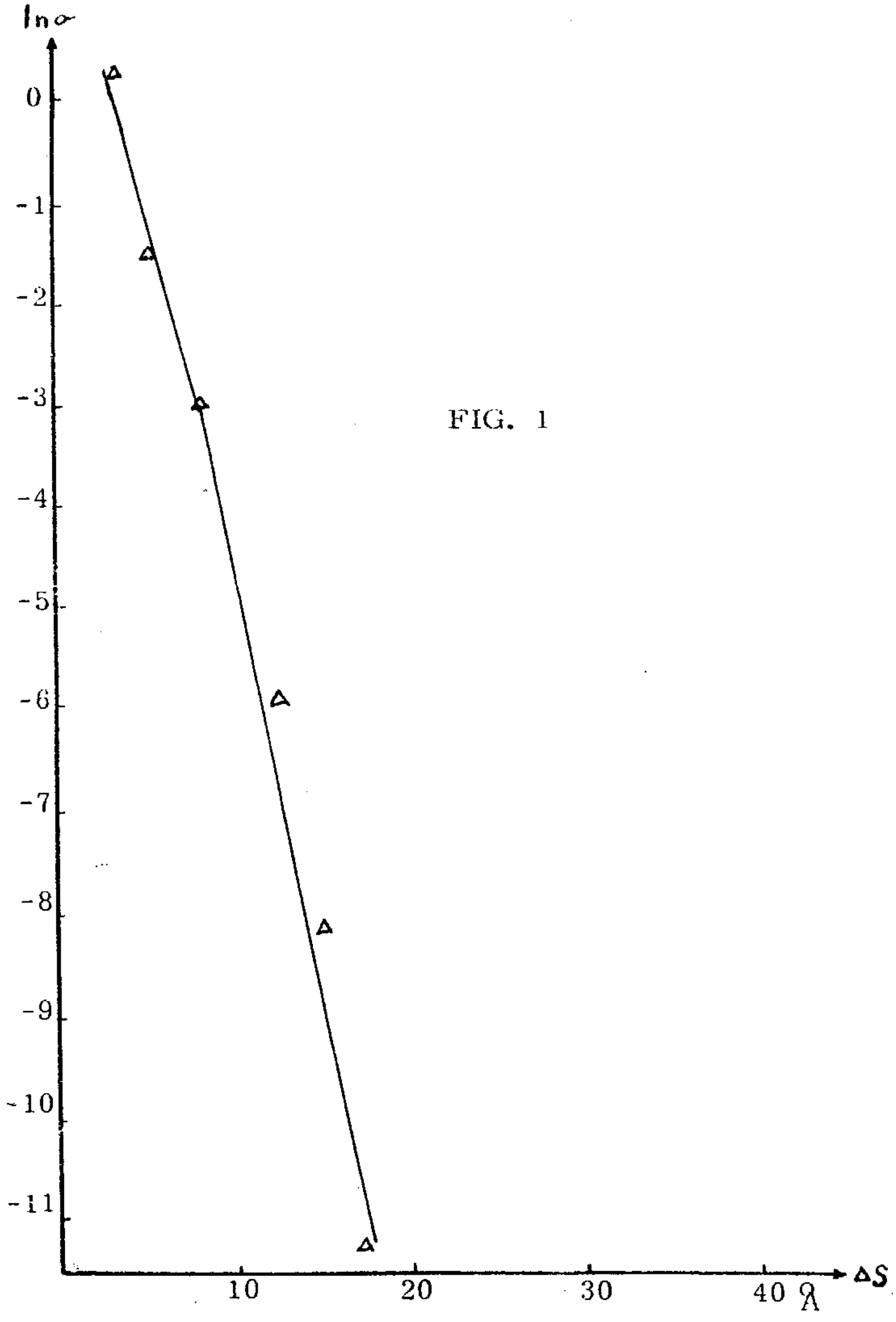

FIG. 1

THE PHASE TRANSITION PRESSURE FROM SOLID MOLECULAR HYDROGEN TO METALLIC HYDROGEN*

Wu-shyong Wu and Shou-yih Wang

Solid state Phys. Division, Institute of Physics
Academia Sinica
The Republic of China

July, 1974

Abstract

The energy-density relations for both the solid molecular hydrogen and metallic hydrogen are computed to explore the possibility of preparing metallic hydrogen under high pressures. The pressure necessary for the transformation is about 2 Mbars. Although the pressure seems to be unattainable with the present techniques, the realization of generating static pressure in excess of 2 Mbars is hopeful.

1. *Introduction*

Our work here is to explore the possibility of preparing metallic hydrogen under high pressure. Metallic hydrogen is of interest for two reasons. First of all, it is expected that the interior of Jupiter and Saturn contains 60 - 80% hydrogen. Under the influence of high gravitational pressures, the form into which hydrogen has condensed may well be metallic. In the second place, as was suggested by Ashcroft,(1) metallic hydrogen may well be a high-temperature superconductor.

To determine theoretically the pressure at which hydrogen undergoes a transformation from the usual molecular crystalline phase to a metallic phase, it is necessary to know accurately the equation of state, or energy-density relation, in the relevant phases. For the molecular crystalline phase, Krumhansl and Wu(2) (KW) performed zero-temperature, variational calculations using Jastrow-Gaussian function and an Ursell-Mayer Cluster expansion for evaluating energy expectation values. The results were somewhat higher than but in reasonably good agreement with experimental data, which are available at low densities. We(3) present another calculation of the energy-density relation for the molecular crystalline phase of hydrogen. The major difference of our work from that of KW lies in the cluster expansion procedure. We employ what is known as the quasicrystal

---

* This work is spousored by National Science Council of the Republic of China.

approximation$^{(4)}$ first developed in connection with solid helium. Such a procedure possesses better convergence properties and is expected to be more reliable expecially at high densities.

For the metallic hydrogen, it is a high-pressure form of hydrogen which may be metastable at atmospheric pressure. Although metallic hydrogen has not been found in nature, it presumably has properties similar to some of the alkali metals, and hence the equation of state can be calculated with reasonably accuracy. We then employ the equation of state of each material to predict the phase transition pressure from solid molecular hydrogen to metallic hydrogen.

2. *Energy-Density Relation for Solid Molecular Hydrogen*

Like Krumhansl and Wu (KW)$^{(2)}$, we begin with a correlated trial wave function:

$$\psi(\vec{\gamma}_1,\vec{\gamma}_2,\dots\vec{\gamma}_N) = \prod_{1\leqslant i\leqslant j\leqslant N} e^{\frac{1}{2}u(\vec{\gamma}_{ij})} \prod_{k=1}^{N} \phi(|\vec{\gamma}_K-\vec{R}_K|) \qquad (1)$$

The first factor on the right hand is known as a Jastrow function. It vanishes rapidly for small r to prevent the overlap of molecules. At large r, U(r) approaches 0 to signify the demise of short-range correlations. The second factor is a product of Gaussians, where

$$\phi(|\vec{\gamma}_K-\vec{R}_K|) = \left(\frac{\alpha}{\sqrt{\pi}}\right)^{\frac{3}{2}} e^{-\frac{1}{2}\alpha^2|\vec{\gamma}_K-\vec{R}_K|^2} \qquad (2)$$

allows the localization of molecules r_k about lattice sites R_K. The coefficient α is related to the width of the Gaussian, and is treated as a variational parameter. The expectation value of Hamiltonian H with respect to the trial function Ψ is to be minimized at each density by varying α and U(r). The Hamiltonian of a system of N H_2 molecules is given by:

$$H = \sum_{i=i}^{N} \frac{-\hbar^2}{2M}\nabla_i^2 + \sum_{1\leqslant i<j\leqslant N} V(\vec{\gamma}_i,\vec{\gamma}_j) \qquad (3)$$

where V represents a pairwise potential. The two-body potential is assumed to be the Lennard-Jones type:

$$V(\gamma) = 4\,\&\,\left[\left(\frac{\sigma}{\gamma}\right)^{12}-\left(\frac{\sigma}{\gamma}\right)^{6}\right] \qquad (4)$$

with $\quad \& = 37^{o}K, \quad \sigma = 2.93\text{Å}$

Our calculation is carried out for a face-centered cubic structure. Lattice summations are performed to include over 30 shells. Good convergence occurs about 10 shells. The densities considered range from 2.67×10^{-2} to $5.57 \times 10^{-2} A^{-3}$, which correspond to molar volumes ranging from 22.47 to 10.80 cm^3/mole. Table I shows the energy-density relations of solid molecular hydrogen for the Lennard-Jones 6 - 12 potential. R(A) denotes the nearest neighbor distance. The binding energy (4.72ev) of molecular hydrogen referred to seperated neutral atoms is not considered here.

Table I

R(A)	V(cc/mole)	E(10^{-14}erg/molecule)
3.75	22.47	-0.9348
3.607	20.00	-0.8655
3.483	18.00	-0.6668
3.356	16.10	-0.2173
3.285	15.10	0.2475
3.233	14.40	0.6900
3.149	13.30	1.7214
3.084	12.50	2.8818
2.982	11.30	5.5609
2.938	10.80	7.0763

3. *Energy-Density Relation for Metallic Hydrogen*

The ground state energy of metallic hydrogen has been calculated by a number of authors, notably Wigner and Huntington[(5)], who applied the Wigner-Seitz method to obtain an approximation solution for the Hartree-Fock equation and added to this solution an estimated "correlation energy". We calculated the ground-state energy of metallic hydrogen within the framework of a perturbation expansion by interpreting the perturbation series as that for two simple systems weakly interacting, one being the electron gas system, the other that of electrons moving in the periodic potential of the lattice neutralized by a uniformly distributed negative charge. For the calculation we use Rayleigh-Schrodinger perturbation theory, with the total of coulomb interactions as the perturbing term. The unperturbed Hamiltonian is the Kinetic energy operator and the perturbing term is

$$V = \tfrac{1}{2} \sum_{i \neq j}\sum \frac{e^2}{\gamma_{ij}} + \tfrac{1}{2} \sum_{i \neq j}\sum \frac{e^2}{R_{ij}} - \sum_{i}\sum_{j} \frac{e^2}{|\vec{\gamma}_i - \vec{R}_j|} \qquad (5)$$

in an obvious notation for the coulomb interaction. The capital R's give the positions of the fixed nuclei, the small r's the corrdinates of the electrons. By adding and subtracting terms to (5) the following expression is obtained:

$$V = V_p + V_{eg} + \tfrac{1}{2}\sum_{i\neq j}\sum \frac{e^2}{R_{ij}} - \tfrac{1}{2}\int\int \frac{e^2\rho^2\, d\vec{\gamma}_1\, d\vec{\gamma}_2}{\gamma_{12}} \tag{6}$$

where ρ is the average density of electrons, or positive charge, and

$$V_p = \sum_i \left[\int \frac{e^2\rho\, d\vec{\gamma}}{|\vec{\gamma}_i - \vec{\gamma}|} - \sum_j \frac{e^2}{|\vec{\gamma}_i - \vec{R}_j|}\right] \tag{7}$$

is the periodic potential energy of electrons moving through a lattice neutralized by a uniform background of negative charge. The term V_{eg} is the coulomb interaction of an electron gas, given by

$$V_{eg} = \tfrac{1}{2}\sum_{i\neq j}\sum \frac{e^2}{\gamma_{ij}} - \sum_i \int \frac{e^2\rho\, d\vec{\gamma}}{|\vec{\gamma}_i - \vec{\gamma}|} + \tfrac{1}{2}\int\int \frac{e^2\rho^2\, d\vec{\gamma}_1\, d\vec{\gamma}_2}{\gamma_{12}} \tag{8}$$

Finally, V may be written as

$$V = V_p - \langle V_p \rangle + V_{eg} + V_L \tag{9}$$

where V_L is the energy of a lattice of positive charge in a uniform background of negative charge. The expression for V_L is

$$V_L = \tfrac{1}{2}\sum_{i\neq j}\sum \frac{e^2}{R_{ij}} - \sum_i \int \frac{e^2\rho\, d\gamma}{|\vec{\gamma} - \vec{R}_j|} + \tfrac{1}{2}\int\int \frac{e^2\rho^2\, d\vec{\gamma}_1\, d\vec{\gamma}_2}{\gamma_{12}} \tag{10}$$

After some calculations, the final result of the ground state energy for the N-electrons is given by

$$E = V_L + E_{eg}(o) + [E_p(o) - \epsilon_o - \langle V_p \rangle] + 0.001N\gamma_s + O(\gamma_s^2\,,\ \gamma_s^2 \ell_n \gamma_s) \tag{11}$$

where ϵ_0 is the Fermi energy of free electrons, $E_{eg}(0)$ is the ground state energy of the electron gas. Table II shows the energy-density relations for metallic hydrogen, r_s denotes the nearest neighbor distance. Our calculation is carried out for a body-centered cubic structure.

Table II

r_s (Å)	V(cc/mole)	E(10^{-12}erg/atom)
1.0051	0.4686	-0.9146
0.9522	0.3996	-1.0889
0.8993	0.3378	-1.1977
0.8464	0.2802	-1.1324
0.7935	0.2317	-0.9364
0.7406	0.1878	-0.6533
0.6877	0.1506	0
0.6348	0.1182	0.9364
0.5819	0.0912	3.0488

4. *Results and Discussion*

In order to predict accurately the phase transition pressure from molecular hydrogen to metallic hydrogen, it is necessary to know the energy-density relation of each material. The transition pressure is found from the common tangent to the energy-density curves for both metallic and molecular hydrogen (Maxwell construction). The pressure necessary for the transformation is about 2 Mbars. Because metallic hydrogen has a simple electronic structure and a high electron density, the potential energy of this system and hence the equation of state can be calculated with reasonable accuracy. However, calculations of the equation of state of the molecular phase are more difficult, and it is necessary to have detailed experiment work available. The pressure under which metallic hydrogen would be stable seems to be unattainable with the present techniques, but the hope for generating static pressure in excess of 2 Mbars is possible in the future. The energy of a body-centered metallic lattice have been calculated only. We hope that another metallic lattice may be much more stable.

References

(1) Ashcroft, N. W., Phys. Rev. Lett. 21, 1748 (1968).

(2) Krumhansl, J. A. and Wu, S. Y., Phys. Lett. 28A, 263 (1968).

(3) Wu, W. S. and Wang, S. Y., Annual Report of the Institute of Physics, Academia Sinica Vol. 3, 73 (1972).

(4) Woo, C. W. and Massey, W. E., Phys. Rev., 177, 272 (1969).

(5) Wigner, E. and Huntington, H. B., J. Chem. Phys. 3, 764 (1935).

INFRARED ABSORPTION SPECTRA OF ATMOSPHERIC WATER VAPOR AND CARBON DIOXIDE IN THE REGION FROM 2.5 TO 40 MICRONS

L. T. Ho (何侗民) and S. S. Tai (戴嵩山)
Institute of Physics
Academia Sinica
The Republic of China

Abstract

The infrared absorption spectra of atmospheric water vapor and carbon dioxide in the region from 2.5 to 40 microns have been measured. Some 600 absorption lines are illustrated in 5 spectrograms and wavelengths, both measured and calibrated, are tabulated.

1. *Introduction*

The vibration-rotation spectra of water vapor and carbon dioxide make a very important contribution to atmospheric absorption in the infrared region. These infrared absorption spectra have been studied and reported by many observers. Due to the improvement of the instruments used in recent years, the wavelengths of the absorption lines can be determined quite precisely. The purpose of this report is to present the vibration-rotation spectra of atmospheric water vapor and carbon dioxide in the region from 2.5 to 40 microns. The wavelengths of the absorption lines, both measured and calibrated comparing with the standard values published in journals, are also tabulated and presented in this report.

2. *Experimental Method and Result*

A Perkin-Elmer grating spectrometer, Model E-13, was used for measuring the spectra. The spectrometer is a building-block system covering the spectral region from the near infrared at 2 microns to the far infrared at 40 microns. The system includes a high resolution grating monochromator, solid-state electronics, light source, detector, recorder, and other related components.

The monochromator, Perkin-Elmer Model E-1, is an Ebert mounted system, linear in wavelength, and operates in double pass. Measurements were made with four plane, replicated diffraction gratings, with 288, 144, 57.6 and 28.8 lines/mm, respectively. All the gratings have 84 by 84 mm ruled areas, ruled on 90 by 90 mm blanks. The gratings are used only in the first order to simplify the problem of filtering out unwanted grating orders and also to minimize the possibility of double diffraction. Wavelength is scanned by rotating the diffraction grating, which is mounted on a heavy table which, in turn, is rotated by means of a reinforced arm riding against a barrel cam. The cam is cut to a sine function so that scanning is linear in wavelength.

Glower is used as the radiation source, which is externally chopped with frequency of 13 cycles per second. To remove higher orders of diffracted radiation than the first, a set of filters is used. A Perkin-Elmer vacuum thermocouple with a cesium-iodide window is used as the detector. Signal from the detector is amplified and the data output is obtained from a Leeds and Northrup Speedomax Model W strip chart recorder.

Absorption Spectra of water vapor and carbon dioxide in the region from 2.5 to 40 microns were measured. All measurements were made under atmospheric conditions of temperature about 23°C and relative humidity about 43-46%. Following are the list of the gratings used, the regions and the spectra measured:

	Grating used (Lines/mm)	Region measured (Micron)	Spectrum measured
(1)	288	2.5-2.9	water vapor
(2)	144	4.95-7.65	water vapor
(3)	57.6	14-16	carbon dioxide
(4)	57.6	16.6-20	water vapor
(5)	28.8	19-40	water vapor

Some 600 lines were measured. They are tabulated and illustrated in five spectrograms. The wavelengths of the lines measured have been corrected after comparing with the standard values published in journals. In cases (1), (2) and (3), comparison is made with the work of Plyer, Danti, Blaine and Tidwell (Journal of Research of the National Bureau of Standards – A. Physics and Chemistry, Vol. 64, No. 1, 1960, p. 29). In cases (4) and (5), values are compared with the work of Blaine, Plyer and Benedict (Journal of Research of the National Bureau of Standards – A. Physics and Chemistry, Vol. 66A No. 3, 1962, p. 223). The absorption spectra measured and the wavelengths, both measured and calibrated, are included in this report.

Absorption Lines of Water Vapor with Grating 288 lines/mm
Wavelength from 2.5 to 2.9 micron

Line Serial Number.	Wavelength Measured (micron)	Wavelength Calibrated (micron)	Line Serial Number.	Wavelength Measured (micron)	Wavelength Calibrated (micron)
1	2.5019	2.5031	27.	2.5429	2.5441
2.	2.5034	2.5046	28.	2.5438	2.5450
3.	2.5046	2.5058	29.	2.5444	2.5456
4.	2.5058	2.5070	30.	2.5465	2.5477
5.	2.5110	2.5122	31.	2.5470	2.5482
6.	2.5137	2.5149	32.	2.5477	2.5489
7.	2.5144	2.5156	33.	2.5498	2.5510
8.	2.5150	2.5162	34.	2.5514	2.5526
9.	2.5160	2.5172	35.	2.5522	2.5534
10.	2.5162	2.5174	36.	2.5589	2.5601
11.	2.5182	2.5194	37.	2.5594	2.5606
12.	2.5230	2.5242	38.	2.5602	2.5614
13.	2.5243	2.5254	39.	2.5618	2.5630
14.	2.5253	2.5265	40.	2.5634	2.5646
15.	2.5262	2.5274	41.	2.5642	2.5654
16.	2.5272	2.5284	42.	2.5668	2.5680
17.	2.5285	2.5297	43.	2.5677	2.5687
18.	2.5305	2.5317	44.	2.5689	2.5701
19.	2.5316	2.5328	45.	2.5724	2.5736
20.	2.5320	2.5332	46.	2.5734	2.5746
21.	2.5340	2.5352	47.	2.5739	2.5751
22.	2.5350	2.5362	48.	2.5761	2.5773
23.	2.5375	2.5387	49.	2.5780	2.5792
24.	2.5379	2.5391	50.	2.5817	2.5829
25.	2.5406	2.5418	51.	2.5828	2.5840
26.	2.5419	2.5531	52.	2.5833	2.5845

53.	2.5856	2.5867	86.	2.6375	2.6388
54.	2.5861	2.5872	87.	2.6404	2.6414
55.	2.5866	2.5877	88.	2.6413	2.6423
56.	2.5873	2.5884	89.	2.6432	2.6442
57.	2.5884	2.5895	90.	2.6449	2.6459
58.	2.5915	2.5926	91.	2.6458	2.6468
59.	2.5937	2.5948	92.	2.6504	2.6514
60.	2.5949	2.5959	93.	2.6516	2.6526
61.	2.5967	2.5977	94.	2.6546	2.6556
62.	2.5988	2.5998	95.	2.6553	2.6563
63.	2.5999	2.6009	96.	2.6560	2.6570
64.	2.6006	2.6016	97.	2.6569	2.6579
65.	2.6025	2.6040	98.	2.6589	2.6599
66.	2.6030	2.6040	99.	2.6594	2.6604
67.	2.6044	2.6054	100.	2.6611	2.6621
68.	2.6066	2.6076	101.	2.6631	2.6641
69.	2.6089	2.6099	102.	2.6641	2.6651
70.	2.6110	2.6120	103.	2.6658	2.6668
71.	2.6114	2.6124	104.	2.6673	2.6683
72.	2.6123	2.6133	105.	2.6673	2.6691
73.	2.6130	2.6150	106.	2.6690	2.6700
74.	2.6140	2.6150	107.	2.6700	2.6710
75.	2.6147	2.6157	108.	2.6718	2.6728
76.	2.6158	2.6168	109.	2.6740	2.6761
77.	2.6163	2.6174	110.	2.6751	2.6761
78.	2.6178	2.6188	111.	2.6760	2.6770
79.	2.6194	2.6204	112.	2.6764	2.6774
80.	2.6258	2.6368	113.	2.6768	2.6778
81.	2.6285	2.6295	114.	2.6775	2.6785
82.	2.6296	2.6306	115.	2.6786	2.6796
83.	2.6313	2.6323	116.	2.6802	2.6812
84.	2.6321	2.6331	117.	2.6812	2.6822
85.	2.6330	2.6340	118.	2.6817	2.6827

119.	2.6825	2.6835	152.	2.7206	2.7217
120.	2.6831	2.6841	153.	2.7234	2.7243
121.	2.6835	2.6845	154.	2.7249	2.7258
122.	2.6840	2.6850	155.	2.7270	2.7279
123.	2.6850	2.6860	156.	2.7313	2.7322
124.	2.6856	2.6866	157.	2.7359	2.7368
125.	2.6871	2.6881	158.	2.7366	2.7375
126.	2.6879	2.6889	159.	2.7378	2.7387
127.	2.6908	2.6918	160.	2.7381	2.7390
128.	2.6926	2.6936	161.	2.7391	2.7400
129.	2.6937	2.6947	162.	2.7408	2.7417
130.	2.6949	2.6959	163.	2.7423	2.7432
131.	2.6954	2.6963	164.	2.7440	2.7449
132.	2.6968	2.6977	165.	2.7445	2.7454
133.	2.6980	2.6980	166.	2.7450	2.7459
134.	2.6994	2.7003	167.	2.7466	2.7475
135.	2.7005	2.7014	168.	2.7479	2.7488
136.	2.7026	2.7035	169.	2.7489	2.7498
137.	2.7032	2.7041	170.	2.7499	2.7508
138.	2.7045	2.7054	171.	2.7510	2.7519
139.	2.7059	2.7068	172.	2.7525	2.7534
140.	2.7062	2.7072	173.	2.7532	2.7541
141.	2.7066	2.7075	174.	2.7542	2.7551
142.	2.7073	2.7082	175.	2.7550	2.7559
143.	2.7082	2.7091	176.	2.7560	2.7569
144.	2.7100	2.7109	177.	2.7574	2.7583
145.	2.7103	2.7112	178.	2.7583	2.7592
146.	2.7130	2.7139	179.	2.7590	2.7599
147.	2.7142	2.7151	180.	2.7595	2.7604
148.	2.7162	2.7171	181.	2.7606	2.7615
149.	2.7168	2.7177	182.	2.7618	2.7627
150.	2.7183	2.7192	183.	2.7632	2.7641
151.	2.7192	2.7201	184.	2.7651	2.7660

185.	2.7656	2.7665	218.	2.8061	2.8070
186.	2.7671	2.7680	219.	2.8071	2.8080
187.	2.7698	2.7707	220.	2.8080	2.8089
188.	2.7706	2.7715	221.	2.8104	2.8113
189.	2.7714	2.7723	222.	2.8130	2.8139
190.	2.7730	2.7739	223.	2.8147	2.8156
191.	2.7740	2.7749	224.	2.8157	2.8166
192.	2.7760	2.7769	225.	2.8174	2.8183
193.	2.7770	2.7779	226.	2.8200	2.8209
194.	2.7781	2.7790	227.	2.8200	2.8209
195.	2.7798	2.7807	228.	2.8206	2.8215
196.	2.7804	2.7813	229.	2.8209	2.8214
197.	2.7810	2.7819	230.	2.8215	2.8224
198.	2.7820	2.7829	231.	2.8268	2.8287
199.	2.7840	2.7849	232.	2.8310	2.8319
200.	2.7857	2.7866	233.	2.8315	2.8324
201.	2.7863	2.7872	234.	2.8328	2.8337
202.	2.7873	2.7882	235.	2.8337	2.8346
203.	2.7883	2.7892	236.	2.8343	2.8352
204.	2.7894	2.7903	237.	2.8355	2.8364
205.	2.7902	2.7911	238.	2.8360	2.8369
206.	2.7915	2.7924	239.	2.8367	2.8376
207.	2.7923	2.7932	240.	2.8377	2.8386
208.	2.7938	2.7947	241.	2.8408	2.8417
209.	2.7947	2.7956	242.	2.8420	2.8429
210.	2.7699	2.7975	243.	2.8456	2.8465
211.	2.7987	2.7996	244.	2.8467	2.8476
212.	2.7997	2.8006	245.	2.8474	2.8483
213.	2.8016	2.8025	246.	2.8485	2.8494
214.	2.8028	2.8037	247.	2.8490	2.8499
215.	2.8035	2.8044	248.	2.8525	2.8534
216.	2.8044	2.8053	249.	2.8529	2.8538
217.	2.8052	2.8061	250.	2.8537	2.8546

251.	2.8543	2.8552
252.	2.8550	2.8564
253.	2.8565	2.8574
254.	2.8590	2.8599
255.	2.8602	2.8611
256.	2.8658	2.8667
257.	2.8671	2.8680
258.	2.8679	2.8688
259.	2.8707	2.8716
260.	2.8721	2.8730
261.	2.8770	2.8779
262.	2.8816	2.8825
263.	2.8835	2.8844
264.	2.8870	2.8879
265.	2.8880	2.8889
266.	2.8888	2.8897
267.	2.8990	2.8999
268.	2.9000	2.9009
269.	2.9018	2.9027
270.	2.9035	2.9044
271.	2.9040	2.9049
272.	2.9121	2.9130
273.	2.9138	2.9147
274.	2.9164	2.9173
275.	2.9204	2.9213
276.	2.9211	2.9220
277.	2.9216	2.9225
278.	2.9226	2.9235

Absorption Lines of Water Vapor using Grating 144 lines/mm

Wavelength from 4.95 to 7.65 micron

Line Serial Number.	Wavelength Measured (micron)	Wavelength Calibrated (micron)	Line Serial Number.	Wavelength Measured (micron)	Wavelength Calibrated (micron)
1.	4.9607	4.9539	27.	5.3260	5.3190
2.	4.9610	4.9542	28.	5.3552	5.3482
3.	4.9652	4.9584	29.	5.3564	5.3494
4.	4.9880	4.9812	30.	5.3604	5.3534
5.	5.0100	5.0032	31.	5.3649	5.3579
6.	5.0249	5.0181	32.	5.3793	5.3723
7.	5.0273	5.0205	33.	5.3874	5.3804
8.	5.0358	5.0290	34.	5.4100	5.4030
9.	5.0906	5.0838	35.	5.4194	5.4124
10.	5.0926	5.0858	36.	5.4260	5.4190
11.	5.0956	5.0888	37.	5.4294	5.4224
12.	5.1218	5.1150	38.	5.4355	5.4285
13.	5.1448	5.1380	39.	5.4502	5.4432
14.	5.1475	5.1407	40.	5.4618	5.4538
15.	5.1545	5.1477	41.	5.4710	5.4640
16.	5.1575	5.5177	42.	5.4740	5.4670
17.	5.1800	5.1732	43.	5.4860	5.4790
18.	5.2068	5.2000	44.	5.4930	5.4960
19.	5.2090	5.2022	45.	5.5090	5.5020
20.	5.2204	5.2136	46.	5.5250	5.5180
21.	5.2425	5.2357	47.	5.5298	5.5228
22.	5.2480	5.2410	48.	5.5398	5.5328
23.	5.2584	5.2514	49.	5.5469	5.5399
24.	5.2837	5.2767	50.	5.5530	5.5460
25.	5.2990	5.2920	51.	5.5582	5.5512
26.	5.3138	5.3068	52.	5.5648	5.5568

53.	5.5670	5.5602	86.	5.8093	5.8025
54.	5.5720	5.5652	87.	5.8160	5.8092
55.	5.5755	5.5687	88.	5.8245	5.8177
56.	5.5778	5.5710	89.	5.8300	5.8232
57.	5.5858	5.5790	90.	5.8375	5.8307
58.	5.5908	5.5840	91.	5.8410	5.8342
59.	5.5990	5.5922	92.	5.8454	5.8386
60.	5.6190	5.6122	93.	5.8542	5.8474
61.	5.6234	5.6166	94.	5.8642	5.8574
62.	5.6283	5.6215	95.	5.8688	5.8620
63.	5.6385	5.6317	96.	5.8700	5.8632
64.	5.6485	5.6417	97.	5.8896	5.8828
65.	5.6520	5.6452	98.	5.8900	5.8832
66.	5.6623	5.6555	99.	5.8988	5.8920
67.	5.6830	5.6762	100.	5.9035	5.8967
68.	5.6934	5.6866	101.	5.9200	5.9132
69.	5.6995	5.6927	102.	5.9300	5.9232
70.	5.7118	5.7050	103.	5.9420	5.9352
71.	5.7164	5.7096	104.	5.9460	5.9510
72.	5.7230	5.7162	105.	5.9578	5.9530
73.	5.7266	5.7198	106.	5.9598	5.9530
74.	5.7280	5.7212	107.	5.9756	5.9688
75.	5.7304	5.7236	108.	5.9900	5.9832
76.	5.7350	5.7282	109.	5.9974	5.9906
77.	5.7385	5.7317	110.	6.0008	5.9940
78.	5.7420	5.7352	111.	6.0210	6.0142
79.	5.7434	5.7366	112.	6.0265	6.0197
80.	5.7552	5.7484	113.	6.0424	6.0356
81.	5.7620	5.7552	114.	6.0560	6.0492
82.	5.7720	5.7652	115.	6.0745	6.0677
83.	5.7760	5.7692	116.	6.0776	6.0708
84.	5.7780	5.7712	117.	6.0830	6.0762
85.	5.7875	5.7807	118.	6.0956	6.0888

119.	6.1030	6.0962	152.	6.5186	6.5122
120.	6.1138	6.1070	153.	6.5264	6.5200
121.	6.1200	6.1132	154.	6.5280	6.5216
122.	6.1220	6.1152	155.	6.5356	6.5292
123.	6.1500	6.1432	156.	6.5488	6.5424
124.	6.1664	6.1596	157.	6.5546	6.5482
125.	6.1798	6.1730	158.	6.5615	6.5551
126.	6.1877	6.1808	159.	6.5640	6.5576
127.	6.1928	6.1860	160.	6.5745	6.5681
128.	6.2205	6.2137	161.	6.5800	6.5740
129.	6.2288	6.2228	162.	6.5844	6.5784
130.	6.2438	6.2370	163.	6.5965	6.5905
131.	6.2518	6.2450	164.	6.5996	6.5936
132.	6.2714	6.2646	165.	6.6010	6.5950
133.	6.2780	6.2712	166.	6.6074	6.6014
134.	6.2885	6.2817	167.	6.6185	6.6125
135.	6.2964	6.2896	168.	6.6262	6.6202
136.	6.3520	6.3452	169.	6.6300	6.6240
137.	6.3770	6.3702	170.	6.6350	6.6290
138.	6.3965	6.3961	171.	6.6443	6.5383
139.	6.4168	6.4104	172.	6.6480	6.6420
140.	6.4236	6.4172	173.	6.6640	6.6580
141.	6.4330	6.4266	174.	6.6780	6.6720
142.	6.4400	6.4336	175.	6.6908	6.6848
143.	6.4495	6.4431	176.	6.7136	6.7076
144.	6.4578	6.4514	177.	6.7180	6.7120
145.	6.4596	6.4532	178.	6.7214	6.7154
146.	6.4780	6.4716	179.	6.7298	6.7238
147.	6.4810	6.4744	180.	6.7378	6.7318
148.	6.4856	6.4792	181.	6.7574	6.7514
149.	6.4910	6.4846	182.	6.7800	6.7740
150.	6.5000	6.4936	183.	6.7932	6.7872
151.	6.5050	6.4986	184.	6.8000	6.7940

185.	6.8340	6.8280
186.	6.8588	6.8528
187.	6.8636	6.8576
188.	6.8700	6.8640
189.	6.8780	6.8720
190.	6.8810	6.8750
191.	6.8925	6.8865
192.	6.9122	6.9062
193.	6.9200	6.9140
194.	6.9260	6.9201
195.	6.9666	6.9606
196.	6.9715	6.9656
197.	6.9835	6.9776
198.	6.9896	6.9836
199.	6.9985	6.9926
200.	7.0074	7.0015
201.	7.0296	7.0236
202.	7.0516	7.0456
203.	7.0610	7.0550
204.	7.0678	7.0618
205.	7.0828	7.0822
206.	7.0900	7.0840
207.	7.0984	7.0924
208.	7.1238	7.1178
209.	7.1535	7.1475
210.	7.1600	7.1540
211.	7.1702	7.1642
212.	7.1775	7.1715
214.	7.1934	7.1873
215.	7.2185	7.2125
216.	7.2544	7.2484
217.	7.2628	7.2568
218.	7.2780	7.2720
219.	7.2850	7.2790
220.	7.2925	7.2871
221.	7.3122	7.3068
222.	7.3413	7.3359
223.	7.3440	7.3386
224.	7.3526	7.3472
225.	7.3690	7.3636
226.	7.3860	7.3806
227.	7.4164	7.4110
228.	7.4660	7.4404
229.	7.4678	7.4616
230.	7.4700	7.4646
231.	7.4728	7.4674
232.	7.4762	7.4708
233.	7.4868	7.4814
234.	7.5250	7.5196
235.	7.5768	7.5714
236.	7.5960	7.5806
237.	7.5865	7.5811
238.	7.5980	7.5026
239.	7.6104	7.6050
240.	7.6178	7.6124
241.	7.6240	7.6186
242.	7.6498	7.6444

Absorption Lines of CO_2 in Atmosphere with Grating 57.6 lines/mm
Wavelength from 14 to 16 micron

Line Serial Number.	Wavelength Measured (micron)	Wavelength Calibrated (micron)	Line Serial Number.	Wavelength Measured (micron)	Wavelength Calibrated (micron)
1.	14.117	14.118	27.	14.955	14.956
2.	14.135	14.135	28.	15.018	15.019
3.	14.152	14.152	29.	15.053	15.054
4.	14.175	14.176	30.	15.089	15.090
5.	14.184	14.185	31.	15.124	15.125
6.	14.217	14.218	32.	15.159	15.160
7.	14.250	14.251	33.	15.195	15.196
8.	14.282	14.284	34.	15.230	15.231
9.	14.317	14.318	35.	15.266	15.267
10.	14.349	14.351	36.	15.302	15.303
11.	14.383	14.384	37.	15.338	15.339
12.	14.417	14.418	38.	15.374	15.375
13.	14.450	14.451	39.	15.408	15.409
14.	14.484	14.485	40.	15.445	15.446
15.	14.517	14.518	41.	15.482	15.483
16.	14.552	14.553	42.	15.518	15.519
17.	14.584	14.585	43.	15.554	15.555
18.	14.619	14.621	44.	15.592	15.593
19.	14.654	14.655	45.	15.626	15.629
20.	14.687	14.689	46.	15.664	15.666
21.	14.721	14.723	47.	15.701	15.702
22.	14.756	14.758	48.	15.735	15.736
23.	14.791	14.793	49.	15.774	15.775
24.	14.826	14.828	50.	15.793	15.794
25.	14.861	14.862	51.	15.849	15.850
26.	14.894	14.895	52.	15.848	15.849

Absorption Lines of Water Vapor with Grating 57.6 lines/mm

Wavelength from 16.6 to 20.0 micron

Line Serial Number.	Wavelength Measured (micron)	Wavelength Calibrated (micron)	Line Serial Number.	Wavelength Measured (micron)	Wavelength Calibrated (micron)
1.	16.662	16.665	15.	18.337	18.338
2.	16.805	16.808	16.	18.478	18.479
3.	16.898	16.899	17.	18.645	18.647
4.	17.101	17.102	18.	18.647	18.649
5.	17.223	17.224	19.	19.012	19.013
6.	17.357	17.358	20.	19.243	19.245
7.	17.501	17.502	21.	19.321	19.323
8.	17.566	17.567	22.	19.343	19.345
9.	17.630	17.631	23.	19.584	19.587
10.	17.755	17.757	24.	19.723	19.726
11.	18.027	18.030	25.	19.823	19.826
12.	18.178	18.181	26.	19.906	19.909
13.	18.253	18.253	27.	19.932	19.935
14.	18.303	18.304			

Absorption Lines of Water Vapor with Grating 28.8 lines/mm

Wavelength from 19.0 to 40.0 micron

Line Serial Number.	Wavelength Measured (micron)	Wavelength Calibrated (micron)	Line Serial Number.	Wavelength Measured (micron)	Wavelength Calibrated (micron)
1.	19.023	19.012	27.	22.558	22.538
2.	19.256	19.241	28.	22.638	22.618
3.	19.327	19.312	29.	22.930	22.910
4.	19.362	19.347	30.	23.016	22.996
5.	19.604	19.589	31.	23.210	23.190
6.	19.742	19.726	32.	23.478	23.458
7.	19.842	19.827	33.	23.525	23.505
8.	19.942	19.927	34.	23.658	23.638
9.	20.250	20.135	35.	23.830	23.810
10.	20.340	20.315	36.	23.921	23.901
11.	20.584	20.569	37.	23.987	23.967
12.	20.675	20.660	38.	24.683	24.663
13.	20.804	20.789	39.	25.000	24.968
14.	21.005	20.990	40.	25.086	25.066
15.	21.173	21.158	41.	25.180	25.160
16.	21.186	21.171	42.	25.242	25.220
17.	21.272	21.257	43.	25.382	25.362
18.	21.350	21.235	44.	25.596	25.576
19.	21.384	21.369	45.	26.002	25.982
20.	21.686	21.661	46.	26.072	26.052
21.	21.860	21.845	47.	26.436	26.416
22.	21.902	21.887	48.	26.600	26.638
23.	22.096	22.081	49.	26.658	26.638
24.	22.160	22.045	50.	26.750	26.730
25.	22.392	22.377	51.	27.052	26.932
26.	22.410	22.395	52.	27.583	27.563

53.	27.913	27.893	65.	32.000	31.950
54.	28.004	27.584	66.	32.350	32.310
55.	28.246	28.221	67.	33.100	33.050
56.	28.440	28.420	68.	33.555	33.505
57.	28.604	28.584	69.	34.560	34.500
58.	28.950	28.930	70.	35.066	35.020
59.	29.160	29.140	71.	35.520	35.480
60.	29.375	29.355	72.	36.090	36.040
61.	29.880	29.840	73.	36.810	36.770
62.	30.580	30.520	74.	37.612	37.562
63.	30.946	30.880	75.	38.040	37.990
64.	31.800	31.740			

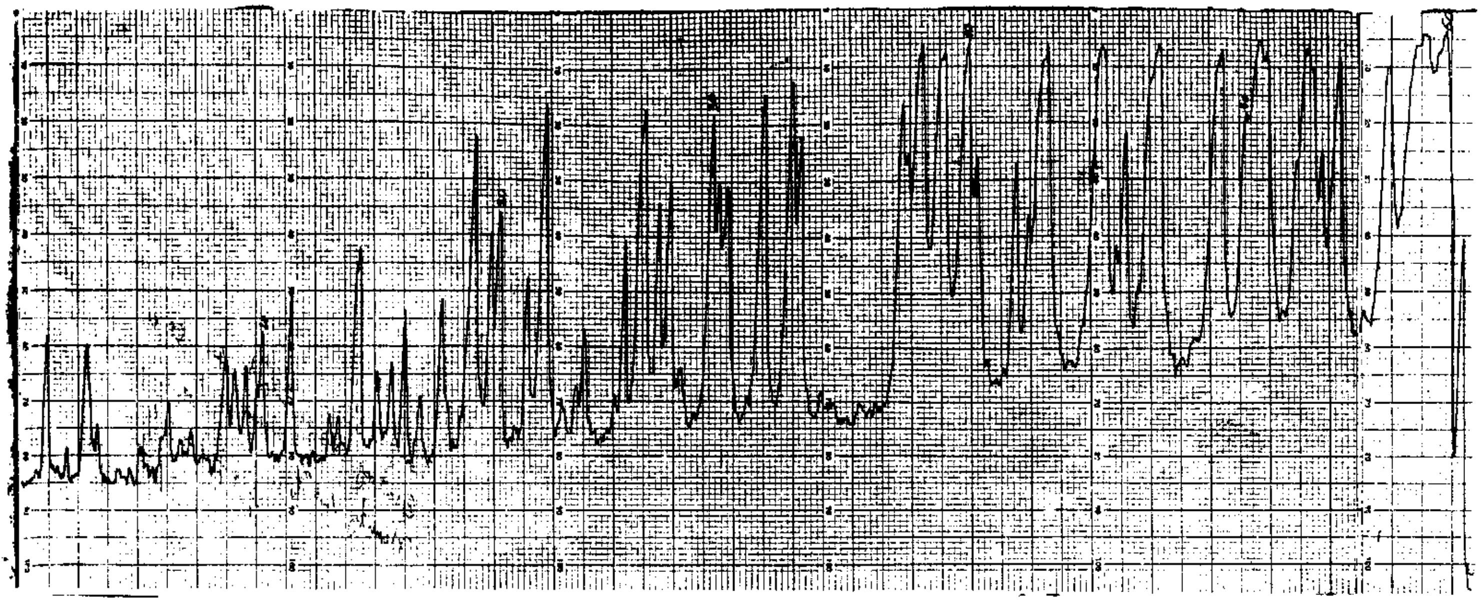

Fig. 1. Absorption Lines of Water Vapor with Grating 288 lines/mm **Wavelength**

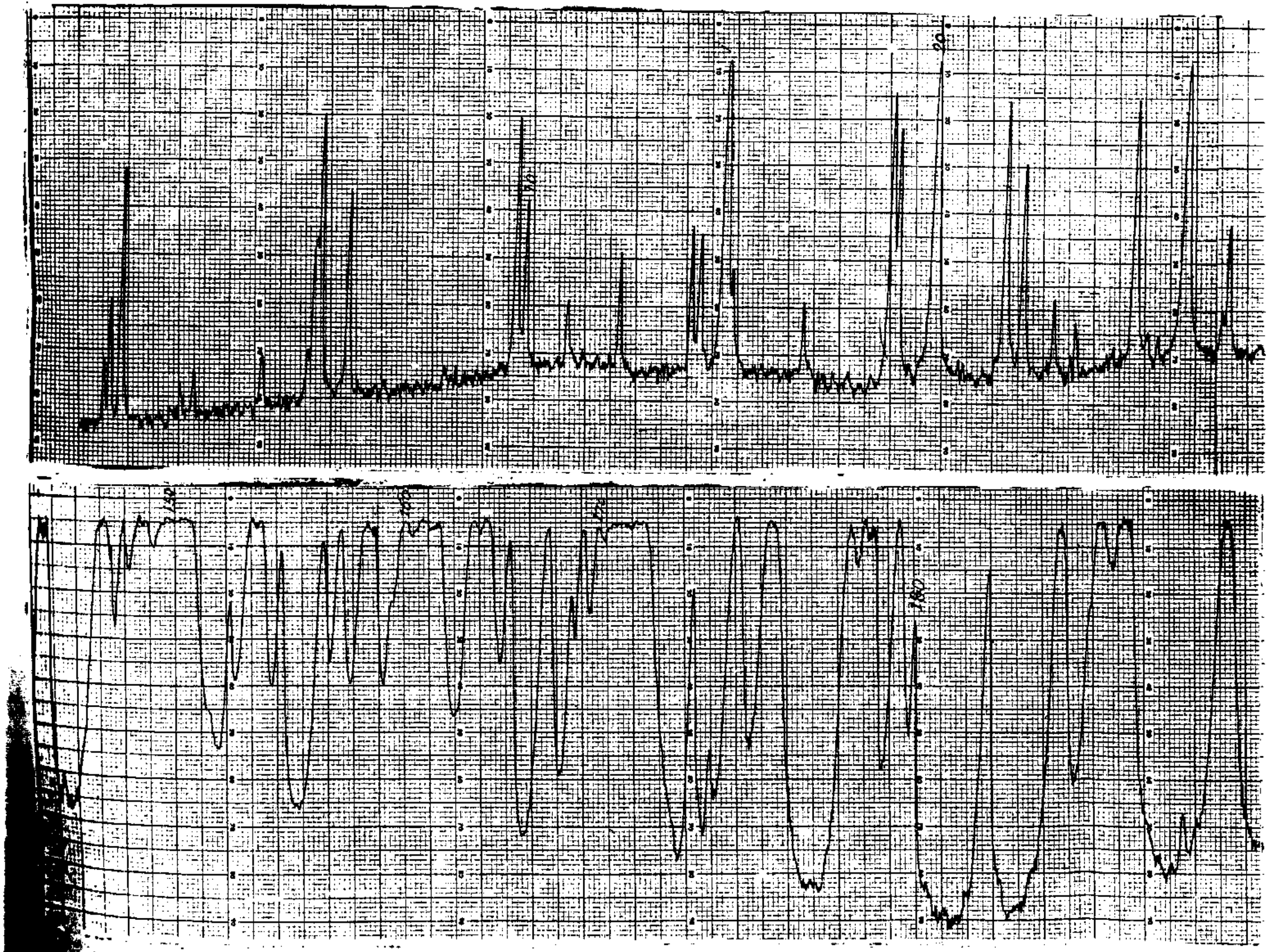

Fig. 2. Absorption Lines of Water Vapor with Grating 144 lines/mm Wavelengt

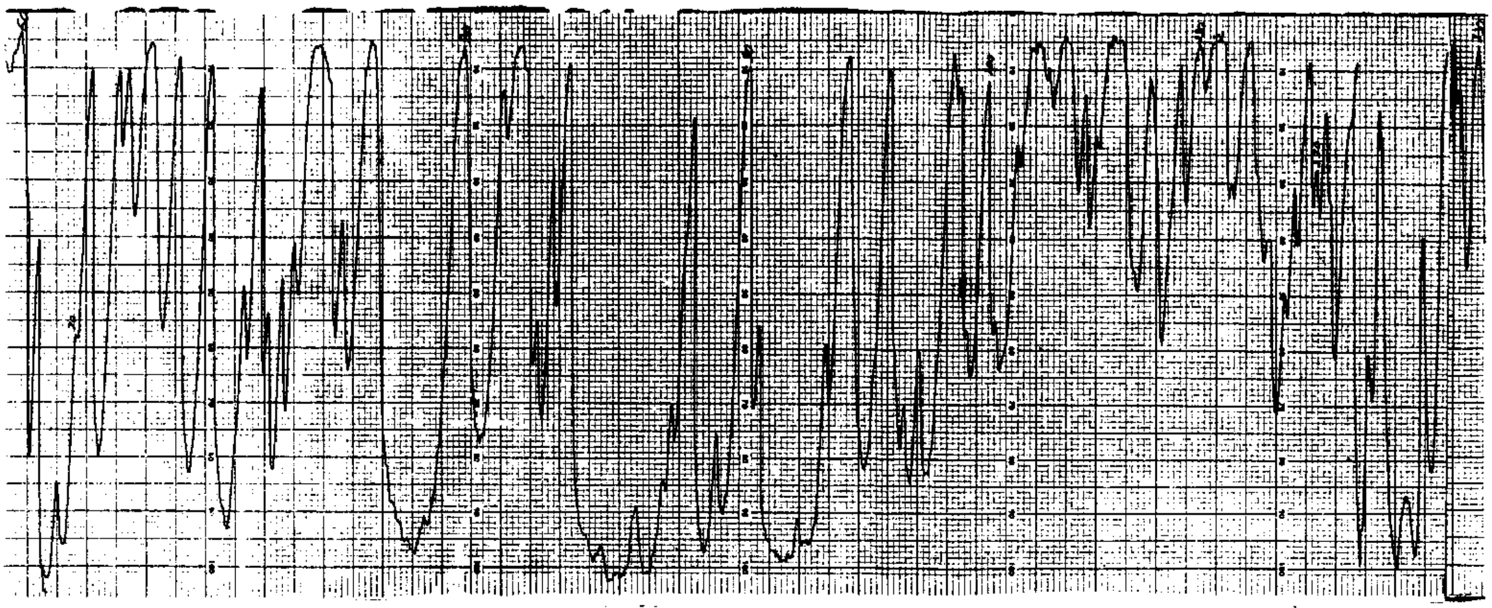

gth from 2.5 to 2.9 micron

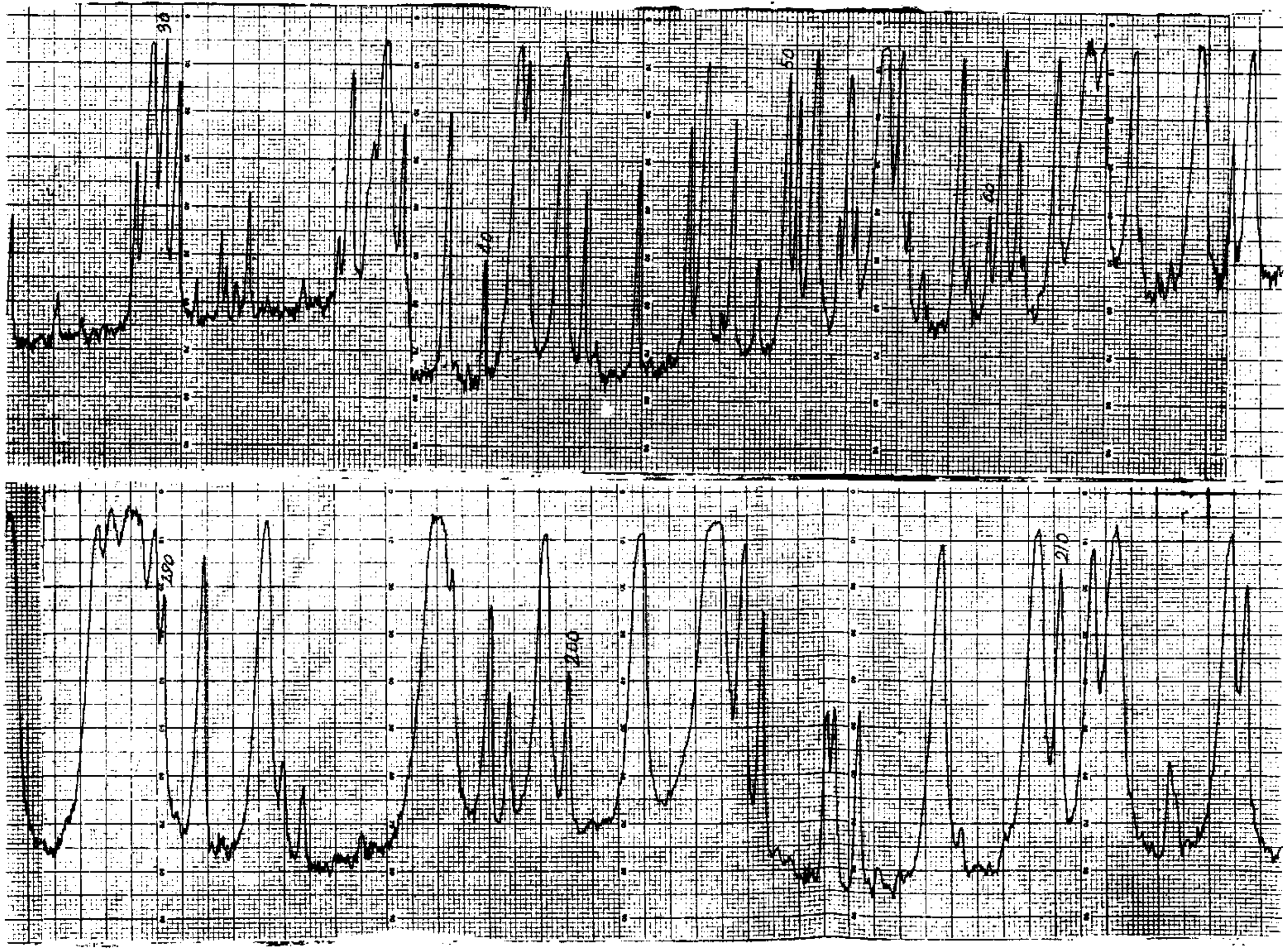

ngth from 4.95 to 7.65 micron

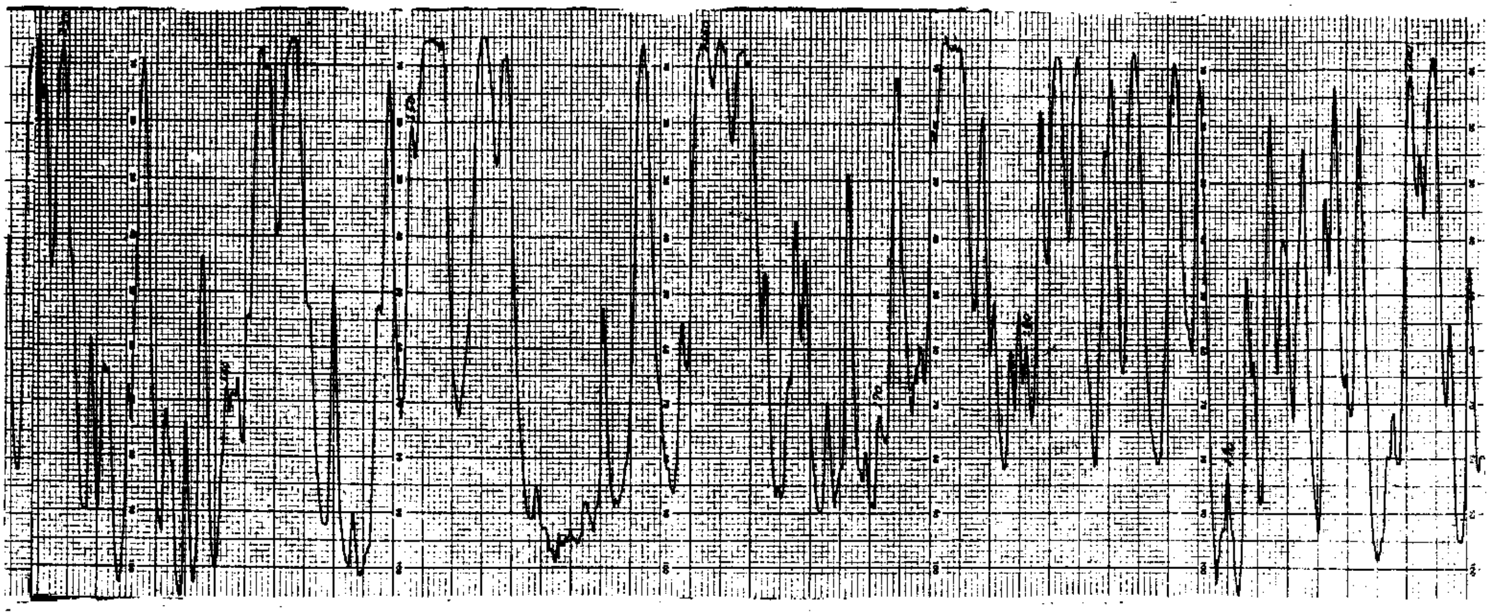

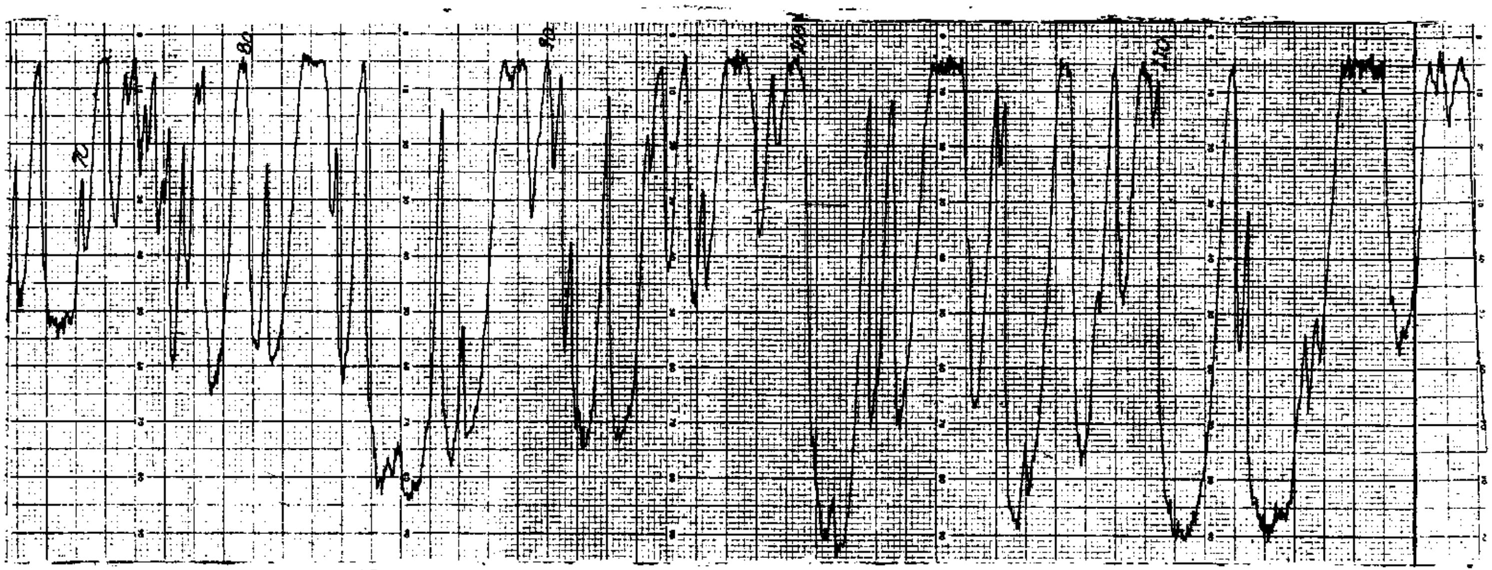
70
80
90
100
110

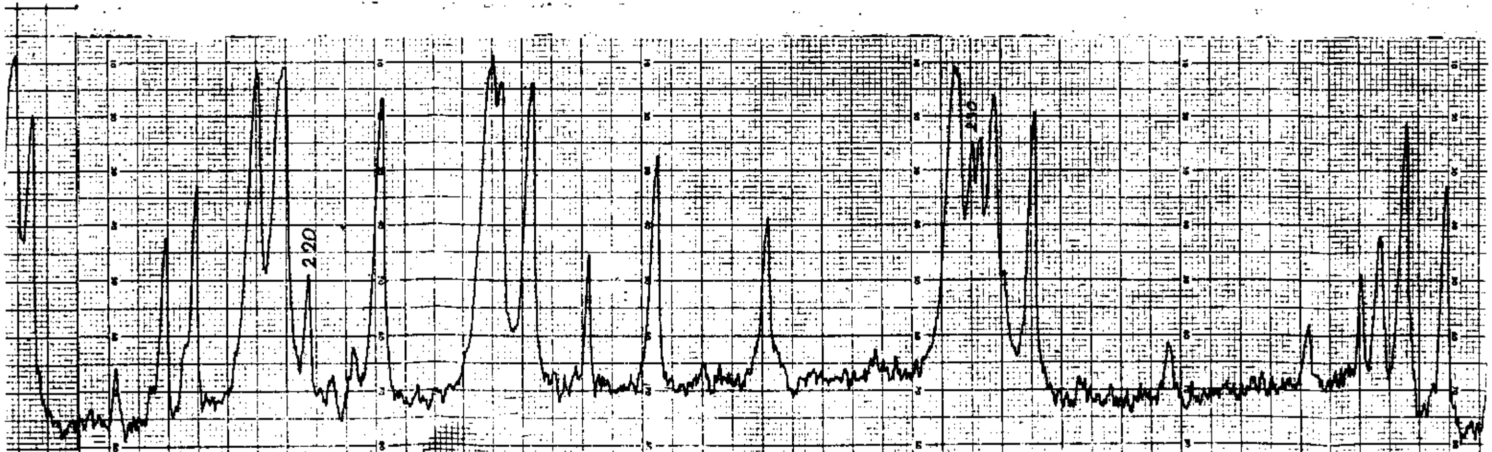
220
230

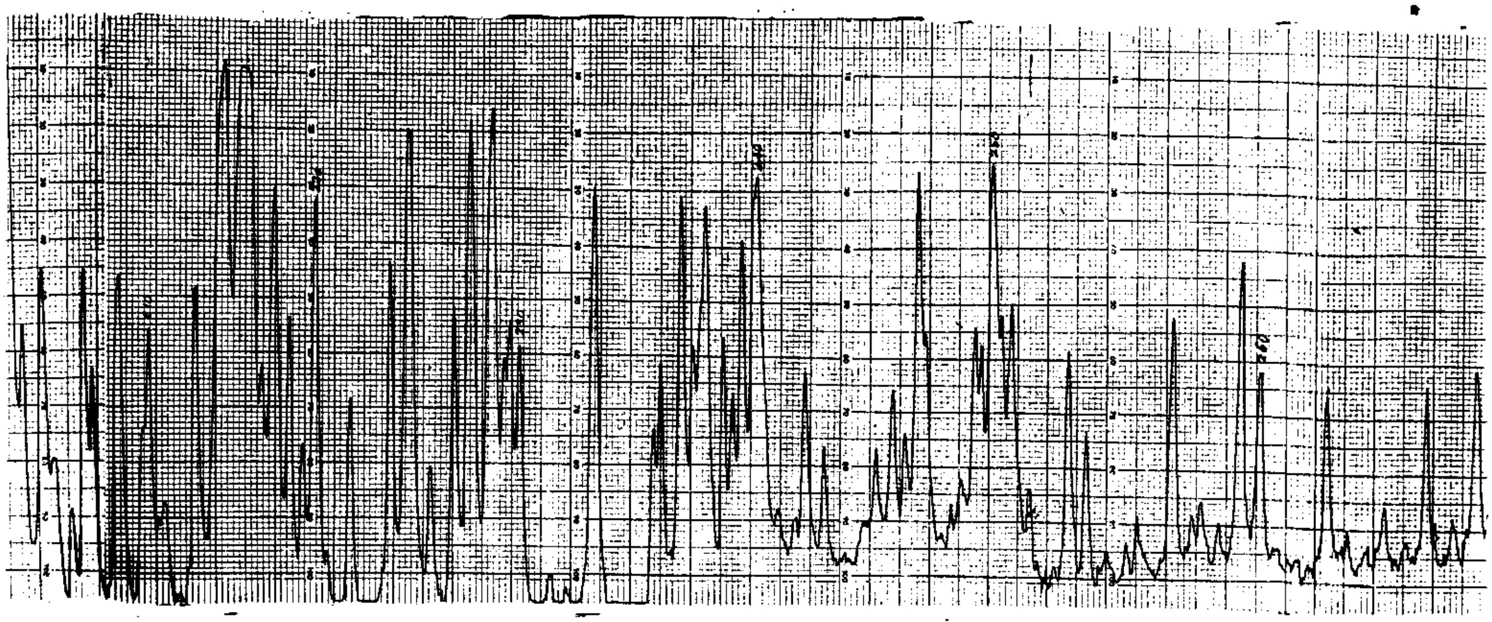

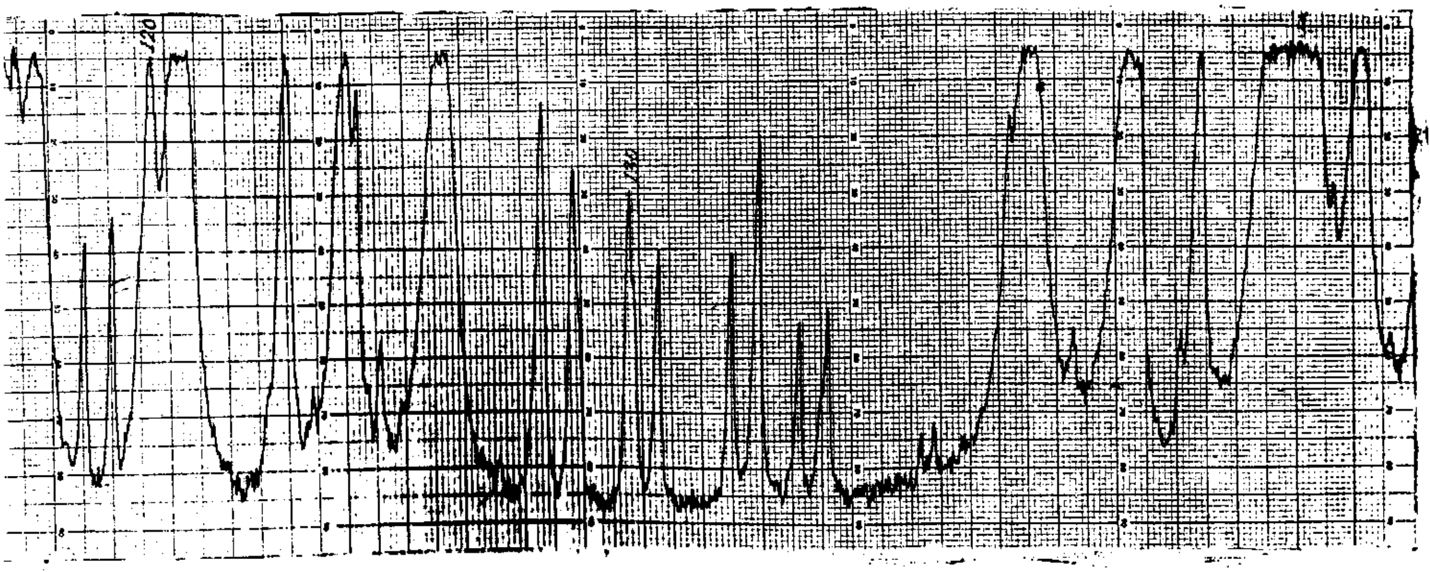
120
120

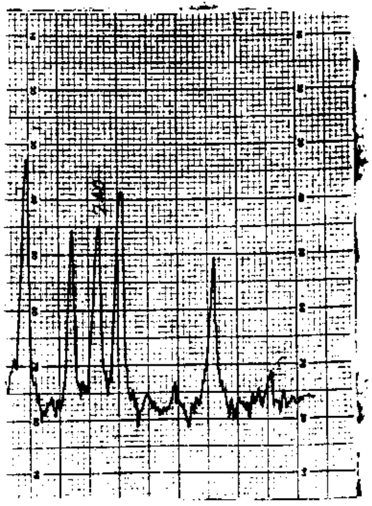
240

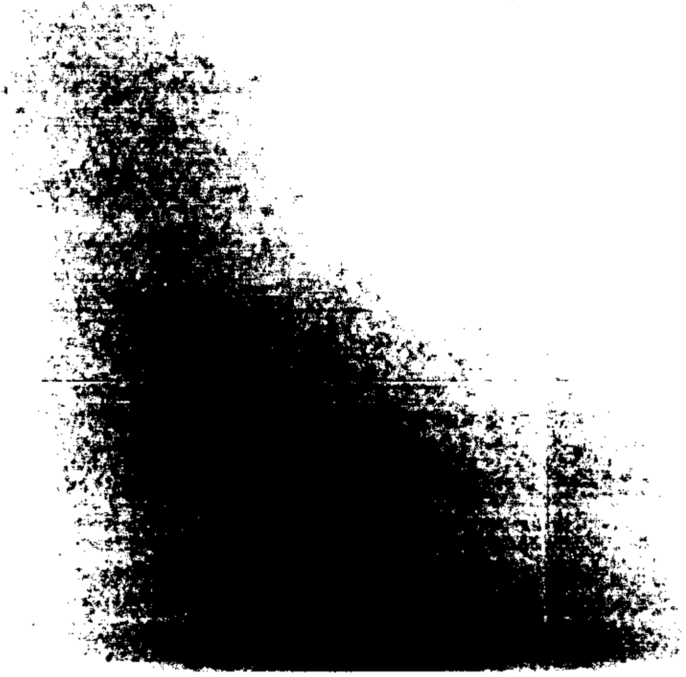

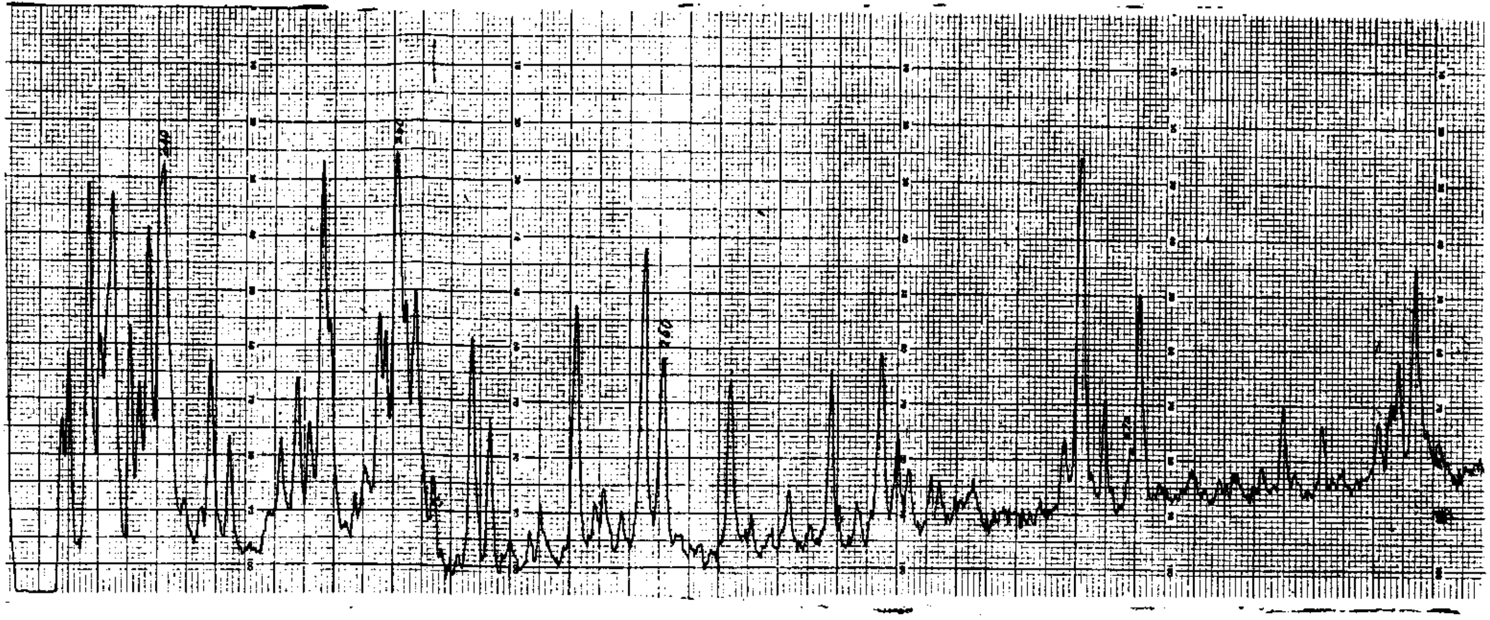
210
190
180

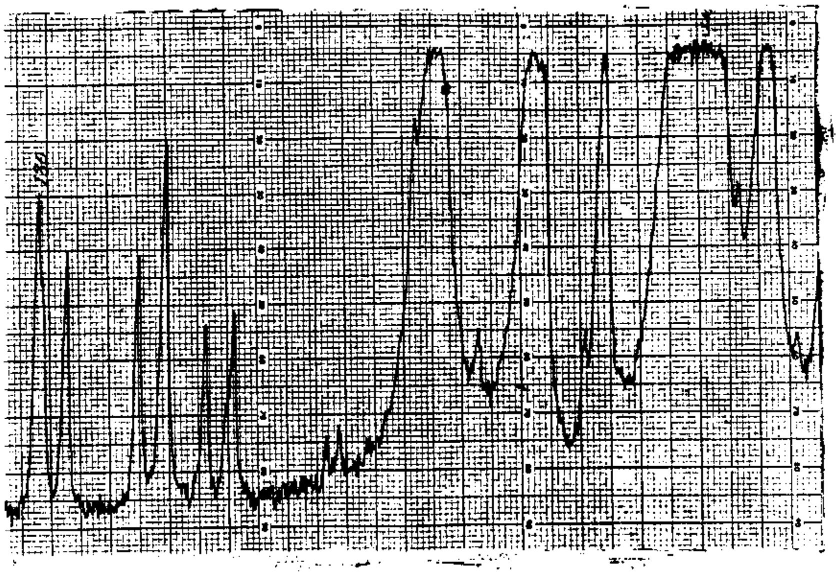
130

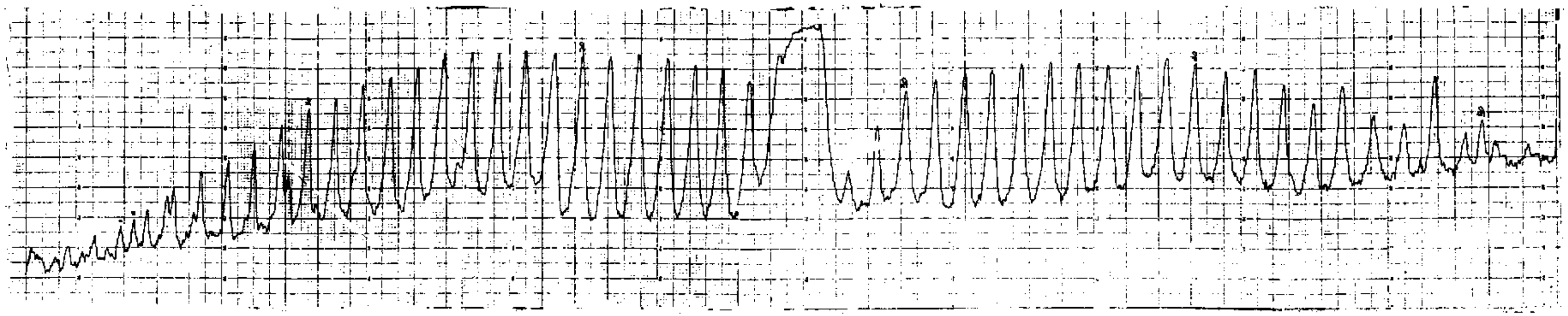

Fig. 3. Absorption Lines of Co_2 in Atmosphere with Grating 57.6 lines/mm Wavelength from 14 to 16 micron

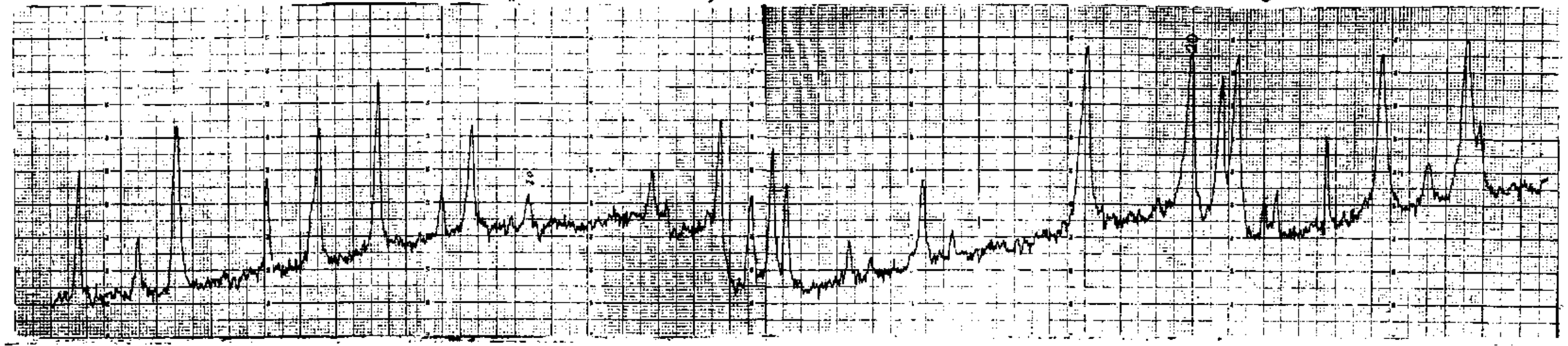

Fig. 4. Absorption Lines of Water Vapor with Grating 57.6 lines/mm Wavelength from 16.6 to 20.0 micron

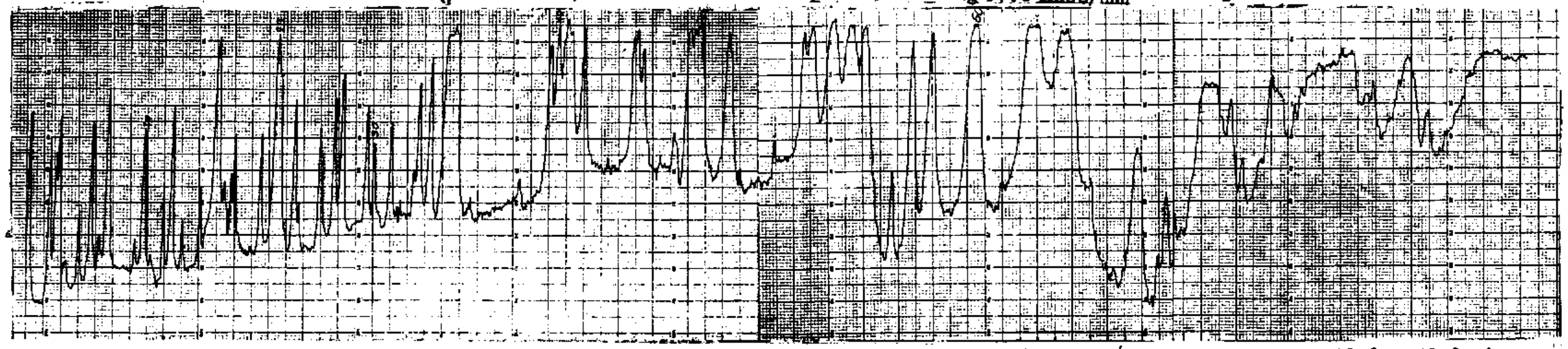

rating 28.8 lines/mm Wavelength from 19.0 to 40.0 micron

A METHOD TO DIFFUSE MAGNESIUM INTO SILICON*

L. T. Ho, (何侗民) S. S. Tai (戴嵩山) and Y. T. Leu (吕燕堂)

Institute of Physics

Academia Sinica

Abstract

A method to diffuse magnesium, a group II element, into unddped silicon is presented. Pure magnesium was deposited by evaporation on the sample surface. After being heated at 1200°C for 2 hours in a helium atmosphere and then quenched in liquid nitrogen, the sample was found to become from high resistivity to low resistivity. Hall effect measurement shows that magnesium is a double donor in silicon and enters into silicon interstitially.

1. *Introduction*

It is well known that semiconductors have an electronic band structure in which a filled valence band is separated from an empty conduction band by a finite energy gap. Early investigations of the properties of semiconductors showed that the intrinsic electric behavior was due to the thermal excitation of electrons across the energy gap while the extrinsic electric behavior originated from the different activation energies of carriers bound to the chemical impurities or defects present in the crystal. Following the recognition that even very small concentration of impurities can significantly change the crystal characteristics, imperfections in semiconductors have been the subject of many important investigations, both experimental and theoretical. For example, the behavior of group III and group V impurities in silicon and germanium represents one of the most extensively studied and best understood aspects of semiconductor physics.(1) Many other impurities have also been studied. Some of the better known cases are lithium in silicon and germanium,(2,3) beryllium in silicon and germanium,(4) sulfur in silicon,(5-7) and zinc,(8,9) mercury(10) in germanium. Other elements as impurities, however, are seldom studied due to doping difficulties. In this report a method to introduce magnesium, a group II element, into silicon is presented and some results are discussed.

2. *Experimental Procedure*

Magnesium-doped silicon samples were made by the diffusion technique. Two

---

* Work supported by the National Science Council of Republic of China.

different kinds of silicon ingots were used for making samples, their resistivity being 1000 and 3000 ohm-cm, respectively. These ingots are both p-type, floating zone material, and purchased from the Materials Division of General Diode Corporation.(11) The magnesium-diffused silicon samples were made in the following manner.

First, samples were cut from the ingot about the size of 2.3 cm long, 6 mm wide and 3 mm thick. A Buehler(12) Model 80-BQ AB DI-MET Cutter with heavy base was used for cutting. In order to minimize the waste of the crystal as well as the damage of the sample surface, the diamond cut-off wheel selected for cutting was very thin, its thickness being 0.012" only. After cutting, the sample surface was ground carefully with silicon carbide powder grit no. 400 to make it as flat as possible. Then the sample was cleaned in acetone and ready for the next step, the evaporation of magnesium onto it.

Magnesium of 99.9948% purity was obtained from Dow Chemical Company.(13) In order to remove the oxidized surface the magnesium had to be etched in hydrochloric acid before being deposited on the surface of silicon sample. A piece of tantalum sheet(14) of 0.002" thick was used to make a boat to hold magnesium. By passing current through it, magnesium sublimes directly onto the silicon sample surface. Since the sublimation temperature of magnesium is 247° C at vacuum pressure of 10^{-6} torr,(15) current used has to be adjusted carefully to avoid magnesium film on the sample surface too thin. The thickness of the magnesium film on the sample surface obtained is usually several hundred microns. The evaporation work was performed using a Varian Model VE-61 vacuum evaporator.(16)

The sample was then put into a high temperature furnace for diffusion. For this purpose, a Lindberg Hevi-Duty Model 1500° C single-zone tube furnace(17) was used. During diffusion (Fig. 1), the sample was kept in a quartz tube;(18) a piece of tantalum sheet separated it from direct contact with the tube in order to avoid diffusion of oxygen from the quartz tube into the sample. Helium gas was used flowing freely in the quartz tube to avoid oxidation. Diffusion temperature was set at 1200° C. Since the boiling point of magnesium is only 1107° C, in order to prevent magnesium from escaping it was found that the sample had to be sandwiched between two other specimens (Fig. 2), all three having magnesium on the surfaces in contact, the sample and the covers weld together and thus the magnesium does not escape into the ambient. For this purpose, two additional silicon pieces, cut from the same silicon ingot about the same size as the sample except only about 1 mm thick, had to be used as the covers for each time of diffusion. After heating for two hours, the sample, together with the covers, was quenched in liquid nitrogen. The covers were then ground off and the sample surfaces were prepared by grinding successively with silicon carbide powder grit no. 400, no. 600, grinding compound 1200 mesh and 3200 mesh.

3. *Experimental Results and Discussion*

The silicon sample, after the diffusion treatment mentioned above, has been found to convert from high resistivity of more than 1000 ohm-cm to low resistivity, its value being variable depending upon the condition of the sample surface prepared, the thickness of the magnesium film deposited on the sample surface as well as the diffusion condition. Specimens subjected to the same heat and quench treatment remained to be high resistivity if no magnesium was deposited initially; this check was made to show that the change from high to low resistivity was indeed associated with magnesium centers. Thus we have proved that magnesium can enter into silicon by the diffusion technique.

Elements as impurities in silicon or germanium can be either substitutional or interstitial. In the substitutional case, the number of outer valence electrons of an impurity atom determines whether the impurity a donor or an acceptor. For example, group III and group V elements are both substitutional, in order to complete the tetrahedral bonds, group III elements have to be acceptors while group V elements become donors. In the interstitial case, however, since there is no need to complete the tetrahedral bonds, all the valence electrons are available to become donors no matter what group this impurity belongs. Therefore, the role of magnesium in silicon would depend on whether its being substitutional or interstitial. Should it be substitutional, it is an acceptor. But, if it is interstitial, it has to be a donor. This can be checked easily by using the Hall effect technique, which tells the sample to be n-type or p-type thus determining whether the impurity a donor or an acceptor. By measuring the Hall constant of our magnesium-diffused silicon sample, we found that the sample, initially p-type, turned out to become n-type. This behavior can be understood only if magnesium is interstitial rather than substitutional as explained above. Thus magnesium in silicon behaves like a donor rather than an acceptor.

Since magnesium is a group II element, it has to be a double donor is silicon. As an interstitial impurity the donor electrons of magnesium are expected to be the two 3s valence electrons. Therefore, both neutral and singly ionized magnesium donors are available to be studied. It is well known that group III and group V impurities are solid state analogs of the hydrogen atom. In our case, the magnesium impurity in silicon should result in a system analogous to the helium atom.

References

(1) W. Kohn, in Solid State Physics, Vol. 5, edited by F. Seitz and D. Turnbull (Academic, New York, 1957), p. 257.
(2) R. L. Aggarwal, P. Fisher, V. Mourzine and A. K. Ramdas, Phys. Rev. 138, A882 (1965).
(3) G. D. Watkins and F. S. Ham, Phys. Rev. B 1, 4071 (1970)

(4) Beryllium in germanium is discussed in the following: H. Shenker, E. M. Swiggard and W. J. Moore, Trans. AIME 239, 347 (1967); W. J. Moore and R. Kaplan, Bull. Am. Phys. Soc. 11, 206 (1966); N. D. Tyapkina, M. M. Krivopolenova and V. S. Vavilov, Fiz. Tverd. Tela 6, 2192 (1964). For beryllium in silicon see J. B. Robertson and R. K. Franks, Solid State Commun. 6, 825 (1968).

(5) W. E. Krag, W. H. Kleiner, H. J. Zeiger and S. Fischler, J. Phys. Soc. Japan Suppl. 21, 230 (1966).

(6) G. W. Ludwig, Phys. Rev. 137, A1520 (1965).

(7) D. L. Camphausen, H. M. James and R. L. Sladek, Phys. Rev. B 2, 1899 (1970).

(8) P. Fisher, R. L. Jones, A. Onton and A. K. Ramdas, J. Phys. Soc. Japan Suppl. 21, 224 (1966); W. J. Moore, Solid State Commun. 3, 385 (1965).

(9) F. Barra and P. Fisher, Phys. Letters 27A, 711 (1968).

(10) R. A. Chapman and W. G. Hutchinson, Phys. Rev. 157, 615 (1967).

(11) General Diode Corporation, Framingham, Massachusetts.

(12) Buehler Ltd., Evanston, Illinois. The cutter equips with hydraulically controlled down-feed, arbor lock for cross-feed, precision spindle quill, 1 HP motor, and 12" diameter rotary table with graduated horizontal and vertical adjustments. Using this cutter, a crystal can be cut to any desired shape and orientation.

(13) Dow Chemical Company, Midland, Michigan.

(14) Products of Fan Steel Metallurgical Corporation, North Chicago, Illinois.

(15) See Handbook of Thin Film Materials, p. 7, published by Sloan Technology Corporation, Santa Barbara, California.

(16) Manufactured by Varian Corporation, Palo Alto, California. A vacuum of the order of 10^{-6} to 10^{-7} torr can be obtained in the vacuum chamber by a 6" oil diffusion pump, with a liquid nitrogen cold trap between the diffusion pump and the chamber, and backed by a mechanical pump. The vacuum chamber is a guarded 18" x 30" Pyrex bell jar. A 2 KVA filament power supply is provided.

(17) Manufactured by Sola Basic Industries, Inc., Milwaukee, Wisconsin. The furnace uses silicon carbide as the heating elements and platinum-platinum 13% rhodium as the thermocouple. Temperature up to 1500°C can be reached. The temperature is controlled by a Lindberg Hevi-Duty Model 59545 control console, which is able to maintain temperatures to ±1°C.

(18) Products of Scientific Glass Apparatus, Inc., Bloomfield, New Jersey.

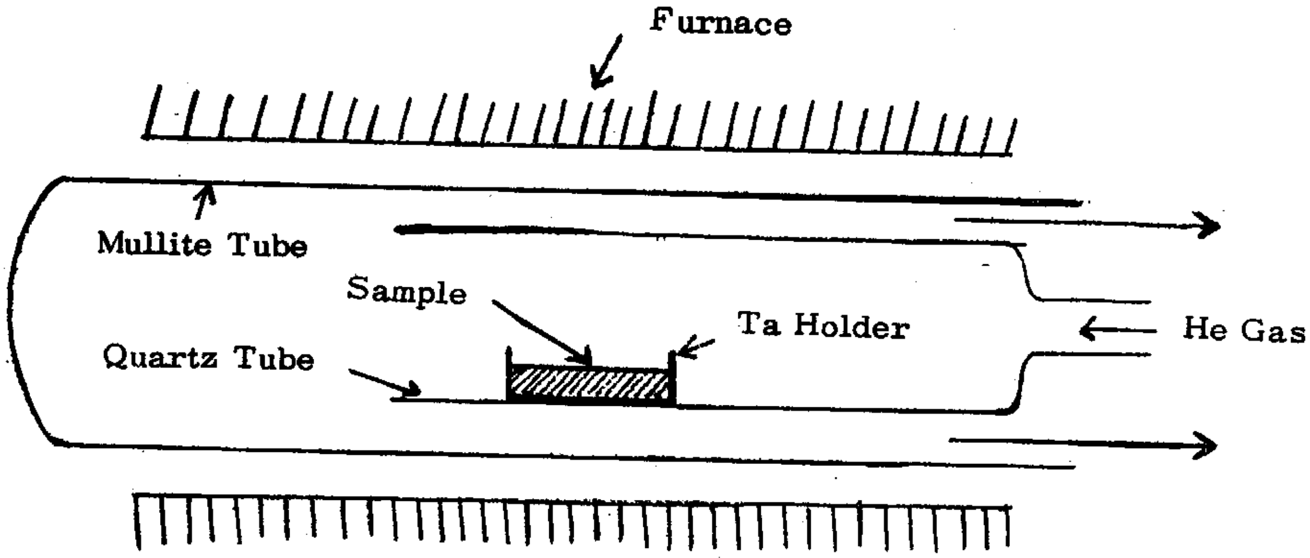
Furnace
Mullite Tube
Sample
Ta Holder
Quartz Tube
He Gas

Fig. 1

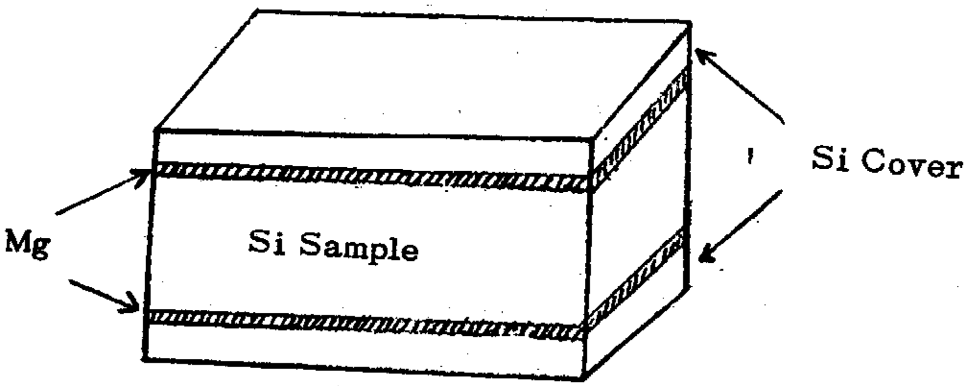
Si Cover
Mg
Si Sample

Fig. 2

A THEORY OF AMBIGUOUS PATTERN PERCEPTION

Chun Chiang

Institute of Physics

Academia Sinica

Nankang, Taipei, Taiwan

The Republic of China

Abstract

A theory of ambiguous pattern perception is formulated. This theory proposes a feature selector (field of attention) based on the time-sequential discrete property of the attention, a short-term memory for storage of the selected features, and a synthesizer (perception) to synthesize the consecuitvely stored features. Since the selected features keep comming in and since the features can only be stored in the short-term memory for a short period, the features which can be synthesized in the synthesizer vary with time. When all the essential features belonging to one pattern happen to be in the synthesizer, the picture is perceived to be that pattern; when all the essential features belonging to another pattern happen to be in the synthesizer, then the picture is perceived to be the other pattern. Thus the picture appears to oscillate between two patterns.

1. *Introduction*

Ambiguous pattern or ambiguous figure has long been a focus of interest, mainly to the psychologist, for the last one hundred years. The fact that a picture can be perceived to be two different objects at different times is a fascinating phenomenon; for example, Fig. 1 can be perceived to be either a vase or two heads facing each other. However, the perception mechanism involved in this phenomenon remains obscure despite the long history of investigation of this subject. Recently, the computer has been introduced, and it is occasionally observed that the computer may also give an ambiguous answer. Under certain circumstance, the output of the computer may fluctuate from one result to another. Thus the computer process may have some similarity to the human perception process. The purpose of this paper is to present a mathematical psychophysical model of the perception process involved in this ambiguous pattern perception.

2. *Theory*

A. Discrete Process

Human perception, like computer data input, is a discrete process, namely, the information contained in the visual stimulus has to be perceived bit by bit. Physiologically, the nerve impulses are composed of a series of discrete electric disturbances, thus if one accepts that the nerve impulses are the physiological process for information perception, then the perception process has to be discrete. Philosophically, one also has tc accept that perception peocess is a discrete process, since it is not possible for any one or for any machine to obtain all the information instantaneouslly, a serious of discrete process is necessary. Chiang [1] has successively utilized this concept to explain the Muller-Lyer illusion, Noton [2], Noton and Stark [3] have measured the scanpath in the eye movement, they have found that in viewing the picture, the subject's eye follows a specific path way and makes pauses at certain locations. This fact also suggests that perception is a discrete process.

B. Pattern Perception

Noton [2] has presented a theory of pattern perception using the concept of matching between the perceived stimulus and the internal representation in the subject. Following his outline, the present paper explores in more detail about the gross pattern perception process, especially with respect to the ambiguous pattern perception. A mathematical formulation is also attempted, furthermore, a time sequential process is emphasized. It can be seen later that this time sequential precess plays a key role in the ambiguous pattern perception, and is the main reason for the alternative apperance of the ambiguous picture.

Before discussing further about the perception process, we would like to define a feature selection function $\delta[x(t), y(t); t']$. Similar to Dirac function in quantum mechanics, we can define $\delta\ [x(t), y(t); t']$ as:

$$\begin{aligned} &\delta[x(t), y(t); t'] = 1 \qquad && \text{if } t = t' \\ &\delta[x(t), y(t); t'] = 0 \qquad && \text{if } t \neq t' \end{aligned} \tag{1}$$

where to and t' represents time, $[x(t), y(t)]$ represents the location of the field of attention at time t. The physical meaning of this feature selection function $\delta[x(t), y(t); t']$ is that it expresses the location of the fixation of the attention at time t where the information can be gathered, this function governs the selection of the features in the stimulus.

Thus if $S(x, y)$ represents the stimulus, then $S(x, y)\delta[x(t), y(t); t']$ represents the selected feature within the stimulus at time t. However a purely selected feature without further processing has no meaning; in order for this selected feature to be associated with some difinite meaning, a complicated short-term memory and identification process is needed. Noton [2] has shown this process and a detailed process in relation to illusion has also been presented by Chiang [4]. We can use P to represent this process, and define

$$I_t = P_t\, S(x, y)\delta[x(t), y(t); t'] \tag{2}$$

where I_t represents the instantaneous perception at time t, P_t is an operator which assigns a pattern to same meaning. Eq. (2) means that the selected feature $S(x,y)\delta[x(t), y(t); t']$ is processed in the brain represented by operator P_t to give an instantaneous perception I.

There are several possibilities P can be: First, P can be zero, which means that the selected feature is discarded and perceived to be nothing. Second, P can be 1, which means that the selected feature is perceived just as it is and no meaning is assigned to it. Third, P can be X or Y, which means that the selected feature is perceived to be X or Y.

This instantaneous perception I represents the perception of only one feature in the stimulus, thus no perception of the whole pattern can yet be obtained. For the perception of the whole pattern, a serious of instantaneous perception has to be made, we can label this as second order perception, thus

$$II_t = \sum_{t=t_{m-\ell}}^{t=t_m} I_t = \sum_{t=t_{m-\ell}}^{t=t_m} P_t\, S(x, y)\delta[x(t), y(t); t'] \tag{3}$$

Eq. (3) means that a serious of instantaneous perception I_t is synthesized together to form the gross pattern perception II_{t_m} at time t_m. Note that a criterion for the above synthesis process to be made at time t_m is that all the instantaneous perception obtained in the period from $t_{m-\ell}$ to t_m has to be remained in the short-term memory. If the time lag between the previous instantaneous perceptions and the present time is too long, then those previous instantaneous perception will be faded away from the short-term memory and could not contribute to the present perception and thus will not be included in the summation in Eq. (3). The number of instantaneous perception which can be included in the perception is determined by ℓ.

C. Ambiguous Pattern Perception

Depending on the environment around the stimulus and the memory stored in the brain, the perceived feature in the stimulus will not always give a unique interpretation.

At one instance, it may be interpreted as one thing, at other instance, it may be interpreted as something else. Thus the selected features processed by P_t may belong to any one of the pattern X, Y····. This is a very confusing situation, because different patterns are coded in the same stimulus and no unique interpretation is possible. However, due to the sequential time discrete process of the perception, it is possible that all the consecutively selected feature stored temporily in the short-term memory may belong to the same pattern, and if those selected features are numerous enough to be identified as pattern X, then a unique identification is made and the stimulus is perceived to be pattern X at that particular moment.

Since the new features keep on feeding into the short-term memory and the old features keep on fading away, it may also happen that all the in-comming features stored in the short-term memory during certain period belong to pattern Y, and thus the stimulus is perceived to be pattern Y at that paticular moment. Thus, we may formulate the condition for ambiguous pattern perception as follows:

$$\begin{cases} II = \sum_{t=t_{m-\ell}}^{t=t_m} I_t = \sum_{t=t_{m-\ell}}^{t=t_m} P_t\, S(x,y)\delta[x(t), y(t); t'] = X, & \\ & \text{if } I_{t_{m-\ell}}, I_{t_{m-\ell+1}} \dots\dots I_{t_m} \in X. \\ II = \sum_{t=t_{m-\ell'}}^{t=t_m} I_t = Y, & \text{if } I_{t_{m-\ell'}}, I_{t_{m-\ell}}, \dots\dots I_{t_m} \in Y. \\ II = \text{no meaning}, & \text{if otherwise.} \end{cases} \tag{4}$$

Since pattern X and pattern Y are of different complexity, thus the number of selected features required for the recognition is different. The number required is indicated by ℓ and ℓ' respectively

3. *Flow Chart of the Perception Process*

In order to give an overall view of the above idea, we present a flow chart about the ambiguous pattern perception process as shown in Fig. 2. Both the terminology commonly used for instruments and that for human perception are indicated in the chart together for comparision.

References

(1) C. Chiang, "A theory of the Muller-Lyer illusion", *Vision Res.* Vol. 13, pp. 347-353, February 1973.

(2) D. Noton, "A theory of visual pattern perception", *IEEE Systems* Science and Cybernetics, Vol. 6, pp. 349-357, October 1970.

(3) D. Noton and L. Stark, "Scanpaths in eye movements during pattern perception", *Science,* Vol. 171 pp. 308-311, January 1971.

(4) C. Chiang, "Illusion and perception", *Ann. Rept. Inst. Phys. Acad. Sin.*, 1973.

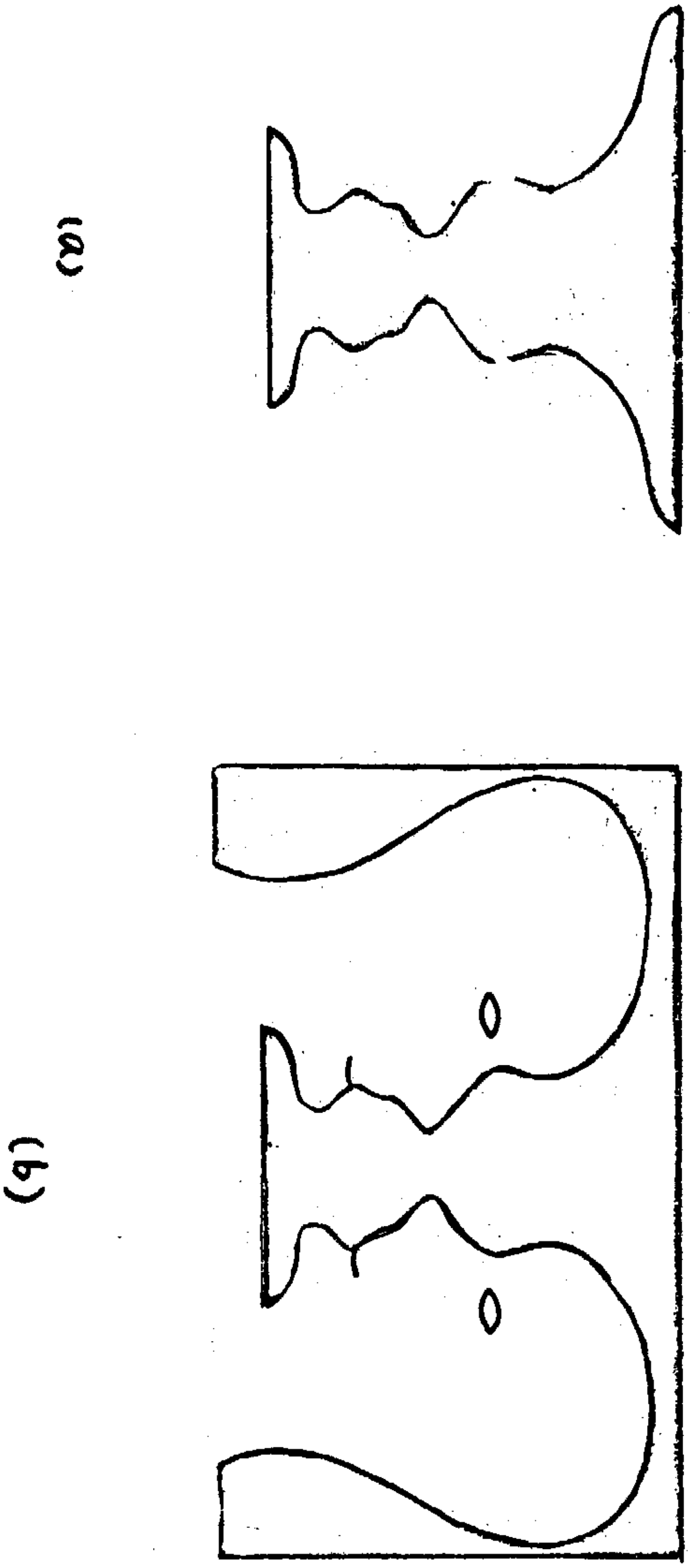

Fig. 1

Fig. 1 A picture showing two alternative patterns; the vase or two heads facing each other.

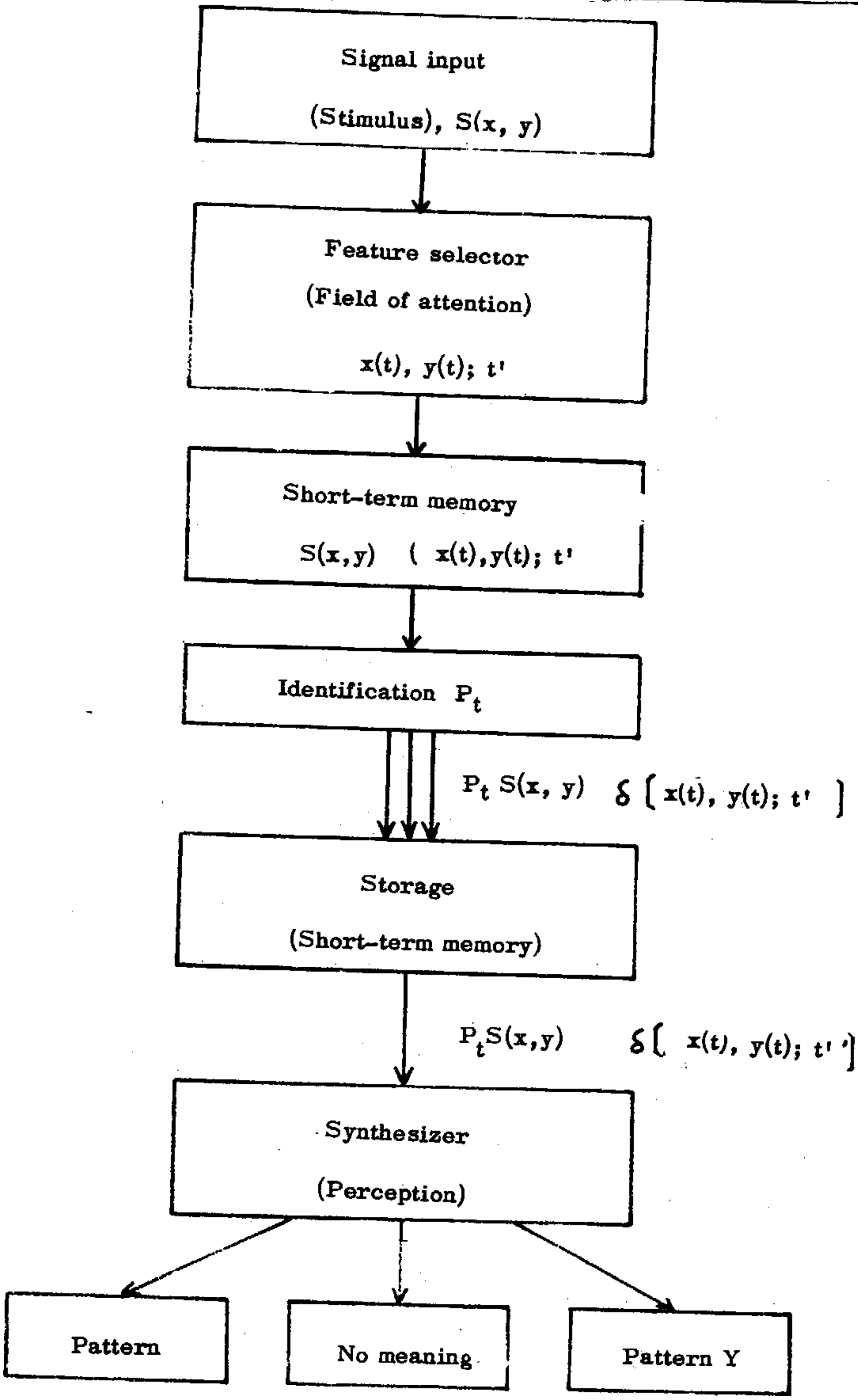

Fig. 2

Fig. 2 A flow chart showing the ambiguous pattern perception process.

ON THE DIPOLE MODEL FOR THE INITIATION OF NERVE IMPULSE

Chyuan-Yih Lee and Chun Chiang

Institute of Physics

Academia Sinica

Nankang, Taiwan, R. O. C.

Abstract

Based on two-state dipole flip-flop theory, the strength-duration relation for cathodic stimulation is derived in this paper. The dipole system is treated classically so that the parameters are easier to evaluate. From this model, the quantitative relation between optimum frequency and temperature is deduced, in agreement with the observation of Hill et al (1936). Observations using constant voltage pulses, instead of constant current pulses, are suggested for further confirmation of this model.

1. *Introduction*

Though many data on nerve excitation has been accumulated, its molecular mechanism is still not very clear. Recently, Wei(1969b, 1971a) proposed a dipole flip-flop model to explain the initiation of nerve impulse. According to this model, a dipole layer exists at the membrane surface. This layer forms a barrier field F, preventing the inward flow of sodium ions (or other cations). A cation of charge q will be subject to a force qF under this barrier. Wei assumed that the membrane dipole has two quantum states with energy E_1 and E_2 respectively ($E_2 > E_1$). If N_1 and N_2 are the numbers of the dipoles corresponding to quantum states E_1 and E_2, the barrier field is proportional to N_1-N_2. When N_2 increases, the barrier will be reduced, this would enable the cation to flow inward and initiats the nerve impulse. With this interesting idea, Wei (1971a) derived a strength-duration relation under the condition that the dipoles are not too far away from the equilibrium.

Recently, Spiegel and Joines(1973) applied a density matrix approach to the membrane dipole system and derived the following strength-duration-frequency relation:

$$\Delta t_o = \left[\gamma + \frac{I^2\gamma_{ab}}{\gamma_{ab}^2 + (\omega - \omega_{ab})^2}\right]^{-1} log \left[\frac{N_o - N_{ss}}{N_t - N_{ss}}\right] \qquad (1)$$

His treatment is quite advanced, however, "no numerical illustrations were presented since it was felt that applicable information regarding the necessary quantities was virtually nil" (Spiegel and Joines, 1973). Noting this difficulty, this paper will follow the same idea, and use a simpler treatment so that the necessary parameters could be accessed and the results could be compared with the observations. Since the dipole flip-flop model is not well confirmed yet, the numerical comparison would be of much significance.

2. *SD-Relation for Constant Field Stimulation*

For any two-state dipole system, neglecting the dipole-dipole interaction, the population change can be described by the following rate equations (for instance, see Frohlich, 1958);

$$
\begin{aligned}
dN_1/dt &= -w_{12}N_1 + w_{21}N_2 \\
dN_2/dt &= w_{12}N_1 - w_{21}N_2
\end{aligned}
\tag{2}
$$

where w_{12} is the probability per unit time for a dipole to make transition from state I to state II, and w_{21} , the probability per unit time for the reverse process. Equation (2) may be transformed to be

$$
d\Delta N/dt = -(w_{21} + w_{12})\Delta N + (w_{21} - w_{12})N \tag{3}
$$

where

$$
\Delta N = N_1 - N_2 \; ; N = N_1 + N_2 \tag{4}
$$

The solution of (3) is

$$
\Delta N = \left(\Delta N^o - N\frac{w_{21} - w_{12}}{w_{21} + w_{12}}\right)e^{-(w_{21}+w_{12})t} + N\frac{w_{21} - w_{12}}{w_{21} + w_{12}} \tag{5}
$$

where ΔN^o is the initial population difference, namely,

$$
\Delta N^o = N_1^o - N_2^o \tag{6}
$$

If we assume that the potential energy difference of the two states in a resting membrane is 2U (corresponding to $E_2 - E_1$ in Wei's paper), then according to Boltzmann distribution

$$N_1^o/N_2^o = exp\ 2U/kT \tag{7}$$

From (4), (6) and (7), we have

$$\Delta N^o = N\ tanh\ U/kT \tag{8}$$

If a constant cathodic field F is applied perpendicularly across the nerve membrane for a sufficiently long time, the system is assumed to reach a new equilibrium, that is, $dN_1/dt = dN_2/dt = 0$. Therefore

$$w_{21}/w_{12} = N_1/N_2 = exp\ 2(U-pF)/kT \tag{9}$$

where p is the dipole mement. We may rewrite (9) as

$$w_{12} = B\ exp\ -(U-pF)/kT\ ;\ w_{21} = B\ exp\ (U-pF)/kT \tag{10}$$

where the ratio constant B has the dimension of $(\text{Time})^{-1}$. Let's choose another constant $\tau = 1/2B$ and call it the "relaxation time". With the aid of (8) and (10), (5) becomes

$$\frac{\Delta N}{N} = (tanh\frac{U}{kT} - tanh\frac{U-pF}{kT})exp(-\frac{t}{\tau}\ cosh\frac{U-pF}{kT}) + tanh\frac{U-pF}{kT} \tag{11}$$

Equation (11) shows that ΔN is exponentially reduced to a steady-state value similar to N(t) in the Spiegel and Joines' paper(1973). Since the barrier force is propotional to ΔN, the cation would flow inward if ΔN is less than a critical value, ΔN_c ; under this condition, the barrier force would be less than the inward driving force. Let the critical value of ΔN be a fraction of ΔN^o, then

$$r = \Delta N_c/\Delta N^o = f_i/f_o \tag{12}$$

where r denotes the fraction, f_o is the original barrier force and f_i the inward driving force. From (8), (12) and let $\Delta N = \Delta N_c$ in (11), the strength-duration relation can be derived as

$$\frac{t_o}{\tau} = \frac{1}{\cosh(U-pF)/kT} \log \frac{\tanh U/kT - \tanh (U-pF)/kT}{\gamma \tanh U/kT - \tanh (U-pF)/kT} \tag{13}$$

Eq. (13) represents the minimum duration t_o for an applied field F to excite the nerve. The field which can just orient the dipoles such that $\Delta N = \Delta N_c$ at $t \to \infty$ is defined here as the rheobasic field F_o. Theoretically, it means that this field is the minimum field which may excite the nerve when the field is applied with an infinite duration. If the applied field is less than F_o, then it is not possible to excite the nerve. From (8), (11) and (12), it can be seen that F_o should satisfy the following equation

$$\tanh (U - pF_o)kT = r \tanh U/kT \tag{14}$$

From (13) and (14) we have

$$\frac{t_o}{\tau} = \frac{1}{\cosh(U-PF)/kT} \log \frac{\tanh U/kT - \tanh(U-pF)/kT}{\tanh(U-pF_o)/kT - \tanh(U-pF)/kT} \tag{15}$$

Equation (15) contains the unknown parameters U, τ and pF_o. U can be obtained by borrowing from Wei's result(Wei, 1971b):

$$U = (E_2 - E_1)/2 \sim 40\ mev/2 = 20\ mev \tag{16}$$

The relaxation time τ, as suggested by Wei(1969b) as in the same order of absolute refractory period, is taken to be 1.5 msec for squid axon (Hodgkin, 1964). pF_o can be obtained from (14) if we know the value of r. In normal axon, the inward driving force for Na^+ is given by its electrochemical potential gradient,

$$f_i = kT \nabla \log[Na] + q \nabla \phi = \frac{kT}{W} \log[Na]_o/[Na]_i - \frac{qV_m}{W} \tag{17}$$

For squid axon, $[Na]_o/[Na]_i = 9$, $V_m = -60$ mv, $W = 70$ Å, and $kT = 24$ mev at $T = 5°C$, then

$$f_i = 1.6 \times 10^5\ ev/cm \tag{18}$$

The potential barrier of a resting membrane has been estimated by many authors to be in the range of 20-26 mv (Hamel and Zimmerman, 1970; Johnson et al. 1954; Wei, 1969a). Let's take the value 20 mv for our problem and assume the thickness of the dipole layer as 10 A (Wei,,1972), then the barrier force for the sodium ion is about

$$f_i = q \times 20\ mv/10Å = 2.0 \times 10^5\ ev/cm. \tag{19}$$

Thus we have r = 0.8. Substituting the values of r and U into (14), we obtain

$$pF_o = 5\ mev. \tag{20}$$

No data on F_0 is available, however, F_0 can be estimated from the threshold voltage of excitation using constant current pulse. From the data of Guttman (1966), the threshold voltage is about 17 mv. Assuming the membrane thickness of 70Å, F_0 can be estimated to be

$$F_o = 17\ mv/70Å = 2.5 \times 10^4\ v/cm \tag{21}$$

and p would be calculated from (21) to be 20 e-Å. Assuming the dipole layer to be 10A, this would indicate that the dipole involves a species with two charges. The above calculation involves with some estimation of parameters. It can be shown that the calculation of p is quite sensitive to the dipole layer thickness. With the assumption of dipole layer thickness of 11Å, the dipole can be calculated to contain only one charge. In any case, the estimation and the calculation seem to be quite reasonable.

The curve of (16) can be plotted in terms of F/F_0 vs. time with the aid of (21) (Figure 1), and is compared with the strength-duration curve observed at constant current pulses for squid axon at T = 5° C (Guttman, 1966).

3. *Optimum Frequency and Relaxation Time*

For sinusoidal alternating stimulus, there exists an optimum frequency at which the stimulus is most effective to excite a membrane. According to the observation of Hill et al.(1936), the optimum frequency lies in the range of 50-200 Hz, increasing with temperature. In the theory of dielectrics, it is known that the maximum absorption of energy from the applied field occurs at the resonant frequency $\omega = \tau^{-1}$ (Fröhlich, 1958). For the membrane dipole system it is quite reasonable to assume that the optimum frequency is just this resonant frequency. In other words, the variation of ΔN is assumed to be the largest when the applied stimulus is at the resonant frequency, and the impulse would be initiated as ΔN_c becomes smaller than ΔN_c .

According to the dipole model of Frohlich(1958), the two states of the dipoles are separated by a potential barrier H as shown in Figure 2 (not to confuse with the energy level difference U). This barrier H is assumed to be large compared with kT, otherwise the diploes with average energy kT would oscillate back and forth between the two states so that thermal equilibrium could never be reached and the initial populations would no longer be distributed as (7). In Figure 2 we can see that the probability for the dipole to transit from I to II and from II to I is respectively

$$w_{12} = \frac{w_o}{2\pi} \exp - (H+U)/kT \, ; \quad w_{21} = \frac{w_o}{2\pi} \exp - (H-U)/kT \tag{22}$$

where $w_o/2\pi$ is the frequency of oscillation of a dipole. Compare with (10) at $F = 0$, we have

$$B = \tfrac{1}{2}\tau = \frac{w_o}{2\pi} \exp - H/kT \tag{23}$$

and

$$\log \tau = \log \pi/w_o + H/kT \tag{24}$$

Since we assumed that the optimum frequency ν_o occured at $(2\pi\tau)^{-1}$, therefore

$$\begin{aligned} \log \nu_o &= \log w_o/2\pi^2 - H/kT \\ &= const - H/kT \end{aligned} \tag{25}$$

Equation (25) shows that the optimum frequency decreases with temperature. This equation can fit the data of Hill et al. (1936) for frog's nerve with H equal to 600 mev. Since $H \gg kT$(24 mev), the result is consistent with our assumption.

4. *Conclusion*

A strength-duration relation has been derived, this relation correlats the applied field F and minimum excitation time t_0 in terms of the relaxation time τ , the energy difference of dipoles U, the dipole moment p and the critical fractional population r. Numerical values have been estimated and the strength-duration relation can be plotted.

However, the available data on strength-duration curve is obtained with constant current pulse, instead of constant voltage pulse across the membrane, so the data can not be directly compared. This paper further deduces the observed relationship of temperature dependence of optimum frequency.

Literature

Frohlich, H. 1958. Theory of Dielectrics. Oxford: Clarendon.

Guttman, R. 1966. "Temperature Characteristics of Excitation in Space-Clamped Squid Axons." J. Gen. Physiol., 49, 1007-1018.

Hamel, B. B. and I. Zimmerman. 1970. "A Dipole Model for Negative Steady-State Resistance in Excitable Membrane." Biophys. J., 10, 1029-1056.

Hill, A. V., B. Katz and D. Y. Solandt. 1936. "Nerve Excitation by Alternating Current." Proc. Roy. Soc. (London), B121, 74-133.

Hodgkin, A. L. 1964. The Conduction of The Nervous Impulse. Springfield, Ill., Charles C Thomas. p. 18.

Johnson, F. H., H. Eyring, and M. J. Polissar. 1954. The Kinetic Basis of Molecular Biology. John Wiley and Sons, Inc., New York. p. 564.

Spiegel, R. J. and W. T. Joines. 1973. "A Semiclassical Theory For Nerve Excitation By A Low Intensity Electromagnetic Field.' Bull. Match. Biology., 35, 591-605.

Wei, L. Y. 1969a. "Role of Surface Dipoles on Axon Membrane." Science, 163, 280-282.

1969b. "Molecular Mechanisms of Nerve Excitation and Conduction." Bull. Math. Biophys., 31, 39-58.

1971a. "Quantum Theory of Nerve Excitation." Ibid., 33, 187-194.

1971b. "Possible Origin of Action Potential and Birefringence Change in Nerve Axon." Ibid., 33, 521-537.

1972. "Dipole Theory of Heat Production and Absorption in Nerve Axon." Biophys. J., 12, 1159-1170.

1973. "Quantum Theory of Time-Varying Stimulation in Nerve." Bull. Math. Biophys., 35, 359-374.

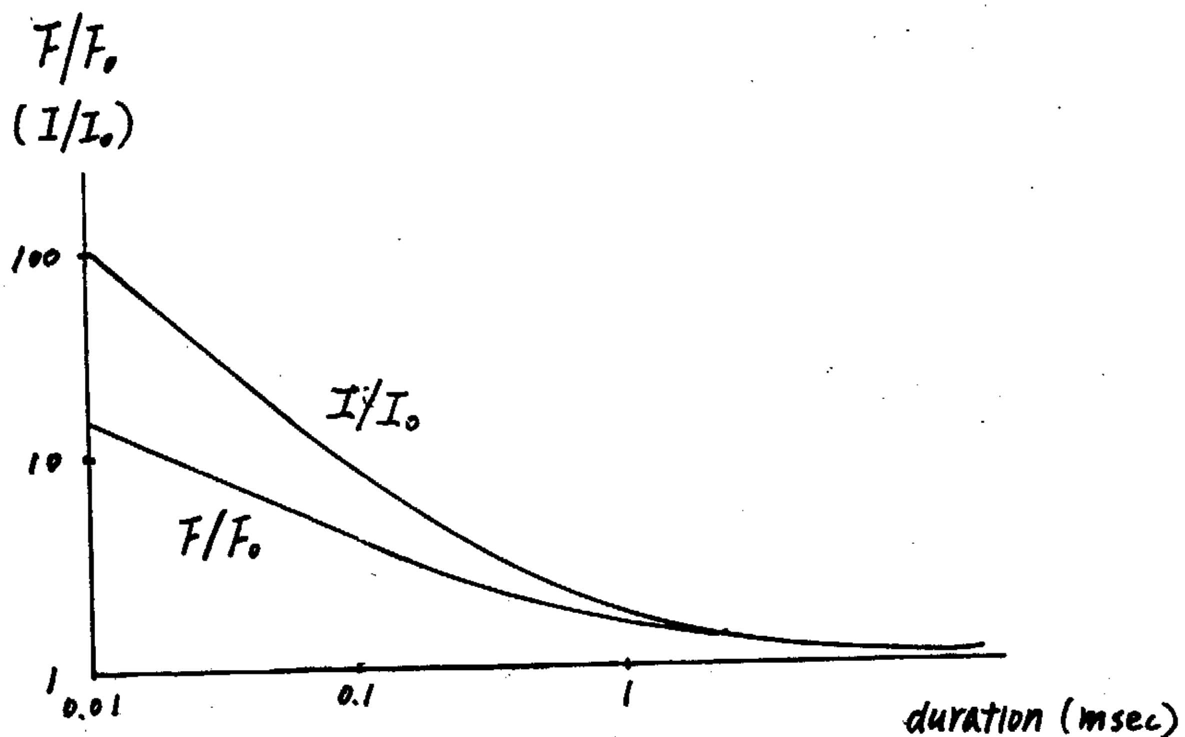

Fig. 1. duration (mse~)

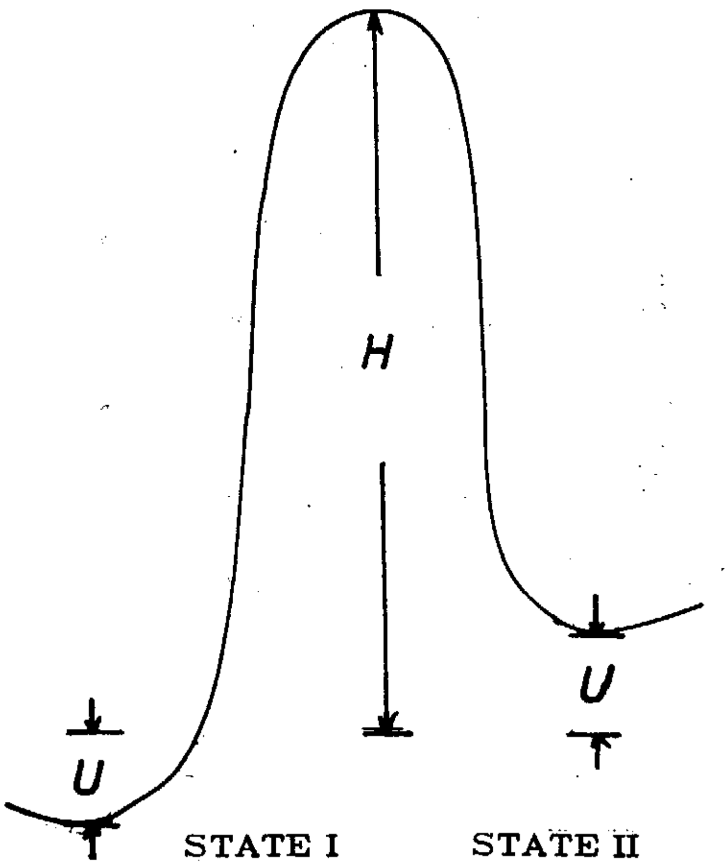

Fig. 2. Potential energy diagram of the dipoles in a resting membrane

ANNUAL REPORT OF THE INSTITUTE OF PHYSICS, ACADEMIA SINICA 1973

THE ENERGY SPLITTING AND RELATIVE INTENSITIES OF ACCEPTOR UNDER ARBITRARY DIRECTIONAL STRESS

Sung-Shan Tai

Institute of Physics, Academia Sinaca

Abstract

This paper presents the theorectical study of excitation spectrum of the imputities in germanium under uniaxial stress in arbitrary direction. Under the action of stress the Γ_8 state splits into two sublevels when $\Delta_{111} > \Delta_{100}$ we found the force in $<111>$ direction will cause the maximum splitting and when the force in (110) plane the energy splitting will greater than any other plane. The relative intensities of transition from Γ_8 to Γ_6, Γ_7, and Γ_8 states are also goven when force in arbitrary direction that can reduce to some special plane and special direction.

1. *Introduction*

The behavior of group-III and group-V impurities in germanium are one of the most extensively studied and understood the properties of semiconductor. The optical properties of semiconductor are affacted by the presence of impurities due to the impurity states produce in the forbident band, the bound states in the energy gap has been studies by Kittel and Mitchell(1) and Luttinger and Kohn(2,3) in effective mass method. The group III impurities in silicon and germanium exist in form of acceptors, the excitation spectrum has been examinated extensively.(4,7) The application of uniaxial stress to a semiconductor produce a strain which reduce the symmetry of material and results in significant changes in energy states. Some of these changes can be determaned from the study of the stress induced variation of the excitation spectrum. From an analysis of these changes, including polarization and intensity, as a function of magnitute and direction of the applied stress, it is possible to measure the deformation potentials and labbel the quantum states of impurity. In the work, we use group theory and base on the method developed by Rodriguez and Fisher(8,9) establish the energy splitting and relative intensities in arbitrary direction stress and reduce to some special plane such as (100), (001), (110) and (120) planes, in some special direction we get the same results as other literature.

2. *Energy Splitting in A Strained Cubic Crystal*

A uniaxial stress applied to germanium or silicon crystal removes the cubic symmetry. The form of Hamiltonian is invariant under the transformation of tetrahedral group and belongs to T(A_1) irreducible representation. Kleiner and Roth$^{(10)}$ have constructed a Hamiltonian in term of the angular momentum operator (J=3/2) to describe the $p_{\frac{3}{2}}$ state at k=0 under uniaxial stress

$$H_e = D_d^v(e_{xx}+e_{yy}+e_{zz}) + \frac{2}{3} D_u [(J_x^2 - \frac{1}{3} J^2)e_{xx} + (J_j^2 - \frac{1}{3} J^2)e_{yy} + (J_z^2 - \frac{1}{3} J^2)e_{zz}]$$

$$+ \frac{2}{3} D_u' [(J_x , J_y)e_{xy} + (J_y , J_z)e_{yz} + (J_x , J_z)e_{xz}] \tag{1}$$

where e_{xx} , e_{yy} , e_{zz} , e_{xy} , e_{yz} and e_{xz} are the conventional strained tensor components and D_d^v , D_u and D_u' are the valence band deformation potential and (J_i , J_j) = ½ (J_iJ_j+ J_jJ_i). Where D_d^v gives the shift of the center of gravity of entire valence band and does not contribute to the splitting. Hence can be neglect.

In order to calculate the energy splitting of a cubic crystal with an applied uniaxial stress in arbitrary direction, we must find the strain components in crystal axes. The procedure is straightforward. We choose a primed system (x′, y′, z′) in which the stress T′ along z′ axis. In this system the stress tensor has the form

$$T_{ij}' = \begin{cases} T' & \text{for } i=j=3 \\ 0 & \text{for otherwise.} \end{cases} \tag{2}$$

The transformation from the crystal system (x, y, z) to primed system can be expressed by a matrix equation of the form

$$\begin{bmatrix} x \\ y \\ z \end{bmatrix} = \begin{bmatrix} \cos\varphi & -\cos\theta\sin\varphi & -\sin\theta\sin\varphi \\ \sin\varphi & \cos\theta\cos\varphi & \sin\theta\cos\varphi \\ 0 & -\sin\theta & \cos\theta \end{bmatrix} \begin{bmatrix} x' \\ y' \\ z' \end{bmatrix}. \tag{3}$$

The angle θ and φ corresponding to the spherical coordinate in crystal coordinate system, This stress tensor can be found by same transformation

$$T_{ii} = \lambda_{ik}\lambda_{jl}T_{kl}' . \tag{4}$$

Hence, the stress tensor in crystal system are

$$T = \begin{bmatrix} T_{xx} \\ T_{yy} \\ T_{zz} \\ T_{xy} \\ T_{xz} \\ T_{yz} \end{bmatrix} = T' \begin{bmatrix} \sin^2\theta \sin^2\varphi \\ \sin^2\theta \cos^2\varphi \\ \cos^2\theta \\ -\sin^2\theta \cos\theta \sin\varphi \\ -\sin\theta \cos\theta \sin\varphi \\ \sin\theta \cos\theta \cos\varphi \end{bmatrix} \tag{5}$$

The strain tensor S_{ij} is obtained

$$S_{ij} = s_{ijkl} T_{kl}, \tag{6}$$

where s_{ijkl} are components of cubic compliance tensor

$$S = \begin{bmatrix} S_{xx} \\ S_{yy} \\ S_{zz} \\ S_{xy} \\ S_{xz} \\ S_{yz} \end{bmatrix} = T' \begin{bmatrix} S_{11}(\sin\theta\sin\varphi)^2 + S_{12}(\sin^2\theta\cos^2\varphi + \cos^2\theta) \\ S_{11}(\sin\theta\cos\varphi)^2 + S_{12}(\sin^2\theta\sin^2\varphi + \cos^2\theta) \\ S_{11}\cos^2\theta \qquad + S_{12}(\sin^2\theta\sin^2\varphi + \sin^2\theta\cos^2\varphi) \\ -\tfrac{1}{2} S_{44}\sin^2\theta\sin\varphi\cos\varphi \\ -\tfrac{1}{2} S_{44}\sin\theta\cos\theta\sin\varphi \\ \tfrac{1}{2} S_{44}\sin\theta\cos\theta\cos\varphi \end{bmatrix}; \tag{7}$$

From the definition of the conventional strain tensor e_{ij} differes from those of tensor by a factor of 2 in the off-diagonal elements, that is

$$e_{ij}=S_{ij} \text{ if } i=j \text{ and } e_{ij}=2S_{ij} \text{ if } i\neq j.$$

When the stress applied in arbitary direction in a cubic crystal, the symmetry group is $\bar{C}_S$ group. The character table is given in Table I. The states designed $\Gamma_3(\bar{C}_S)$ and $\Gamma_4(\bar{C}_S)$ are degenerate under time reversal operator and will not be split by application of uniaxial stress. The $\Gamma_6(\bar{T}_d)$ and $\Gamma_7(\bar{T}_d)$ states will not split, but $\Gamma_8(\bar{T}_d)$ states will not split, but $\Gamma_8(\bar{T}_d)$ states will decompose into two sublevels $\Gamma_3(\bar{C}_S)+\Gamma_4(\bar{C}_S)$ denoted $\Gamma_{3+4}(\bar{C}_S)$. Using a matrix representation for J_x, J_y, J_z (2) we have H_e in matrix form

$$H_e = \begin{bmatrix} \epsilon_1 & -\epsilon_2 e^{-i\varphi} & \epsilon_4+i\epsilon_3 & 0 \\ -\epsilon_2 e^{i\varphi} & -\epsilon_1 & 0 & \epsilon_4+i\epsilon_3 \\ \epsilon_4-i\epsilon_3 & 0 & -\epsilon_1 & \epsilon_2 e^{-i\varphi} \\ 0 & \epsilon_4-i\epsilon_3 & \epsilon_2 e^{i\varphi} & \epsilon_1 \end{bmatrix}, \tag{8}$$

where

$$\begin{aligned} \epsilon_1 &= \frac{2}{3} D_u T'(S_{11}-S_{12})\,(\cos^2\theta-\frac{1}{2}\sin^2\theta)\,, \\ \epsilon_2 &= -\frac{1}{\sqrt{3}} D_u' T' S_{44} \sin\theta\cos\theta\,, \\ \epsilon_3 &= -\frac{1}{\sqrt{3}} D_u' T' S_{44} \sin^2\theta\cos\varphi\sin\varphi\,, \\ \epsilon_4 &= -\frac{1}{\sqrt{3}} D_u T'(S_{11}-S_{12})\sin^2\theta(\cos^2\varphi-\sin^2\varphi)\,. \end{aligned} \tag{9}$$

Table I. Character table for the double value group $\overline{C}_S$.

$\overline{C}_S$	E	E	σ	$\overline{\sigma}$
3	1	-1	$-i$	i
4	1	-1	i	$-i$

The diagonalization of H_e is accomplished by the unitary transformation matrix R

$$R = \frac{1}{N} \begin{bmatrix} 1 & \dfrac{\epsilon_2 e^{-i\varphi}}{\epsilon_1+\delta} & \dfrac{i(\epsilon_3-i\epsilon_4)}{\epsilon_1+\delta} & 0 \\ \dfrac{-\epsilon_2 e^{i\varphi}}{\epsilon_1+\delta} & 1 & 0 & \dfrac{-i(\epsilon_3-i\epsilon_4)}{\epsilon_1+\delta} \\ \dfrac{i(\epsilon_3+i\epsilon_4)}{\epsilon_1+\delta} & 0 & 1 & \dfrac{\epsilon_2 e^{-i\varphi}}{\epsilon_1+\delta} \\ 0 & \dfrac{-i(\epsilon_3+i\epsilon_4)}{\epsilon_1+\delta} & \dfrac{-\epsilon_1 e^{i\varphi}}{\epsilon_1+\delta} & 1 \end{bmatrix}, \tag{10}$$

where

$$\delta = (\epsilon_1^2+\epsilon_2^2+\epsilon_3^2+\epsilon_4^2)^{½} ,$$

N is normalized constant.

The eigenvalue are ± δ . The $\Gamma_8(\overline{T}_d)$ levels split into two sublevels with energy difference 2δ .

3. *Relative Intensive of Electric Dipole Transition*

The transition probability induced by electric dipole from state χ^i_m *to* χ^f_m *is* proportional to the square of the transition matrix $<\chi^f_{m'}|\vec{Q}|\chi^f_m>$ where $\vec{Q}$ is the electric dipole moment operator of the system. Without external perturbation, the system belong to T_d group and impurity levels labeled by double-valued representation Γ_6, Γ_7, Γ_8. The ground state is characterized by $\Gamma_8(\overline{T}_d)$. The components of Q belong to the single-valued representation $\Gamma_5(T_d)$. From elementary group theory, we have $\Gamma_5 \times \Gamma_6 = \Gamma_7 + \Gamma_8$, $\Gamma_5 \times \Gamma_7 = \Gamma_6 + \Gamma_8$, and $\Gamma_5 \times \Gamma_8 = \Gamma_6 + \Gamma_7 + 2\,\Gamma_8$. Thus the transition induced by electric dipole are permitted between Γ_8 and Γ_6, Γ_7, Γ_8 states.

The eigenstates under applied stress are given by appreciated linear combination of perturbed wave functions.

$$\chi^i_{m'} = \Sigma\, R_{\nu m'}\, \psi^i_\nu ,$$
$$\chi^f_m = \Sigma\, R_{\mu m}\, \psi^f_\mu . \tag{11}$$

where (ψ^i_ν) and (ψ^f_μ) are the unperturbed wave function of the impurty levels. Thus, the transition matrix is

$$\vec{M}^{i\rightarrow,f}_{mm'} = (R'^{+}\vec{Q}\,R)_{mm'} . \tag{12}$$

Case 1. $\Gamma_8 \rightarrow \Gamma_6$

The transition from Γ_8 to Γ_6, only one complex parameter are needed to described the transition matrix Q, since in the direct product of $\Gamma_5 \times \Gamma_6 = \Gamma_7 + \Gamma_8$, Γ_8 appear only once.

Using elementary group theorem one gets

$$\vec{Q}^{8\rightarrow 6} = D_0 \begin{bmatrix} \sqrt{3}\,(\hat{x} + i\hat{y}) & -2i\hat{z} & (\hat{x} + \hat{y}i) & 0 \\ 0 & i(\hat{x} + i\hat{y}) & 2\hat{z} & \sqrt{3}i(\hat{x} - i\hat{y}) \end{bmatrix}, \tag{13}$$

where D_0 is a complex parameter that can be obtained by unperturbed wave function. To get the transition matrix $\vec{Q}$ when applied force in arbitrary direction, one can have transition R′ is 2 × 2 unit matrix and R is given in Eq. (8). From Eq. (12), the components of transformed transition matrix are

$$\begin{aligned} Q'_x &= \frac{D_o}{N} \begin{bmatrix} \sqrt{3}+A & -\sqrt{3}B^{*} & -\sqrt{3}A^{*} & -B^{*} \\ Bi & (1-3A)i & \sqrt{3}Bi & (A^{*}+\sqrt{3})i \end{bmatrix}, \\ Q'_y &= \frac{D_o}{N} \begin{bmatrix} (\sqrt{3}-A) & -\sqrt{3}B^{*}i & -(\sqrt{3}A^{*}+1)i & B^{*}i \\ -B & -(1+\sqrt{3}A) & \sqrt{3}B & \sqrt{3}-A^{*} \end{bmatrix}, \\ Q'_z &= \frac{D_o}{N} \begin{bmatrix} -2Bi & -2i & 0 & -2A^{*}i \\ 2A^{*} & 0 & 2 & -2B^{*} \end{bmatrix}, \end{aligned} \tag{14}$$

where

$$\begin{aligned} A &= \frac{i(\epsilon_3 + i\epsilon_4)}{\epsilon_1 + \delta}, \\ B &= \frac{-\epsilon_2 e^{i\varphi}}{\epsilon_1 + \delta}. \end{aligned} \tag{15}$$

Since we require the components of Q one along the direction of force and the other two perpendicular direction, we choose a Cartesian coordinate system x', y', z' where z' parallel to F and x', y' are two perpendicular axes. The three components of transition matrix $Q_{x'}, Q_{y'}, Q_{z'}$ along x', y', z' respectively. Thus we have

$$Q_{x'} = Q'_x \cos\varphi + Q'_y \sin\varphi,$$

$$Q_{y'} = -Q'_x \cos\theta \sin\varphi + Q'_y \cos\theta \sin\varphi - Q'_z \sin\theta,$$

$$Q_{z'} = -Q'_x \sin\theta\sin\varphi + Q'_y \sin\theta\cos\varphi + Q'_z \cos\theta\,. \tag{16}$$

The relative intensities along three axes are proportional to the square of transition matrix are presented in Table II.

Case 2. $\Gamma_8 \rightarrow \Gamma_7$

The transition from Γ_8 to Γ_7, same as case 1, only one parameter are needed to express the transition matrix

$$\vec{Q}^{8\rightarrow 7} = D'_o \begin{bmatrix} -(\hat{x}+\hat{y}i) & 0 & \sqrt{3}(\hat{x}+\hat{y}i) & 2\hat{z}i \\ -2\hat{z} & \sqrt{3}(\hat{x}+\hat{y}i)i & 0 & -i(\hat{x}+\hat{y}i) \end{bmatrix}, \tag{17}$$

where D'_o is a complex parameter that can be derived from the unperturbed wave functions. In arbitrary direction applied force, one make use of the transition matrix R and R′ given in Eq.(8). The transformed Transition matrix Q′ are

$$Q'_x = \frac{D'_o}{N} \begin{bmatrix} -1+\sqrt{3}A & B^* & A^*+\sqrt{3} & -\sqrt{3}B^* \\ \sqrt{3}Bi & (\sqrt{3}+A)i & -Bi & (\sqrt{3}A^*-1)i \end{bmatrix},$$

$$Q'_y = \frac{D'_o}{N} \begin{bmatrix} (1+\sqrt{3}A)i & -B^*i & (\sqrt{3}-A)i & \sqrt{3}B^*i \\ \sqrt{3}B & \sqrt{3}-A & B & \sqrt{3}A^*+1 \end{bmatrix}, \tag{18}$$

$$Q'_z = \frac{D'_o}{N} \begin{bmatrix} 0 & -2Ai & 2Bi & 2i \\ -2 & 2B^* & 2A^* & 0 \end{bmatrix}.$$

The relative intensities are listed in Table II.

Case 3. $\Gamma_8 \rightarrow \Gamma_8$

The transition of $\Gamma_8 \rightarrow \Gamma_8$, we note that $\Gamma_8 \times \Gamma_8 = \Gamma_6 + \Gamma_7 + 2\,\Gamma_8$, here Γ_8 appears twice. The transition matrix Q must be in term of two complex parameters D and D′

$$\vec{Q}^{8\rightarrow 8} \begin{bmatrix} 0 & -(D+2D')(\hat{x}+i\hat{y}) & -(D-D')i\hat{z} & 3D'(\hat{x}-i\hat{y}) \\ D(-\hat{x}+i\hat{y}) & 0 & 3D'(\hat{x}+i\hat{y}) & -(D+3D')i\hat{z} \\ (D+3D')i\hat{z} & 3D'(-\hat{x}+i\hat{y}) & 0 & D(\hat{x}+i\hat{y}) \\ 0 & (D-D')i\hat{z} & (D+3D')(\hat{x}-i\hat{y}) & 0 \end{bmatrix} \qquad (19)$$

In this case, the transformation matrix R is given in Eq. (8) and R$'$ is given below

$$R' = \frac{1}{M} \begin{bmatrix} 1 & -G^* & -F^* & 0 \\ G & 1 & 0 & F^* \\ F & 0 & 1 & -G^* \\ 0 & -F & G & 1 \end{bmatrix}, \qquad (20)$$

where M, F, G have the same form as A, B, C but with different deformation potential.

The components of transformed transition matrix $\vec{Q}$ are

$$Q'^{8\rightarrow 8}_{x} = \frac{1}{MN} \left[\begin{array}{ll} -D(B+G^*)+D'(-2B+\sqrt{3}G^*A-\sqrt{3}F^*B) & D(G^*B^*-1-F^*A)+D'(-\sqrt{3}A-\sqrt{3}F^*-2) \\ D(GB-F^*A-1)+D'(2GB+\sqrt{3}A+\sqrt{3}F^*-2F^*A) & D(G+B^*)+D'(\sqrt{3}GA-\sqrt{3}F^*B^*+2G) \\ D(FB+G^*A)+D'(2FB-\sqrt{3}B-3G^*+2G^*A) & D(F-A)+D'(\sqrt{3}AF+\sqrt{3}B^*G^*+2F-\sqrt{3}) \\ D(-F+A)+D'(\sqrt{3}AF+\sqrt{3}GB+2A-\ 3) & D(FB^*+AG)+D'(\sqrt{3}B^*+\sqrt{3}G) \end{array} \right.$$

$$\left. \begin{array}{ll} D(F^*B+G^*A^*)+D'(\sqrt{3}B+\sqrt{3}G^*) & D(-A^*+F^*)+D'(-\sqrt{3}F^*A^*-\sqrt{3}G^*B^*-2A^*+\sqrt{3}) \\ D(A^*-F^*)+D'(-\sqrt{3}GB-\sqrt{3}F^*A^*-2F^*+\sqrt{3}) & D(A^*G+F^*B^*)+D'(2F^*B^*+2A^*G-\sqrt{3}G-\sqrt{3}B^*) \\ D(B+G^*)+D'(\sqrt{3}G^*A^*-\sqrt{3}FB+2G^*) & D(FA^*-G^*B^*+1)+D'(2FA^*-2G^*B^*-\sqrt{3}F-\sqrt{3}A^*) \\ D(-GB^*+1+A^*F)+D'(\sqrt{3}F+\sqrt{3}A^*+2) & D(-G-B^*)+D'(\sqrt{3}GA^*-\sqrt{3}B^*F-2B^*) \end{array} \right]$$

$$Q'^{8\rightarrow 8}_{y} = \frac{i}{MN} \left[\begin{array}{ll} D(G^*-B)+D'(\sqrt{3}BF^*+\sqrt{3}G^*A-2B) & D(-AF^*-B^*G-1)+D'(\sqrt{3}F^*+\sqrt{3}A-2) \\ D(BG+F^*A+1)+D'(2BG+2AF^*+\sqrt{3}A+\sqrt{3}F^*) & D(G-B^*)+D'(-\sqrt{3}F^*B^*-\sqrt{3}AG+2G) \\ D(FB-G^*A)+D'(2FB-2AG^*-\sqrt{3}G^*+\sqrt{3}B) & D(F-A)+D'(\sqrt{3}B^*G^*-\sqrt{3}AF+2F-\sqrt{3}) \\ D(F-A)+D'(\sqrt{3}FA-\sqrt{3}BG-2A-\sqrt{3}) & D(GA-FB^*)+D'(-\sqrt{3}G+\sqrt{3}B^*) \end{array} \right.$$

$$\begin{matrix} D(BF^{*}-A^{*}G^{*})+D'(\sqrt{3}G^{*}-\sqrt{3}B) & D(F^{*}-A^{*})+D'(\sqrt{3}A^{*}F^{*}-\sqrt{3}B^{*}G^{*}-2A^{*}-\sqrt{3}) \\ D(F^{*}-A^{*})+D'(\sqrt{3}BG-\sqrt{3}F^{*}A^{*}+2F^{*}+\sqrt{3}) & D(A^{*}G-F^{*}B^{*})+D'(2GA^{*}-2F^{*}B^{*}+\sqrt{3}G-\sqrt{3}B) \\ D(B-G^{*})+D'(\sqrt{3}FB+\sqrt{3}G^{*}A^{*}-2G^{*}) & D(FA^{*}+B^{*}G^{*}+1)+D'(2FA^{*}+2B^{*}G^{*}+\sqrt{3}A^{*}+\sqrt{3}F) \\ D(-A^{*}F-GB-1)+D'(\sqrt{3}A^{*}+\sqrt{3}F-2) & D(B^{*}-G)+D'(-\sqrt{3}B^{*}F-\sqrt{3}GA^{*}+2B^{*}) \end{matrix}\Bigg] \qquad (21)$$

,

$$Q_z^{\prime 5\to 8}=\frac{i}{MN}\left[\begin{matrix} D(-A+F^{*})+D'(A+3F^{*}) & D(G^{*}A-F^{*}B^{*})+D'(3G^{*}A-3F^{*}B^{*}) \\ D(GA-F^{*}B)+D'(F^{*}B-GA) & D(A-F^{*})+D'(F^{*}+3A) \\ D(AF+BG^{*}+1)+D'(3-AF-G^{*}B) & D(G^{*}-B^{*})+D'(-G^{*}-3B^{*}) \\ D(-G+B)+D'(-B-3G) & D(FA+GB^{*}+1)+D'(3GB^{*}+3FA-1) \end{matrix}\right.$$

$$\left.\begin{matrix} D(-1-G^{*}B-A^{*}F^{*})+D'(1-3G^{*}B-3A^{*}F^{*}) & D(B^{*}-G^{*})+D'(-B^{*}-3G^{*}) \\ D(G-B)+D'(-G-3B) & D(-B^{*}G-F^{*}A^{*}-1)+D'(B^{*}G+F^{*}A^{*}-3) \\ D(F-A^{*})+D'(-F-3A^{*}) & D(G^{*}A^{*}-B^{*}F)+D'(B^{*}F-G^{*}A^{*}) \\ D(-BF+GA^{*})+D'(3GA^{*}-3BF) & D(-F+A^{*})+D'(-3F-A^{*}) \end{matrix}\right].$$

The relative intensities are very complicate and there are not compact form to be given.

Table II. Relative intensitis for force in arbitary direction

Zero-stress Transition	Components	Relative Intensity
	A. Transverse Polarization along x'	
$\Gamma_8 \rightarrow \Gamma_6$	$\Gamma_{3+4}(\pm\frac{3}{2}) \rightarrow \Gamma_{3+4}$ THX	$(f+b)/4N^2$
	$\Gamma_{3+4}(\pm\frac{1}{2}) \rightarrow \Gamma_{3+4}$ TLX	$(g-b)/4N^2$
$\Gamma_8 \rightarrow \Gamma_7$	$\Gamma_{3+4}(\pm\frac{3}{2}) \rightarrow \Gamma_{3+4}$ THX	$(g-b')/4N^2$
	$\Gamma_{3+4}(\pm\frac{1}{2}) \rightarrow \Gamma_{3+4}$ TLX	$(f+b')/4N^2$
	B. Transverse Polarization along y'	
$\Gamma_8 \rightarrow \Gamma_6$	$\Gamma_{3+4}(\pm\frac{3}{2}) \rightarrow \Gamma_{3+4}$ THY	$[(f+b)\cos^2\theta + j\sin\theta\cos\theta + 4k\sin^2\theta]/4N^2$
	$\Gamma_{3+4}(\pm\frac{1}{2}) \rightarrow \Gamma_{3+4}$ TLY	$[(g+b)\cos^2\theta - j\sin\theta\cos\theta + 4\sin^2\theta))]/4N2$
$\Gamma_8 \rightarrow \Gamma_7$	$\Gamma_{3+4}(\pm\frac{3}{2}) \rightarrow \Gamma_{3+4}$ THY	$[(f-g)\cos^2\theta + j\sin\theta\cos\theta + 4\sin^2\theta]/4N^2$
	$\Gamma_{3+4}(\pm\frac{1}{2}) \rightarrow \Gamma_{3+4}$ TLY	$[(g+b')\cos^2\theta - j\sin\theta\cos\theta + 4k\sin^2\theta]/4N^2$
	C. Longitudinal Polarization	
$\Gamma_8 \rightarrow \Gamma_6$	$\Gamma_{3+4}(\pm\frac{3}{2}) \rightarrow \Gamma_{3+4}$ THZ	$[(f-b)\sin^2\theta - j\sin\theta\cos\theta + 4k\cos^2\theta]/4N^2$
	$\Gamma_{3+4}(\pm\frac{1}{2}) \rightarrow \Gamma_{3+4}$ TLZ	$[(g+b)\sin^2\theta + j\sin\theta\cos\theta + 4\cos^2\theta]/4N^2$
$\Gamma_8 \rightarrow \Gamma_7$	$\Gamma_{3+4}(\pm\frac{3}{2}) \rightarrow \Gamma_{3+4}$ THZ	$[(g+b')\sin^2\theta - j\sin\theta\cos\theta + 4k\cos^2\theta]/4N^2$
	$\Gamma_{3+4}(\pm\frac{1}{2}) \rightarrow \Gamma_{3+4}$ TLZ	$[(f-b')\sin^2\theta + j\sin\theta\cos\theta + 4k\cos^2\theta]/4N^2$

where

$f = 3 + AA^* + BB^*$ $b = \sqrt{3}A\exp(-2i\varphi) + \sqrt{3}A^*\exp(2i\varphi)$

$g = 1 + 3AA^* + 3BB^*$ $j = 2\sqrt{3}[B^*\exp(i\varphi) + B\exp(-i\varphi)]$

$k = BB^* + AA^*$ $b' = \sqrt{3}A^*\exp(-2i\varphi) + \sqrt{3}A\exp(2i\varphi).$

4. *Summary and Conclusions*

When the stress is applied, the Γ_8 state splits into two sublevels with energy difference 2δ, the high state designed $\Gamma_8(\pm\frac{3}{2})$ and the low state designed $\Gamma_8(\pm\frac{1}{2})$. The energy splitting of Γ_8 state is shown in Fig. 1. calculated with $\Delta_{100} = 1.585$mev and $\Delta_{111} = 1.826$mev which are energy splitting when force in $<100>$ direction and $<111>$ direction respectively. From this figure we note that when force in (100) plane, the energy splitting is like cosin function but if force in other plane there are less symmetry than in (100) plane. In the case of $\Delta_{111} > \Delta_{100}$, the occurrence of the greatest splitting change from 45° force in (100) plane to about 54° force in (110) plane. We also note that when force in (110) plane the energy splitting of Γ_8 state is greater than force in any other plane in all range of θ, the maximum splitting come to force in $<111>$ direction. The energy difference between $\Gamma_8(\pm\frac{3}{2})$states are shown in Fig.6. which calculates with $\Delta_{100} = 1.585$mev, $\Delta_{111} = 1.826$mev and $\Delta'_{100} = 1.492$mev, $\Delta'_{111} = 1.286$mev. The curve has the same shape and character as Fig.1. because the two Γ_8 states have the same shape. When force along $<001>$ direction the energy difference is 0.093mev.

The relative intensities we calculated are not the exact relative intensities because we assume that all initial sublevels are equally populated. The compact form of the relative intensities of the transition from Γ_8 to Γ_7 and Γ_6 states list in Table II. The numerical results for some special plane are given in Fig. 2 to Fig. 5 which calculated with the parameter same as before. In Fig. 2 we know that the relative intensity of $\Gamma_8(\pm\frac{3}{2}) \to \Gamma_6$ and $\Gamma_8(\pm\frac{1}{2}) \to \Gamma_7$, $\Gamma_8(\pm\frac{1}{2}) \to \Gamma_6$ and $\Gamma_8(\pm\frac{3}{2}) \to \Gamma_7$, polarization along x′ are equal to each other just as prediction in Table II. The transition from Γ_8 to Γ_6 longitudinal polarization and one of transverse polarization(x′) are monotonic function of the action angle. The other transverse polarization(y′), the transition from high state of Γ_8 to Γ_6 is greater than the other component in all (100) plane. When θ=45° in Fig. 1 this corresponds to force in $<101>$ direction the symmetry group of the system belonged to $\overline{C}_{2v}$. The general furture of the intensities still obey. One of transverse polarization(x′), the relative intensities of $\Gamma_8(\pm\frac{3}{2}) \to \Gamma_6$ and $\Gamma_8(\pm\frac{1}{2}) \to \Gamma_7$, $\Gamma_8(\pm\frac{1}{2}) \to \Gamma_6$ and $\Gamma_8(\pm\frac{2}{3}) \to \Gamma_7$ equal to each other. The intensities of the components TYL, TYH, TZH, TZL of the transition from Γ_8 to Γ_6 are equal to that of TZH, TZL, TYL, TYH of Γ_8 to Γ_7 transition. In the case of force in (110) plane, Fig. 3, in Γ_8 to Γ_7 transition, one of the transverse polarization(x′) are nearly independent of the direction of force in this plane, the other transverse polarization(y′) and the logitudinal polarization are function of θ symmetry about $<110>$ direction. If force in (001) plane as Fig 5. The inensities of $\Gamma_8 \to \Gamma_6$ seemed very simple nearly independent of the direction of force in this plane, Specially, when polarization along x′ the relative intensities are constant and equal to land0, that is $\Gamma_8(\pm\frac{3}{2})\rightarrow\Gamma_7$ is forbiden. In $\Gamma_8\rightarrow\Gamma_7$ transition only longhtudial polarization are nearly constant. In Fig. 3 $\theta=45°$ and Fig. 5 $\varphi=90°$ correspond to the case of force in <110> direction. The corresponding components must have same intensities as the figure shown. The relative intensities of the components TXH, TXL, TYH, TYL, TZH, TZL in $\Gamma_8\rightarrow\Gamma_6$ transition and that of components TZL, TZH, TYL, TYH, TXL, TXH in $\Gamma_8\rightarrow\Gamma_7$ transition equal to one another respectively. Force in other plane, for example (120) plane, there are not have such high symmetry as in special plane. From Fig. 2 to Fig. 5 one would notice that in $\Gamma_8\rightarrow\Gamma_6$ transition the logitudinal polarization and one of transverse polarization(x') are function of 2θ and are monotonic function of θ in (hk0) plane and the other transverse polarization is periodic function of θ symmetry about $\theta=45°$. The intensities of transition from Γ_8 to Γ_6 are greater than the other component in all (hk0) plane. For the case of force in <001> direction the transverse polarization apprach to 0.25 and 0.75 and that of logitudinal polarization apporach to 1 and 0. In $\Gamma_8\rightarrow\Gamma_8$ transition, the result are very tedious there are no compact form are obtained but the numerical result calculated with parameter Δ_{100} = 1.492mev , Δ_{111} = 1.826mev , Δ_{100} = 1.492mev , Δ_{111} = 1.286 and u=0.23, v=0.1 are plotted Fig. 7 to Fig. 8 for some special planes. The state $\Gamma_8(\pm\frac{3}{2})$ desinged H, the state $\Gamma_8(\pm\frac{1}{2})$ designed L the transition $\Gamma_8(\pm\frac{3}{2})\rightarrow\Gamma_8(\pm\frac{1}{2})$ designed by HL. Force in (001) plane, the components of HH and LL coincident as prediction and has high symmetry. If force along <001> direction this corresponding to force in (hk0) plane $\theta=0°$, the relative intensities are same as other literature.(8)

Acknowledgement

It is a pleasure to express the hearty thank to Dr. L. T. Ho of Academia Sinica for his guidance and encouragement and all members of computer center of Tsing-Hua University for their generous assistance.

References

1. C. K. Kittel and A. H. Mitchell Phys. Rev. 96, 1488 (1954).
2. J. M. Luttinger and W. Kohn Phys. Rev. 96, 802 (1954).
3. W. Kohn and J. M. Luttinger Phys. Rev. 98, 915 (1955).
4. A. Onton, P. Fisher and A. K. Ramdans Phys. Rev. 163, 686 (1967).
5. D. H. Diskey and J. O. Dimmock J. Phys. Chem. Solids 28, 529 (1967).
6. F. Barra and P. Fisher Phys. Rev. B7, 5285 (1973).
7. P. Fisher and H. Y. Fan Phys. Rev. Lett. 5, 195 (1960).
8. S. Rodriguez, P. Fisher and F. Barra Phys. Rev. B5, 2219 (1972).
9. K. Anadi, Bhattacharjee and S. Rodriguez Phys. Rev. B6, 3836 (1972).
10. W. H. Kliener and L. M. Roth Phys. Rev. Lett. 2, 334 (1959).

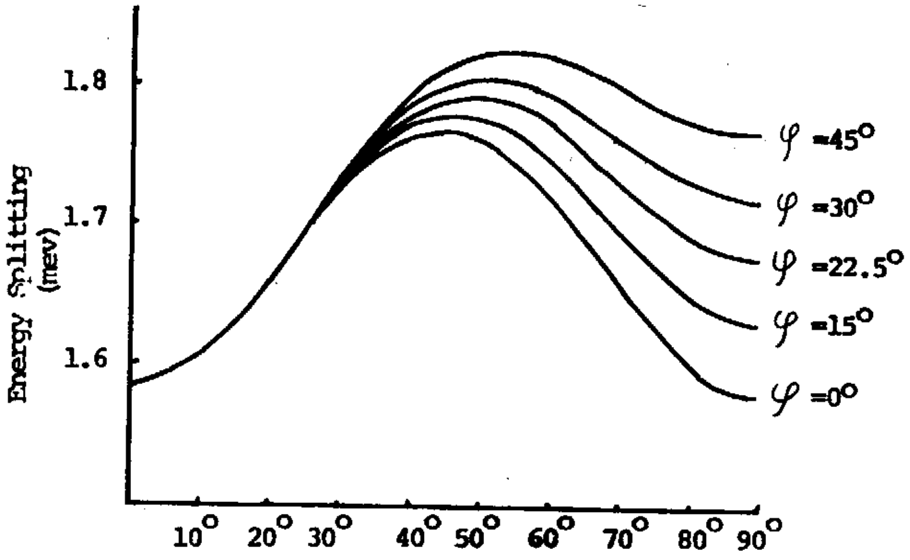

Fig. 1. Energy splitting of Γ_8 state for stress in different plane.

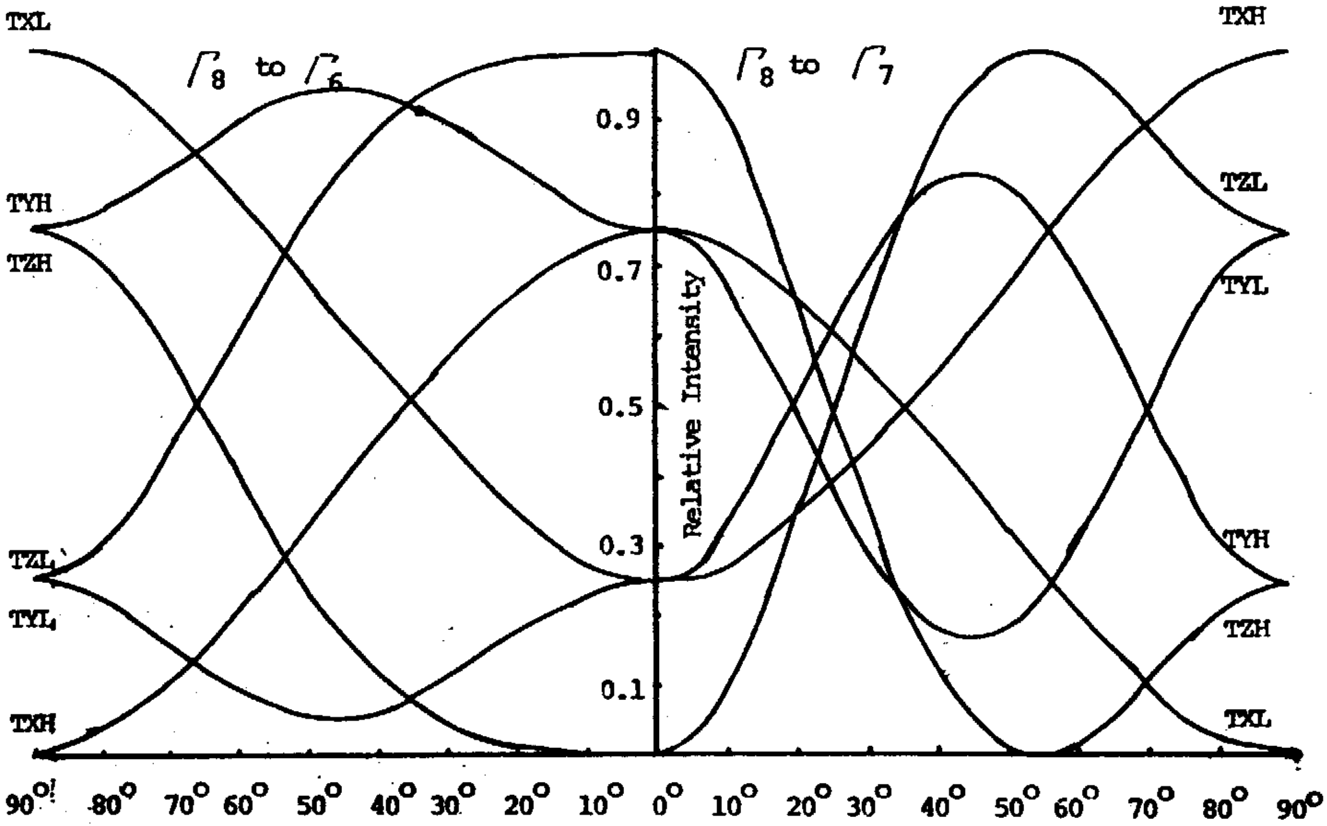

Fig. 2. Relative intensities of Γ_8 to Γ_6 and Γ_7 transition for stress in (100) plane.

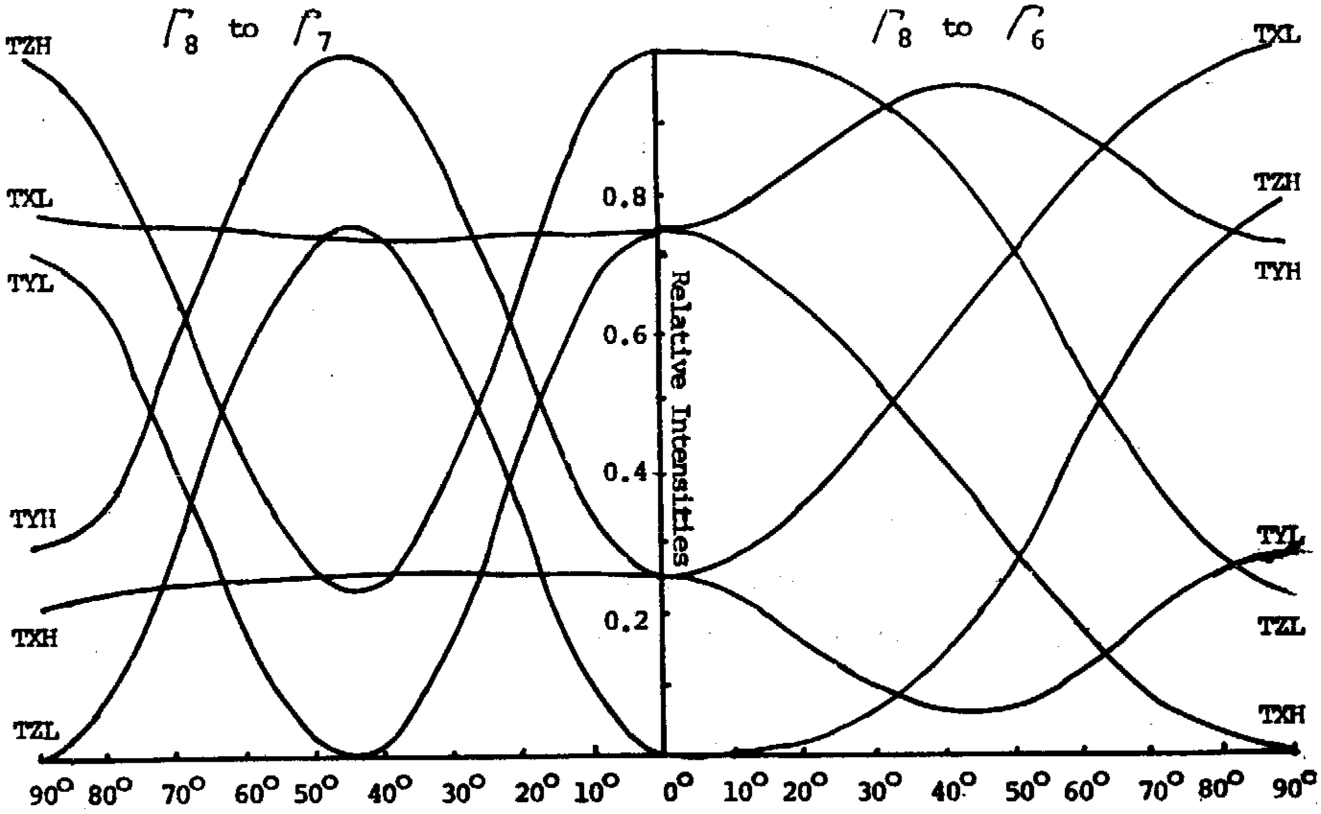

Fig. 3. Relative intensities of Γ_8 to Γ_7 and Γ_6 transition for stress in (110) plane.

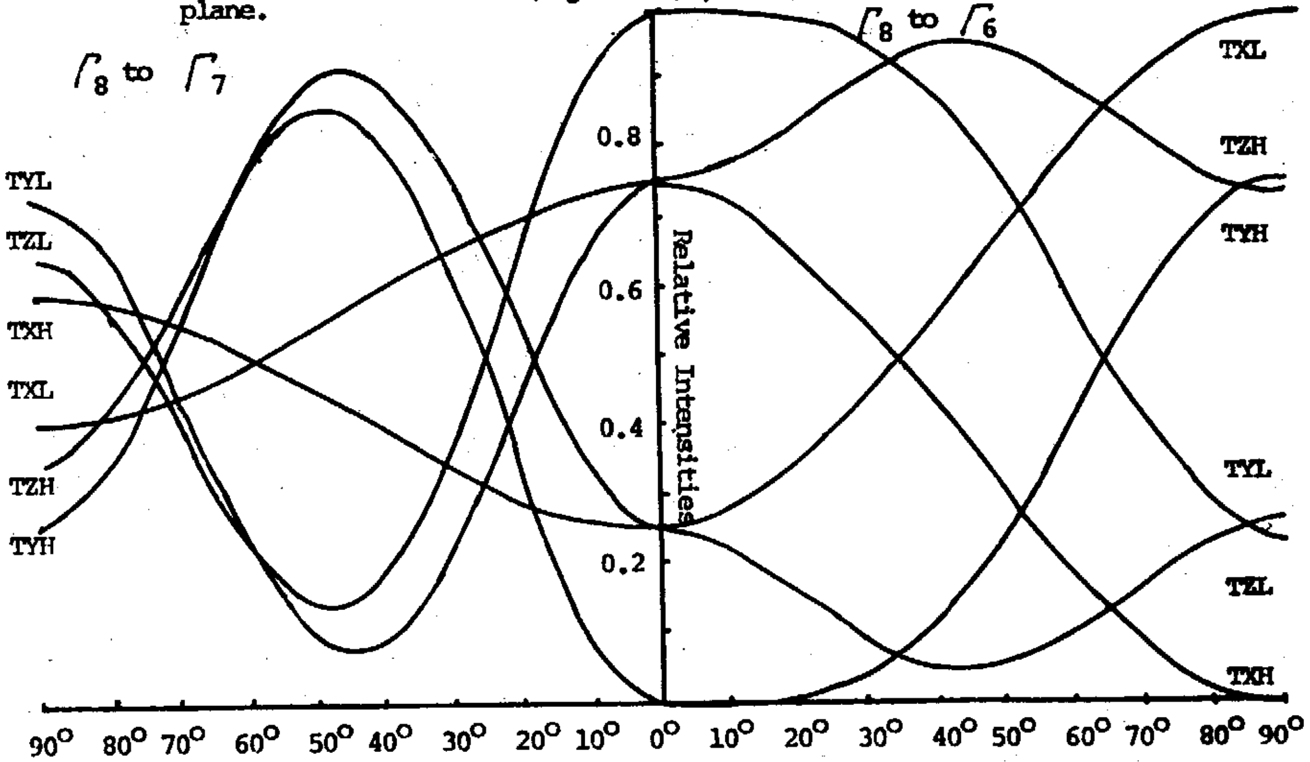

Fig. 4. Relative intensities of Γ_8 to Γ_7 and Γ_6 transition for stress in (120) plane.

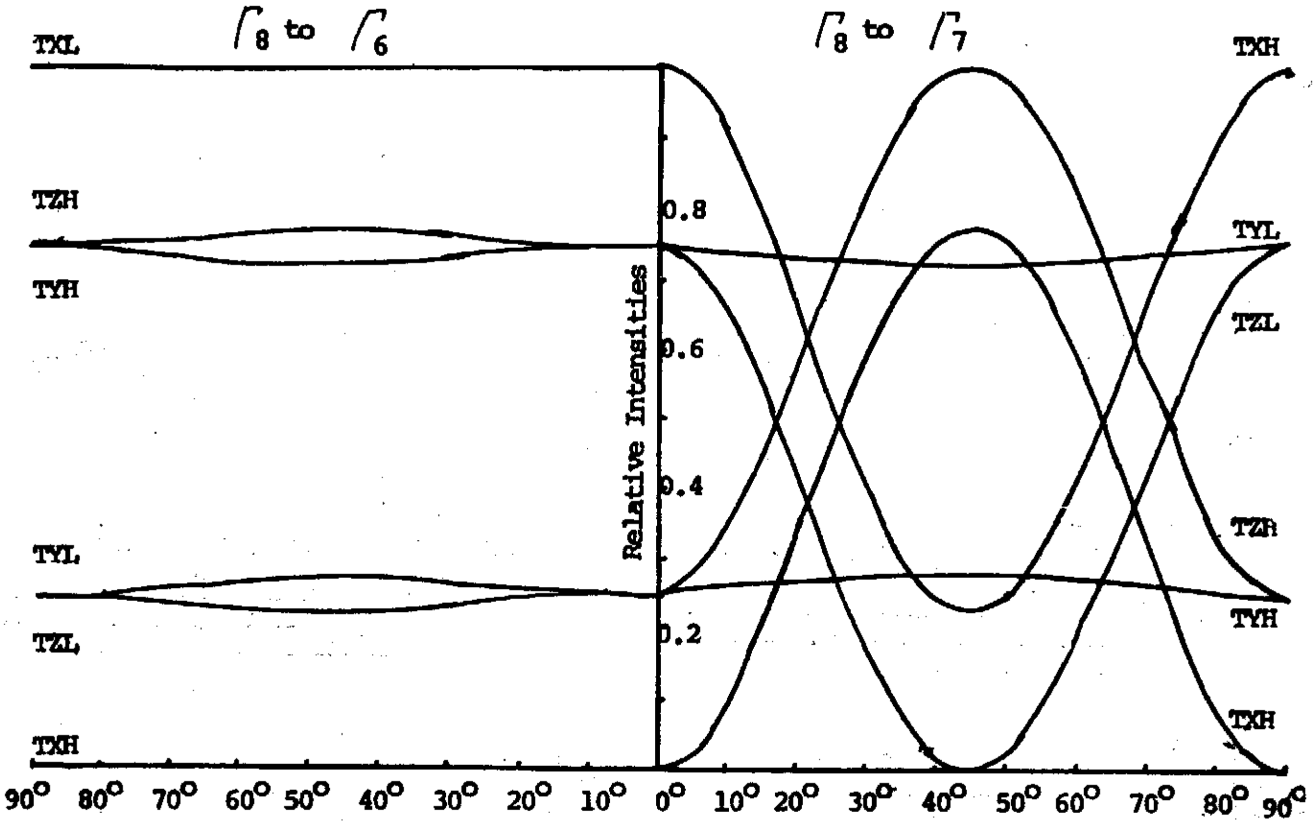

Fig. 5. Relative intensities of Γ_8 to Γ_6 and Γ_7 transition for stress in (001) Plane.

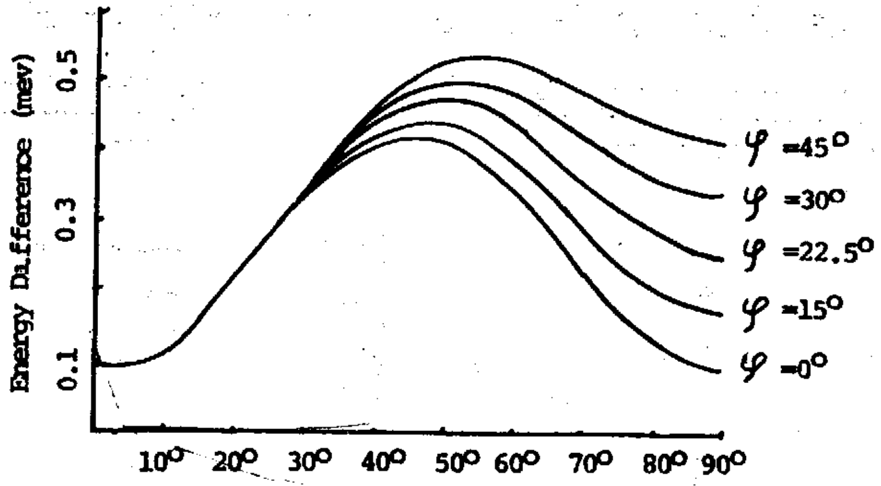

Fig. 6.Energy difference between two

$_8$ states(2/3 → 2/3).

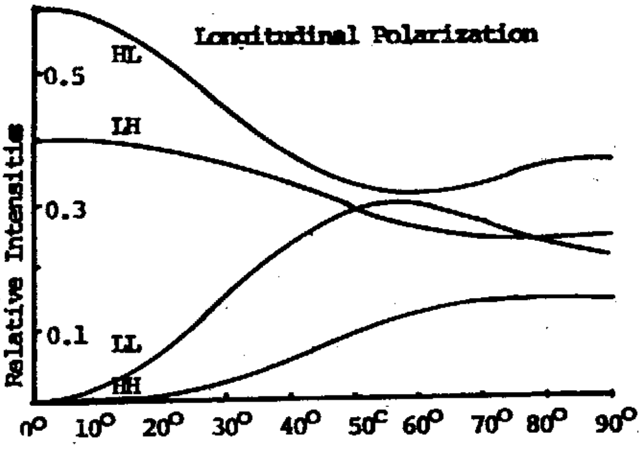

Fig. 7. Relative intensities of Γ_8 to Γ_8 polarization in z' direction for stress in (100) plane.

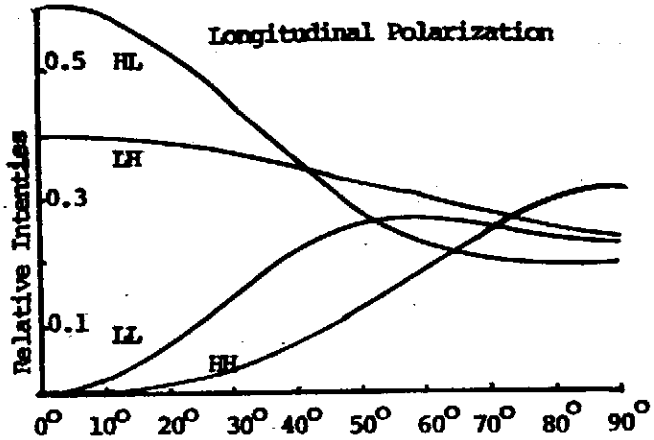

Fig. 10. Relative intensities of Γ_8 to Γ_8 polarization in z' direction for stress in (110) plane.

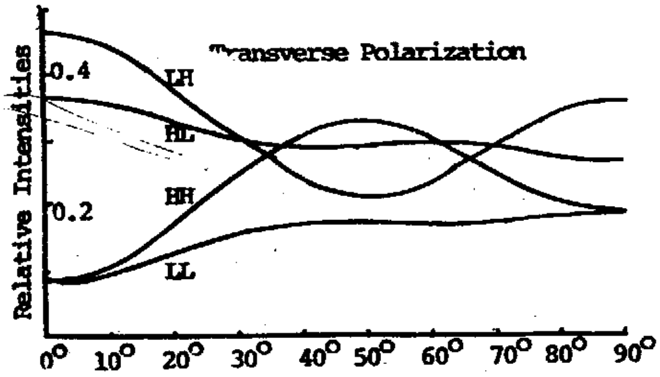

Fig. 8. Relative intensities of $_8$ to Γ_8 polarization in y' direction for stress in (100) plane.

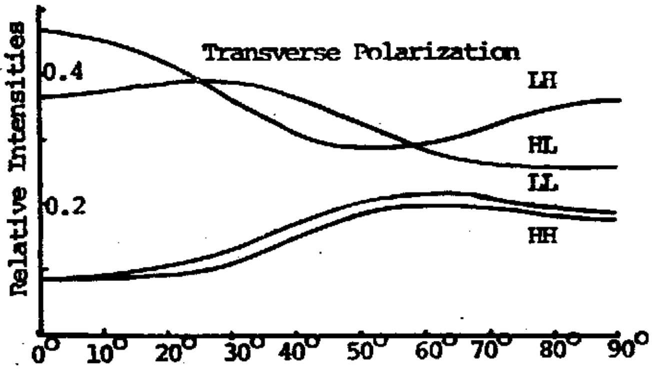

Fig. 11. Relative intensities of Γ_8 to Γ_8 polarization in y' direction for stress in (110) plane.

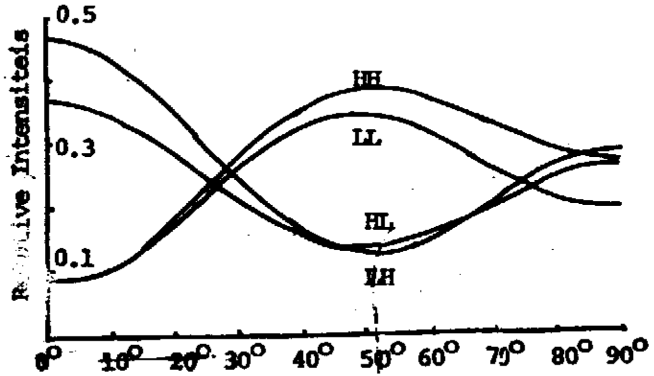

Fig. 9. Relative intensities of Γ_8 to Γ_8 polarization in x' direction for stress in(100) plane.

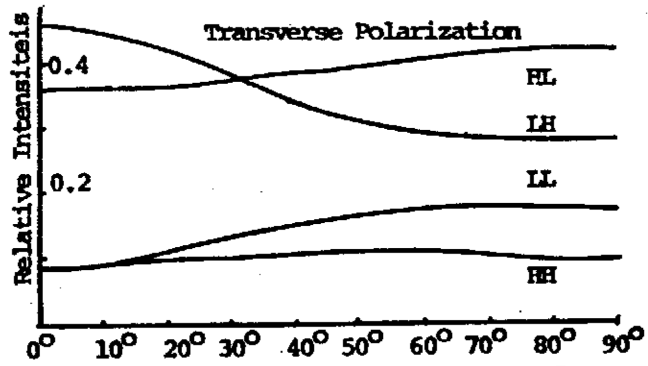

Fig. 12. Relative intensities of Γ_8 to Γ_8 polarization in x' direction for stress in (110) plane.

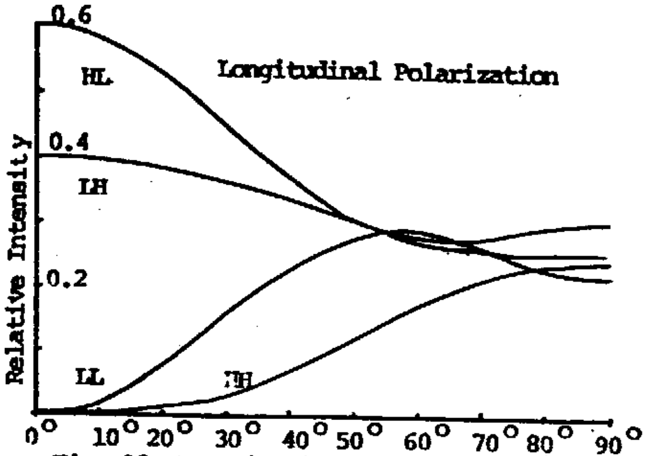

Fig. 13. Repative intensities of Γ_8 to Γ_8 polarization in z' direction for stress in (120) plane.

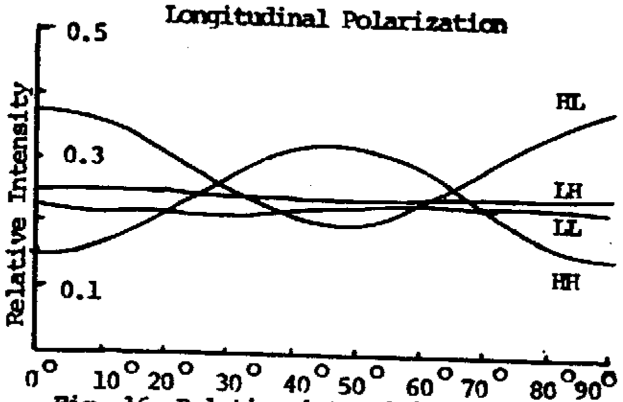

Fig. 16. Relative intensities of Γ_8 to Γ_8 polarization in z' direction for stress in (001) plane.

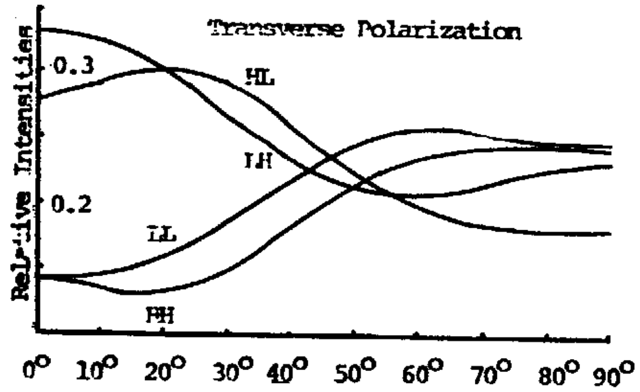

Fig. 14. Relative intensities of Γ_8 to Γ_8 polarization in y' direction for stress in (120) plane.

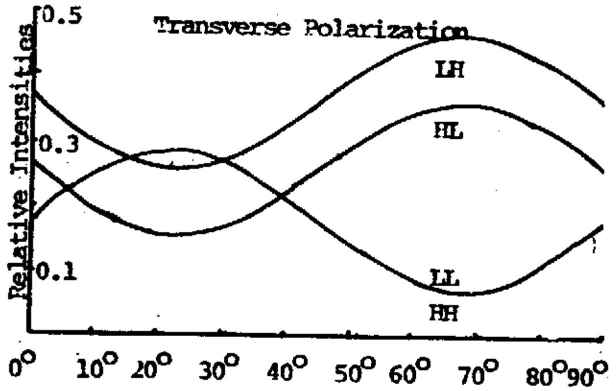

Fig. 17. Relative intensities of Γ_8 to Γ_8 polarization in y' direction for stress in (001) plane.

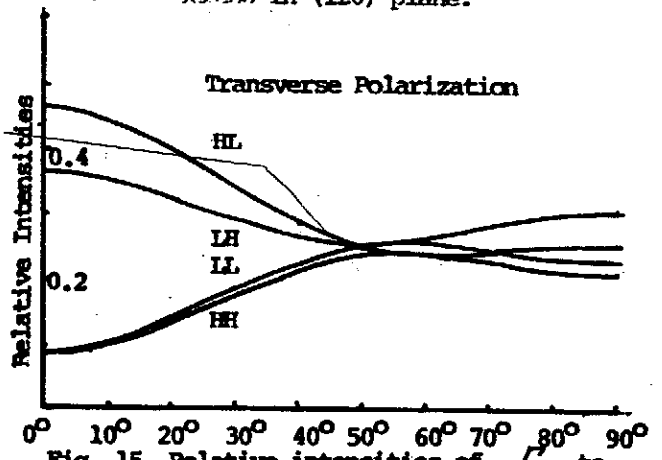

Fig. 15. Relative intensities of Γ_8 to Γ_8 polarization in x' direction for stress in (120) plane.

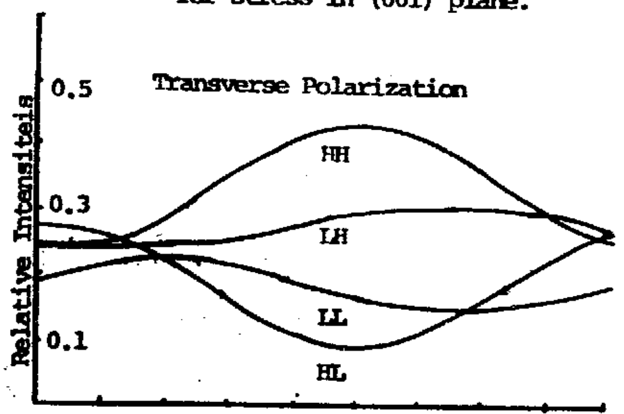

Fig. 18. Relative intensities of Γ_8 to Γ_8 polarization in x' direction for stress in (001) plane.

氣象鐵塔簡介

汪群從 *(Chun-Tsung Wang)*

I 前記

民國 61 年筆者代表我國出席在非律賓、馬尼剌市由聯合國教科文組舉辦之風力對建築物影響研討會。返國後，鑒於舉凡風力對建築物之影響、微氣象空氣污染等皆極需一氣象鐵塔作爲研究之工具，乃先後邀請邱昌平、蔡益超、馬天驥、胡仲英等先生參與，承彼等同心協力，得在建築材料波動之際，順利完成此一氣象鐵塔，特此致謝。另則行政院國科會、台灣大學及本院各單位支援之情亦一併誌謝。

II 氣象鐵塔

鐵塔高約 35 公尺，底座約 6 公尺見方，塔頂約 1 公尺見方，係利用電子計算機之 Stress Program 設計。鐵塔本體前視圖如圖一所示，各層間置有安全鐵絲網，上下經由分段之鐵梯。爲使該鐵塔便利各有關機構使用，鐵塔設置於台北市台灣大學大氣科學系附近。

儀器分東北、東南、西南、西北四個方向裝設，詳細裝置位置參閱表一。由於鐵塔所在位置強風多爲東北風，故五具風速計皆裝設於東北方向。儀器的安裝係在鐵塔母體的粗角鋼上向外搭接一較細角鋼，上置儀器墊板或承座用以固定儀器。每種儀器其設計細節均不相同。今僅以水平風速計的安裝設計示於圖二，以供參考。四個方向的儀器裝設高度大致均在 3 米、7 米、14 米、21 米、28 米與塔頂，以便在不影響所想得的觀測資料之前提下，達到整齊劃一，增進瞻觀的目的。所有儀器的記錄器均置放於鐵塔旁的活動小木屋內。

各種儀器有關資料列表如后：

儀器種類	儀器名稱	規格	數量	用途	備註
1	水平風速風向計		1		
2	水平風速計	OTA KEIKI Cat. No. 21-B	4	測水平風速	
3	風速風向計	OTA KEIKI Cat. No. 112	1	測水平風速與風向	
4	水平及垂直風向自計	W.M. Cat. No. 17002	1	測三度空間的風向	
5	風壓感應器	KISTLER MODEL 202 C5	8	測風速壓	
6	溫濕儀	KMC C4	6	測溫度、濕度	有六個感應器
7	垂直風速自計	W. M. Cat. No. 27101	2	測垂直風速	
8	記錄器	BRYANS SOUTHERN Model F10-313	1	記錄8個風壓應感器信號	本記錄器有 12 頻道 現只裝 8 chanels
9	發電機	Honda E 1500A	1	提供緊急電源用	

Ⅲ 結論

歐、美、日諸國均根據其實測的風速資料加以理論的研究而定出風速隨高度的變化及風力與風速之關係式，做爲全國建築設計的主要參考。此部份工作絕不可引用他國研究的研究結果，若風力計算過低，將成爲建築物受強風侵襲而倒塌的主因。風力計算過高，則使設計者浪費材料。

本計劃已在台灣大學大氣科學系建立高達三十五公尺的鐵塔，分五層安裝風速風向計二具、風速計四具、風壓感應計八具、垂直風速儀兩具、垂直水平風向儀一具及六測點溫、濕自計器。今後可利用這些儀器建立台灣地區自有的資料，以期瞭解此區的風速垂直結構，風力垂直分佈及風力對建築物造成的影響，爲建築物的耐風研究奠下基礎。同時亦歡迎各有關機構利用此鐵塔進行微氣象、空氣汚染等研究工作。

儀器編號	儀器名稱	裝設方向	angle頂面距地表面高度 m	測點高度m	備　　註
1	水平風速風向計 Beeckman & whigle	東北	2·90	3·00	
2	水平風速計	〃	6·45	1·00	
3	水平風速計	〃	13·45	14·00	
4	水平風速計	〃	20·45	27·00	
5	水平風速計	〃	27·45	28·00	
6	水平風速計	〃	置於塔頂	35·79	
7	水平及垂直風向自計 Gill Bivane	東南	2·90	3·00	
8	風壓感應器	〃	13·85	14·00	兩個風壓感應器朝N(北)與E(東)
9	風壓感應器	〃	27·85	28·00	
10	溫濕儀	西南	2·90	3·00	
11	溫濕儀	〃	6·90	7·00	
12	濕濕儀	〃	13·90	14·00	
13	溫濕儀	〃	20·90	21·00	
14	溫濕儀	〃	27·90	28·00	
15	溫濕儀	〃	34·70	34·80	
16	垂直風速自計 Gill Propeller Anemometer.	西北	2·90	3·00	
17	風壓感應器	〃	13·85	14·00	兩個風壓感應器朝S(南)與W(西)
18	風壓感應器	〃	27·85	28·00	
19	垂直風速自計 Gill Propeller Anemometer	〃	34·70	34·80	

儀器裝設位置一覽表　（表一）

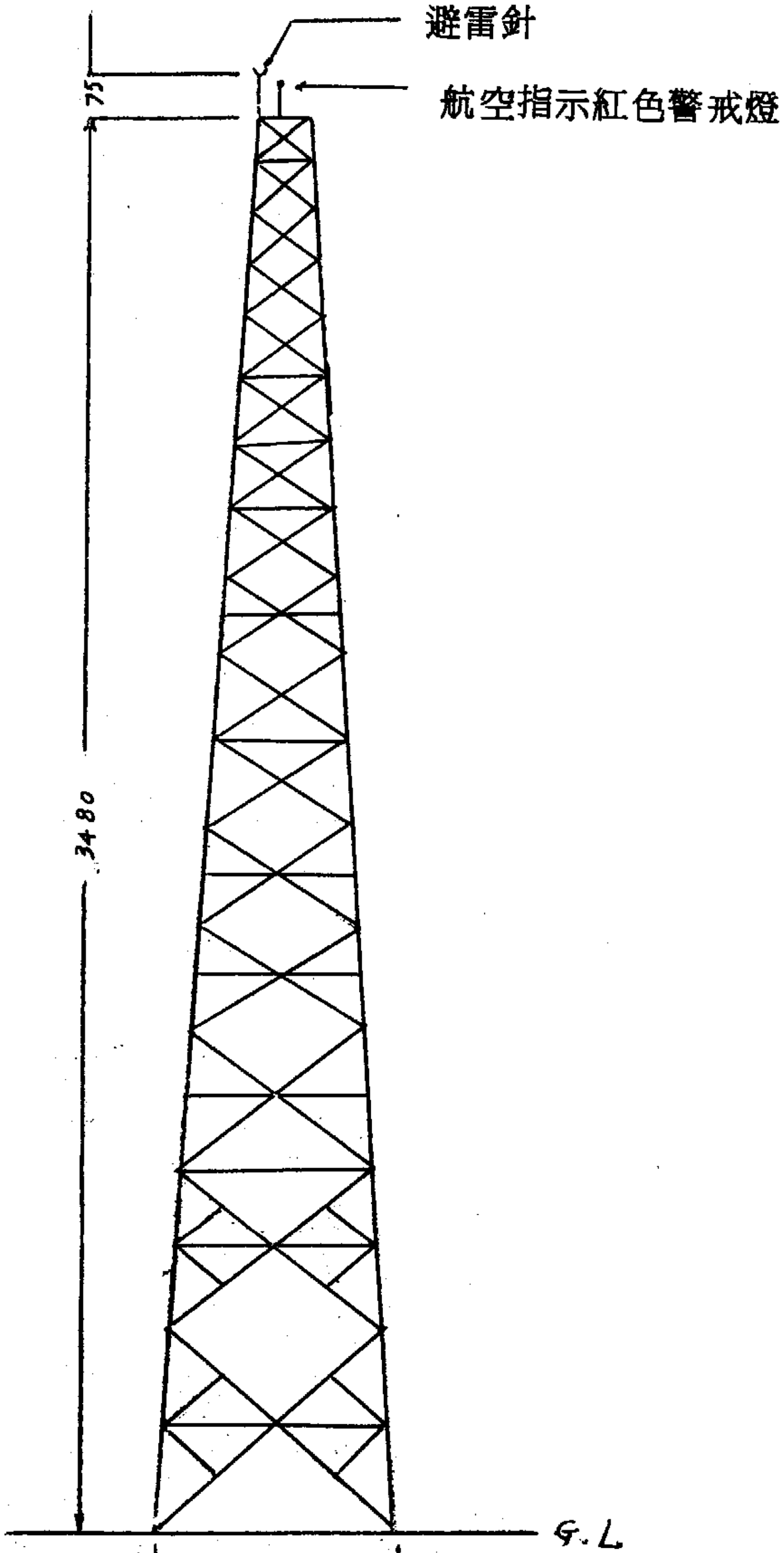

單位： cm

圖一：颱風觀測鐵塔前視圖（比例尺1:200 ）

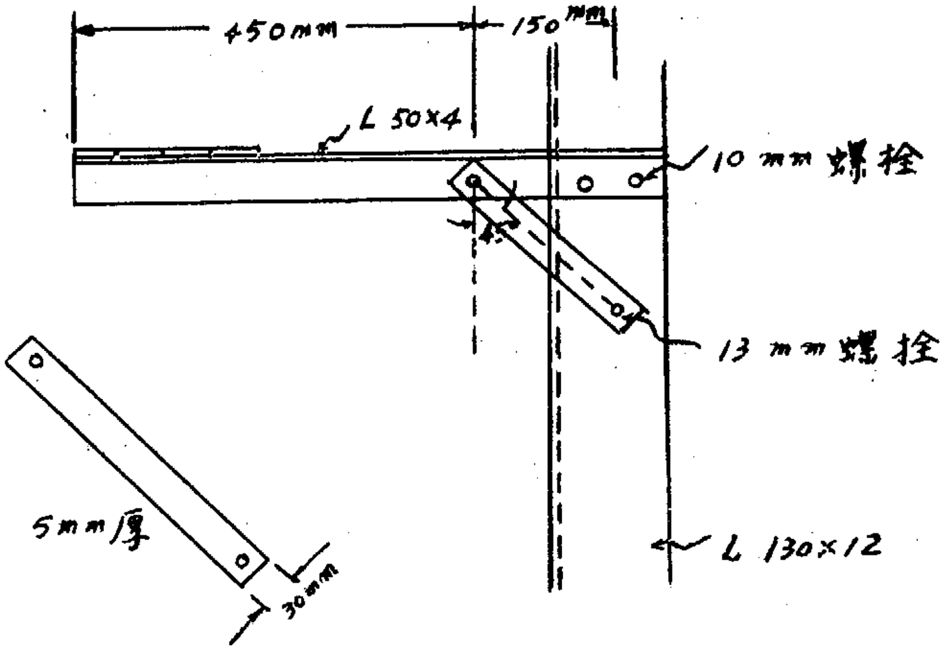

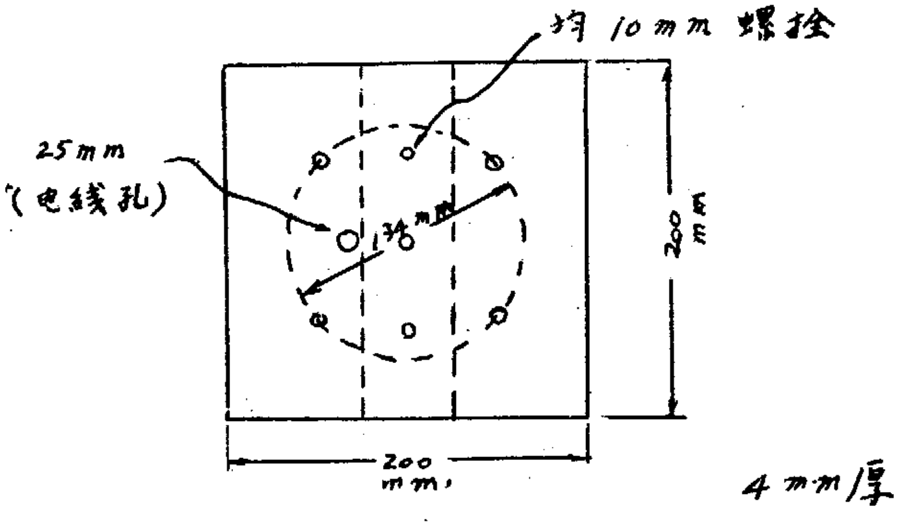

儀器墊板詳細圖

圖二：水平風速計安裝支架構造詳圖

A STUDY ON THE DIAGNOSTIC BALANCE MODEL FOR TYPHOON BESS

Chun-Tsung Wang and Lai-Chen Chien

Inst. Physics

Academia Sinica

1. *Introduction*

The governing equations for air movement, in the x, y, p, t coordinates, are the vorticity equation, the balance equation, the energy equation and the equation of continuity (Haltiner, 1971; Hawkins, 1972)

$$\nabla^2\frac{\partial\psi}{\partial t} = -J(\psi,\eta) - \nabla\chi\cdot\nabla f + f\frac{\partial\omega}{\partial p} \tag{1}$$

$$\nabla^2\phi = f\nabla^2\psi + \nabla f\cdot\nabla\psi \tag{2}$$

$$\frac{\partial^2}{\partial t\partial p} + J(\psi,\frac{\partial\phi}{\partial p}) + \nabla\chi\cdot\nabla\frac{\partial\phi}{\partial p} + \sigma\omega = -\frac{R}{pC_p}\cdot\frac{d(Q-\bar{Q})}{dt} \tag{3}$$

$$\nabla^2\chi = -\frac{\partial\omega}{\partial p} \tag{4}$$

where ψ is the stream function, ϕ is the geopotential height, χ is the velocity potential, ω is the vertical velocity, η is the absolute vorticity about the vertical, f is the Coriolis parameter, R is the specific gas constant, (= 287 m^2/sec^2-K°), c_p is the specific heat capacity at constant pressure (= 1004 m^2/sec^2-K°), Q is the heat energy, $\frac{d\bar{Q}}{dt}$ is the spatially constant radiational cooling (staff members, 1966), and $\sigma = -\frac{1}{\sigma g\theta}\frac{\partial\theta}{\partial p}$ is the static stability, where ρ is the air density, θ is the potential temperature.

The heating rate is approximated by (staff members, 1966)

$$\frac{dQ}{dt} = \frac{dQ_s}{dt} + \frac{dQ_L}{dt} \tag{5}$$

the sensible heating rate is (Gambo, 1963)

$$\frac{dQ_s}{dt} = A \cdot |V_{1000}|(T_{sea}-T_{1000}) \cdot (\frac{P}{P_{1000}})^2$$

$$A = 0.001 \quad when \quad T_{sea} > T_{1000}$$

$$A = 0.0001 \quad when \quad T_{sea} < T_{1000} \qquad (6)$$

$$|V_{1000}| \cong 0.7\, |V_{900}|$$

and the latent heating rate is (Danard, 1966; Miller et. al. 1972)

$$\frac{dQ_L}{dt} = -LF^* S \qquad when \quad \omega < 0$$

$$= 0 \qquad when \quad \omega \geqslant 0 \; or \; P \leqslant 700\; mb \qquad (7)$$

where T_{sea} and T_{1000} are temperature at sea surface and 1000 mb level, V_{1000} and P_{1000} are velocity and pressure at 1000 mb level, V_{900} is velocity at 900 mb level, L is the heat of condensation (= 2.27 x $10^6 m^2/sec^2$), and (Kuo, 1965; Haltiner & Martin, 1957)

$$F^* = [(\frac{\partial q^*}{\partial p})_T + \frac{RT}{c_p p} (\frac{\partial q^*}{\partial T})_p] \cdot [1 + \frac{L}{c_p} (\frac{\partial q^*}{\partial T})_p]^{-1} \qquad (8)$$

$$q^* = 0.622e\, [p-0.378e\,]^{-1}$$

$$T = -\frac{p}{R} \cdot \frac{\partial \phi}{\partial p} \quad , \qquad e = 6.11\, [\frac{273}{T}]^{5.31} EXP\, [\, 25.22(1-\frac{273}{T})\,]$$

$$\Delta S = 1 - \frac{T-T_d}{\Delta T'} \geqslant 0 \qquad (9)$$

where T_d is the dew point temperature, $\Delta T'$ is an empirical constant.

It is convenient to combine Eqs. 1, 2, 3, 4, 5, & 7 into the ω-equation

$$\nabla^2 \sigma^* \omega + f^2 \frac{\partial^2 \omega}{\partial p^2} = -\nabla^2 [\, J(\psi, \frac{\partial \phi}{\partial p}) + \nabla\chi \cdot \nabla \frac{\partial \phi}{\partial p} + \frac{R}{c_p p} \cdot \frac{dQ_s}{dt}\,]$$

$$+\frac{\partial}{\partial p}[-\frac{\partial}{\partial t}\nabla f\cdot\nabla\psi+fJ(\psi,\eta)+f\nabla\chi\cdot\nabla f \tag{10}$$

where

$$\begin{aligned}\sigma^{*} &= \sigma-\frac{R}{c_p p}LF^{*}S\geqslant 0.2\,\sigma && \textit{when }\ \omega<0\ \textit{ and }\ p>500\,mb\\ &= \sigma && \textit{when }\ \omega\geqslant 0\ \textit{ or }\ p\leqslant 500\,mb\end{aligned} \tag{11}$$

2. *Numerical Scheme*

Theoretically speaking, Equations 1, 2, 4 and 10 can be used to solve the four unknowns ϕ,ψ,χ, and ω. Yet no analytical solution is available up to date, and numerical methods have to be pursued.

First, geopontential height data, $\phi'_{i,j}$, taken from weather map are horizontally manipulated by

$$\begin{aligned}\phi_{i,j} = \frac{1}{16}[\,4\,\phi'_{i,j}&+2(\phi'_{i+1,j}+\phi'_{i-1,j}+\phi'_{i,j+1}+\phi'_{i,j-1})\\ &+(\phi'_{i+1,j+1}+\phi'_{i+1,j-1}+\phi'_{i-1,j+1}+\phi'_{i-1,j-1})\,]\end{aligned} \tag{12}$$

and vertically manipulated by

$$\phi_k=\phi'_k+\frac{1}{4}[\,2(\phi'_k-\overline{\phi'_k})+\overline{\phi'_k}\,(\frac{\phi'_{k-1}-\overline{\phi'_{k-1}}}{\overline{\phi'_{k-1}}}+\frac{\phi'_{k+1}-\overline{\phi'_{k+1}}}{\overline{\phi'_{k+1}}})\,] \tag{13}$$

to filter our high frequency gravity inertia waves, where "-" stands fro the p-level average in x and y directions.

Then [$2\nabla^2\phi+f^2$]$_{i,j,k}$ is checked pointwise to make sure it is greater than zero, in order to avoid imaginaty solution in the full balance eq.

$$\nabla^2\phi=f\nabla^2\psi+\psi_y f_y+2J(\psi_x,\psi_y) \tag{14}$$

If [ ]$_{i,j,k}$ is less than zero at certain grid point, it is set equal to zero, and corresponding values at neighboring four points are each reduced by | [ ]$_{i,j,k}$|/4. Balanced values are thereafter evaluated from

$$\nabla^2 \psi + f = [(\psi'_{xx} - \psi'_{yy})^2 + 4\, \psi'^2_{xy} + 2\nabla^2 \phi + f^2 - 2\, \psi'^f_{yy}]^{1/2} \qquad (15)$$

where $\psi' = \phi/\bar{f}$. And balanced ϕ values are obtained via Eq. 14.

The computation loop now proceeds as

(1) With given ϕ, ψ, and ω (to start with zero initially) fields at time t, χ field at time t is computed via Eq.4. $\chi_{boundary}$ is set equal to zero, and iteration accuracy used in solving Eq.4 is 100_{sec}^{-1}.

(2) $\frac{\partial \psi}{\partial t}$ at time t is computed via Eq.1 with an iteration accuracy of 0.05 m^2/sec^2. In solving Eq.1, $\frac{\partial \psi}{\partial t})_{boundary}$ is set equal to zero in the iteration process and then substituted by a weighted value according to Eq.12 (Hawkins, 1972).

(3) ψ at time t+Δt is computed from $\frac{\partial \psi}{\partial t}$ directly. (staff members, 1973)

(4) ϕ at time t+Δt is computed via Eq.2 with an iteration accuracy of 0.3 m^2/sec^2

(5) ω is computed via Eq.10 with an iteration accuracy of 10^{-6} mb/sec, while $\omega_{boundary}$ is set equal to zero.

–value computed at step (5) is compared with original ω–value at time t, if the difference exceeds certain value ω_{ϵ}, the new ω–value is substituted for the original ω–value, and steps (1) to (5) are repeated; otherwise ω–value computed at step(5) is is adapted as ω at time t+Δt, and the loop proceeds. Iteration procedures are similar to those used by Staff Members (1973) and will not be repeated here.

3. *Typhoon Bess*

Simulation study on Typhoon Bess of September 21, 1971 by using a four-level baroclinic model incorporating heat and surface friction had been successfully modelled by Staff Members (1973). At that time, it was found that data directly obtained from weather map were poor in quality, and thus a feasibility study on modelling typhoon Bess by a diagnostic balance model is first made.

The computation domain and grid systems (Fig.1) used are idential to those used by Staff Members (1973), the smoothed geopotential data are presented in Fig.2. After the first time step (0.25 hr later), the field is balanced, but Fig.3 shows that typhoon Bess disappears, indicating that the weather data used are not suitable for balance model study.

Figure 4 shows the geopontential field after 24 hrs, although the cyclone no longer appears, the steering flow still moves in the right direction. Thus it is decided that further study should be pursued on diagnostic balance model, but better initial weather data should be incorporated (e.g. data obtained by Japan Meteoro. Agency).

References

Danard, M. B., A Quasi-geostrophic Numerical Model Incorporating Effects of Release of Latent Heat, J. Appl. Met., 5, 85, 1966.

Gambo, K., The Role of Sensible and Latent Heats in the Baroclinic Atmosphere, J. Meteo. Soc. Japan, 41, 233, 1963.

Haltiner, G. J., Numerical Weather Prediction, John Wiley & Sons, Inc., N. Y., 1971.

Haltiner, G. J. & F. L. Martin, Dynamical and Physical Meteorology, McGraw-Hill Book Co., 1957.

Hawkins, H. F. Jr., Development of a Seven-level, Balanced, Diagnostic Model and its Application to Three Disparate Tropical Disturbances, NOAA-TM-ERL-NHRL 98, 1972.

Kuo, H. L., On Formation and Intensification of Tropical Cyclones through Latent Heat Release by Cumulus Convection, J. Atm. Soc., 22, 40, 1965.

Miller, B. I. et. al., Numerical Prediction of Tropical Weathering Systems, MWR, 100, 825, 1972.

Staff Members of Electronic Computation Center, 72-hr Baroclinic Forecast by the Diabatic Quasi-Geostrophic Model, J. Met. Soc. Japan, 43, 246, 1965.

Staff Members of Atmospheric Division, Simulation Model for Atmospheric Motion: III: Heat and Friction, Ann. Rept., Inst. Phys., Academia Sinica, 1973.

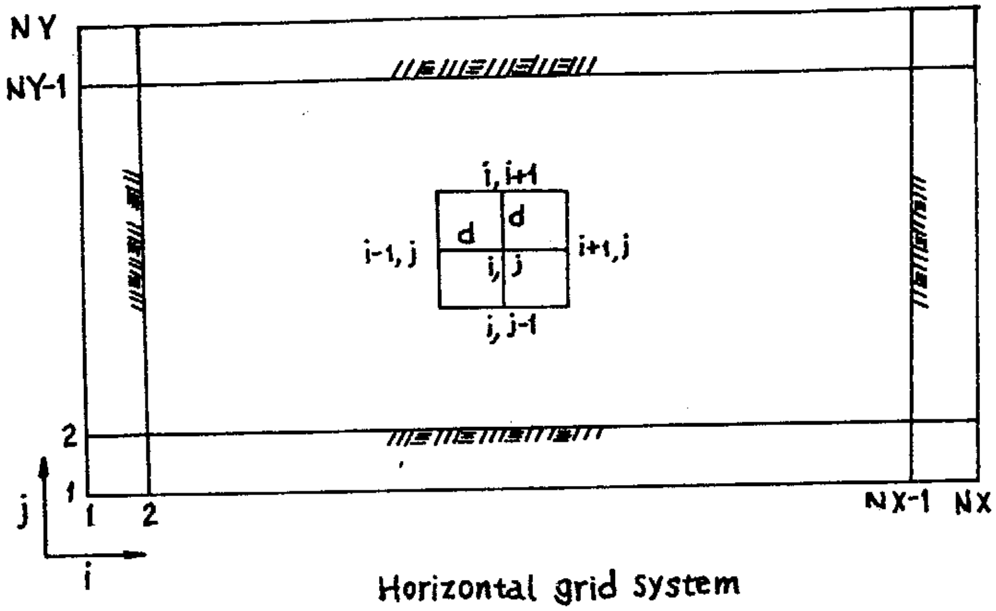

Horizontal grid system

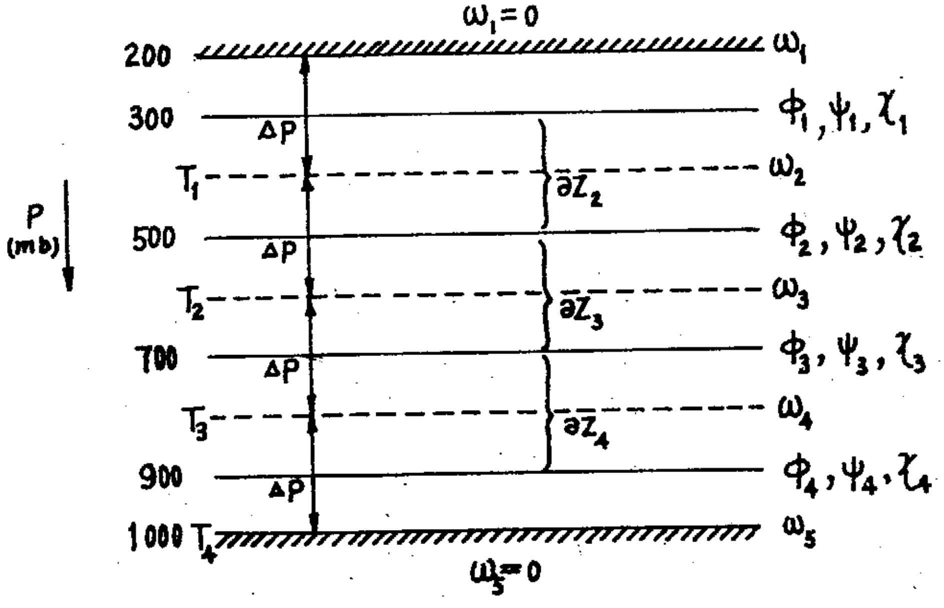

Vertical grid system

Fig.1. Grid systems

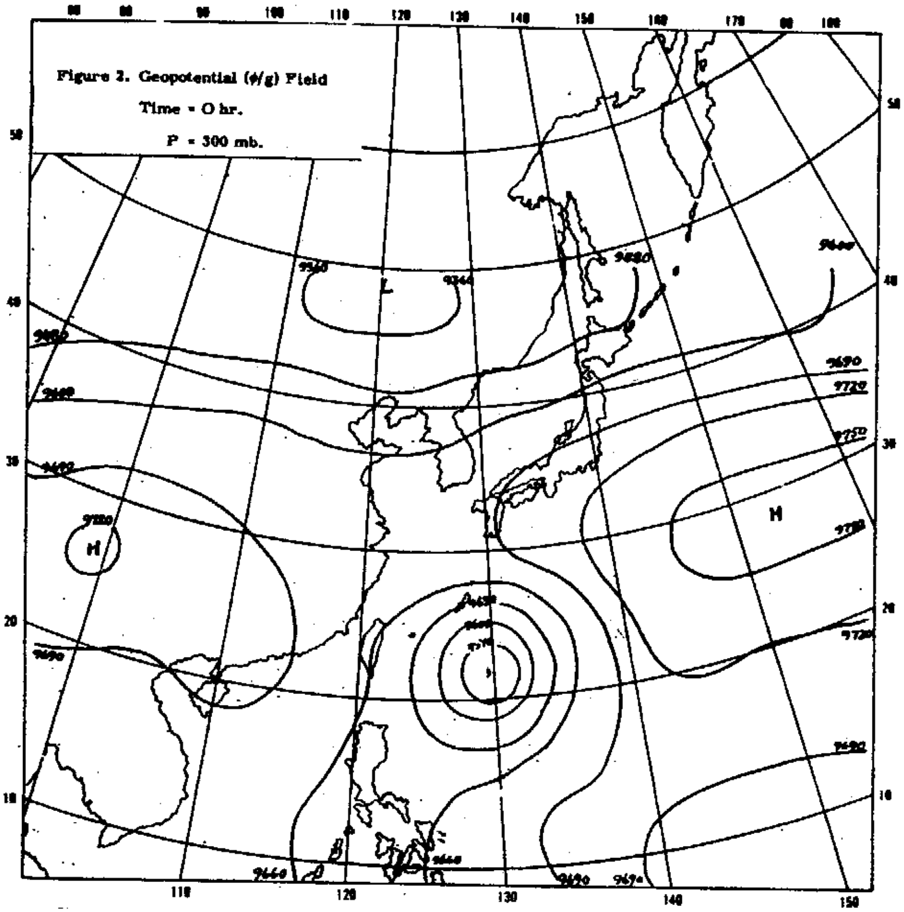
Figure 2. Geopotential (φ/g) Field
Time = O hr.
P = 300 mb.

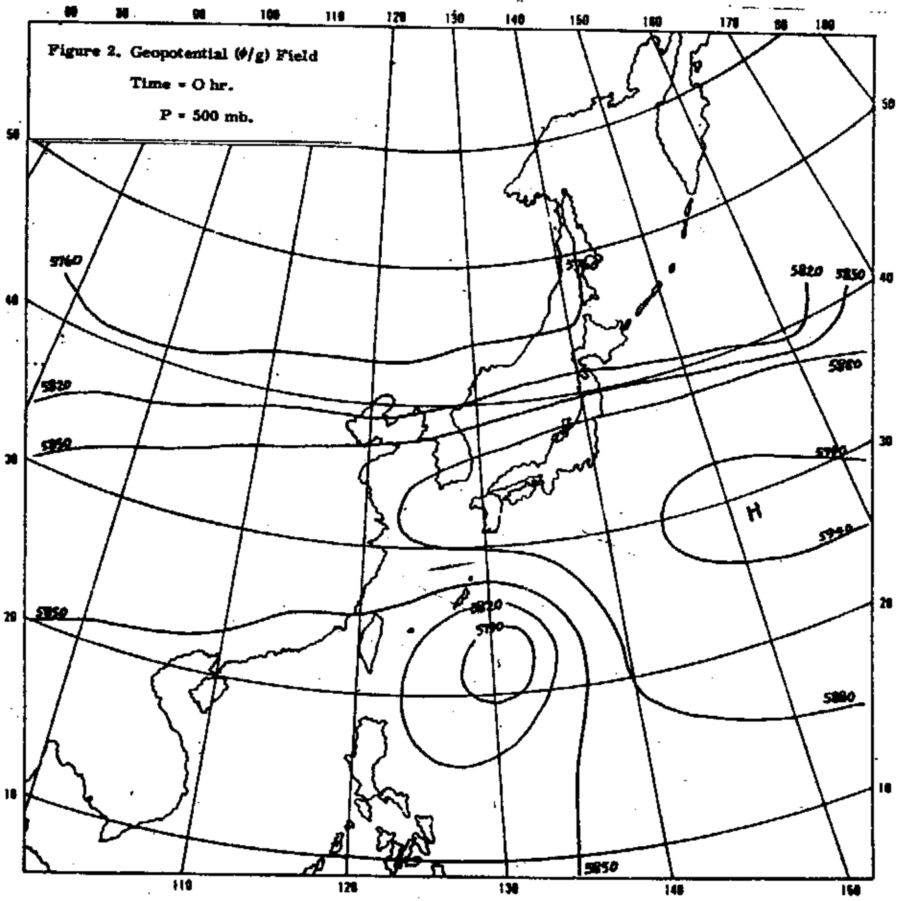
Figure 2. Geopotential (φ/g) Field
Time = O hr.
P = 500 mb.

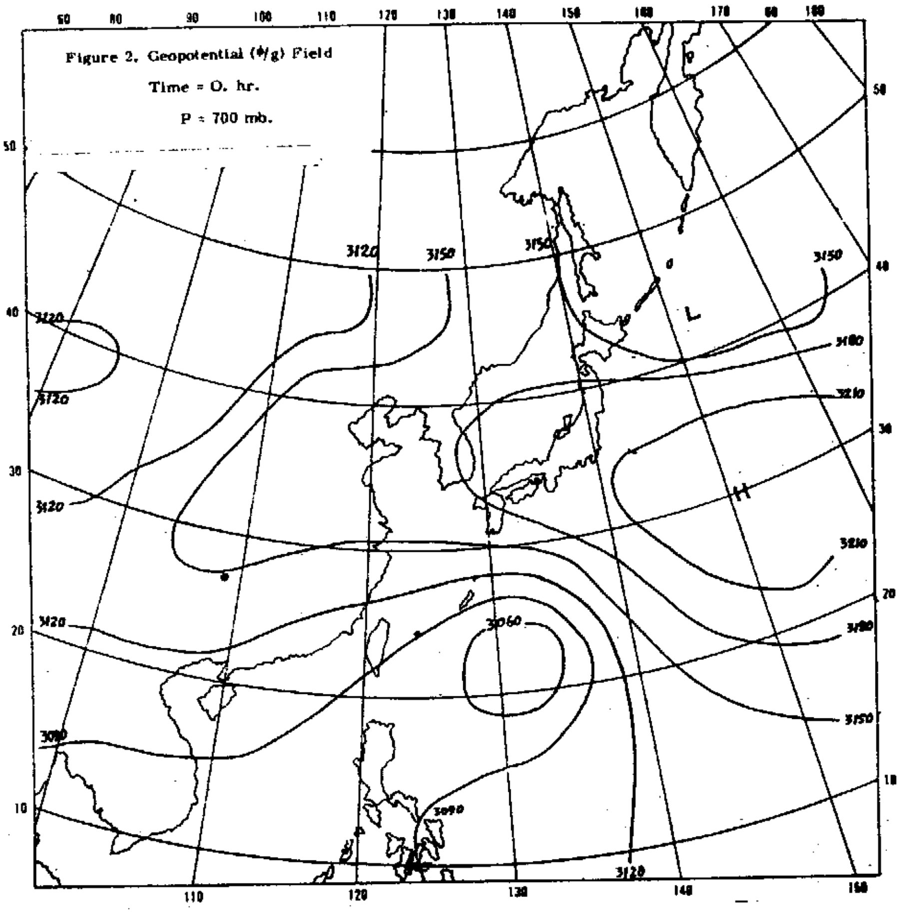

Figure 2. Geopotential (φ/g) Field

Time = O. hr.

P = 700 mb.

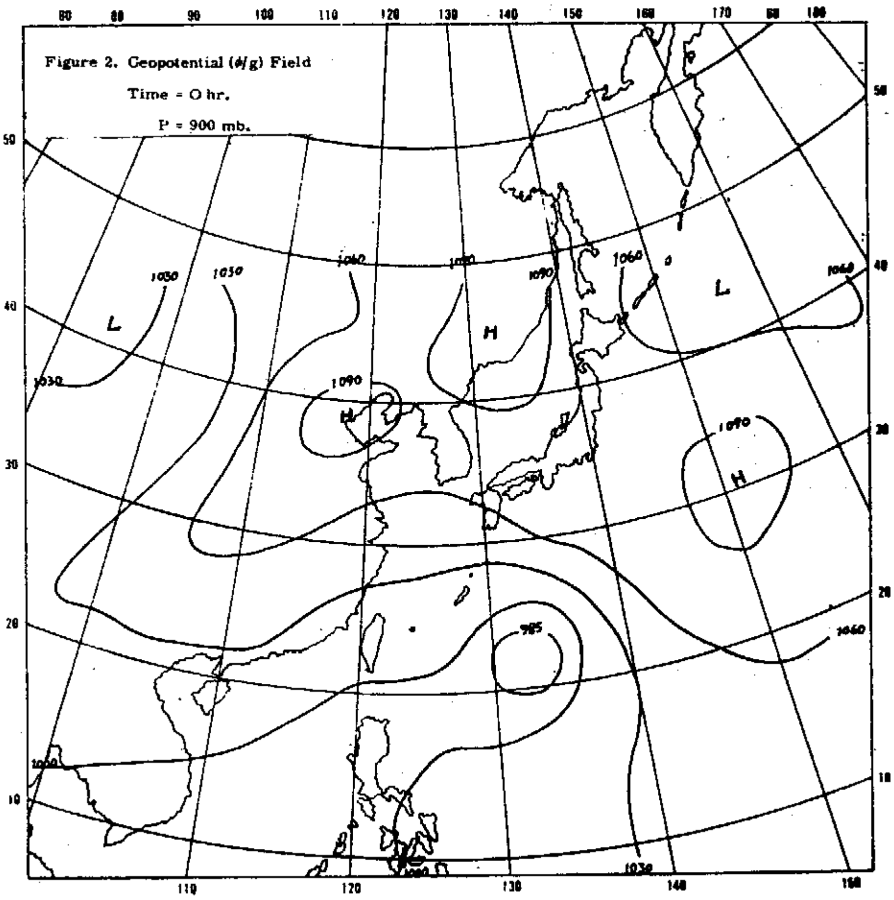

Figure 2. Geopotential (φ/g) Field

Time = O hr.

P = 900 mb.

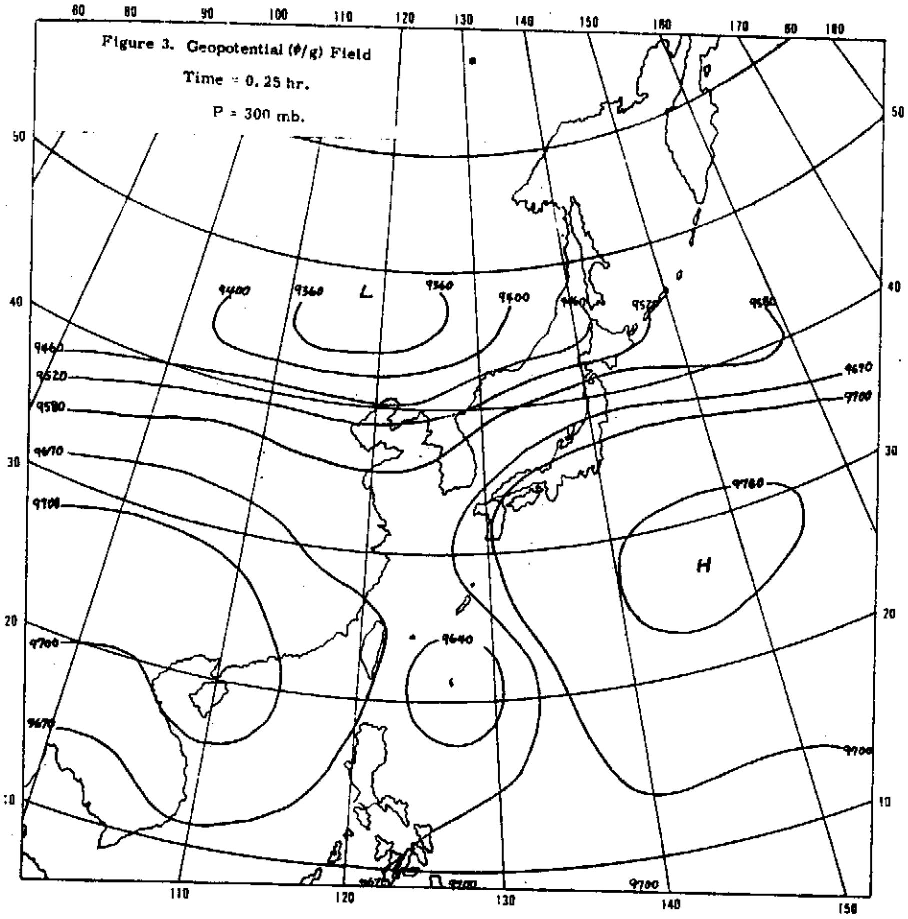

Figure 3. Geopotential (φ/g) Field

Time = 0.25 hr.

P = 300 mb.

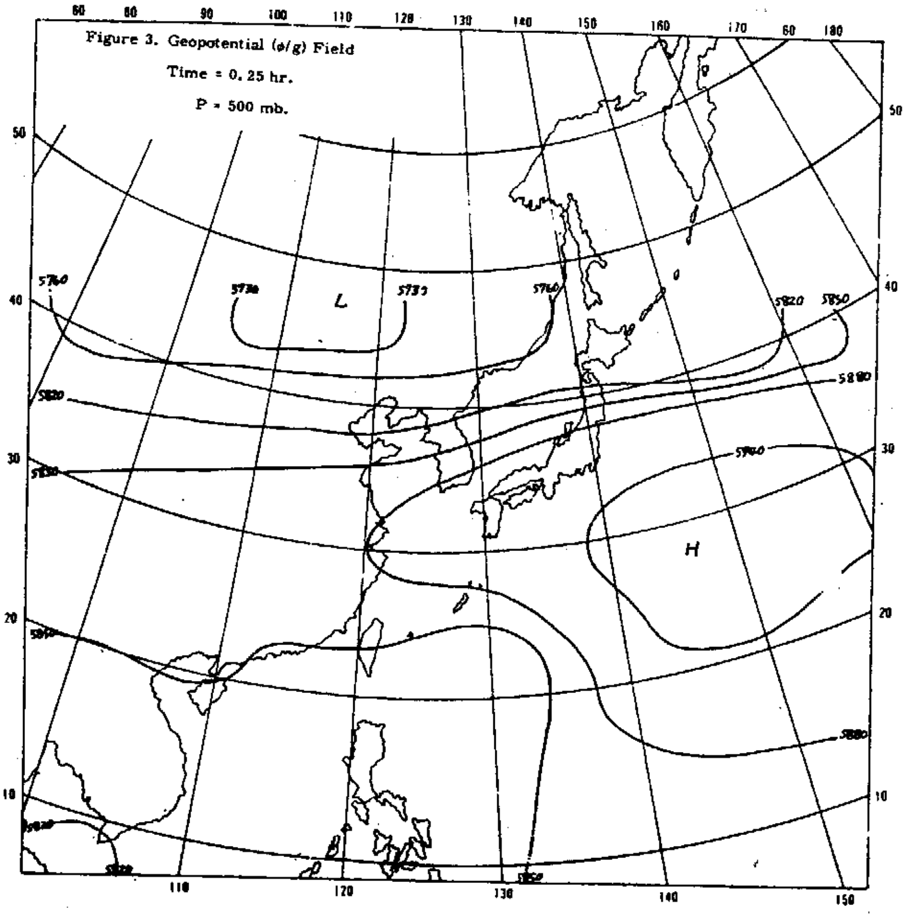

Figure 3. Geopotential (φ/g) Field

Time = 0.25 hr.

P = 500 mb.

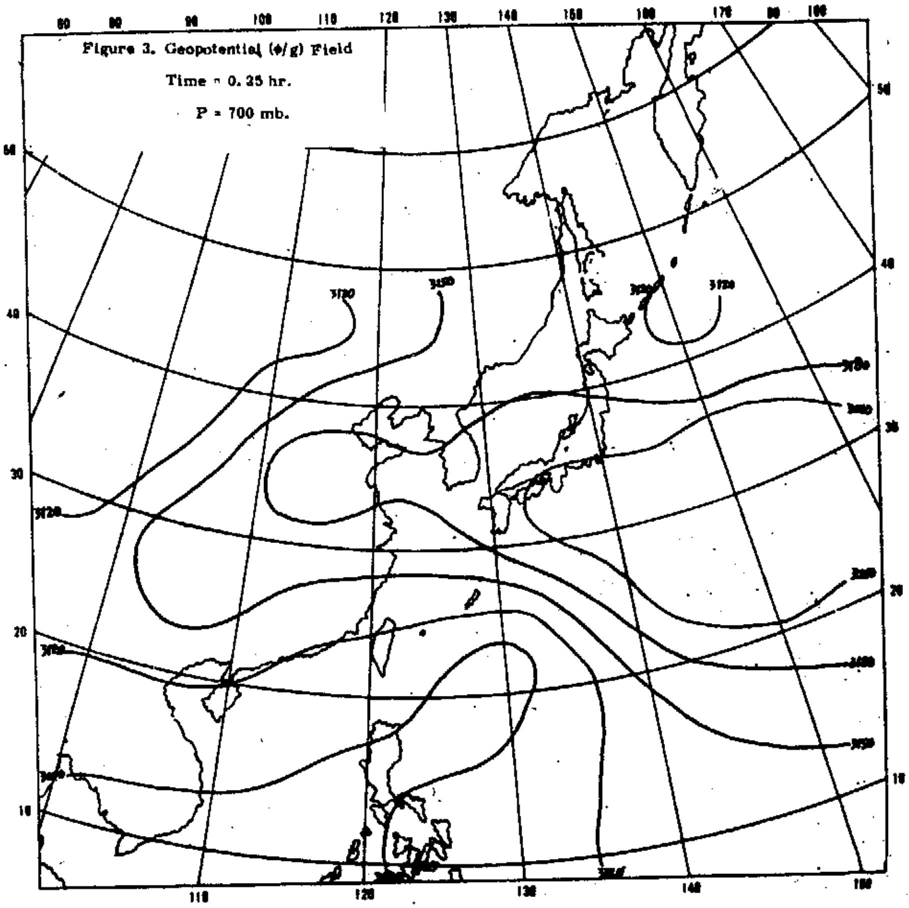

Figure 3. Geopotential (φ/g) Field
Time = 0.25 hr.
P = 700 mb.

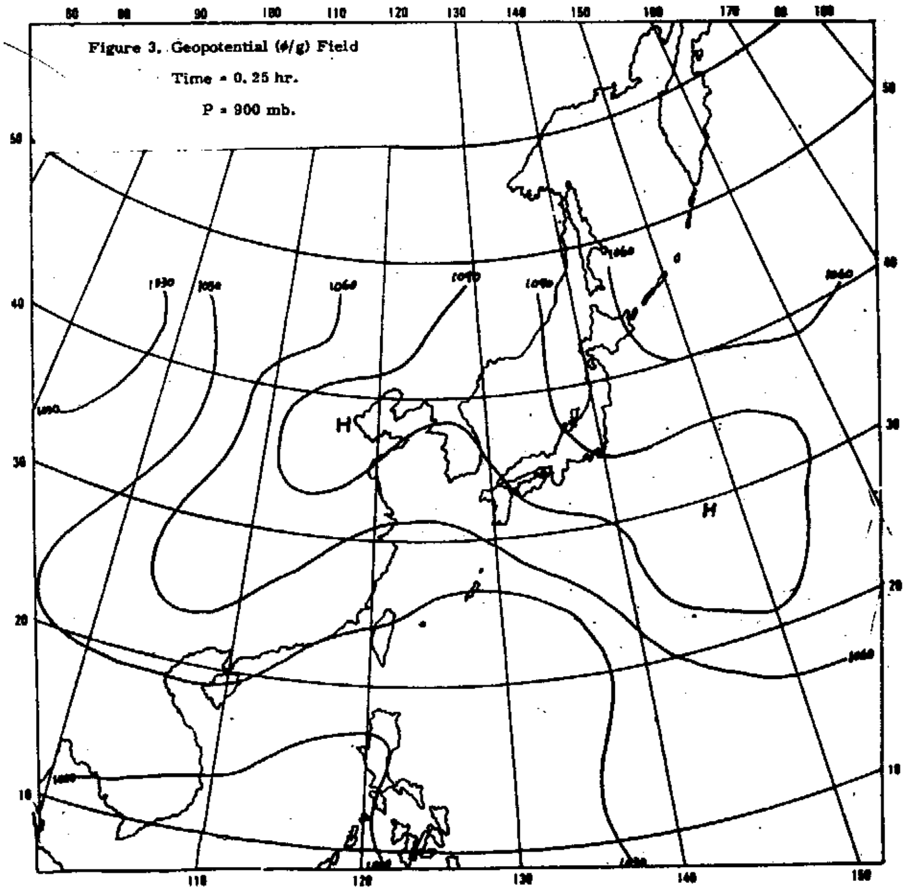

Figure 3. Geopotential (φ/g) Field
Time = 0.25 hr.
P = 900 mb.

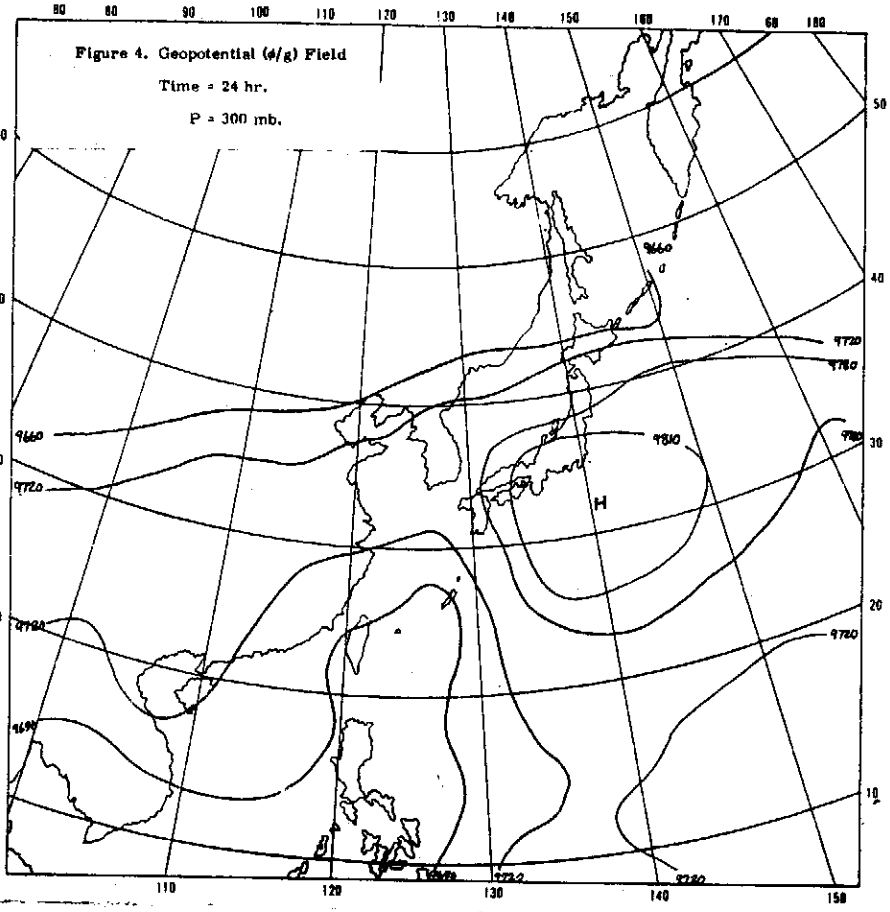

Figure 4. Geopotential (φ/g) Field

Time = 24 hr.

P = 300 mb.

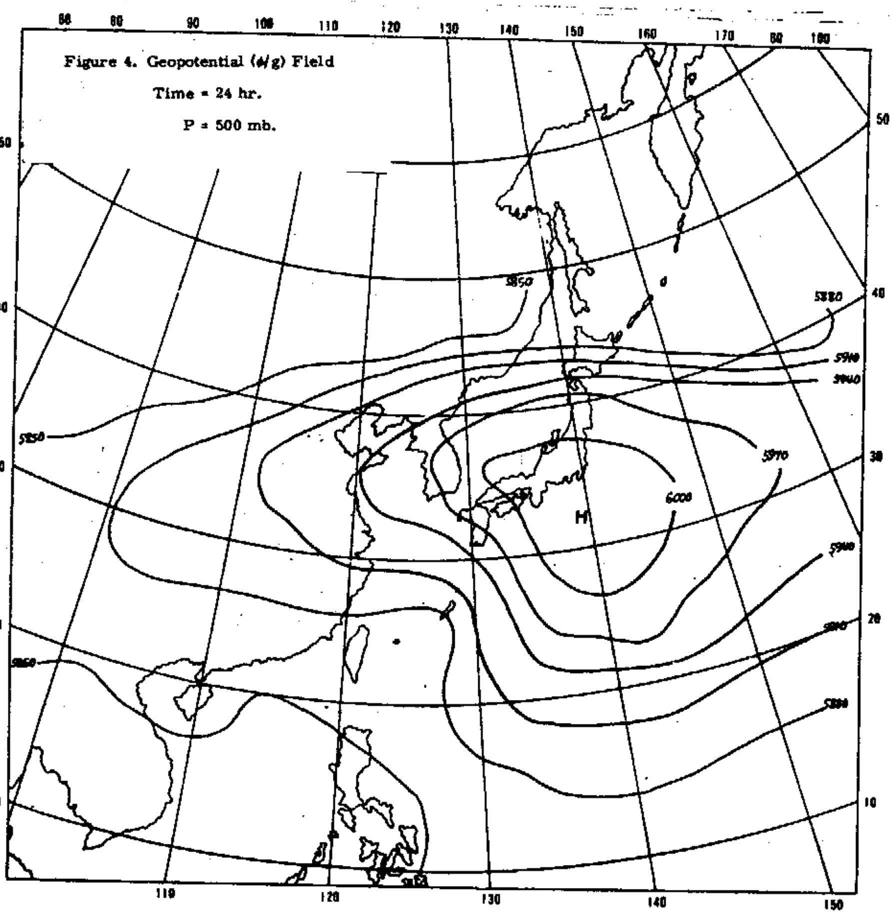

Figure 4. Geopotential (φ/g) Field

Time = 24 hr.

P = 500 mb.

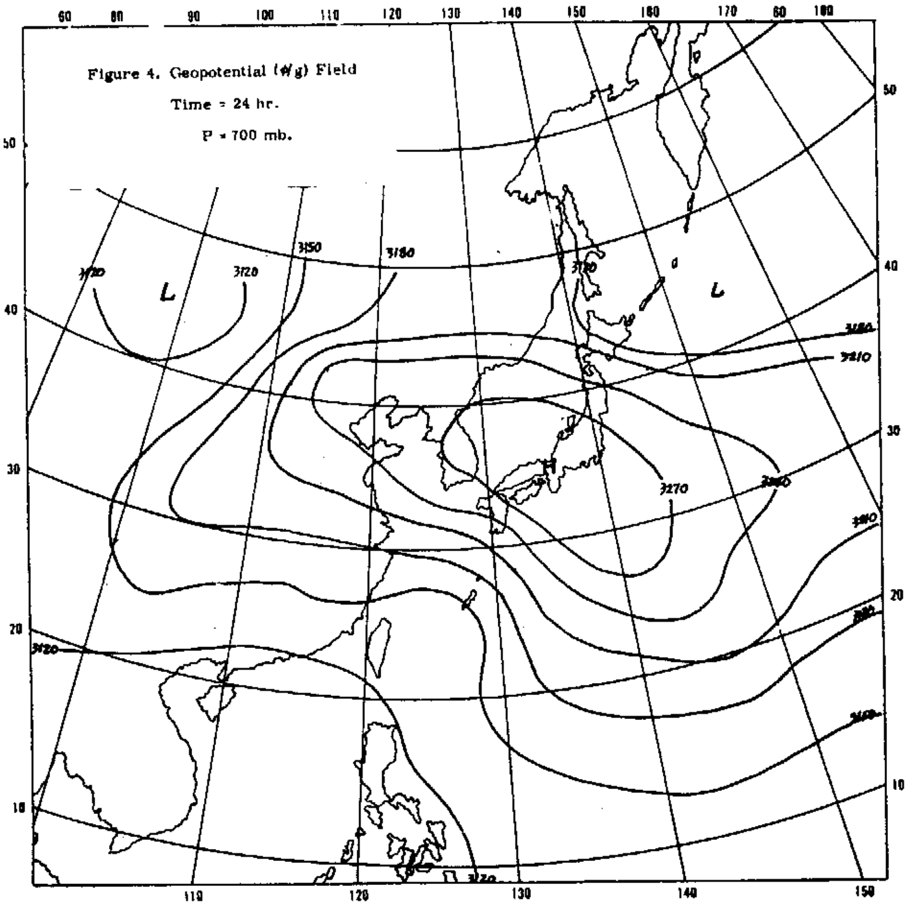

Figure 4. Geopotential (ϕ/g) Field

Time = 24 hr.

P = 700 mb.

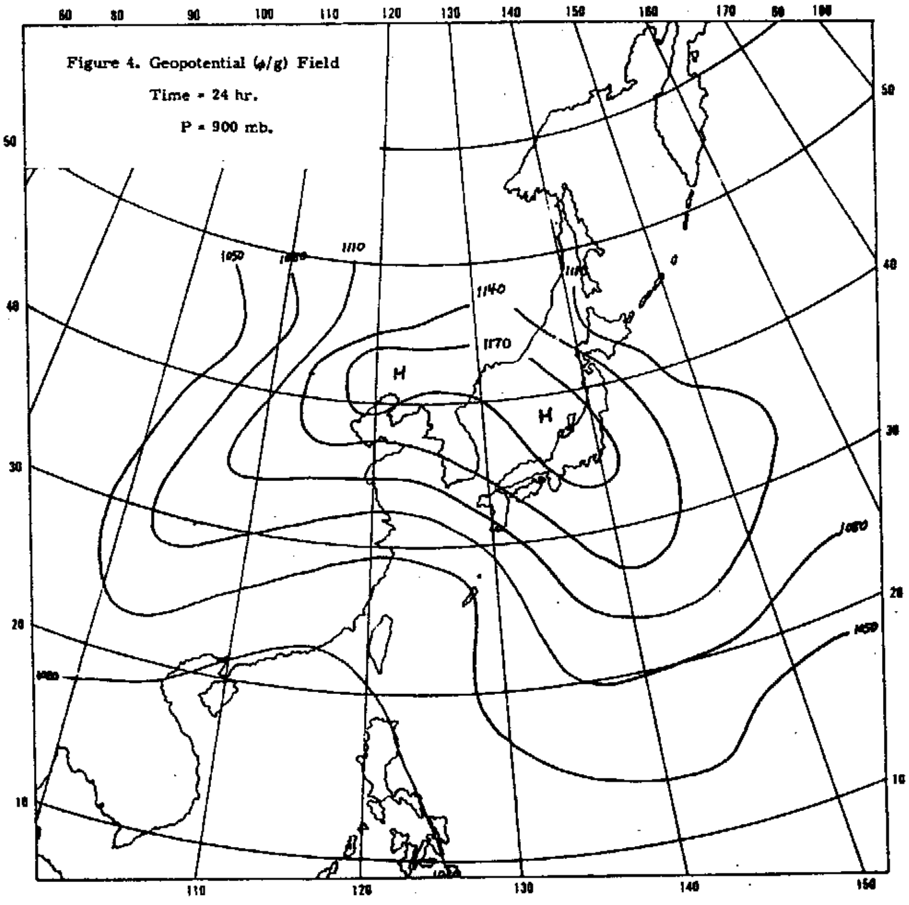

Figure 4. Geopotential (ϕ/g) Field

Time = 24 hr.

P = 900 mb.

利用有限區域細網格探討娜定颱風之運動

蕭錫璋 *(C.J. Shiau)* 胡仲英 汪群從 *(C.T. Wang)*

摘要

本文採用二層斜壓大氣數值模式，利用粗細網格之配合，探討娜定 Nadine) 颱風（民國六十年七月二十四日）的運動。

首先將細網格場 (Fine-mesh grids) 的中央放置於颱風中心，利用粗網格場 (Coarse-mesh grids) 計算Δt時間 250 mb ，750mb 的高度場及 500mb 垂直速度場 (ω-field) 。然後藉同時刻細網格場的計算結果修正其間的共同點值 (Common Points) 。

計算結果顯示：粗細網格之配合使用，可較單獨使用粗網格計算提供更淸楚之運動變化現象。

I 引言

研究大氣運動問題，在有限區域網格上，將控制方程式積分時，必須考慮格點尺度 (Grid scale) 與流體運動尺度相互配合的問題。而一般處理此種數值問題，基於電子計算機的容量 (Memory space) 及使用經費，均選用粗網格的計算，但在粗網格上無法顧及若干重要的天氣現象。例如：颱風、鋒面、颮線 (Squall line) 等。但若完全選用細網格，則不僅過份浪費電子計算機的容量及時間，而且很可能造成計算不穩定 (Harrison Jr. 1973) 。基於上述理由，吾人提出一粗細網格配合使用的數值模式；亦即吾人考慮大尺度運動和小尺度運動的相互影響。

處理的方法是同時做粗細網格的預報。在粗細網格交界處，細網格點值由粗網格點值內插，再由同時刻細網格計算值修正共同點值 (Birchfield, 1960)。如此對於颱風等較小尺度的大氣現象而言，細網格的計算優於粗網格者，又粗細網格在時間上同時積分，積分過程中有二者相互影響的作用。

本文採用二層斜壓大氣數值模式，利用渦旋度方程式 (Vorticity eq.) 及垂直速度方程式 (ω-eq) 來研究颱風的運動。將細網格中央置於颱風中心，颱風渦旋由細網格的計算決定。同時也考慮颱風周圍環境的影響。

II 物理數學模式

數值模式中有兩種網格。粗網格有 20 × 20 點，各格點間的距離 $d = 300$ km ，覆蓋的區域由 90°E ～ 160°E，6°N～60°N（如圖 1）。使用蘭勃特正角錐投影 (Lambert conformal conic mapping)。細網格有 13 × 13 點，各格點的距離 $d' \doteq \frac{d}{2} = 150$ km。每隔一格點有一共同點。粗網格的時間間隔 (Time interval) Δt，經計算約爲 20 分鐘左右，而細網格的時間間隔 $\Delta t'$ 爲顧及颱風中心風速較大，取爲 $\frac{1}{4}\Delta t$。

本文的重點在研究粗細網格間如何配合；故暫不考慮熱量變化、摩擦效應及地形影響。垂直剖面分爲二層，每層厚 500mb（如圖 2）。並假設壓力分佈爲流體靜力平衡 (Hydrostatic) 。在（x，y，p，t）坐標，利用大氣運動方程式，連續方程式 (Eq·of continuity) ，流體靜力方程式 (Hydrostatic·

eq.) ，狀態方程式 (eq. of state) 及熱力學第一定律。經濾波、化簡手續，可得下列二預報方程式 (Thompson, 1961).

$$\nabla^2 \frac{\partial z}{\partial t} + J(z, \zeta + f) - \frac{\bar{f}^2}{g} \frac{\partial \omega}{\partial p} = 0 \qquad (1)$$

$$\sigma \nabla^2 \omega - \frac{\bar{f}^2}{g} \frac{\partial^2 \omega}{\partial p^2} = \frac{g}{\bar{f}} \nabla^2 J\left(z, \frac{\partial \omega}{\partial p}\right) - \frac{\partial}{\partial p} J(z, \zeta + f) \qquad (2)$$

其中 σ 爲靜力穩定度 (Static stability) (Saito, 1963)

$$\sigma = \frac{1}{g\sigma\theta} \frac{\partial \theta}{\partial p} = -\frac{\partial^2 z}{\partial p^2} + \frac{c_v}{c_p p} \frac{\partial z}{\partial p} \qquad (3)$$

其餘符號可參見 List of Symbols.

(1)、(2) 式經改寫爲定差方程式如下：

$$\sigma \nabla^2 \omega_{2k} - \frac{\bar{f}^2 d^2}{g m^2 (\Delta p)^2} (\omega_{2k-1} - 2\omega_{2k} + \omega_{2k+1}) = \frac{g}{8 \bar{f} d^2 \Delta p} \nabla^2 m^2 J$$

$$(z_{k+1} + z_k, z_{k-1} - z_k) - \frac{1}{4\Delta p} \left[J(z_{k+1}, \zeta_{k+1} + f) - J(z_k, \zeta_k + f) \right] \equiv G_{ijk}$$

$$(k = 1, \text{ at } 500\,\text{mb}) \qquad (4)$$

$$\nabla^2 \left(\frac{\partial z}{\partial t}\right)_k = -\frac{1}{4} J(z_k, \zeta_k + f) + \frac{\bar{f}^2 d^2}{g m^2 \Delta p} (\omega_{k+1} - \omega_k) \equiv H_{ijk}$$

$$(k = 1, 2, \text{ at } 250, 750\,\text{mb}) \qquad (5)$$

其中 $\zeta = \frac{g m^2}{\bar{f} d^2} \nabla^2 z$

由(4)、(5) 式使用緩和法 (Modified Gauss relaxation method, Wang 1970) 經 interation procedure 解得 500mb 的 ω-field 及 250mb、750mb 的 $\frac{\partial z}{\partial t}$。再由 $\frac{\partial z}{\partial t}$ 利用 time forword difference method (t=0) 及 central difference method (t > 0) 計算下一時刻的 Z-field。

方程式中 J (Jacobian) 的計算參考 Staff members of Electronic Computer center (1965). ，由 12 點的資料求出其值。結果較爲準確，合乎能量守恒原則，而仍不失其穩定度。

計算過程中使用的初值條件 (Initial conditions) 及邊界條件 (Boundary conditions) 如下：

(1)初值條件：由天氣圖中讀取 200，300，500，700，850mb 的高度場及溫度場資料，利用流體靜力原理計算出 250mb，750mb 的高度場（廖學鎰，1959），再經 Smooth (Shuman, 1957)。用此 Smoothed value，作爲 initial Z-field 值，開始計算。至於 ω-field, 則假設 $t = 0$ 時，$\omega = 0$。

(2)邊界條件：

(a)上界和下界 (Upper & lower B.C.)

$\omega = 0$ at $p = 0$，1000mb

(b)橫向邊界條件（對粗網格而言）。（如圖 3 ）由不滑動邊界條件 (Free ship B.C.) 假設大氣在邊界不受摩擦阻力，可以自由流動。即在 x －方向$\frac{\partial v}{\partial x} = 0$，在 y 方向$\frac{\partial u}{\partial y} = 0$，（大氣物理組同仁，1971），可導出：

$$Z_{boundary}\text{外一層} = 2\,Z_{boundary} - Z_{boundary}\text{內一層}$$

至於ω的邊界條件爲：假設每一層邊界$\frac{\partial z}{\partial t} = 0$，

$$\text{由}\quad \frac{\partial}{\partial t}\left(\frac{\partial z}{\partial p}\right) + \frac{g}{f}J\left(z, \frac{\partial z}{\partial p}\right) - \sigma\omega = 0$$

$$\text{可得}\quad \omega_{boundary} = \frac{g}{\sigma f}J\left(z, \frac{\partial z}{\partial p}\right)$$

Ⅲ 細網格的應用

將細網格中央置於颱風中心，在一完全的時間間隔內計算步驟如下：

(1) 先由渦旋度方程式，上升速度方程式及上述的初值條件、邊界條件、求出 t + 1 時刻，粗網格上的 z 及ω值。

(2) 在細網格邊界上，利用已知的 t，t+1 時刻，粗網格的 z 及ω值，求出時間變量(Tendency value)

$$\left(\frac{\partial z}{\partial t}\right)_{r,s} = \left(z_{i,j}^{t+1} - z_{i,j}^{t}\right)\quad 4\Delta t$$

$$\left(\frac{\partial \omega}{\partial t}\right)_{r,s} = \left(\omega_{i,j}^{t+1} - \omega_{i,j}^{t}\right)\quad 4\Delta t'$$

其中 (r,s), (i,j) 分別表示細網格點及粗網格點的位置。由此求出粗細網格邊界上，共同點的 z，ω時間變量，再內挿該邊界處細網格點的時間變量。

(3) 利用 (2)中的時間變量，求細網格各時間間隔（粗網格每一時間間隔內，細網格有四個時間間隔）的邊界值：

$$z_{r,s}^{t+\Delta t'} = z_{r,s}^{t+\frac{1}{4}\Delta t} = z_{r,s}^{t} + \left(\frac{\partial z}{\partial t}\right)_{r,s}\Delta t'$$

$$\omega_{r,s}^{t+\Delta t'} = \omega_{r,s}^{t+\frac{1}{4}\Delta t} = \omega_{r,s}^{t} + \left(\frac{\partial \omega}{\partial t}\right)_{r,s}\Delta t'$$

由此求出細網格的邊界值後，利用渦旋度方程式及上升速度方程式，可得細網格內各點 $t+\frac{1}{4}\Delta t$，$t+\frac{2}{4}\Delta t$，$t+\frac{3}{4}\Delta t$，$t+\Delta t$之 z 及ω值。

(4) 由細網格內共同點上計算出的 z 、ω值取代原先粗網格點計算的值。再加上法，重覆使用，求 $t+2\Delta t$，$t+3\Delta t$……，$t+n\Delta t$之 z，ω 值。

由於颱風移動速度一般很少超過25km/hr， 則 24 小時內也不過移動兩個格點，颱風

中心仍在細網格中央附近，爲方便起見，吾人保持細網格不隨颱風移動。

四、 資料的準備及處理

爲試驗上述模式，採用1971 年7月 24 日娜定颱風爲研究對象（承中央氣象局供給原始天氣資料，謹致謝意）。24 日22 時 30 分，氣象局發佈海上陸上颱風警報。是日爲此颱風生命期中的全盛期。本文取08 時的200,300,500,700,850mb 的高度場及溫度場做爲初值資料，利用中山科學研究院 CDC Cyber 72 Computer（謹致謝意）開始運算。

至於細網格上的值，最初是由粗格點上的值內插，以避免資料稀少，造成讀圖的誤差。

V 計算結果之分析

本文主旨在探討粗細網格配合使用可能造成運動模型的影響。經計算分析後，由圖4顯示：

250mb颱風中心原來在（13,6）格點位置，卽約在19°N，129°E，呂宋島東北方海面，中心高度場爲10870 m，經 12 小時後，移向西北西方，位於(10,5)格點，約17°N，123°E，高度場增爲10920 m。24小時後又向西移至(8,5）格點，高度場爲10920 m。與實際情況比較，250mb 颱風中心移動太快。

在此高度層內，庫頁島西方有一氣旋，中心位於（14,16）格點，高度場爲 10530 m，槽線由此中心向西南延伸，經日本海至日本南方。12 小時後東移至（17,17）格點，高度場升爲 10610 m，24 小時後又東移至（20,18）格點，高度場又升爲10690 m。此氣旋中心一面東移一面塡塞，與實際天氣情況相較，頗爲接近。

太平洋高壓原以30°N爲主軸，向西伸展至（16,10）格點。12 小時後向東北退縮，引致槽線東進。高壓中心先由11110 m升至11160 m，又降爲 11140 m。另外青康藏高原上有一高壓，與太平洋高壓遙遙相對，逐漸發展，擴大範圍，並且東移。此層颱風移動速度過快，即可能受此壓駛流(Steering flow) 影響。新疆西北有一氣旋，向東移動同時分裂爲二。

750mb 颱風中心原來在（13,6）格點位置，高度場爲 2305 m，經 12 小時，移向西北西，至（12,6）格點，約19.5°N，127°E，中心高度場爲2388 m。略爲塡塞。 小時後大約移至21°N，126°E，中心高度場爲 2407 m，與實際情況比較，颱風中心移動的方向及速度計算結果相當良好。

以30°N 爲主軸的太平洋高壓，向西伸展，深入華南，24 小時內此高壓脊增強。颱風的移動係受制於此脊線南緣的導引氣流，高緯度槽線均爲此強有力的脊線所阻隔，使颱風向西北西方向移動，不受槽線影響而轉向。

在蒙古北方、中南半島及卡洛林群島附近，都有氣旋向西移動。

至於500mb 的垂直速度場，12 小時後，颱風中心西北有一上升氣流區域，最大値在（11,7）格點，約21.5°N,123°E 。強度爲 -20.7×10^{-5}mb/sec。颱風中心東南則有一下降氣流區域，最大値在（11,5）格點，約18°N，125°E，強度爲+14.2×10^{-5}mb sec。顯示颱風進行方向大致爲西北西。又在日本海上空之槽線前方有上升氣流，後方有下降氣流。此種趨勢與實際情況符合，同時垂直速度場的強度非常合理。

本文又將相同的初値，以粗格點計算，所得的結果由圖5顯示。

250mb 高空，24 小時計算已看不出颱風環流存在。750mb 上颱風中心，24 小時後移至

(10,7)格點，約 21.5°N，120.5°E 與實際情況比較，移動過快，且颱風中心塡塞亦太快。500 mb 上垂直速度場在颱風西北方有上升氣流區，最大值爲 -13.5×10^{-5}mb/sec ，東南有一下降氣流區，最大值爲 15.1×10^{-5} mb/sec 。

在本文中，粗細網格配合使用的計算結果比只用粗網格的計算結果爲詳盡。同時粗細網格交界處的計算結果非常穩定，等值線很平滑。顯示粗細網格的配合情況尙稱良好。

由於本文未考慮熱量變化，摩擦效應及地形影響，可能使颱風中心塡塞較快，同時也可能是颱風速度移動稍快的原因之一。若加入這些效應，當可得到更爲合理的結果。對於熱量變化、摩擦效應、地形影響等，吾人將繼續研究。

REFERENCES

Edward J. Harrison, Jr., Three-dimensional numerical mumerical simulations of tropical systems utilizing nested finite grids, J. A. S. Vol. 30, No. 8, Nov. 1973.

Gene E. Birchfield, Numerical prediction of hurrican mavement with the use of a fine grid, Journal of met. 7, 406-414, 1960.

Saito, On the four-lovel geostrophic model (the 2-nd) report, Tech, rep. of the Japan agency, No. 24, 13-32, 1963.

Shuman F. G., Numerical methods in weather prediction II, Smoothing and filtering, MWR, 85, 357, 1957.

Staff members of Electronic Computer Center, 72-hrs. baroclinic forecast by the diabatic quasi-geostrophic model, J. met, Soc. of Japan, 43, 246, 1965.

Thompson, Numerical Weather Analysis and Prediction, 104, 1969.

中央研究院物理研究所大氣物理組同仁研究報告 I. 大氣及颱風運動模型， 1972 。

廖學鎰：厚度圖對於天氣分析和預報之應用。氣象學報 Vol. V, T-11, 1959。

中央氣象局研究室；民國六十年颱風調査報告。 Vol. 18, No. 1, p. 38-44, 1972 。

空軍氣象聯隊：六十年度七月份侵台娜定颱風之檢討，氣象預報與分析 Vol. 51, No, 366, 1972。

List of Symbols

z : geopotential height
w : $\frac{dp}{dt}$ p-velocity
ζ : relative vorticity
f : Coriolis parameter
$\bar{f}$: the averaged Coriolis parameter
g = 9.8m/sec^2 gravitational acceleration
p : pressure
Δp : thickness between the levels (500mb)
d, d' : grid interval of the coarse and fine mesh respectively (300km, 150km)
m : mapping factor
σ : static stability
R : gas constant
θ = $T(\frac{P_o}{P})^{R/C_p}$
C_v, C_p : specific heat of air at constant volume and pressure respectively
P_o = 1000mb

C. J. SHIAN 胡仲英, C. T. WANG

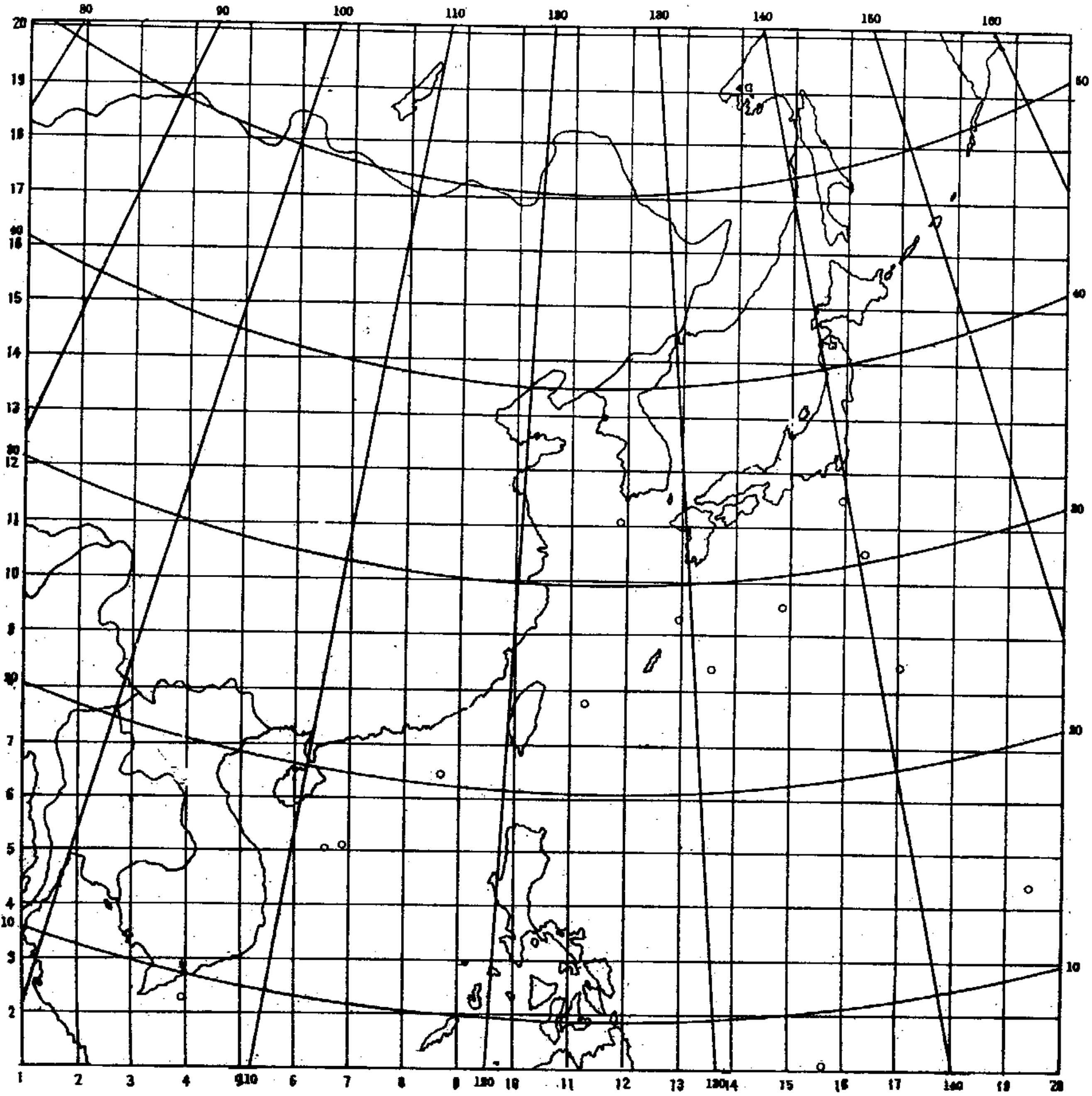

Fig. 1. Computation Domain

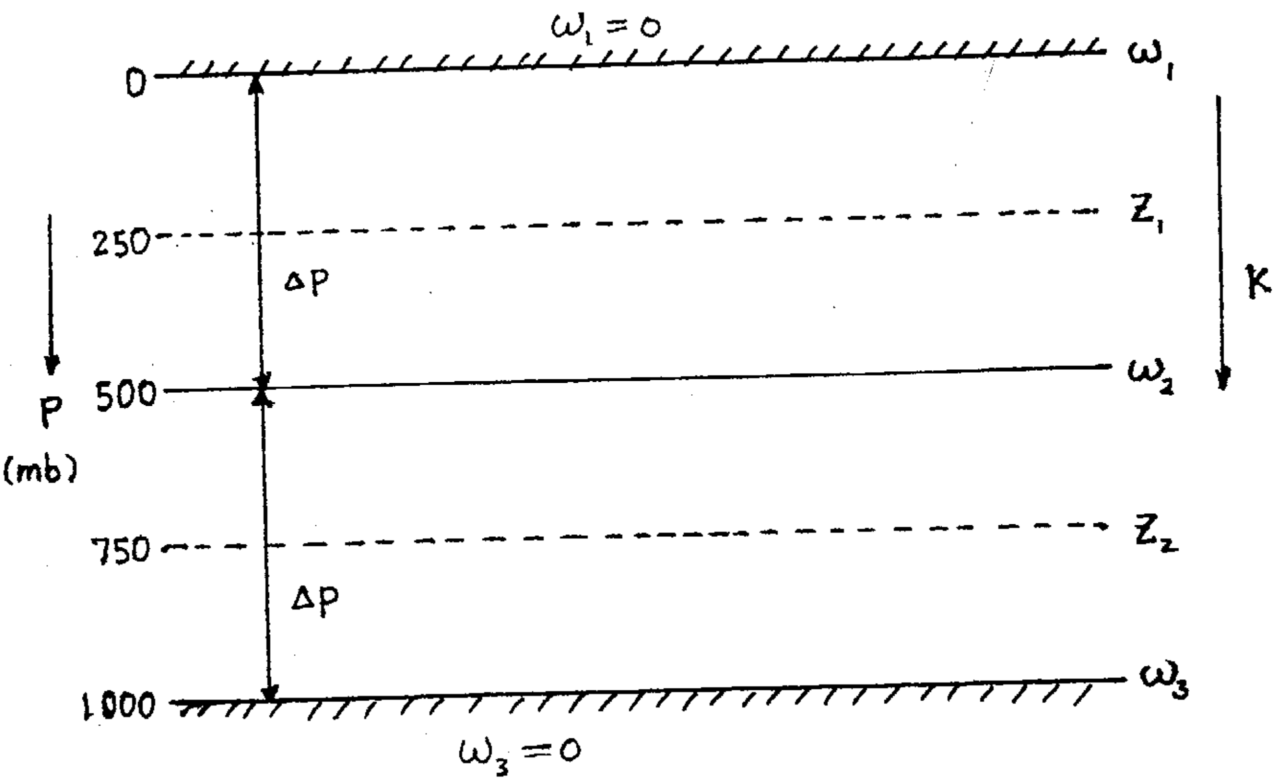

Fig. 2. Vertical Grid System

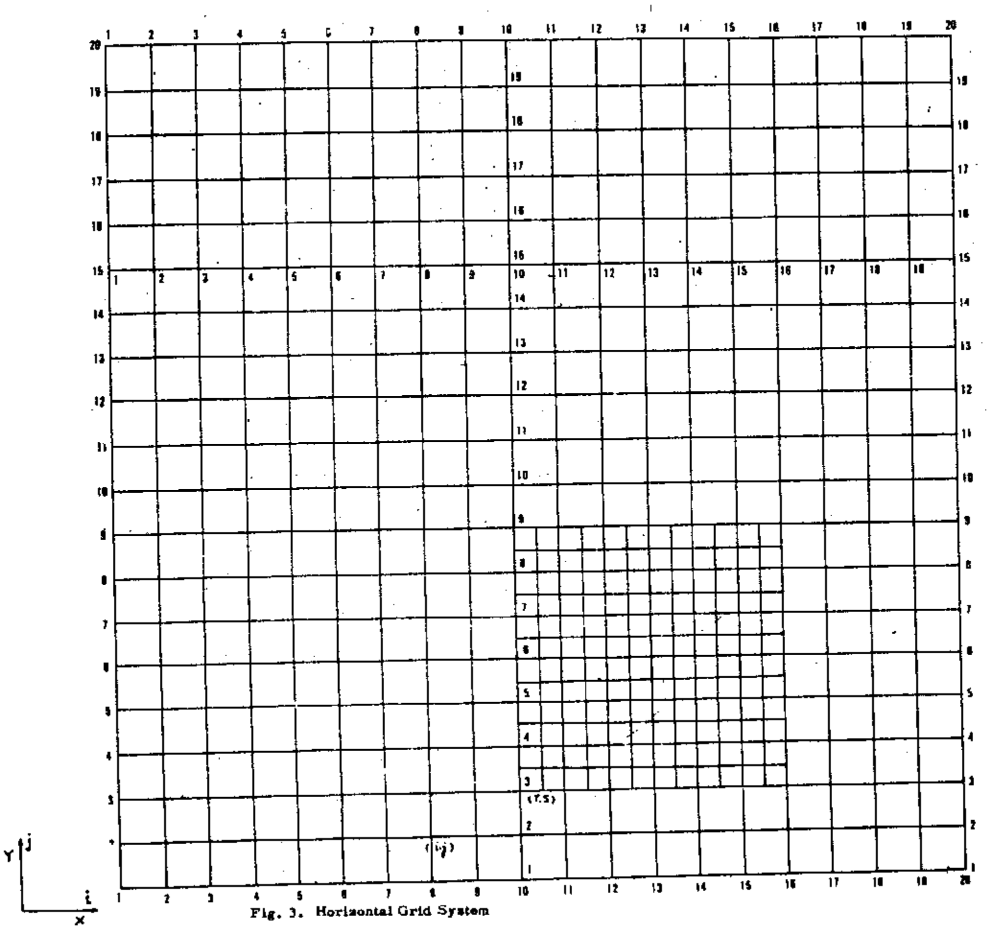

Fig. 3. Horizontal Grid System

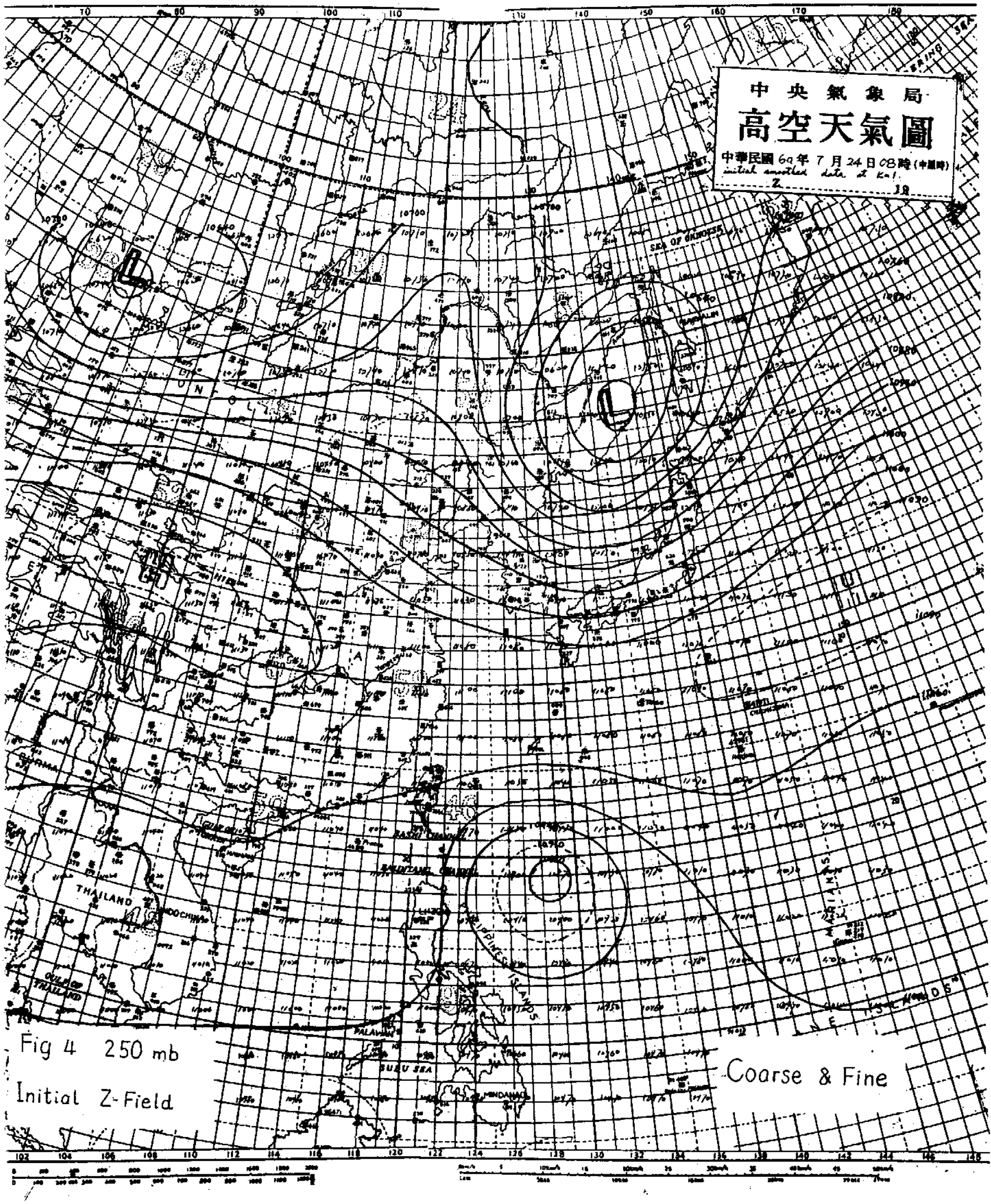

Fig 4 250 mb Initial Z-Field

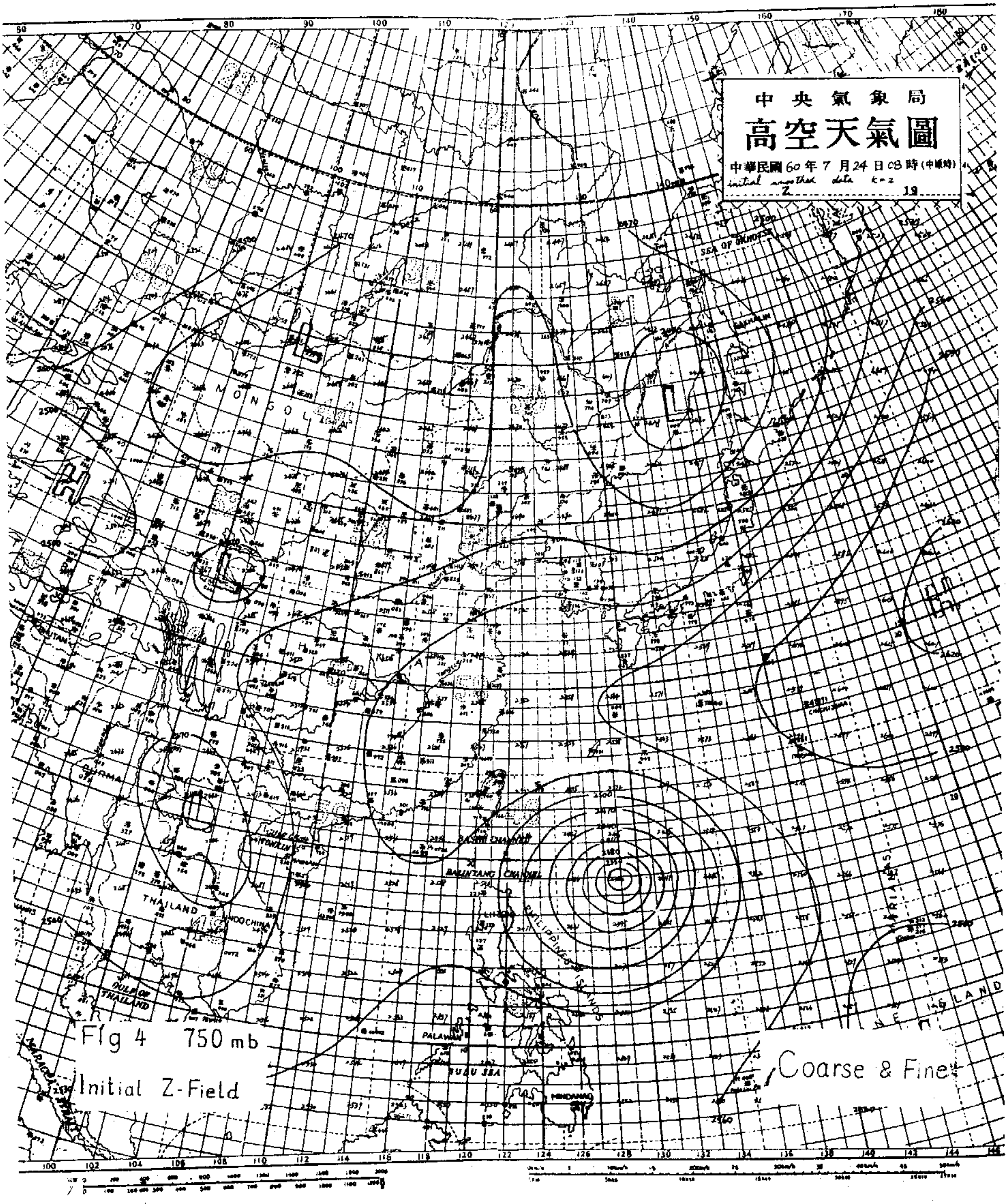

Fig 4 750 mb Initial Z-Field

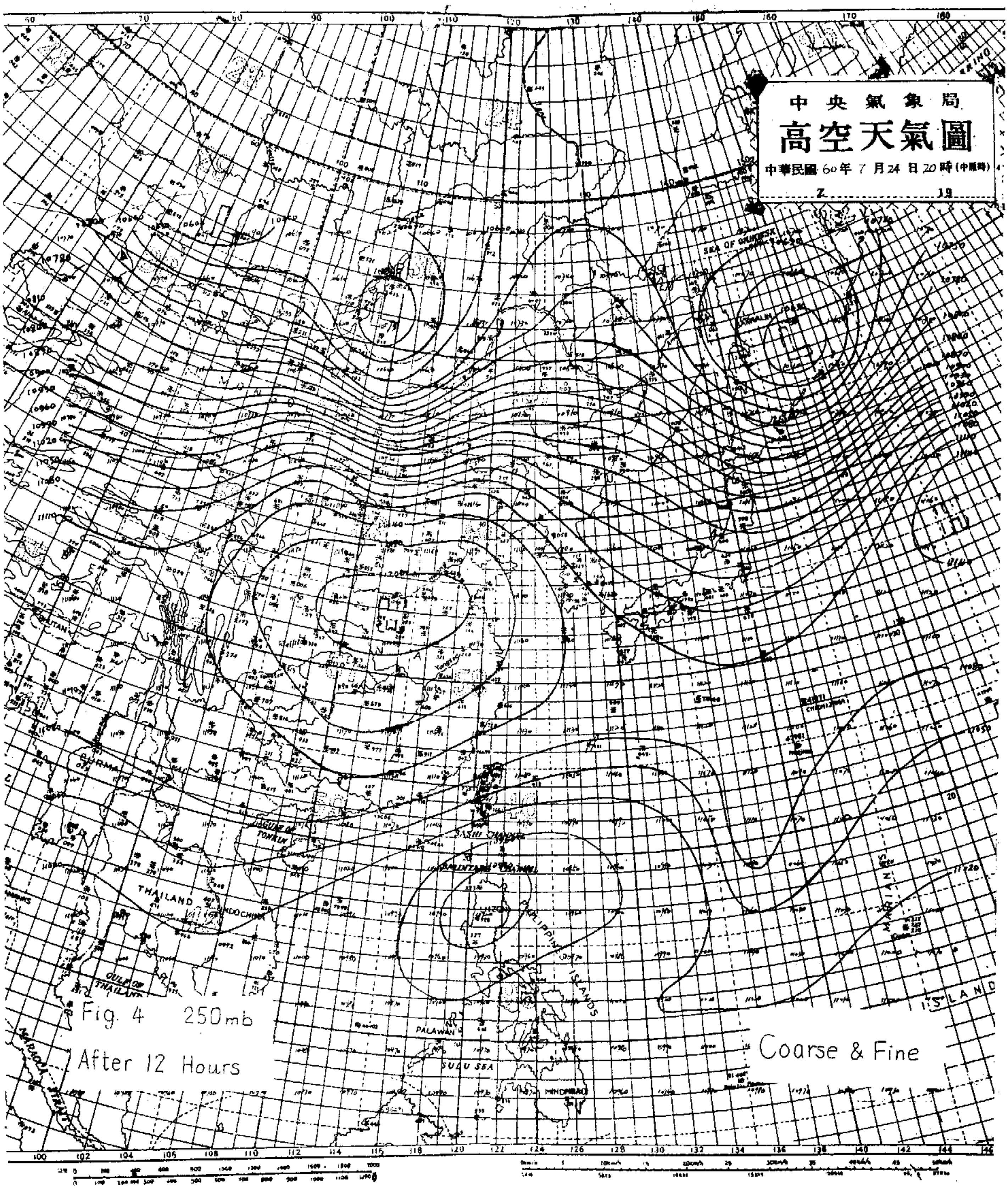

Fig. 4 250mb After 12 Hours

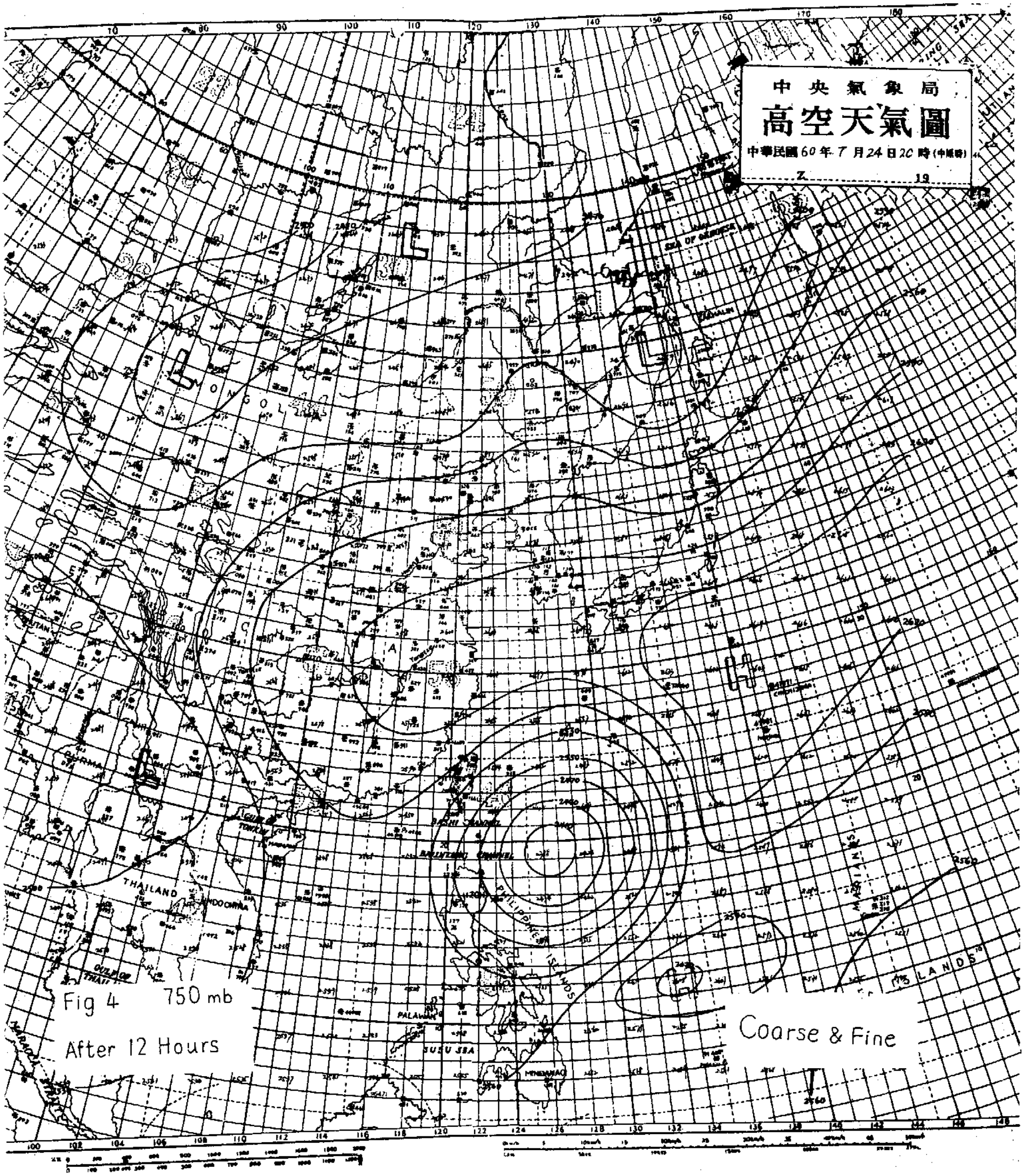

Fig 4 750 mb

After 12 Hours

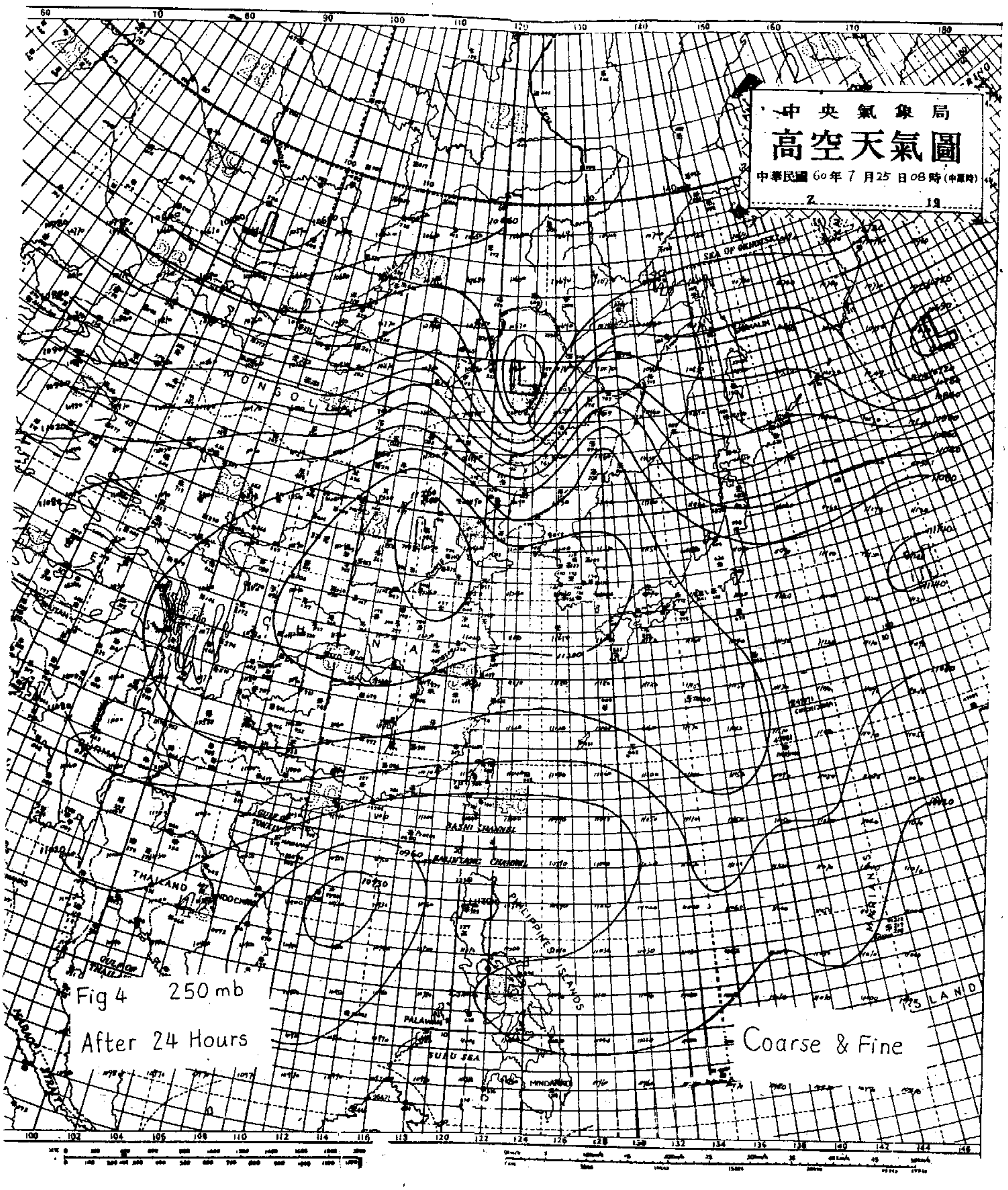

Fig 4 250 mb

After 24 Hours

Coarse & Fine

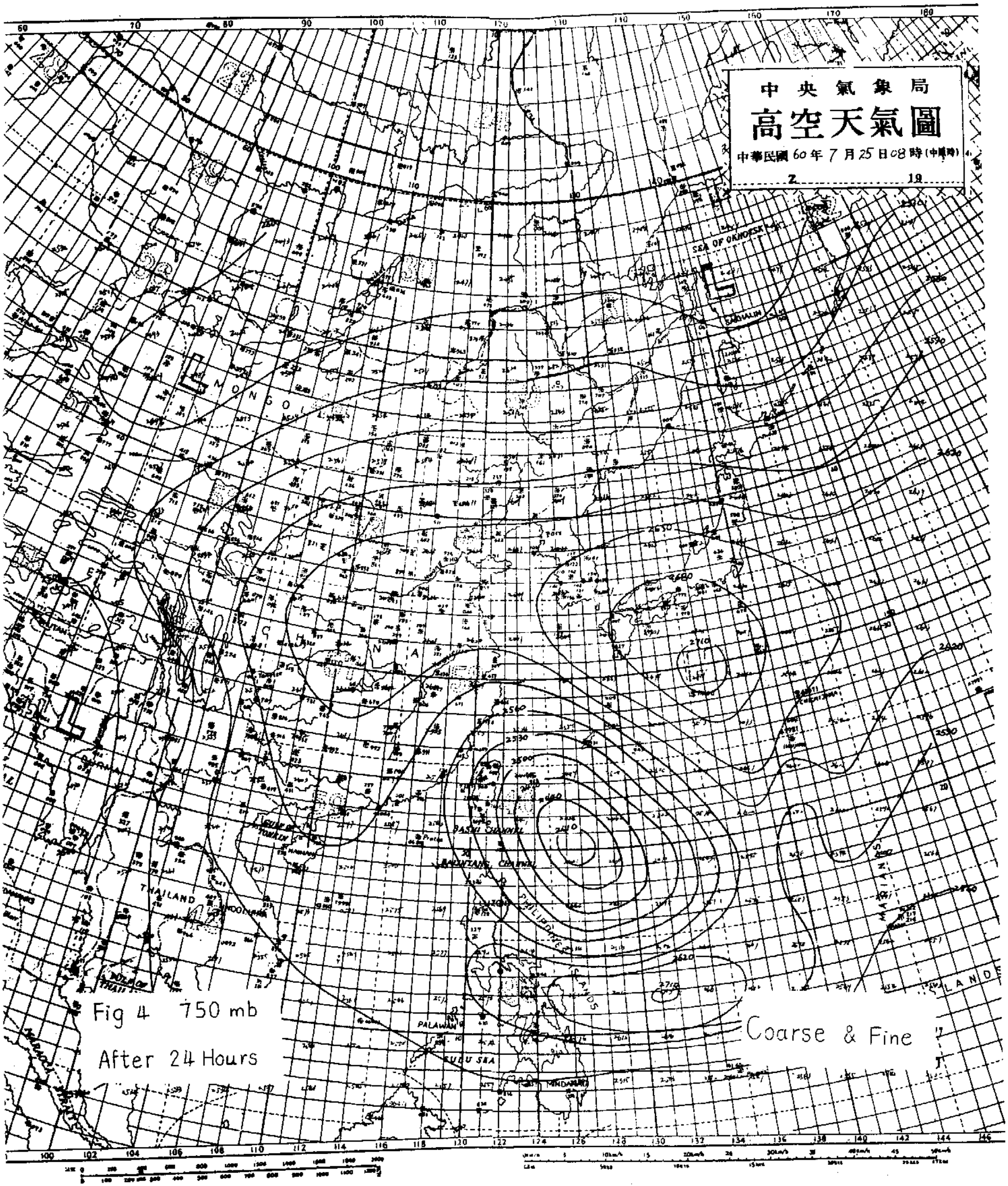

Fig 4 750 mb

After 24 Hours

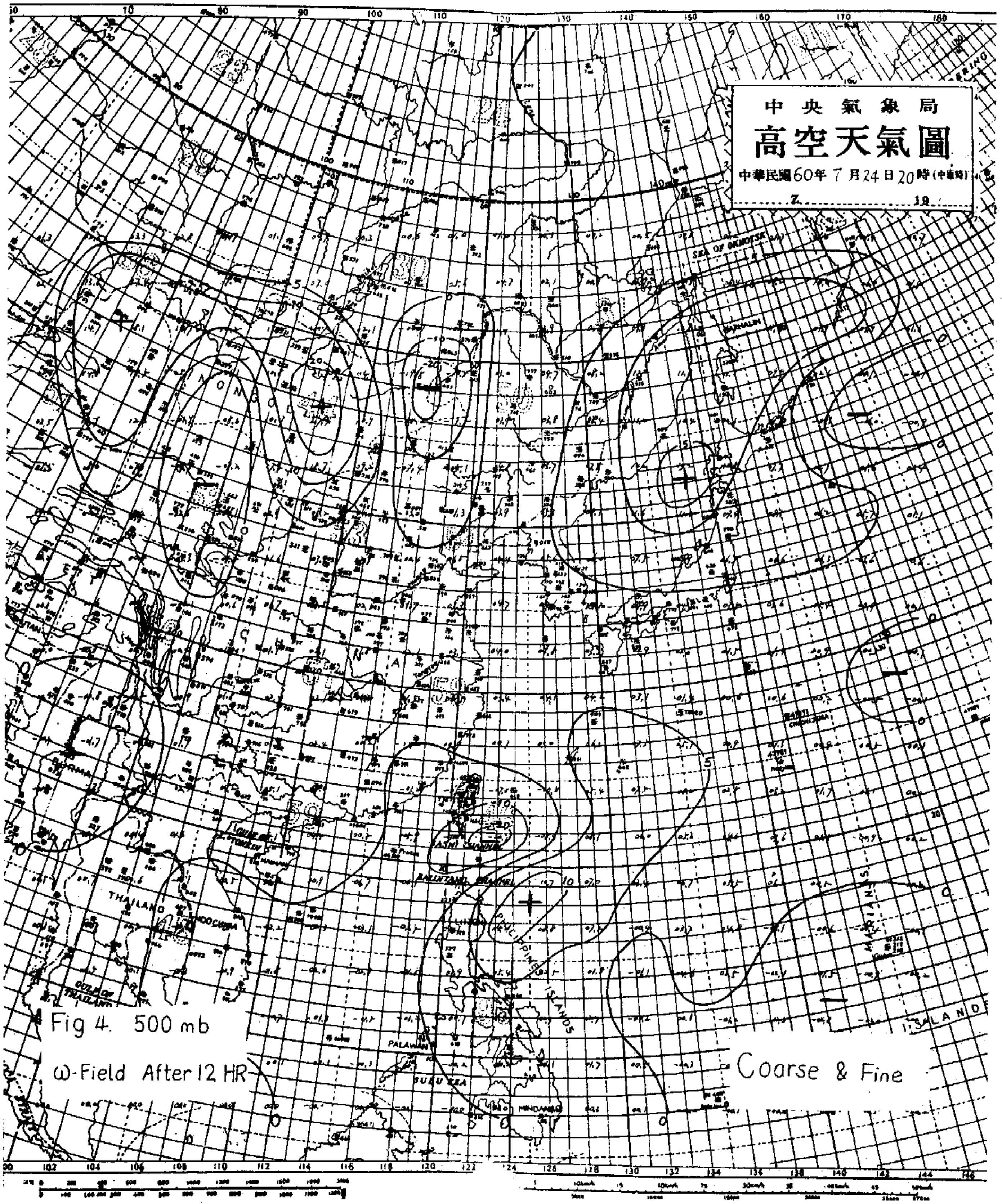

Fig 4. 500 mb ω-Field After 12 HR

Coarse & Fine

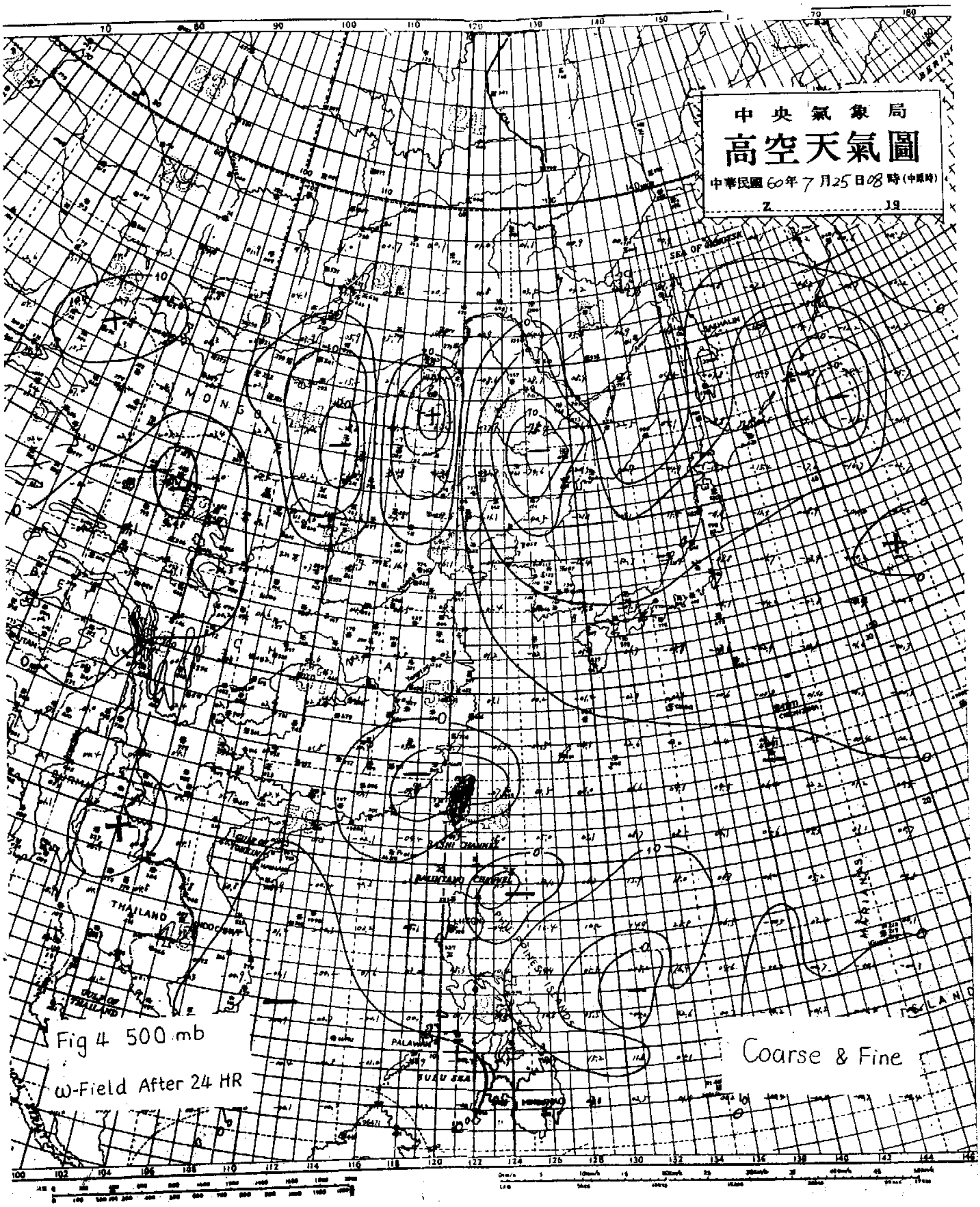

Fig 4 500 mb
ω-Field After 24 HR

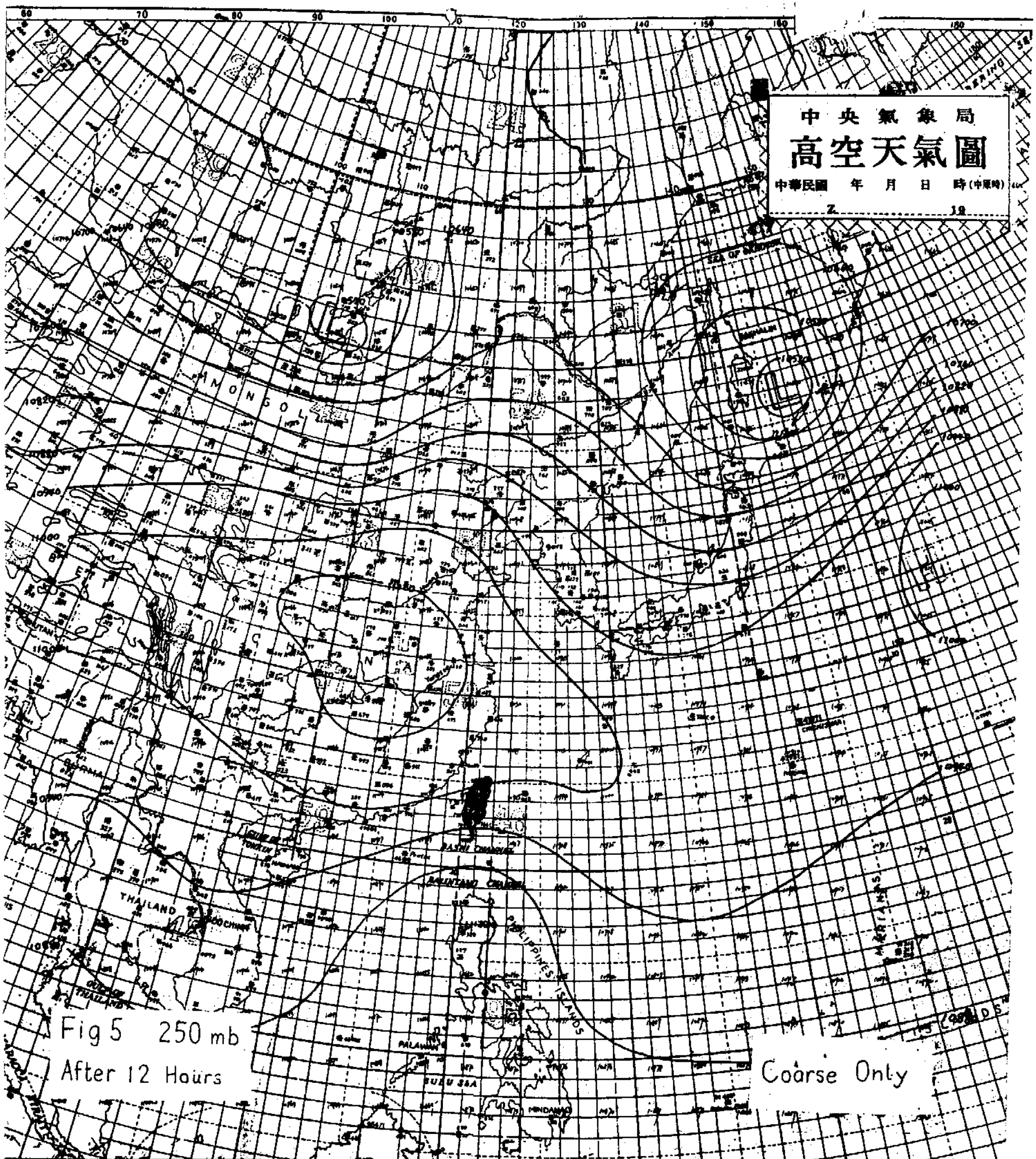

Fig 5 250 mb
After 12 Hours

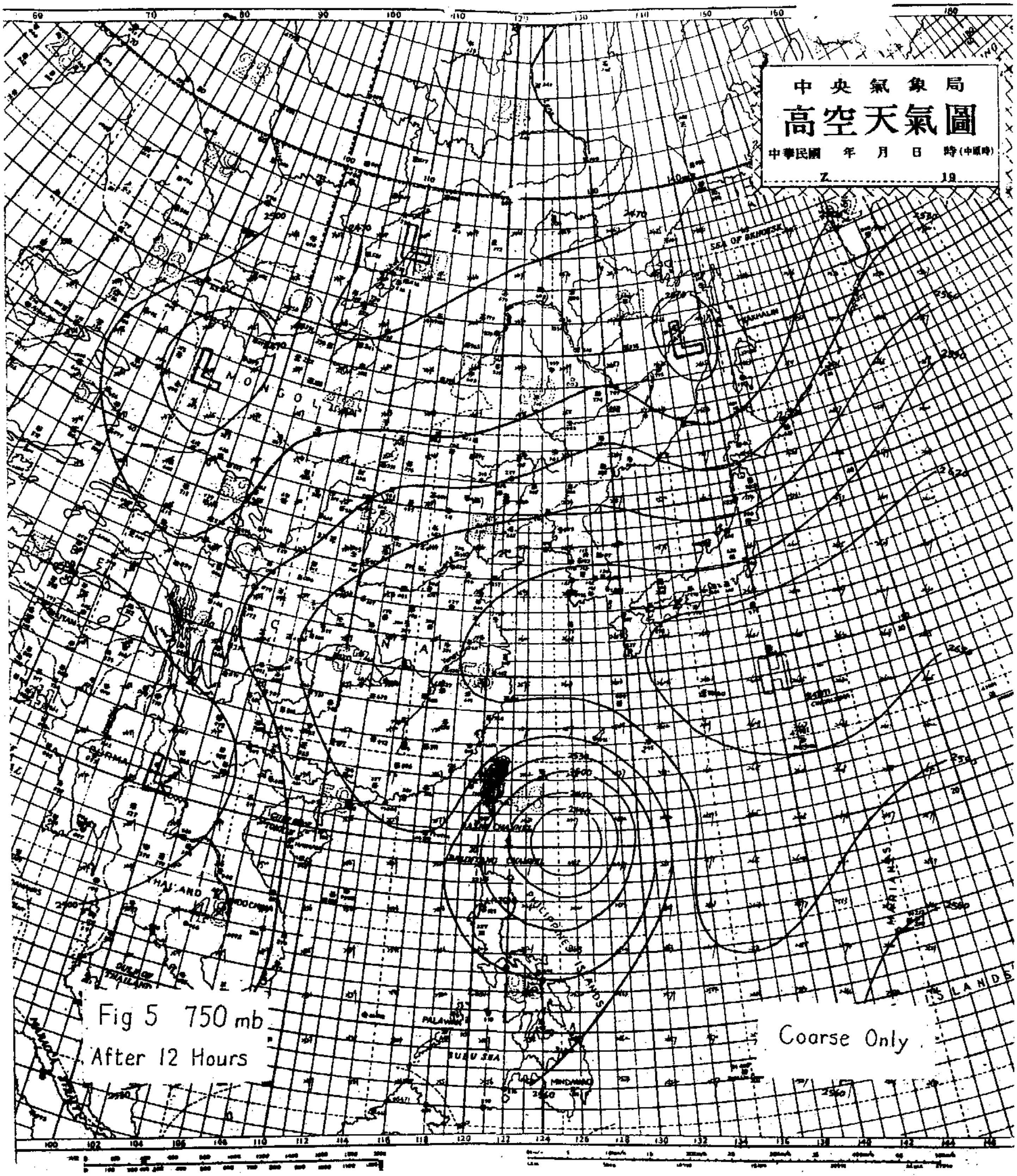

Fig 5 750 mb
After 12 Hours

Coarse Only

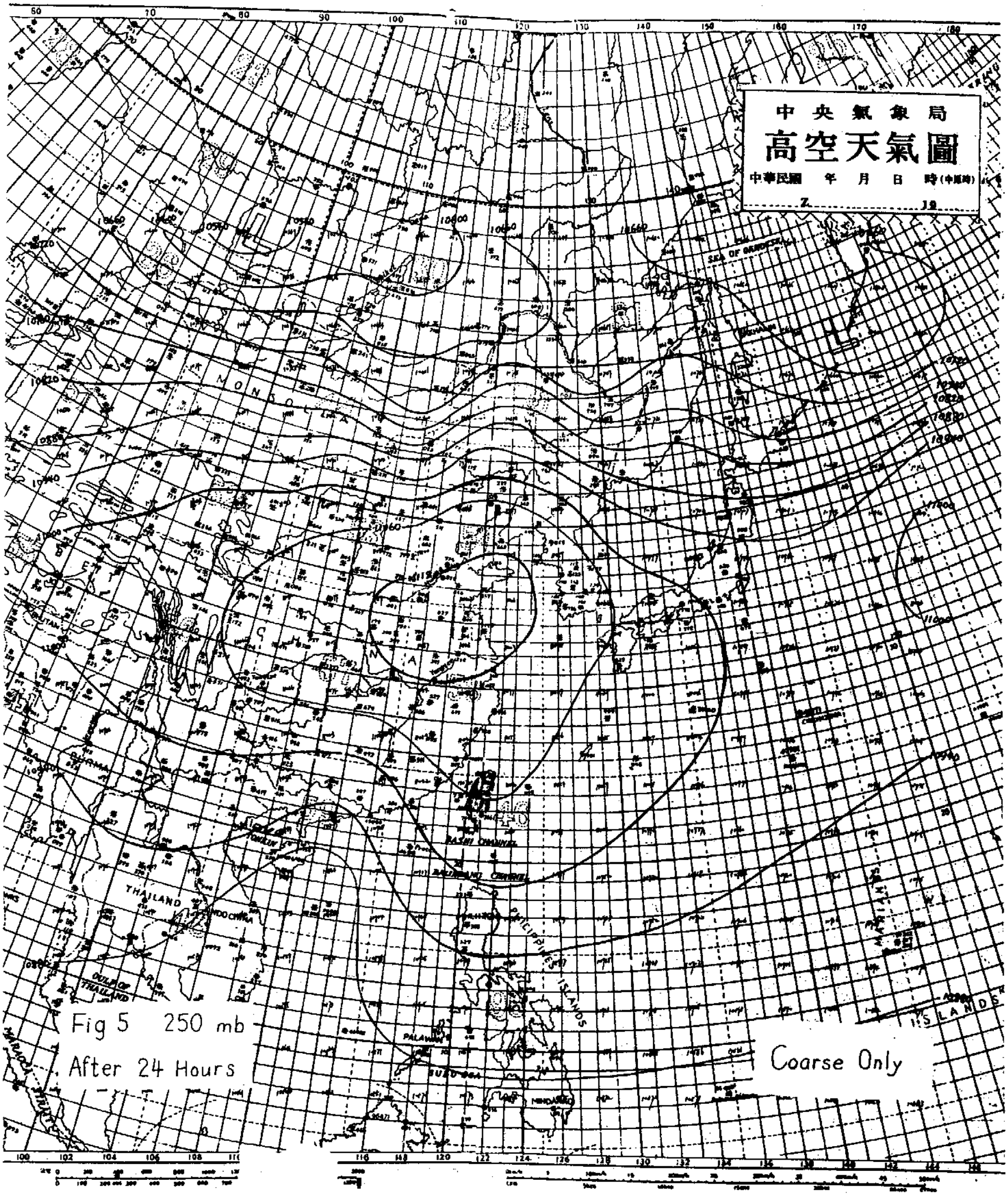

Fig 5 250 mb After 24 Hours

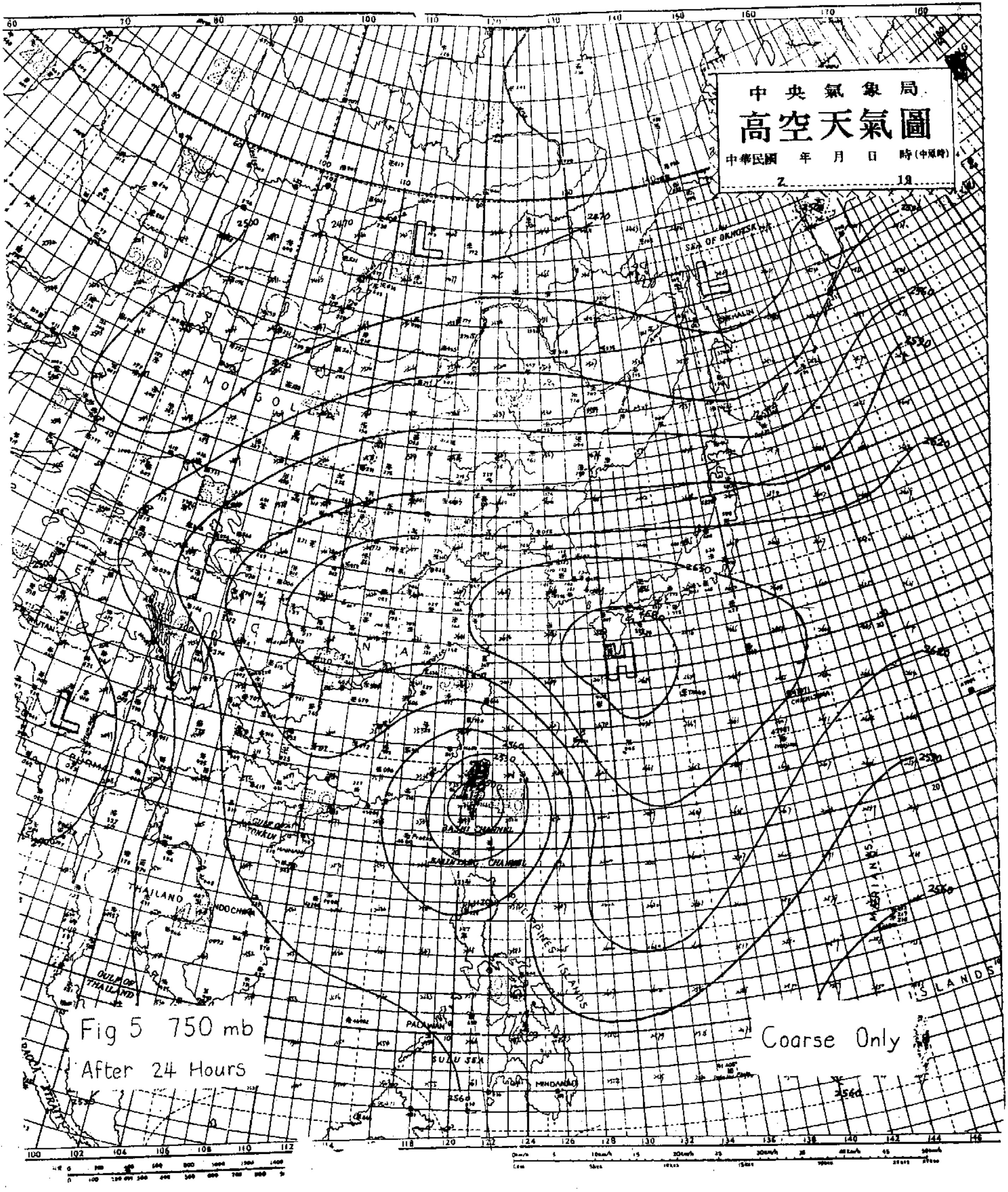

Fig 5 750 mb
After 24 Hours

Coarse Only

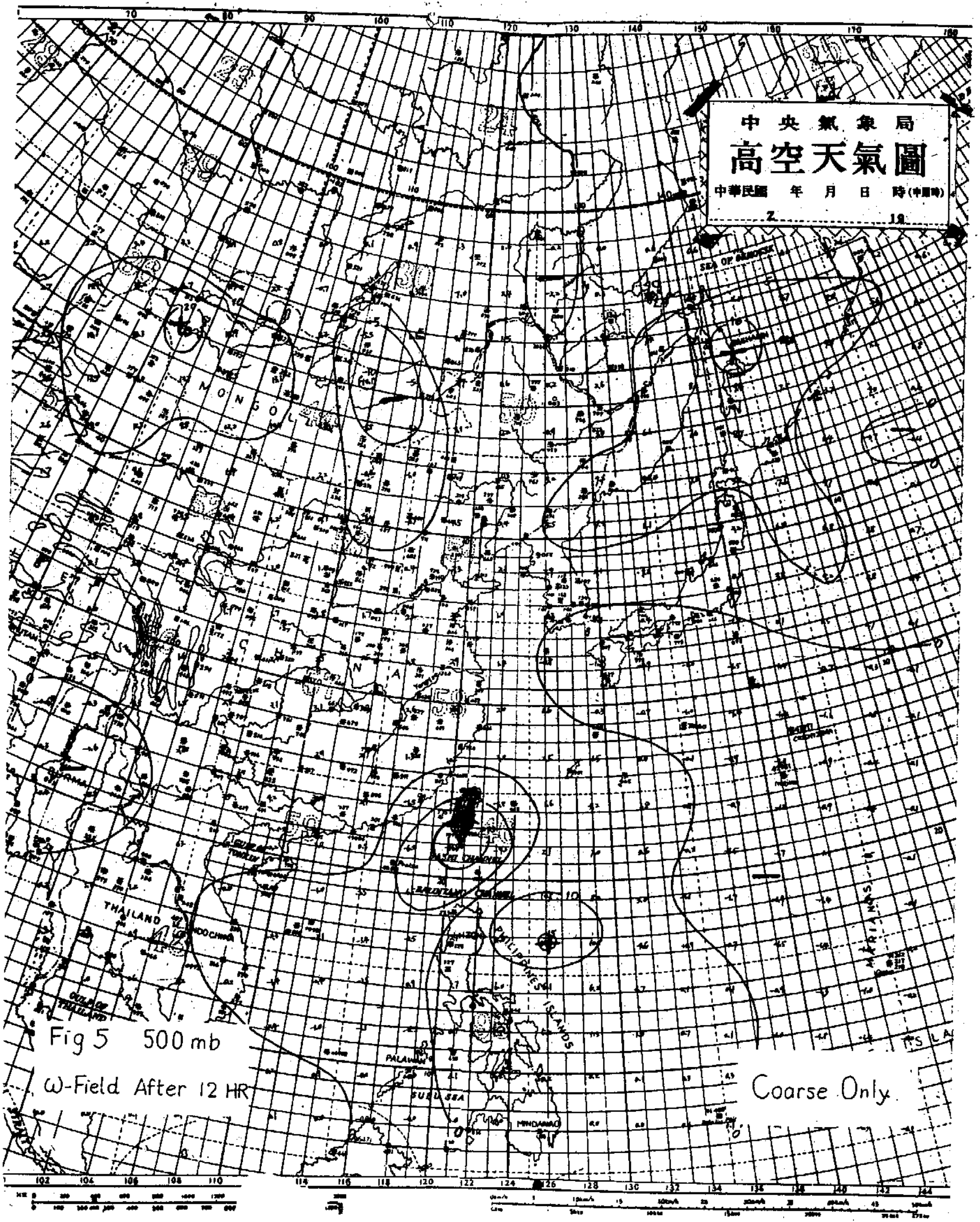

Fig 5 500 mb ω-Field After 12 HR

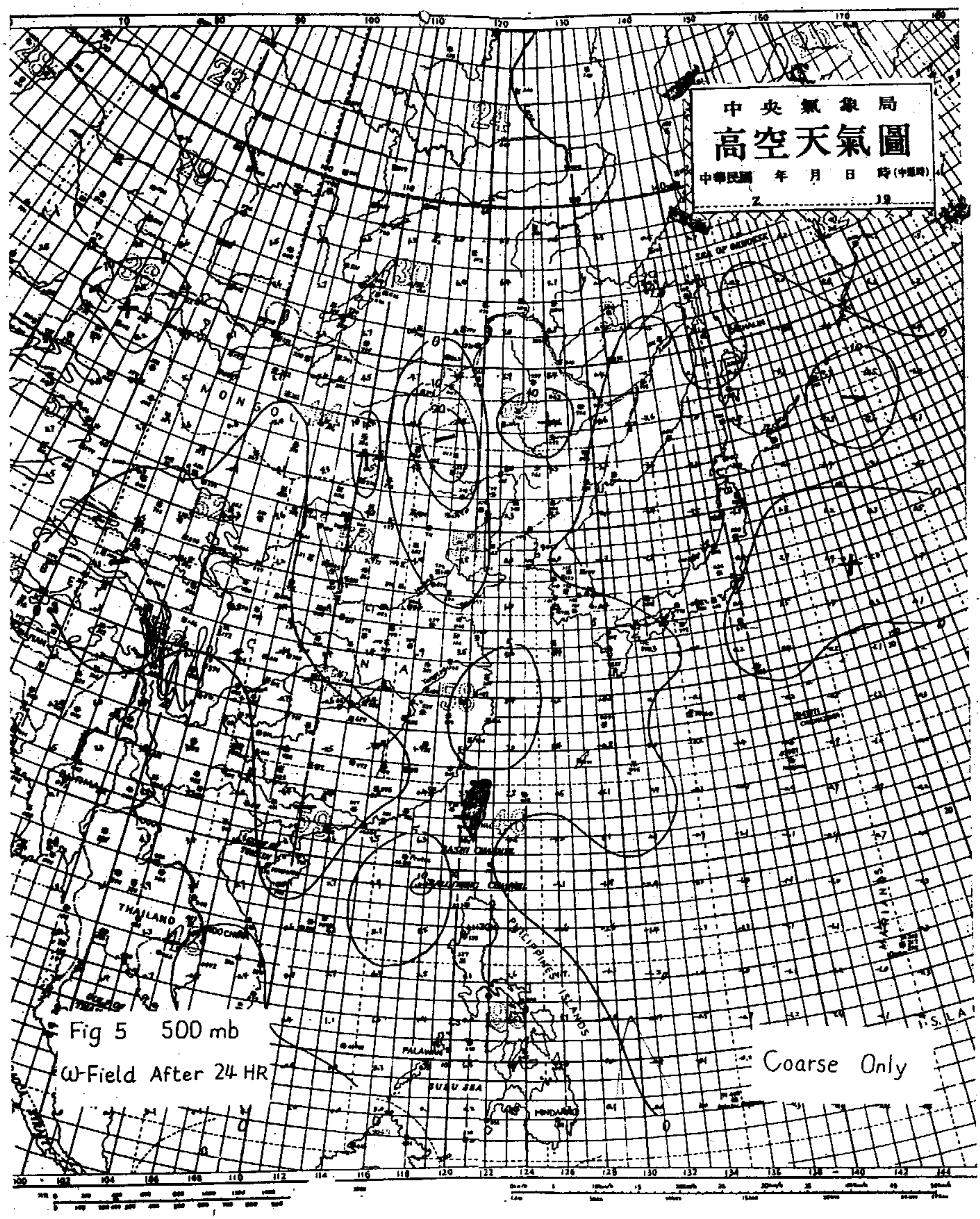

Fig 5 500 mb ω-Field After 24 HR

Coarse Only

大氣及颱風運動模型：III A，不等間距斜壓模式

戴治台　汪群從 *(Chun-Tsung Wang)* **簡來成** *(Lai-Chen Chien)*

在大氣及颱風運動模型、III、熱及摩擦阻力 (1973) 一文中，曾利用四層斜壓模式預測台灣附近颱風運動情況，獲得良好結果。該文探討時利用 300、500、700及 900 mb之高度場，而一般制式天氣圖應用 300、500、700及850mb 處之高度場，本文之目的即在直接應用天氣圖資料供預報作業。

本文所用方法同於大氣物理組同仁 (1973)，（以下節稱C案）不同的地方祇是在數值處理高度場方向不等間距時，採用 Sundquist (1970)

$$f' = \frac{h_{i-1}}{h_i + h_{i-1}} \cdot f_{i+\frac{1}{2}} + \frac{h_i}{h_i + h_{i-1}} \cdot f'_{i-\frac{1}{2}}$$

$$= \frac{1}{h_i + h_{i-1}} \cdot \left[\frac{h_{i-1}}{h_i} \cdot f_{i+1} + \left(\frac{h_i}{h_{i-1}} - \frac{h_{i-1}}{h_i} \right) f_i - \frac{h_i}{h_{i-1}} f_{i-1} \right] \quad \cdots (1)$$

$$f'' = \frac{2\left[h_{i-1} \cdot f_{i+1} - f_i (h_{i-1} + h_i) + h_i f_{i-1} \right]}{h_i h_{i-1} (h_i + h_{i-1})} \quad \cdots (2)$$

或採用 Maine (1972)

$$f' = R_{i-1} f_{i-1} - R_i f_i - R_{i+1} f_{i+1} \quad \cdots (3)$$

式中

$R_{i-1} = D_1 (D_2 \cdot D_3)$

$R_i = (D_1^2 - D_2^2)(D_1 \cdot D_2 \cdot D_3)$

$R_{i+1} = D_2 (D_1 \cdot D_3)$

$D_1 = h_{i+1} - h_i$

$D_2 = h_i - h_{i-1}$

$D_3 = h_{i+1} - h_{i-1}$

$$f'' = T_{i+1} f_{i+1} - T_i f_i + T_{i-1} f_{i-1} \quad \cdots (4)$$

式中

$T_{i+1} = 2 / (D_1 \cdot D_3)$

$T_i = 2 / (D_1 \cdot D_2)$

$T_{i-1} = 2 / (D_2 \cdot D_3)$

上二式形式雖不同，計算所得結果一致。

圖一顯示經過過濾後，850mb 處高度場分佈情形（300，500 及700mb 同於C案，，圖2顯示 12 及 24 小時後，使用不等間距斜壓模式所得 300，500，700及 850 mb 之高度場。與C案比較可

以看出 300mb 天氣圖形類似，不過C案 deepping 強些，500及700 mb 之高度場與C案極爲相近。850mb 之高度場變化也與實際天氣變化類似。是則不等間距之斜壓大氣模式可直接利用天氣圖資料進行天氣預測工作。

參考文獻

大氣物理組同仁，大氣及颱風運動模型： III、熱及摩擦阻力，中研院物理所集刊，211. Aug., 1973.

R. Maine, A Filtered Equation Model For Operational & Research, J. Appl, Meteo., Vol. 11, No. 1, PP. 7-15, 1972.

Sundquist, H. & G, Veronis, A Simple Finite-Difference Grid with Non-Constant Intervals, Tellus, Vol. 22, P. 26-31, 1970.

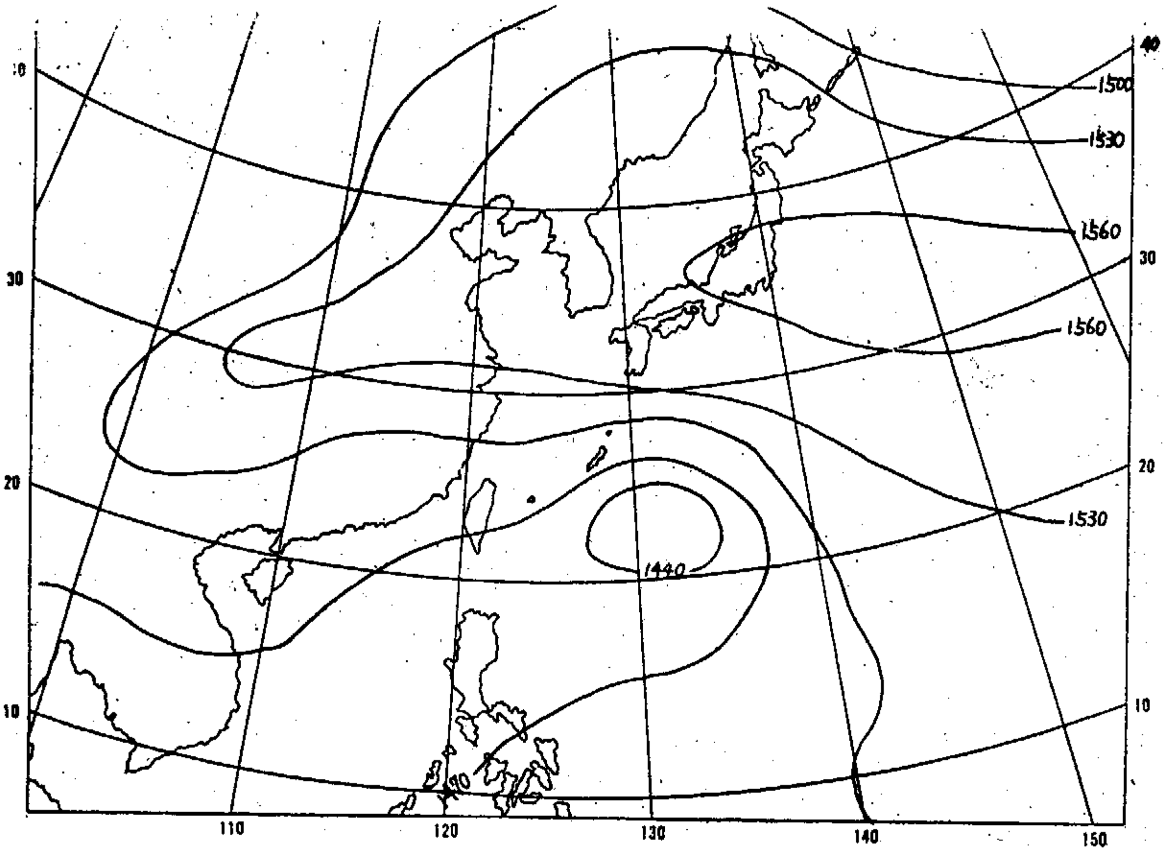

Fig. 1 經過過濾後，850mb 處高度場之分佈。

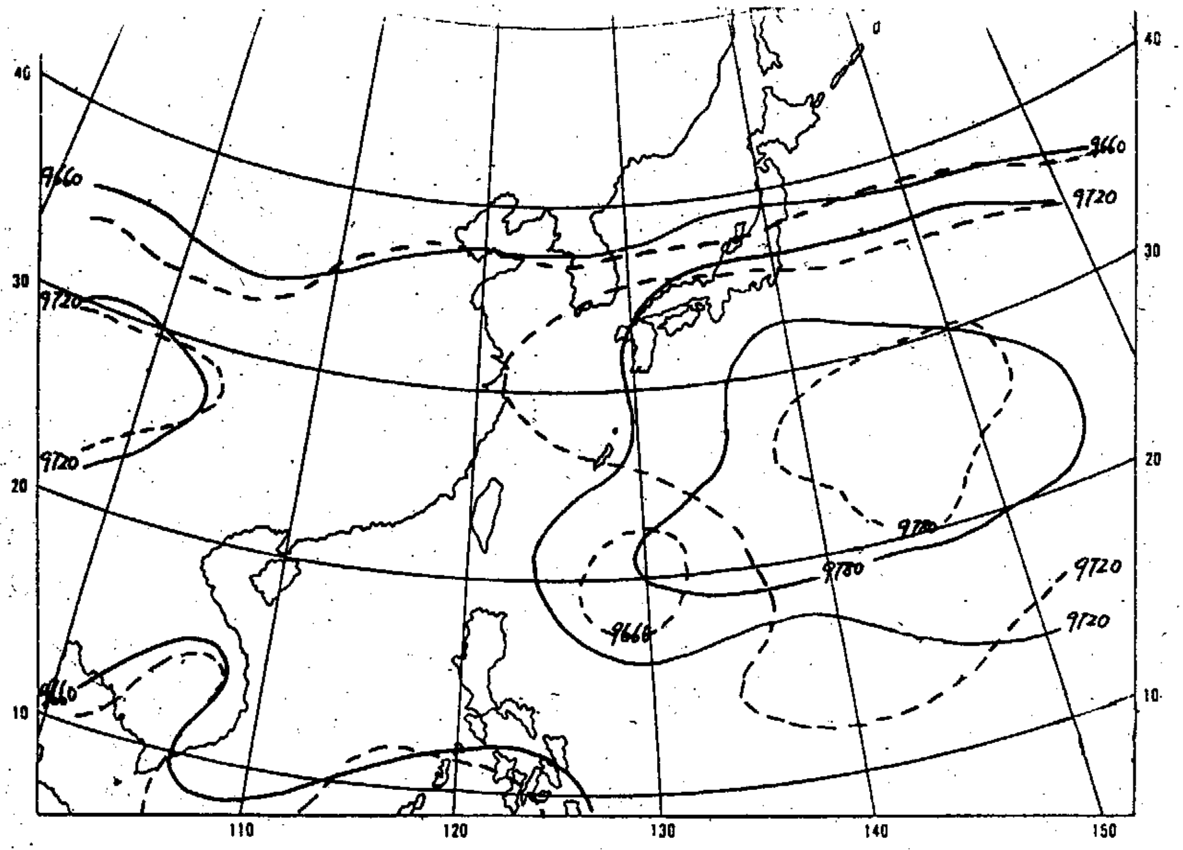

Fig. 2—1 12及24小時後使用不等間距斜壓模式，300mb 高度場。

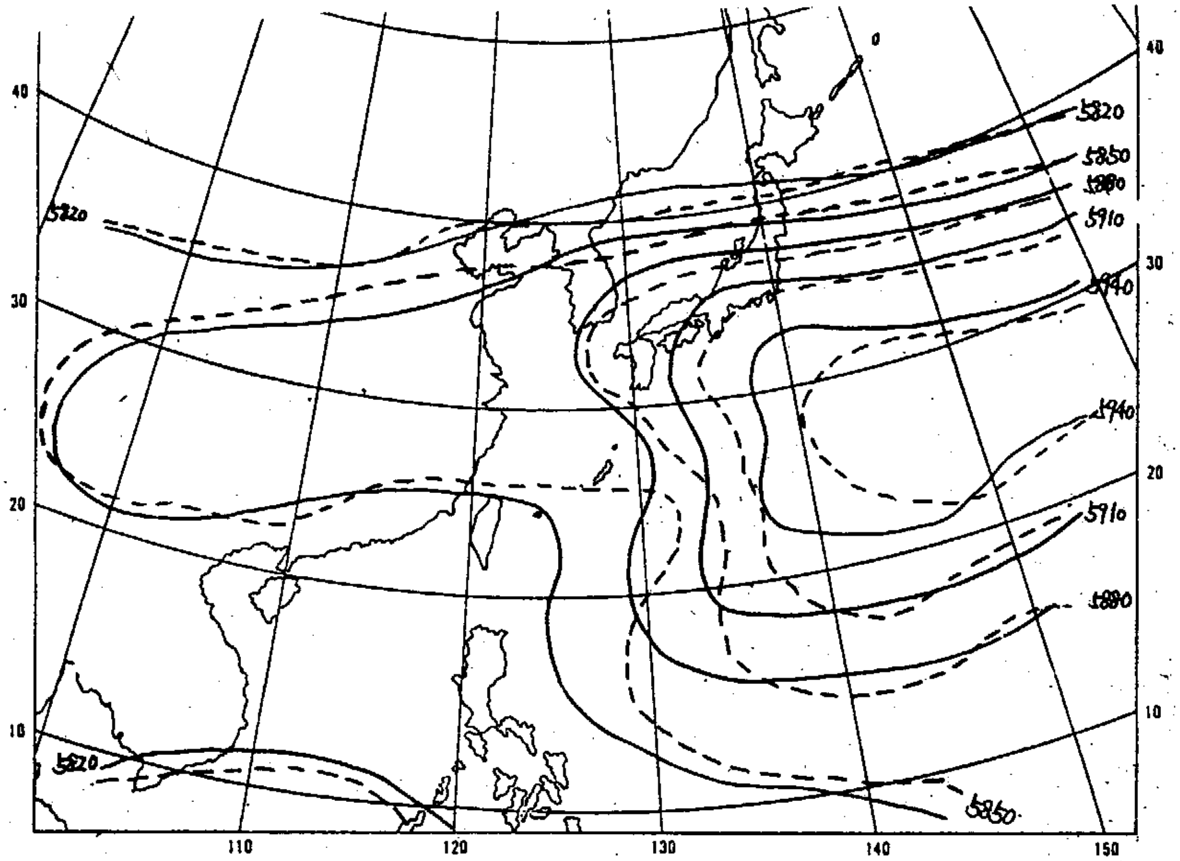

Fig. 2—2 12及24小時後，使用不等間距斜壓模式，500mb高度場。

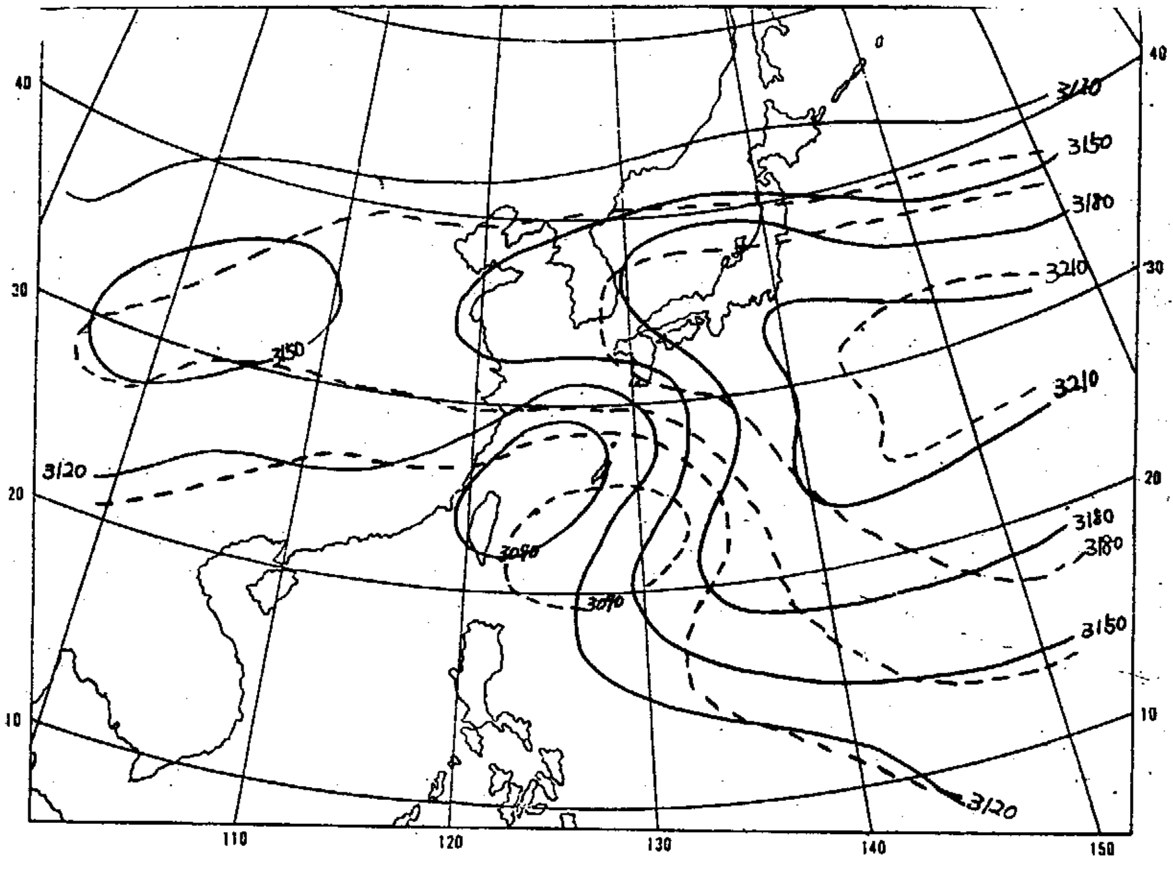

Fig. 2—3 12及24小時後，使用不等間距斜壓模式，700mb高度場。

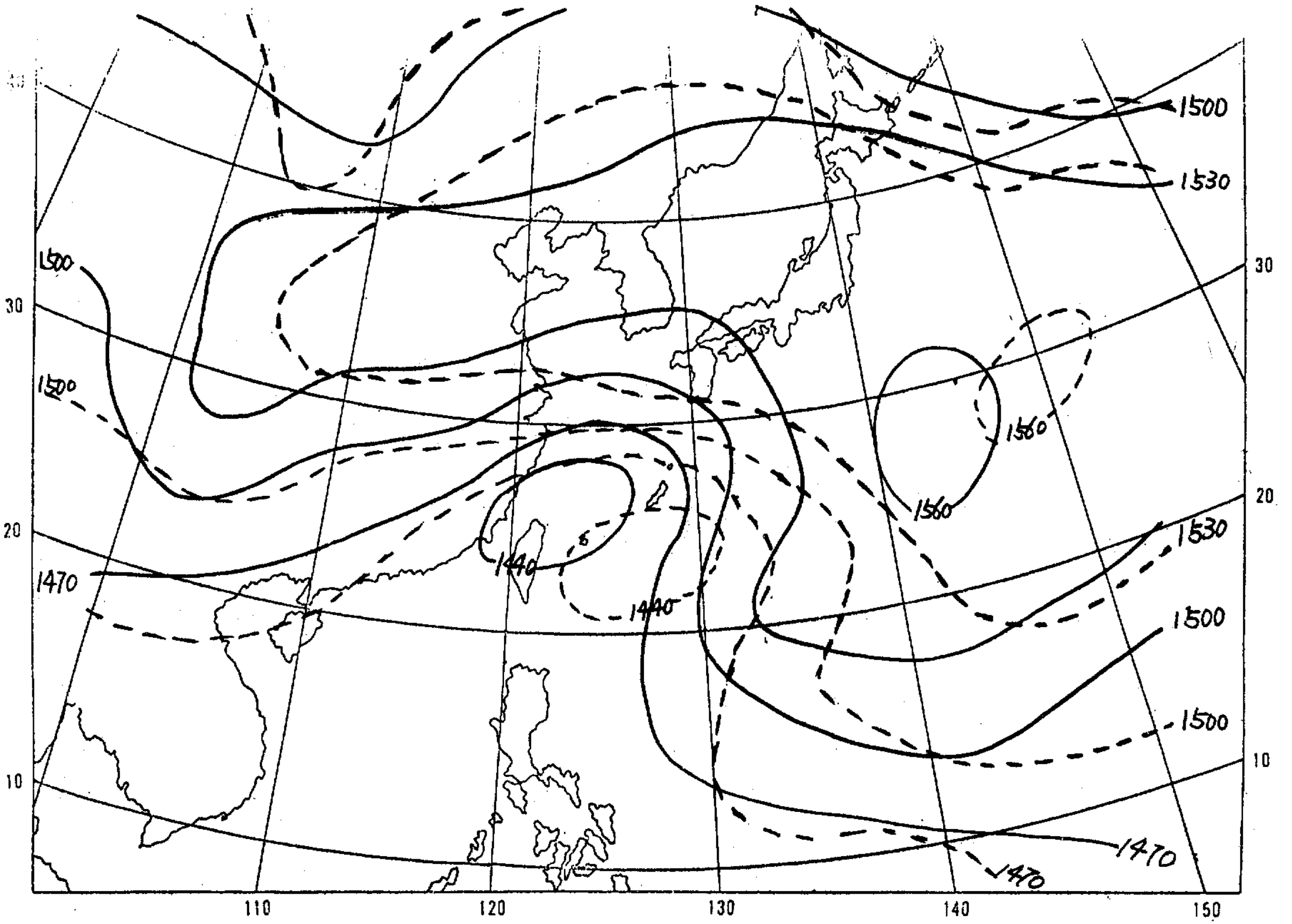

Fig. 2—4　12及24小時後，使用不等間距斜壓模式，850mb 高度場。

SOME FURTHER STUDY ON JET FLOWS WITH FREE SURFACE

C. T. Wang, W. L. Chang, T. C. Ma
Institute of Physics
Academia Sinica
Nankang, Taipei, Taiwan
The Republic of China

1. *Introduction*

In 1972, an experimental study of a circular jet in uniform flow field under the effect of free surface was made in the National Taiwan University$^{(1)}$. It was noticed that when there was no uniform flow, the jet flows were different from that obtained by Maxwell & Pazwash$^{(2,3)}$. Recently some further experimental study on jet flows were conducted in the Fluid Dynamics Laboratory of this Institute by using of a set of hot film anemometer system, in hope that data obtained previously by pitot tube measurement could be checked.

The experimental set-up has been mentioned elsewhere$^{(4)}$ and will not be repeated here. Data obtained are too much to be listed that a typical velocity profile is shown in Fig. 1 for illustration. It is seen that under the effect of free surface, as jet flows downstream, the maximum flow section deviates more and more from the original flow centerline.

2. *Results and Discussion*

As shown in Fig. 2, a uniform jet of diameter D and of velocity U_o is discharged at an angle θ from a circular nozzle with distance Z_o from the free surface. At a distance x from the nozzle, the distance between the point where local maximum velocity U_m occurs and the point where the velocity equals half of U_m is defined as the diffusion half width $D_{½}$. Figure 3 shows the relationship between U_o/U_m versus x/D, it is seen that U_o/U_m increases linearly as x/D increases

$$\frac{U_o}{U_m} = 0.1735\left(\frac{x}{D} - 1\right)$$

and is not a function of Z_0/d and U_0^2/gd. It is also shown that as x/d increases, the velocity pattern tends to deviate from that of a deeply submerged jet. This relationship agrees with previous data (1,2,3). It should also be mentioned that at $\theta = \pm 2.5°$, experimental data show that the relationship shown in Eq. 1 still holds.

Figure 4 shows the linear relationship between diffusion half width $D_{1/2}$ and downstream distance x as

$$D_{1/2} = 0.1\, x$$

this tends to disagree with previous data (1), however data obtained by Maxwell and Pazwash (2) fit Eq. 2 nicely although test conditions between the two are quite different.

References

(1) Wang, S. T., Wang, C. T. & Y. N. Chen, An Experimental Study of a Circular Jet in Uniform Flow Field Under the Effect of Free Surface, NTU-SHL-07, Ship Hydrodynamics Laboratory, National Taiwan University, July, 1972.

(2) Maxwell, W. H. C., & H. Pazwash, Basic Study of Jet Flow Patterns Related to Stream and Reservoir Behavior, Res. Rept. No. 10, Water Resources Center, Uni. Illinois, July, 1967.

(3) Maxwell, W. H. C., & H. Pazwash, Boundary Effects on Jet Flow Patterns Related to Water Quality and Pollution, Res. Rept. No. 28, Water Resources Center, Uni. Illinois, Jan., 1970.

(4) Chang, Y. C., An Experimental Study on Blockage Effect of a Rectangle in a Rectangular Channel, M. S. Thesis, Civil Engr. Dept., NTO, 1974.

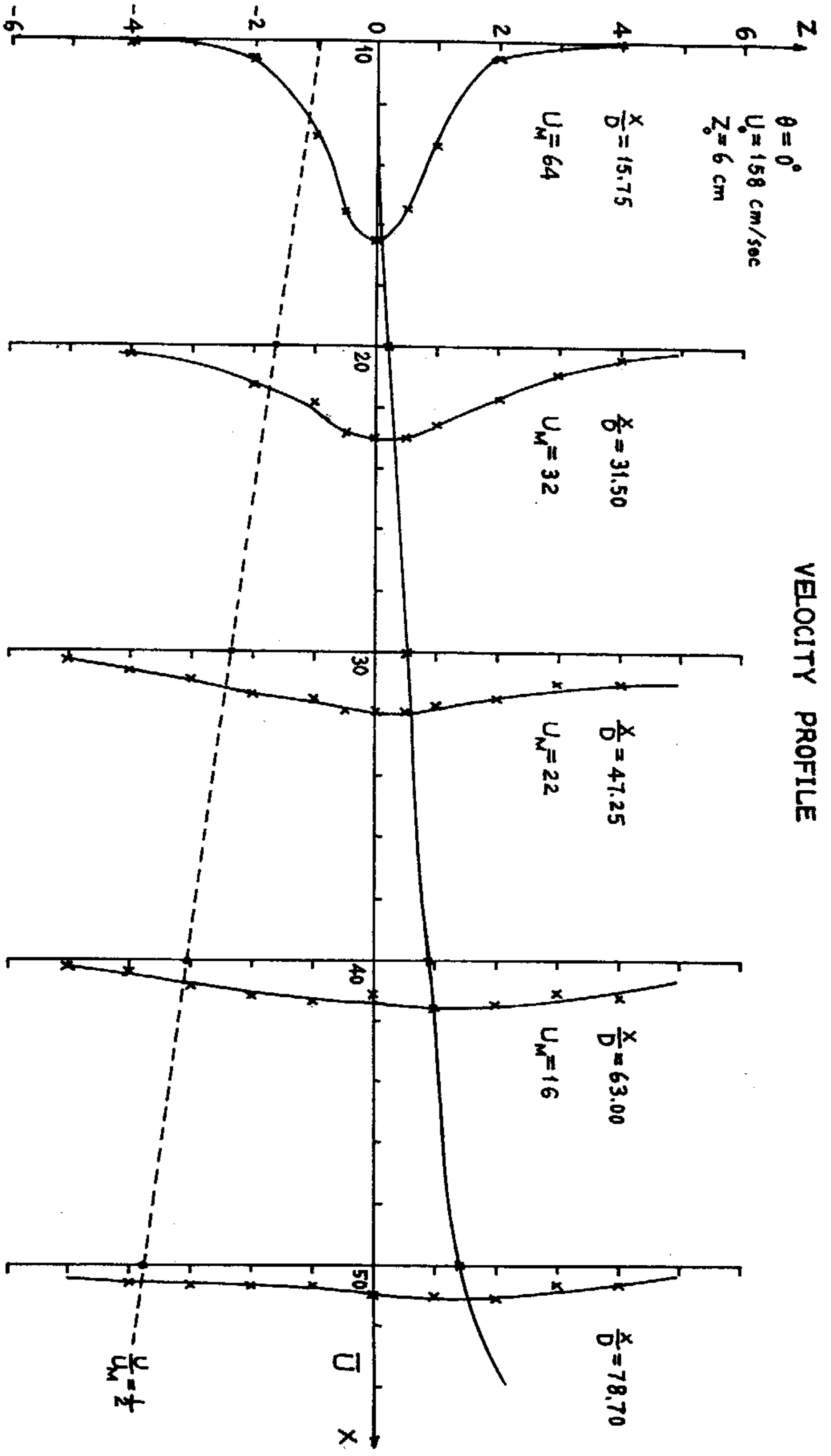

Nozzle diameter D= 0.635 cm

Figure 1 Velocity Profiles

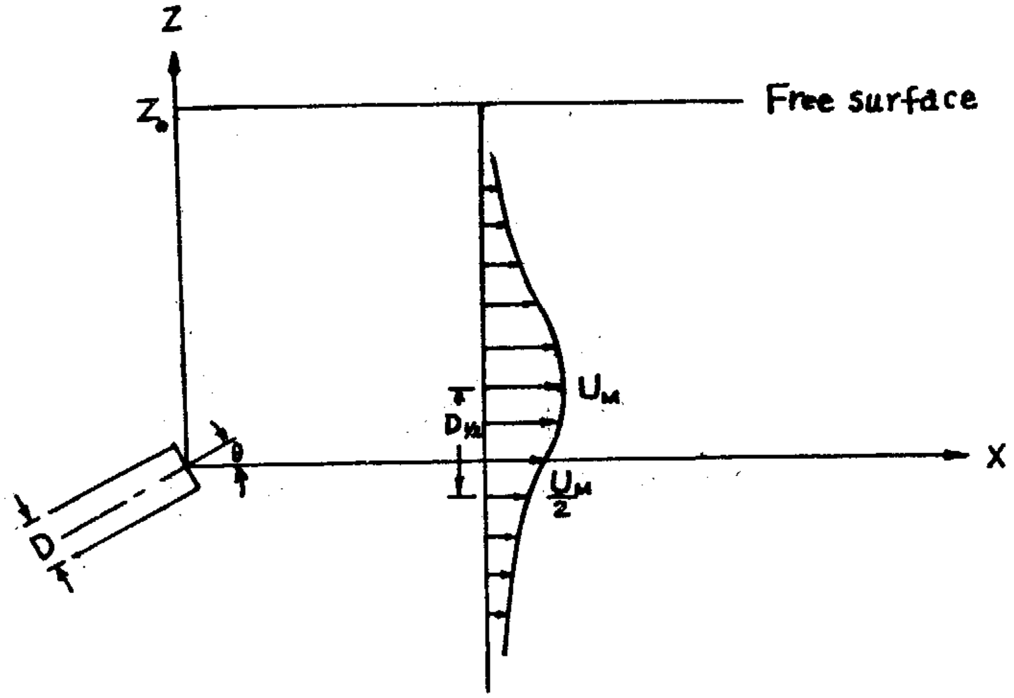

Figure 2. Test Condition

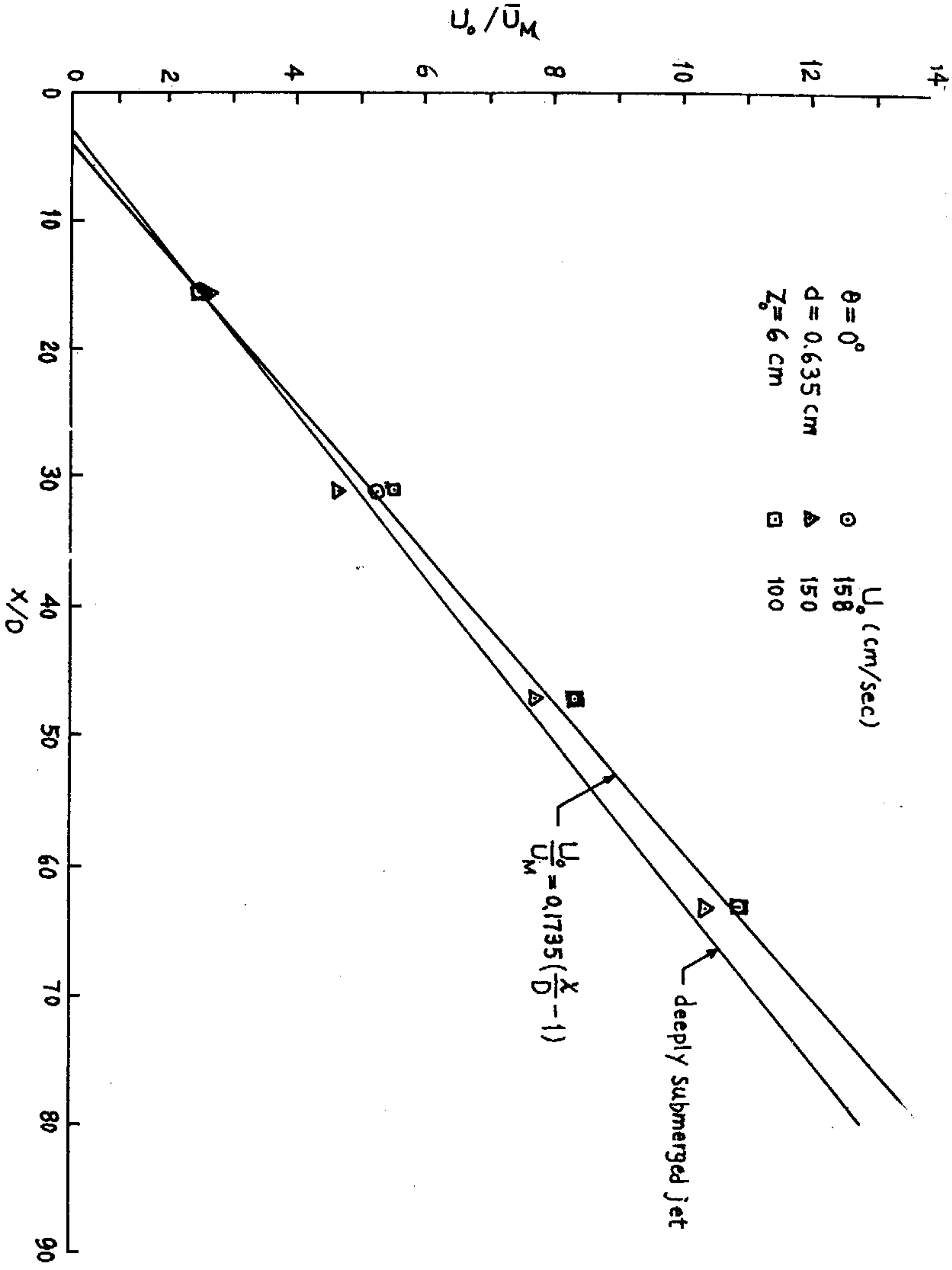

Figure 3 Maximum Velocity Variation

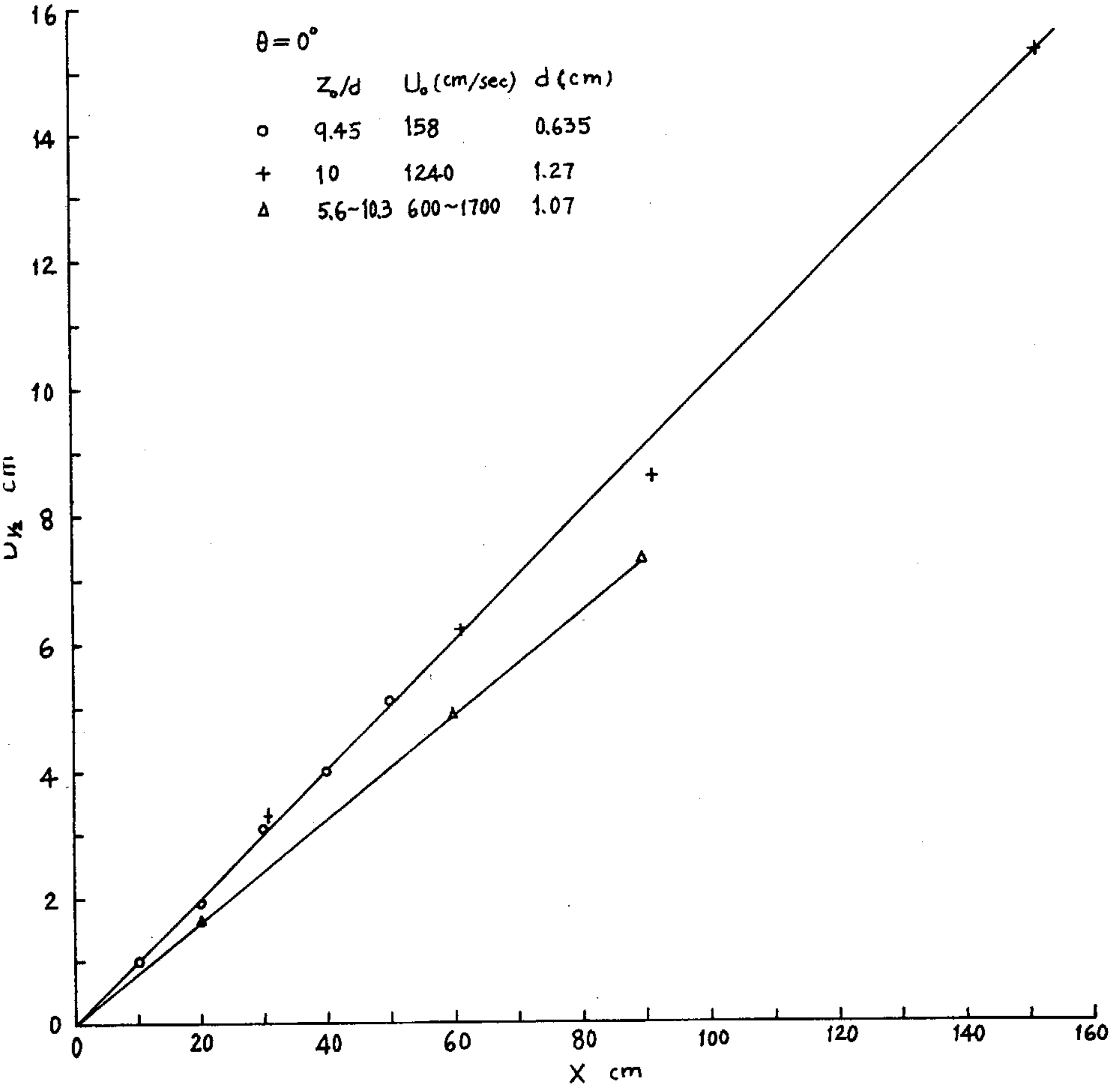

Figure 4. Half Width Variation

經網格擾動二平行水流經隔板之試驗探討

陳芳正　汪群從 *(Chun–Tsung Wang)*　魏濟邦

Ⅰ 簡介

在氣體流動方面，因熱線流速儀 (Hot-wire Anemometer) 之應用，廣泛的增加了實測資料的獲得及對紊流之了解。在水流方面，由於熱膜流速儀 (Hot-film Anemometer) 在試驗技術方面仍有若干問題存在（5，8，9），故在水流之研究方面，進展較爲緩慢。

李察遜和麥昆夫（9，10）及賴希蘭（6）應用絲型探針探討，渠流中不同深度(relative turbulent intensity)、巨尺度 (Macroscale)、微尺度 (Microscale) 及能量譜 (Energy Spectrum) 之特性。

本文利用拋物線型探針進行，經過隔板二平行水流沿水流方向之各種紊流特性之試驗探討。

Ⅱ 實驗裝置

實驗水槽爲 1 公分厚透明壓克力板所做成之水平槽，長600 公分，寬 60 公分，高 30 公分。在距水槽入口100 公分處，架設網格，槽寬之中央以 0·3 公分厚、80 公分長、25 公分高之透明壓克力板分隔水流，隔板兩側之網格，分別以鐵絲網及壓克力棒爲之，其裝置如圖 1 所示，試驗流況如表一所示。

Ⅲ 實驗結果及分析

本試驗取水面下 5 公分 (Z = +5cm) 之水平截面爲實驗面。各流之探測沿其中心線，以避免側邊界面之影響。測點測線之表示座標，如圖 1 所示。

1　紊度變化

圖 2-1 顯示沿各分流中心線之相對紊度 $(\frac{u'}{\bar{U}})$ 減衰變化。u′爲波動速度 (root-mean-square of the velocity fluctuation in x-direction), $\bar{U}$ 爲 x 方向當地平均速度，圖中顯示離網格愈遠，相對紊度越小。在流速變化不大時 (22cm/sec .VS. 29.6cm/sec) 鐵絲網後方紊度減衰情形類同。圖 3 顯示匯流後，各網側分流因受另一柵分流紊度之影響，減衰情形稍有不同，匯合之柵側分流紊度較大時，因傳遞之動量較多，減衰較慢。

關於網格紊度減衰，可區分爲初始段，轉變段及終了段。在初始段，減衰情形主要受慣性因素影響，即流本身動力傳遞。其後粘性阻滯效應逐漸顯著，到了終了段時，減衰完全受粘性因素作用。本試驗中初始段與終了段間之轉變段約在 x/M 爲15 與 20 之間。圖 2 - 2 顯示在初始段紊度之減衰是 $(\frac{\bar{U}}{u})^2 \sim x/M$ 之線性關係，在終了段，紊度之減衰是 $(\frac{\bar{U}^2}{u^2})^{2/5}$ 之關係，其詳細關係如表二所示。

本試驗所得水中網格產生紊度之減衰情形與風洞實驗結果相似。（2，3，11，12，13），但二者間轉變段之分界值不同（空氣中約爲 $x/M = 200 \sim 600$ ）。

2　板後匯流之紊度及流速分佈

網側分流和槽側分流在隔板後方，即 x = 70 cm 處匯合，因兩流紊度、流速不同，所造成的紊度流速分佈並不對稱，不同於均勻流場中之對稱尾流 (1)。圖 4 顯示在實驗 I 情況下，兩側分流之流速近乎相等，所以匯流後，流速對紊度沒有顯著之影響，其紊度分佈曲綫隨流行距離減衰而漸趨平滑，中央之紊度尖峰消失。其尾流區紊度亦無顯著之擴散，＋y 方向由 2cm 增大到 5cm ，－y 方向維持在 5cm 左右。

圖 5 顯示在實驗 II情況下，兩側分流之流速相差一倍，除尾流所產生之紊度外，更加上不同流速流體間動量傳遞所造成之紊度。這所增加之紊度使紊度分佈曲綫之中央尖峰雖有減衰但歷久不減。流速差也增大尾流區紊度之擴散，＋y 方向由2cm增加到8cm，－y 方向由 3.5cm增加到 8cm 。

3　能量譜分析

使用訊號調節器 (Signal conditioner) 可測出紊流能量對頻率之分佈區綫 (7)。因訊號調節器在低頻率時不甚準確，故在若干測點同時實測瞬時流速變化，計算能量譜。

能量譜 F(n) 爲 (3)

$$F(n) = \frac{W(n)}{(u')^2} \qquad \cdots\cdots (1)$$

試中 n 爲頻率，W(n) 爲能量譜函數

並且 $$\int_0^\infty F(n)\,dn = 1 \qquad \cdots\cdots (2)$$

自相關函數 R(τ) (Auto-correlation) 爲

$$R(\tau) = \frac{\overline{u(t)u(t-\tau)}}{(u')^2} \qquad \cdots\cdots (3)$$

試中 t 爲時間，τ 爲遲滯時間

能量譜函數 F(n) 與自相關函數 R(τ) 可經由傅利葉餘弦轉變相互推求，

$$R(\tau) = \int_0^\infty F(n)\cos 2\pi n\tau\,dn \qquad \cdots\cdots (4)$$

$$F(n) = 4\int_0^\infty R(\tau)\cos 2\pi n\tau\,d\tau \qquad \cdots\cdots (5)$$

由 $R(\tau)$ 積分後乘以平均流連 U 可求出 x 方向巨尺度 L_x (Macroscale)

$$L_x = U\int_0^\infty R(\tau)\,d\tau \qquad \cdots\cdots (6)$$

另由能量譜積分可求出 x 方向微尺度 λ_x (Microscale)

$$\frac{1}{\lambda_x^2} = \frac{4\pi^2}{U^2}\int_0^\infty n^2 F(n)\,dn \qquad \cdots\cdots (7)$$

圖 6 顯示三組能量譜分佈曲綫以爲代表，可看出訊號調節器與記錄器所得之曲綫相當吻合。同時顯示水流中紊度能量分佈主要在 $n \doteq 100$ 以下。

圖 7 顯示微尺度和巨尺度大致上沿水流而增大。不過其變化情形略不同於空氣中情況（圖 8 ）(2)。

Ⅳ 結論

本實驗所得結果顯示：

1. 水中網格後方紊度之減衰，在初始段爲 $\left(\frac{U}{\overline{u'}}\right)^{2} \sim x/M$ ；在終了段時 $\left(\frac{\overline{U}^{2}}{u'^{2}}\right)^{2/5} \sim x/M$。其間轉變段之分界值約在 $x/M = 15 \sim 20$。
2. 分流之速度差影嚮板後匯流之紊度分佈。速度差大時，不但延緩尖峰之減衰且增大尾流之擴散。
3. 微尺度和巨尺度沿流之增大趨勢爲 $\lambda_x^2 \sim x/M$ ，$L_x^2 \sim x/M$。

本試驗所得水中紊流情形與空氣中者不完全相同，初步結果亦未能由粘滯度之關係去解釋其不同現象，似宜進一步加以研討。

表一　實驗水力資料表

總流量 = 20800 cm^3/Sec，　坡度 = 0，　水溫 = 68°± 3°F

編號		網格距 M，cm	寬度 b，cm	水深 d，cm	水力半徑 r，cm	平均流速 $\bar{u}$，cm/Sec	弗勞德數 $N_F = \frac{\bar{u}}{\sqrt{gd}}$	雷諾數 $N_R = \frac{4r\bar{u}}{\upsilon}$
I	鐵絲網	0.312	0.09	16	7.73	22.0	0.176	69,600
	壓克力格柵	5.00	1.0	16	7.73	21.5	0.172	68,600
II	鐵絲網	0.312	0.09	16	7.73	29.6	0.236	93,600
	壓克力格柵	2.50	1.0	16	7.73	13.8	0.110	43,600

表二　紊度減衰式表

	實驗 I		實驗 II	
	網側分流	柵側分流	網側分流	柵側分流
初始段 x/M < 15	$(\frac{\bar{U}}{u'})^2 \sim 1.15(\frac{x}{M})$	$(\frac{\bar{U}}{u'})^2 \sim 1.18(\frac{x}{M})$	$(\frac{\bar{U}}{u'})^2 \sim 1.15(\frac{x}{M})$	$(\frac{\bar{U}}{u'})^2 \sim 0.4(\frac{x}{M})$
終了段 x/M > 20	$(\frac{\bar{U}}{u'^2})^{2/5} \sim 0.11(\frac{x}{M})$	$(\frac{\bar{U}^2}{u'^2})^{2/5} \sim 0.11(\frac{x}{M})$	$(\frac{\bar{U}^2}{u'^2})^{2/5} \sim 0.11(\frac{x}{M})$	$(\frac{\bar{U}^2}{u'^2})^{2/5} \sim 0.11(\frac{x}{M})$

參 考 文 獻

1. Chevay, R. and Kovasznay, L. S. G: "Turbulence Measurements in the Wake of a thin Flat Plate", AIAA Journal, Vol. 7, No. 8, August, 1969, pp. 1641-1.
2. Naudascher E. and C. Farell: "Unified Analysis of Grid Turbulence" Journal of Engineering Mechanics Division, ASCE, Vol. 96, No. EM2, proc.paper 7214, April, 1970, pp. 121-141.
3. Hinze, J. O.: Turbulence, An Introduction to Its Mechanism and Theory; McGrew-Hill Book Co., Inc., New York, 1959.
4. "Hot-Film and Hot-Wire Anemometry, Theory and Application".—Bulletin TB5, Thermo-System Inc.
5. Kanevcé, G. and S. Oka: "Correcting Hot- Wire Readings for Influence of Flui Temperature Variation" DISA Information, No. 15, October, 1973, pp. 21-24.
6. Raichlen, F.: "Some Turbulence Masurement in Water", Journal of Engineering Mechanies Division, ASCE, Vol. 93, No. EM2, proc. paper 5195, April, 1967, pp. 73-97.
7. Rasmussen, C. G.: "Measurement of Turbulence Characteristics", DISA Information, No. 3, Jonuasy, 1966, pp. 9-20.
8. Rassmussen, C. G. "The Air Bubble Problem in Water Flow Hot-Film Anemometry DISA Information, No. 5, June, 1967, pp. 21-26.
9. Richardson, E. V. and R. S. McQuivey: "Measurement of Turbulence in Water Journal of Hydraulic Division, ASCE, Vol. 94, No. HY2, Proc. Paper 5855, March. 1968, pp. 411-430.
10. Richardson, E. V. and R. S. McQuivey: "Some Turbulence Measurements in Open-Channel Flow", Journol of Hydraulic Division, ASCE, Vol. 95, No. HYI, Proc. Paper 6349, Jenuary, 1969, pp. 209-223.
11. Deissler R. C.: "On the Decay of Homogeneous Turbulence before the Final Period", The Physics of Fluids, Vol. 1, No. 2, March-April, 1958, pp. 111-121.
12. Deissler, R. C.: "Decay of Homogeneous Turbulence from a given Initial State", The Physics of Fluids, Vol. 14, No. 8, August, 1971, pp. 1629-1638.
13. Robertsen, J. M.: "A Turbulence Primer", Engineering Experiment Station Circular No. 79, University of Illinois Bulletin.

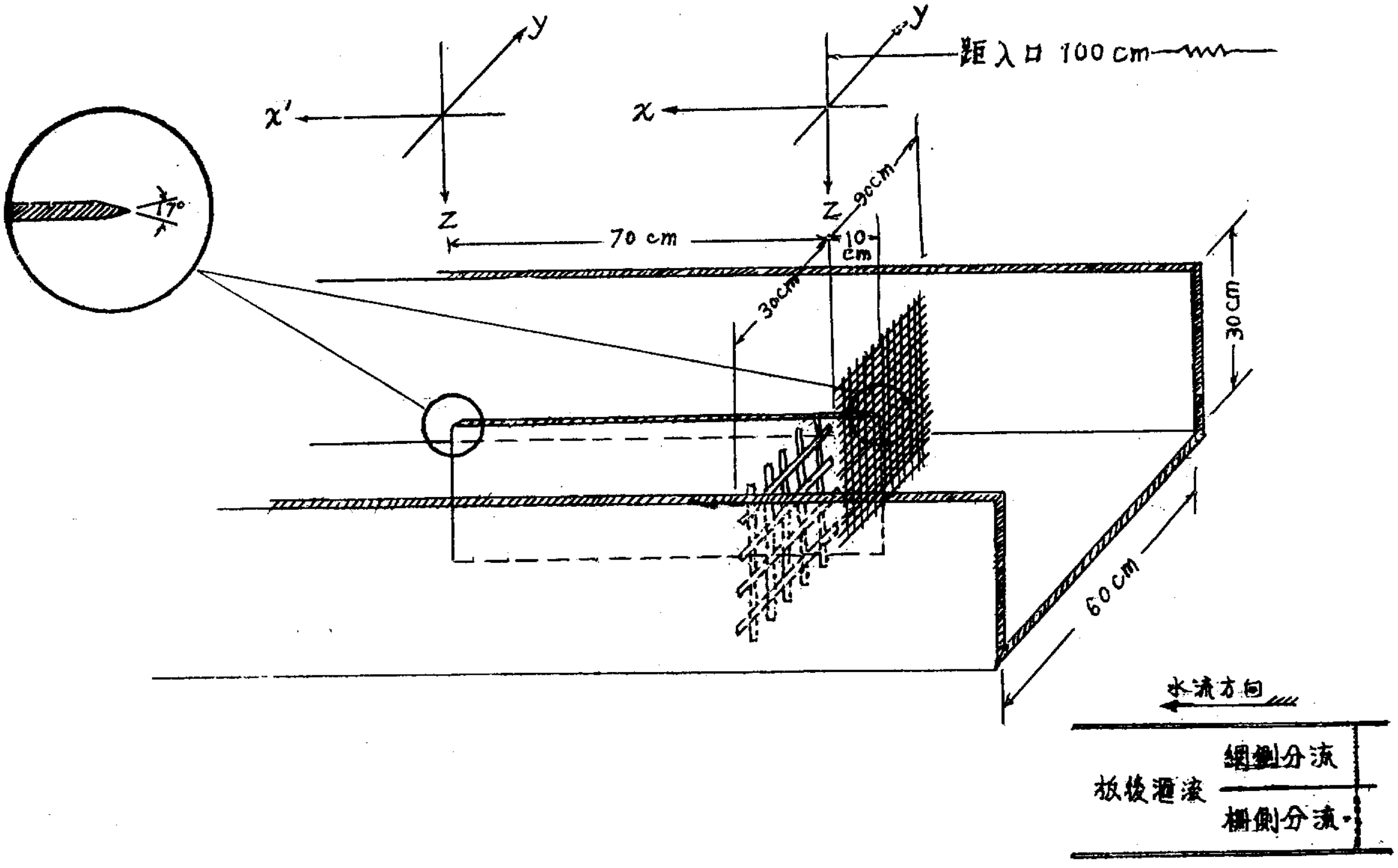
y
y
距入口 100 cm
x'
x
Z
Z
7°
70 cm
90cm
10 cm
30cm
30cm
60cm
水流方向
網側分流
板後迴漩
柵側分流

圖一：實驗裝置圖

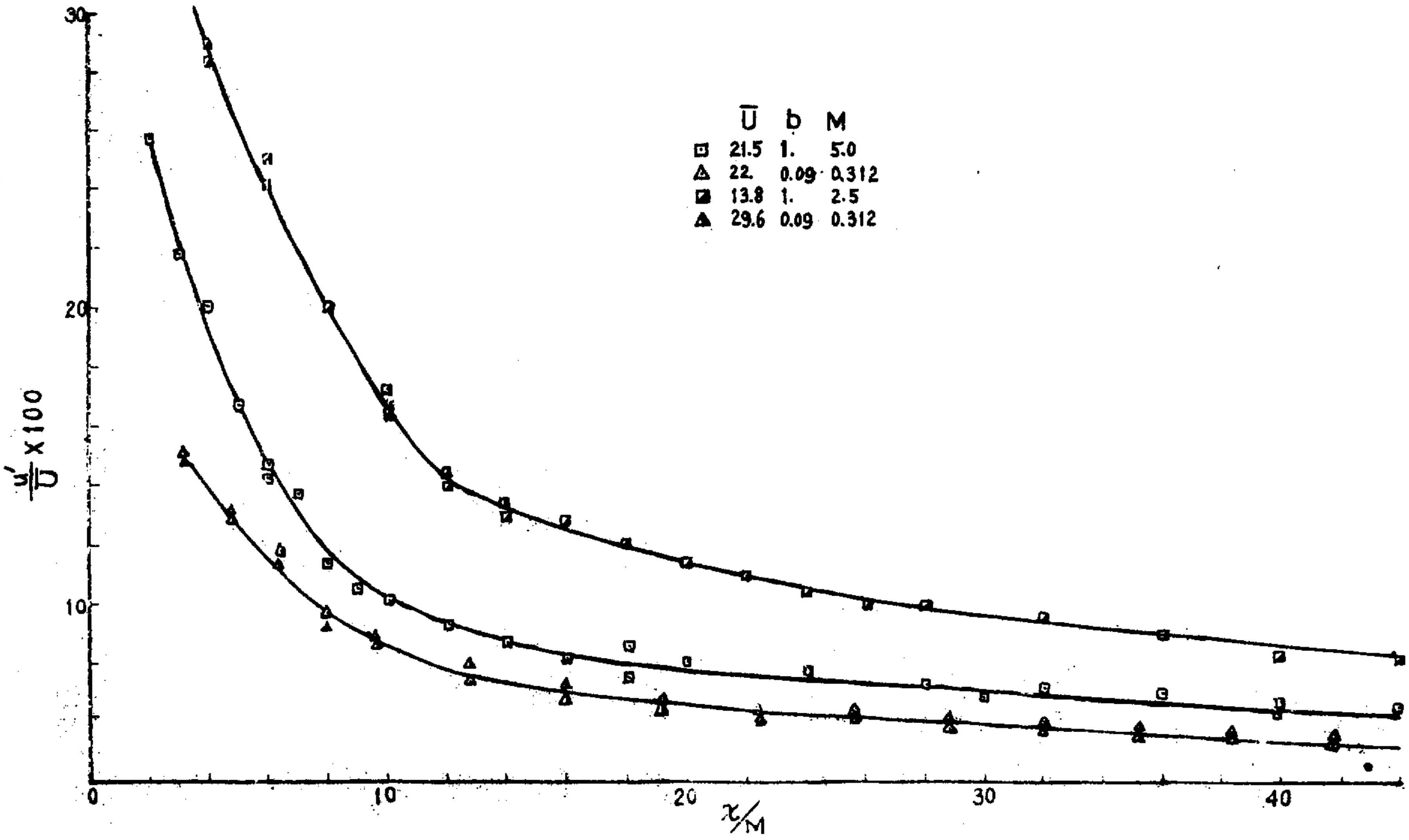

圖 2 - 1 各分流中心線沿流紊度減衰變化

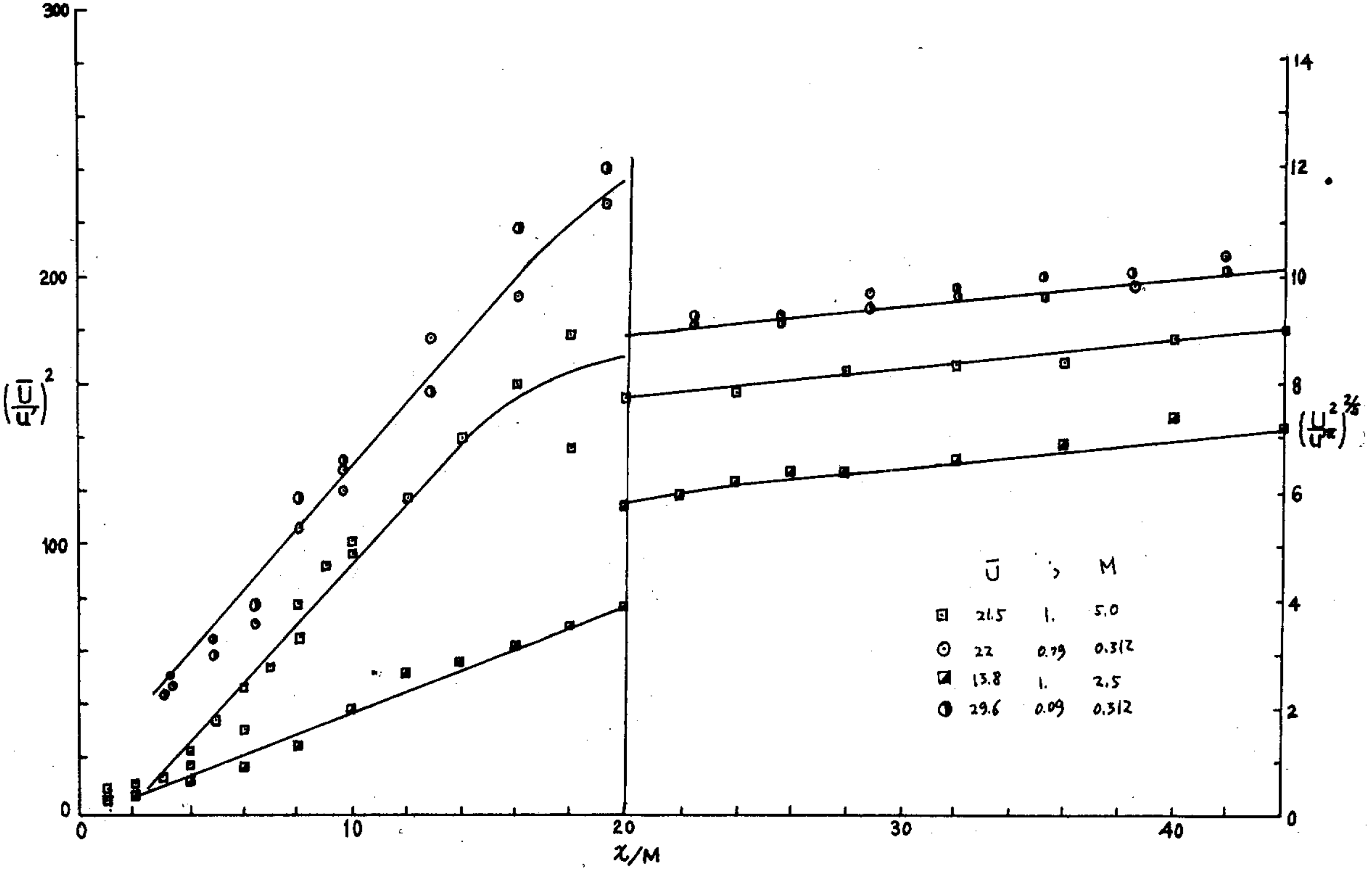

圖 2-2 初始段.終了段紊度變化

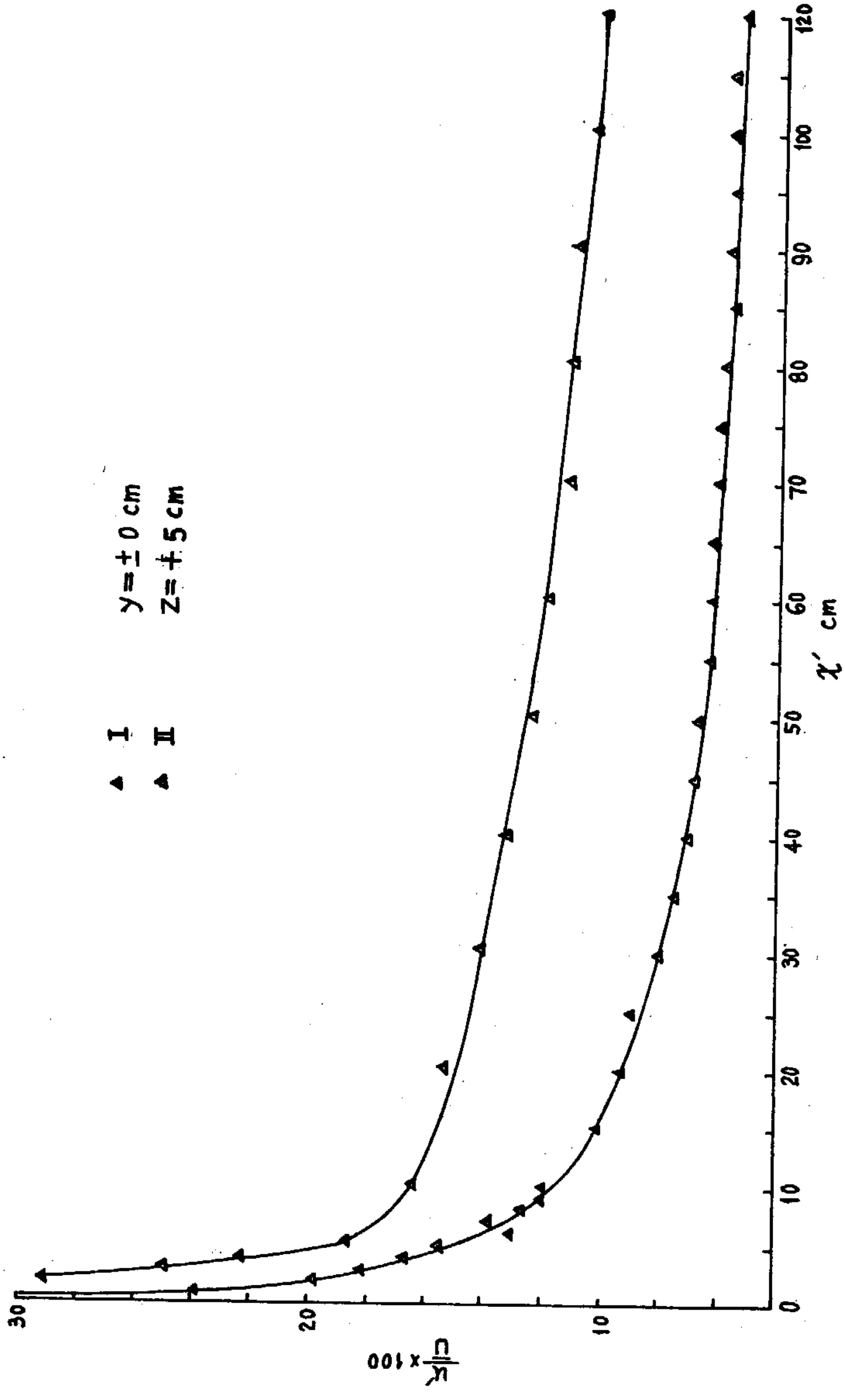

圖 3 板後迴流中心線紊度之減衰变化

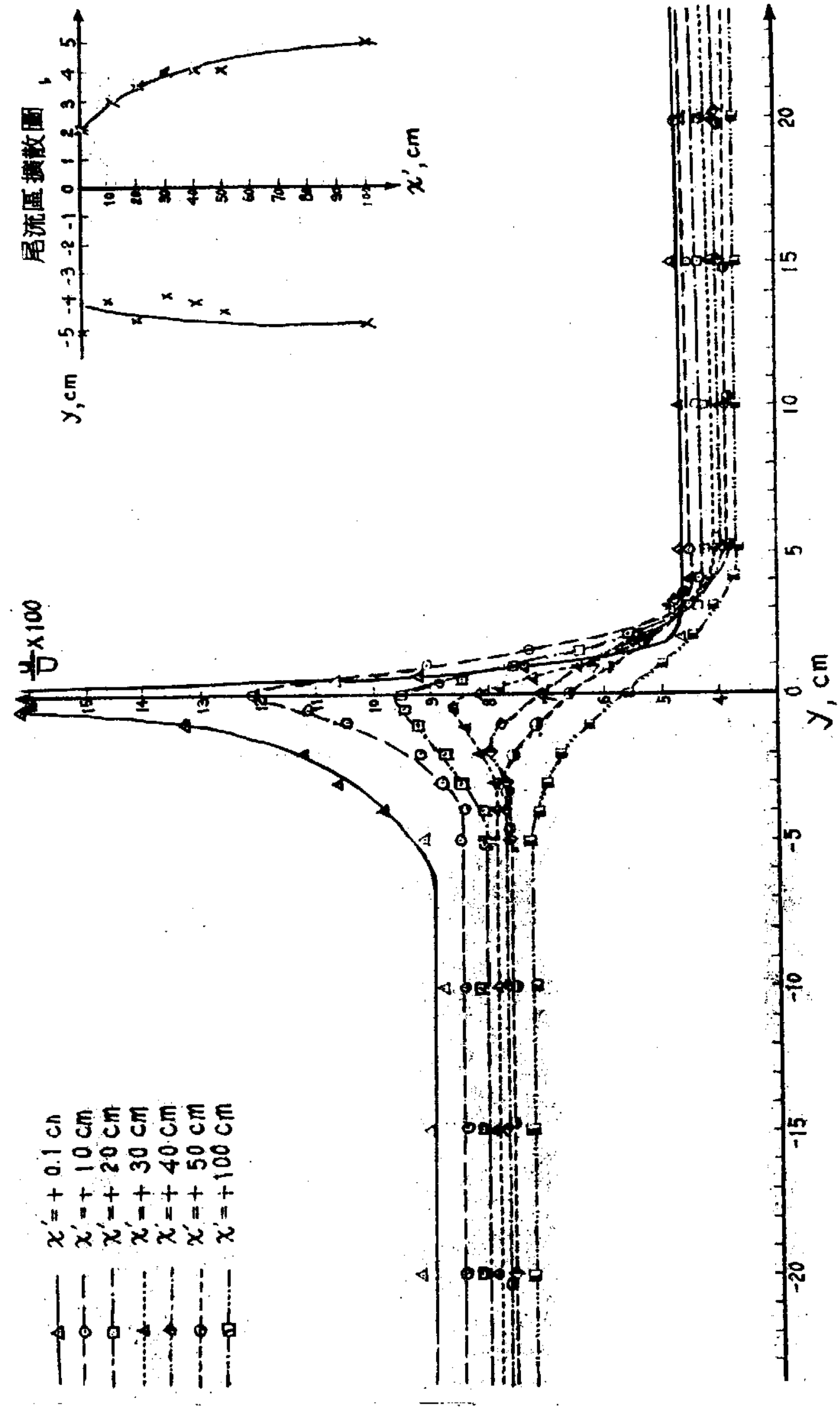

圖 4-1 實驗 I 板後匯流紊度分佈圖

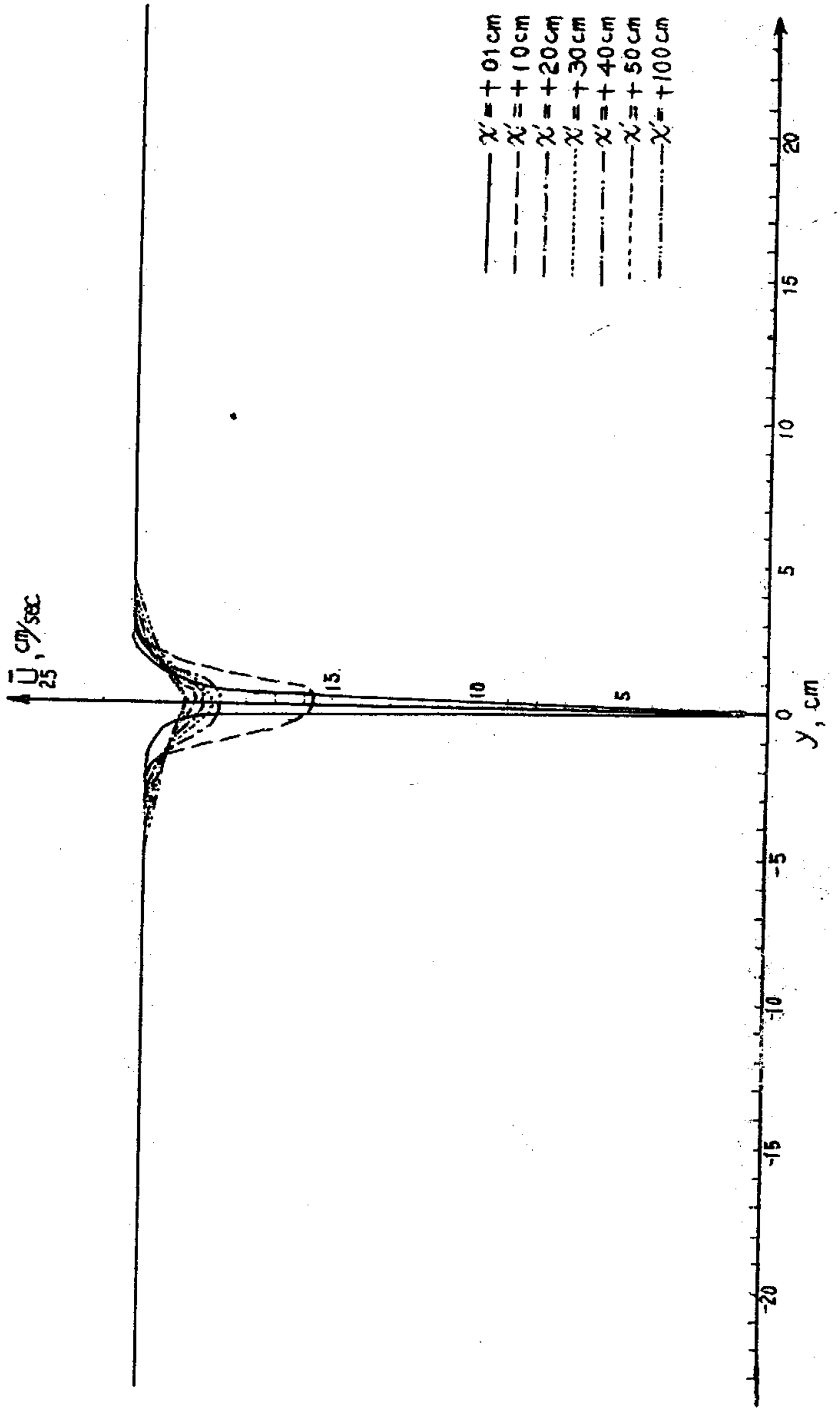

圖 4-2 實驗 1 板後匯流平均流速分佈圖

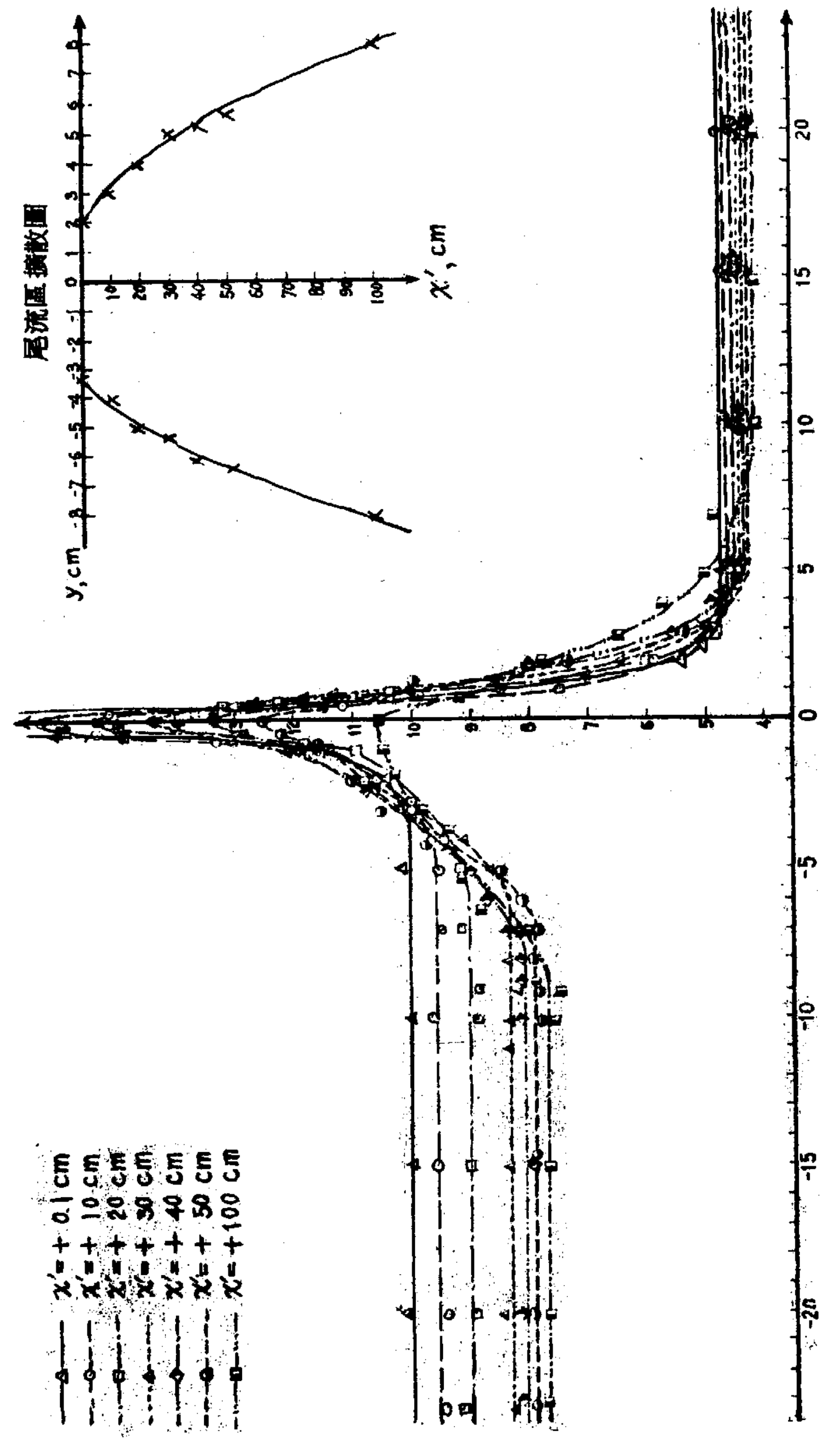

圖5-1 實驗II 板後匯流紊度分佈圖

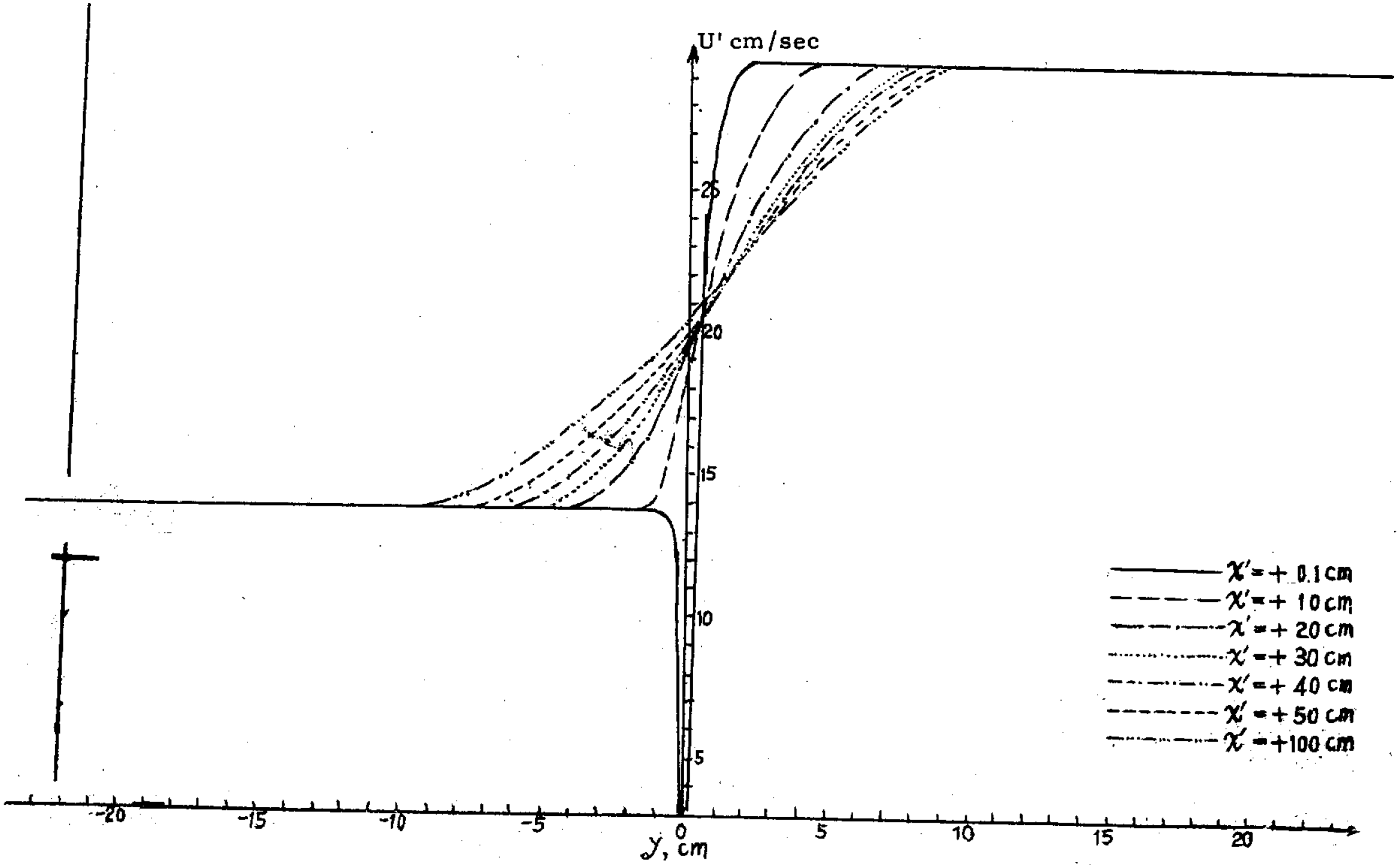

圖 5 - 2 實驗 11 板後匯流平均流速分佈圖

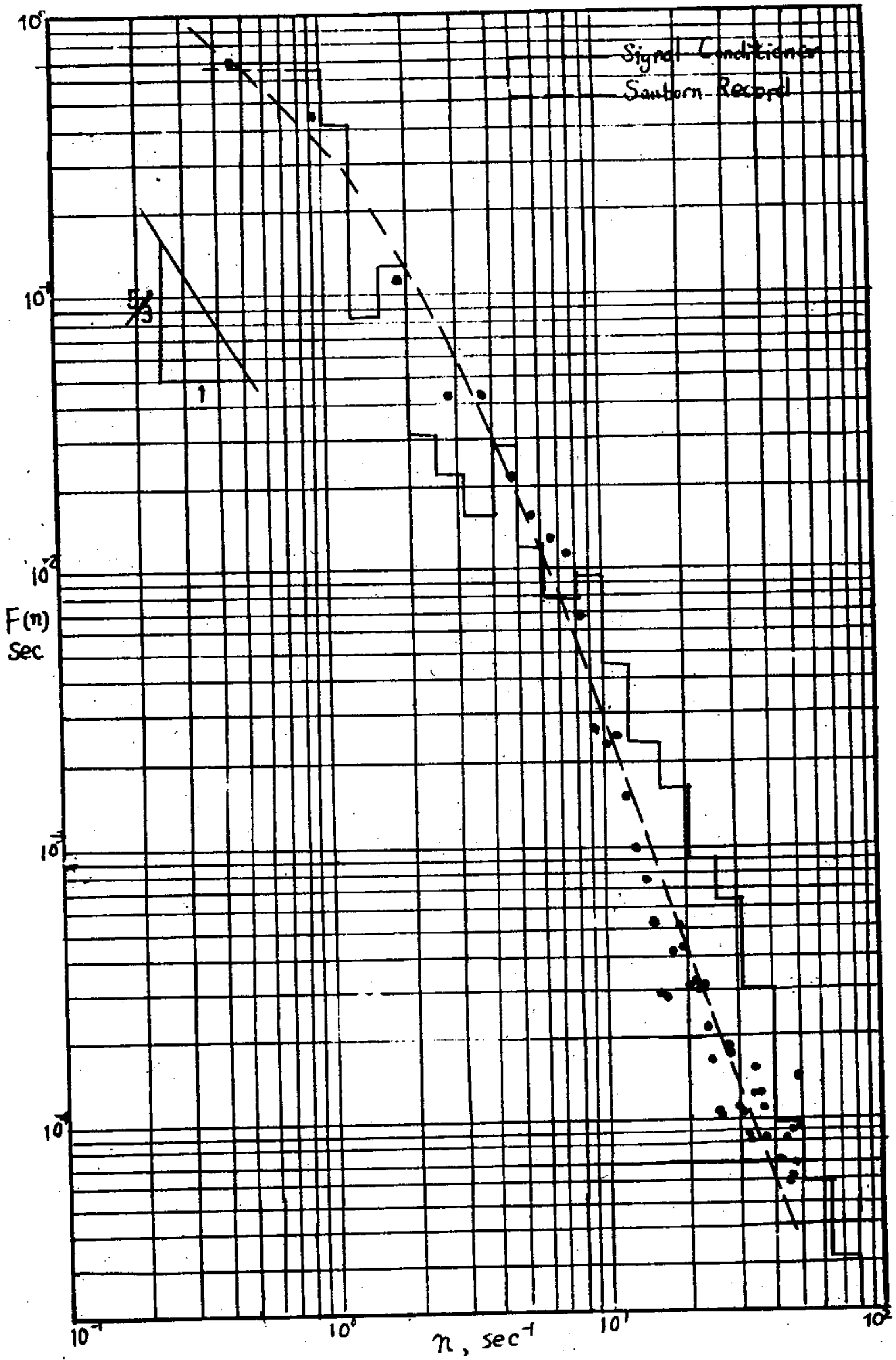

圖 6-1 能量譜 Ⅱ $x=+90$ cm $y=-15$ cm

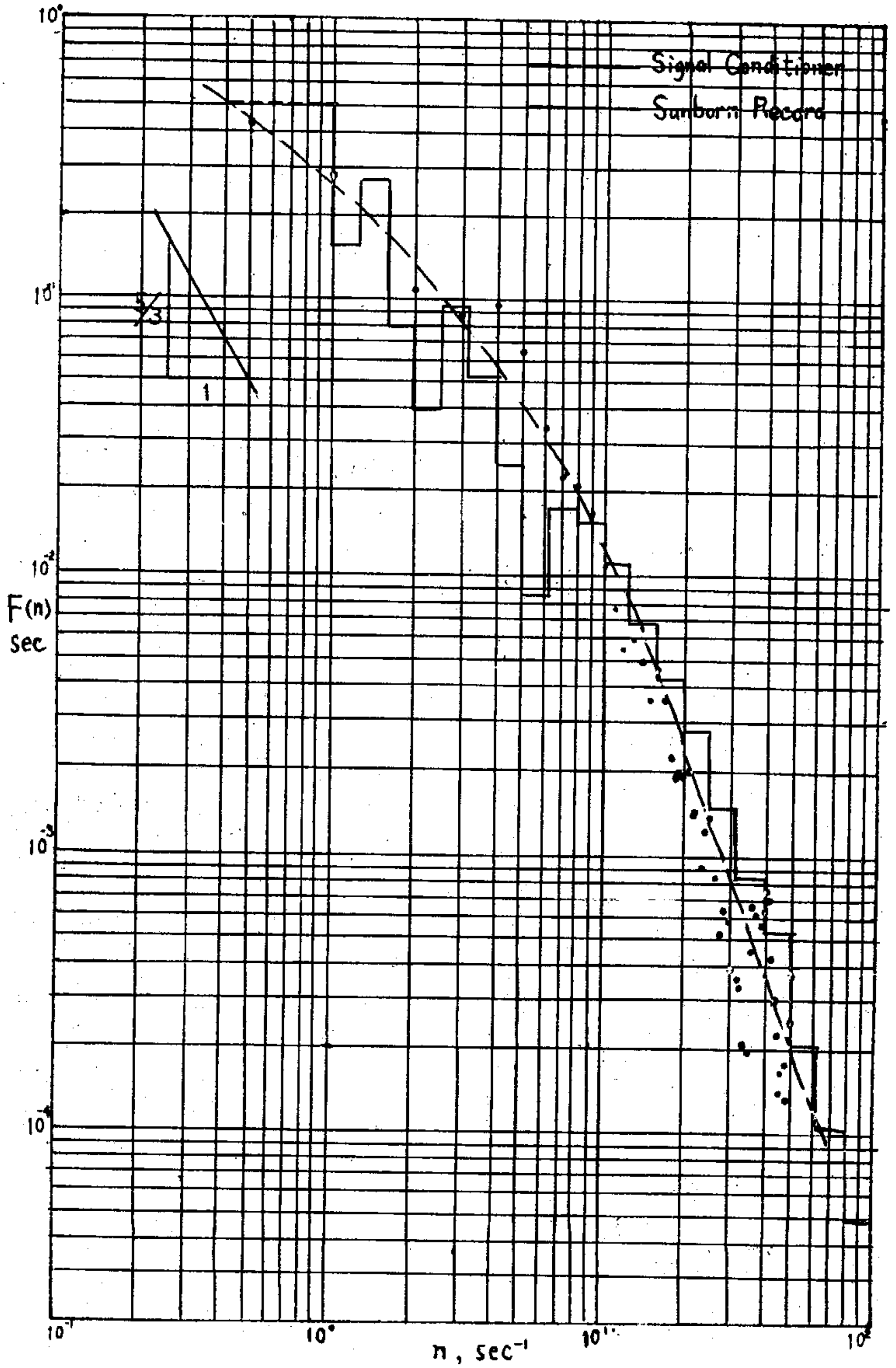

圖 6 - 2 能量譜　　Ⅱ　$\chi = +90$ cm　$y = +15$ cm

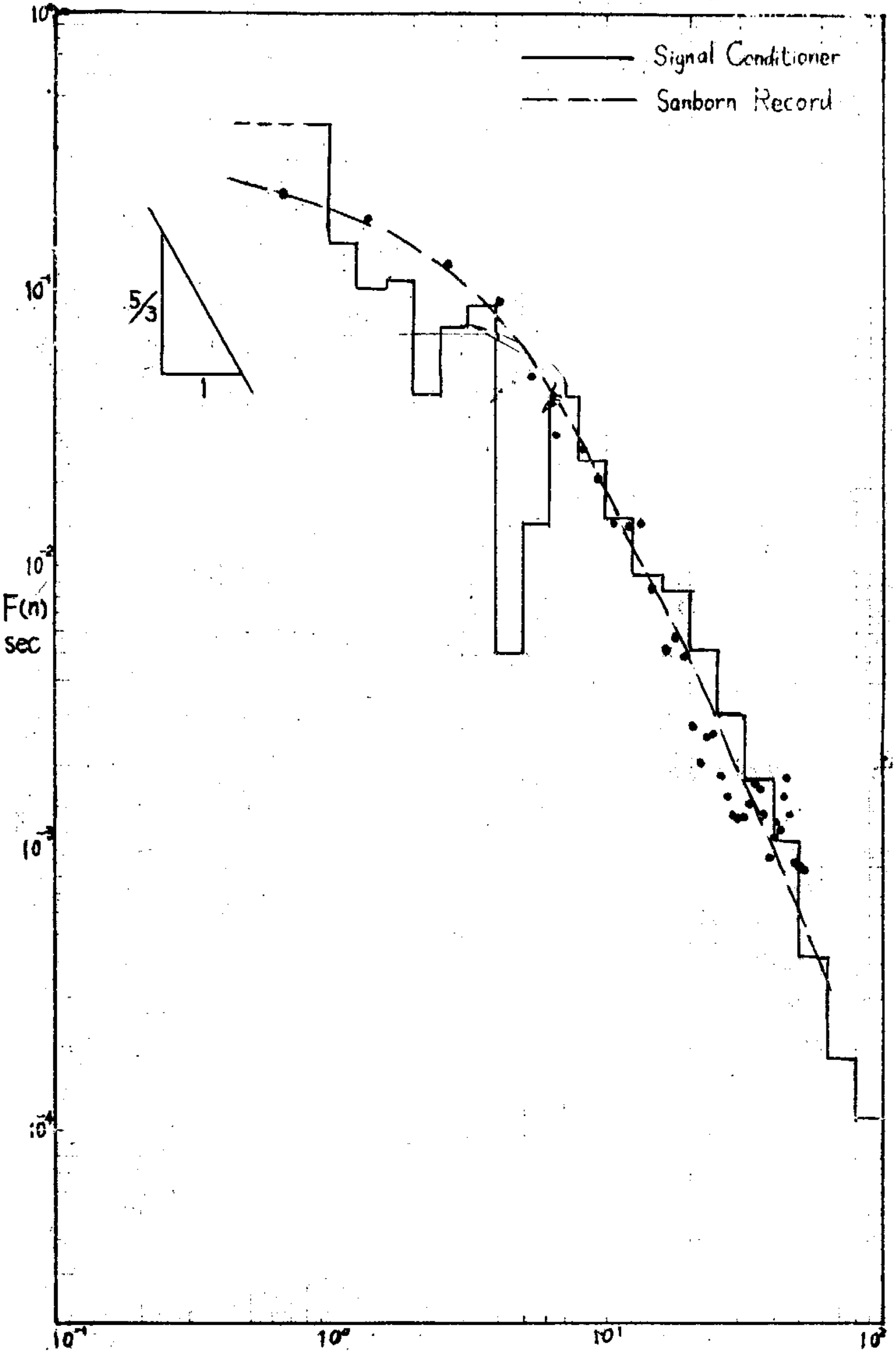

圖 6-3 能量譜　　Ⅱ　$x'=+10$ cm　$y=\pm 0$ cm

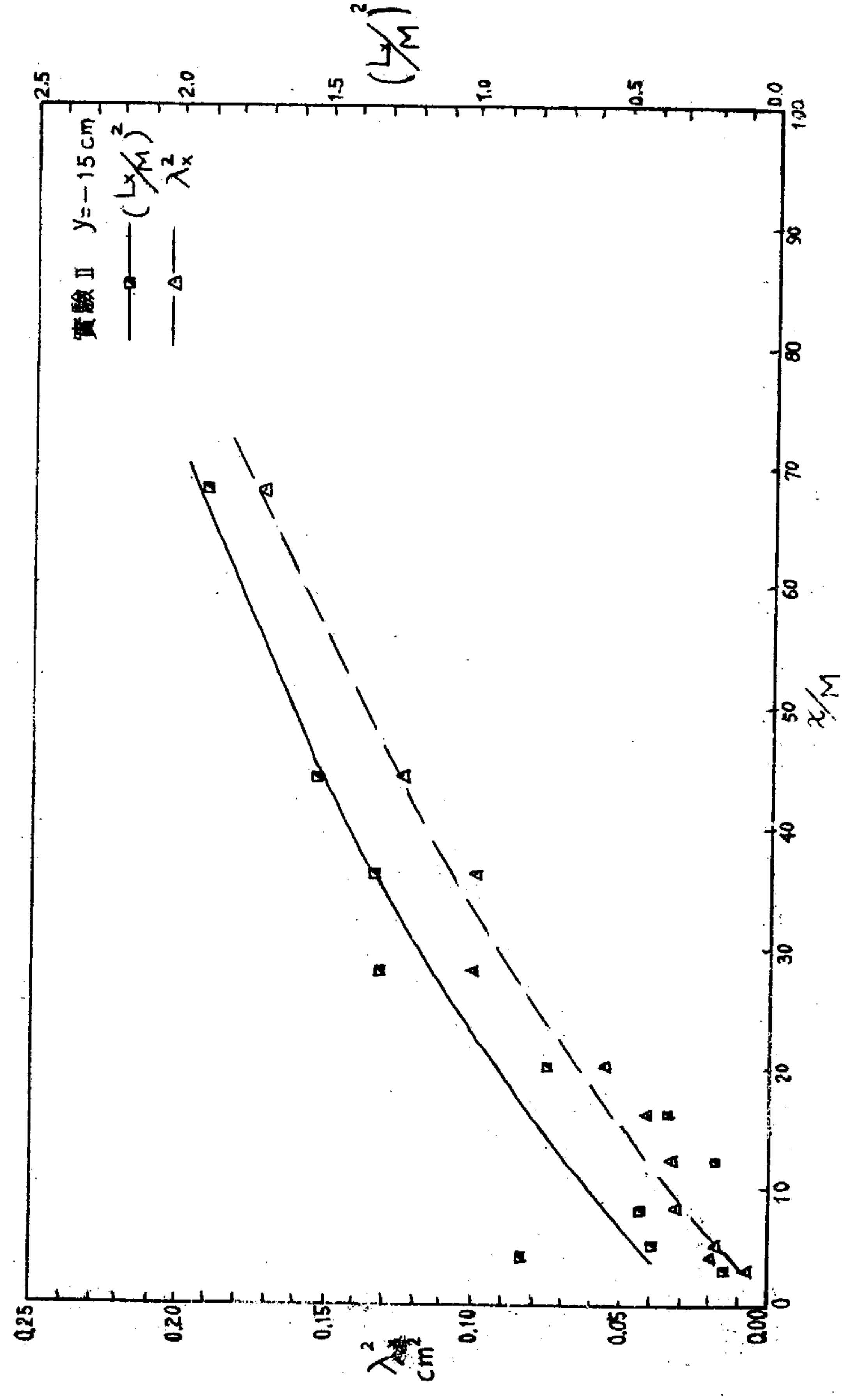

圖7-1 橫側分流巨尺度及微尺度沿流之變化

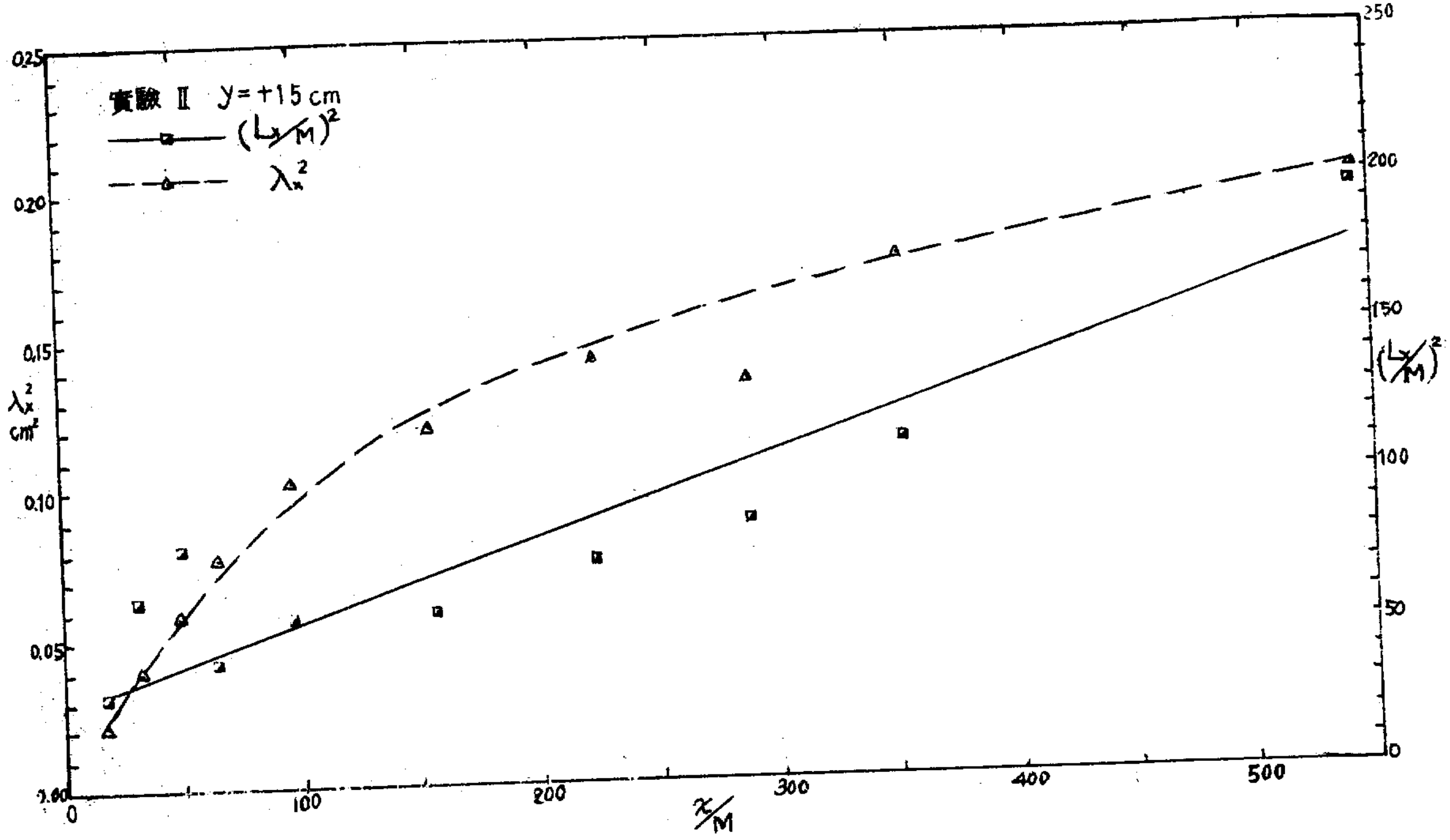

圖 7-2 網側分流巨尺度及微尺度沿流之變化

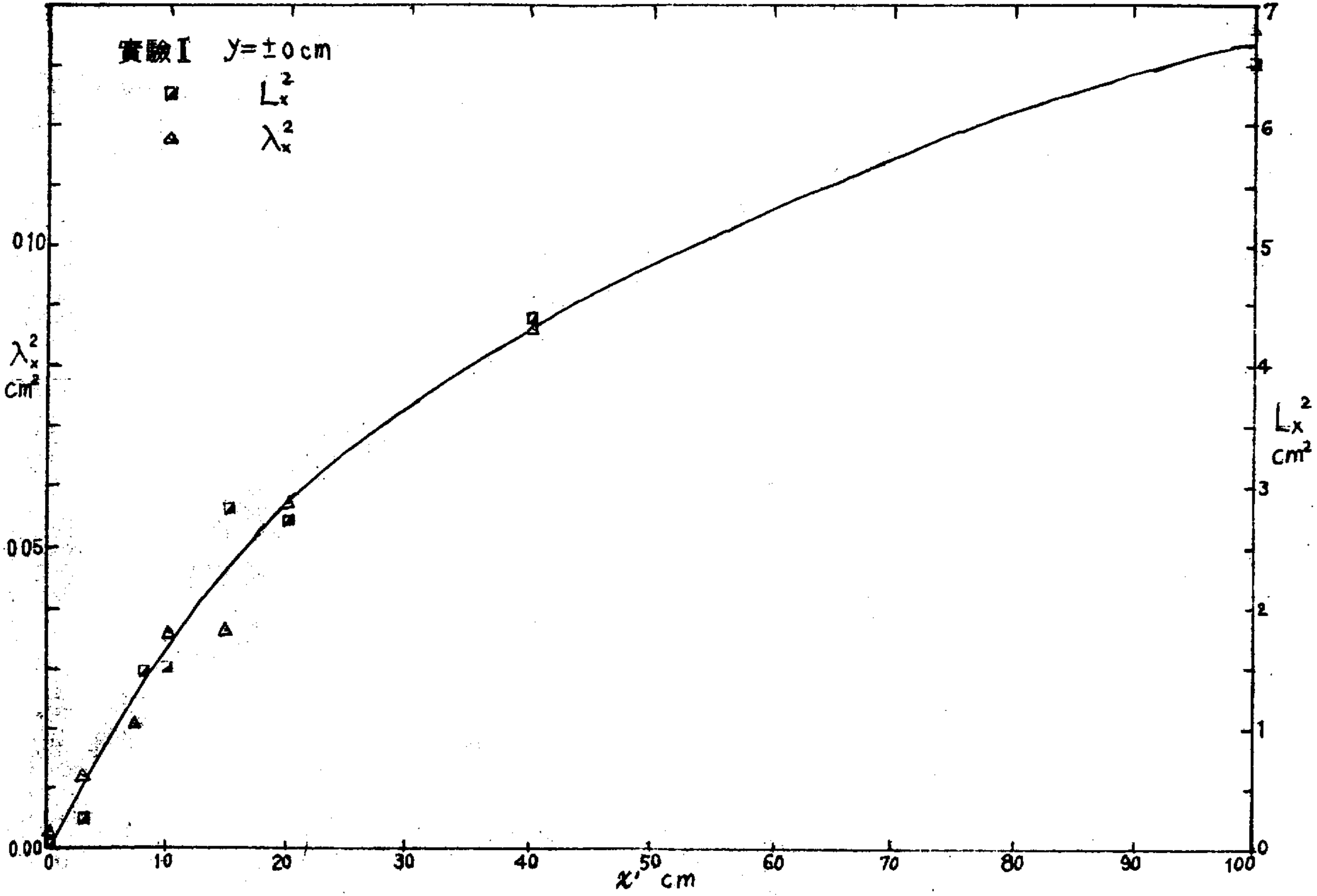

圖 7 - 3 板後漩流巨尺度及微尺度沿流之變化

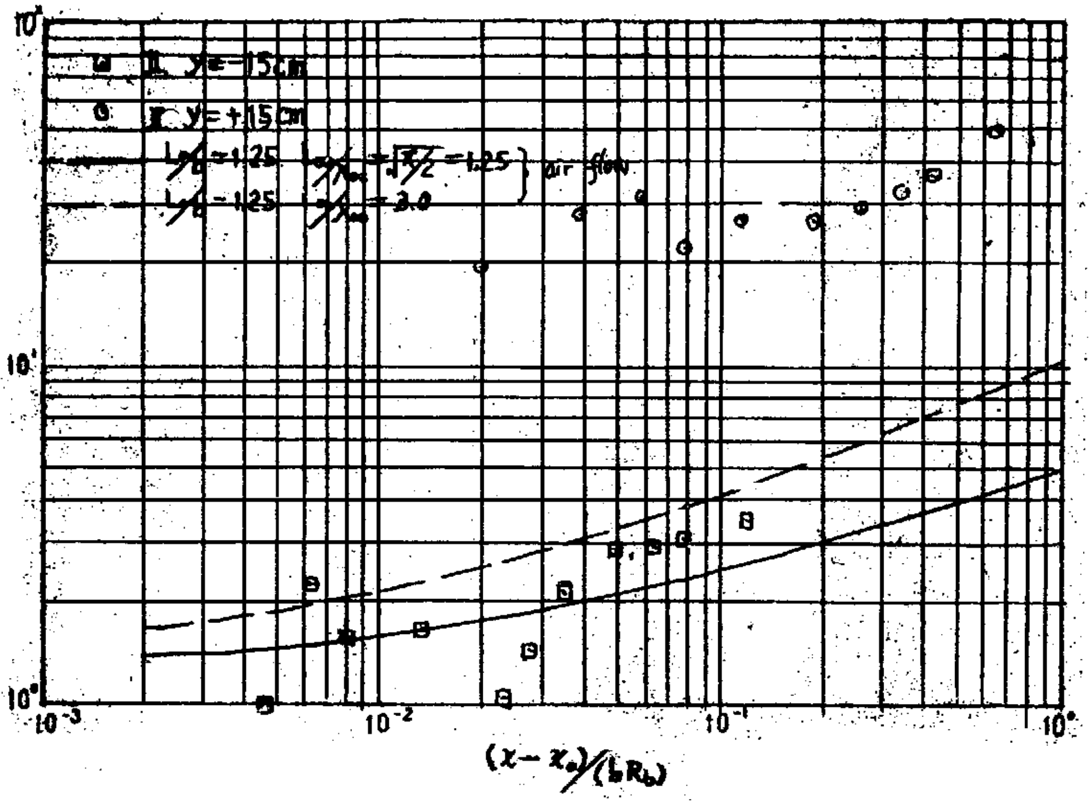

圖 8　空氣與水中紊度變化比較

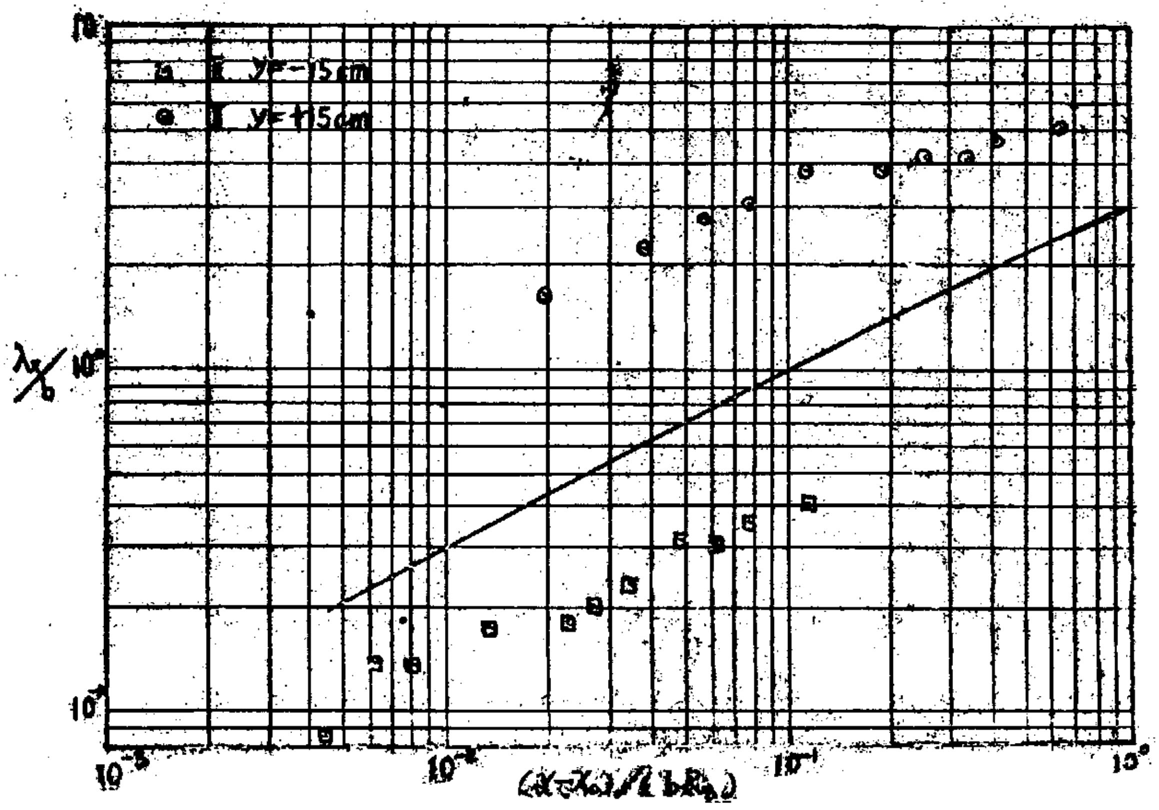

矩形槽中矩形物體尺寸影響之初步探討

張月珠　汪群從 *(Chun–Tsung Wang)*

I 簡介

在實驗室利用水槽進行試驗探討工作時，常需要避免水槽槽壁對被試驗物體之影響，嚴格的說，祇有水槽趨近於無限大時，才沒有槽壁影響。可是在實驗室中設置的水槽皆有一定大小，爲了了解試驗物體所受槽壁影響，本文擬藉實驗方法初步探討矩形槽中矩形物體受槽壁之影響。

II 實驗裝置

本試驗係在60 公分寬、30 公分高之水平矩形槽中進行，試驗流量 20,800 立方公分／秒，水深 15 公分。試驗用矩形物長 10 公分，高 16 公分，寬度 (W)爲 1 公分、5 公分、10 公分、30 公分和 60 公分五種。

試驗時，逐漸減少矩形物與槽底之淨矩（Z），量度矩形物中心正下方之槽底壓力變化（△hr：即有矩形物及無矩形物之壓力差），及矩形物中心正下方接近槽底之速度分佈情形。前者係藉靜壓力管 (piozometric opening) 量度，後者係藉熱片流速計 (hot-film anemometer system) 量度。

III 實驗結果及分析

不同寬度之矩形物體在不同浸水深度時槽底壓力變化如圖一所示。當流經矩形物之水流完全不受水槽影響時，槽底壓力應無變化，圖一顯示矩形物寬度爲 1 公分時，近乎不受水槽影響；寬度爲 5 公分時，矩形物與槽底淨距大於 7 公分時亦近乎不受影響。同樣的現象在圖二亦可看出。圖二速度分佈曲線中顯示在上敍二種情況時，接近槽底之流速情況未受矩形物浸埋之影響。在此二種情況以外，接近槽底流況變化愈來愈大，顯示槽底水流愈來愈受矩形物浸埋之影響。此二種情況約相當於矩形物浸埋截面積爲水槽浸水截面積之百分之五。

以上結果顯示在矩形槽中進行水工試驗時，當不太長之矩形物浸埋面積小於水槽浸水截面積百分之五時，矩形物附近之流況可假設爲不受水槽槽壁影響。

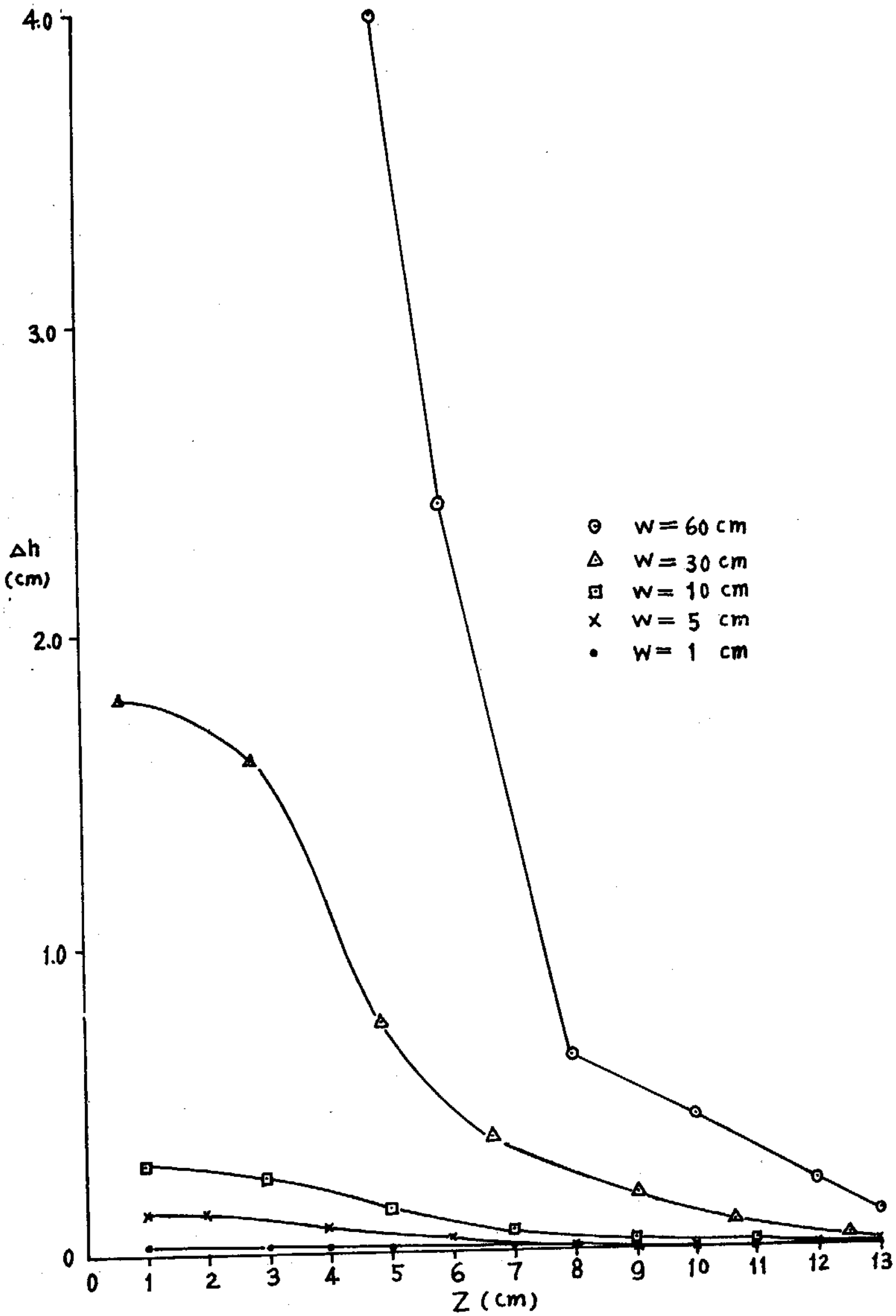
4.0
3.0
2.0
1.0
0
Δh
(cm)
0
1
2
3
4
5
6
7
8
9
10
11
12
13
Z (cm)
⊙ w = 60 cm
△ w = 30 cm
⊡ w = 10 cm
× w = 5 cm
• w = 1 cm

圖一. 槽底壓力之变化

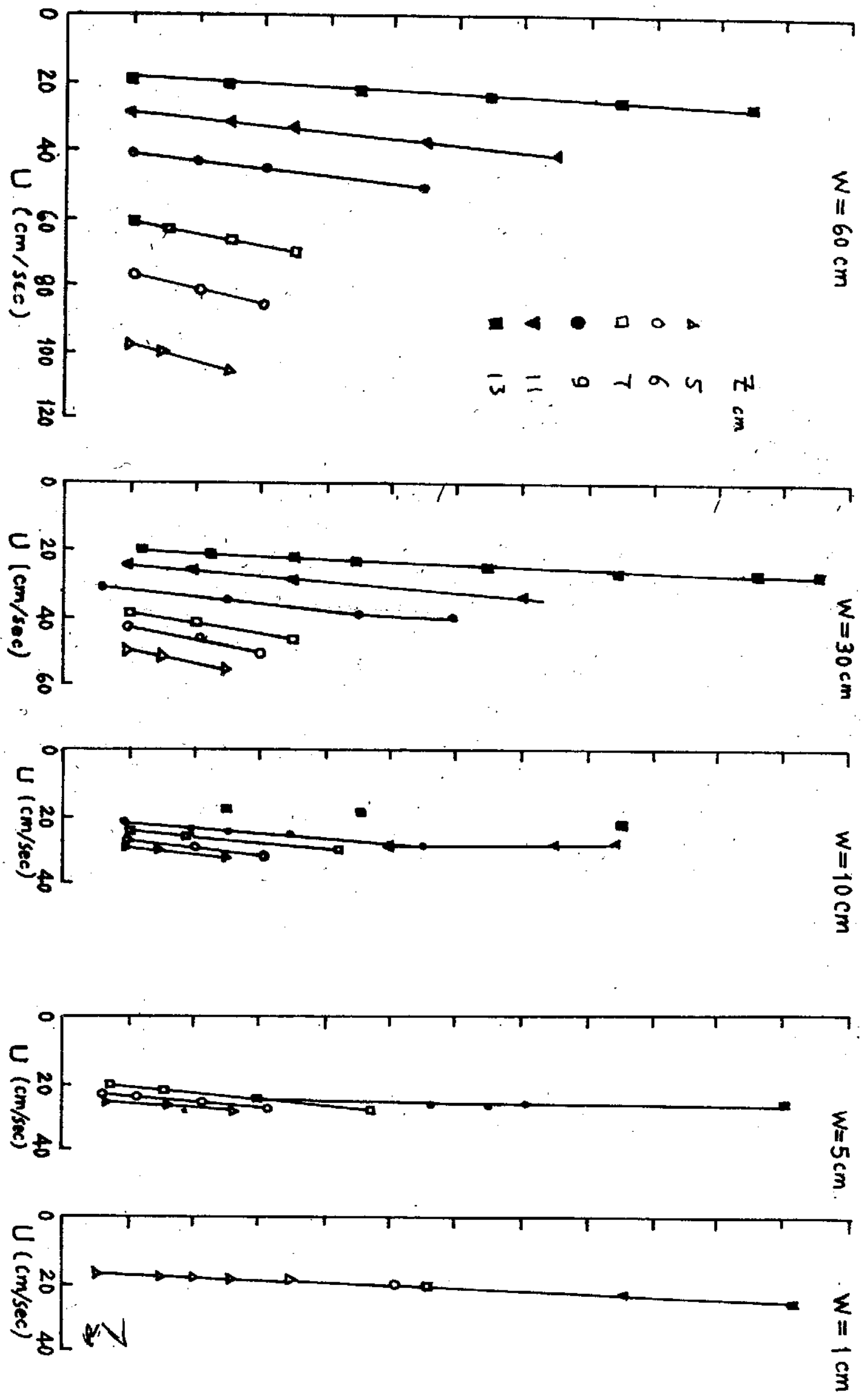
W = 60 cm
W=30cm
W=10cm
W=5cm
W = 1cm
U (cm/sec)
0
20
40
60
80
100
120
Z cm
▲ 5
○ 6
□ 7
● 9
▼ 11
■ 13
Z

圖二. 速度分佈圖

WAVE DISTURBANCES IN WINTER OVER THE COASTAL AREA OF SOUTHEASTERN CHINA CONTINENT

Shun-Der Ko* (柯順德)

Abstract

Wave disturbances in winter at the constant pressure levels of from 850 mb to 200 mb over the coastal area of southeastern China continent are studied by the spectral method. A high-pass filter covering a period range up to 25 days is used prior to the spectral analysis. Two predominent types of wave disturbances are obtained. One is that with period around 17 days for both zonal and meridional components throughout the troposphere above 850 mb, the other is that with 4- to 5.5-day period for the meridional wind component throughout the entire troposphere over the whole area.

Horizontal and vertical structures of the disturbances are studied by examining the cross spectrum. The large type of wave disturbance in the southwest area leads that in the northeast region. The meridional wind disturbance with period of 4 to 5.5 days changes phase in the region between Makung and Swatow.

1. *Introduction*

In winter the polar high, the Aleutian low, the cyclone over Japan and Eastern China Sea, and the blocking high over Far and Middle East are responsible for the weather over the coastal area of southeastern China continent. However, the information about the source causing wave disturbances is not known exactly and little is known about the dynamic structure of the wave disturbances in this area.

Nitta et al. (1973) studied the wave disturbances over China continent and the Eastern China Sea in February 1968. They divided this region into four blocks and observed two types of disturbances, one is that with 4-5 day period over the area to the south of 32° N; the other 1.5-2 day period in the lower troposphere over the southern part of the Eastern China Sea. However, the author (1974a) studied the wave disturbances over northern Taiwan in winter and found two distinct types of disturbances with period of 8-10 days throughout the troposphere and of 3-4 days in the lower and upper troposphere. Thus the results obtained are not in fair agreement with each other. It seems interest to study the wave disturbances in winter more quantitatively.

---

* Associate Professor, Taipei Inst. Tech., and Visitor, Inst. Phys., Academia Sinica

In this study we intend to investigate the wave disturbances over the coastal area of southeastern China continent, which is approximately the block II studied by Nitta et al., by a spectral analysis covering a period range up to 25 days. We shall first analyze the power spectra of both zonal and meridional wind components and next examine the cospectrum, quadrature-spectrum, coherence and phase difference for both components to gain more information about the features of structure of the prevailing disturbances throughout the entire troposphere over the above area.

2. *Data and Method of Analysis*

The data used in this study are the upper wind observations over the coastal area of southeastern China continent from 1 December 1968 to 28 February 1969. The including upper air observation stations are Fuchow (26.05 N, 119.18 E), Taoyuan (25.03 N, 121.13 E), Makung (23.31 N, 119.34 E), Swatow (23.21 N, 116.40 E), Kuangchow (23.10 N, 113.20 E) and Tuangkang (22.28 N, 120.28 E). The locations of these stations are shown in Fig. 1. The data are available twice a day (0000 GMT and 1200 GMT) at Fuchow, Taoyuan, Swatow and Kucngchow, but once a day (1200 GMT) at Makung and Tungkang. Analysis is made for the wind speed and wind direction at the constant pressure levels of 850, 700, 500, 400, 300 and 200 mbs except for Fuchow. For Fuchow we made the same analysis by excluding 200-mb level due to a large amount of missing data. There are also many missing data at the levels above 400 mb for all stations. In this study, computations are made by excluding all the missing data.

A high-pass filter is applied prior to the spectral analysis of wave disturbances. The frequency response of the high-pass filter is illustrated in Fig. 2. The response is almost kept constant up to about 25 days. The frequency interval is 0.02 cpd (cycles per day) and the largest frequency is limited to 0.5 cpd. We obtain 26 spectral estimates for the maximum lag number of 25. In order to compute the cross spectrum between twice- and once-daily data, we reduce the twice-daily one to the once-daily one by taking weighted average to the successive three original data. The detailed method of the spectral analysis used in this study were given in the author's previous papers (1973, 1974a).

3. *Power Spectra and Cross Spectra of Wave Disturbances*

Fig. 3 shows the u-spectra and Fig. 4 the v-spectra of 850, 700, 500, 400, 300 and 200 mbs at Taoyuan, Tungkang, Makung, Swatow, Kuangchow and Fuchow respectively.

To get a general idea about the wave disturvances in winter over the coastal area of southeastern China continent we first investigate the period ranges at which the prevailing peaks of the u- and v-spectra exhibit. At Taoyuan, Tungkang, Makung, Swatow, Kuangchow and Fuchow, we find remarkable peaks exist around 17-day period at 700, 500,

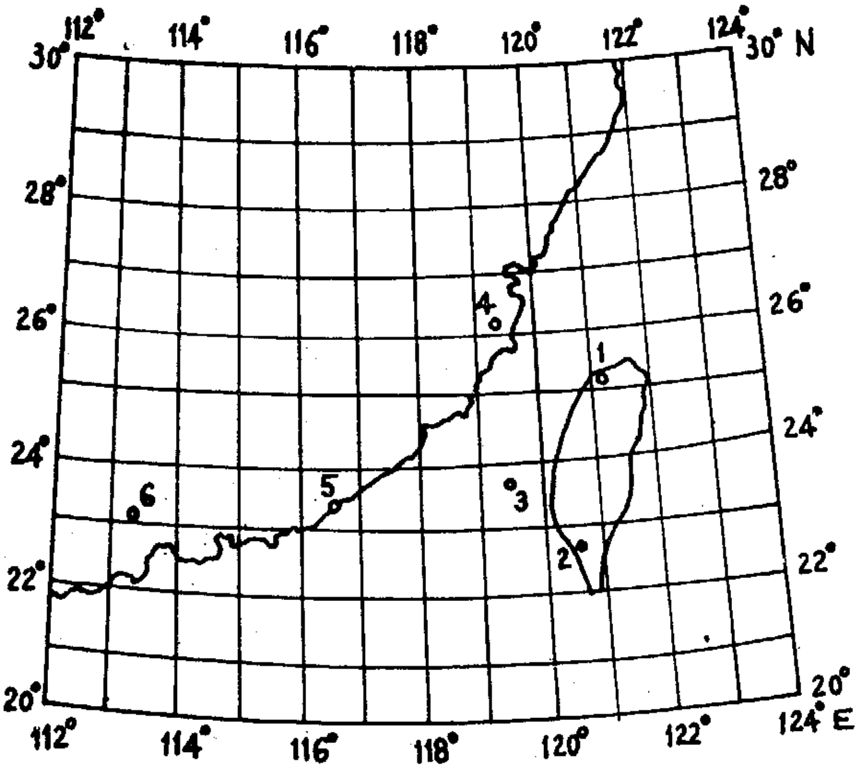

Fig. 1. Upper observation stations over the coastal area of southeastern China continent.
1 : Taoyuan, 2 : Tungkang, 3 : Makung,
4 : Fuchow, 5 : Swatow, 6 : Kuangchow.

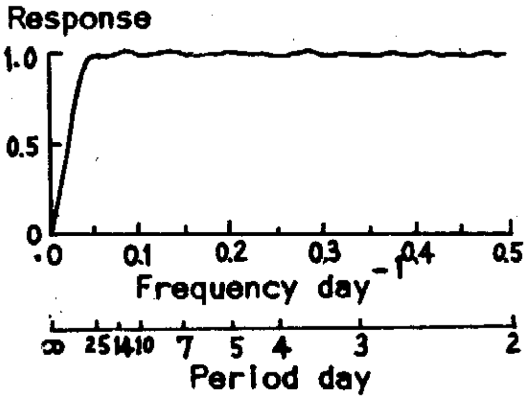

Fig. 2. Response of the high-pass filter used in this study.

400, 300 mbs in the u-spectra and 700, 500, 400, 300, 200 mbs in the v-spectra. It is also worthy mentioning that the v-spectra at almost all levels over all stations exist predominent maxima in the period range of 4-5.5 days. At Kuangchow there are also large peaks in the u-spectra at the period around 6 days for all levels except 200 mb. At Tungkang evident peaks in the u-spectra are found at 4- to 5-day period. In addition, the u-spectra at both 850- and 200-mb levels and the v-spectra at 200-mb level for all stations show conspicuous peaks at the period around 25 days.

The cospectra and quadrature-spectra between u and v disturbances at the same level for each station are shown in Fig. 5. From this figure we find, at 500-, 400-, and 300-mb levels for all stations, the cospectra have evident minima and quadrature-spectra maxima at about 17-day period. At this period range the coherences are larger than 0.8 and the phase differences are about +130° as shown in Table 1. These results may imply that the meridional wind disturbance lead the zonal one and that the axis of disturbance is directed generally from southeast to northwest throughout the middle troposphere over each station. The former deduction is the same as that obtained in the author's previous study (1974a) but the latter not.

As mention above, the zonal wind disturbance in the entire troposphere above 850 mb reveals the periodicity of around 17 days at almost all stations and the meridional one shows two types of disturbance with periods of around 17 and 4-5.5 days respectively. Therefore we shall particularly pay attention to these types of disturbances in investigating the structures of the wave disturbances.

Table 1. Phase differences(θ) and coherences(R) between u and v disturbances at each level at the period of about 17 days for Taoyuan(TA), Tungkang(TU), Makung(MA), Swatow(SW), Kuangchow(KU) and Fuchow(FU)

Stations	TA		TU		MA		SW		KU		FU	
Levels	R	θ	R	θ	R	θ	R	θ	R	θ	R	θ
500 mb	0.9	140	0.8	135	0.7	133	0.9	129	1.0	125	0.9	147
400 mb	0.9	155	0.8	125	0.9	145	0.9	112	1.0	127	1.0	116
300 mb	0.9	145	0.9	114	0.9	163	0.9	161	1.0	61	1.0	148

4. *Structures of Wave Disturbance*

4-1. Vertical Structure

In order to investigate the vertical structure of u- and of v-component, we calculate

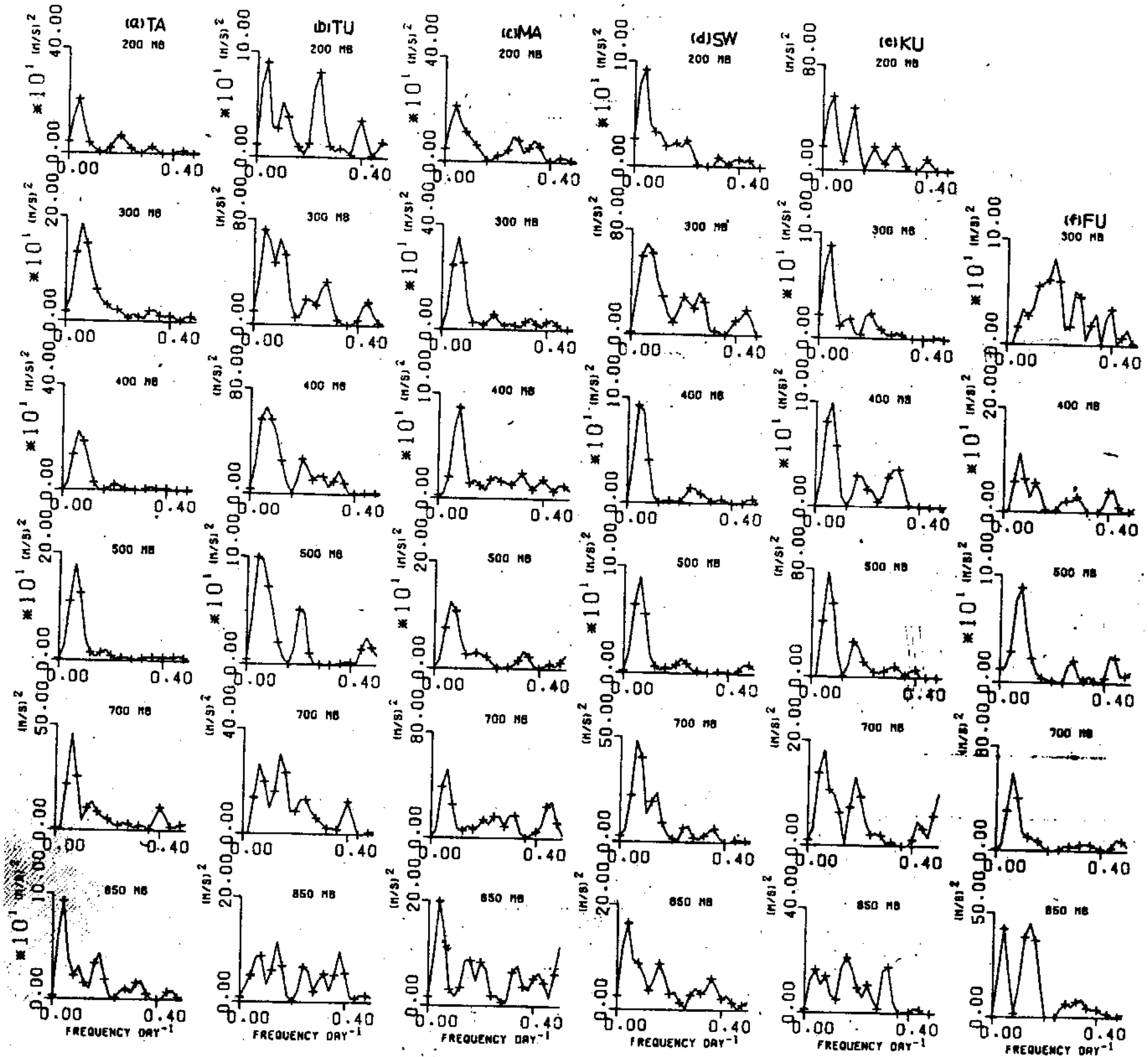

Fig. 3. U-spectra at various levels over (a) Taoyuan, (b) Tungkang, (c) Makung, (d) Swatow, (e) Kuangchow and (f) Fuchow.

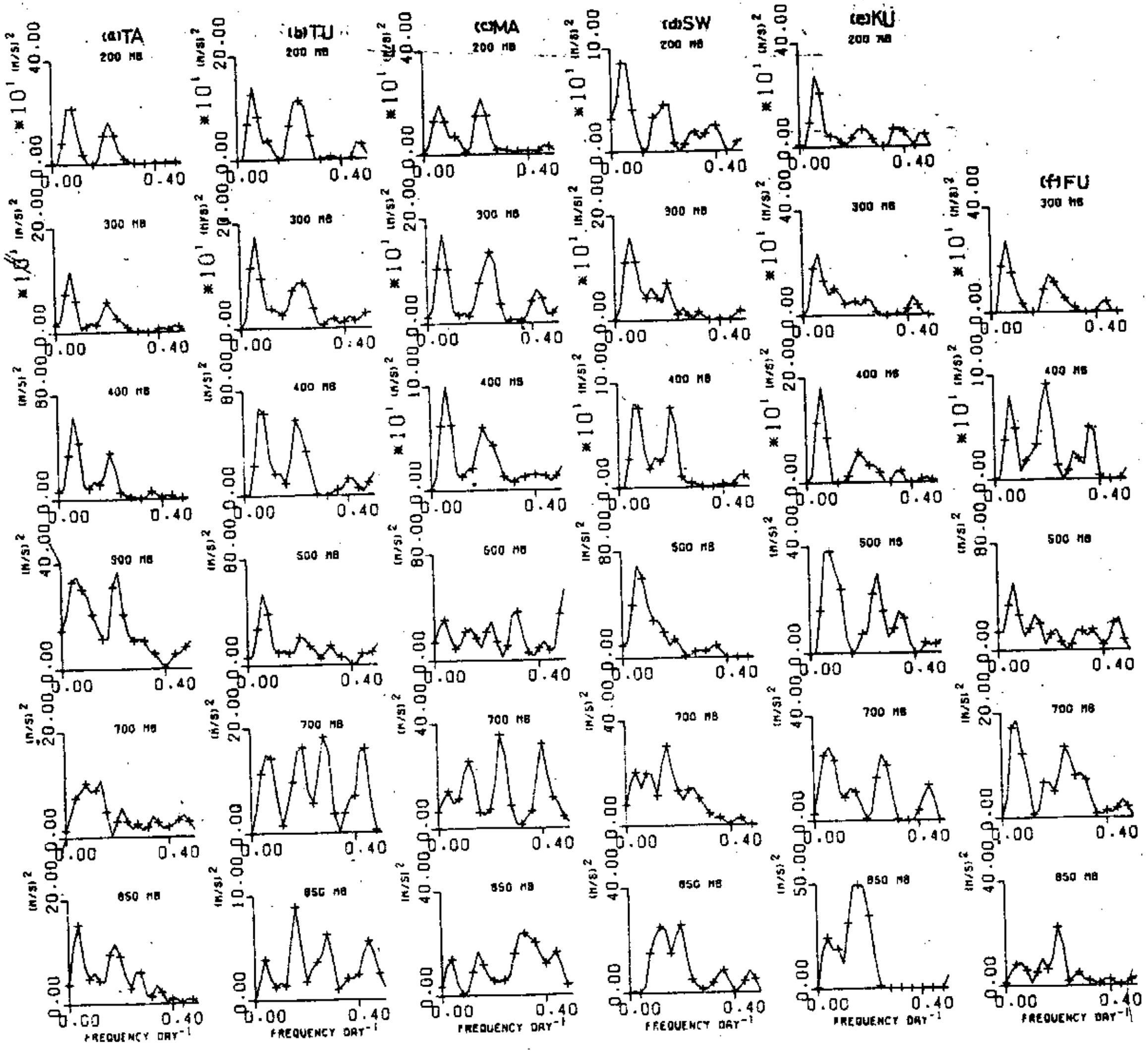

Fig. 4. V-spectra at various levels over (a) Taoyuan, (b) Tungkang, (c) Makung, (d) Swatow, (e) Kuangchow and (f) Fuchow.

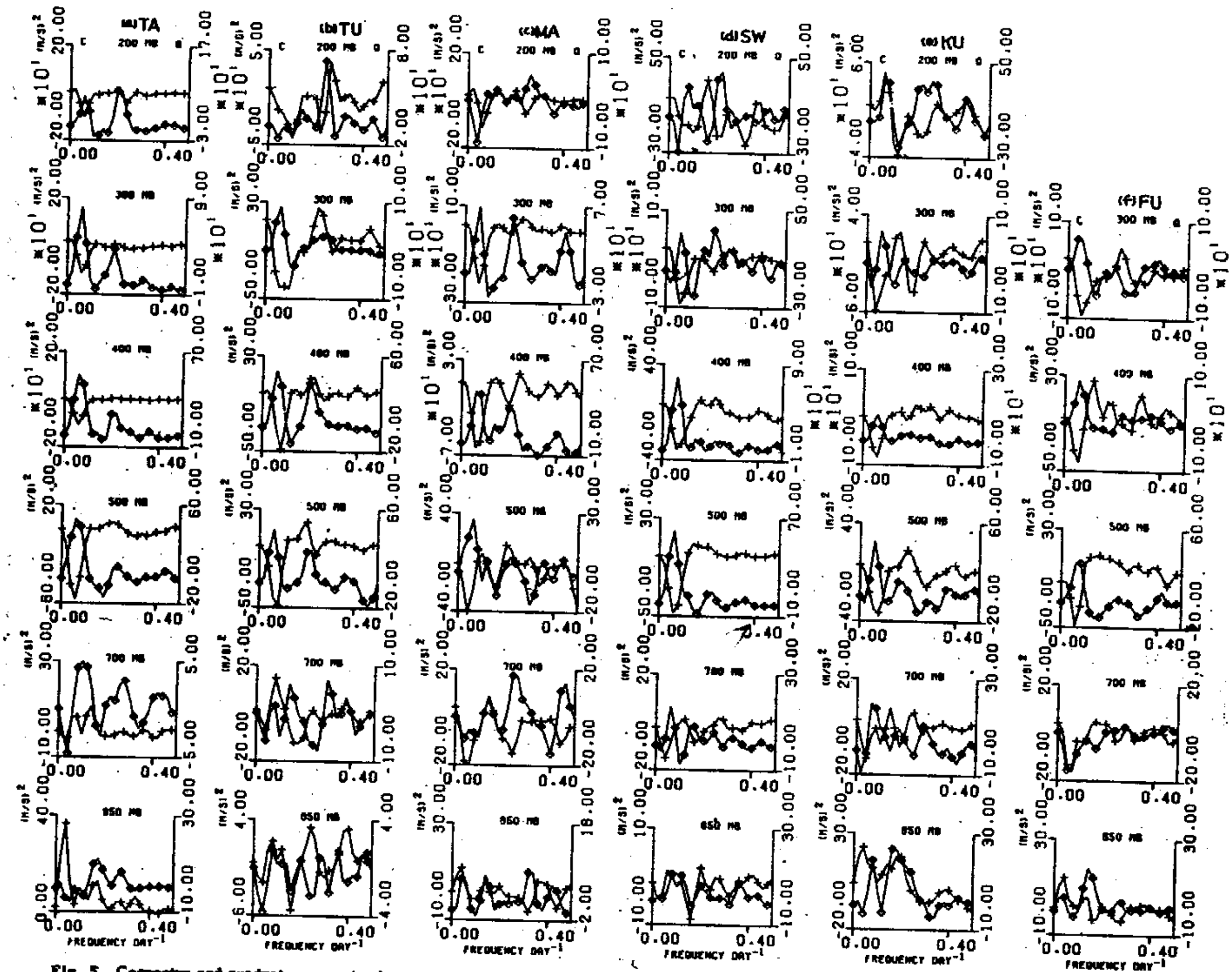

Fig. 5. Cospectra and quadrature-spectra between u and v components at the same level over (a) Taoyuan, (b) Tungkang, (c) Makung, (d) Swatow, (e) Kuangchow and (f) Fuchow.

the cospectrum, quadrature-spectrum, coherence and phase difference for both components on the basis of 850 mb. The cospectra and quadrature-spectra between 850 mb and other level are illustrated in Fig. 6 for u component and Fig. 7 for v respectively at Taoyuan, Tungkang, Makung, Kuangchow, Swatow and Fuchow. Their phase differences with coherences for some selected period ranges are shown in Fig. 8.

First, we shall investigate the vertical structure of the zonal component around the period of 17 days in Fig. 6. The phase differences at this period for various stations are shown in Fig. 8. (first column). At Taoyuan the cospectra for all levels except 200 mb show large minima and quadrature-spectra maxima, with the phase differences all about +140° and the coherences larger than 0.6. This means that the zonal disturbances above 850 mb are nearly in the same phase at the period around 17 days. At Tungkang, Makung, Swatow and Kuangchow, the cospectra also show predominent peaks with large quadrature-spectra. The phase lead at Tungkang increases slightly with altitute. At Makung the phases above 700 mb are nearly the same except 300 mb. At Fuchow, Swatow and Kuangchow the u disturbance at upper level leads that at lower one. Generally speaking, the upper zonal wind disturbance over the stations to the west of coastal line of southeastern China continent leads the lower one but is nearly in the same phase as the lower one to the east.

Next, let us examine the vertical structure of the meridional component around both 17-and 5-day periods. The cospectra and quadrature-spectra between v component at 850 mb and that at other levels for various stations are presented in Fig. 7. At the period around 17 days, the cospectra and quadrature-spectra show somewhat complicated situation. For Taoyuan there are large cospectra with small quadrature-spectra at 500-, 400-, and 300-mb levels around 17-day period. For Makung, Swatow and Kuangchow the quadrature-spectra show relative maxima with small cospectra at 400-, 300- and 200-mb levels at this period range. These facts suggest that the phase lead of upper v disturbance relative to lower one at Taoyuan is smaller than that at Makung, Swatow and Kuangchow respectively. This deduction may also be certified by comparing the phase differences of each station shown in second column of Fig. 8. From this figure we note in general the meridional wind disturbance at upper level lead that at lower one. As for period around 5 days, we observe minima cospectra exist at Taoyuan, Makung and Tungkang. The phase differences above 700 mb are all positive and nearly equal except 200 mb. That is, the v disturbances at 500, 400, and 300 mbs are nearly in the same phase, but lead those at 700 and 200 mbs. At Fuchow, Swatow and Kuangchow we also find minima cospectra occur at about 5-day period but with negative phase difference except 200 mb. Therefore we may conclude that in the lower and middle troposphere the merdional disturbance at upper level lags that at lower one over these stations.

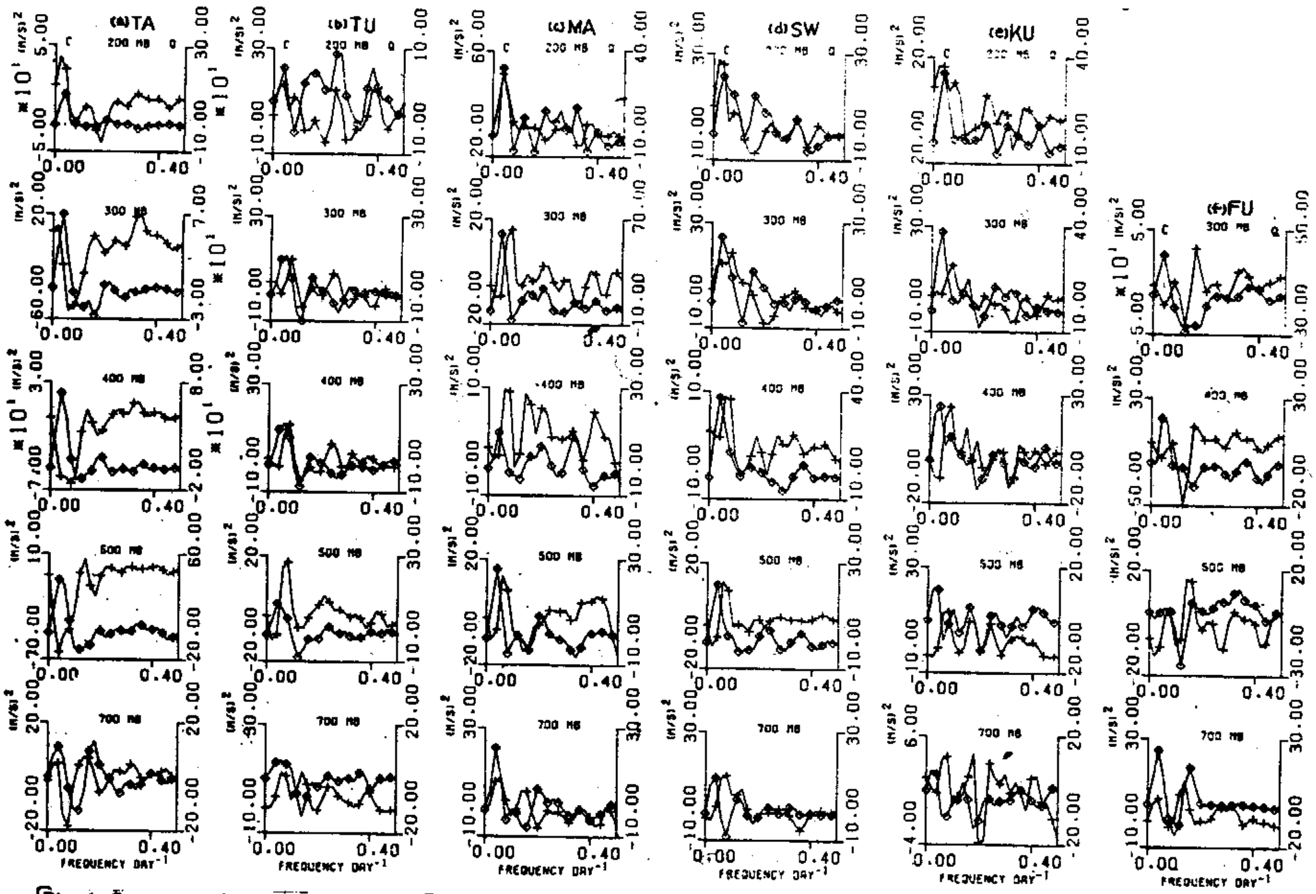

Fig. 6. Cospectra and quadrature-spectra between u component at 850mb level and that at other levels over (a) Taoyuan, (b) Tungkang, (c) Makung, (d) Swatow, (e) Kuangchow, and (f) Fuchow.

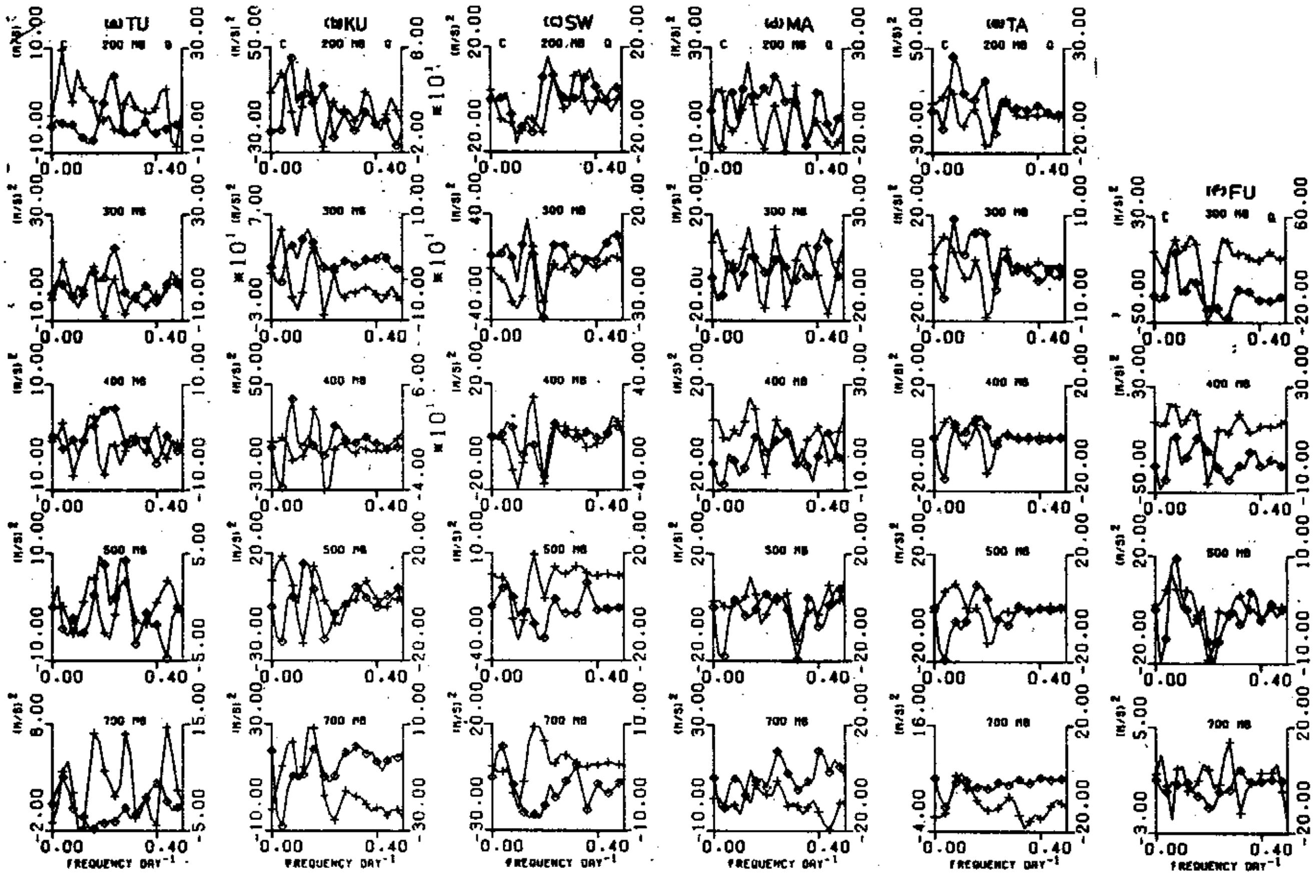

Fig. 7. Cospectra and quadrature-spectra between v component at 850mb level and that at other levels over (a) Tungkang, (b) Kuangchow, (c) Swatow, (d) Makung, (e) Taoyuan and (f) Fuchow .

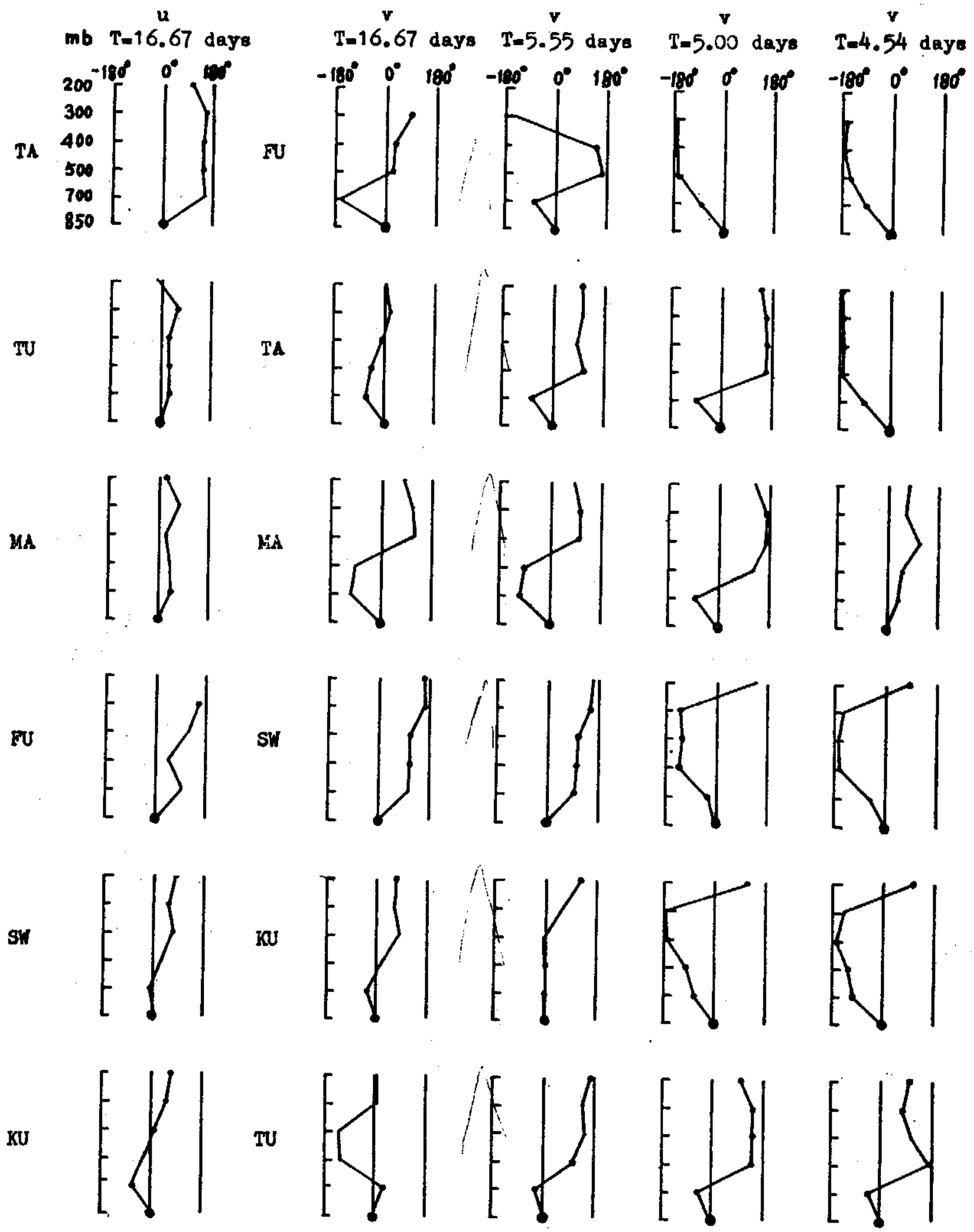

Fig.8. Vertical phase differences of u and of v on the basis of 850-mb level four period ranges at Taoyuan(TA), Tungkang(TU), Makung(MA), Fuchow(FU), Swatow(SW) and Kuangchow(KU). Large dot denotes the data whose coherence is larger than 0.6.

4-2. Horizontal Structure

In this subsection we shall study the horizontal structure of the wave disturbances. First, we shall analyze the cross spectrum between the u component at Taoyuan and that at other stations. Next, we shall interprete the same items for the v component. As stated in above section we shall pay attention only to the prevailing period (around 17 and 5 days).

Fig. 9 shows the cospectra and quadrature-spectra between u component at Taoyuan and that at other stations for 850, 700, 500, 400, 300, and 200 mbs respectively. From this figure we find, with a few exception, both the cospectra and the quadrature-spectra at 700, 500, 400, 300 mbs have large maxima with coherences larger than 0.8 around the period of 17 days. This implies that around this period range the zonal wind disturbance at Taoyuan has close relationship with other stations but is not in the same phase. In addition, at 850 mb both the cospectra and the quadrature-spectra also show large peaks around the period of 25 days.

Fig. 10 shows the cospectra and quadrature-spectra between v component at Taoyuan and that at other stations for 850, 700, 500, 400, 300 and 200 mbs respectively. In section 3, we see that the v component reveals two types of disturbance. Therefore we shall particularly investigate the cospectra and quadrature-spectra of these two types. Around 17-day period both the cospectra and the quadrature-spectra have sharp peaks with coherences larger than 0.8 above 700-mb level. This implies that in the middle and upper troposphere the meridional wind disturbances over all stations have the same period of about 17 days but are not simultaneous. In the vicinity of 5-day period, we also find large peaks exist in the cospectra at 850-, 500-, 400-, 300-, and 200-mb levels. It follows that in the middle and upper troposphere the v disturbance at Taoyuan leads or lags that at other stations by less than about 60° or shorter than one day.

In order to see the horizontal structure more explicitly, we illustrate in Fig. 11 the phase differences between wind components for all levels over Taoyuan and those at the same levels over other stations in the period ranges of 16.67 and 4.16-5.55 days. In this figure, the stations are arranged downward in order from east to west according to their longitudes for u component and latitudes from north to south for v component. In Fig. 11 we notice, around 17-day period, the wind disturbances in the west and in the south slightly lead those in the east and in the north respectively. It follows that the wind disturbance in southwest area lead that in the northeast region. Consequently, the disturbances with period around 17 days propagate from southwest to northeast. At the period of 4 to 5.5 days, the u disturbance change phase at Makung and v between Makung and Swatow. That is, to the east of Makung the phase lead for the u component increases with longitude but in the opposite situation to the west. For the v component, the phase

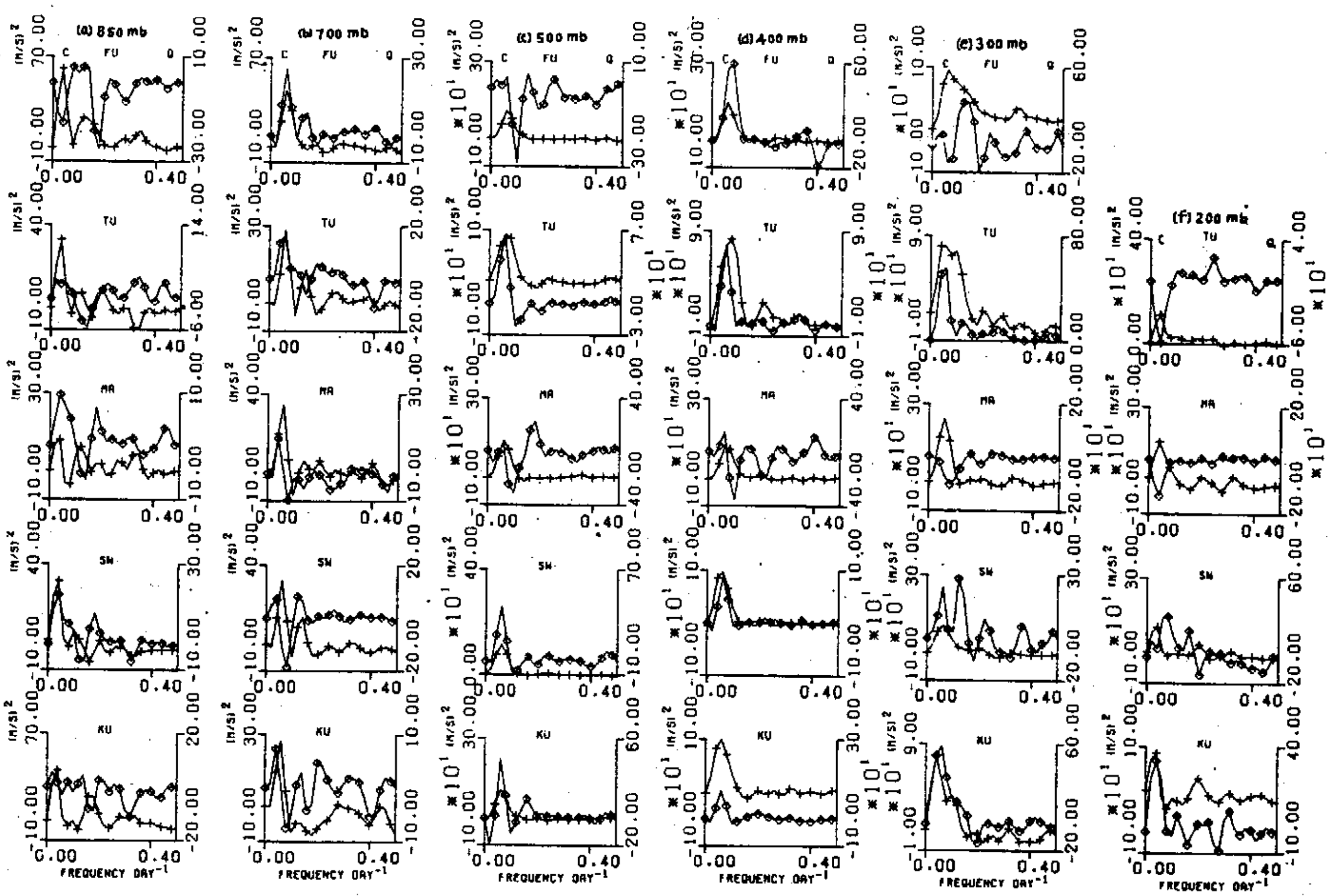

Fig. 9. Cospectra and quadrature-spectra between u component at Taoyuan and that at other stations for (a) 850-, (b) 700-, (c) 500-, (d) 400-, (e) 300-, and (f) 200-mb level.

lead increases with latitude to the north of Makung and to the south of Swatow. These facts may imply that over the coastal area of southeastern China continent the front wave often appears in the region between Makung and Swatow in winter season, and that the period at which the front wave emerges is about 5 days.

5. *Conclusions and Recommendations*

Wave disturbances are studied by the spectral method for the upper wind observation data over the coastal area of southeastern China continent during 1 December 1968 through 28 February 1969. The including upper air observation stations are Taoyuan, Tungkang, Makung, Fuchow, Swatow and Kuangchow. From the investigation of power spectra and cross spectra of the wave disturbances over the above stations the following deductions may be made:

a. The zonal wind component in the troposphere above 850-mb level reveals one remarkable type of disturbance with period around 17 days.

b. The meridional wind component exhibits two types of disturbance. One is the large-scale disturbance with the same period range as that of the zonal component, the other is a smaller one with period of 4 to 5.5 days.

c. In general, the upper zonal wind disturbance over the stations to the west of coastal line of southeastern China continent leads the lower one but is nearly in the same phase as the lower one to the east (over the sea region).

d. For the 17-day type of disturbance, the upper meridional wind component leads the lower one in the troposphere above 850 mb at Fuchow, Swatow and Kuangchow.

e. For the 4- to 5.5-day type of disturbance, the meridional component at upper level lags that at lower one over Fuchow, Swatow and Kuangchow in the lower and middle troposphere.

f. The disturbance with period of about 17 days generally propagates from southwest to northeast over the coastal area of southeastern China continent.

g. The meridional disturbance in the period range of 4 to 5.5 days change phase in the region between Makung and Swatow.

As mention above, there are two predominent types of winter wave disturbance over the coastal area of southeastern China continent. The large type with period about 17 days is prevaling above 850-mb level and is generally propagating from southwest to northeast. Therefore it is probably generated by the blocking high over Far and Middle East. The smaller meridional disturbance with period of 4 to 5.5 days is prevailing at almost all levels and is probably developed due to the passage of front wave of polar outbreaks.

The above concluding features are not exactly the same as those in earlier studies of

Nitta et al. (1973) and Ko (1974a). The wave disturbances appear to be nonstationary and unpredictable. It seems not easy to establish modes for the disturbances and to interprete why the observed features appear as they are. Consequently, further statistical investigation as well as theoretical work is called for in the future. To make a complete analysis, other considerations must be taken into account, spectral method extended to other variables, such as temperature, vertical wind component, geopotential height, etc., seems necessary, and further appropriate filters should be designed to pick up the prevailing period ranges.

Acknowledgements

The author is grateful to Drs. Chun-Tsung Wang and Li Peng, Research Fellows of the Institute of Physics, Academia Sinica, for their encouragement and valuable suggestions. All the computations in this study are made at the Computer Center of Taipei Institute of Technology and of the Physics Research Center, National Science Council.

This research is supported through a grant from the National Science Council, Republic of China.

References

Blackman, R. B., and J. W. Tukey, 1958: The measurement of power spectra from the point of view of communications engineering. Dover publications, New York, 190pp.

Holloway, J. L., 1958: Smoothing and filtering of time series and space fields. Advances in Geophys., Ed. by H. E. Lansberg and J. Van Mieghem, Vol. 4, Academic Press(New York), 351-389.

Izawa, T., 1972: Some considerations on the continous space-time spectral analysis of atmospheric disturbances. Papers in Meteor. and Geophys., 23, 33-71.

Julian, P. R., 1971: Some aspects of variance spectra of synoptic scale tropospheric wind components in midlatitudes and in the tropics. Mon. Wea. Rev., 99, 954-965.

Ko, S. D. et al., 1973: Power spectra of upper wind over Taiwan in summer. Ann. Rept. Inst. Phys. Acad. Sin., 3, 239-256. (with Staff Members Atmos. Div., Acad. Sin.)

Ko, S. D., 1974a: Spectrum analysis of wave disturbances over northern Taiwan in winter. Atmos. Sci., Meteor. Soc. ROC, 1, 45-60.

Ko, S. D., 1974b: Normalized weights of Gaussian filtering function. J. Tai. Inst. Tech., 7,83-97.

Maruyama, T., 1968a: Time sequence of power spectra of disturbances in the equatorial lower stratosphere in relation to the quasi-biennial oscillation. J. Meteor. Soc. Japan, 46, 327-341.

Maruyama, T., 1968b: Upward transport of westerly monentum due to large-scale disturbances in the equatorial lower stratosphere. J. Meteor. Soc. Japan, 46, 404-417.

Nitta, T., 1970: Statistical study of tropospheric wave disturbances in the tropical Pacific region. J. Meteor. Soc. Japan, 48, 47-60.

Nitta, T., M. Nanbu, and M. Yoshizaki, 1973: Wave disturbances over the China continent and the Eastern China Sea in February 1968. J. Meteor. Soc. Japan, 51, 11-28.

Weather Wing, CAF, 1969: The weather and circulation of the East Asia during December 1968-February 1969. Quart. J. Meteor. ROC, 39, 37.

Yanai, M., and M. Murakani, 1970: A further study of tropical wave disturbances by the use of spectrum analysis. J. Meteor. Soc. Japan, 48, 185-197.

双舭船型截面垂直自由液面振盪時附加質量係數之計算

林同慶　劉衿友　汪群從 *(C.T. Wang)* 戴堯天 *(Y.T.Dai)*

I 導言

附加質量的數據在船體振動，船體運動性能，以及船體結構上的計算極爲重要。除了簡單形體外，一般物體不易求出附加質量的理論數值，故對複雜的物體（如船體）實用上是以截面法 (strip method) 來計算，此法是將物體分成數個等距的截面，首先計算每一個截面的附加質量（假定此截面上的流體是二維的），而後沿著縱向將這些值積分可得整個物體的附加質量。但每段截面的計算通常依近似方法求得，簡單形體亦有理論的結果，例如F.M. Lewis [1]利用Schwarz-Christoffel轉換式計算矩形及三角形截面的附加質量係數，Vugts [2] 再以實驗結果比較起伏、横搖及側移的理論值，其中包括了矩形及三角形截面，所得結果相當接近。最近 Hwang [3] 及 Hwang 和 Kim [4] 計算了 12 種稜形柱體及單舭船型的垂直向振盪附加質量，並推論得截面上之稜角大小對附加質量的影響並不亞於截面的面積係數。

其他簡單形體，如雙舭船型均未曾討論，此種具有二個稜角的截面形常出現於快艇、驅逐艦、直板簡易船型及方形船艉上。本文考慮雙舭船體的各種相對尺寸大小對附加質量的影響，其結果和單舭船體比較甚爲合理。

II 理論分析

取一直角座標系統，其原點位於自由液面及截面之垂直對稱線的交點上，y 軸和自由液面一致，x 軸垂直於 y 軸上，如圖 1 所示。

爲了使問題可以用勢流理論來求解，本文只考慮二維柱體以高頻率振盪，並忽略液面上波動的影響。同時因浮體在水中運動的動能及附加質量可視爲其水下部分及逆像部分 (mirror image) 所組成之截面完全浸在無限水域時的動能及附加質量值的一半。此種假設並不適用於水平向的運動 [5] 。

圖 1 所示之雙舭船形是半浸於無限大的水域中，船型及其逆像對 x 軸及 y 軸均爲對稱。柱體在自由液面的垂直向振盪時的邊界條件爲：

(i) 自由液面的條件：

線性化的液面條件爲

$$\phi_{tt} - g\phi_x = 0$$

ϕ 爲振盪時之勢函數，又 ϕ 可視爲 ωt 的簡諧函數，且於 $\omega \to \infty$ 時，上式變成

$$\phi_{x=0} = 0$$

(1)

(ii) 柱體上的邊界條件：

$$\frac{\partial\phi}{\partial n} = V_n \tag{2}$$

V_n 爲表面上速度的垂直分量。又因流體的運動對 x 軸對稱，所以

$$\phi(x, y, t) = \phi(x, -y, t) \tag{3}$$

(iii) 流體底部的條件

若於底部有固體表面時，$\phi_x = 0$，若沒有固體邊界時，則

$$\phi_x \to 0 \qquad 當\ x \to \infty \tag{4}$$

(iv) $y = \pm\infty$ 時，設流體之動能爲零。

因柱體作上下之週期運動的勢函數可視爲流體流過靜止柱體的勢函數 ϕ_1，加上均勻流的勢函數。流體流過靜止柱體的情形，可經 Schwarz Christoffel 轉換式變成爲 ζ 平面上的均勻流，其複數勢函數 (Complex potential) 爲

$$\begin{aligned} w &= \zeta \\ &= \phi_1 + i\xi_1 \end{aligned}$$

因柱體的截面對 x 軸及 y 軸爲對稱，且半浸之柱體的附加質量爲完全浸入柱體的一半。故流過 OPQR～Q′P′O 柱體的均勻流，可視爲流過UVST～PQRS多邊形的均勻流。

考慮圖 1 之雙舭船型，其使用之 Schwarz-Christoffel 轉變式爲，

$$Z = \int (\phi_1^2 - 1)^{\alpha-1} (\phi_1^2 - SK^2)^{\beta-1} (\phi_1^2 - SJ^2)^{2-\overline{\alpha+\beta}} d\phi_1$$

ϕ_1 爲流體均勻地流過雙舭船型（靜止的）的勢函數，上式係將圖 1 之截面形的邊界對應至 ζ 平面的實軸上。設 r_0、r_1及 r_k爲雙 船形的各邊長，如圖 1 所示，則利用複變數的關係，各邊長爲；

$$r_o = |Z_p - Z_o| = \int_o^{SK} (1-\phi_1^2)^{\alpha-1} (SK^2-\phi_1^2)^{\beta-1} (SJ^2 - \phi_1^2)^{2-\overline{\alpha+\beta}} d\phi_1 \tag{5}$$

$$r_1 = |Z_Q - Z_P| = \int_{SJ}^{SK} (1-\phi_1^2)^{\alpha-1} (SK^2 - \phi_1^2)^{\beta-1} (\phi_1^2 - SJ^2)^{2-\overline{\alpha+\beta}} d\phi_1 \tag{6}$$

$$r_k = |Z_R - Z_Q| = \int_{SK}^{1} (1-\phi_1^2)^{\alpha-1} (\phi_1^2 - SK^2)^{\beta-1} (\phi_1^2 - SJ^2)^{2-\overline{\alpha+\beta}} d\phi_1 \tag{7}$$

由上述三式可知 r_o，r_1 及 r_k 均爲 SK，SJ，α，β 等四變數的函數。SK及SJ 各爲稜角 α 及 β 所對應的單位位能。設H及 b 代表浸水深度及半寬，利用圖 1 的幾何性質可知

$$H = r_o + r_1 \cos(\alpha+\beta)\pi + r_k \cos(1-\alpha)\pi \tag{8}$$

$$b = r_k \sin(1-\alpha)\pi - r_1 \sin(\alpha+\beta)\pi \tag{9}$$

而截面形面積A爲，

$$A = r_k \sin(1-\alpha)\pi \cdot [2(H-r_o) - r_k \cos(1-\alpha)\pi] + r_1 \cdot \sin(2-\overline{\alpha+\beta})\pi \cdot$$

$$〔2 r_o + r_1 \cos(2-\overline{\alpha+\beta})\pi〕$$

由圖 2 可知，

$$A = HB - (H-r_o)^2 \tan(2-\overline{\alpha+\beta}) \tag{10}$$

故面積係數

$$\sigma = \frac{A}{H \cdot B} = 1 - (1-\frac{r_o}{H})^2 \cdot \frac{H}{B} \cdot \tan(2-\overline{\alpha+\beta})$$

$$= \sigma(\alpha, \beta, B/H, r_o/H) \tag{11}$$

故若 α，β，B/H及 r_o/H 爲已知時，σ 值即可決定。

柱體周圍的動能可根據能量公式爲：

$$2T_{II} = -\rho \int \phi \frac{\partial \phi}{\partial n} ds$$

因 $\phi = \phi_1 - x$ 及 $\frac{\partial \phi_1}{\partial n} = 0$，故上式可寫爲

$$2T_{II} = +\rho \int (\phi_1 - x) \frac{\partial x}{\partial n} ds$$

今沿若柱體計算時，

$$2T_{II} = 2\rho \{ \int_{SJ}^{SK} 〔-\sin(\alpha+\beta)\pi〕 \cdot \phi_1 dr_1 + \int_{SK}^{1} 〔\sin(1-\alpha)\pi〕 \cdot \phi_1 dr_k -$$

$$\int x \frac{\partial x}{\partial n} d\acute{s} \}$$

因

$$dr_1 = (1-\phi_1^2)^{\alpha-1} (SK^2-\phi_1^2)^{\beta-1} (\phi_1^2 - SJ^2)^{2-\overline{\alpha+\beta}} d\phi_1$$

$$dr_k = (1-\phi_1^2)^{\alpha-1} (\phi_1^2 - SK^2)^{\beta-1} (\phi_1^2 - SJ^2)^{2-\overline{\alpha+\beta}} d\phi_1$$

故最後可得

$$2T = 2\rho \{ -\sin(\alpha+\beta)\pi \int_{SJ}^{SK} (1-\phi_1^2)^{\alpha-1} (SK^2-\phi_1^2)^{\beta-1} (\phi_1^2 - SJ^2)^{2-\overline{\alpha+\beta}}$$

$$\phi_1 d\phi_1 + \sin(1-\alpha)\pi \int_{SK}^{1} (1-\phi_1^2)^{\alpha-1} (\phi_1^2 - SK^2)^{\beta-1} \cdot$$

$$(\phi_1^2 - SJ^2)^{2-\overline{\alpha+\beta}} \cdot \phi_1 \alpha \phi_1 - \frac{A}{2} \} \tag{12}$$

Hwang [3] 設附加質量係數爲 C_Z 其定義爲

$$C_Z = \frac{16T}{\pi \rho B^2} \tag{13}$$

而每單位截面之附加質量 m 爲

$$m = C_Z \frac{\pi \rho B^2}{8}$$

Ⅲ 計算結果及比較

對所討論之雙舭船型，若已知 SK，SJ，α及β的值，則 r_0，r_1，r_k，H，B，σ，A及C_Z的值可由計算而得，故知此類問題具有四個變數，可以各種的配合值計算之。但必須滿足下列的條件：

(i) SK 值必須大於 SJ 值而小於 1。

(ii) $1.5 < \alpha+\beta < 2.0$

因σ由α，β，r_0/H，B/H 等四個實用變數所決定，故計算所得結果以α，β，r_0/H，B/H 作變數，而以 SJ 爲中間變數，步驟如下：

(i) 以 SJ ，α，β，r_0/H 作參數，劃圖表示每一組α，β，B/H，及r_0/H 所對應的 SJ 值。

(ii) 由 SJ 值及α，β，B/H 值作出 C_Z 的曲線圖。

計算結果如圖 3 到圖 5 所示，其結果和三角形及矩形截面比較甚爲合理。

五、 參考資料

[1] F.M. Lewis, "The inertia of the water surrounding a vibration ship" SNAME 1929. Vol. 37, p. 37, p. 1-20.

[2] J.H. Vugts, "The hydrodynamics Coefficiento for swaying, heaving and rolling cylinder in a Free surface" I.S.P. 1969. Vol. 15 pp. 251-276.

[3] J.H. Hwang, "Added mass of two dimensional cylinder with the sections of straight framed oscillating vertically in a free surface." I.S.P. 1969. Vol. 16 pp. 169-181.

[4] J.H. Hwang and K.C. Kim, "A study on the added mass associated with the vertical Oscillating of the straight frame ships in a free surface" Science and Engineering Report, Seoul National University, 1968.

[5] L.C. Burrill, W. Robsor and R.L. Townsin, "Ship vibration: entrained water experiments" - I.N.A. 1962. Vol. 104 No. pp. 415-445.

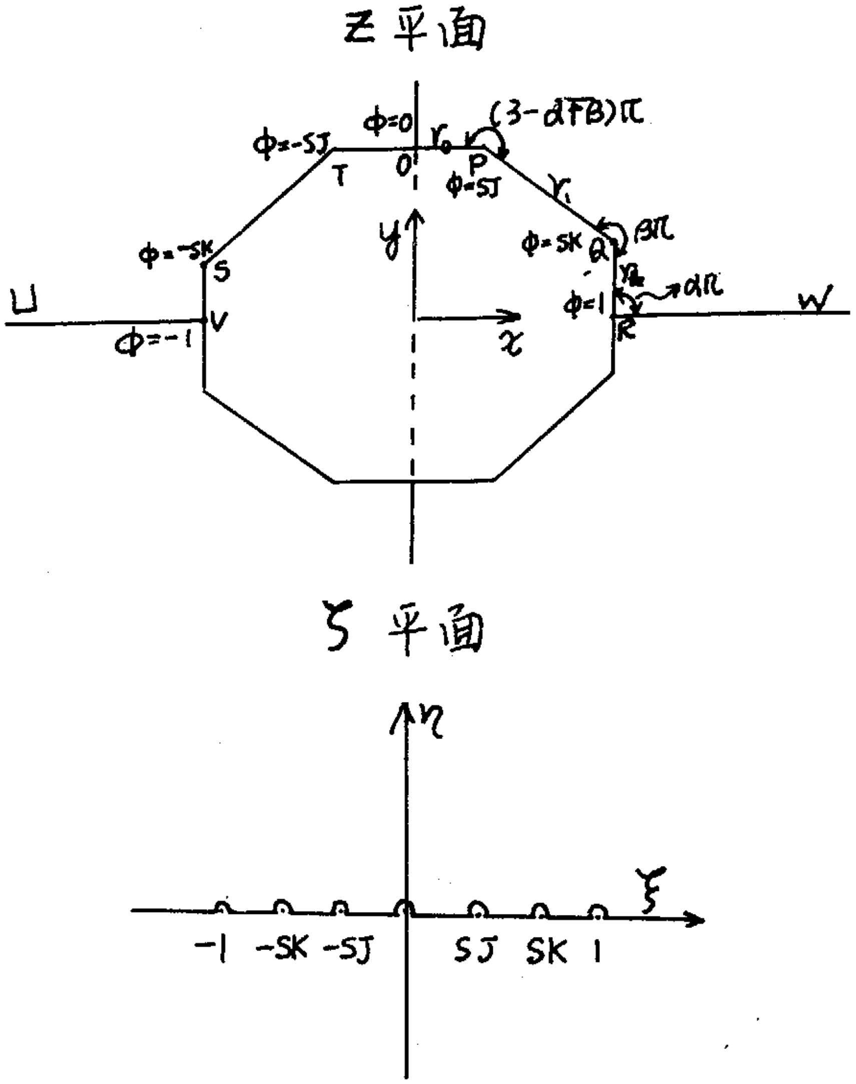

圖 1　具有平底及垂直邊的雙舨船型。

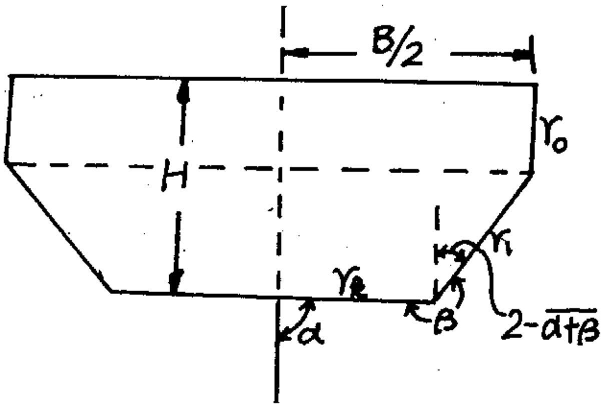

圖 2　$\alpha = 90°$ 之截面形。

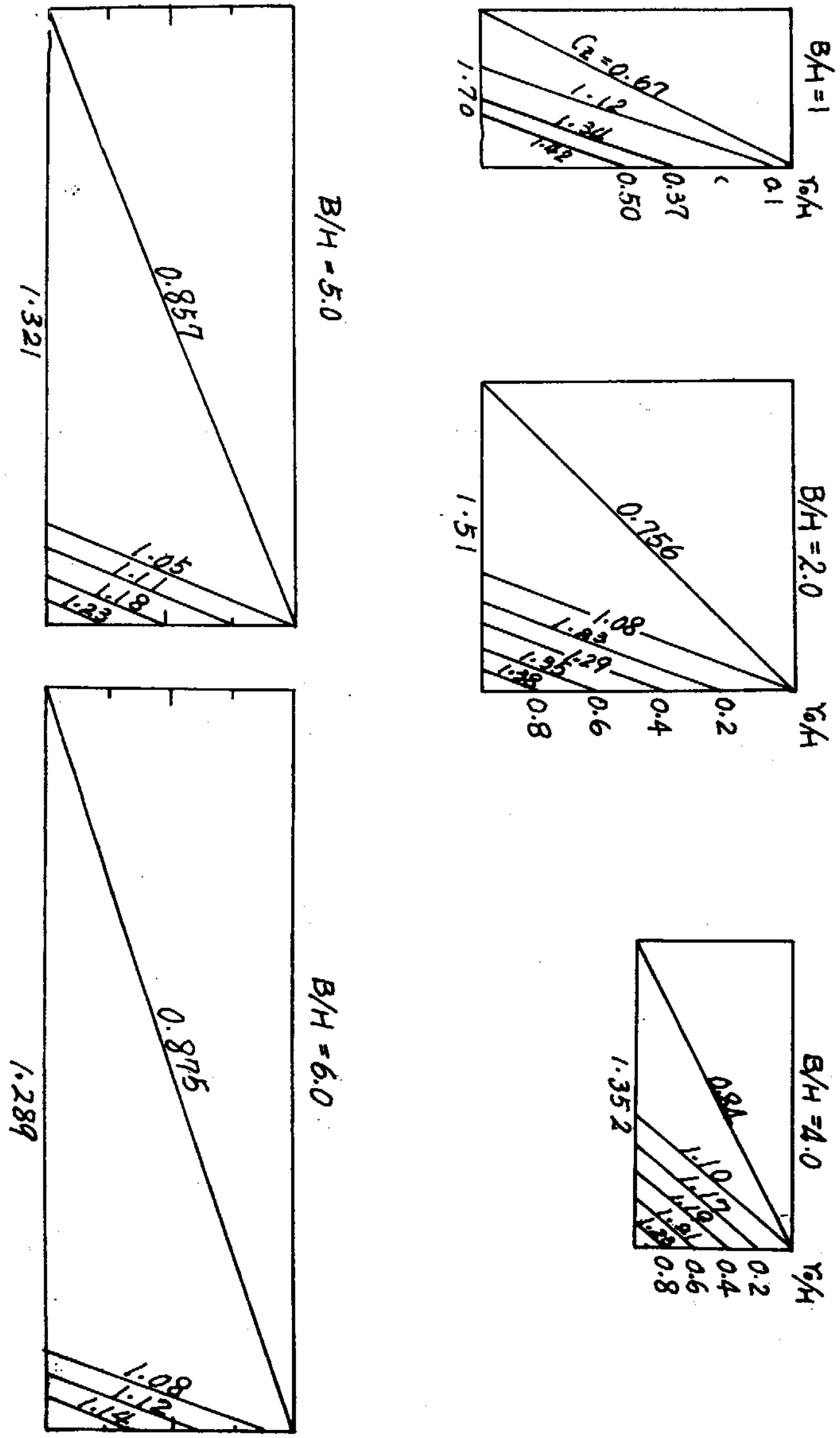

圖3　附加質量係數及截面形（α=0.60，β=1.45）

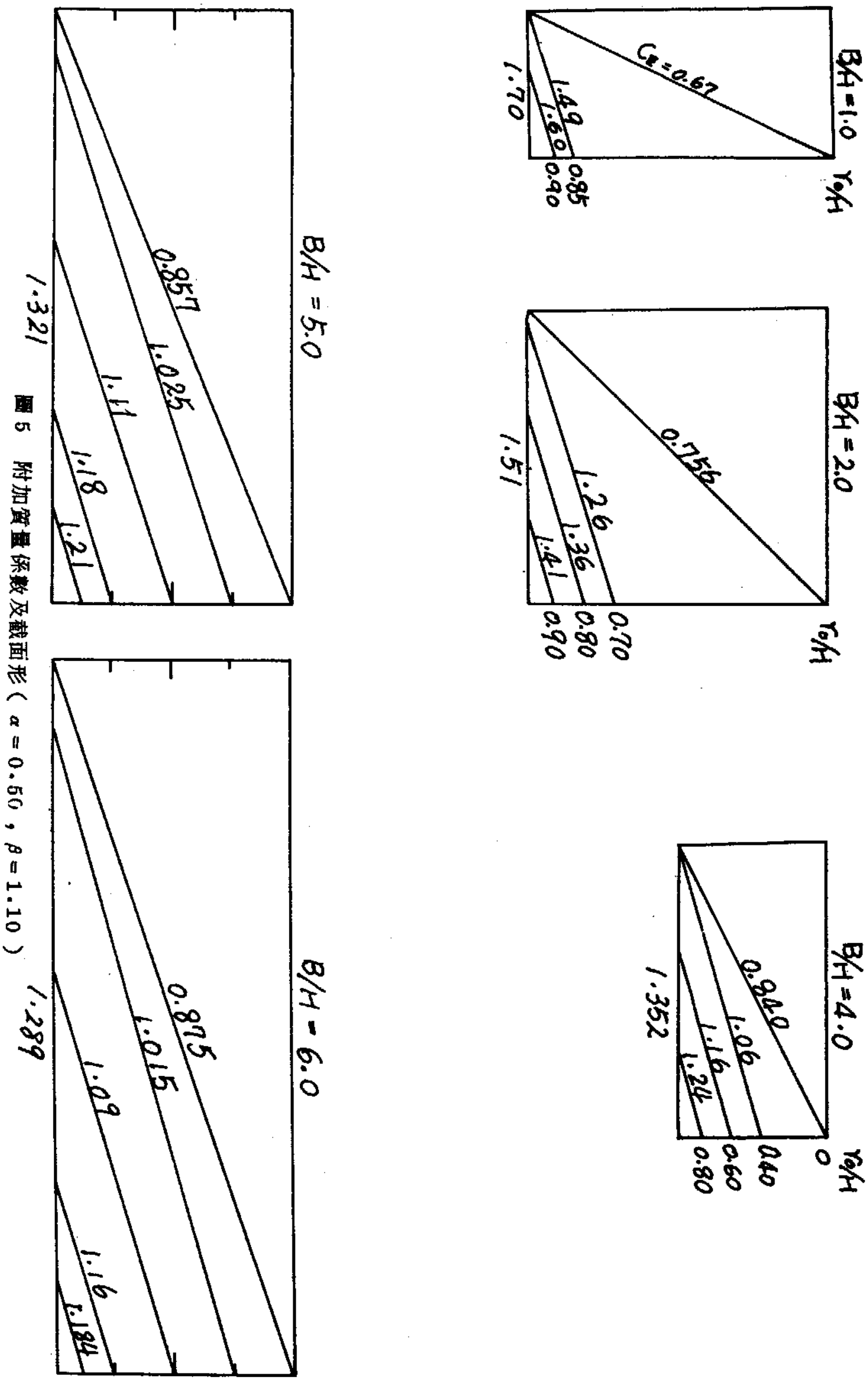

圖 5　附加質量係數及截面形（α = 0.50，β = 1.10）

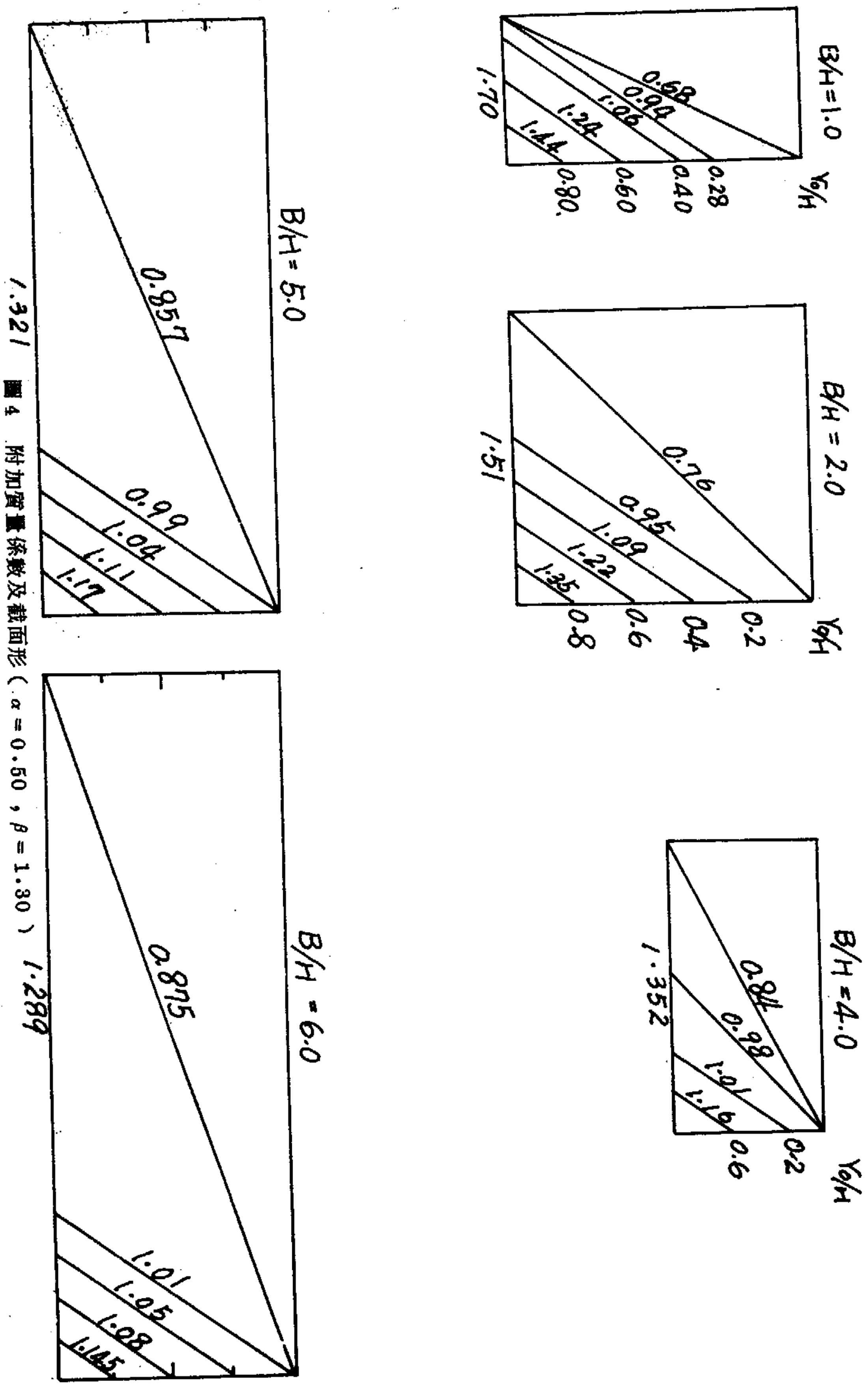

圖4 附加質量係數及截面形（α＝0.50，β＝1.30）

NEW SEISMIC DATA OF TAIWAN REGION

Y. B. Tsai, T. L. Teng*, Y. M. Hsiung and C. M. Lo

Seismology Division, Institute of Physics

Academia Sinica

The Republic of China

Abstract

A modern telemetered seismic network has been established in Taiwan. Currently 13 stations are in operation. This network, when completed, will consist of 19 stations distributed throughout Taiwan and its offshore islands. Seismic signals are telemetered to Taipei and recorded both by drums and on magnetic tapes as well as on films. Seismic data obtained thus far have shown (1) a marked increase in the number of detected and located events through a significant lowering of detection threshold from magnitude 4 to 2; (2) a great improvement in epicenter location from an uncertainty of 25 km to less than 5 km for most of the events; and (3) the most active and widespread seismic zone of Taiwan is on the east coast of Taiwan extending from Suao southward, passing through Hualien and ending at Taitung. Two other active seismic zones are the Miaoli-Taichung area in the northwest and the Chiayi-Tainan area in the southwest of Taiwan.

1. *Introduction*

Taiwan is located on the Circum-Pacific seismic belt. It suffered from numerous damaging earthquakes in the past. In view of the accelerating pace of major engineering and housing constructions at home plus the staggering dollar loss caused by devastating earthquakes abroad in recent years, it has become apparent that the nation can no longer afford to take seismic hazards lightly if severe destructions from future earthquakes are to be avoided. Thanks to its farsightedness the government of the Republic of China, through its National Science Council, inaugurated a comprehensive earthquake research program in 1972. Since then an islandwide telemetered short-period seismograph network has been installed in Taiwan as an integral part of the program. The purpose of this article is to give a brief description of the modern Taiwan Seismograph Network and to present some new seismic data obtained thereof.

2. *A New Seismic Network in Taiwan*

The Central Weather Bureau maintains an old seismic network in Taiwan installed some seventy years ago. The instruments are obsolete and the data are poor in quality in

---

* Department of Geological Sciences University of Southern California Los Angeles, California, U.S.A.

terms of modern standards. It is thus natural that installation of a modern seismic network should have become the first major item of a comprehensive seismic research program. In view of the excellent telecommunication facilities available in Taiwan and in order to ensure high data quality, it was decided at the outset that the new islandwide seismograph network would be a telemetered one with a recording center located in Taipei. Following several months of program planning and personnel training, actual installation of this network got under way in August 1972. By the end of 1972 nine seismograph stations were in operation. Since then four other stations have been added. Still six more stations in more remote areas or the offshore islands are being installed or planned. When completed the new Taiwan Seismic Network will consist at least nineteen stations distributed throughout Taiwan and its offshore islands. Figure 1 shows the locations of these new seismic stations in operation (solid dots) and to be installed (open Circles). The coordinates of the thirteen stations in operation are given in Table 1. Most of our stations are occupied by a Mark Products L-4C vertical-component seismometer. A few stations are equipped with a Mark Products L-4-3D three-component seismometer. The natural frequency of these short-period seismometers is 1 H_Z. In addition to the seismometer, each telemetered seismic channel also consists of a Develco VCO/Amplifier, a Develco discriminator and a recording device. The recording devices presently available at our recording center include a Geotech develocorder, two Bell & Howell 14-track analog tape units and twelve kinemetric drum recorders. Our system is essentially the same as the one operating in Central California by the National Earthquake Research Center of the U. S. Geological Survey. A typical system response curve is shown in Figure 2. An ELDORADO crystal clock and time code generator is used to provide timing signals to all seismic channels at our Taipei recording center. The new Taiwan telemetered seismic system may be summarized by a block diagram in Figure 3.

3. *Some* Seismic *Data of Taiwan*

The new islandwide telemetered seismic system began to operate as a network since the winter of 1972. Seismic data obtained so far showed that a marked increase in the number of detected and located events through a significant lowering of threshold magnitude from 4 to 2. Figure 4 shows the epicenteres of earthquakes located by means of the new seismic network during the first three months of 1973. According to the data, three active seismic zones can be recognized. The most active and widespread seismic zone is located on the east coast extending from Suao southward passing through Hualien, Yuli until Tatung, Lutao. Two other less active zones are found in Miaoli-Taichung area in the northwest and in Chiayi-Tainan area in the southwest, respectively, This spatial pattern of seismic activity apparently persisted into the following three months from April to June as shown in Figure 5. It is noticed however that some subtle changes in epicentral distribution did take place in the same time. For instance, in Taipei-Taoyuan area in northern Taiwan, there were some earthquakes appeared in the second quarter whereas none was located during the preceding quarter. On the other hand, in the area between Lutao and Lanhsu, the two offshore islands off the southeast coast of Taiwan, the seismic activity appeared to have subsided from the first quarter to the second quarter of 1973. Apart from these temporal changes, seismic data of small earthquakes ($M > 2.0$) obtained from the first six months of operation of the new network generally showed a similar pattern of epicentral distribution as seismic data of larger earthquakes ($M > 4.0$) obtained by the World-wide Network of Standard Seismographs in the preceding twelve years, as shown in Figure 6. Furthermore, the b parameter in the relation $\log N = a - bM$ determined from new seismic data, as shown in Figure 7, is found to have the same value of 1.0 as that determined from past seismic data, as shown in Figure 8. The similarities between these two sets of data in both the epicentral distribution pattern and the b parameter value are suggestive that the small earthquakes located presently by the new seismic network and the larger earthquakes located previously in the same areas by the old seismic network might have originated from common tectonic processes. This is particularly reassuring because we can now use the more numerous small earthquakes recorded by the new network as convenient intermediaries for understanding the less frequent devastating earthquakes which are our main concerns after all.

The new seismic network in Taiwan not only detect more earthquakes but also provide better locations of the earthquake epicenters. The uncertainty of epicenter location is improved significantly from about 25 km to less than 5 km for most of the earthquakes, especially for those located inside the network. This improvement has been verified by excellent agreements in epicenters of same earthquakes independently located by using the telemetered network data and by using local array data. Two actual examples are presented below to illustrate this point. Figure 9 shows the epicenters of a $M = 3.8$ earthquake occurred in Tainan area near the telemetered station TWN on 31 August 1973 and its aftershocks. Following the main shock a local array of four temporary stations was set up to operate in the epicentral area. The epicenters of aftershocks in the first three days defined an elongated zone denoted by the dashed curve in Figure 9. The epicenter of main shock determined by means of the telemetered network, as shown by the big dot in Figure 9, fits right into the aftershock zone. The second example concerns a $M = 4.5$ earthquake occurred near our telemetered station TWT at Tachien area in the Central Mountain Range on 24 December 1973. Three days after the main shock a local array of five temporary stations was set up to operate in the area for two weeks. More than 200 aftershocks were located by the local network. The epicenters of these aftershocks are shown in Figure 10. The epicenters of the main shock and the largest aftershock, as located by means of the islandwide seismic network, again fit right into the aftershock zone. Since the aftershock epicenters have been precisely located by means of local array data, these excellent agreements are undoubtedly indicative of the high precision of epicenter location resulting from the new islandwide telemetered seismic network.

4. *Conclusions*

A modern telemetered seismic network has been installed throughout Taiwan since late 1972. High-quality seismic data obtained thus far, showed a marked increase in the number of events detected and located resulting from a significant lowering of detection threshold from magnitude 4 to 2. Moreover, a substantial improvement of epicenter location was also realized. The uncertainty of epicenter location was reduced from 25 km to less than 5 km. Although some subtle temporal variations of seismicity were recognized, the present pattern of seismic activity in Taiwan is essentially the same as in the past. There exist three major active seismic zones in Taiwan. The most active and widespread seismic zones is on the east coast extending from Suao southward through Hualien until Taitung. The other two active zones are in Miaoli-Taichung area in the northwest and Chiayi-Tainan area in the southwest, respectively. Seismic data from the new telemetered network in Taiwan are being routinely processed and published in a quarterly entitled "Catalog of Earthquakes in Taiwan" since the beginning of 1973.

Acknowledgements

Our special thanks are due to Drs. W. H. K. Lee, C. Y. King, F. T. Wu and S. K. Yiu for their enthusiatic participation in planning the new seismic network in Taiwan. The work was supported by the National Science Council, Republic of China.

Table 1 Station Codes and Coordinates of Taiwan Seismic Network

CODE	LOCATION	LAT-N	LONG-E
TWA	MUCHA	24 58.82	121 35.02
TWC	SUAO	24 36.55	121 50.93
TWD	CHIAWAN	24 04.89	121 35.73
TWF	YULI	23 20.95	121 17.75
TWG	PINGLANG	22 49.24	121 04.30
TWK	HENGCHUN	22 00.03	120 45.18
TWM	SHOUSHAN	22 38.50	120 15.09
TWN	HSINYING	23 16.00	120 29.28
TWO	MEISHAN	23 34.57	120 32.97
TWQ	TUNGSHIH	24 16.48	120 50.15
TWR	CHUTUNG	24 38.41	121 04.72
TWS	KUANGYINSHAN	25 07.70	121 24.87
TWT	TACHIEN	24 15.20	121 10.55

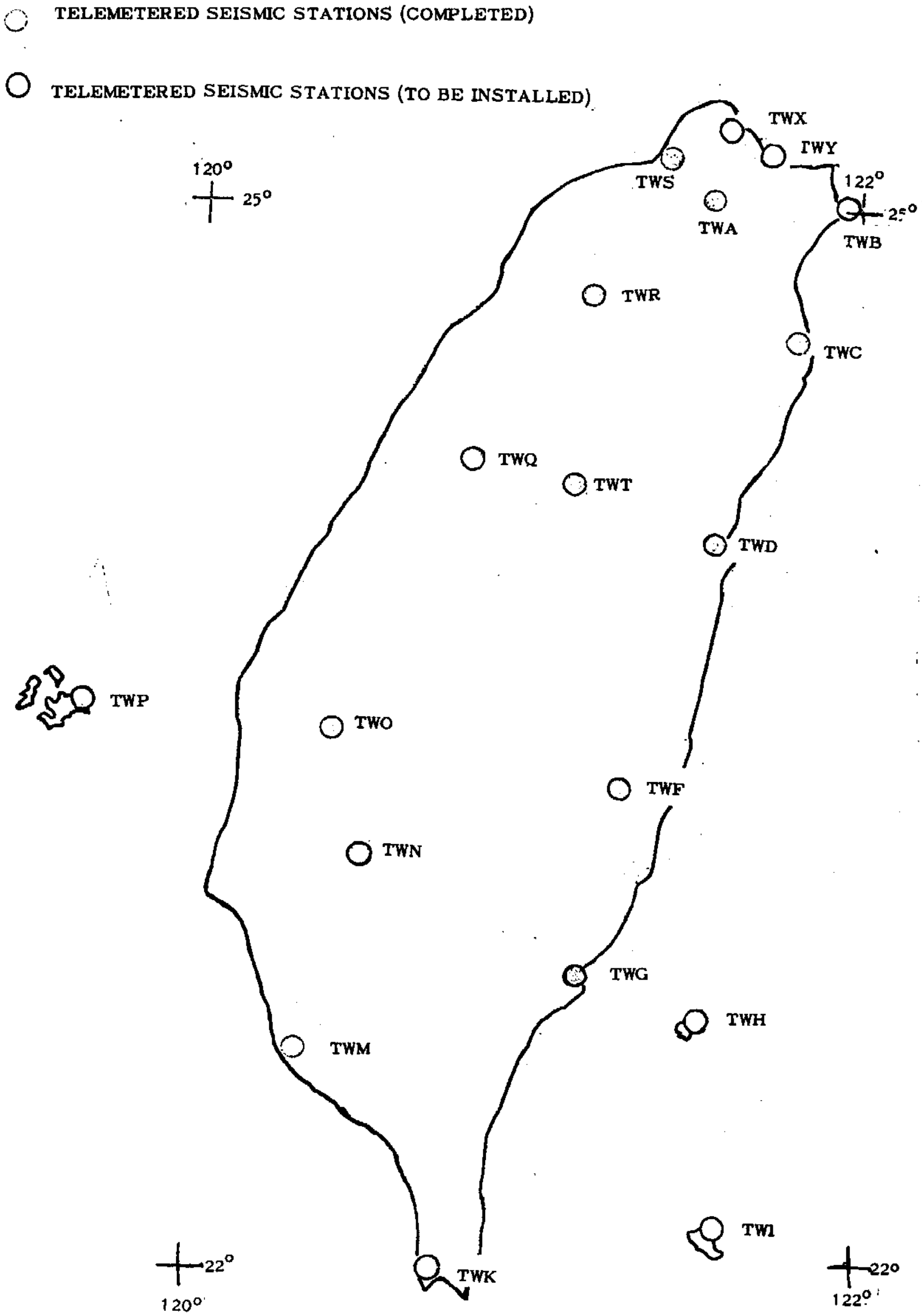

Figure 1. TAIWAN SEISMIC NETWORK

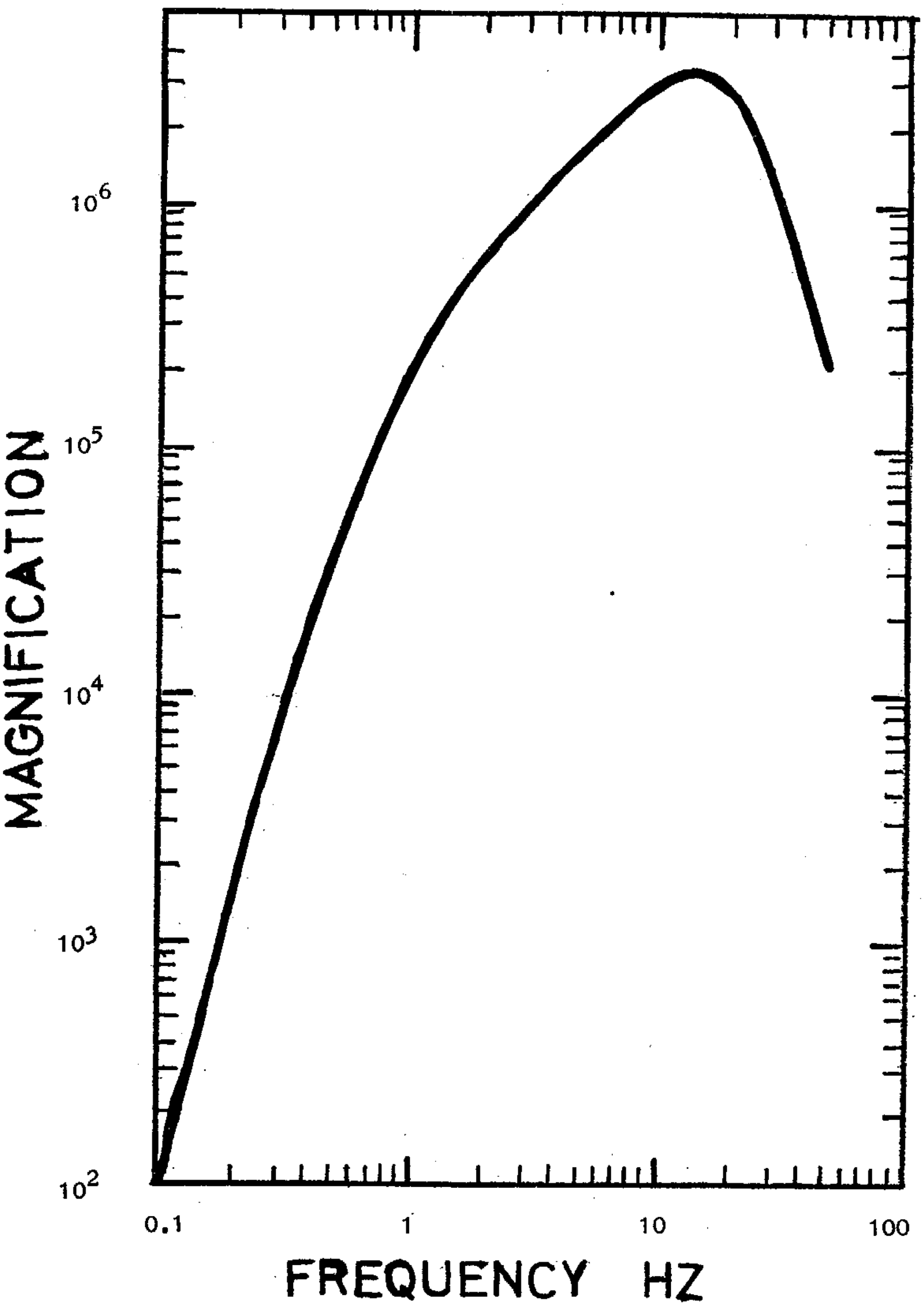

Figure 2 SYSTEM RESPONSE OF A TYPICAL CERC TELEMETERED SEISMOGRAPH STATION.

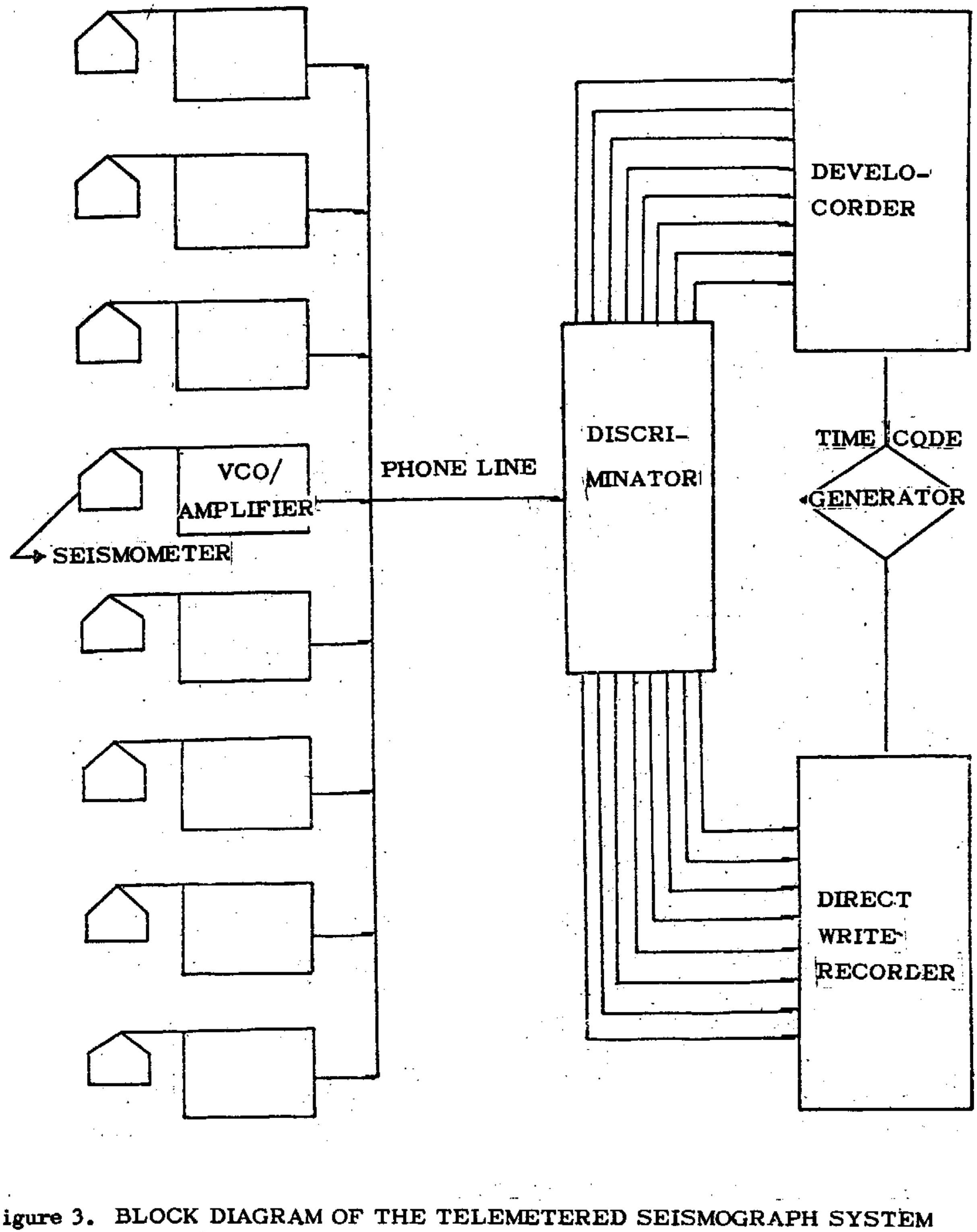

Figure 3. BLOCK DIAGRAM OF THE TELEMETERED SEISMOGRAPH SYSTEM

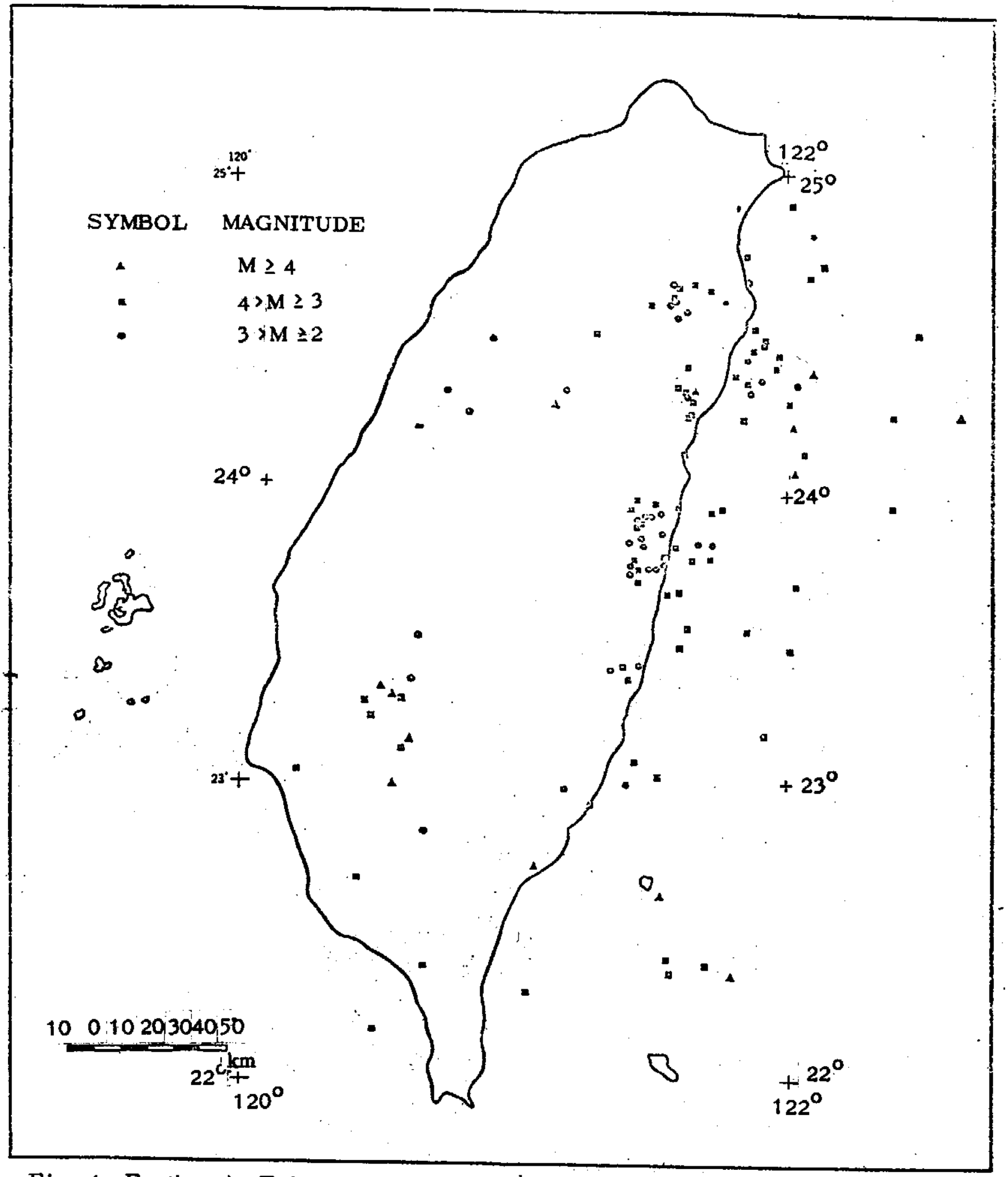

Fig. 4 Earthquake Epicenters from Jan 1 to Mar 31 1973

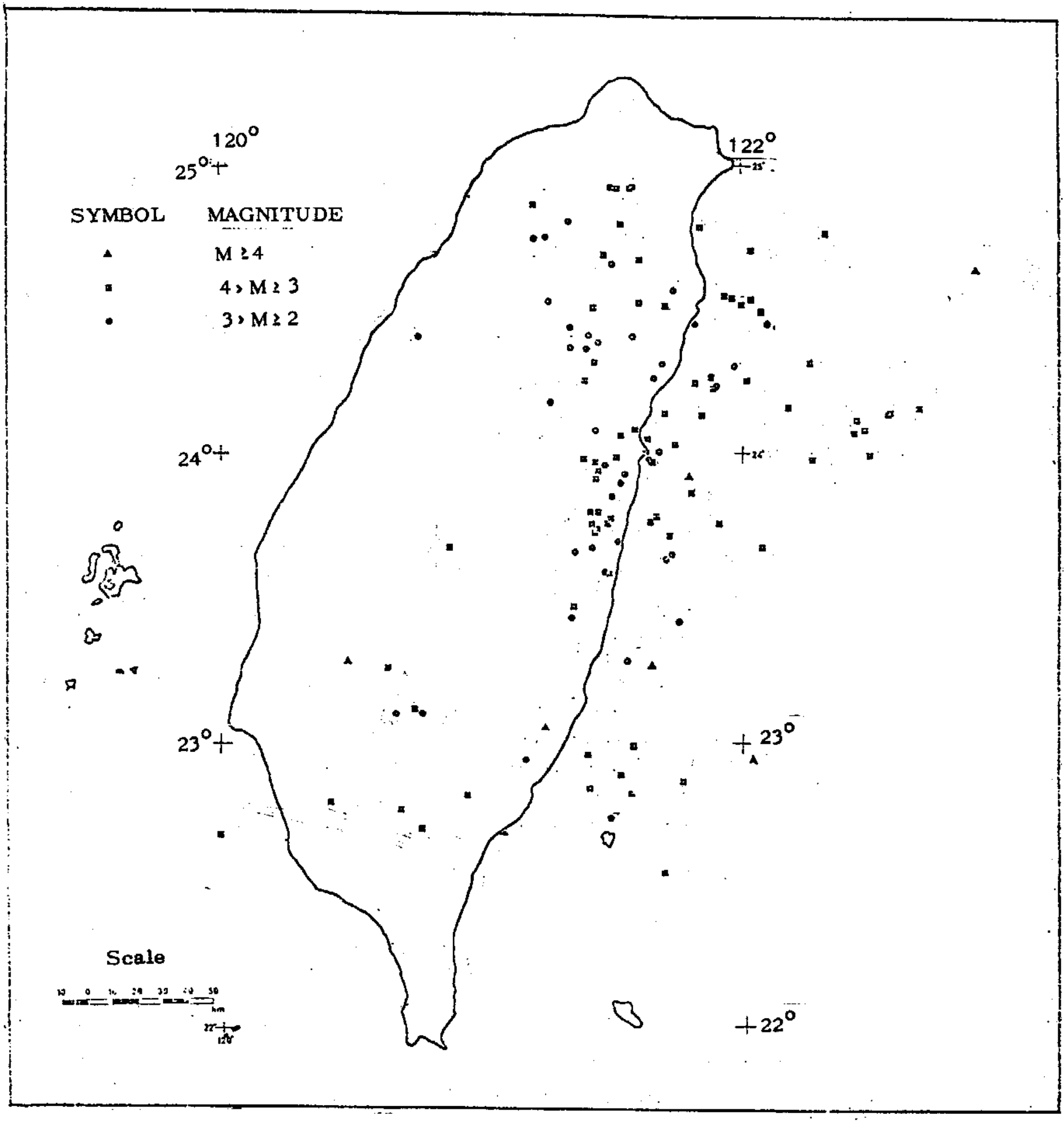

Fig. 5 Earthquake Epicenters from April 1 to June 30 1973

Fig. 6 SEISMICITY OF TAIWAN 1961-1972

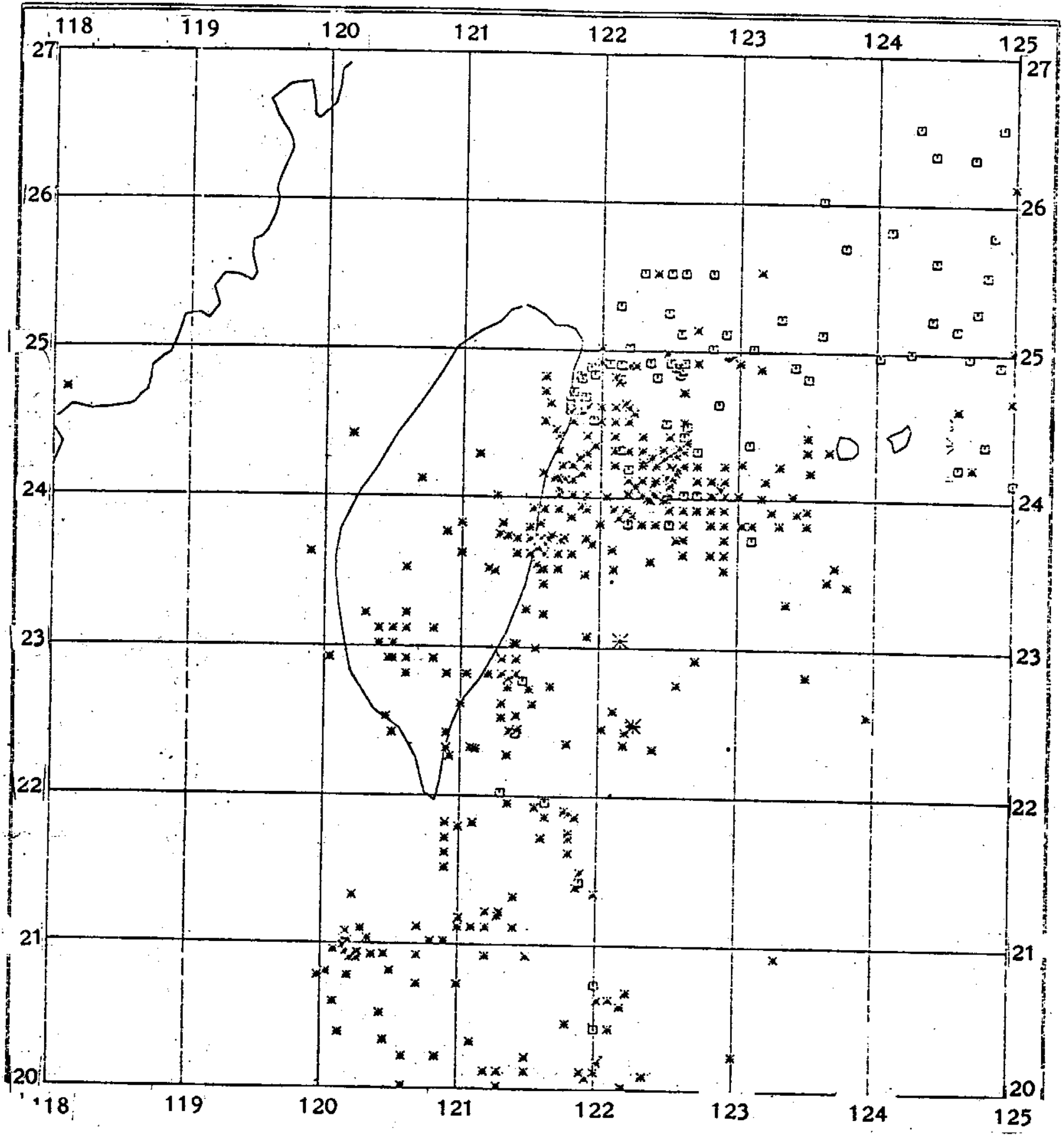

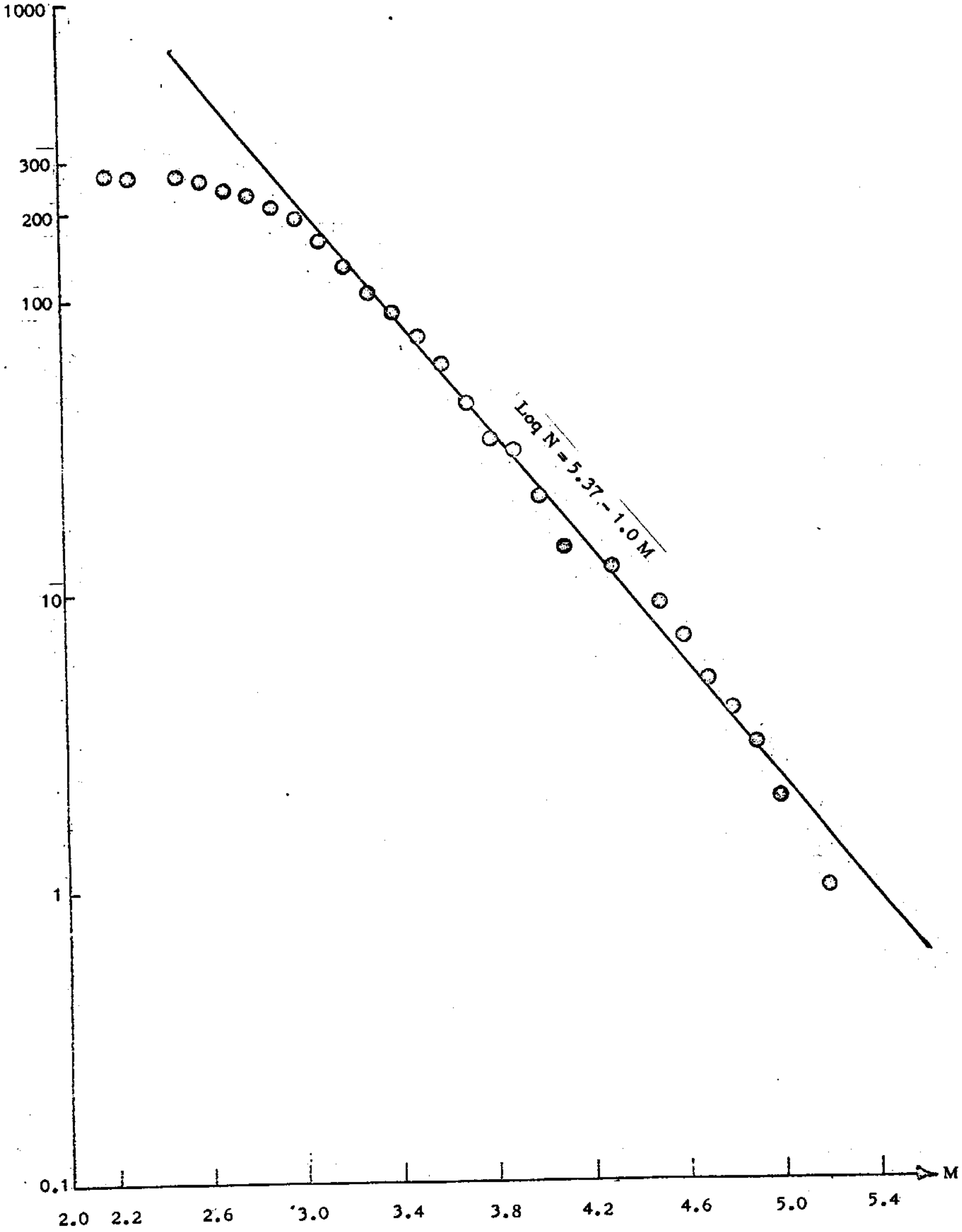

Fig. 7 THE NUMBER OF EARTHQUAKES VERSUS MAGNITUDE FROM Jan 1973 TO June 1973

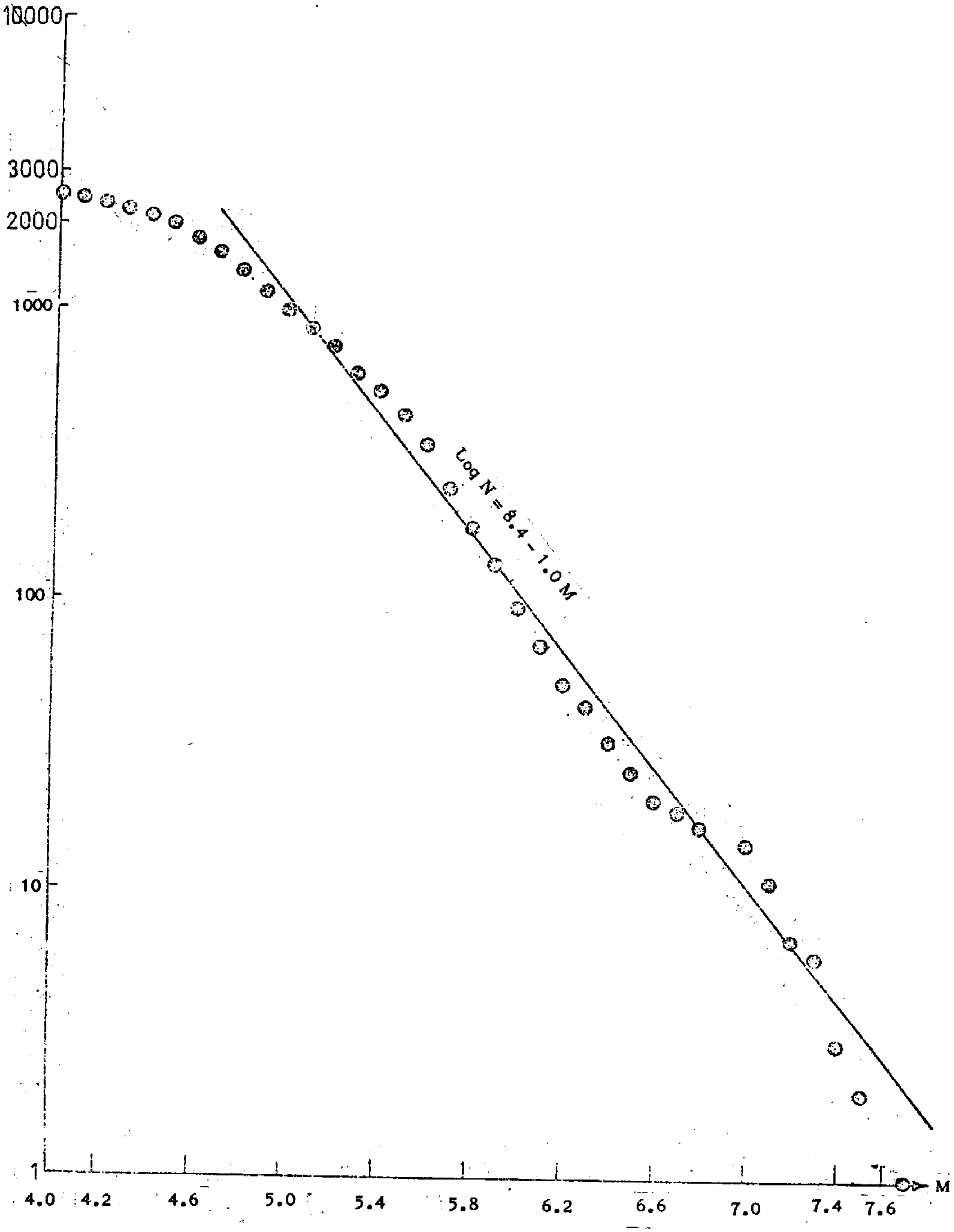

Fig. 8 THE NUMBER OF EARTHQUAKES VERSUS MAGNITUDE

Fig 9 EARTHQUAKE EPICENTERS IN THE CHIAYI-TAINAN AREA(Aug. 27 to Sep. 30, 1973)

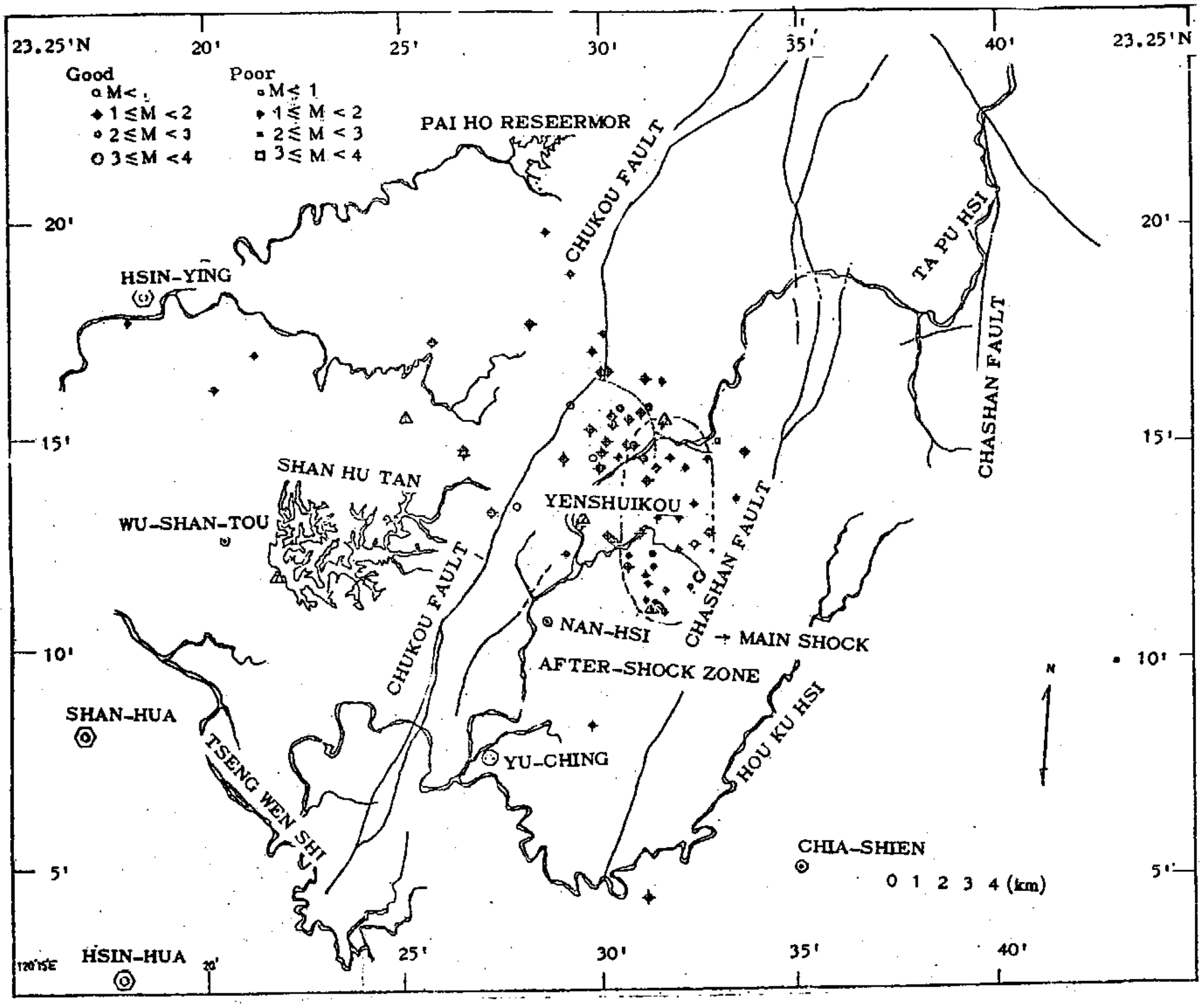

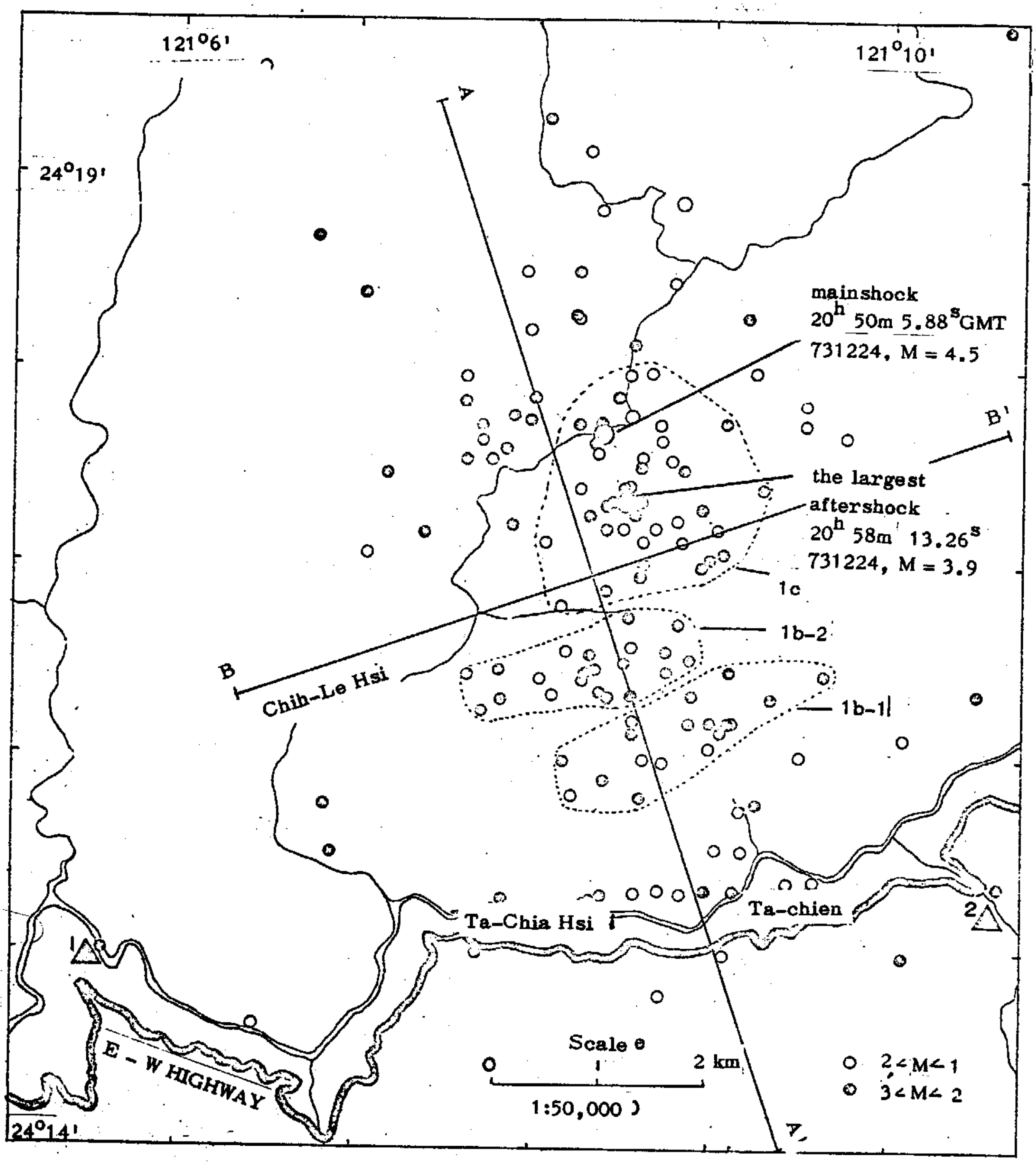

Fig. 10. Epicenters of the mainshock and aftershocks of the Tachien sequence.

ANNUAL REPORT OF THE INSTITUTE OF PHYSICS, ACADEMIA SINICA 1973

A STUDY OF MICROEARTHQUAKES IN THE TATUN VOLCANIC REGION IN NORTHERN TAIWAN

Y. B. Tsai, H. B. Liaw and C. C. Feng
Seismology Division, Institute of Physics
Academia Sinica
The Republic of China

July, 1974

Abstract

Microearthquakes have been observed in the southern zone of Tatun Volcanic Region in northern Taiwan. A close spatial relationship between microearthquakes and geothermal activity in the area is recognized. Microearthquakes are located primarily on or near the faults adjacent to rather than inside the zones of hydrothermal alteration. The focal depths of these microearthquakes are confined mostly in the upper six kilometers of the crust. Both normal faulting and thrust faulting types of earthquake source mechanism are found in the Tatun Volcanic Region. No earthquake with magnitude greater than 4 is known to have occurred in the Tatun geothermal area in the past several decades.

1. *Introduction*

Occurrence of small earthquakes in major geothermal areas is common (Ward, 1972). A study of microearthquakes in a geothermal area can be useful in the following ways:

1. Faults in many geothermal areas appear to provide zones of high permeability allowing convection of heat to the surface. Since earthquakes take place on faults, the location of potentially permeable zones at depth beneath a geothermal region can be determined by accurately locating the earthquakes. The best production wells might be drilled near these potentially permeable zones.
2. Fault motion during earthquakes may increase or decrease the flow of hot water from depth and thus could profoundly affect the longevity of a geothermal field. Prior knowledge about the properties of these earthquakes will be helpful in determining how geothermal fluids should be extracted and reinjected.
3. Finally, earthquake hazards need to be considered when building structures in the geothermal areas.

The purpose of this paper is to present new data from recent observations on where microearthquakes occur in the Tatun Volcanic Region in northern Taiwan and what are the properties of these earthquakes.

The Tatun Volcanic Region occupies an area 18 km x 18 km at the northern tip of Taiwan. It is divided by the northeast striking Chinshan Fault into a northern zone of more basic andesites and a southern zone of less basic andesites. All the hot springs, fumaroles and four young volcanoes in the Tatun Volcanic Region are located in the southern zone. The volcanic formations have been mapped as Pleistocene, but the four young volcanoes in the southern zone can be regarded as Recent. Underlying the volcanic rocks with pronounced uncomformity are formations of Miocene sandstones and shales. The sandstone formations generally strike northeast and dip southeast at angles of 10° to 20°. Sandstones are not exposed in the southern zone of the Tatun Volcanic Region except at a few places. The Chinshan Fault is an overthrust fault striking east-northeast and dipping southeast. The southern boundary of the Tatun Volcanic Region is defined by the Kanchiao Fault which is another overthrust fault parallel to the Chinshan Fault. Aparts from these two major faults there are numerous minor faults inside the Tatun Volcanic Region.

2. *Microearthquake Activity in the Tatun Volcanic Region*

A first survey of microearthquakes in the Tatun Volcanic Region was made during February 1974. Nine temporary stations equipped with sensitive portable seismographs and two permanent stations, TWA and TWS, of the islandwide telemetered seismographic network were deployed in the Tatun Region and the Hsintien Region, northeast and southeast of the capital city of Taipei, respectively. The total area covered during this survey was approximately 1600 km^2. The location of these stations is given in Table 1 and also shown by the open triangles in Figure 1. Each portable seismograph consists of a short-period vertical seismometer, a smoke-paper drum recorder and a chronometer. The system is battery powered. Normally, the internal timing was checked with the standard time broadcasting both at the beginning and the end of each record.

The computer program HYPO71 using the Geiger's method for locating earthquake hypocenter and origin time was adopted for the present study. The program was developed originally by Eaton (1969) and modified later by Lee and Lahr (1971) for studying earthquakes in California. In order to locate an event, at least three readings of P-wave first arrival time plus one reading of S-wave arrival time must be available simultaneously at three stations. Thus, the number of locatable earthquakes is considerably less than the number of events recorded at individual stations. In general, the precision of reading the P-wave first arrival times is within 0.05 second, whereas the precision of reading the S-wave arrival times is poorer and can be as large as 0.2 second.

Since the elevation of stations differed as much as 790 meters, a correction of arrival times for elevation was made approximately according to the following formula:

$$\delta t_e = -\frac{H}{V}$$

where H is station elevation in kilometers, V is seismic wave velocity of rocks above the mean-sea level in kilometer/second. Finally, δt_e represents the correction of arrival time in seconds to be added to the observed arrival time. According to the coring data obtained from the southern zone of Tatun Volcanic Region by the Mining Research and Service Organization (MRSO), the P-wave velocity of the volcanic rocks ranges from 2.8 km/sec to 4.3 km/sec. A medium value of 3.3 km/sec is adopted for the present purpose. The corresponding elevation corrections of P-wave arrivals for all stations are also given in Table 1. The crustal model used for hypocentral location is given in Table 2. The precision of hypocentral location is believed to be well within one kilometer for earthquakes inside the recording seismographic network.

Finally, the earthquake magnitude M is defined according to the following formula:

$$M = -0.87 + 2.0 \log \tau + 0.0035 \Delta$$

where τ represents the total signal duration in seconds and Δ is epicentral distance in kilometers.

In all, twelve earthquakes were located during one month of recording. Three of these events were located in the Hsintien Region and nine in the Tatun Volcanic Region. Pertinent data of these earthquakes are given in Table 3. The epicenters of these microearthquakes are further shown in Figure 1. It is evident from the figure that microearthquake activity in the Tatun Volcanic Region is confined in a small area centered at Station 11 in the southern zone. The magnitudes of these events range from 0.8 to 2.1. Most of these microearthquakes were located in the upper 6 kilometers. Only one out of the twelve events were determined at a greater depth of 9.3 kilometers. It is also interesting to note that none of the events located in the Tatun Region took place south of the Kanchiao Fault. In addition to the nine locatable events mentioned above there were twenty-three more local microearthquakes with P-S intervals less than 1.5 seconds observed at Station 1 or Station 11. These events were too small to be recorded at other stations, and thus could not be located precisely. They were however probably all in the southern zone of Tatun Volcanic Region just like the nine larger locatable events.

In order to examine more closely the relation between geothermal activity and microearthquakes, epicenters of the nine events are superimposed on the geologic map of the southern zone of Tatun Volcanic Region. As shown by dots in Figure 2, the nine events determined in this first survey were all located outside the hydrothermal areas even though there were faults in these areas. This is not suprising since in all likelihood rocks directly beneath hydrothermal areas might have been too weakened to sustain sufficient tectonic strains for earthquake to occur. Instead, these microearthquakes appear to take place on or near faults in the areas immediately adjacent to the hydrothermal areas.

In order to follow up the first survey mentioned above, a second survey of microearthquakes was made specifically over the southern zone of the Tatun Volcanic Region centering around Station 11 for 16 days from 25 April to 10 May 1974. Five temporary stations were set up in a small area centered at Station 11 with a radius of approximately 5 kilometers. The coordinates of these stations are given in Table 4. They are also shown in Figure 1 by open squares. During this period of sixteen days seventy-one microearthquakes with magnitude $M \geqq 0.1$ were recorded at one or more stations. Among them only eleven events were large enough to be located. Pertinent data of these earthquakes are given in Table 5. Their epicenters are again shown by crossed circles in Figure 2 along with the nine other events located during the first survey. It is seen from this figure that the microearthquakes located in the second survey are more widespread than the first one. This is probably due to artificial difference in the configuration of recording networks employed in the two surveys. It is again found that all microearthquakes were located on or near faults in the areas adjacent to the hydrothermal areas instead of inside these hydrothermal zones. The fact that microearthquakes took place in adjacent areas of the hydrothermal zone appears to suggest that hot water at depth may play an important role in causing microearthquakes on faults immediately outside the hydrothermal areas. The most widely accepted mechanism for this effect of fluids on earthquake occurrence involves pore pressure (Hubbert and Rubey 1959). If T is the shear stress on a fault plane, T_o is the intrinsic strength, S_n is the normal stress across the fault plane, P is the pore pressure, and μ is the coefficient of friction, then

$$T = T_o + \mu(S_n - P)$$

The effect of increasing the pore pressure is thus to reduce the frictional resistance to slippage by decreasing the normal stress across the fault plane.

Similar to earlier results from the first survey, the focal depths of these eleven microearthquakes were confined primarily at 4 or 5 kilometers.

After reviewing earthquake activity in many geothermal areas in various parts of the world, Ward (1972) has pointed out that earthquakes with magnitudes greater than about 4.5 seem to be very rare in the crust under geothermal areas even though most geothermal areas occur near the major seismic belts around the world. The Tatun Volcanic Region appears to have this phenomenon too. Figure 3 shows the epicenters of all earthquakes with magnitudes greater than 4.0 located in Northern Taiwan between the years 1936 and 1969 (Hsu, 1971). There was only one earthquake with magnitude between 4.0 and 4.9 took place in the Tatun Volcanic Region during the 34-year period. In other words, earthquake activity in the Tatun Volcanic Region can be considered as typical among the geothermal areas in that microearthquakes are frequent and shallow, but their magnitudes rarely exceeds 4.5. Thus, it appears that local seismicity will not be a major concern in terms of earthquake hazards in the Tatun Volcanic Region. Nevertheless, vibrations due to large earthquakes in the Ilan area could be strong enough to cause structural damages in the Tatun region.

In order to find what are the properties of microearthquakes in the Tatun Volcanic Region, two composite fault plane solutions based on an equal-area projection of the lower hemisphere of the polarities of P-wave first motion are obtained from records of four earthquakes located near Station 11 in the first survey during February 1974. These two composite fault plane solutions represent two distinctively different types of source mechanism for earthquakes in the Tatun Volcanic Region. Figure 4 shows the first type of earthquake source mechanism representing a normal fault. One nodal plane strikes N 37° E and dips N 50° W. Another nodal plane strikes N 45° E and dips S 40° E. The first nodal plane is consistent with surface faults in the area and thus may be taken as the actual fault plane. Figure 5 shows a second type of earthquake source mechanism representing an overthrust fault in the same general area as the first type of normal faulting earthquakes. One of the two orthogonal nodal planes is found to strike N 60° E and dip S 50° E. The other nodal plane strikes N 14° E and dip N 30° W. The first nodal plane possesses properties similar to the underlying Chinshan Fault and thus may represent a physical fault plane. In any case, these fault plane solutions indicate that both normal and overthrust faults are present in the Tatun Geothermal Area near Matsao.

3. *Conclusions*

Two detailed surveys of microearthquakes in the Tatun Volcanic Region were made during February and April 1974, respectively The outcomes can be summarized as the following:

1. All microearthquakes recorded in the Tatun Volcanic Region occurred in the southern zone defined by the Chinshan Fault on the northwest side and the Kanchiao Fault on the southeast side. Microearthquake activity was associated with local faults adjacent to the areas of greatest geothermal activity observed at the surface.

2. Most microearthquakes in the Tatun Volcanic Region occurred at depths of less than 6 km. Some events were as deep as 9 km.

3. Past data showed that earthquakes with magnitudes greater than 4.0 did not occurred in the southern zone of Tatun Volcanic Region where microearthquake activity was present.

4. Two distinct types ot source mechanism were found from microearthquakes in

the Tatun Volcanic Region. Microearthquakes having overthrust faulting source mechanism were probably related to the Chinshan Fault, whereas microearthquakes having normal faulting source mechanism were related to other minor normal faults observed in the Tatun Volcanic Region.

Acknowledgements

We thank Messrs. Y. T. Yeh, W. S. Liu, Y. S. Cheng and C. C. Hsu for their assistance in the field operations. Cooperation with the Mining Research and Services Organization was appreciated. The project was supported partly by Taiwan Power Company and partly by the National Science Council, Republic of China.

References

1. Eaton J. P., Hypolayr - a computer program for determining hypocenters of local earthquakes in an earth consisting of uniform flat layers over a half space, *U. S. Geological Survey*, Open File Report, 155 p., 1969.
2. Hsu. M. T., Seismicity of Taiwan & Some Related problems, Bulletin of International Institute of Seismology and Earthquake Engineering vol. 8 pp. 41 - 160, 1971.
3. Hubbert M. K., Rubey W. W. - Role of fluid pressure in mechanics of overthrust faulting. I mechanics of fluidfilled porous solids and its application to overthrust faulting. Bull. Geol. Soc. Amer. 70, 115 p., 1959.
4. Lee W. H. K., J. C. Lahr, HYPO71 – a computer program for determining hypocenter, magnitude & first motion pattern of local earthquakes, *U. S. Geological Survey*, Open File Report, 100 p., 1972.
5. Ward P. L., Microearthquakes – Prospecting tool & possible hazard in the Development of Geothermal Resources, Geothermics vol. 1, No. 1, pp. 3-12, 1972.

Table 1 Seismic recording stations in the Tatun and Hsintien Regions between 1 February and 6 March 1974

Station No.	Lat. (N)	Long. (E)	Elevation (M)	Station correction (sec)
1	25° 10.32′	121° 33.17′	790	- 0.26
2	25° 14.46′	121° 36.60′	30	- 0.01
3	25° 11.90′	121° 33.47′	0	0.0
4	25° 06.46′	121° 40.15′	210	- 0.07
5	25° 06.36′	121° 35.15′	210	- 0.07
6	24° 51.74′	121° 32.85′	200 200	- 0.07
7	24° 59.04′	121° 29.04′	150	- 0.05
8	24° 55.76′	121° 25.21′	90	- 0.03
19	24° 57.55′	121° 37.50′	465	- 0.14
11	25° 10.14′	121° 33.54′	790	- 0.26
TWA	24° 58.82′	121° 35.02′	260	- 0.09
TWS	25° 07.70′	121° 24.87′	300	- 0.09

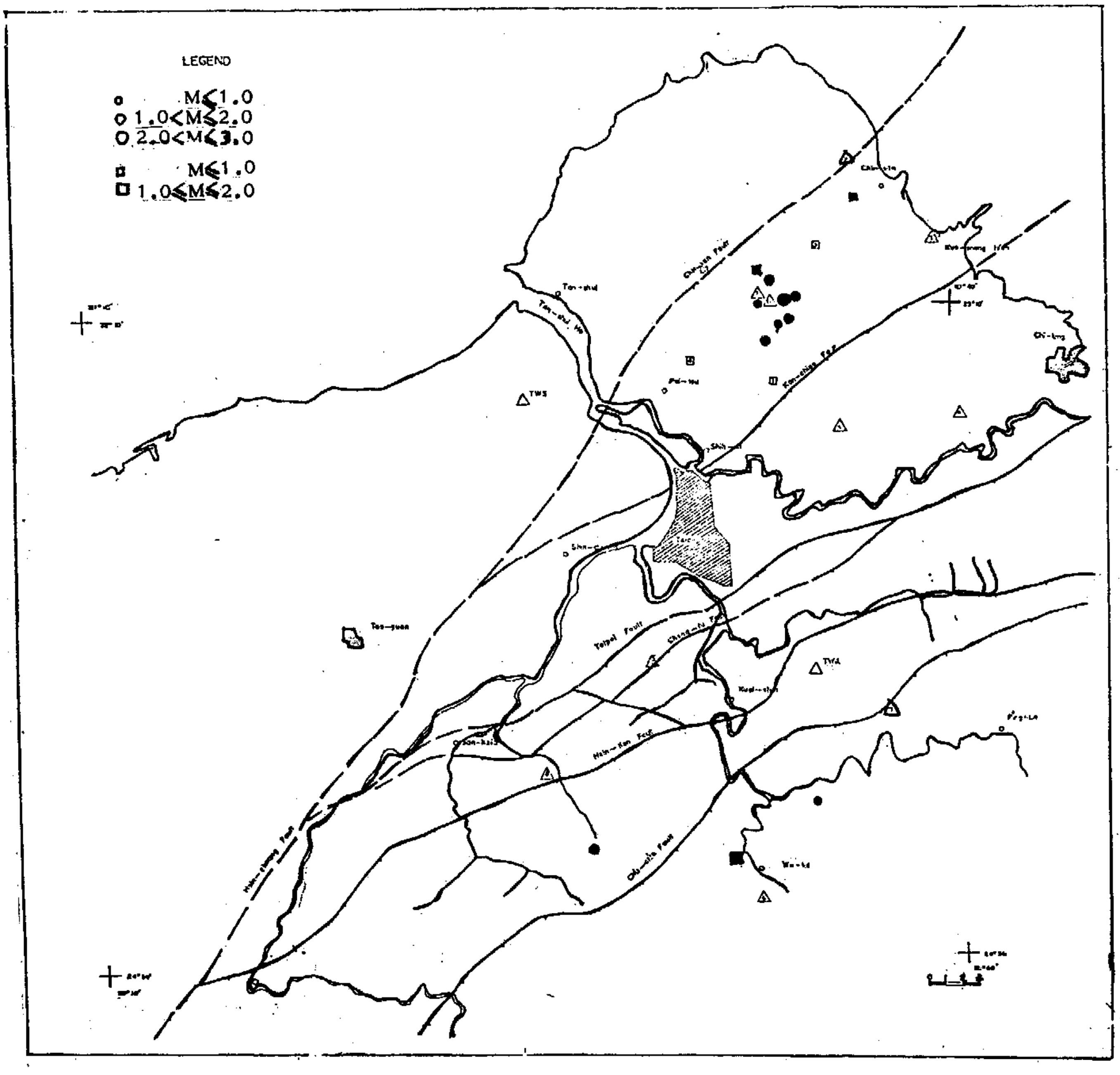

Figure 1. Locations of seismic stations, denoted by open triangles and squares, set up to observe microearthquakes in Tatun and Hsintien areas in northern Taiwan. Epicenters of microearthquakes located during February-March 1974 are shown by the solid dots and squares.

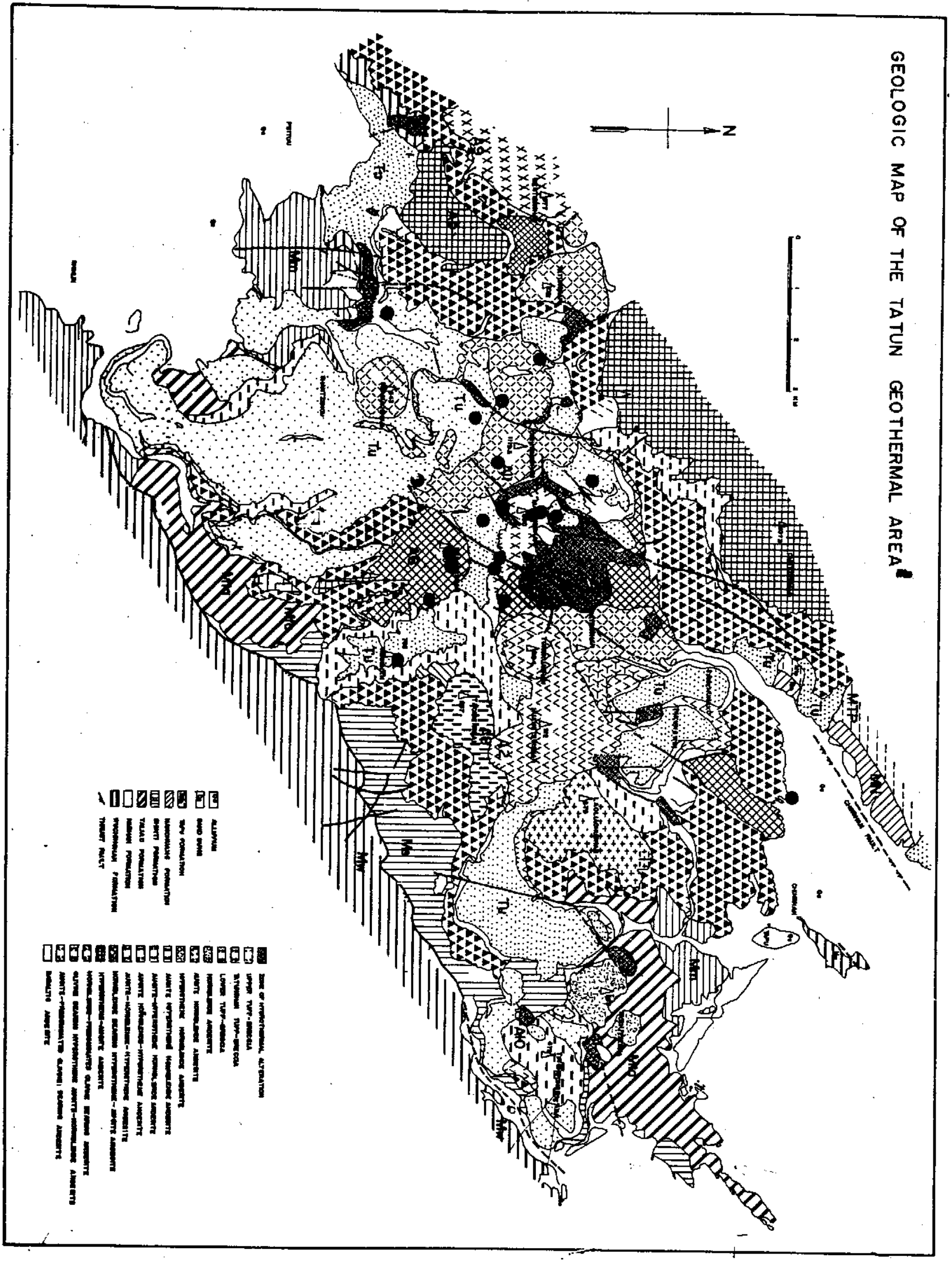

Figure 2. Epicenters of microearthquakes shown on the geologic map of the Tatun Volcanic Region.

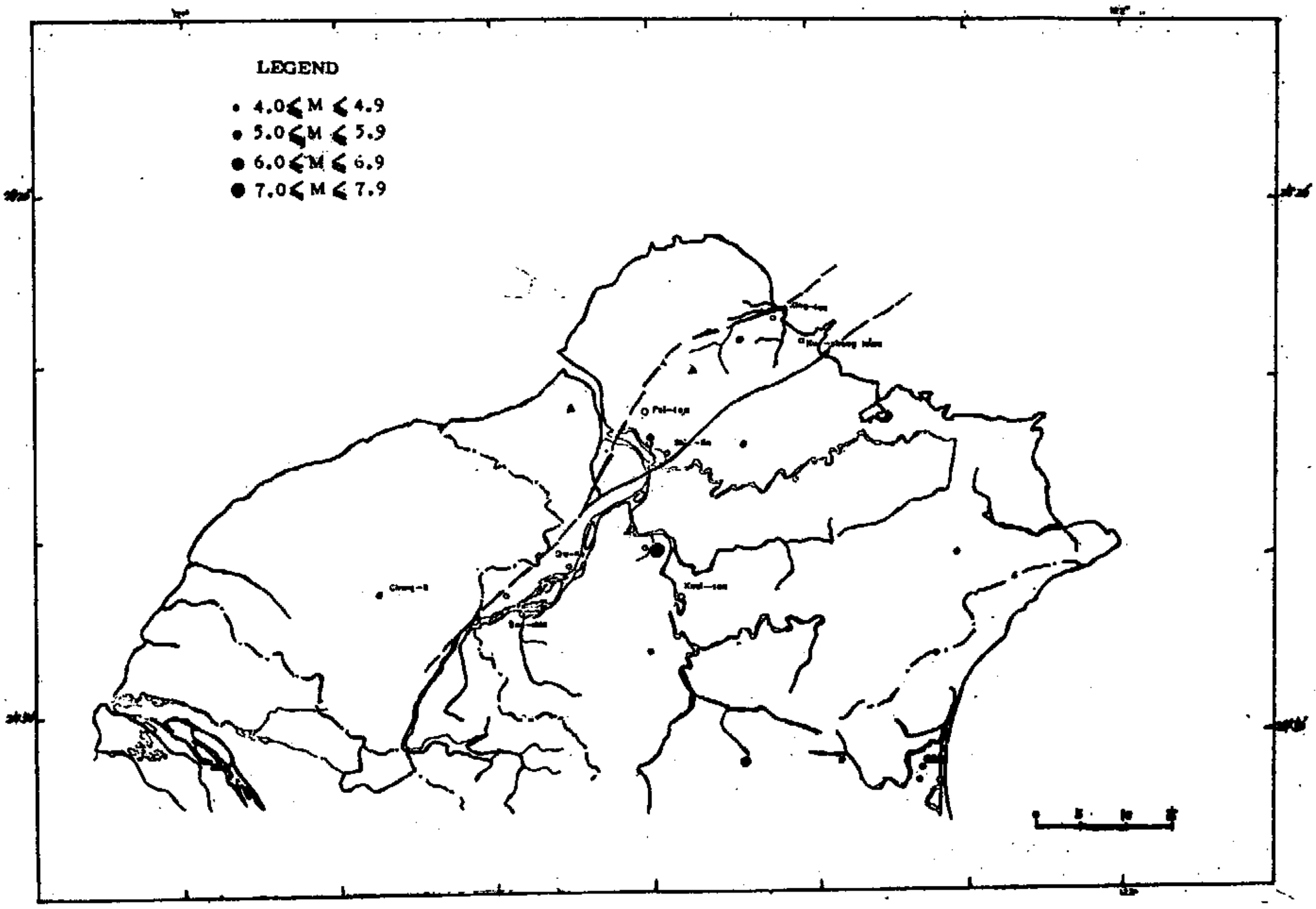

Figure 3. Epicenters of earthquakes located in northern Taiwan during 1936-1969.

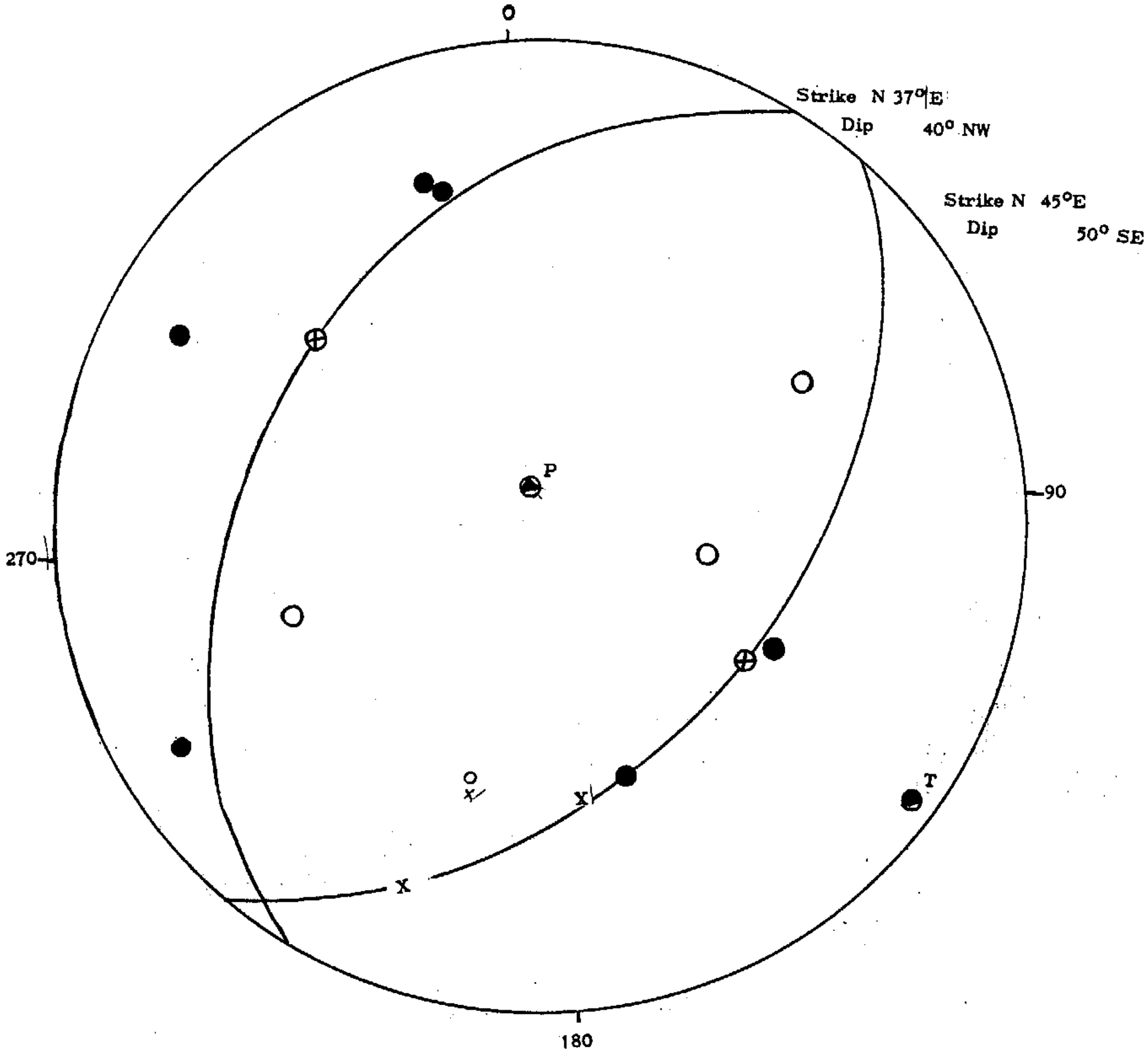

Figure 4. Fault plane solution representing normal faulting earthquake source mechanism in the Tatun Volcanic Region.

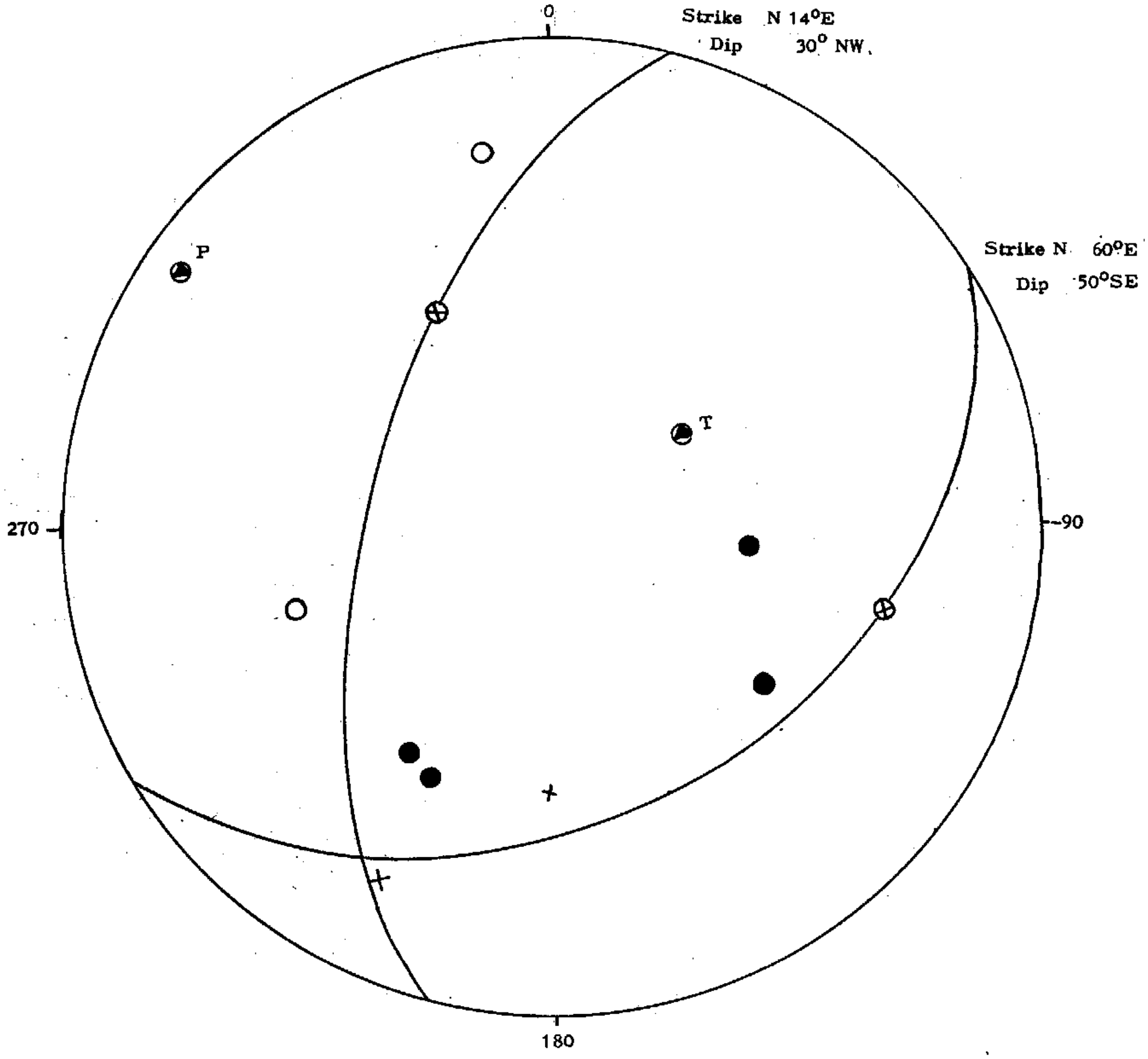

Figure 4. Fault plane solution representing normal faulting earthquake source mechanism in the Tatun Volcanic Region.

A SEISMIC REFRACTION STUDY OF EASTERN TAIWAN

Y. B. Tsai, Y. M. Hsiung, H. B. Liaw, H. P. Lueng, T. H. Yao, Y. H. Yeh and Y. T. Yeh

Seismology Division Institute of Physics

Academia Sinica

May, 1974

Abstract

A seismic refraction study was made in eastern Taiwan in August 1973. Three profiles with varying lengths from about 20 to 60 km were studied by using nine portable seismographs to record seismic waves generated by six dynamite explosions in deep boreholes. The results from analyzing the travel-time data of P-wave first arrivals can be summarized as follows:

(1) Profile I or II traversing the southern portion of the Eastern Coastal Range is characterized by a top layer whose thickness and P-wave velocity are determined as 3.9 km and 3.50 km/sec respectively. The basement formation is found to have a P-wave velocity of 5.41 km/sec.

(2) Profile III lying along the west side of the Longitudinal Valley is characterized by a relatively thin top layer whose thickness and P-wave velocity are determined as 2.0 km and 2.96 km/sec, respectively. The P-wave velocity of the substratum is estimated at 5.97 km/sec, the highest value found in Taiwan so far.

The results show that the subsurface seismic sections underneath the Eastern Coastal Range and the west side of the Longitudinal Valley differ from each other appreciably.

1. *Introduction*

Seismicity of Taiwan shows clearly that eastern Taiwan is the most active seismic zone of the island (see Figures la and lb). In order to lay ground for detailed seismological studies of eastern Taiwan in the future, a seismic refraction study was conducted during August of 1973. The field operations were carried out jointly by Taiwan Petroleum Exploration Division of the Chinese Petroleum Corporation, the Mining Research and Service Organization of the Ministry of Economic Affairs and the Seismology Division of the Institute of Physics, Academia Sinica.

The immediate objective of the study was to determine the upper crustal structures underneath the Longitudinal Valley and the Eastern Coastal Range. Information on the crustal structures will in turn be used to improve location of earthquake epicenters in eastern Taiwan. It was also hoped that the seismic refraction data from this study might shed new lights for resolving some highly complicated geological problems of eastern Taiwan.

2. *Field Operations*

The field operations consisted of borehole drilling, borehole shooting and signal recording.

The task of borehole drilling was carried out by a drilling team of the Mining Research and Service Organization. Three criteria were considered in selection of a borehole site: (a) It was at least 500 meters away from private dwellings or public facilities to ensure human safety and avoid property damages; (b) It was accessible to the drilling equipment and had sufficient water supplies for the drilling operations; (c) It was located on the outcrop of hard basement rock or at a point where the soft superficial layer was thin. This would not only minimize many drilling difficulties but also increase the efficiency of seismic wave generation. Even in the relatively sparsely populated eastern Taiwan, not many prospective borehole sites could meet these stringent criteria simultaneously. Consequently, most boreholes were located on the edges of river beds. Picture 1 shows drilling operation on one of the eight boreholes which were drilled from December 1972 to April 1973. The diameter and average depth of these boreholes were 13 cm and 70 m, respectively. Iron casing was lowered into the borehole to prevent collapse. Concrete was then poured around the casing just few inches below its upper end. The casing was capped to prevent unwanted filling of the borehole (see Picture 2).

Shooting and recording in the field were originally scheduled to be carried out near the end of 1973 when delivery of ten additional portable seismographs on order was expected. Unfortunately, due to misconcept of the experiment by some local people, one of the boreholes was ruined beyond repair. In order to avoid recurrence of similar incident to other boreholes, it was decided to move up the schedule. Field operations were subsequently executed in August 1973. Incidentally, August was the peak irrigation season for the rice paddies in eastern Taiwan and shooting at three of the remaining seven boreholes in the northern part of eastern Taiwan had to be withheld at the request of the local irrigation bureau. Consequently, only four boreholes were used for shooting in the present experiment. These boreholes were SP-2 near Fenglin, SP-6 near Chihshang, SP-7 near Taiyuan and SP-8 near Pinlang (see Figure 2).

Loading and detonation of dynamite in the borehole were carried out by a shooting crew of the Chinese Petroleum Corporation. The amount of dynamite used for each shooting was adjusted in accordance with the profile length. The concreted iron casing made it difficult to expand the bottom of borehole into a cavity for dynamite loading. Thus, all dynamite lowered down to the borehole was confined inside the borehole casing. Normally, the borehole was filled with water prior to detonation. Soon after explosion of dynamite a column of steam and smoke rushed up in the air for several tens of meters (see Picture 3). It was indeed quite a sight.

Two types of recording instruments were used for each profile. A spread of 24 geophones complete with a central recording unit was deployed next to the shot hole by a seismic reflection team of the Chinese Petroleum Corporation. Results derived from this type of recordings are reported in a separate article (Chen, 1974). The second type of recording instruments consisted of nine MEQ-800 portable seismographs operated by the Seismology Division of the Institute of Physics, Academia Sinica. Each portable seismograph is consisted of a vertical seismometer (see Picture 4), a smoke-paper recorder (see Picture 5), a crystal clock and a pair of batteries for power supply. Its magnification can range from 10^3 to 10^6 at 10 Hz depending on the noise background. Internal timing was checked with the standard time broadcasting by means of WWVB radio receivers both at the beginning and the end of each record. Prior to each shot these portable seismographs were placed along a profile at approximately equal intervals of a few kilometers (see Figure 2). One portable unit was always deployed side-by-side with a CPC geophone near the shot point in order to provide information necessary for reducing the travel-time data.

In total six events were made with dynamite charges ranging from approximately 250 to 650 kilograms. Detailed information about these events are given in Table I. Among them Events C, D and A, E were two pairs of overlapping reverse shootings over Profiles I and II, respectively, whereas Events B and F constituted a third pair of nonoverlapping reverse shootings over Profile III (see Figure 2).

3. *Data Processing and Interpretation*

Depending on the distance and background noise of a recording site, the recorded seismic signals varied in strength. Occasionally, some sismographs might fail to pick up any signal at all. Figure 3 shows a typical sample of seismograms obtained along Profile I from Event D detonated at Taiyuan (SP-7).

Following each event the first arrival times were read from individual seismograms. Corrections for internal colck drifting of individual seismographs were subsequently made on these readings. The corrected arrival times were reduced to travel times by subtracting from all readings of the same profile a constant amount of time which was determined by correlating the readings from the closest portable seismogram and the neighboring CPC geophone output. Tables IIa, IIb, IIc summarize the data resulting from the six events conducted for Profiles I, II, III respectively. In the tables the names of recording sites, their coordinates, elevations, distances from shot points, the recorded arrival times, the clock corrections the corrected arrival times and the reduced travel-times are given in increasing order from column 1 to column 8.

Preliminary examination showed that no systematic difference could be found between the two sets of travel time data from the same pair of reverse shootings for all three profiles. Thus, the standard model of horizontal velocity layers was adopted for intepreting these travel-time data. A schematic diagram and the corresponding travel-time curve for a horizontal two-layer model are shown in Figure 4. It is well known that the slopes of the first and second linear segments of the travel-time curve are equal to the P-wave slownesses of the first and second layers, respectively. The thickness Z of the first layer can also be determined by $Z = \frac{T_i}{2} \frac{V_1 V_0}{\sqrt{V_1^2 - V_0^2}}$, where V_0, V_1 are the P-wave velocities of the first and second layers, respectively. T_i represents the intercept time of the second linear segment of the travel-time curve (see Figure 4). This simple model will enable us to find out the gross features of the subsurface seismic sections beneath individual profiles. Since only a few data points with relatively large spacings are available, a more sophisticated model for interpretation seems unwarranted. In Figure 5 the observed data from Profiles I, II, III are compared with the theoretical travel-time curves. The two-layer seismic sections corresponding to these theoretical curves are also shown in the upper-left corner of the same figure.

Profile I has a length of approximately 30 km. It traverses from SP-8 to SP-7 in a northeasterly direction over the Eocene and Oligocene formations of the eastern front of the Central Mountain Range, the Alluvium of the Longitudinal Valley and the Miocene and Pliocene formations of the Eastern Coastal Range (see Figure 6). The seismic data shown in Figure 5 suggest that the top layer has an average P-wave velocity of about 3.50 km/sec and a gross thickness of approximately 3.9 km. The basement formation underneath the top layer has a P-wave velocity of about 5.41 km/sec.

Profile II has a length of only about 20 km. It lies between SP-6 and SP-7 in a southeasterly direction over the Alluvium of the Longitudinal Valley and the Miocene and Pliocene formations of the Eastern Coastal Range (see Figure 6). According to present seismic data, the top layer has an average P-wave velocity of about 3.70 km/sec and a gross thickness of about 3.3 km. The P-wave velocity of the basement formations was given as 5.42 km/sec. It should be mentioned that Profile II was relatively short and these parameter estimates may contain greater uncertainties than that of Profile I. Bearing this in mind, it may be said that Profiles I and II have essentially the same subsurface seismic section. Since these two profiles meet at SP-7 approximately at right angle, the similarity in seismic data appears to suggest that the top layer over the triangular area defined by SP-6, SP-7 and SP-8 is essentially horizontal.

Profile III was composed of two separate spreads with an overlapping segment of about 10 km. One spread extends for about 57 km from SP-8 in a north-northeasterly direction passing beyond SP-6. The second spread extends for about 60 km from SP-2 in a south-southwesterly direction. The two spreads overlap each other for some 10 km between the towns of Fuli and Yuli (see Figure 2). The whole profile practically lies on the border line separating the Mesozoic and Paleozoic formations of the Central Mountain Range on the west and the Alluvium of the Longitudinal Valley on the east (see Figure 6). According to present seismic data shown in Figure 5, the top layer underneath Profile III has an average P-wave velocity of 2.96 km/sec and a gross thickness of about 2.0 km. The basement formation is found to have a relatively high P-wave velocity of 5.97 km/sec. The relatively thin soft top layer is apparently related to the alluvium deposits of the Longitudinal Valley.

A comparison of Profile III on one hand with Profile I or II on the other makes it clear that they differ substantially from each other both in the travel-time data and in the vertical cross-sections of P-wave velocity. Briefly speaking, both the thickness and the P-wave velocity of the top layer are appreciably smaller for Profile III than for Profile I or II. Furthermore, the P-wave velocity of the basement formation is significantly higher for Profile III than for Profile I or II. This is in accordance with the geological evidence that the top formations in the Eastern Coastal Range are older, and thus having higher P-wave velocity than recent alluvium deposits in the Longitudinal Valley. According to present seismic data, the basement formations underneath the west side of the Longitudinal Valley, as revealed by Profile III, are probably consisted of the relatively old metamorphic rocks of the Central Mountain Range. On the other hand, the basement formations underlying the Eastern Coastal Range, as revealed by Profiles I and II, have much smaller P-wave velocity, and thus, may be composed of quite different kinds of rock, as compared with Profile III. As for the difference in thickness of the top layer between Profile III and Profile I or II, it may be taken as a crude evidence for the existence of at least one major fault lying to the east of Profile III. Hopefully microearthquake data being collected in this region may result in more precise information about faults in the Longitudinal Valley and the Eastern Coastal Range.

Acknowledgements

The authors wish to thank Mr. J. S. Chen, the third seismic team of the Chinese Petroleum Corporation, the drilling team of the Mining Research and Service Organization and the staff members of the Seismology Division for their valuable help in field operations. Thanks are due Drs. C. Y. King, W. H. K. Lee, C. Y. Meng, T. L. Teng and S. K. Yiu who conceived the project. We are also indebted to Dr. C. Y. Meng and Mr. H. H. Liu who critically read the manuscript and made valuable suggestions, and to Professor C. S. Ho who made his unpublished geologic map of Taiwan available to us. This study was supported by the National Science Council of the Republic of China.

References

1. Chen, J. S., et al., 1974, Seismic Survey conducted in eastern Taiwan: Petroleum Geol. Taiwan,

no.11, p. 147–163.

2. Ho, C. S., 1974, Geologic map of Taiwan, unpublished.

Table I Data of the six shot events

Event	Date	Time	Shot Point	Coordinate Y	Coordinate X	Elevation m	Location	Charge kg
A	73/8/5	14.00	SP-6	11.92	59.05	350	Chihshand	234
B	73/8/7	14.00	SP-8	01.67	23.80	140	Pinlang	500
C	73/8/7	14.00	SP-8	01.67	23.80	140	Pinlang 25	250
D	73/8/10		14.30	SP-7	25.53	43.41		
E	73/8/11	14.00	SP-7	25.53	43.41	30	Taiynan	350
F	73/8/14	12.00	SPd-	38.39	24.86	150	Fenglin	640

Table IIb Arrival times from Profile II

Recording Site	Coordinates Y	Coordinates X	Elevation m	Distance km	Recorded arrival time	Clock coorection	Coorected arrival time	Reduced travel time
A_1	13.25	58.90	330	1.20	12.30	+0.05	12.35	0.46
A_2	15.00	56.50	295	4.00	13.00	-0.20	12.80	0.91
A_3	17.00	55.52	320	6.19	13.60	±0.00	13.60	1.71
A_4	17.00	54.00	300	7.16	13.80	±0.00	13.80	1.91
A_5	17.80	52.00	370	9.18	/	=0.05	/	/
A_6	21.32	49.83	255	13.17	15.60	±0.00	15.60	3.71
A_7	22.90	48.42	110	15.30	/	±0.00	/	/
A_8	22.61	46.60	110	16.41	/	±0.00	/	/
A_9	25.89	43.84	100	20.60	/	-0.02	/	/
E_1	25.39	43.22	30	0.24	1.38	+0.07	1.45	0.09
E_2	24.21	44.83	120	1.94	2.00	+0.14	2.14	0.78
E_3	22.61	46.62	110	4.34	2.35	+0.08	2.43	1.07
E_4	21.33	49.82	255	7.66	3.10	=0.00	3.10	1.74
E_5	17.80	52.01	370	11.56	4.30	+0.07	4.37	3.01
E_6	17.00	54.00	300	13.60	5.00	+0.03	5.03	3.67
E_7	16.73	55.35	275	14.83	5.40	+0.00	5.40	4.04
E_8	15.00	56.50	385	17.10	6.00	+0.05	6.05	4.69
E_0	11.44	58.02	360	20.30	6.20	+0.08	6.28	4.92

Table IIa Arrival Times from Profile I

Recording Site	Coordinates Y .	X	Elevation m,	Distance km	Recorded arrival time	Clock Coorection	Coorected arrival time	Reduced travel timke
C_1	1.55	23.50	100	1.04	3.63	-0.08	3.55	0.34
C_2	4.07	27.69	195	4.54	4.25	+0.01	4.26	1.05
C_3	9.53	28.42	200	9.12	5.80	+0.04	5.84	2.63
C_4	10.44	32.26	345	12.19	6.50	-0.02	6.48	3.27
C_5	16.65	38.54	180	21.02	8.90	±0.00	8.90	5.69
C_6	19.10	40.82	153	24.36	9.10	-0.08	9.02	5.81
C_7	21.36	43.07	50	27.55	/	+ 0.01	/	/
C8	23.38	43.65	100	29.51	10	+0.10	10.30	7.09
C_9	25.60	43.60	250	30.50	10.70	+0.20		
D_1	25.60	43.60	250	0.36	2.85	+0.20	3.05	0.13
D_2	23.38	43.65	100	2.20	3.70	+0.01	3.80	0.88
D_3	21.36	43.07	50	4.80	4.20	+0.01	4.21	1.20
D_4	19.10	40.82	150	6.94	5.10	-0.08	5.02	2.10
D_5	16.65	39.54	180	10.30	5.60	±0.00	5.60	2.68
D_6	10.44	32.26	345	18.79	7.50	-0.02	7.48	4.56
D_7	9.53	28.42	200	21.90	/	+0.04	/	/
D_8	4.07	27.69	195	26.60	9.45	=0.01	9.46	6.54
D_9	1.55	23.50	100	29.80	10.40	-0.08	10.32	7.40

Table IIc Arrigal times from Profile III

Recording Site	Coordinates Y	X	Elevation m	Distance km	Recorded arrival time	Clock coorection	Coorected arrival time	Reduced travel time
B_1	2.00	23.60	120	1.55	3.35	-0.43	2.92	0.44
B_2	3.51	31.10	310	7.53	4.90	=0.00	4.90	2.42
B_3	5.52	37.67	380	14.43	6.10	+0.04	6.14	3.66
B_4	7.85	42.75	350	19.93	6.50	+0.70	7.20	4.72
B_5	9.03	47.54	250	24.85	7.40	+0.50	7.90	5.42
B_6	10.63	52.39	300	29.96	8.15	+0.50	8.65	6.17
B_7	14.48	60.98	300	39.31	10.00	+0.40	10.40	7.92
B_8	20.12	67.05	220	47.02	11.25	+0.45	11.70	9.22
B_9	23.90	76.24	170	56.96	13.70	+0.50	14.20	11.72
F_1	37.40	23.60	150	1.54	1.71	+0.09	1.80	0.36
F_2	37.72	18.95	215	5.95	3.70	-0.23	3.47	2.03
F_3	33.43	12.11	200	13.68	3.80	+1.00	4.80	3.36
F_4	33.07	3.24	105	22.26	6.20	+0.05	6.25	4.81
F_5	30.84	92.60	130	33.13	/	-0.65	/	/
F_6	25.70	83.05	190	43.70	9.72	±0.00	9.72	8.28
F_7	29.60	82.56	140	43.20	/	±0.00	/	/
F_8	26.30	74.51	180	51.78	/	±0.00	/	/
F_9	20.12	67.05	220	60.63	/	±0.00	/	/

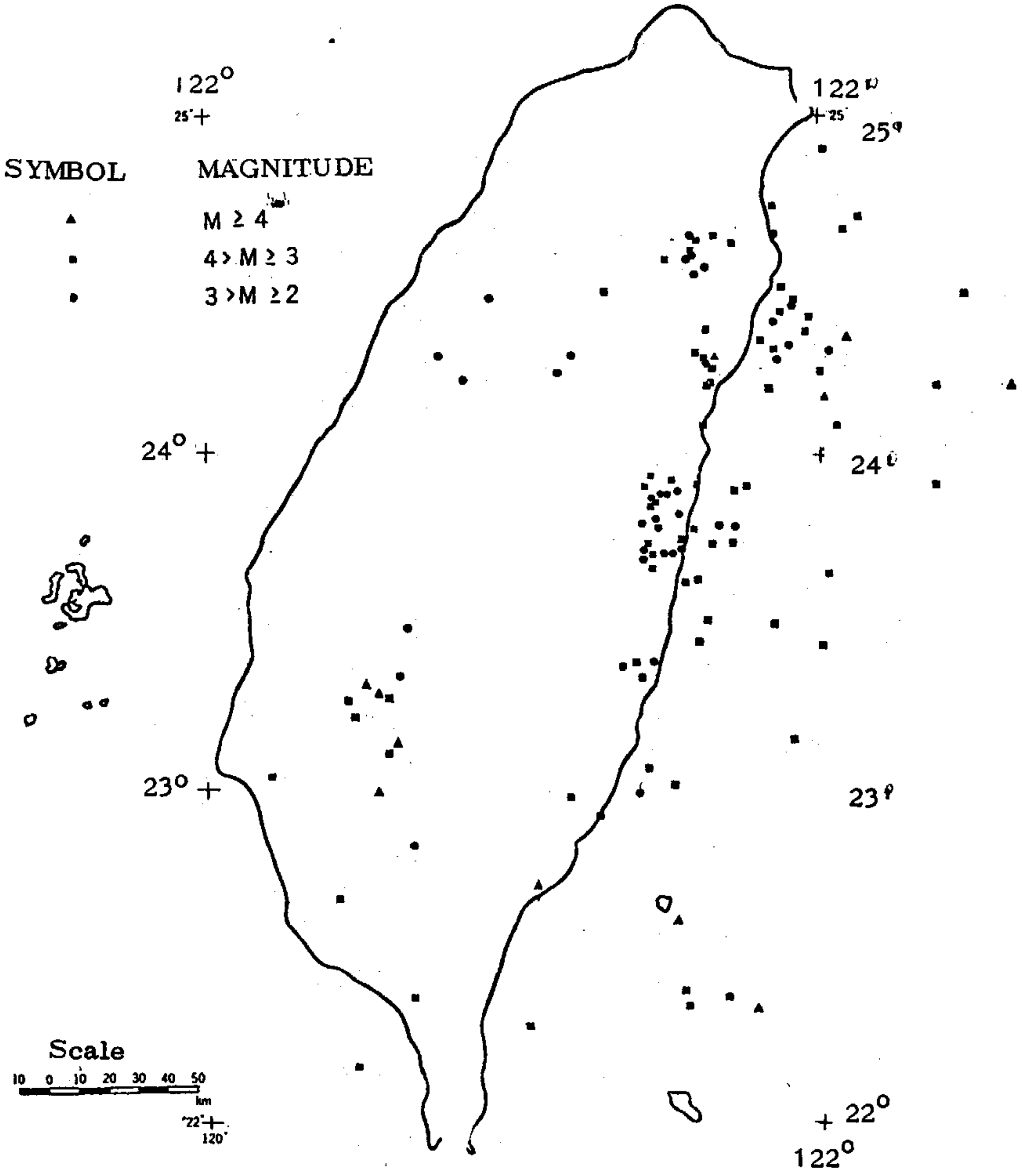

Figure 1b Seismicity of Taiwan January - March 1973

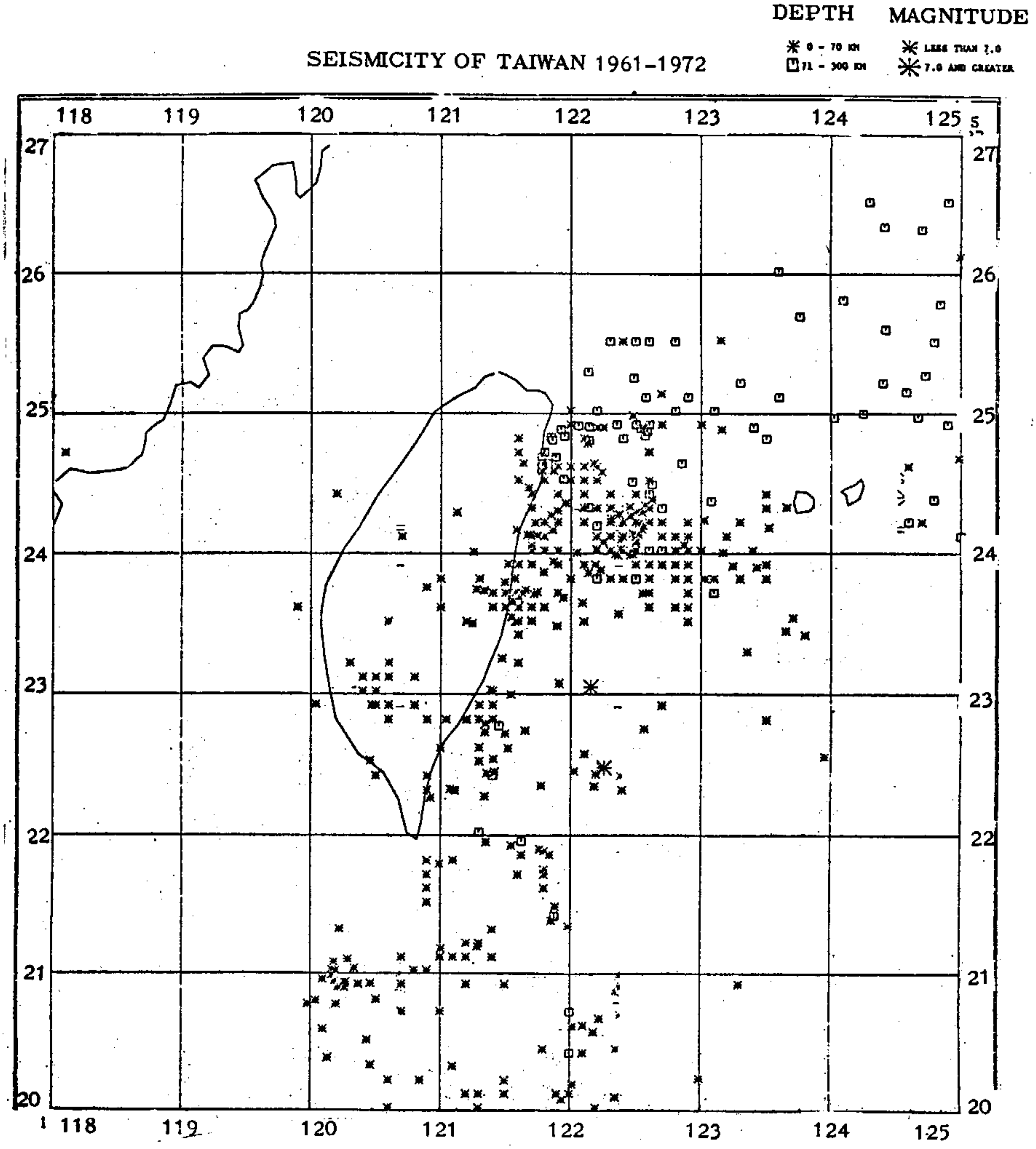

Figure la Seismicity of Taiwan 1961-1972

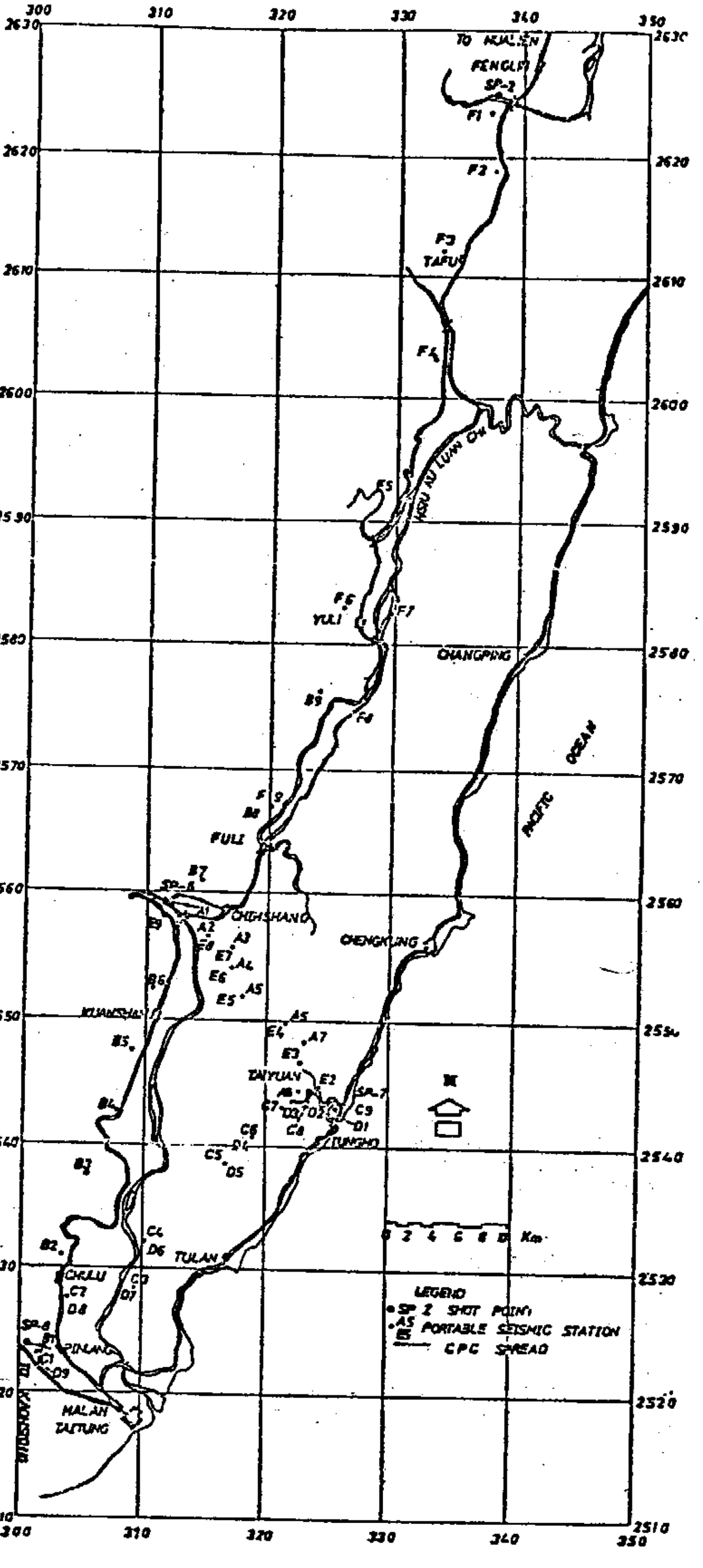

Figure 2 Locations of shot points and recording sites

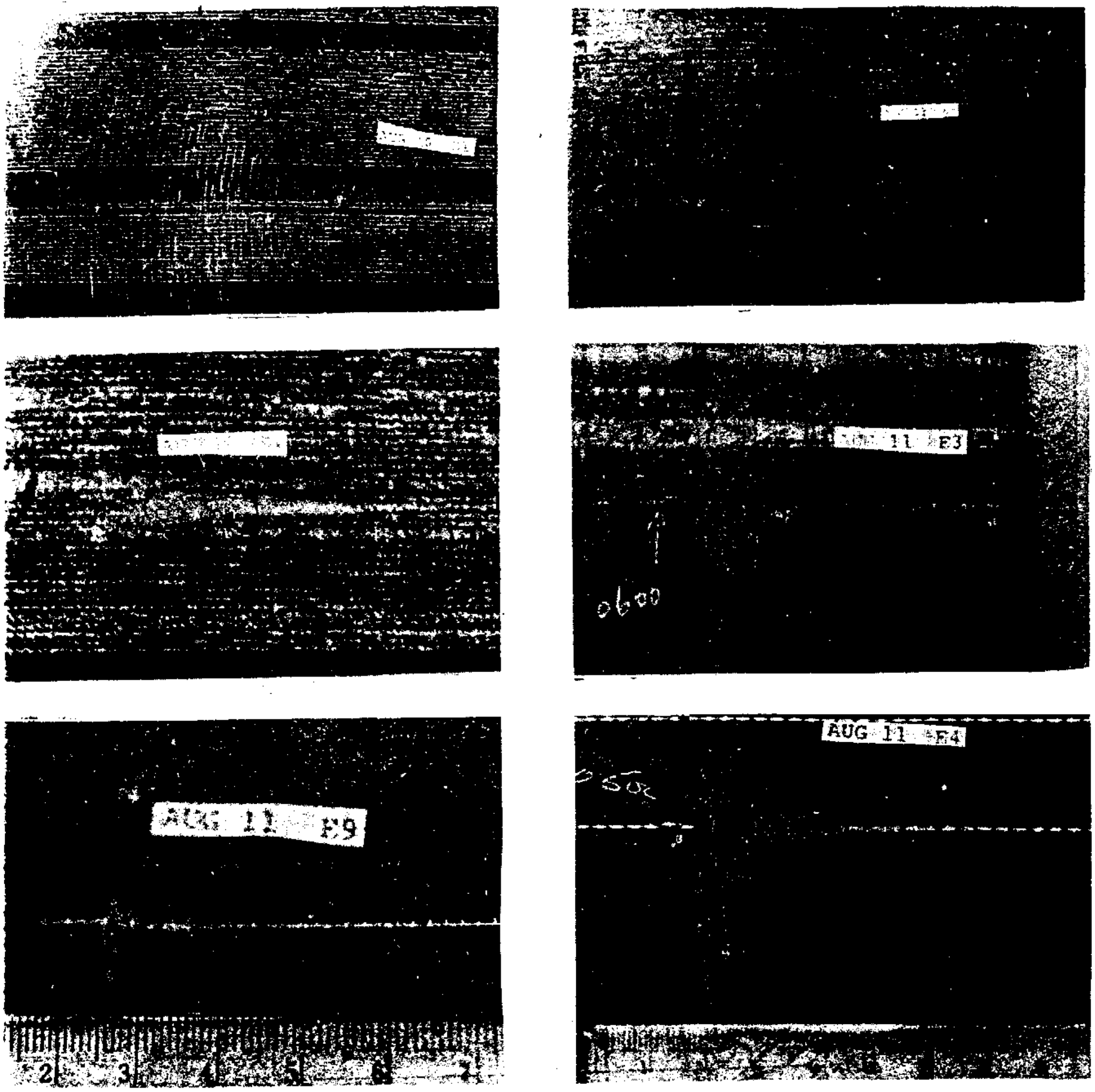

Figure 3 Sample seismograms from event D

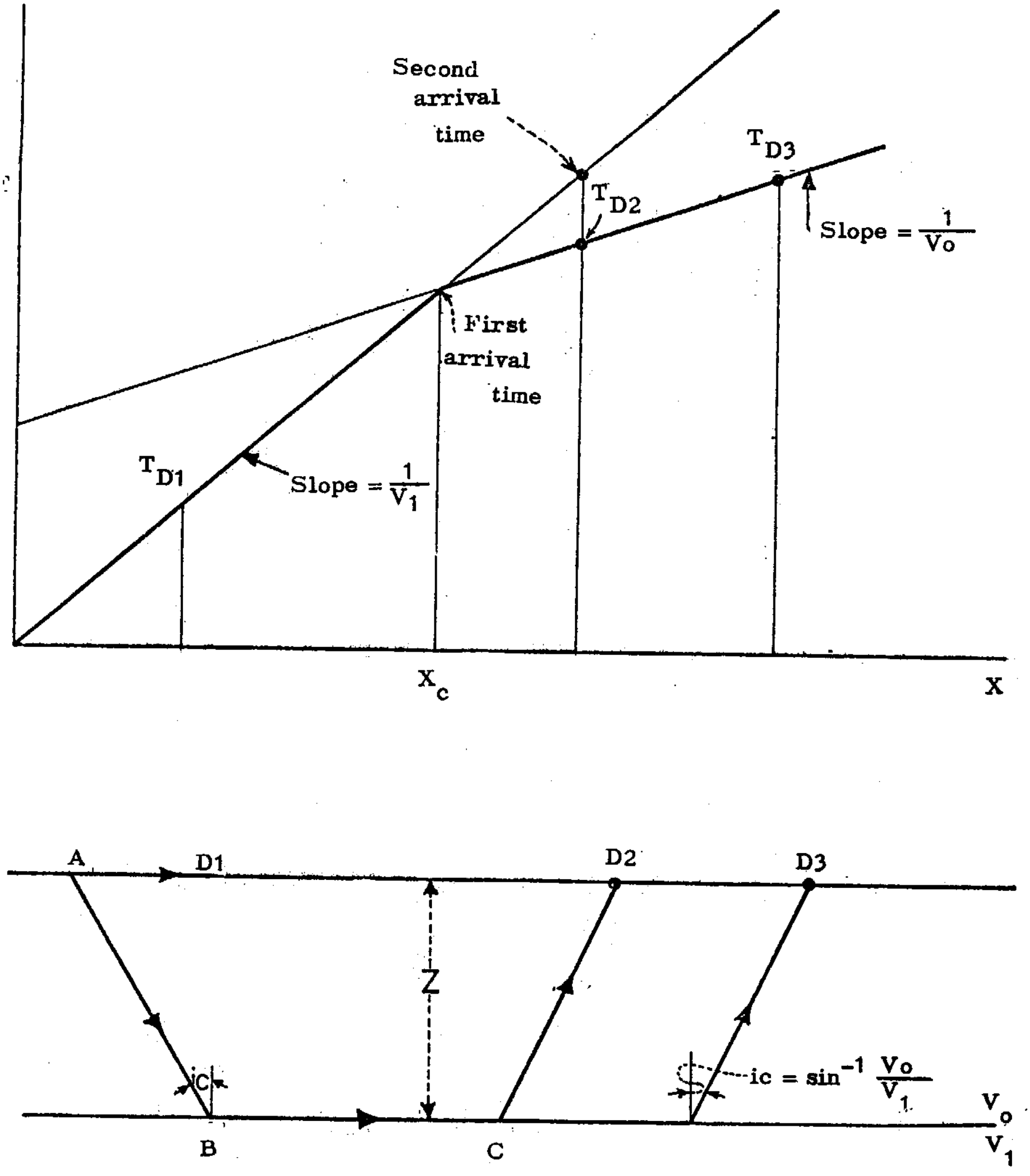

Figure 4. Ray paths of least time and time–distance curve for two layers separated by a horizontal interface

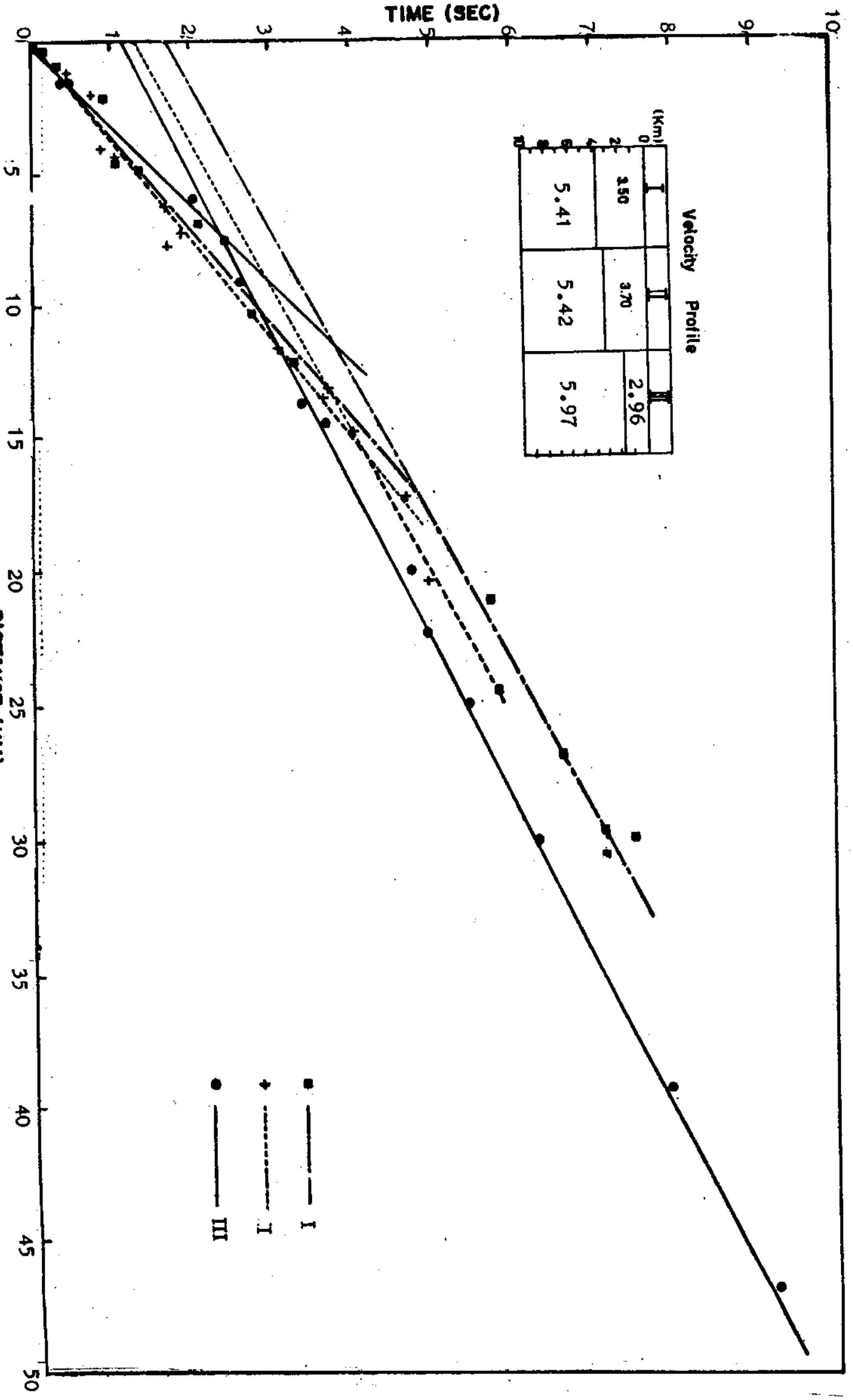

Figure 5 Seismic travel time curves

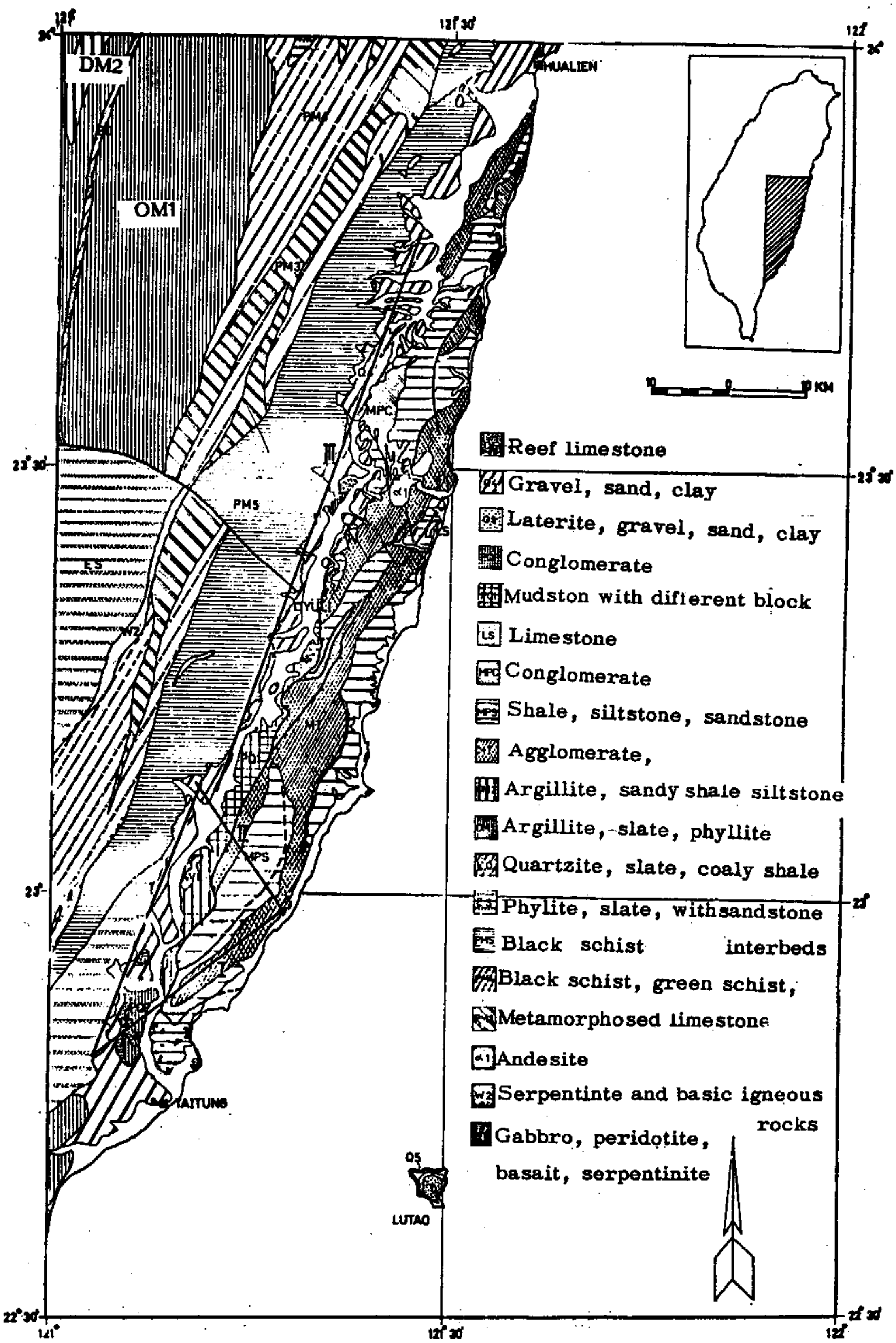

Figure 6 Seismic refraction profiles and geologic map of eastern Taiwan (after C. S. Ho, 1974).

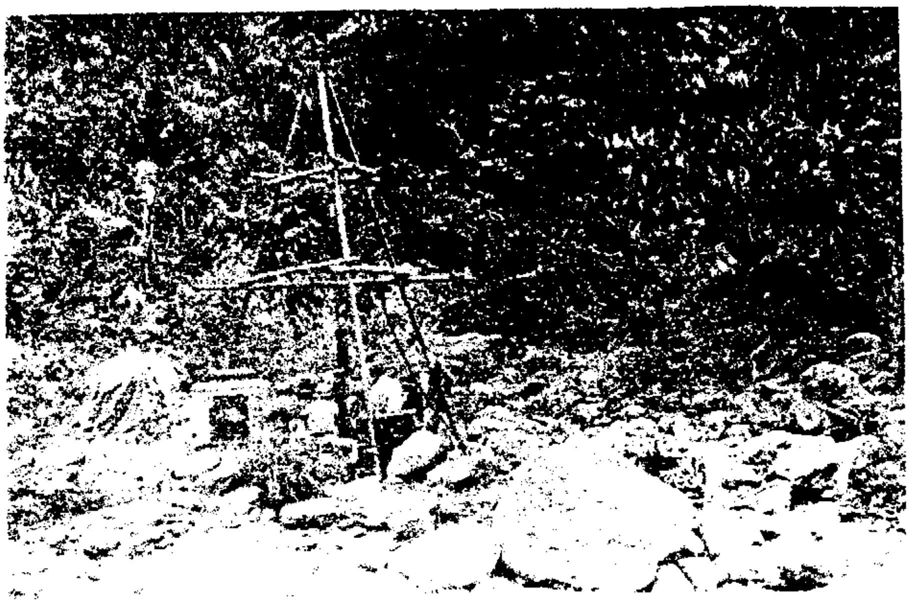

Picture 1

Picture 2

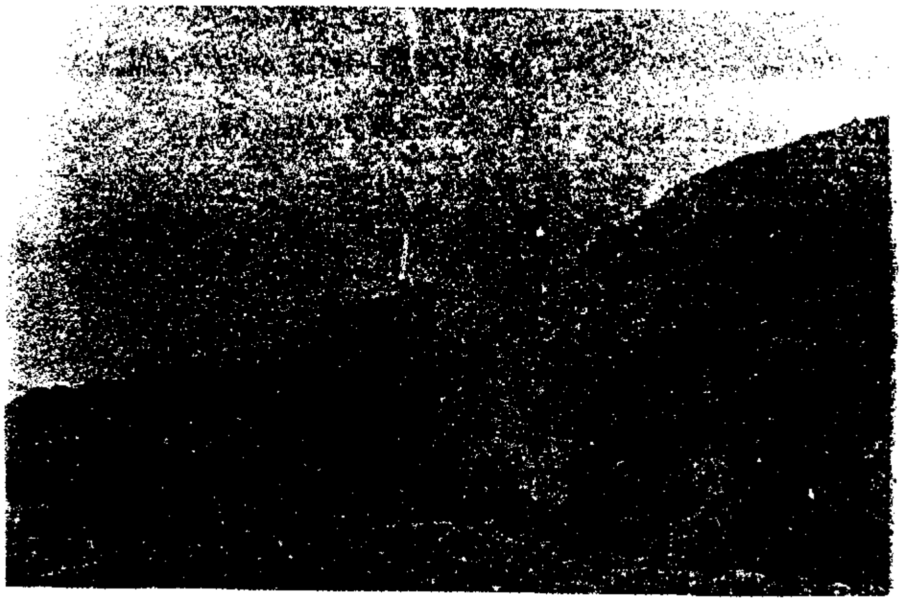

Picture 3

Picture 4

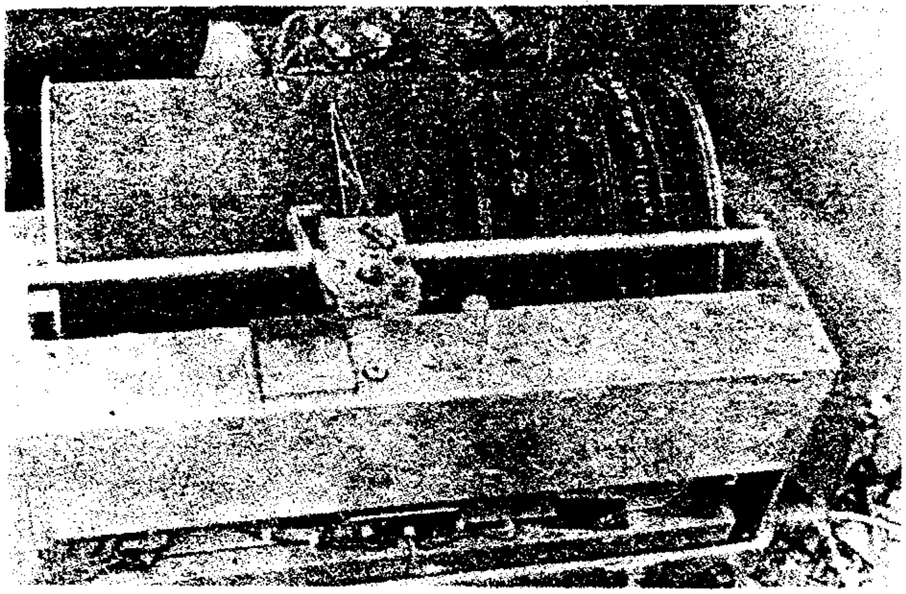

Picture 5

Figure 5. Fault plane solution representing overthrust faulting earthquake source mechanism in the Tatun Volcanic Region.

A CONCENTRATED LINE LOAD ACTING IN THE INTERIOR OF AN ELASTIC WEDGE SHAPED MEDIUM

Y. C. Teng（鄧玉瓊）
Seismology Division, Institute of Physics
Academia Sinica
The Republic of China

July, 1974

Abstract

As an extension of a previous work by the author, the problem of a single wedge subjected to an internally applied line load is considered. The formal solutions of stresses and displacements are obtained by means of the Papkovitch functions. The stresses and displacements for $r < r_o$ and $r > r_o$, where r_o is the position of load in r-direction, are evaluated separately by means of the residue theorem. The solutions thus obtained agree with the known expressions for the two limiting cases, viz, (a) surface loading, (b) vertex loading.

1. *Introduction*

The problem of stress distribution in a single wedge has been treated by many investigators [1 to 10] *. Most recently, Teng and Kuo [11 and 12] studied the problem of an infinite elastic wedge subjected to an arbitraryly oriented surface line load by means of Papkovitch functions. The approach by starting with the Papkovitch functions offers the advantage for determining the stresses and displacements simultaneously. Therefore, some wedge problems of the more general kind, such as a line load applied internally or a point load applied on the surface or internally can be solved by using this approach.

In the present paper, we shall consider the problem of an arbitrarily oriented concentrated line load applied internally to an infinite elastic wedge with arbitrary wedge angle.

2. *Statement and Boundary Conditions*

Consider a wedge shaped, elastic, isotropic and homogeneous medium as shown in

---

* Numbers in brackets designate References at end of paper.

Figure 1. The origin of the polar coordinates is placed at the vertex of the wedge, and the wedge surfaces are bounded by $\theta = -\alpha$ and $\theta = +\alpha$. A static line load P_o (force per unit length) is located at the point (r_o, θ_o) and makes an angle β with respect to the wedge surface $\theta = \theta_o$. $P(r,\theta)$ is the observation point.

The boundary conditions for the traction free wedge surfaces are

$$\tau^{(1)}_{\theta\theta}\Big|_{\theta=+\alpha} = \tau^{(1)}_{\theta r}\Big|_{\theta=+\alpha} = \tau^{(2)}_{\theta\theta}\Big|_{\theta=-\alpha} = \tau^{(2)}_{\theta r}\Big|_{\theta=-\alpha} = 0 \tag{1}$$

where the superscripts $i = 1,2$ represent the first and second region respectively as shown in Figure 1. At the surface $\theta = \theta_o$, there must be continuity of the displacements. In the present problem these boundary conditions are

$$u^{(1)}_{r}\Big|_{\theta=\theta_o} = u^{(2)}_{r}\Big|_{\theta=\theta_o} \qquad (2) \qquad u^{(1)}_{\theta}\Big|_{\theta=\theta_o} = u^{(2)}_{\theta}\Big|_{\theta=\theta_o} \tag{3}$$

Let us now consider the applied force as boundary conditions, then at the surface $\theta = \theta_o$, we have

$$\tau^{(2)}_{\theta\theta}\Big|_{\theta=\theta_o} - \tau^{(1)}_{\theta\theta}\Big|_{\theta=\theta_o} = -P_o \sin\beta\, \delta\,(r-r_o) \tag{4}$$

$$\tau^{(2)}_{\theta r}\Big|_{\theta=\theta_o} - \tau^{(1)}_{\theta r}\Big|_{\theta=\theta_o} = -P_o \cos\beta\, \delta\,(r-r_o) \tag{5}$$

Letting $r = r' e^{\rho}$, $r_o = r' e^{\rho_o}$, and taking $r' = 1$, we have

$$\delta\,(r-r_o) = e^{-\rho}\,\delta\,(\rho-\rho_o) = \frac{e^{-\rho}}{2\pi}\int_{-\infty}^{\infty} e^{in(\rho-\rho_o)}\,dn \tag{6}$$

The boundary conditions (4) and (5) can be written as

$$\left.\overset{(2)}{\tau}_{\theta\theta}\right|_{\theta=\theta_o} - \left.\overset{(1)}{\tau}_{\theta\theta}\right|_{\theta=\theta_o} = \frac{-P_o e^{-\rho}\sin\beta}{2\pi}\int_{-\infty}^{\infty} e^{in(\rho-\rho_o)}\,dn \tag{7}$$

$$\left.\overset{(2)}{\tau}_{\theta r}\right|_{\theta=\theta_o} - \left.\overset{(1)}{\tau}_{\theta r}\right|_{\theta=\theta_o} = \frac{-P_o e^{-\rho}\cos\beta}{2\pi}\int_{-\infty}^{\infty} e^{in(\rho-\rho_o)}\,dn \tag{8}$$

3. *Formal Solutions of Stresses and Displacements*

Using an approach similar to that of surface loading wedge problem in Reference [11], the general expressions of stresses and displacements can be written as

$$\begin{aligned}\overset{(i)}{\tau}_{rr} = -e^{-\rho}\int_{-\infty}^{\infty} in\,\{\,&(in-3)\,[B_n^{(i)}\cos(in-1)\,\theta\\&+F_n^{(i)}\sin(in-1)\,\theta\,]\\&+(in+1)\,[Y_n^{(i)}\cos(in+1)\theta\\&+Z_n^{(i)}\sin(in+1)\,\theta\,]\,\}\;e^{in\rho}\,dn\end{aligned} \tag{9}$$

$$\begin{aligned}\overset{(i)}{\tau}_{\theta\theta} = e^{-\rho}\int_{-\infty}^{\infty} in(in+1)\,[\,&B_n^{(i)}\cos(in-1)\,\theta + F_n^{(i)}\sin(in-1)\,\theta\\&+Y_n^{(i)}\cos(in+1)\,\theta\\&+Z_n^{(i)}\sin(in+1)\,\theta\,]\;e^{in\rho}\,dn\end{aligned} \tag{10}$$

$$\begin{aligned}\overset{(i)}{\tau}_{\theta r} = e^{-\rho}\int_{-\infty}^{\infty} in\,\{\,&(in-1)\,[\,B_n^{(i)}\sin(in-1)\,\theta - F_n^{(i)}\cos(in-1)\,\theta\,]\\&+(in+1)\,[\,Y_n^{(i)}\sin(in+1)\,\theta\\&-Z_n^{(i)}\cos(in+1)\,\theta\,]\,\}\;e^{in\rho}\,dn\end{aligned} \tag{11}$$

$$u_\theta^{(i)} = \frac{1}{2\mu}\int_{-\infty}^{\infty} \{ (\frac{Q}{S}+in) [B_n^{(i)} \sin(in-1)\theta - F_n^{(i)} \cos(in-1)\theta]$$

$$+ (in+1) [Y_n^{(i)} \sin(in+1)\theta - Z_n^{(i)} \cos(in+1)\theta] \} e^{in\rho} dn$$

$$- B_o^{(i)} \sin\theta - F_o^{(i)} \cos\theta - F_1^{(i)} r \qquad (12)$$

$$u_r^{(i)} = \frac{1}{2\mu}\int_{-\infty}^{\infty} \{ (\frac{Q}{S}-in) [B_n^{(i)} \cos(in-1)\theta + F_n^{(i)} \sin(in-1)\theta]$$

$$- (in+1) [Y_n^{(i)} \cos(in+1)\theta + Z_n^{(i)} \sin(in+1)\theta] \} e^{in\rho} dn$$

$$+ B_o^{(i)} \cos\theta - F_o^{(i)} \sin\theta \qquad (13)$$

where i = 1,2. And

$$S = \frac{\lambda+\mu}{2(\lambda+2\mu)} \qquad (14)$$

$$Q = \frac{\lambda+3\mu}{2(\lambda+2\mu)} \qquad (15)$$

λ and μ are the lame's constants, $B_o^{(i)}$, $F_o^{(i)}$, $F_1^{(i)}$ are the rigid body motion constants.

Substituting equations (10) to (13) into equations (1), (2), (3), (7) and (8), we obtain

$$B_o^{(1)} = B_o^{(2)} \qquad (16)$$

$$F_o^{(1)} = F_o^{(2)} \qquad (17)$$

$$F_1^{(1)} = F_1^{(2)} \qquad (18)$$

$$B_n^{(1)} = b_n + B_n \qquad (19)$$

$$B_n^{(2)} = b_n - B_n \tag{20}$$

$$F_n^{(1)} = f_n + F_n \tag{21}$$

$$F_n^{(2)} = f_n - F_n \tag{22}$$

$$Y_n^{(1)} = y_n + Y_n \tag{23}$$

$$Y_n^{(2)} = y_n - Y_n \tag{24}$$

$$Z_n^{(1)} = z_n + Z_n \tag{25}$$

$$Z_n^{(2)} = z_n - Z_n \tag{26}$$

$$B_n = - \frac{P_o e^{-in\rho_o} \sin [\, (in-1)\theta_o - \beta \,]}{4\pi\, in\, (\frac{Q}{S} + 1\,)} \tag{27}$$

$$F_n = \frac{P_o e^{-in\rho_o} \cos [\, (in-1)\theta_o - \beta \,]}{4\pi\, in\, (\frac{Q}{S} + 1\,)} \tag{28}$$

$$Y_n = \frac{P_o\, e^{-in\rho_o}}{4\pi\, in(in+1)} \Big\{ \sin [\, (in+1)\theta_o + \beta \,] + \frac{1}{(\frac{Q}{S} + 1\,)} \big(a_3(\theta_o) \sin [(in-1)\theta_o - \beta] - a_2(\theta_o) \cos [(in-1)\theta_o - \beta] \big) \Big\} \tag{29}$$

$$Z_n = \frac{P_o e^{-in\rho_o}}{4\pi\, in\, (in+1)} \Big\{ -\cos [\, (in+1)\theta_o + \beta \,] + \frac{1}{(\frac{Q}{S} + 1\,)} \big(a_1(\theta_o) \sin [\, (in-1)\theta_o - \beta \,] + a_4(\theta_o) \cos [\, (in-1)\theta_o - \beta \,] \big) \Big\} \tag{30}$$

$$b_n = \frac{P_o e^{-in\rho_o}}{4\pi in\, a_1} \Big\{ \cos[(in+1)\theta_o + \beta]$$

$$+ \frac{1}{(\frac{Q}{S}+1)} \Big([a_4 - a_4(\theta_o)] \cos[(in-1)\theta_o - \beta]$$

$$- a_1(\theta_o) \sin[(in-1)\theta_o - \beta] \Big) \Big\} \tag{31}$$

$$f_n = \frac{P_o e^{-in\rho_o}}{4\pi in\, a_2} \Big\{ - \sin[(in+1)\theta_o + \beta]$$

$$+ \frac{1}{(\frac{Q}{S}+1)} \Big([a_3 - a_3(\theta_o)] \sin[(in-1)\theta_o - \beta]$$

$$+ a_2(\theta_o) \cos[(in-1)\theta_o - \beta] \Big) \Big\} \tag{32}$$

$$y_n = \frac{P_o e^{-in\rho_o}}{4\pi in\,(in+1)\, a_1} \Big\{ - a_3 \cos[(in+1)\theta_o + \beta]$$

$$+ \frac{1}{(\frac{Q}{S}+1)} \Big(a_3 a_1(\theta_o) \sin[(in-1)\theta_o - \beta]$$

$$+ [a_3 a_4(\theta_o) - (n^2+1)] \cos[(in-1)\theta_o - \beta] \Big) \Big\} \tag{33}$$

$$z_n = \frac{P_o e^{-in\rho_o}}{4\pi in\,(in+1)\, a_2} \Big\{ - a_4 \sin[(in+1)\theta_o + \beta]$$

$$+ \frac{1}{(\frac{Q}{S}+1)} \Big(a_4 a_2(\theta_o) \cos[(in-1)\theta_o - \beta]$$

$$+ [\, a_4 a_3(\theta_o) - (n^2+1) \sin[(in-1)\theta_o - \beta] \Big) \Big\} \tag{34}$$

where

$$\begin{matrix} a_1 \\ a_2 \end{matrix} = \sin 2in\,\alpha \pm in \sin 2\alpha \tag{35}$$

$$\begin{matrix} a_3 \\ a_4 \end{matrix} = \cos 2in\,\alpha \pm in \cos 2\,\alpha \tag{36}$$

$$\begin{matrix} a_1(\theta_o) \\ a_2(\theta_o) \end{matrix} = \sin 2in\theta_o \pm in \sin 2\theta_o \tag{37}$$

$$\begin{matrix} a_3(\theta_o) \\ a_4(\theta_o) \end{matrix} = \cos 2in\theta_o \pm in \cos 2\theta_o \tag{38}$$

4. *Evaluation of Stresses and Displacements*

The stresses and displacements in equations (9) to (13) contain simple poles in either the upper half or the lower half of the complex n-plane depending on either $r < r_o$ or $r > r_o$. By means of the residue theorem, these integrals can be evaluated as (see [11])

$$\begin{aligned} \tau_{rr}^{(i)}(r_>, \theta) = {} & \frac{2P_o \cos(\theta_o+\beta)}{(2\alpha+\sin 2\alpha)} \frac{\cos\theta}{r} + \frac{2P_o \sin(\theta_o+\beta)}{(2\alpha-\sin 2\alpha)} \frac{\sin\theta}{r} \\ & + \frac{P_o}{2} \Big\{ \sum_{p_n>0} \big[(p_n+3)A_1(r_>)\cos(p_n+1)\theta \\ & - A_3(r_>)\cos(p_n-1)\theta \big] \frac{r_o^{\,p_n}}{r^{p_n+1}} \\ & - \sum_{q_n>0} \big[(q_n+3)A_2(r_>)\sin(q_n+1)\theta \\ & - A_4(r_>)\sin(q_n-1)\theta \big] \frac{r_o^{\,q_n}}{r^{q_n+1}} \Big\} \end{aligned} \tag{39}$$

$$\begin{aligned}
\tau^{(i)}_{rr}(r_<,\theta) = \frac{P_o}{2}\Big\{ & \sum_{p_n>0} [\,(p_n-3)A_1(r_<)\cos(p_n-1)\theta \\
& + A_3(r_<)\cos(p_n+1)\theta\,]\,\frac{r^{p_n-1}}{r_o^{\;p_n}} \\
& + \sum_{q_n>0} [\,(q_n-3)A_2(r_<)\sin(q_n-1)\theta \\
& + A_4(r_<)\sin(q_n+1)\theta\,]\,\frac{r^{q_n-1}}{r_o^{\;q_n}}\ \Big\}
\end{aligned} \tag{40}$$

$$\begin{aligned}
\tau^{(i)}_{\theta\theta}(r_>,\theta) = \frac{P_o}{2}\Big\{ & \sum_{p_n>0} [\,-(p_n-1)A_1(r_>)\cos(p_n+1)\theta \\
& + A_3(r_>)\cos(p_n-1)\theta\,]\,\frac{r_o^{\;p_n}}{r^{p_n+1}} \\
& + \sum_{q_n>0} [\,(q_n-1)A_2(r_>)\sin(q_n+1)\theta \\
& - A_4(r_>)\sin(q_n-1)\theta\,]\,\frac{r_o^{\;q_n}}{r^{q_n+1}}\ \Big\}
\end{aligned} \tag{41}$$

$$\begin{aligned}
\tau^{(i)}_{\theta\theta}(r_<,\theta) = \frac{-P_o}{2}\Big\{ & \sum_{p_n>0} [\,(p_n+1)A_1(r_<)\cos(p_n-1)\theta \\
& + A_3(r_<)\cos(p_n+1)\theta\,]\,\frac{r^{p_n-1}}{r_o^{\;p_n}} \\
& + \sum_{q_n>0} [\,(q_n+1)A_2(r_<)\sin(q_n-1)\theta
\end{aligned}$$

$$+ A_4(r_<)\sin(q_n+1)\theta\ ]\ \frac{r^{q_n-1}}{r_o^{\,q_n}}\ \} \tag{42}$$

$$\tau^{(i)}_{\theta r}(r_>,\theta) = \frac{P_o}{2}\ \{\ \sum_{p_n>o}\ [\ (p_n+1)A_1(r_>)\sin(p_n+1)\theta$$

$$- A_3(r_>)\sin(p_n-1)\theta\ ]\ \frac{r_o^{\,p_n}}{r^{p_n+1}}$$

$$+ \sum_{q_n>o}\ [\ (q_n+1)A_2(r_>)\cos(q_n+1)\theta$$

$$- A_4(r_>)\cos(q_n-1)\theta\ ]\ \frac{r_o^{\,q_n}}{r^{q_n+1}}\ \} \tag{43}$$

$$\tau^{(i)}_{r\theta}(r_<,\theta) = -\frac{P_o}{2}\ \{\ \sum_{p_n>o}\ [\ (p_n-1)A_1(r_<)\sin(p_n-)\theta$$

$$+ A_3(r_<)\sin(p_n+1)\theta\ ]\ \frac{r^{p_n-1}}{r_o^{\,p_n}}$$

$$+ \sum_{q_n>o}\ [\ -(q_n-1)A_2(r_<)\cos(p_n-1)\theta$$

$$- A_4(r_<)\cos(q_n+1)\theta\ ]\ \frac{r^{q_n-1}}{r_o^{\,q_n}}\ \} \tag{44}$$

$$u^{(i)}_r(r_>,\theta) = B_o\cos\theta - F_o\sin\theta$$

$$+ \frac{P_o}{4\mu(2\alpha+\sin 2\alpha)}\ \{\ -(\frac{Q}{S}+1)\cos(\theta_o+\beta)\cos\theta\,\ln(\frac{r_o}{r})$$

$$+ (\frac{Q}{S}-1)\ [\ \cos(\theta_o+\beta)\ ]\ \theta\sin\theta + 2\sin\theta_o\sin\beta\cos\theta$$

$$- (\frac{Q}{S} - 1)\theta_o \sin(\theta_o + \beta)\cos\theta \Big\}$$

$$+ \frac{P_o}{4\mu(2\alpha - \sin 2\alpha)} \Big\{ -(\frac{Q}{S} + 1)\sin(\theta_o + \beta) \sin\theta \ln(\frac{r_o}{r})$$

$$- (\frac{Q}{S} - 1) [\, \sin(\theta_o + \beta) \,]\, \theta \cos\theta - 2 \sin\beta \cos\theta_o \sin\theta$$

$$+ (\frac{Q}{S} - 1)\, \theta_o \cos(\theta_o + \beta)\sin\theta \Big\}$$

$$+ \frac{P_o}{4\mu} \Big\{ - \sum_{p_n > o} \frac{1}{p_n} [\, (\frac{Q}{S} + p_n) A_1(r_>) \cos(p_n + 1)\theta$$

$$- A_3(r_>) \cos(p_n - 1)\theta \,] \frac{r_o^{\,p_n}}{r^{p_n}}$$

$$+ \sum_{q_n > o} \frac{1}{q_n} [\, (\frac{Q}{S} + q_n) A_2(r_>) \sin(q_n + 1)\theta$$

$$- A_4(r_>) \sin(q_n - 1)\theta \,] \frac{r_o^{\,q_n}}{r^{q_n}} \Big\} \qquad (45)$$

$$u_r^{(i)}(r_<, \theta) = B_o \cos\theta - F_o \sin\theta$$

$$- \frac{P_o}{4\mu} \Big\{ \sum_{p_n > 0} \frac{1}{p_n} [\, (\frac{Q}{S} - p_n) A_1(r_<) \cos(p_n - 1)\theta$$

$$- A_3(r_<) \cos(p_n + 1)\theta \,] \frac{r^{p_n}}{r_o^{\,p_n}}$$

$$+ \sum_{q_n > 0} \frac{1}{q_n} [\, (\frac{Q}{S} - q_n) A_2(r_<) \sin(q_n - 1)\theta$$

$$- A_4(r_<) \sin(q_n + 1)\theta \,] \frac{r^{q_n}}{r_o^{\,q_n}} \Big\} \qquad (46)$$

$$u_\theta^{(i)}(r_>,\theta) = -B_o \sin\theta - F_o \cos - F_1 r$$

$$+ \frac{P_o}{4\mu(2\alpha+\sin 2\alpha)} \Big\{ (\frac{Q}{S}+1)\cos(\theta_o+\beta)\sin\theta \ln(\frac{r_o}{r})$$

$$+ (\frac{Q}{S}-1)\ [\cos(\theta_o+\beta)]\ \theta\cos\theta - 2\cos\theta_o \cos\beta\sin\theta$$

$$+ (\frac{Q}{S}-1)\sin(\theta_o+\beta)\sin\theta \Big\}$$

$$+ \frac{P_o}{4\mu(2\alpha-\sin 2\alpha)} \Big\{ -(\frac{Q}{S}+1)\sin(\theta_o+\beta)\cos\theta \ln(\frac{r_o}{r})$$

$$+ (\frac{Q}{S}-1)\ [\sin(\theta_o+\beta)]\ \theta\sin\theta + 2\sin\theta_o \cos\beta\cos\theta$$

$$+ (\frac{Q}{S}-1)\ \theta_o \cos(\theta_o+\beta)\cos\theta \Big\}$$

$$+ \frac{P_o}{4\mu} \Big\{ \sum_{p_n>0} \frac{1}{p_n} \Big[(\frac{Q}{S}-p_n) A_1(r_>)\sin(p_n+1)\theta$$

$$+ A_3(r_>)\sin(p_n-1)\theta \Big] \frac{r^{p_n}}{r_o^{p_n}}$$

$$+ \sum_{q_n>0} \frac{1}{q_n} \Big[(\frac{Q}{S}-q_n) A_2(r_>)\cos(q_n+1)\theta$$

$$+ A_4(r_>)\cos(q_n-1)\theta \Big] \frac{r^{q_n}}{r_o^{q_n}} \Big\} \tag{47}$$

$$u_\theta^{(i)}(r_<,\theta) = -B_o \sin\theta - F_o \cos\theta - F_1 r$$

$$- \frac{P_o}{4\mu} \Big\{ \sum_{p_n>0} \frac{1}{p_n} \Big[(\frac{Q}{S}+p_n) A_1(r_<)\sin(p_n-1)\theta$$

$$+ A_3(r_<)\sin(p_n+1)\theta\,]\,\frac{r^{p_n}}{r_o^{\,p_n}}$$

$$+ \sum_{q_n>0} \frac{1}{q_n}\,[\,-(\frac{Q}{S}+q_n)A_2(r_<)\cos(q_n-1)\theta$$

$$- A_4(r_<)\sin(q_n-1)\theta\,]\,\frac{r^{q_n}}{r_o^{\,q_n}}\,\} \tag{48}$$

where $r_>$ means $r > r_o$, $r_<$ means $r < r_o$, p_n and q_n are the roots of the transcendental equations, by setting equations (35), a_1 and a_2, to zero with in = -p, +q, viz:

$$\sin 2p\alpha + p\sin 2\alpha = 0 \tag{49}$$

$$\sin 2q\alpha - q\sin 2\alpha = 0 \tag{50}$$

$$A_1(r_>) = \frac{1}{\Delta_1}\,\{\cos[\,(p_n-1)\theta_o-\beta\,]$$

$$+ \frac{1}{(\frac{Q}{S}+1)}\,([\,a_3'-a_3'(\theta_o)\,]\cos[\,(p_n+1)\theta_o+\beta\,]$$

$$- a_1'(\theta_o)\sin[\,(p_n+1)\theta_o+\beta\,])\} \tag{51}$$

$$A_1(r_<) = \frac{1}{\Delta_1}\,\{\cos[\,(p_n+1)\theta_o+\beta\,]$$

$$+ \frac{1}{(\frac{Q}{S}+1)}\,([\,a_4-a_4(\theta_o)\,]\cos[\,(p_n-1)\theta_o-\beta\,]$$

$$- a_1(\theta_o)\sin[\,(p_n-1)\theta_o-\beta\,])\} \tag{52}$$

$$A_2(r_<) = \frac{1}{\Delta_2} \{ \sin [(q_n - 1)\theta_o - \beta]$$

$$- \frac{1}{(\frac{Q}{S} + 1)} ([b_4 - b_4(\theta_o)] \sin [(q_n + 1)\theta_o + \beta]$$

$$+ a_2'(\theta_o) \cos [(q_n + 1)\theta_o + \beta]) \} \tag{53}$$

$$A_2(r_<) = \frac{1}{\Delta_2} \{ - \sin [(q_n + 1)\theta_o + \beta]$$

$$+ \frac{1}{(\frac{Q}{S} + 1)} ([b_3' - b_3'(\theta_o)] \sin [(q_n - 1)\theta_o - \beta]$$

$$+ b_2'(\theta_o) \cos [(q_n - 1)\theta_o - \beta]) \} \tag{54}$$

$$A_3(r_>) = \frac{1}{\Delta_1} \{ - a_4' \cos [(p_n - 1)\theta_o - \beta]$$

$$+ \frac{1}{(\frac{Q}{S} + 1)} ([a_4' a_1'(\theta_o) \sin [(p_n + 1)\theta_o + \beta]$$

$$+ [a_4' a_3'(\theta_o) + (p_n{}^2 - 1)] \cos [(p_n + 1)\theta_o + \beta]) \} \tag{55}$$

$$A_3(r_<) = \frac{1}{\Delta_1} \{ - a_3' \cos [(p_n + 1)\theta_o + \beta]$$

$$+ \frac{1}{(\frac{Q}{S} + 1)} (a_3' a_1'(\theta_o) \sin [(p_n - 1)\theta_o - \beta]$$

$$+ [a_3' a_4'(\theta_o) + (p_n{}^2 - 1)] \cos [(p_n - 1)\theta_o - \beta]) \} \tag{56}$$

$$A_4(r_>) = \frac{1}{\Delta_2}\Big\{ b_3' \sin[(q_n-1)\theta_o-\beta]$$

$$+\frac{1}{(\frac{Q}{S}+1)}\Big(-b_3'b_2'(\theta_o)\cos[(q_n+1)\theta_o+\beta]$$

$$+[b_3'b_4'(\theta_o)+(q_n^2-1)]\sin[(q_n+1)\theta_o+\beta]\Big)\Big\} \tag{57}$$

$$A_4(r_<) = \frac{1}{\Delta_2}\Big\{ -b_4' \sin[(q_n+1)\theta_o+\beta]$$

$$+\frac{1}{(\frac{Q}{S}+1)}\Big(b_4'b_2'(\theta_o)\cos[(q_n-1)\theta_o-\beta]$$

$$-[b_4'b_3'(\theta_o)+(q_n^2-1)]\sin[(q_n-1)\theta_o-\beta]\Big)\Big\} \tag{58}$$

$$\begin{matrix} a_1' \\ a_2' \end{matrix} = \sin 2p_n\alpha \pm p_n \sin 2\alpha \tag{59}$$

$$\begin{matrix} a_3' \\ a_4' \end{matrix} = \cos 2p_n\alpha \pm p_n \cos 2\alpha \tag{60}$$

$$\begin{matrix} a_1'(\theta_o) \\ a_2'(\theta_o) \end{matrix} = \sin 2p_n\theta_o \pm p_n \sin 2\theta_o \tag{61}$$

$$\begin{matrix} a_3'(\theta_o) \\ a_4'(\theta_o) \end{matrix} = \cos 2p_n\theta_o \pm p_n \cos 2\theta_o \tag{62}$$

$$\begin{matrix} b_1' \\ b_2' \end{matrix} = \sin 2q_n\alpha \pm q_n \sin 2\alpha \tag{63}$$

$$\begin{matrix} b_3' \\ b_4' \end{matrix} = \cos 2q_n\,\alpha \pm q_n \cos 2\alpha \tag{64}$$

$$\begin{matrix} b_1'(\theta_o) \\ b_2'(\theta_o) \end{matrix} = \sin 2q_n\,\theta_o \pm q_n \sin 2\theta_o \tag{65}$$

$$\begin{matrix} b_3'(\theta_o) \\ b_4'(\theta_o) \end{matrix} = \cos 2q_n\,\theta_o \pm q_n \cos 2\theta_o \tag{66}$$

$$\Delta_1 = 2\alpha \cos 2p_n\alpha + \sin 2\alpha \tag{67}$$

$$\Delta_2 = 2\alpha \cos 2q_n\alpha - \sin 2\alpha \tag{68}$$

The rigid body motion constants can be fixed by choosing a particular point $(r_1\ , 0)$, where r_1 is sufficiently large that

$$u_r(r_>, \theta)\Big|_{\substack{r=r_1\\ \theta=0}} = 0 \tag{69}$$

$$u_\theta(r_>, \theta)\Big|_{\substack{r=r_1\\ \theta=0}} = 0 \tag{70}$$

$$\frac{\partial u_\theta(r_>, \theta)}{\partial r}\Bigg|_{\substack{r=r_1\\ \theta=0}} = 0 \tag{71}$$

From equations (45) and (47), we obtain

$$B_o = \frac{P_o}{4\mu(2\alpha+\sin 2\alpha)} \; \{ \; (\frac{Q}{S}+1)\cos(\theta_o+\beta)\ln(\frac{r_o}{r_1})$$

$$+ (\frac{Q}{S}-1)\theta_o \sin(\theta_o+\beta) - 2 \sin\theta_o \sin\beta \; \}$$

$$+\frac{P_o}{4\mu}\sum_{p_n>0}\frac{1}{p_n}\left[\left(\frac{Q}{S}+p_n\right)A_1(r_>)-A_3(r_>)\right]\frac{r_o^{\,p_n}}{r_1^{\,p_n}} \tag{72}$$

$$F_1=-\frac{P_o}{4\mu}\left\{\sum_{q_n>0}\left[\left(\frac{Q}{S}-q_n\right)A_2(r_>)+A_4(r_>)\right]\frac{r_o^{\,q_n}}{r_1^{\,q_n+1}}\right\}$$

$$+\frac{P_o}{4\mu(2\alpha-\sin 2\alpha)}\left[\left(\frac{Q}{S}+1\right)\sin(\theta_o+\beta)\right]\frac{1}{r_1} \tag{73}$$

$$F_o=\frac{P_o}{4\mu(2\alpha-\sin 2\alpha)}\left\{-\left(\frac{Q}{S}+1\right)\sin(\theta_o+\beta)\left[1+\ln\left(\frac{r_o}{r_1}\right)\right]\right.$$

$$\left.+\left(\frac{Q}{S}-1\right)\theta_o\cos(\theta_o+\beta)+2\sin\theta_o\cos\beta\right\}$$

$$+\frac{P_o}{4\mu}\sum_{q_n>0}\left(1+\frac{1}{q_n}\right)\left[\left(\frac{Q}{S}-q_n\right)A_3(r_>)+A_4(r_>)\right]\frac{r_o^{\,q_n}}{r_1^{\,q_n}} \tag{74}$$

5. *Limiting Cases*

(1) Case A: for $\theta_o=\alpha$, that is, the load is applied on one of the wedge surfaces (Figure 2). Equations (39) to (47) reduce to

$$\tau_{rr}^{(2)}(r_>,\theta)=\frac{2P_o}{r}\left[\frac{\cos(\alpha+\beta)\cos\theta}{2\alpha+\sin 2\alpha}+\frac{\sin(\alpha+\beta)\sin\theta}{2\alpha-\sin 2\alpha}\right]$$

$$+\sum_{p_n}\frac{P_o}{2\Delta_1}\left\{(p_n+3)(d_3+d_8)\cos(p_n+1)\theta\right.$$

$$\left.-\left[(p_n+1)d_1+(p_n-1)d_6\right]\cos(p_n-1)\theta\right\}\frac{r_o^{\,p_n}}{r^{\,p_n+1}}$$

$$+\sum_{q_n}\frac{P_o}{2\Delta_2}\left\{-(q_n+3)(d_4-d_7)\sin(q_n+1)\theta\right.$$

$$+ [\,(q_n-1)d_2-(q_n+1)d_5\,]\,\sin(q_n-1)\theta \}\,\frac{r_o^{\,q_n}}{r^{q_n+1}} \tag{75}$$

$$\tau_{rr}^{(2)}(r_<,\theta)=\sum_{p_n}\frac{P_o}{2\Delta_1}\,\{\,-(p_n-3)(d_1-d_6)\cos(p_n-1)\theta$$

$$+ [\,(p_n-1)d_3-(p_n+1)d_8\,]\,\cos(p_n+1)\theta\,\}\,\frac{r^{p_n-1}}{r_o^{\,p_n}}$$

$$-\sum_{q_n}\frac{P_o}{2\Delta_2}\,\{\,(q_n-3)(d_2+d_5)\sin(q_n-1)\theta$$

$$-[\,(q_n+1)d_4+(q_n-)d_7\,]\,\sin(q_n+1)\theta\,\}\,\frac{r^{q_n-1}}{r_o^{\,q_n}} \tag{76}$$

$$\tau_{\theta\theta}^{(2)}(r_>,\theta)=\sum_{p_n}\frac{P_o}{2\Delta_1}\,\{-(p_n-1)(d_8+d_3)\cos(p_n+1)\theta$$

$$+ [\,(p_n+1)d_1+(p_n-1)d_6\,]\,\cos(p_n-1)\theta\,\}\,\frac{r_o^{\,p_n}}{r^{p_n+1}}$$

$$+\sum_{q_n}\frac{P_o}{2\Delta_2}\,\{\,(q_n-1)(d_4-d_7)\sin(q_n+1)\theta$$

$$+ [\,(q_n+1)d_5-(q_n-1)d_2\,]\,\sin(q_n-1)\theta\,\}\,\frac{r_o^{\,q_n}}{r^{q_n+1}} \tag{77}$$

$$\tau_{\theta\theta}^{(2)}(r_<,\theta)=\sum_{p_n}\frac{P_o}{2\Delta_1}\,\{-(p_n+1)(d_6-d_1)\cos(p_n-1)\theta$$

$$- [(p_n-1)d_3-(p_n+1)d_8] \cos(p_n+1)\theta \} \frac{r^{p_n-1}}{r_o^{p_n}}$$

$$+ \sum_{q_n} \frac{P_o}{2\Delta_2} \{ (q_n+1)(d_2+d_5)\sin(q_n-1)\theta$$

$$- [(q_n-1)d_7+(q_n+1)d_4] \sin(q_n+1)\theta \} \frac{r^{q_n-1}}{r_o^{q_n}} \tag{78}$$

$$\tau_{\theta r}^{(2)}(r_>, \theta) = \sum_{p_n} \frac{P_o}{2\Delta_1} \{ (p_n+1)(d_3+d_8)\sin(p_n+1)\theta$$

$$- [(p_n+1)d_1+(p_n-1)d_6] \sin(p_n-1)\theta \} \frac{r_o^{p_n}}{r^{p_n+1}}$$

$$+ \sum_{q_n} \frac{P_o}{2\Delta_2} \{ (q_n+1)(d_4-d_7)\cos(p_n+1)\theta$$

$$- [(q_n-1)d_2-(q_n+1)d_5] \cos(p_n-1)\theta \} \frac{r_o^{q_n}}{r^{q_n+1}} \tag{79}$$

$$\tau_{\theta r}^{(2)}(r_<, \theta) = \sum_{p_n} \frac{-P_o}{2\Delta_1} \{ (p_n-1)(d_1-d_6)\sin(p_n-1)\theta$$

$$+ [(p_n+1)d_3+(p_n-1)d_8] \sin(p_n+1)\theta \} \frac{r^{p_n-1}}{r_o^{p_n}}$$

$$- \sum_{q_n} \frac{P_o}{2\Delta_2} \{ (q_n-1)(d_2+d_5)\cos(q_n-1)\theta$$

$$- [(q_n+1)d_4+(q_n-1)d_7] \cos(q_n+1)\theta \} \frac{r^{q_n-1}}{r_o^{q_n}} \tag{80}$$

$$
\begin{aligned}
u_r^{(2)}(r_>, \theta) = {} & \frac{P_o}{4\mu(2\alpha+\sin 2\alpha)} \left\{ \left[2\sin\alpha \sin\beta - \left(\frac{Q}{S}-1\right) \alpha \sin(\alpha+\beta) \right] \cos\theta \right. \\
& \left. + \cos(\alpha+\beta) \left[\left(\frac{Q}{S}-1\right)\sin\theta + \left(\frac{Q}{S}+1\right)\cos\theta \ln\left(\frac{r}{r_o}\right) \right] \right\} \\
& + \frac{P_o}{4\mu(2\alpha-\sin 2\alpha)} \left\{ \left[\left(\frac{Q}{S}-1\right) \alpha \cos(\alpha+\beta) - 2\cos\alpha \sin\beta \right] \sin\theta \right. \\
& \left. - \sin(\alpha+\beta) \left[\left(\frac{Q}{S}-1\right)\theta\cos\theta - \left(\frac{Q}{S}+1\right)\sin\theta \ln\left(\frac{r}{r_o}\right) \right] \right\} \\
& + \sum_{p_n} \frac{P_o}{4\mu p_n \Delta_1} \left\{ -\left(\frac{Q}{S}+p_n\right)(d_3+d_8)\cos(p_n+1)\theta \right. \\
& \left. + \left[(p_n+1)d_1 + (p_n-1)d_6 \right] \cos(p_n-1)\theta \right\} \frac{r_o^{p_n}}{r^{p_n}} \\
& + \sum_{q_n} \frac{P_o}{4\mu q_n \Delta_2} \left\{ \left(\frac{Q}{S}+q_n\right)(d_4-d_7)\sin(q_n+1)\theta \right. \\
& \left. - \left[(q_n-1)d_2 - (q_n+1)d_5 \right] \sin(q_n-1)\theta \right\} \frac{r_o^{q_n}}{r^{q_n}} \\
& + B_o\cos\theta - F_o\sin\theta \qquad (81)
\end{aligned}
$$

$$
\begin{aligned}
u_r^{(2)}(r_<, \theta) = {} & B_o\cos\theta - F_o\sin\theta \\
& + \sum_{p_n} \frac{P_o}{4\mu p_n \Delta_1} \left\{ \left(\frac{Q}{S}-p_n\right)(d_2-d_6)\cos(p_n-1)\theta \right. \\
& \left. + \left[(p_n-1)d_3 - (p_n+1)d_8 \right] \cos(p_n+1)\theta \right\} \frac{r^{p_n}}{r_o^{p_n}}
\end{aligned}
$$

$$+ \sum_{q_n} \frac{P_o}{4\mu q_n \Delta_2} \left\{ \left(\frac{Q}{S} - q_n\right)(d_2+d_5)\sin(q_n-1)\theta \right.$$

$$\left. + \left[(q_n+1)d_4 + (q_n-1)d_7 \right] \sin(q_n+1)\theta \right\} \frac{r^{q_n}}{r_o^{q_n}} \tag{82}$$

$$u_\theta^{(2)}(r_>, \theta) = -B_o \sin\theta - F_o \cos\theta - F_1 r$$

$$+ \frac{P_o}{4\mu(2\alpha+\sin 2\alpha)} \left\{ \left[\left(\frac{Q}{S} - 1\right)\alpha \sin(\alpha+\beta) - 2\cos\alpha\cos\beta \right] \sin\theta \right.$$

$$\left. + \cos(\alpha+\beta) \left[\left(\frac{Q}{S} - 1\right)\theta\cos\theta - \left(\frac{Q}{S} + 1\right)\sin\theta \ln\left(\frac{r}{r_o}\right) \right] \right\}$$

$$+ \frac{P_o}{4\mu(2\alpha-\sin 2\alpha)} \left\{ \left[\left(\frac{Q}{S} - 1\right)\alpha \cos(\alpha+\beta) + 2\sin\alpha\cos\beta \right] \cos\theta \right.$$

$$\left. + \sin(\alpha+\beta) \left[\left(\frac{Q}{S} - 1\right)\theta\sin\theta + \left(\frac{Q}{S} + 1\right)\cos\theta \ln\left(\frac{r}{r_o}\right) \right\} \right.$$

$$+ \sum_{p_n} \frac{P_o}{4\mu p_n \Delta_1} \left\{ \left(\frac{Q}{S} - p_n\right)(d_3+d_8)\sin(p_n+1)\theta \right.$$

$$\left. + \left[(p_n+1)d_1 + (p_n-1)d_6 \right] \sin(p_n-1)\theta \right\} \frac{r_o^{p_n}}{r^{p_n}}$$

$$+ \sum_{q_n} \frac{P_o}{4\mu q_n \Delta_2} \left\{ \left(\frac{Q}{S} - q_n\right)(d_4-d_7)\cos(q_n+1)\theta \right.$$

$$\left. + \left[(q_n-1)d_2 - (q_n+1)d_5 \right] \cos(q_n-1)\theta \right\} \frac{r_o^{q_n}}{r^{q_n}} \tag{83}$$

$$
\begin{aligned}
u_{\theta}^{(2)}(r_{<},\theta) = & -B_o \sin\theta - F_o \cos\theta - F_1 r \\
& + \sum_{p_n} \frac{P_o}{4\mu p_n \Delta_1} \left\{ \left(\frac{Q}{S} + p_n\right)(d_1 - d_6)\sin(p_n-1)\theta \right. \\
& \left. - \left[(p_n-1)d_3 - (p_n+1)d_8 \right] \sin(p_n+1)\theta \right\} \frac{r^{p_n}}{r_o^{p_n}} \\
& - \sum_{q_n} \frac{P_o}{4\mu q_n \Delta_2} \left\{ \left(\frac{Q}{S} + q_n\right)(d_2 + d_5)\cos(q_n-1)\theta \right. \\
& \left. - \left[(q_n+1)d_4 + (q_n-1)d_7 \right] \cos(q_n+1)\theta \right\} \frac{r^{q_n}}{r_o^{q_n}}
\end{aligned}
\tag{84}
$$

$$d_1 = \sin(p_n+1)\alpha \sin\beta \tag{85}$$

$$d_2 = \sin(q_n+1)\alpha \cos\beta \tag{86}$$

$$d_3 = \sin(p_n-1)\alpha \sin\beta \tag{87}$$

$$d_4 = \sin(q_n-1)\alpha \cos\beta \tag{88}$$

$$d_5 = \cos(q_n+1)\alpha \sin\beta \tag{89}$$

$$d_6 = \cos(p_n+1)\alpha \cos\beta \tag{90}$$

$$d_7 = \cos(q_n-1)\alpha \sin\beta \tag{91}$$

$$d_8 = \cos(p_n-1)\alpha \cos\beta \tag{92}$$

Equations (75) to (84) are identical to those given in Reference [11].

(2) Case B: for $r_o = 0$, that is, the load is applied to the vertex of the wedge (Figure 3), equations (39), (41), (43), (45) and (47) reduce to

$$\tau_{rr}^{(i)}(r_>,\theta)\Big|_{r_o=0} = \frac{2P_o\cos(\theta_o+\beta)}{(2\alpha+\sin 2\alpha)}\,\frac{\cos\theta}{r} + \frac{2P_o\sin(\theta_o+\beta)}{(2\alpha-\sin 2\alpha)}\,\frac{\sin\theta}{r} \qquad (93)$$

$$\tau_{\theta\theta}^{(i)}(r_>,\theta)\Big|_{r_o=0} = \tau_{\theta r}^{(i)}(r_>,\theta)\Big|_{r_o=0} = 0 \qquad (94)$$

$$\begin{aligned} u_r^{(i)}(r_>,\theta)\Big|_{r_o=0} = {} & \frac{P_o\cos(\theta_o+\beta)}{4\mu(2\alpha+\sin 2\alpha)}\left\{ \left(\frac{Q}{S}-1\right)\theta\sin\theta \right. \\ & \left. + \left(\frac{Q}{S}+1\right)\ln\left(\frac{r}{r_1}\right)\cos\theta \right\} \\ & + \frac{P_o\sin(\theta_o+\beta)}{4\mu(2\alpha-\sin 2\alpha)}\left\{ \left(\frac{Q}{S}+1\right)\ln\left(\frac{r}{r_1}\right)\sin\theta \right. \\ & \left. + \left(\frac{Q}{S}-1\right)\left[\sin\theta-\theta\cos\theta\right] \right\} \end{aligned} \qquad (95)$$

$$\begin{aligned} u_\theta^{(i)}(r_>,\theta)\Big|_{r_o=0} = {} & \frac{P_o\cos(\theta_o+\beta)}{4\mu(2\alpha+\sin 2\alpha)}\left\{ \left(\frac{Q}{S}-1\right)\theta\cos\theta \right. \\ & \left. - \left(\frac{Q}{S}+1\right)\ln\left(\frac{r}{r_1}\right)\sin\theta - 2\sin\theta \right\} \\ & + \frac{P_o\sin(\theta_o+\beta)}{4\mu(2\alpha-\sin 2\alpha)}\left\{ \left(\frac{Q}{S}-1\right)\theta\sin\theta \right. \\ & \left. + \left(\frac{Q}{S}+1\right)\left[\ln\left(\frac{r}{r_1}\right)\cos\theta - \frac{r}{r_1} + \cos\theta\right] \right\} \end{aligned} \qquad (96)$$

Solutions for stresses and displacements, equations (93) to (96), are the same as given by Michell [2] and Teng [11].

6. *Remarks*

It is understood that the solution of the problem for a wedge subjected to an interior multipoleline load may similarly be obtained.

For the plane strain or plane stress problems of a single wedge, the stresses are independent of the elastic properties of the medium if a load applied on the free surface, whereas the stresses depend on the elastic properties of the medium if a load applied internally.

For a single wedge problem, the transcendental equations obtained for the present interior loading case, equations (35), are exactly the same as those obtained for the surface loading case.

Acknowledgement

The authoress wishes to express her appreciation to Professor John T. Kuo and Dr. Chung Gong. (郭宗汾教授，龔鐘博士) for their fruitful discussion.

References

(1) Levy, M., "Mecánique Appliquée - Sur L'équilibre élastique d'un barrage in Macon-nerie à section triangulaires"Comptes Rendus Hebdomaires des Seances, Vol. 127, 1898, pp. 10-15.

(2) Michell, J. H., "Elementary Distributions of Plane Stress," Proceeding of the London Mathematical Society, Vol. 32, 1900, pp. 35-63.

(3) Brahtz, J. H. A., "Stress Distribution in Wedges with Arbitrary Boundary Forces," Journal of Applied Physics, Vol. 4, 1936, pp. 56-65.

(4) Shepherd, W. M., "Stress Systems in an Infinite Sector," Proceedings of the Royal Society, London, Series A, Vol. 148, 1935, pp. 284-303.

(5) Carothers, S. D., "Plane Strain in a Wedge with Applications to Masonary Dams," Proceedings of the Royal Society, Edinburgh, Vol. 33, 1913, pp. 292-306.

(6) Tranter, C. J., "The Use of the Mellin Transform in Finding the Stress Distribution in an Infinite Wedge," Quarterly Journal of Mechanics and Applied Mathematics, Vol. 1, 1948, pp. 125-130.

(7) Sternberg, E., and Koiter, W. T., "The Wedge Under a Concentrated Couple: A Paradox in the Two-Dimensional Theory of Elasticity," JOURNAL OF APPLIED MECHANICS, Vol. 25, TRANS. ASME, Vol. 80, 1958, pp. 575-581.

(8) Buchward, V. T., "Eigenfunctions of plane Elastostatics III, the Wedge," Journal of the Australian Mathematical Society, Vol. 5, 1965, pp. 241-257.

(9) Hetényi, M., "A Method of Solution for the Elastic Quarter-Plane," JOURNAL OF APPLIED MECHANICS, Vol. 27, TRANS. ASME, Vol. 82, Series E, 1960, pp. 289-296.

(10) Karp, S. N., and Karal, F. C., Jr., "The Elastic Field Behavior in the Neighborhood of a Crack of Arbitrary Angle," Communications on Pure and Applied Mathematics, Vol. 15, No. 4, 1962, pp. 413-421.

(11) Teng, Y. C., "Displacements and Stresses in a Two-Dimensional Wedge Shaped Medium," PhD dissertation, Columbia University in the City of New York, N. Y. 1971; or Kuo, J. T., et al., "Loading Problems of Multilayered and Wedge-Shaped Media," report prepared for Air Force Cambridge Research Laboratories, Contract No. AF19(628)-6011, Mar. 1971.

(12) Teng, Y. C., and J. T. Kuo, "Displacements and Stresses in a Two-Dimensional Wedge Shaped Medium," JOURNAL OF APPLIED MECHANICS, Paper No. 74-APM-M.

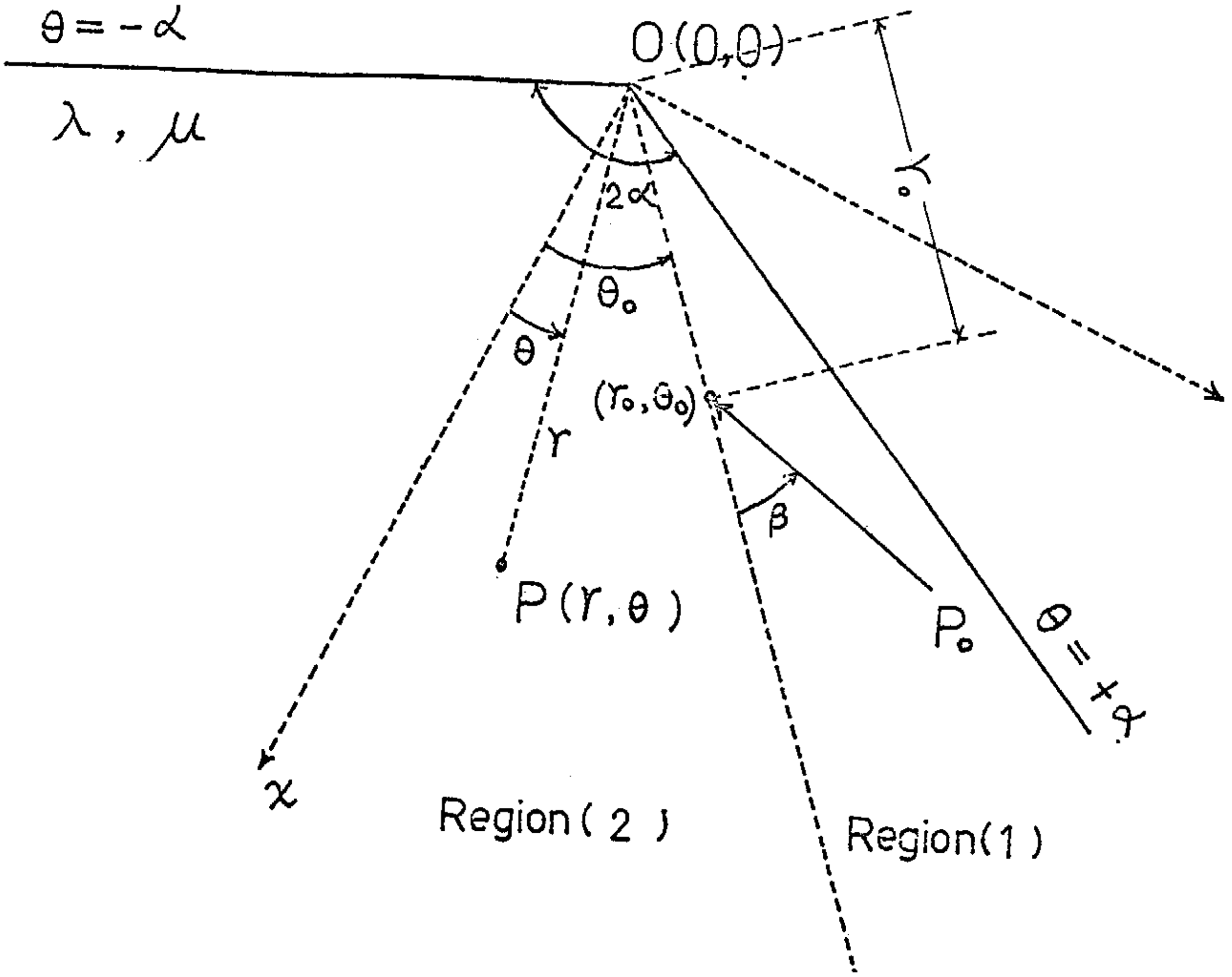

Fig. 1 . An elastic wedge subjected to an interior line load

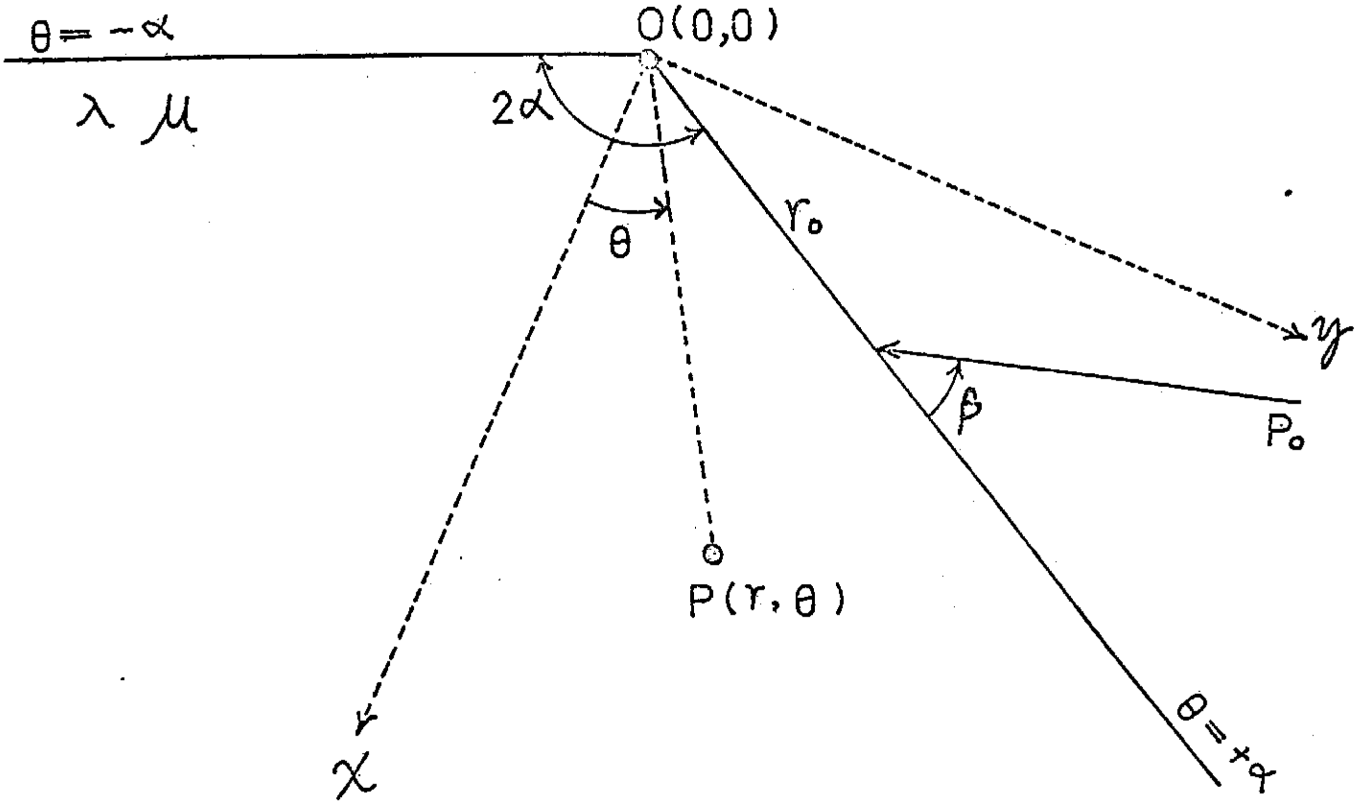

Fig. 2. An elastic wedge subjected to a surface line load

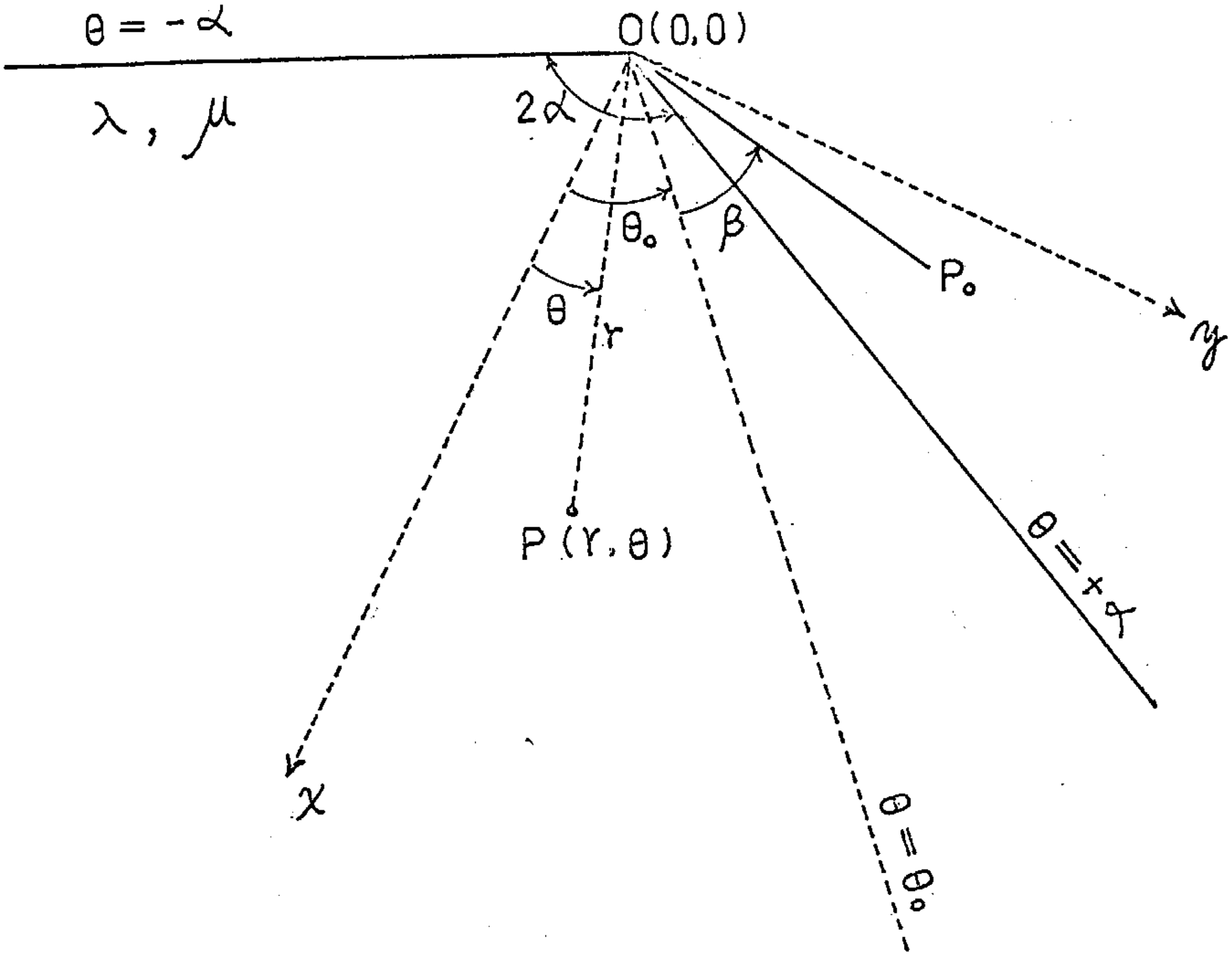

Figure 3 An Elastic Wedge Subjected to a Line Load at the Vertex

ANNUAL REPORT OF THE INSTITUTE OF PHYSICS, ACADEMIA SINICA 1973

TWO DIMENSIONAL INTERPRETATION OF A GRAVITY PROFILE ACROSS TAIWAN

Chih-Ping Lu* and Francis T. Wu
Department of Geological Sciences
SUNY at Binghamton
Binghamton, New York 13901
U. S. A.

Abstract

Crustal thicknesses of about 35 km under the Central Range and about 22 km under the coastal range are inferred from the gravity profile.

1. *Introduction*

Although gravity interpretation is theoretically non-unique, with some additional controls the results had proven to be of value (Talwani et al., 1959a and b). Taiwan has now almost complete coverage along the rim of the island and two profiles across the island along the new cross-island highways. A number of interesting features are revealed. In the absence of extensive deep seismic crustal refractive data, such data can provide some insight into the deep structure underneath Taiwan. In this short research note we will use a two dimensional interpretation, aiming at a preliminary understanding of the crustal thickness and the nature of the Eastern Coastal Range.

2. *The Data*

The gravity data used in this study is mainly obtained from the gravity contour maps of Liu (1964) and Hsieh and Hu (1971) (Fig. la & b). In both maps, all the gravity values established in the survey were referred to the zero gravity base located at the gate of the building of Taiwan Petroleum Exploration Division at Miaoli (Hsieh and Hu, 1971).

* Present address: Seismology Division (C.E.R.C.)
Institute of Physics
Academia Sinica
P. O. Box 58937
Taipei, Taiwan
The Republic of China

According to these maps, the international tie at Taipei Military Air Transport Service Terminal (TMATS) has an anomaly of 23 mgals. Since at TMATS the true Bouguer anomaly is 0.1 mgal, base maps can be converted to Bouguer anomaly maps when subtracted by 23 mgals (Dr. I-Chi Hsu, personal communication, 1972).

The interpretation would be more significant if the gravity data is studied in conjunction with subsurfacial data such as drilling wells or seismic refractive profilings, or from both. Along the profile we have chosen (C-C' in Figure 2) subsurface data is quite abundant near Peikang and on Penhu Islands.

Near the town of Peikang (Fig. 2), two drilling wells (pk-2 & pk-3) were operated by the Chinese Petroleum Corporation (CPC). It was found that Neogene sediments which lie unconformably over a paleocene (Huang, 1968) indurated metamorphic stratum, the Peikang Massif, have a thickness of 1460 metres at pk-2 and 1962 metres at pk-3. It thickness to the east after crossing the Yichu Marginal Hinge Fault (HF) and reaches a thickness of more than 6 km., 30 km. east of Peikang City (Bosum et al., 1970, among others). The similar stratigraphic relationship was also found in Penhu Islands in Taiwan Strait from the drilling well TL-1 (Pan, 1967). The Peikang Massif was found at 500

The reconnaissance aeromagnetic survey gives us a clue as to the thickness of the Peikang Massif. The large area anomalies of low amplitude are the prominent features in Taiwan Strait and were interpreted to be originated from a deep "magnetic basement" which lies underneath the Peikang Massif. The depth of the top of this basement is estimated to be 4 km at Penhu Islands and 7 km at Peikang, as was mapped in Figures 1-10 & 1-17 of Bosum et al (1970). To the west of Penhu, this magnetic basement deepens from 4 km to 10 or 11 km with local variations.

With this information, we can roughly draw boundary lines between the three upper layers for the area west of HF. No subsurfacial data is available for the central and eastern part of Taiwan.

To obtain a starting model, we shall adapt the idea of most of the Taiwan geologists that the island is a product of a miogeosyncline with a sedimentary wedge thickening to the east (Ho, 1967, among others). Accordingly, we extend the substrata beneath west coast of Taiwan to the central and east parts. Boundary lines A, B, and C in Figure 2 are considered to be intersection of boundary surfaces of equal density layers with the earth surface. Through lithostratigraphic correlations between the outcrops of regions A, B, and C and the subsurfacial information from drilling wells of Peikang and Penhu Islands, we suggest a three-layered crustal model for west of the East Taiwan Rift (region E in Fig. 2 and 3b) bounded from below by the magnetic basement.

The structure line between the Central Range and the Coastal Range is the Central

Range fault. To the east of this fault, we assume that the East Coastal Range lies on a "modified oceanic crust" (i.e. with thicker gabbroic layer below oceanic theolite). Starting from this rough model, we have attempted by trial and error to find a crustal model, including layer thicknesses and moho depth that fits the Bouguer anomaly along C-C'.

3. *The Computation*

The method of computing the gravitational profile is that of Talwani et al (1959a), as modified by Corbato (1965).

We start our calculation from a 3-layered crust on both sides of the Central Range fault. As was noticed in the previous paragraphs, in this model only the boundaries between the Penhu Islands and the Foothill Zone (Fig. 2) are certain. The density of the layers are assigned according to the rock types (Table 1). For the layer below these three, we suppose it to be the basement of the crust and has a uniformly density. We use 2.9 g/cm^3 and 3.4 g/cm^3 to be densities of this layer and the mantle underneath respectively, as were suggested by Talwani et al (1959b) for Puerto Rico. The fit of the calculated Bouguer anomalies to the observed ones requires varying constantly, not only the location of moho but also the locations of boundaries and densities of each layer, especially for the part east of the hinge fault (Fig. 4b). The computation was terminated when the difference between the calculated and observed profiles differ by less than 10 mgal on the average.

It is found that in the final model (Fig. 4b) any attempt to vary the configuration of moho will generate pronounced difference between the calculated and the observed anomalies. The agreement between calculated and observed lines (Fig. 4a) could only be improved by shifting the boundaries of layers in the crust and varying the densities slightly. This test suggests that the location of moho is rather dependable. As a consequence, the model gives us thickness of the crust along C-C'.

Three segments in Fig. 4a have to be explained. Judging from the appearance of basaltic layers found in the drilling well of TL-1, the disagreement around Penhu may come from the existence of a basaltic magmatic chamber underneath. Around the hinge fault the observed anomaly may imply a more complicated fault configuration in the vicinity. The abrupt change near the region of East coast Range demands a steep and deep fault zone as well as different crustal structures on both its sides.

Discussion

The preliminary results presented here have some interesting implications:

(1) The variation in the thickness of moho seems to indicate the thickening of an originally

thinner crust perhaps as a consequence of the collosion of the coastal range with the miogeosyncline (Jahn, 1972, Chai, 1972; Biq, 1969).

(2) Under the coastal range, the high density (2.9) layer is very close to the surface and the crustal thickness is much thinner than that under the central range.

Until there is more complete gravity coverage and more refraction or reflection seismic data on Taiwan, the uniqueness of our interpretation cannot be ensured.

References

1. Biq, C., 1969, Role of gravitational gliding in Taiwan tectogneiss, Bull. Geol. Survey Taiwan, no. 20, 2-39.
2. Bosum, W., G. D. Burton, S. H. Hsieh, E. G. Kind, A.Schreiber, and C. H. Tang, 1970, I. Aeromagnetic survey of offshore Taiwan, COOP Tech. Bull. 3, 1-34.
3. Chiai, B. H. T., 1972, Structure and tectonic evolution of Taiwan, 1972, Amer. J. Science, 272, 389-422.
4. Corbato, C. E., 1965, A least-squares procedure for gravity interpretation, Geophysics, 30, 228-233.
5. Ho, C. S., 1967, Structural evolution and major tectonic forms of Taiwan, Mem. Geol. Soc. China, 1, 3-24.
6. Hsieh, S. H., C. C. Hu, Gravimetric and magnetic studies of Taiwan, Sino-American Science Cooperation Colloquium on Ocean Resources, Preprints, Vol. 7, 87-145, 1972.
7. Huang, T., 1968, Some paleocene planktonic foraminiferids from well pk-3 at Peikang, Yuanling, Taiwan, Proc. Geol. Soc. China, no. 11, 34-44, for 1967.
8. Jahn, B. M., Reinterpretation of Geologic evolution of the Coastal Range, East Taiwan. Bull. Geol. Soc. Am., 83, 241-248, 1972.
9. Jakosky, J. J., Exploration geophysics, Trija, Los Angeles 1950.
10. Liu, H. H., A preliminary study on the regional Bouguer Anomalies of Taiwan, Petroleum Geol. Taiwan, 3, 1975-183, 1964.
11. Pan, Y. S., 1967, The regional gravity of the Penhu Islands, Taiwan, China, Petro. Geol. Taiwan, no. 5, 117-130.
12. Talwani, M., J. L. Worzel, and M. Landisman, 1959a, Rapid gravity computations for two-dimensional bodies with application to the Medocino submarine fracture zone, J. Geophys. Res., 64, 49-59.
13. Talwani, M., G. D. Burton and J. L. Worzel, 1959b, A crustal section across the Puerto Rico trench, J. Geophs. Res., 64, 1545, 1556.

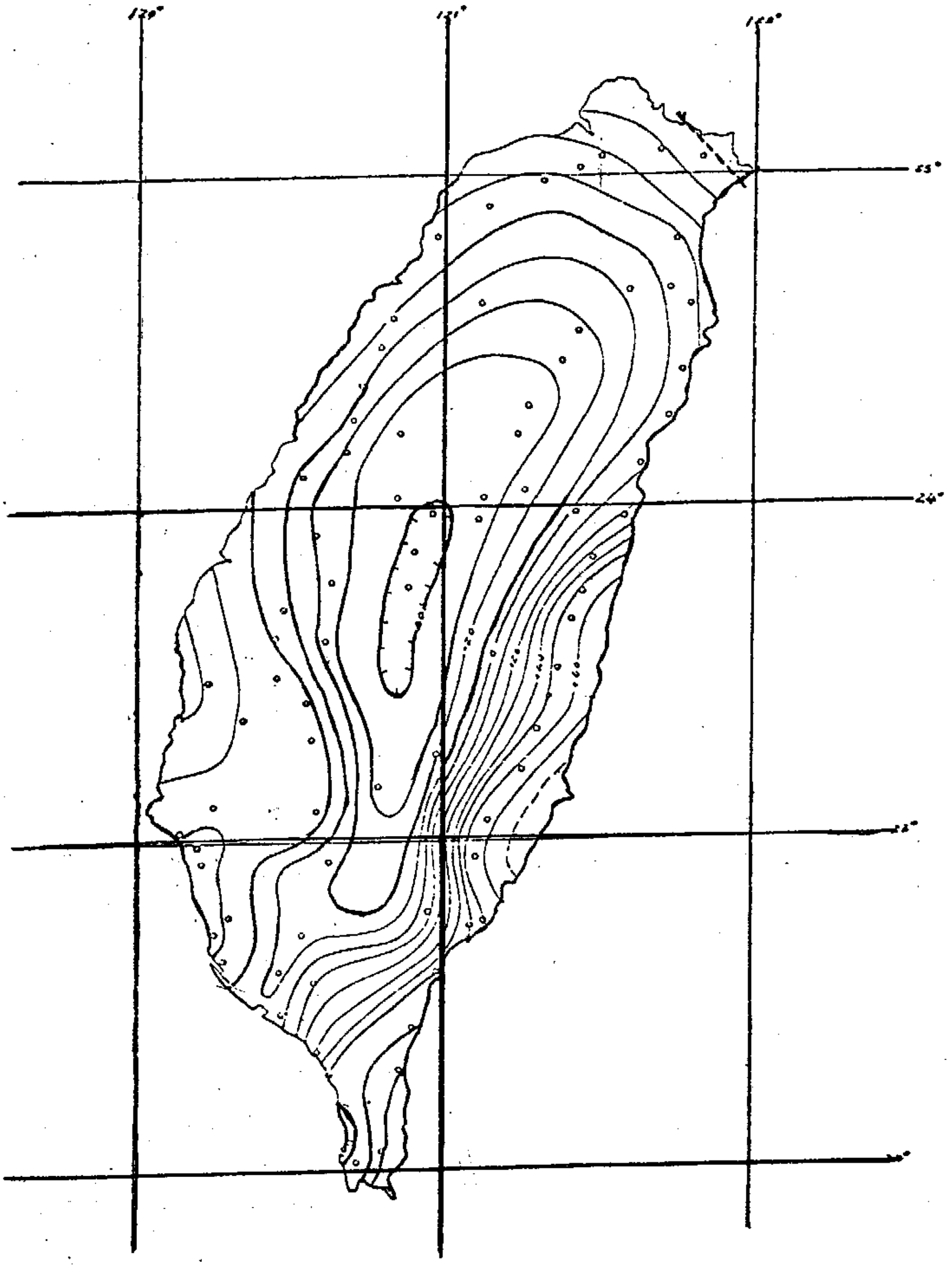

Fig. la Simplified, Bouguer gravity map of Taiwan (Liu, 1964). The values should be subtracted by 23.

Incomplete Bouguer gravity of Taiwan. Contour interval 2 mgal (from Hsieh & Hu, 1972). All the values should be subtracted by 23 mgal. The data used in this report is based on this map, supplemented by data in Fig. la.

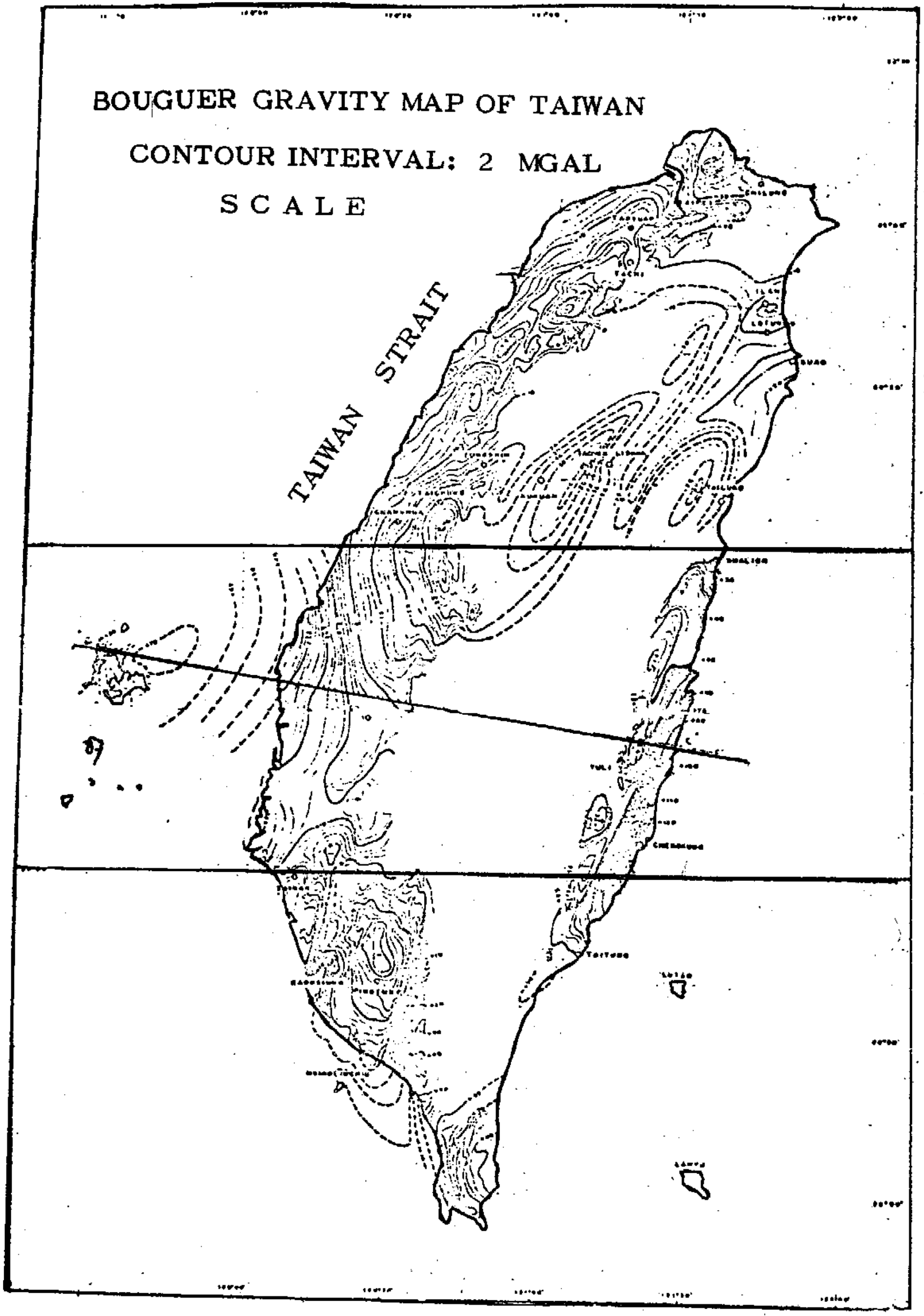

Fig. 2 Simplified structural boundaries of Taiwan. P, paleogene; N, neogene; PT, pre-Tertiary basement (Modified from Biq, 1971).

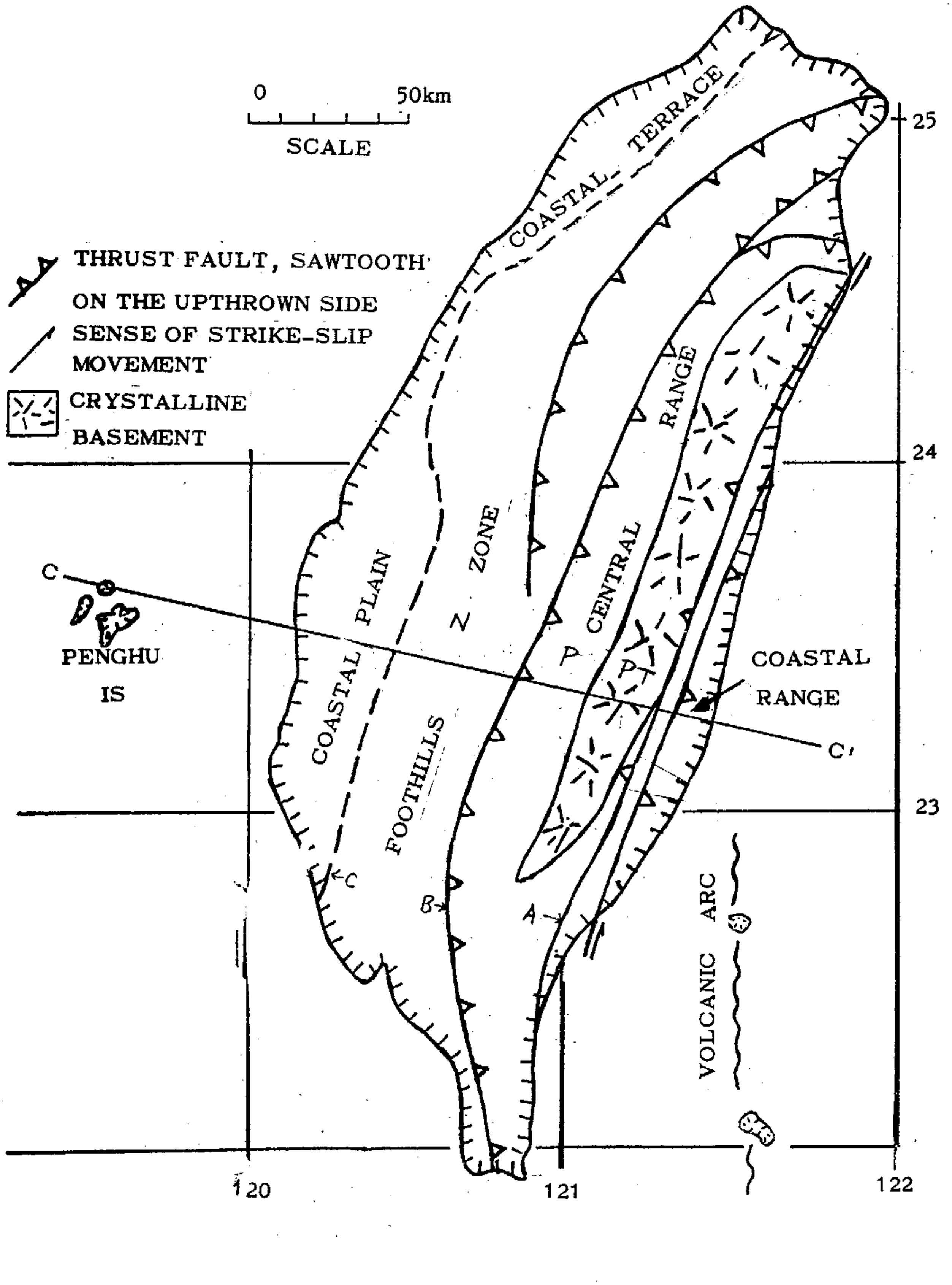

Fig. 3a Data and computed gravitational anomalies from the model.

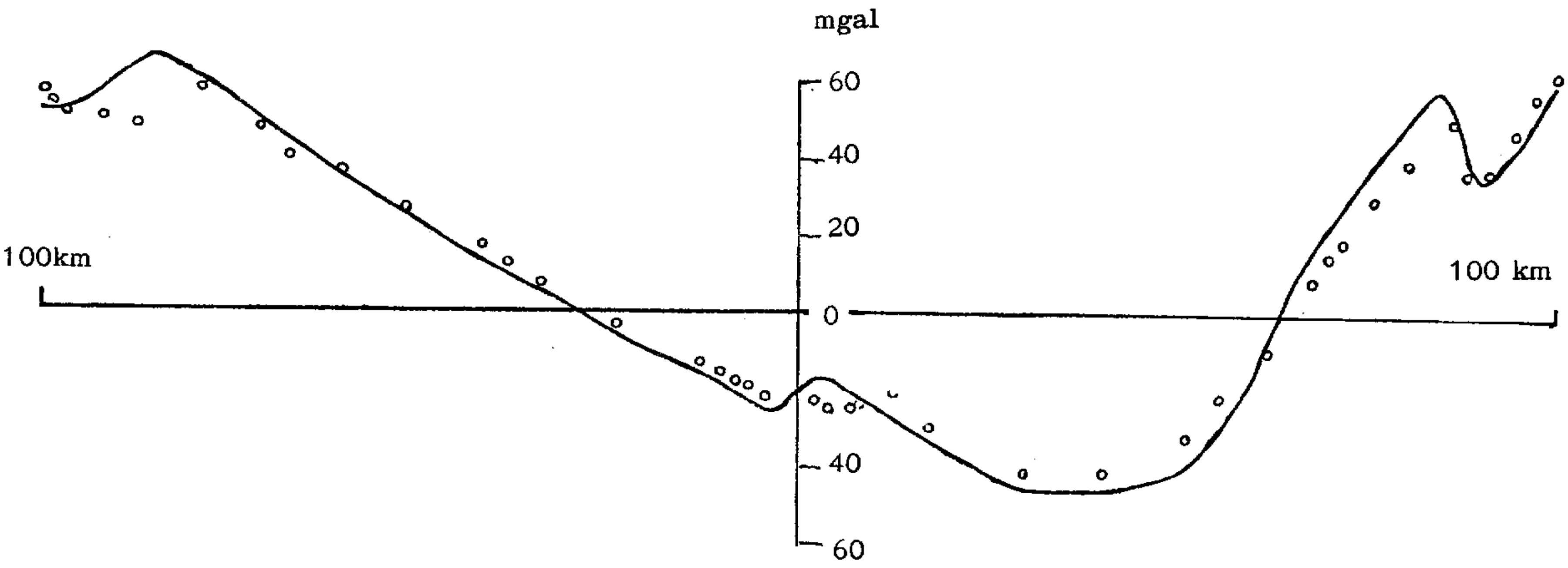

Fig. 3b The model adopted

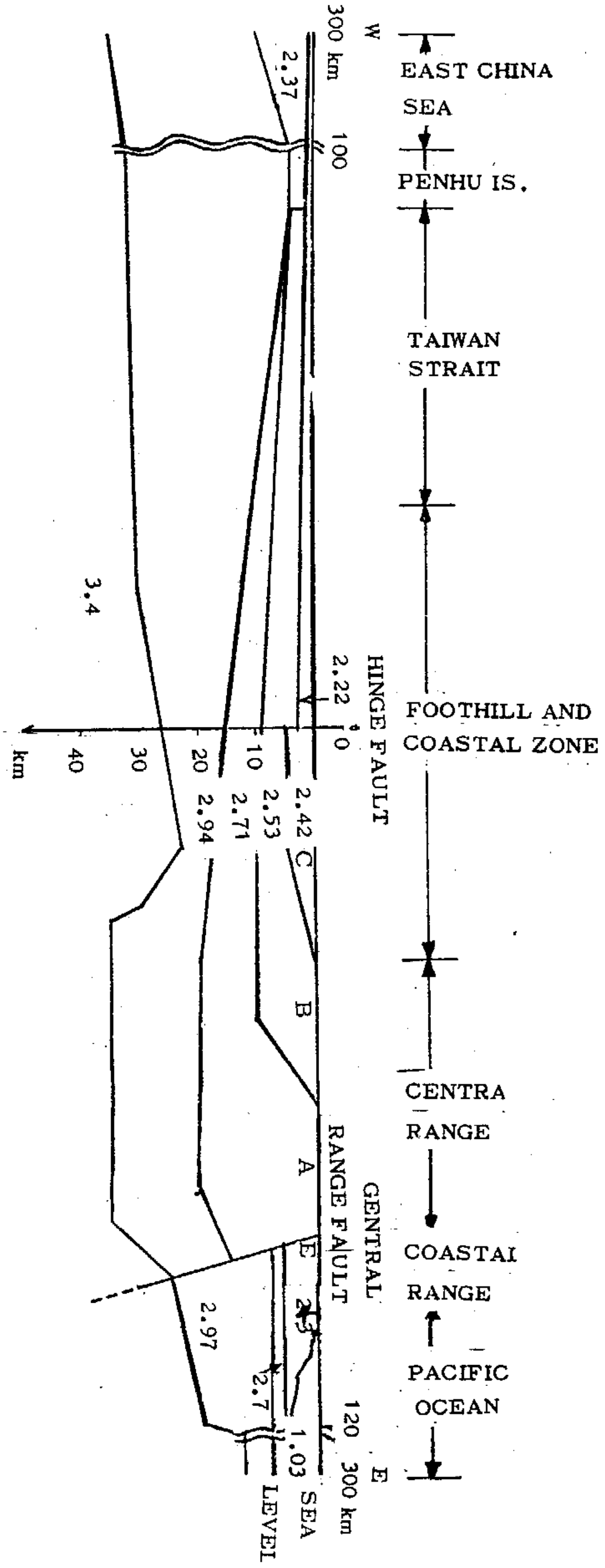
W
300 km
2.37
100
EAST CHINA SEA
PENHU IS.
TAIWAN STRAIT
3.4
2.22
HINGE FAULT
FOOTHILL AND COASTAL ZONE
0
10
20
30
40
km
2.42
2.53
2.71
2.94
C
B
A
CENTRA RANGE
GENTRAL RANGE FAULT
E
COASTAI RANGE
2.97
2.5
2.7
1.03
PACIFIC OCEAN
120
300 km
E
SEA LEVEL

IMPLICATIONS FROM AFTERSHOCKS OF TACHIEN EARTHQUAKE OF 24 DECEMBER 1973

Chih-Ping Lu
Seismology Division, Institute of Physics
Academia Sinica
The Republic of China

July, 1974

Abstract

Over 200 aftershocks of the Tachien earthquake of 24 December 1973 have been analyzed in detail. The results suggest a left-lateral strike-ship fault which strikes N24°W and dips almost 80° to the northeast. It is also found that the pattern of long term variations in the daily frequency of microearthquakes may be used as a practical criterion for predicting local earthquakes.

1. *Introduction*

An overwhelming majority of earthquakes occur because of sudden release of tectonic strain along pre-existed faults. Immediately following a large earthquake, numerous aftershocks will usually take place in the vicinity of the fault zone in order to release the residual strain. Based on this concept, focal mechanism of large earthquakes can be deduced from aftershock studies.

At 20^h 50^m 5.88^s (GMT) of 24 December 1973, a large earthquake (compare to other local events) with $M_L = 4.5$ hit the Tachien area on East-West Highway (Fig. 2). Eight minutes later, a strong aftershock ($M_L = 3.9$) occurred, and a tremendous amount of smaller events came after. Before these events, little is known about the seismicity and geology of the area. However, in local people's memory, the area has never been quiet seismically. It is only after TPC (Taiwan Power Company) people came that the first strong motion seismograph began to record locally (in 1972). In October 1973 a telemetered seismographic station (TWT) was installed here by the Chinese Earthquake Research Center, and a systematic monitoring of the local events has then become possible.

Like most parts of the Central Mountain Range, geologic work of Tachien area is not very detailed. The only faults known to pass close by the area shaken by this earthquake sequence are Kuantaoshan fault to the west and Wulin fault to the east, both of them strike NNE and are located about 5 kilometers away from the area. Judging from the direction of wave propagation, these faults do not appear to have any relation with those events. Thus, a detailed study on Tachien aftershocks will give us an effective way for delineating local active faults.

2. *Data acquisition and processing*

Two days after the mainshock, we set up five temporary seismographic stations in the area and deployed them for two weeks (from 28 December 1973 to 11 January 1974). Each station was equipped with a vertical component of 1 H_Z seismometer (Mark products L-4C) and a portable seismographic system (Sprengnether MEQ-800). The seismographic system consists of an amplifier (with a maximum electronic gain of 1 million at 1 H_Z), a smoke-paper drum recorder, an accurate chronometer, and internal batteries. The internal time signals at each station have been checked with time signals sent out from a fixed radio station so that accuracy in time can be kept within 0.05 sec.

In order to locate aftershocks precisely, we tried to find a local velocity model. We put three stations on a line aim at the aftershock area (stations 2, 3 and 5, Fig. 1), and pick up earthquakes which are shallow and occurred either on or very close to this line. These two requirements can be achieved by events which give maximum time difference between any two of the three stations. According to this criterion appropriate events were chosen to form a local travel-time curve (Fig. 3), and P and S wave velocities of the first layer were then derived. The preliminary results are $V_p = 5.6$ km/sec and $V_s = 3.0$ km/sec.

During the surveying period we recorded more than 250 aftershocks. Over 200 events were processed through computer program HYPO02 (modified by Lee, 1973). P-arrivals, S-arrivals and the velocities derived above (applied as a half space) are used in this calculation. Appendix I gives a list of these aftershocks.

3. *Nature of Faulting of the Tachien Earthquake Sequence*

Fig. 2 shows the spatial distribution of the aftershocks. The epicenters, as one will notice, seem to arrange in a elongated zone trending NNW. If we draw a longitudinal section (A-A') and a transversal section (B-B') passing through the epicentral zone and project the epicenters onto these vertical sections, interesting phenomena emerge. The aftershock projections were distributed evenly all over the A-A' plane. While on the B-B' plane, the distribution is confined to a linear vertical zone (Fig. 4). These patterns imply that the fault zone associated with the aftershocks strike NNW with a very steep dip.

Furthermore, the properties of earthquake faulting can be found from composite fault plane solutions of the aftershocks. These solutions, as appeared in Fig. 5, reveal the same features no matter where the events were located. They all suggest a left lateral strike-slip fault which strikes N24° W and dips almost 80° to the northeast. This seem to be reasonable since during the time of the mainshock, landslides occurred extensively on the East-West Highway, right at the intersection with the southern extension of the inferred fault strike.

Fig. 6 is a plot of the cumulative number of the aftershocks against their focal depths. The concentration of aftershocks at a depth of 5 kilometers may be due to systematic bias, since in the calculation our first trial depth for hypocenters is 5 kilometers. However, the "bimodal" structure should not be neglected. The concentration of aftershocks at depths of 3.7 and 5.0 kilometers may actually arise from cumulation of the residual stress and define the width of the main fault plane. This is consistent with investigations in other parts of the world (Eaton et al., 1970, Hamilton, 1971).

4. *A Possible Way Towards Prediction*

Since October of 1973, a tremendous amount of local earthquakes has been recorded by CERC's telemetered station TWT at Tachien (Fig. 1). With a gain of 84 db, the vertical component short-period seismometer successfully registered local events down to a magnitude 0.5, and provided us full information before and after the mainshock of Tachien earthquakes.

Fig. 7 shows daily variations on the number of local events down to magnitude 0.5 from October, 1973 to March, 1974. The increase in the daily seismicity after the main event is expectable. On the other hand, the variations before 24 December 1973, in the long term level of seismicity, seems significant. It reveals that local seismicity, which originally kept a steady level of around twelve events per day, began to decline on 7 November 1973 and stayed at a lower level of about seven events per day for nearly seven weeks. The seismicity resumed to its original level on 24 December 1973, and then the big shock occurred. This phenomenon, if further confirmed to be a characteristic property of this area, may be used as a practical criterion for predicting local earthquakes.

5. *Concluding Remarks*

From the existing documents, it is found that this area has never been quiet (Fig. 1). In 1938, two large earthquakes with magnitudes greater than 6 occurred nearby. The preceding evidences all lead us to believe that the area is under stress at the present time so that some local faults are active. The potential of having large earthquakes (M > 6) in the area can not be ruled out. It is hoped that more detailed investigation on the local active faults can be made in the near future.

Acknowledgement

The field operations were assisted by W. S. Liu and D. A. Lee of the Division. Dr. Y. B. Tsai critically reviewed the manuscript and made many valuable suggestions. This work was funded by the National Science Council, Republic of China.

References

1. Eaton, J. P., M. E. O'Neill, and J. N. Murdock, 1970, Aftershocks of the 1966 Parkfield – Cholame, California earthquake: A detailed study, Bull. seismol. Soc. Amer., 60, 1151-1197.
2. Hamilton, R. M., 1971, Aftershocks of Borrego Mountain earthquake from April 12 to June 12, 1968, U. S. Geol. Survey Prof. paper.
3. Lee, W. H. K., 1973, HYPOC2, a modified computer program of HYPO71 (Lee and Lahr, 1972) for the Chinese Earthquake Research Center.
4. Lee, W. H. K., and J. C. Lahr, 1972, HYPO71: A computer program for determining hypocenter, magnitude, and first pattern of local earthquakes, U. S. Geological Survey, Open File Report.

Appendix I

LISTING OF TACHIEN AFTERSHOCKS

DATE	HR	MN	SEC	LAT-N	LONG-E	DEPTH	MAG	NO	GAP	RMS	ERH	ERZ	Q
731229	08	42	18.62	24° 15.30'	121° 08.33'	5.00	1.80	3	167	0.14			C
	08	58	48.37	24° 15.30'	121° 07.85'	5.00	1.80	3	170	0.01			C
	11	05	13.58	24° 17.68'	121° 07.83'	6.81	1.85	4	210	0.00			C
	11	30	25.17	24° 15.60'	121° 06.89'	5.00	1.95	4	185	0.19			C
	12	20	40.96	24° 15.30'	121° 09.04'	5.00	1.60	3	163	0.03			C
	12	48	48.97	24° 16.39'	121° 07.66'	0.55	2.04	4	192	0.03			C
	13	39	58.95	24° 17.76'	121° 08.06'	5.00	1.41	3	209	0.00			C
	13	46	13.17	24° 10.98'	121° 18.07'	5.00	2.43	4	222	0.19			C
	13	47	47.97	24° 15.30'	121° 09.64'	5.00	1.75	3	160	0.07			C
	14	19	00.13	24° 14.77'	121° 06.43'	19.72	1.75	4	170	0.03			C
	14	25	53.88	24° 15.30'	121° 10.64'	5.00	2.53	3	170	0.38			D
	15	15	20.98	24° 17.72'	121° 07.96'	7.47	2.07	4	209	0.00			C
	16	08	32.31	24° 20.65'	121° 28.82'	5.00	2.94	3	316	0.14			C
	16	10	21.53	24° 18.45'	121° 07.01'	7.33	1.83	4	228	0.00			C
	16	20	39.49	24° 17.04'	121° 09.03'	5.00	2.07	4	190	0.13			C
	16	52	46.98	24° 17.12'	121° 07.32'	0.82	1.86	4	207	0.02			C
	17	20	49.37	24° 17.88'	121° 07.68'	5.79	1.83	4	214	0.00			C
	17	41	21.23	24° 17.75'	121° 08.21'	7.16	1.82	5	207	0.05	1.0	1.2	C

DATE	HR	MN	SEC	LAT-N	LONG-E	DEPTH	MAG	NO	GAP	RMS	ERH	ERZ	Q
	18	33	36.94	24° 17.66'	121° 07.82'	4.71	1.48	4	210	0.00			C
	21	31	0.05	24° 16.79'	121° 08.12'	4.05	1.08	4	194	0.00			C
	22	12	32.80	24° 17.54'	121° 07.62'	5.20	1.90	4	210	0.00			C
	22	51	15.62	24° 17.96'	121° 07.66'	6.64	1.46	4	215	0.00			C
	23	50	12.51	24° 16.12'	121° 08.56'	3.25	1.91	4	180	0.00			C
	23	53	13.75	24° 15.30'	121° 08.59'	3.35	1.57	4	165	0.02			C
740101	04	33	36.26	24° 19.13'	121° 08.25'	1.89	1.78	5	231	0.07	2.3	10.8	C
	04	30	16.95	24° 15.30'	121° 08.98'	5.00	2.20	3	191	0.02			C
	09	14	30.17	24° 17.20	121° 08.50'	5.23	1.49	5	200	0.01	0.2	0.4	C
	18	21	49.21	24° 16.36'	121° 08.92'	5.55	2.75	5	179	0.02	0.4	0.6	C
	18	35	34.89	24° 16.21'	121° 09.00'	5.80	1.80	7	175	0.03	0.5	0.2	B
	19	23	13.11	24° 16.46'	121° 08.26'	4.10	1.93	5	188	0.04	1.0	1.4	C
	19	23	29.28	24° 16.16'	121° 07.87'	6.72	1.44	5	186	0.02	0.8	0.5	C
	23	09	7.10	24° 14.99'	121° 09.10'	7.78	1.63	5	203	0.15	8.4	2.7	D
	23	26	46.40	24° 16.21'	121° 07.72'	3.80	2.32	4	180	0.00			C
740102	00	24	17.75	24° 21.02'	121° 19.56'	7.34	1.75	6	300	0.12	2.8	1.2	D
	00	24	30.38	24° 20.50'	121° 17.50'	5.00	1.87	3	289	0.01			C
	07	40	47.09	24° 16.82'	121° 19.88'	5.00	2.46	4	224	0.16			C
	08	11	37.59	24° 16.13'	121° 08.65'	5.20	1.67	7	176	0.12	1.2	1.4	C
	08	35	1.41	24° 15.30'	121° 08.88'	3.56	1.50	5	169	0.02	0.7	0.3	C
	08	45	8.44	24° 15.79'	121° 08.17'	5.04	1.75	6	173	0.06	0.8	0.6	B
	09	30	34.58	24° 18.72'	121° 06.76'	1.00	2.11	6	244	0.25	3.3	22.5	D

DATE	HR	MN	SEC	LAT-N	LONG-E	DEPTH	MAG	NO	GAP	RMS	ERH	ERZ	Q
	11	57	56.43	24° 16.44'	121° 08.25'	3.31	2.53	4	187	0.02			C
	13	40	44.25	24° 17.18'	121° 22.51'	4.42	1.80	4	266	0.01			C
	14	42	37.98	24° 15.83'	121° 22.13'	5.00	4.39	4	258	0.27			C
	19	30	30.53	24° 17.38'	121° 09.26'	0.48	1.99	6	195	0.08	0.8	7.1	D
	19	31	46.80	24° 17.69'	121° 08.76'	0.57	1.59	7	205	0.10	0.9	7.9	D
	20	00	48.29	24° 15.97'	121° 08.63'	5.22	1.31	6	173	0.05	0.8	0.4	B
	22	00	27.11	24° 15.97'	121° 08.16'	4.13	1.98	7	178	0.08	0.9	0.7	B
	22	03	9.00	24° 17.53'	121° 07.71'	0.17	1.68	4	215	0.07			C
	23	15	40.04	24° 17.28'	121° 08.32'	2.38	1.88	4	203	0.06			C
	23	34	04.16	24° 14.99'	121° 05.60'	5.00	2.52	4	202	0.20			C
740103	04	58	13.24	24° 16.76'	121° 8.83'	3.16	2.31	5	188	0.10	2.1	4.3	C
	04	58	31.66	24° 15.30	121° 8.29'	5.64	2.13	4	168	0.07			C
	04	59	29.81	24° 17.56'	121° 8.84'	5.00	1.81	3	202	0.00			C
	07	29	44.58	24° 18.87'	121° 8.27'	5.17	1.42	9	228	0.04	0.3	0.5	C
	10	19	0.89	24° 16.37'	121° 8.05'	0.35	1.62	6	240	0.04	1.6	7.1	D
	11	12	42.18	24° 16.89'	121° 8.39	7.18	1.88	5	195	0.02	0.5	0.9	C
	11	53	57.97	24° 19.08'	121° 4.59'	3.20	1.47	6	275	0.08	1.3	2.7	C
	14	26	28.55	24° 17.44'	121° 8.21'	6.22	1.71	5	207	0.02	0.4	0.7	C
	14	50	20.74	24° 16.77'	121° 8.52'	3.65	2.09	5	191	0.00	0.1	0.1	C
	14	51	55.78	24° 16.58'	121° 8.29'	4.15	1.92	5	190	0.01	0.2	0.3	C
	15	04	10.40	24° 17.88'	121° 8.41'	6.37	1.95	5	212	0.02	0.3	0.7	C
	16	29	38.00	24° 16.46'	121° 8.72'	4.01	2.44	5	183	0.00	0.0	0.0	C

DATE	HR	MN	SEC	LAT-N	LONG-E	DEPTH	MAG	NO	GAP	RMS	ERH	ERZ	Q
740104	02	57	32.34	24° 14.66'	121° 19.64'	5.00	1.59	3	288	0.00			C
	03	52	40.23	24° 15.30'	121° 8.29'	5.00	1.53	3	192	0.09			C
	06	13	14.45	24° 14.81'	121° 8.70'	3.11	1.84	7	166	0.15	2.5	1.9	C
	07	02	29.24	24° 17.76'	121° 8.00'	7.31	2.08	5	214	0.02	0.5	0.8	C
	08	40	5.18	24° 17.73'	121° 8.73'	5.00	1.65	4	206	0.01			C
	09	30	55.08	24° 18.14'	121° 26.52'	12.71	2.63	5	300	0.07	0.2	0.1	C
	09	40	57.68	24° 14.99'	121° 7.68'	5.00	1.90	4	178	0.03			C
	09	51	34.15	24° 6.83'	121° 5.60'	5.00	2.66	5	289	0.20	0.2	0.3	C
	11	0	12.26	24° 17.81'	121° 8.53'	7.10	1.55	5	209	0.02	0.5	1.1	C
	12	1	33.56	24° 16.29'	121° 8.59'	2.54	1.54	5	180	0.03	0.7	1.0	C
	12	35	19.14	24° 17.11'	121° 8.64'	5.95	1.82	5	196	0.01	0.2	0.3	C
	13	24	53.47	24° 17.61'	121° 8.83'	5.55	1.86	5	202	0.00	0.0	0.0	C
	14	05	42.02	24° 17.22'	121° 8.84'	5.66	1.88	5	196	0.02	0.3	0.6	C
	14	36	59.22	24° 16.03'	121° 9.47'	5.44	1.67	5	168	0.03	0.6	0.7	C
	15	42	36.00	24° 17.73'	121° 8.52'	5.53	1.66	5	208	0.01	0.2	0.3	C
	17	14	30.96	24° 15.59'	121° 17.32'	1.15	2.36	9	165	0.08	0.4	3.3	C
	17	48	48.44	24° 17.68'	121° 8.40'	5.86	1.42	5	208	0.00	0.0	0.0	C
	18	17	33.08	24° 15.63'	121° 17.57'	0.83	1.96	5	171	0.02	0.2	5.0	D
	18	26	31.09	24° 17.14'	121° 9.04'	3.59	1.45	4	252	0.03			C
	18	34	5.65	24° 18.23'	121° 7.96'	5.32	1.69	5	222	0.01	0.2	0.4	C
	18	44	11.67	24° 10.98'	121° 18.07'	1.90	2.96	5	222	0.14	0.8	0.8	C
	19	52	58.65	24° 17.93'	121° 8.50'	6.15	1.69	5	211	0.02	0.4	0.8	C

DATE	HR	MN	SEC	LA T-N	LONG-E	DEPTH	MAG	NO	GAP	RMS	ERH	ERZ	Q
	21	37	58.77	24° 17.61'	121° 6.64'	4.72	1.78	5	233	0.04	1.1	1.5	C
	23	09	37.21	24° 6.24'	121° 16.38'	8.41	2.67	7	293	0.22	3.7	4.7	D
	23	45	2.07	24° 15.95'	121° 10.07'	3.45	1.90	5	162	0.01	0.2	0.2	C
740105	03	16	48.82	24° 17.42'	121° 8.50'	6.71	1.76	6	203	0.08	0.8	1.5	C
	06	54	50.95	24° 10.98'	121° 18.07'	5.00	2.25	4	223	0.33			D
	08	44	29.70	24° 23.76'	121° 20.82'	4.61	2.38	6	314	0.07	1.6	1.5	C
	10	03	50.05	24° 10.98'	121° 18.07'	5.00	2.34	4	223	0.19			C
	14	11	35.83	24° 15.53'	121° 9.18'	5.00	1.44	4	159	0.02			C
	14	29	1.12	24° 18.47'	121° 7.77'	8.09	1.15	4	228	0.03			C
	14	53	5.96	24° 13.86'	121° 24.77'	5.00	2.88	4	288	0.14			C
	15	47	57.13	24° 17.09'	121° 8.86'	7.15	1.34	4	194	0.00			C
	16	12	13.76	24° 16.11'	121° 9.07'	3.53	1.35	5	172	0.02	0.2	0.9	C
	18	44	31.31	24° 10.98'	121° 18.07'	5.00	2.09	4	223	0.24			C
	20	25	7.34	24° 10.98'	121° 18.07'	5.00	2.48	4	223	0.46			D
	22	50	57.62	24° 16.44'	121° 8.32'	6.28	2.00	4	187	0.00			C
740106	05	43	9.77	24° 16.43'	121° 7.90'	2.33	2.35	4	192	0.00			C
	06	58	27.75	24° 15.30'	121° 9.13'	5.00	2.51	3	169	0.08			C
	12	41	27.47	24° 16.34'	121° 8.11'	1.82	1.75	5	187	0.01	0.2	0.7	C
	13	03	28.25	24° 16.59'	121° 8.77'	7.07	2.04	5	185	0.01	0.1	0.2	C
	15	15	10.87	24° 16.35'	121° 10.46'	1.19	1.89	5	167	0.06	0.9	2.9	C
	16	07	1.30	24° 16.29'	121° 7.77'	4.22	2.01	5	190	0.01	0.0	0.0	C
	16	40	20.01	24° 16.55'	121° 8.80'	9.11	2.05	10	184	0.12	0.8	0.8	C

DATE	HR	MN	SEC	LAT-N	LONG-E	DEPTH	MAG	NO	GAP	RMS	ERH	ERZ	Q
	17	29	33.03	24° 16.28'	121° 8.54'	3.41	2.18	5	181	0.00	0.1	0.1	C
	18	21	2.92	24° 20.50'	121° 18.77'	5.00	1.67	5	281	0.12	7.1	6.9	D
	18	58	21.85	24° 17.12'	121° 8.06'	3.87	1.79	5	203	0.00	0.0	0.0	C
	19	33	59.79	24° 17.80'	121° 9.53'	6.63	2.29	9	199	0.07	0.4	0.8	C
	21	44	01.29	24° 20.82'	121° 7.96'	5.00	1.49	3	304	0.05			C
	21	56	43.22	24° 0.47'	121° 14.68'	8.96	2.60	5	313	0.15	3.3	2.5	D
	22	15	6.16	24° 19.76'	121° 10.64'	5.00	1.89	3	292	0.12			C
	22	43	9.49	24° 20.63'	121° 5.43'	0.24	1.80	4	272	0.09			C
	23	20	19.08	24° 16.91'	121° 8.63'	5.89	2.12	8	193	0.09	0.9	1.0	C
740107	04	07	30.52	24° 17.49'	121° 7.14'	13.83	2.60	4	224	0.00			C
	05	17	1.16	24° 13.94'	121° 9.07'	5.00	1.70	3	188	0.00			C
	05	44	56.95	24° 15.58'	121° 9.04'	5.88	1.93	5	161	0.03	0.5	0.7	C
	07	33	56.91	24° 17.15'	121° 8.39'	5.23	2.07	5	200	0.09	1.6	2.8	C
	07	34	10.30	24° 16.95'	121° 8.93'	4.69	2.17	5	190	0.08	1.6	2.2	C
	09	31	29.90	24° 17.30'	121° 8.30'	5.62	1.95	5	204	0.02	0.6	0.9	C
	11	04	22.46	24° 15.87'	121° 8.30'	0.87	2.07	5	173	0.01	0.2	0.8	C
	12	36	39.55	24° 18.80'	121° 18.72'	11.98	3.09	4	246	0.10			C
	15	16	38.73	24° 16.04'	121° 8.98'	5.50	1.68	5	172	0.00	0.1	0.1	C
	15	20	20.60	24° 16.13'	121° 9.07'	3.61	2.46	5	173	0.01	0.2	0.3	C
	15	30	43.83	24° 16.28'	121° 9.06'	3.66	1.93	5	175	0.03	0.5	0.8	C
	15	56	31.69	24° 17.75'	121° 7.89'	4.35	1.89	5	216	0.01	0.2	0.4	C
	16	08	47.63	24° 16.16'	121° 9.10'	1.86	1.60	5	173	0.03	0.5	0.9	C

DATE	HR	MN	SEC	LAT-N	LONG-E	DEPTH	MAG	NO	GAP	RMS	ERH	ERZ	Q
	16	10	37.36	24° 17.21'	121° 8.57'	4.69	1.96	10	199	0.09	0.7	0.9	C
	16	26	25.10	24° 17.01'	121° 8.98'	4.72	1.91	5	191	0.01	0.3	0.5	C
	17	05	18.89	24° 17.30'	121° 8.41'	0.32	2.12	4	202	0.01			C
	17	07	2.50	24° 17.73'	121° 7.71'	11.15	2.05	4	218	0.02			C
	18	41	11.64	24° 15.78'	121° 6.82'	1.05	2.33	4	192	0.19			C
	19	23	12.04	24° 17.37'	121° 8.91'	2.93	2.21	8	198	0.27	1.9	4.0	C
	22	33	46.37	24° 17.66'	121° 8.44'	3.76	2.03	4	208	0.00			C
	23	26	32.61	24° 17.29'	121° 8.54'	2.08	2.04	4	201	0.00			C
	23	58	41.10	24° 16.99'	121° 8.62'	4.74	2.17	4	194	0.00			C
740108	0	29	25.50	24° 17.38'	121° 8.52'	2.60	1.81	4	203	0.00			C
	09	08	32.41	24° 16.40'	121° 9.13'	4.15	1.98	5	178	0.05	0.9	1.4	C
	09	28	18.05	24° 16.29'	121° 8.31'	0.60	1.93	4	236	0.03			C
	10	55	18.76	24° 16.18'	121° 9.13'	5.87	2.64	5	173	0.03	0.5	0.9	C
	10	56	21.94	24° 15.71'	121° 9.23'	4.12	2.06	4	216	0.01			C
	10	56	34.65	24° 16.49'	121° 8.47'	7.91	2.68	5	186	0.10	2.3		C
	10	57	42.10	24° 16.27'	121° 9.32'	0.31	2.61	5	174	0.14	1.0	11.7	D
	11	14	1.23	24° 23.52'	121° 17.96'	4.57	1.93	5	307	0.08	8.4	4.5	D
	11	35	45.58	24° 18.22'	121° 8.55'	3.01	1.99	5	216	0.06	1.2	4.0	C
	11	55	21.88	24° 18.20'	121° 8.24'	5.29	1.91	5	219	0.01	0.2	0.4	C
	12	18	6.66	24° 16.15'	121° 8.82'	4.22	2.22	5	175	0.02	0.3	0.5	C
	13	18	0.52	24° 17.95'	121° 10.63'	3.33	1.75	4	248	0.01			C
	13	52	22.93	24° 17.53'	121° 20.15'	5.00	2.65	5	233	0.31	1.0	2.2	C

DATE	HR	MN	SEC	LAT-N	LONG-E	DEPTH	MAG	NO	GAP	RMS	ERH	ERZ	Q
	14	24	47.40	24° 17.00'	121° 5.99'	3.12	1.60	4	281	0.01			C
	14	46	26.57	24° 17.97'	121° 9.19'	1.06	1.68	6	264	0.05	1.9	6.7	D
	17	0	46.57	24° 6.25'	121° 17.65'	7.43	2.63	6	304	0.02	0.5	0.6	C
	17	32	0.61	24° 3.12'	121° 14.40'	5.00	3.04	7	312	0.28	4.1	15.7	D
	17	54	49.64	24° 13.77'	121° 7.48'	3.56	1.88	5	195	0.20	0.8	1.6	C
	19	1	26.31	24° 17.74'	121° 9.09'	1.99	2.19	5	203	0.14	0.1	0.4	C
	19	54	4.15	24° 17.55'	121° 8.59'	5.03	2.11	5	201	0.04	0.8	1.6	C
	23	7	44.38	24° 17.88'	121° 8.01'	6.29	2.04	5	273	0.12	2.4	2.7	C
	23	24	35.93	24° 19.23'	121° 8.09'	5.00	1.84	3	290	0.03			C
740109	12	39	4.73	24° 18.53'	121° 7.95'	4.80	1.37	5	226	0.02	0.7	1.3	C
	12	52	12.94	24° 17.23'	121° 8.32'	2.87	2.30	5	202	0.02	0.4	0.9	C
	14	55	8.50	24° 16.62'	121° 8.18'	3.51	1.43	5	192	0.04	0.6	1.0	C
	17	06	4.99	24° 16.65'	121° 8.50'	2.34	1.84	4	189	0.00			C
	19	33	11.41	24° 18.13'	121° 8.53'	6.57	2.12	5	214	0.02	0.4	0.8	C
	19	33	18.17	24° 17.59'	121° 8.39'	9.99	2.18	4	207	0.00			C
	20	03	35.26	24° 21.97'	121° 19.29'	5.00	2.51	7	305	0.18	3.8	3.2	D
	23	41	38.36	24° 18.37'	121° 8.22'	4.62	1.58	5	221	0.00	0.0	0.1	C
	23	56	33.05	24° 17.38'	121° 11.86'	8.25	1.75	5	174	0.22	4.5	9.9	D
	23	56	33.16	24° 17.65'	121° 10.64'	5.00	1.75	6	187	0.39	5.6	12.6	D
	23	59	36.75	24° 15.30'	121° 8.66'	5.00	1.55	4	191	0.10			C
740110	11	20	5.75	24° 17.74'	121° 8.44'	2.12	2.17	5	210	0.01	0.2	0.9	C
	16	02	40.25	24° 17.19'	121° 7.89'	0.02	2.02	5	207	0.07	1.1	136.7	D

DATE	HR	MN	SEC	LAT-N	LONG-E	DEPTH	MAG	NO	GAP	RMS	ERH	ERZ	Q
	20	6	29.87	24° 17.20'	121° 8.70'	3.93	1.32	5	197	0.05	0.9	2.0	C
	21	11	26.16	24° 18.83'	121° 8.32'	1.77	1.25	5	285	0.01	0.3	1.2	C
740111	06	54	11.40	24° 15.69'	121° 9.14'	3.73	1.65	5	163	0.01	0.1	0.2	C
	07	48	16.78	24° 15.84'	121° 8.61'	0.71	2.74	4	170	0.03			C
	09	30	46.21	24° 15.30'	121° 10.64'	5.77	1.92	5	147	0.04	0.7	1.0	C
	11	52	39.94	24° 15.96'	121° 8.69'	2.36	1.39	4	224	0.01			C
	13	54	36.82	24° 17.06'	121° 7.06'	5.00	1.67	3	358	0.03			C
	14	13	12.26	24° 20.50'	121° 17.96'	16.83	2.37	5	296	0.23	1.0	6.7	D

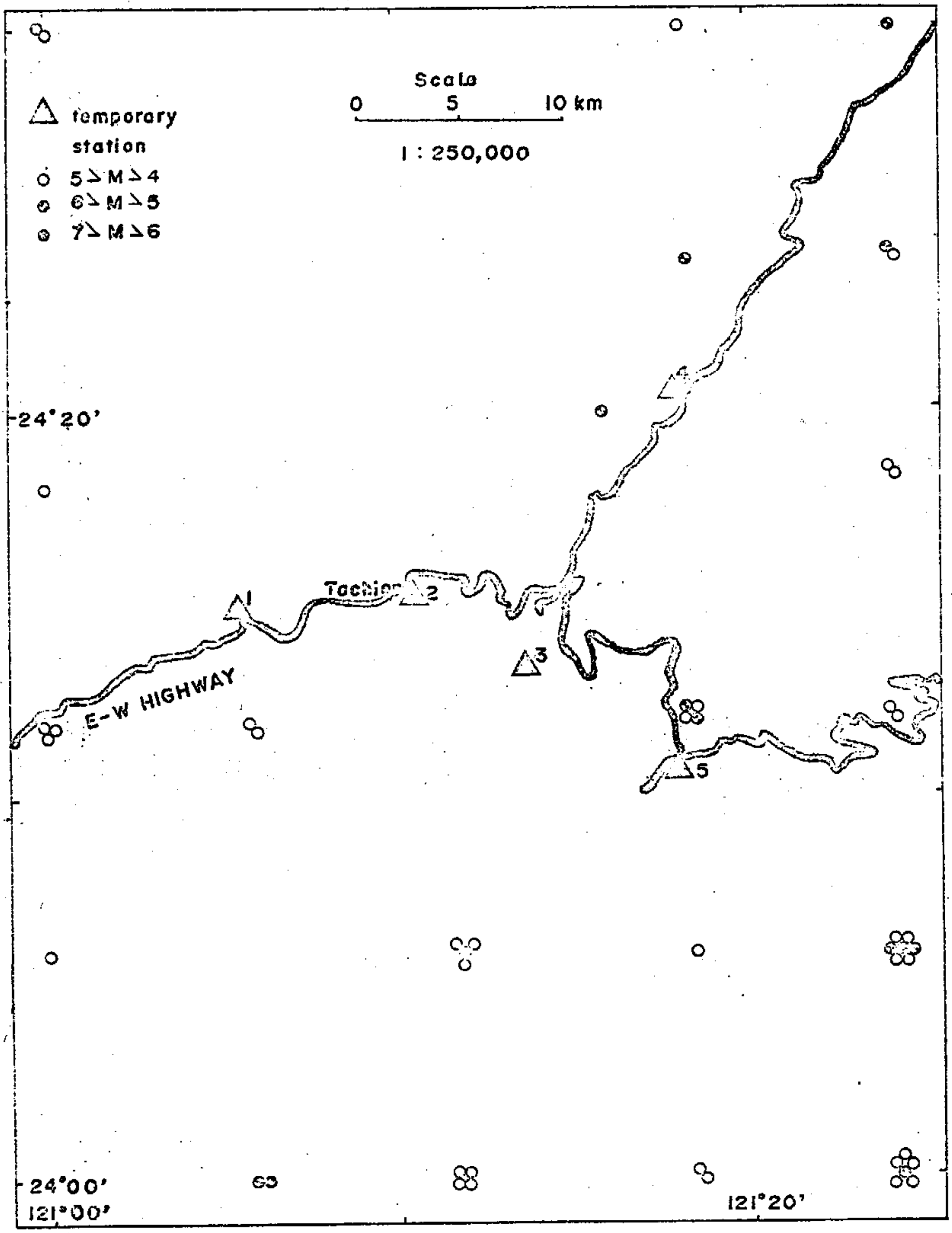

Fig. 1. Seismicity map of the central part of E-W Highway (1936-1967) and locations of temporary seismographic stations during the surveying period (December 28, 1973-January 11, 1974).

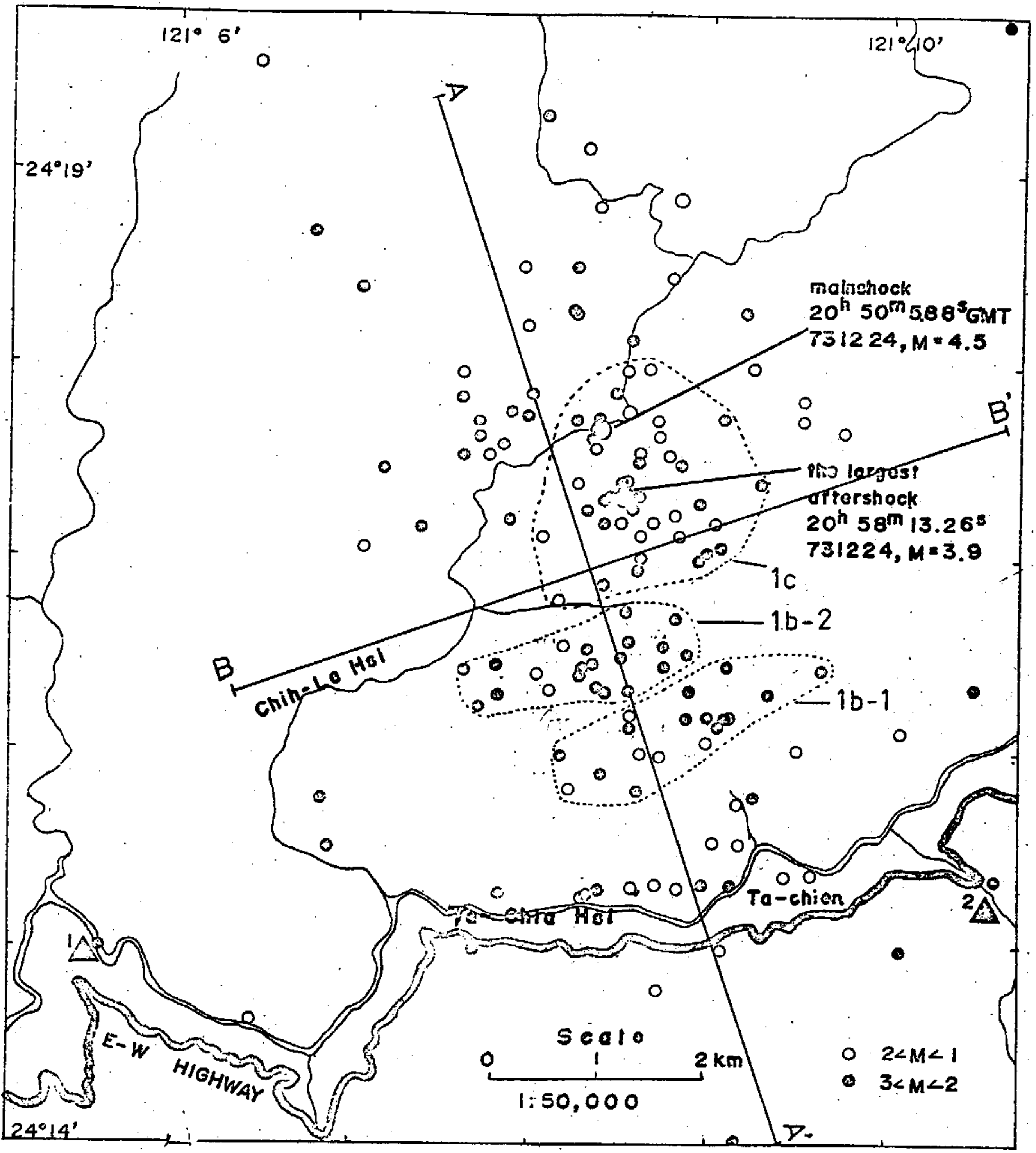

Fig. 2. Epicenters of the mainshock and aftershocks.

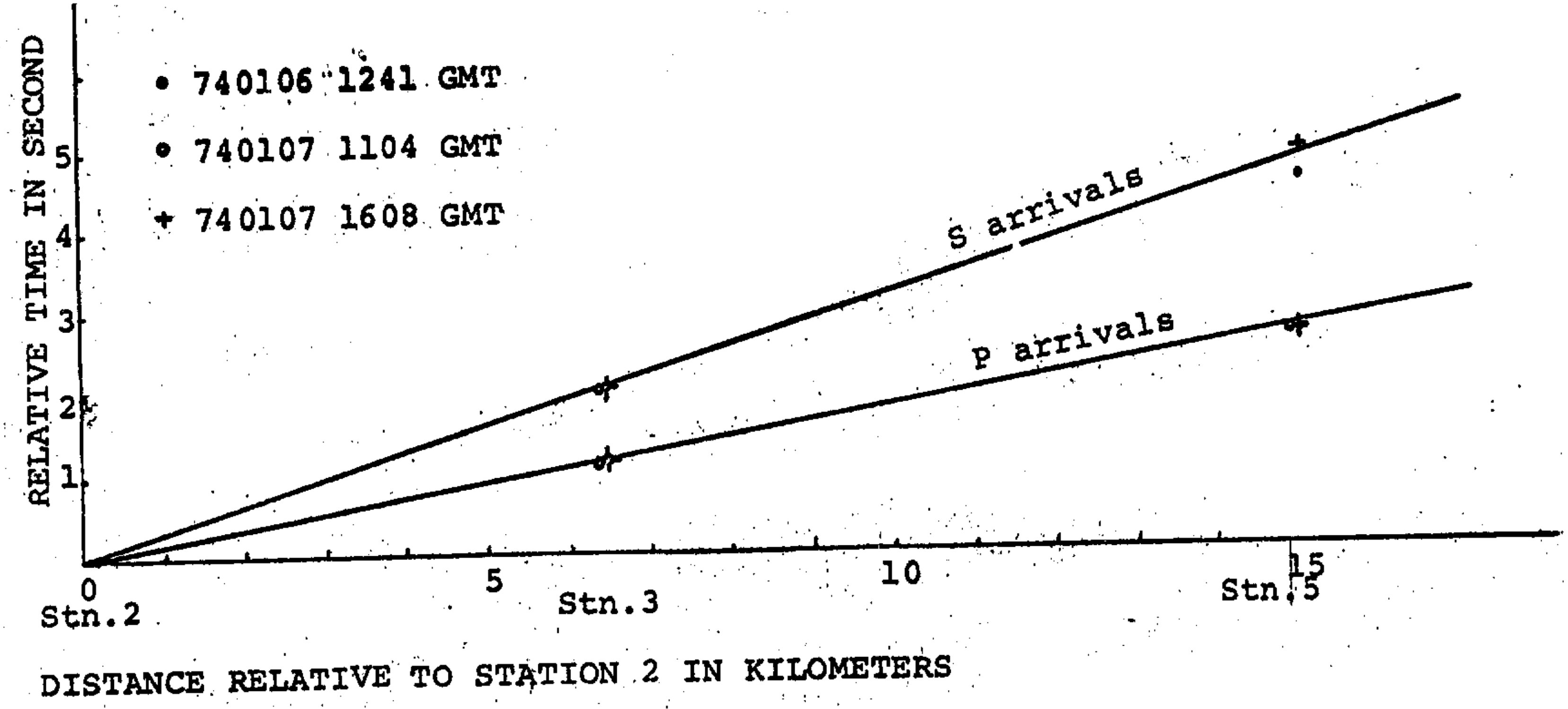

Fig. 3. A local travel-time curve for Tachien area.

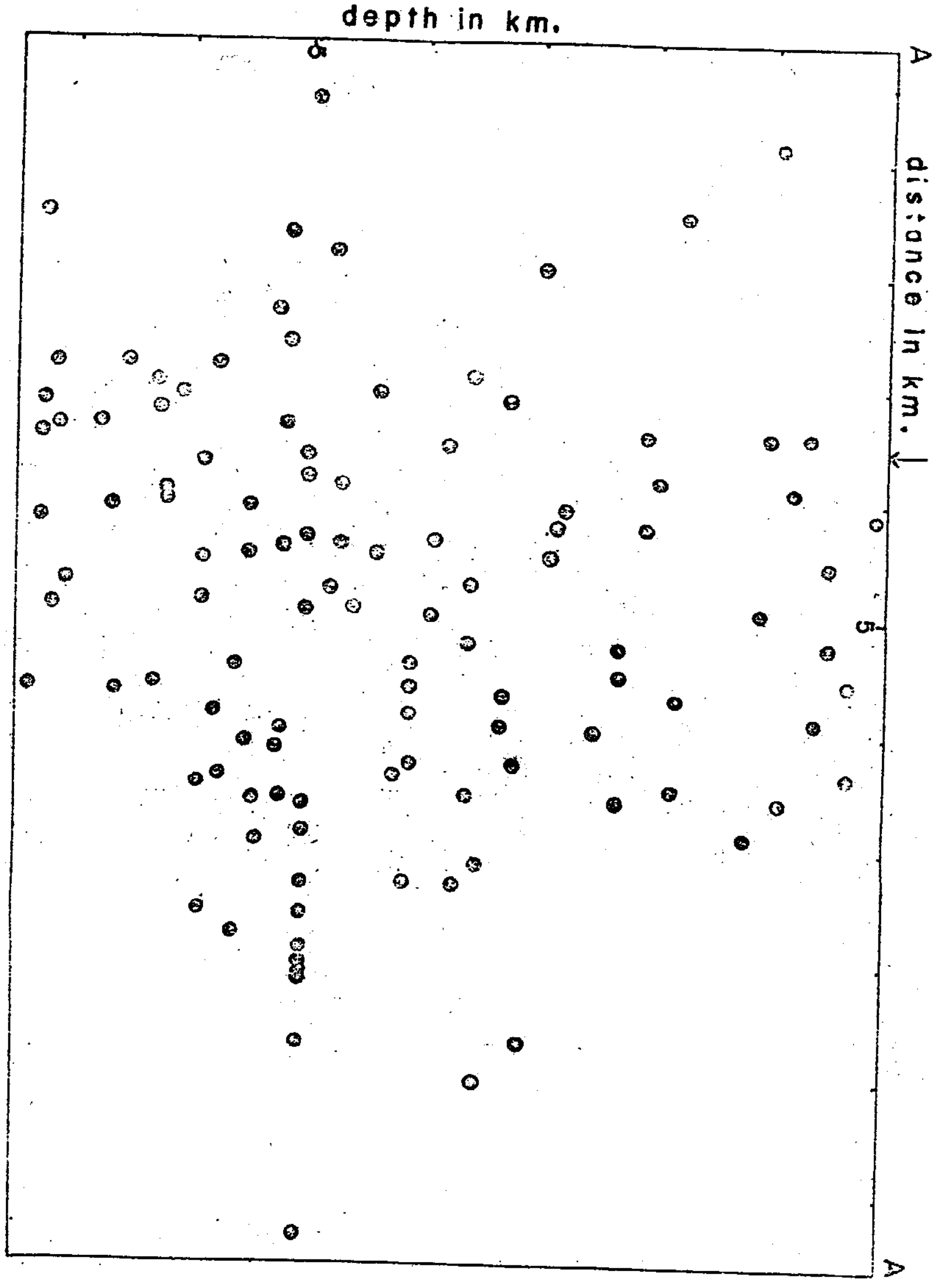

Fig. 4a. Aftershocks as projected on A-A, plane. Arrow indicate the projection of the mainshock.

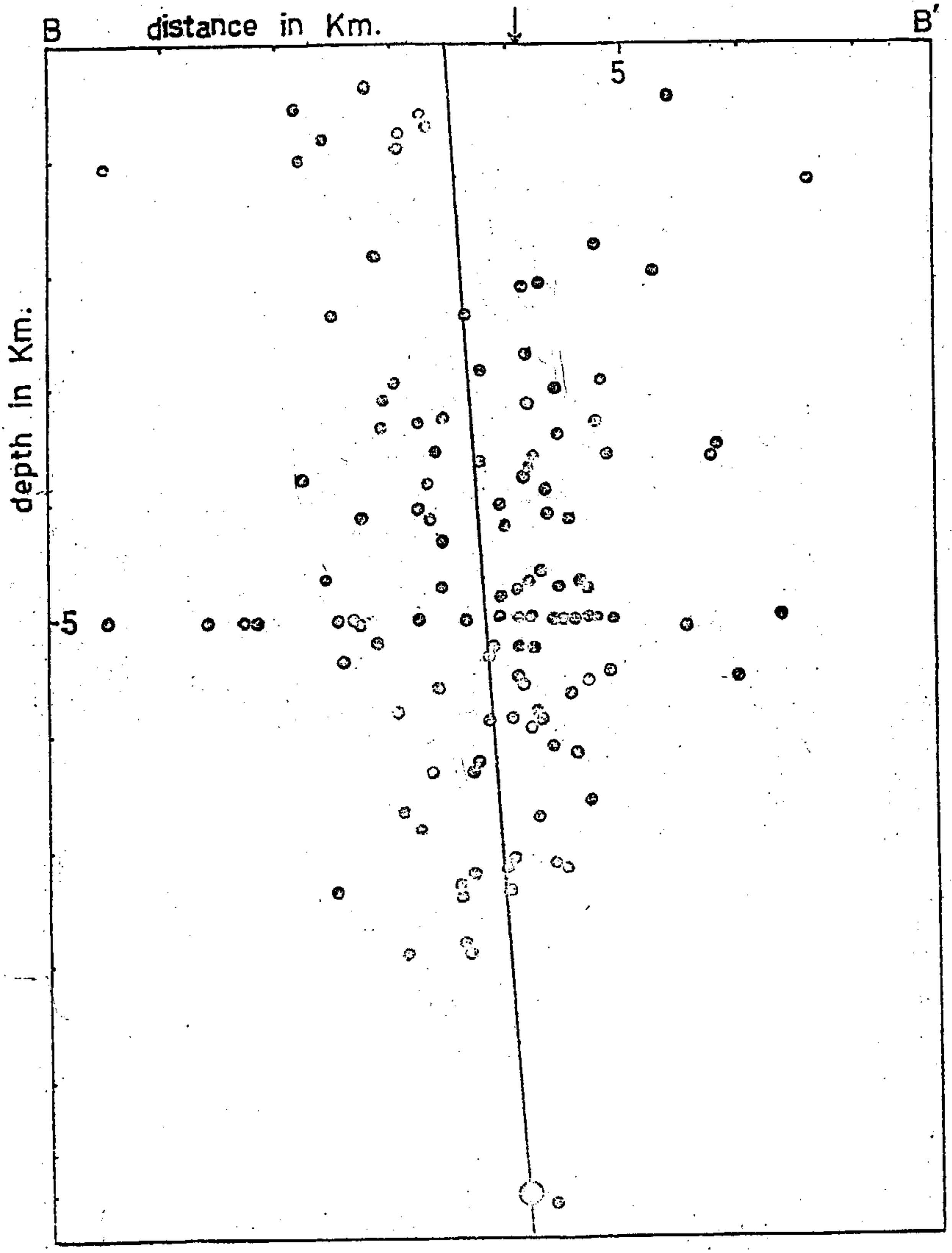

Fig. 4b. Aftershocks as projected on B-B' plane.

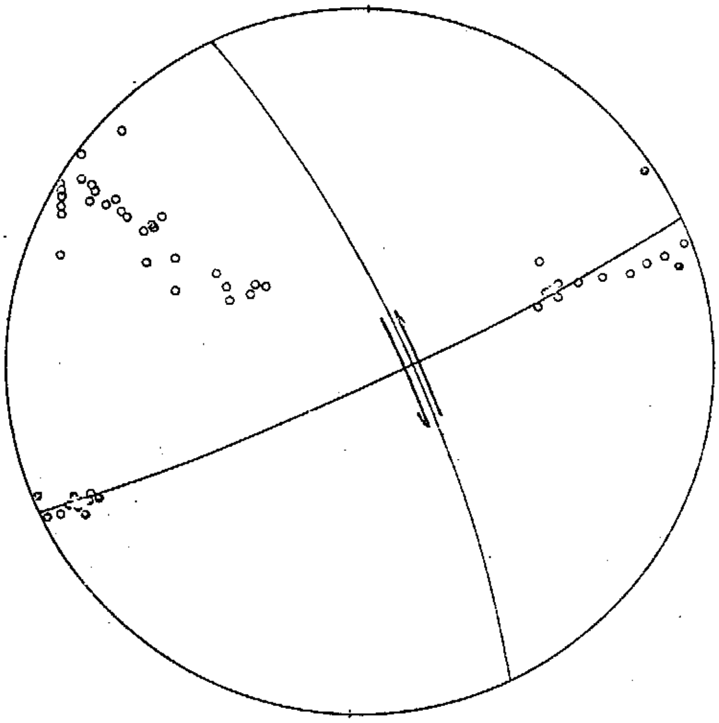

group 1b-1

Fig. 5. Composite fault plane solutions of aftershocks. All of them have the same result no matter where the events are chosen.

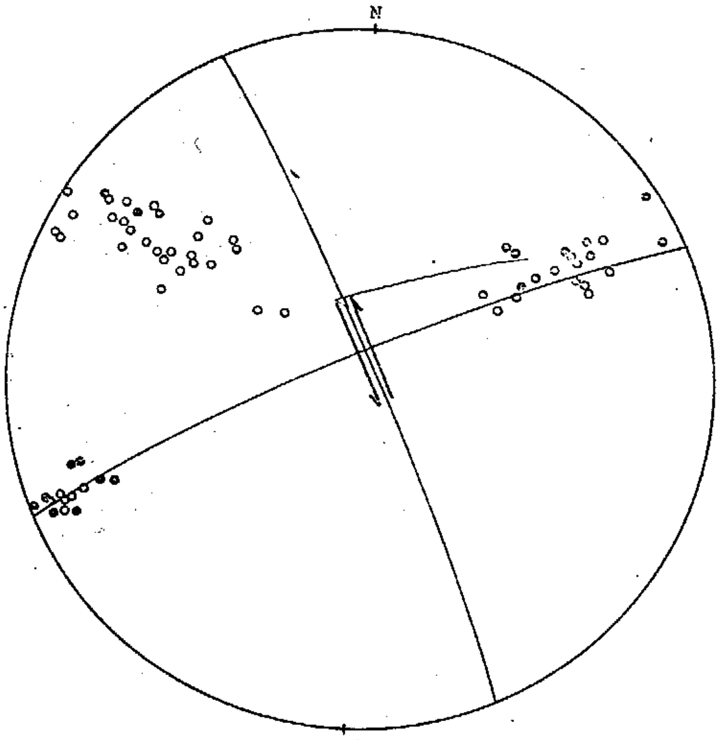

Fig. 5. (continued) group 1b-2

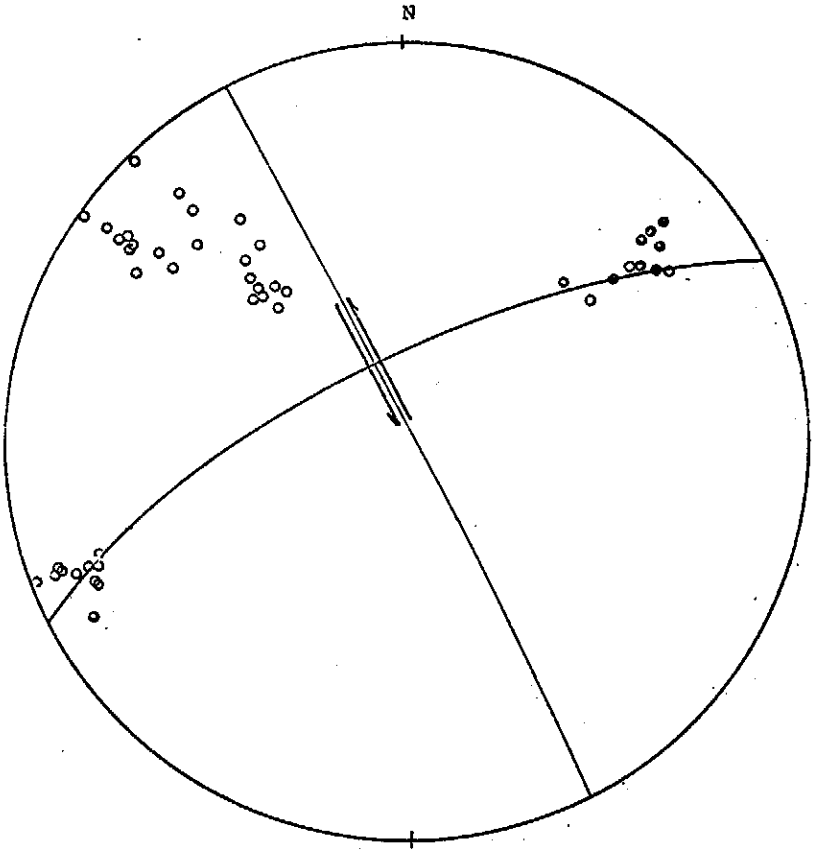

group 1c

Fig. 5. (continued)

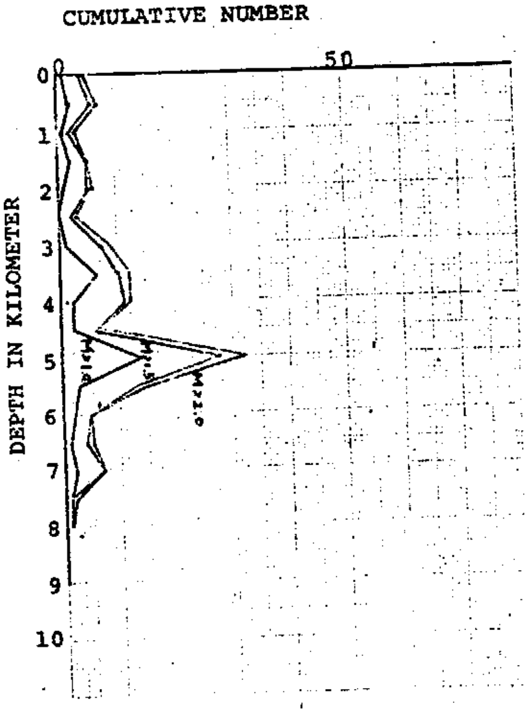

Fig. 6. Depth distribution of Tachien aftershocks.

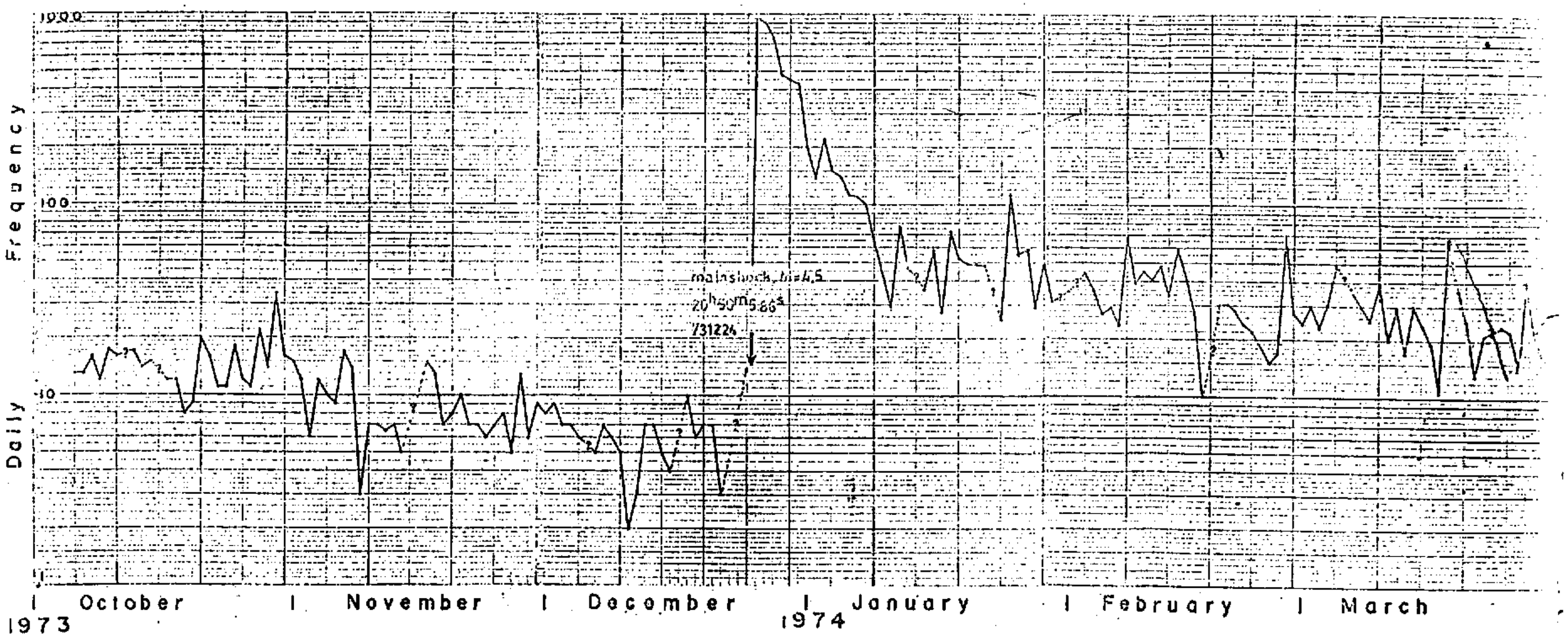

Fig. 7. Variations in the daily seimicity of Tachien microearthquakes.

ESTIMATING MAGNITUDE OF EARTHQUAKES IN TAIWAN AREA FROM TOTAL DURATION OF OSCILIATION

S. K. Yiu and Z. S. Lin*

Seismology Division, Institute of Physics
Academia Sinica
The Republic of China

July, 1974

Abstract

General expressions are derived for the magnitude of earthquakes in terms of epicentral distance and total duration of oscillation. Magnitude scale for local earthquakes is established by the regression analysis of earthquake records in and around Taiwan area. The scale is tested to be rationally accurate.

1. *Introduction*

The basic concept of magnitude was originated by C. F. Richter (1935) as a convenient means of comparing the relative sizes of different earthquakes. The concept has been developed and related to earthquake energy by various authors; and is now well established in several variations as the standard means of comparison of earthquake size (see e.g., Gutenberg and Richter, 1942, 1956A, 1956B; Bath, 1955, 1958, 1966; Gutenberg, 1956; Richter, 1958; Bath and Duda, 1964; Solove'v, 1965; Tsumura, 1967; Howell and Yiu, 1970). For local earthquakes, the version most widely employed is the use of total duration for estimating magnitude, which is defined as

$$M = a_1 + a_2 \log \tau + a_3 \Delta$$

where τ is the total duration of oscillation; Δ is the epicentral distance; and a_1, a_2 and a_3 are arbitrary constants.

The measure of relative sizes of local earthquakes is believed to be affected by the regional structures of geology as well as the characteristics of local earthquakes. Therefore, it is an obvious advantage to establish the local magnitude scale by collecting the

---

* Institute of Oceanography National Taiwan University, Taipei, Republic of China.

earthquake data from the network of seismograph stations in Taiwan area (Fig. 1). However, since the task has to be accomplished by the use of the philosophy of statistics, one is expected to refine the present scale by collection of more earthquake data as the input of our computer program. Up to now, we have established the empirical formula of magnitude scale for Taiwan area as:

$$M = 0.6325 + 1.6673 \log \tau + 0.000582\, \Delta$$

where τ is in seconds, and Δ is in kilometers.

2. *Theoretical Considerations*

Assume that all the energy of an earthquake is radiated as elastic waves and that it spreads equally in all directions from the focus. Suppose that at the seismometer the principal part of the energy arrives as a series of N equal sinusoidal waves of lenth λ, amplitude A_0, and period T_0. Then the kinetic energy (Howell, 1959) can be written as

$$E = \frac{4\pi^3 \Delta^2 N \lambda \rho A_o^{\,2}}{T_o^{\,2}} \tag{1}$$

where Δ is the hypocentral distance, and ρ is the average density of the rocks.

The relation between the kinetic energy E and the magnitude of earthquake M (Gutenberg and Richter, 1942; 1956B) may be assumed as

$$M = \xi + \tfrac{1}{2} \log E \tag{2}$$

where ξ is a constant.

By neglecting bodily force (Bullen, 1962), the equation of motion for an elastic body with mass m, friction coefficient b, and elastic constant k is expressed as

$$m\frac{dx^2}{dt^2} + b\frac{dx}{dt} + kx = 0$$

Letting $\frac{b}{m} = 2\beta$, $\frac{k}{m} = \omega_o^2$, and considering the case of permissible oscillation or $\omega_1^2 = \omega_0^2 - \beta^2 > 0$, then the displacement is given as

$$x(t) = A_o\, e^{-\beta t} \operatorname{Cos}(w_1 t - \delta)$$

The displacement curve and its envelope is shown in Fig. 2. In the case of phase angle $\delta = 0$, the relatively maximum displacement becomes

$$X_{max}(t) = \pm A_o e^{-\beta t} \tag{3}$$

Taking logarithm and combining Eqs. (1),(2), and (3), then applying Taylor expansion for $\log \tau$ and $\log \Delta$ at τ_o and Δ_o, respectively, we have the first order approximation of magnitude M in terms of total duration of oscillation τ and epicentral distance Δ as.

$$M = a_1 + a_2 \log \tau + a_3 \Delta \tag{4}$$

With

$$a_1 = \xi + ½ \log (4\pi^3 N \lambda \rho) - (\log e)(\beta + k_o)(\tau_o \log \tau_o - \tau_o) + \log T_o + \log \Delta_o - 1$$

$$a_2 = (\beta + k_o)(\log e)\, \tau_o$$

and $$a_3 = \frac{1}{\Delta_o} + k_o \log e$$

One can clearly recognize that those arbitrary constants are evidently controlled by structures of regional geology and characteristics of local earthquakes. Therefore, it is expected to have a local magnitude scale of reliability by the use of statistical treatment of local earthquake data. For short epicentral distances, the third term in Eq. (4) is considered to be less important and may be neglected, then Eq. (4) becomes

$$M' = b_1 + b_2 \log \tau \tag{5}$$

where b_1 and b_2 are arbitrary constants.

3. *Curve Fitting*

Let magnitude reported by PDE cards (USGS, 1973) be the standard earthquake magnitudes used in this study and designated them as M_{PDE}

Then the difference, $(M_{PDE}-M)$, is a function of the epicentral distance Δ. There must have a proportional relation expressed by

$$M_{PDE} - M' = b_3 + b_4 \Delta \tag{6}$$

where b_3 and b_4 are arbitrary constants.
From Eqs (5) and (6); we have

$$M_{PDE} = (b_1 + b_3) + b_2 \log \tau + b_4 \Delta \tag{7}$$

Note that Eqs. (4) and (7) are the same if one puts arbitrary constants $a_1 = b_1 + b_3$, $a_2 = b_2$, and $a_3 = b_4$.

In order to determine the constants in Eq. (7) or Eq. (4) suitable to the data obtained from the Taiwan seismographic network (Table 1), the total duration of oscillation τ is plotted against M_{PDE} as shown in Fig. 3. By the use of linear regression method through a computer program, the following results are produced:

$b_1 = 0.728298 \pm 0.129950,$
$b_2 = 1.667354 \pm 0.021476,$
$b_3 = -0.095710 \pm 0.030480,$
and $b_4 = 0.000582 \pm 0.000010.$

Therefore, we obtain

$$M = 0.632588 + 1.667354 \log \tau + 0.000582 \Delta \tag{8}$$

By neglecting the term of epicentral distance, a similar form of fomula is

$$M = 0.728298 + 1.667354 \log \tau \tag{9}$$

where τ is in seconds, and Δ is in kilometers.

4. *Discussions*

Using the data of durations and distances in table 1, magnitudes of different earthquakes are determined by Eqs. (8) and (9). Standard deviations defined as $\sigma = \sqrt{\frac{\sum_{i=1}^{N}(M-\bar{M})^2}{N-1}}$ are calculated then. The standard deviations associates with the results calculated by Eq(8) and Eq(9) are 0.108 and 0.101, respectively. The negligible difference in standard deviation ensures us that Eq. (9) is more conveniently applied in the case of epicentral distances less than 200 km.

Comparing the accuracy of the magnitude formula, currently used by Chinese Earthquake Research Center (CERC), in the form of $M_L = -0.87 + 2.00 \log \tau + 0.0035 \Delta$ (Lee, et al., 1972) with Eq. (8) of this paper, the standard deviations are 0.287 and 0.168, respectively, as shown in table 2. The achievement of precision obtained from the formula of this paper is quite natural, because we have taken the advantage of averaging the locally geological and seismological features through a statistical treatment of local earthquake data.

In estimating the magnitude of local earthquakes, the argument in the logarithmic term is concerned. Since the logarithm is a convex function, it follows that

$$\frac{\log \tau_1 + \log \tau_2}{2} \leqq \log \frac{(\tau_1 + \tau_2)}{2}$$

Thus, the question of whether first to take logarithms of observations and then forming the average, or vice versa, is not trivial.

Eq. (4) is regressionally analyzed by taking logarithms of observations first and then forming the average, the variances of b_1 and b_2 are 0.129950 and 0.021476, respectively. If by taking the logarithm of the average of the observations, the variances of b_1 and b_2 become 0.700884 and 0.115352, respectively. The variance of the latter is greater than that of the former. The former process is therefore the better means of estimation.

5. *Summary*

The conclusions we have drawn from this study are:

1) Using the data of total durations and epicentral distances from CERC observations, an empirical formula of magnitude, which correlates with the magnitude of PDE reported, is given as

$$M = 0.632588 + 1.667354 \log \tau + 0.000582 \Delta$$

For earthquakes of short epicentral distances (less than 200 km), one may neglect the distance term and apply the simple form

$$M = 0.728298 + 1.667354 \log \tau$$

which is more convenient

2) For an earthquake, it is generally happened to have some slight differences in observational values of total duration at different stations. It is found that taking logarithm of the observations first and then forming the average (e.g. $(\log \tau_1 + \log \tau_2)/_2$)is very essential.

3) It has been justified by the statistical tests of standard deviations that the magnitude formula derived in this paper is more realistic than the equation (e.g. $M_L = -0.87 + 2.00 \log \tau + 0.0035 \Delta$) for estimating the magnitude of earthquakes in Taiwan region.

Acknowledgements

We are indebted to the staffs of Chinese Earthquake Research Center (CERC), Institute of Physics, Academia Sinica for supplying the seismograms used in this study. Especially the assistance of Dr. Yi-Ben Tsai, Mr. Y. M. Hsiung, and Mr. C. P. Lu of CERC during this study is gratefully acknowledged.

References

Båth, M. (1955). The relation between magnitude and errergy of earthquakes. Trans. Am. Geoph. Union. 36, 861-865.

Båth, M. (1958). The energy of seismic body waves and surface waves. In contributions in Geophysics in Honor of Beno Gutenberg, pp. 1-16, pergamoss press.

Båth, M. (1966). Earthquake energy and magnitude. Physics and Chemistry of the Earth. 7, 115-165.

Båth, M. and S. J. Dula (1964). Earthquake volume, fault plane area, seismic energy, strain, deformation and related quantities. Ann. Geofis, 17, 353-368.

Bullen, K. E. (1962). An introduction to the theory of seismology. pp. 80-81, Cambridge Univ. press.

Gutenberg, B. (1956). The energy of earthquakes, Quart. J. Geol. Soc. London, 112, 1-14.

Gutenberg, B. and C. F. Richter (1942). Earthquake magnitude, intensity, energy and acceleration. Bull. seism. Soc. Am. 32, 163-191.

Gutenberg, B. and C. F. Richter (1956A). Earthquake magnitude, intensity, energy and acceleration (2nd paper). Bull. Seism. Soc. Am. 46, 105-145.

Gutenberg, B. and C. F. Richter (1956B). Magnitude and energy of earthquakes. Ann. Geofis. 9, 1-15.

Howell, B. F. Jr. (1959). Introduction to geophysics. pp. 126-128. McGraw-Hill.

Howell, B. F. Jr. and S. K. Yiu (1970). Integrated and frequency-band magnitude, two alternative measures of the size of an earthquake. Bull. Seism. Soc. Am. 60, 917-937.

Lee, W. H. K., R. E. Bennett and K. L. Meagher (1972). A method of estimating magnitude of local earthquakes from signal duration. U. S. Geological Survey, Open file report.

Richter C. F. (1935). An instrumental earthquake magnitude scale. Bull. Seism. Soc. Am. 25, 1-32.

Richter, C. F. (1958). Elementary Seismdogy. W. H. Freeman, 768 pp.

Solove'v, S. L. (1965). Seismisity of Sakhalin, Bull. Earthq. Res. Ins. 45, 95-102.

Tsumura, K. (1967). Determination of earthquake from total duration of oscillation, Bull. Earthq. Res. Ins. 45, 7-18.

Table 1. Local earthquakes recorded by the network of seismographic stations of CERC (Magnitudes ranged from 3.9 to 5.8)

DATE	HRMN	SEC	LAT.N	LONG.E	DEPTH	MAG	SIN	DIST	HRMN	P-SEC	EMP(SEC)
730129	2133	39.6	23.9	123.4	53	4.9	TWD	0.2	2124	4.40	240
							TWQ	80.2	2124	14.00	250
							TWA	99.4	2124	11.20	265
							TWO	120.6	2124	20.90	---
							TWG	149.8	2124	16.40	278
730206	0530	02.0	27.9	127.7	---	5.7	TWA	139.8	0531	37.90	247
							TWS	162.4	0531	39.10	---
							TWQ	203.4	0531	48.50	190
							TWO	251.3	0531	56.30	251
							TWG	254.0	0531	53.20	254
730210	0332	26.76	24-17.16	121-38.36	1.23	4.8	TWD	23.1	0332	31.70	388
							TWQ	81.6	0332	41.90	320
							TWS	96.0	0332	40.90	400
							TWG	172.3	0332	49.20	400
							TWM	210.7	0332	60.65	---
730325	0627	16.87	24-21.93	121-51.03	10.00	4.0	TWC	27.0	0627	25.40	155
							TWD	40.8	0627	29.30	115
							TWA	73.3	0627	29.80	157
							TWR	79.8	0627	32.80	180
							TWQ	103.5	0627	39.50	150
							TWO	158.6	0627	46.20	141
730326	0237	47.64	24-13.14	121-59.86	28.61	5.5	TWR	101.8	0238	4.00	410
							TWQ	118.2	0238	7.20	413
							TWO	163.8	0238	9.00	390
							TWA	94.2	0238	3.00	410
730326	2253	27.62	24-19.55	122-7.90	6.14	4.8	TWD	60.8	2253	38.30	---
							TWA	91.3	2253	43.10	350
							TWS	114.8	2253	47.20	237
							TWQ	131.7	2253	49.60	194

							TWC	198.7	2253	58.50	340
							TWC	42.5	2253	35.40	260
730328	2356	5.20	23-48.03	122-08.7	37.35	5.3	TWD	64.2	2356	18.00	500
							TWQ	143.3	2356	31.7	450
							TWR	146.9	2356	29.00	450
							TWG	154.5	2356	25.00	452
							TWS	164.7	2356	30.00	308
							TWA	142.6	2356	27.00	300
730329	1522	26.69	23-53.89	121-35.82	18.48	4.4	TWD	20.4	1522	34.20	180
							YWQ	88.0	1522	47.20	---
							TWA	119.9	1522	43.00	194
							TWG	130.8	1522	40.20	200
							TWS	137.6	1522	47.00	200
							TWM	195.7	1522	55.00	220
730423	1329	13.03	23-55.65	121-40.46	0.55	5.2	TWD	18.8	1329	16.10	---
							TWC	77.5	1329	26.20	400
							TWQ	93.5	1329	28.30	450
							TWR	111.0	1329	32.20	350
							TWS	135.6	1329	36.00	550
							TWM	203.6	1329	46.00	350
730605	1329	48.11	23-31.33	121-04.39	20.00	4.6	TWO	53.8	1329	0.00	299
							TWG	77.7	1329	57.00	250
							TWM	128.8	1329	10.00	225
							TWA	169.6	1329	14.00	338
							TWS	181.2	1320	16.00	250
730608	0610	0.98	22-36.73	121-01.07	20.00	4.4	TWM	78.9	0610	14.00	286
							TWA	268.5	0610	39.00	320
							TWS	281.6	0610	40.00	250
730609	1415	47.92	21-57.71	121-16.14	20.00	4.7	TWM	129.1	1416	7.00	150
							TWO	193.4	1416	18.00	190
							TWQ	259.9	1416	26.00	210
							TWA	335.8	1416	35.00	160
							TWS	351.0	1416	35.00	169

730622	0329	47.41	22-49.34	122-05.21	20.00	4.7	TWG	104.2	0329	4.00	200
							TWD	148.2	0329	8.50	300
							TWN	165.6	0329	14.00	280
							TWO	178.1	0329	16.00	224
							TWQ	205.4	0329	11.00	220
							TWA	244.4	0329	24.00	330
							TWS	264.4	0329	24.00	240
730625	0720	27.59	24-23.34	121-35.12	49.08	5.7	TWA	65.5	0720	10.00	522
							TWQ	77.1	0720	34.00	650
							TWS	83.7	0720	11.90	---
							TWO	138.6	0720	50.00	609
							TWG	181.4	0720	39.90	480
							TWM	236.7	0720	40.00	440
730628	1049	47.87	22-39.60	120-15.19	20.00	5.2	TWO	107.7	1050	16.00	350
							TWQ	190.2	1050	13.50	440
							TWR	267.3	1050	15.00	438
							TWS	299.6	1050	10.00	661
730630	1743	32.09	23-06.89	121-05.85	29.07	5.2	TWN	59.6	1743	42.90	500
							TWQ	131.2	1743	53.00	540
							TWA	212.5	1743	61.00	560
							TWS	225.3	1743	63.20	520
730721	1147	8.12	22-44.35	120-27.24	10.00	5.0	TWM	23.4	1147	13.10	190
							TWO	93.2	1147	24.00	220
							TWQ	174.5	1147	35.2	240
							TWD	189.0	1147	33.20	---
							TWA	273.6	1147	48.20	260
730721	1309	48.97	23-10.46	120-42.77	5.08	3.9	TWM	75.6	1310	2.00	110
							TWQ	122.5	1310	8.30	160
							TWD	134.9	1310	7.10	---
							TWC	196.6	1310	15.10	100
							TWA	218.7	1310	26.00	120
							TWS	227.9	1310	37.50	100

730723	1434	13.22	22-38.60	120-58.14	10.00	5.0	TWO	111.9	1434	33.20	450
							TWD	171.7	1434	39.00	500
							TWQ	181.2	1434	42.50	350
							TWA	266.3	1434	47.40	426
730728	1753	42.32	23-02.01	121-16.38	5.23	5.4	TWN	79.0	1753	55.50	664
							TWO	95.3	1753	59.20	600
							TWD	120.6	1753	01.20	685
							TWS	232.5	1753	18.00	694
730729	9433	27.47	23-59.40	123-58.74	10.00	4.4	TWD	242.7	0433	2.00	179
							TWA	266.4	0433	6.00	200
							TWS	288.7	0433	9.00	170
							TWQ	321.1	0433	13.50	165
							TWO	352.8	0433	17.20	170
							TWn	364.1	0433	18.50	282
730806	0227	33.82	22-35.97	120-44.14	12.83	3.2	TWG	42.3	0227	42.0	247
							TWM	50.0	0227	43.20	270
							TWQ	185.8	0228	02.00	297
							TWD	186.2	0228	02.00	298
							TWC	249.9	0228	09.90	289
730817	0142	22.69	23-47.86	122-48.60	20.00	5.4	TWD	128.2	0142	42.20	450
							TWC	134.1	0142	43.40	445
							TWA	182.1	0142	50.30	487
							TWS	205.7	0142	53.10	400
							TWO	231.8	0142	57.00	480
							TWM	290.8	0143	02.00	415
730825	2150	43.51	23-12.55	119-21.19	20.00	5.1	TWO	128.9	2152	03.40	300
							TWG	181.4	2151	51.00	350
							TWR	268.4	2151	22.00	200
							TWS	298.4	2151	25.10	350
							TWA	299.9	2151	24.20	400

731029	2125	21.99	24–08.08	121–49.02	20.00	4.3	TWD	24.3	2125	27.10	332
							TWC	52.7	2125	31.00	328
							TWQ	101.9	2125	38.80	322
							TWS	117.7	2125	41.50	245
							TWO	144.1	2125	46.50	313
							TWG	164.7	2125	46.70	312

Table 2. Comparison of the accuracy between two magnitude formulas

DATE	HR MN	SEC	LAT.N	LONG.E	DEPTH	STN	DIS	DURATION	M^*_{CERC}	M_{CERC}	CERC	M^{**}	$\overline{M}$	
0603	1507	21.8	24°31.3'	122°55.5'	20	TWA	141.2	193	4.2			4.52		
						TWS	162.5	131	3.9			4.25		
						TWR	168.4	94	3.7			4.01		
						TWQ	215.3	185	4.4	4.23	0.316	4.53	4.33	0.185
						TWØ	267.8	176	4.6			4.53		
						TWG	274.8	117	4.2			4.23		
						TWN	291.9	115	4.3			4.23		
						TWM	350.1	133	4.6			4.37		
0605	1329	48.11	23-31.33	121-04.39	20.00	TWG	71.5	250	4.2			4.66		
						TWØ	107.6	299	4.5			4.82		
						TWQ	131.6	348	4.7			4.94		
						TWM	151.5	255	4.4	4.50	0.195	4.63	4.75	0.139
						TWR	176.7	200	4.4			4.56		
						TWA	187.5	338	4.8			4.95		
						TWS	204.4	250	4.6			4.66		
0607	0622	2.6	22°41.4'	121°4.6'	15.6	TWM	85.0	470	4.8			5.13		
						TWØ	112.1	460	4.8			5.14		
						TWQ	177.3	500	5.1	5.17	0.470	5.23	5.22	0.012
						TWA	258.9	598	5.6			5.41		
						TWS	272.3	500	5.5			5.22		
0615	1008	20.5	23°59.3'	121°35.2'	14.2	TWQ	83.2	205	4.0			4.53		
						TWR	102.7	130	3.7			4.20		
						TWA	110.8	200	4.1	3.92	0.159	4.53	4.36	0.156
						TWØ	115.0	140	3.8			4.26		
						TWS	128.4	140	3.9			4.27		
0615	1432	0.8	23°51.7'	121°46.5'	22.9	TWD	30.5	150	3.6			4.27		

$^*M_{CERC}$ denotes magnitude determined by the formula of CERC

$^{**}M$ denotes magnitude determined by the formula of this paper

						TWQ	105.9	204	4.1			4.54		
						TWR	121.8	148	3.9			4.31		
						TWA	125.5	157	4.0	3.90	0.216	4.36	4.317	0.146
						TW0	128.9	158	4.0			4.37		
						TWS	145.1	100	3.6			4.04		
						TWM	206.2	135	4.1			4.30		
0622	6329	47.41	22-49.34	122-05.21	20.00	TWG	98.8	200	4.1			4.52		
						TWD	139.3	300	4.6			4.84		
						TWN	158.4	280	4.6			4.80		
						TW0	169.7	224	4.4	4.50	0.287	4.64	4.67	0.182
						TWM	184.8	168	4.2			4.44		
						TWQ	196.0	220	4.5			4.64		
						TWR	231.5	160	4.3			4.43		
						TWA	236.0	330	5.0			4.96		
						TWS	255.7	240	4.8			4.74		
0629	2158	49.5	23°26.6'	123°18.8'	20.07	TWS	285.7	151	4.5			4.42		
						TWQ	287.8	150	4.5	4.62	0.394	4.43	4.51	0.252
						TW0	301.0	120	4.3			4.27		
						TWN	304.6	300	5.2			4.93		
0630	1743	32.09	23-06.89	121-05.85	29.07	TWN	59.6	500	4.7			5.16		
						TWM	101.4	300	4.4			4.81		
						TWQ	131.2	540	5.1	4.95	0.403	5.26	5.12	0.222
						TWR	194.5	300	4.8			4.87		
						TWA	212.5	560	5.4			5.33		
						TWS	225.3	520	5.4			5.28		
			TOTAL								0.287			0.168

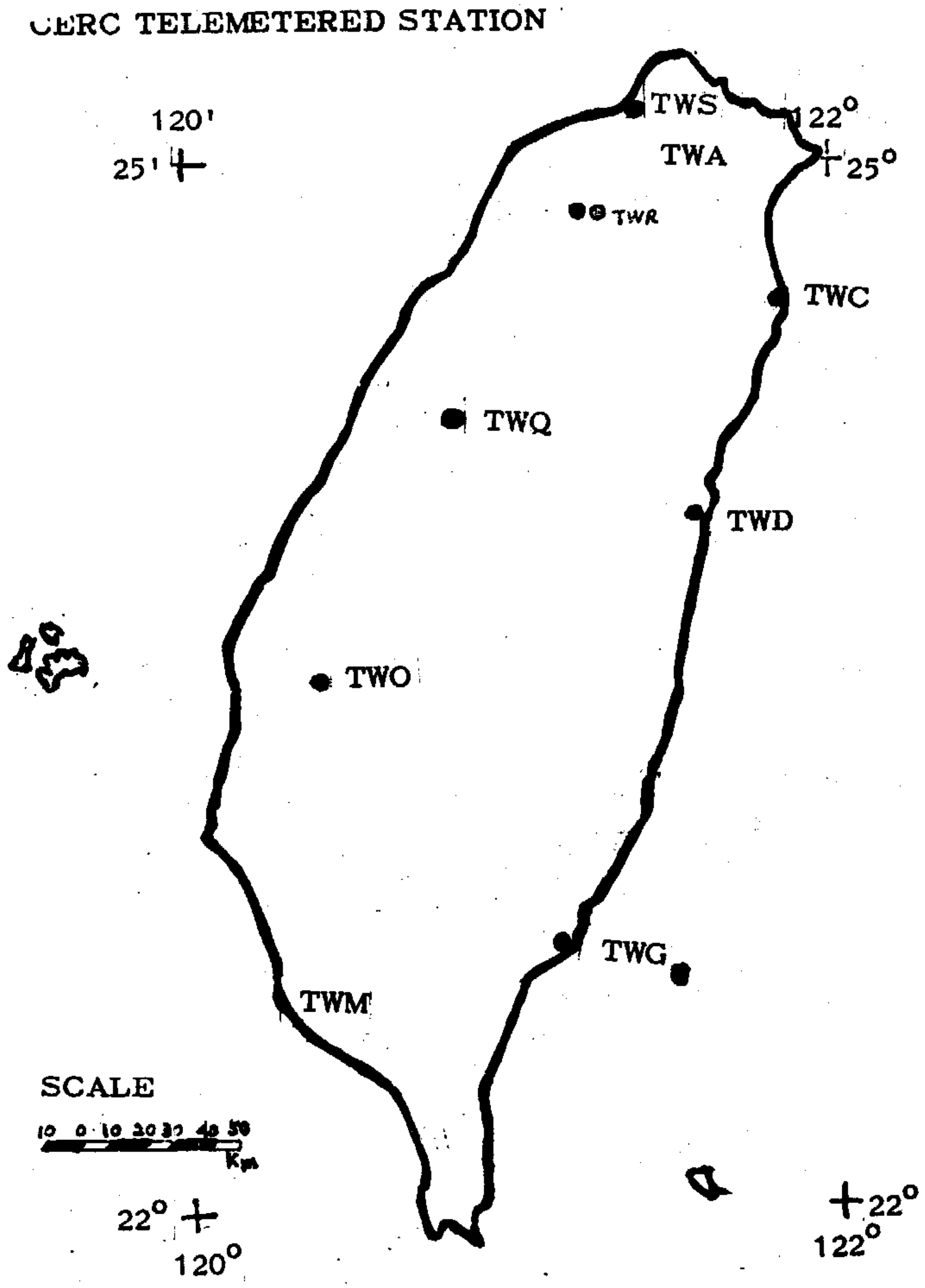

FIG. 1 TELEMETERED STATIONS IN TA IWAN

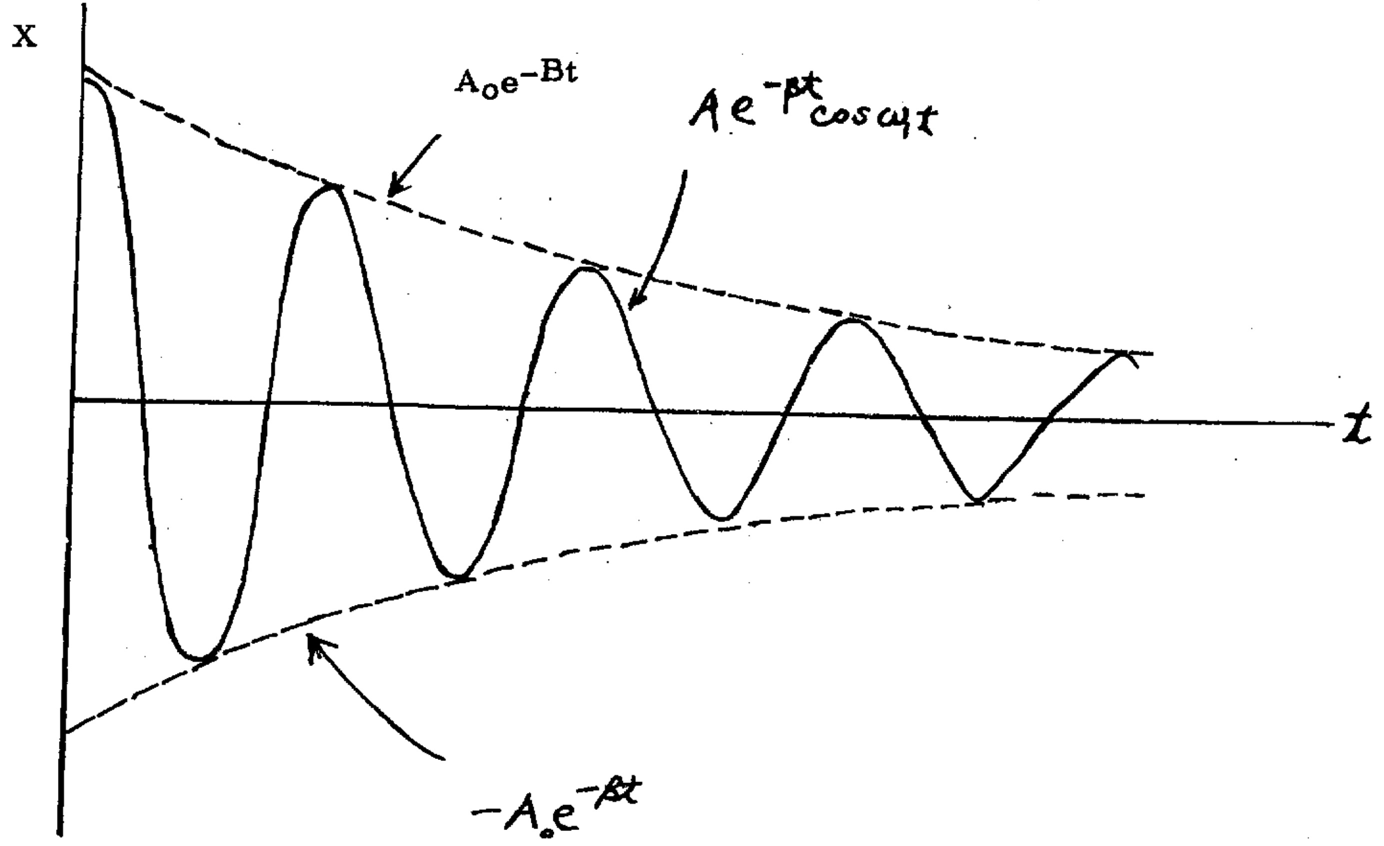

FIG. 2 THE ENVELOPE OF THE DISPLACEMENT VERSUS TIME CURVE

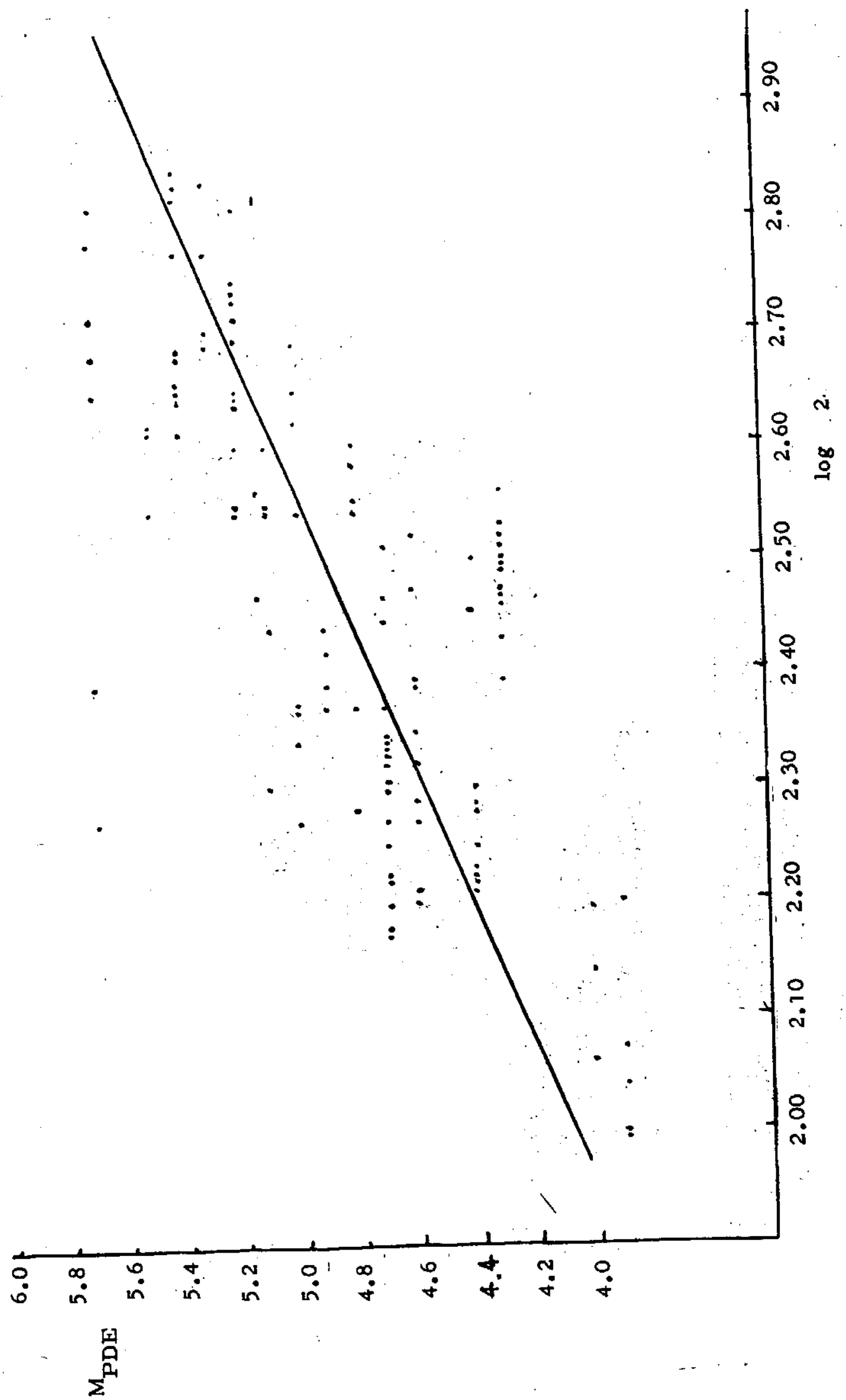

FIG. 3 CORRELATION BETWEEN MAGNITUDE (FROM PDE AND THE LOGARITHM OF TOTAL DURATION